

**CIVIL ENGINEERING STUDIES**  
Structural Research Series No. 584



ISSN: 0069-4274

# **FINITE ELEMENT ANALYSIS OF REINFORCED CONCRETE SHEAR WALLS**

By

**Chadchart Sittipunt  
and  
Sharon L. Wood**

A Report to the  
**National Science Foundation**  
Research Grant BCS 89-12992

**Department of Civil Engineering  
University of Illinois at Urbana-Champaign  
Urbana, Illinois**

**December 1993**



<b>REPORT DOCUMENTATION PAGE</b>	1. REPORT NO. UILU-ENG-93-2015	2.	3. Recipient's Accession No.
4. Title and Subtitle Finite Element Analysis of Reinforced Concrete Shear Walls		5. Report Date December 1993	6.
7. Author(s) Chadchart Sittipunt and Sharon L. Wood		8. Performing Organization Report No. SRS 584	
9. Performing Organization Name and Address University of Illinois at Urbana-Champaign Department of Civil Engineering 205 North Mathews Avenue Urbana, Illinois 61801		10. Project/Task/Work Unit No.	11. Contract(C) or Grant(G) No. BCS 89-12992
12. Sponsoring Organization Name and Address National Science Foundation 4201 Wilson Boulevard, Room 545 Arlington, VA 22230		13. Type of Report & Period Covered	
15. Supplementary Notes		14.	
16. Abstract (Limit: 200 words)  The primary objective of this study was to use the finite element method to study the cyclic response of slender, reinforced concrete shear walls. Material models which represent the cyclic response of concrete and reinforcing steel in shear walls were developed in this investigation. These material models were verified both at the element and structural levels; the results of the finite element analyses were compared with the experimental data from several experimental programs. After the material models had been satisfactorily tested, the finite element method was used to extend the scope of the investigation of the response of slender reinforced concrete shear walls with different configurations, reinforcement details, and loading histories.			
17. Document Analysis a. Descriptors  Concrete, Cyclic Loading, Energy Dissipation, Failure Modes, Finite Element Analysis, Nonlinear Response, Reinforced Concrete, Reinforcing Steel, Shear Walls  b. Identifiers/Open-Ended Terms  c. COSATI Field/Group			
18. Availability Statement		19. Security Class (This Report) UNCLASSIFIED	21. No. of Pages 384
		20. Security Class (This Page) UNCLASSIFIED	22. Price





## ACKNOWLEDGEMENT

Financial support for this study was provided by the National Science Foundation under Grant No. BCS 89-12992 at the University of Illinois.

The writers would like to express their sincere gratitude to the following persons for their valuable contribution to this project:

Professor R.H. Dodds for his help and advice during the implementation of the material models in FINITE.

Professors W.L. Gamble, N.M. Hawkins, D.A.W. Pecknold, W.C. Schnobrich, and M.A. Sozen for their valuable criticism and advice.

W.R. Lackner and C.J. Wolschlag for their help during the experimental phase of this project.

H. Dalrymple, M.J. Lawson, and D.C. Hines, Jr. for assistance with instrumentation and data acquisition during the experimental phase of the project.

C. Swan and the machine shop staff for fabrication the test specimens and the testing hardware.

Acknowledgements are also due to the Civil Engineering Apollo Network (CEAN) for the use of the Apollo DN-10000 workstation in the initial stage of this study and the Civil Engineering Research Network (CERN) for the use of the HP9000/720 workstations in the final stage of this study. This study could not have been completed without these computer facilities.

This report was prepared as a doctoral dissertation by C. Sittipunt, directed by S.L. Wood.



# TABLE OF CONTENTS

<b>1. INTRODUCTION</b> .....	<b>1</b>
1.1 OVERVIEW .....	1
1.2 OBJECTIVE AND SCOPE .....	3
<b>2. FINITE ELEMENT ANALYSIS OF REINFORCED CONCRETE MEMBERS</b> .....	<b>5</b>
2.1 LITERATURE REVIEW .....	5
2.1.1 OVERVIEW .....	5
2.1.2 PREVIOUS WORK ON R/C SHEAR WALLS .....	6
2.1.3 PREVIOUS WORK ON CYCLIC RESPONSE OF R/C MEMBERS .....	7
2.1.4 APPLICATIONS OF THE FINITE ELEMENT METHOD .....	9
2.2 CRACK MODELLING .....	10
2.2.1 CRACK REPRESENTATION .....	10
2.2.2 CRACK INITIATION AND CRACK PROPAGATION .....	12
2.2.3 CONSTITUTIVE MODELLING OF CRACKED CONCRETE .....	14
2.2.3.1 FIXED CRACK MODEL .....	15
2.2.3.2 ROTATING CRACK MODEL .....	16
2.2.3.3 NON-ORTHOGONAL MULTI-CRACK MODEL .....	17
2.3 MODELLING OF STEEL REINFORCEMENT .....	19
2.3.1 STEEL REINFORCEMENT REPRESENTATION .....	19
2.3.2 STRESS-STRAIN RELATIONSHIP OF REINFORCING STEEL .....	20
2.4 PROPOSED MATERIAL MODELS .....	21
2.4.1 PROPOSED CONCRETE MODEL .....	21
2.4.2 PROPOSED STEEL MODEL .....	23
<b>3. MATERIAL MODEL FOR CONCRETE</b> .....	<b>24</b>
3.1 NORMAL STRESS FUNCTION .....	25
3.1.1 TENSION STIFFENING .....	26
3.1.2 CRACK CLOSING AND REOPENING .....	28
3.1.3 COMPRESSION SOFTENING .....	32
3.1.4 CONFINED CONCRETE .....	34
3.1.5 DEGRADATION OF CONCRETE PROPERTIES UNDER CYCLIC LOADINGS ...	35

3.2	SHEAR STRESS FUNCTION .....	39
3.2.1	SHEAR STIFFNESS DUE TO INTERFACE SHEAR TRANSFER .....	41
3.2.2	SHEAR STIFFNESS DUE TO DOWEL ACTION .....	43
3.2.3	EFFECT OF CYCLIC LOADING .....	46
3.3	SUMMARY .....	47
<b>4.</b>	<b>MATERIAL MODEL FOR REINFORCING STEEL .....</b>	<b>49</b>
4.1	CYCLIC STRESS-STRAIN RELATIONSHIP .....	49
4.2	PROPOSED STEEL MODEL .....	51
4.2.1	MONOTONIC CURVE .....	51
4.2.2	ENVELOPE CURVES .....	52
4.2.3	LOAD REVERSALS FROM YIELD PLATEAU .....	58
4.3	EVALUATION OF THE STEEL MODEL .....	59
4.4	SUMMARY .....	60
<b>5.</b>	<b>FINITE ELEMENT PROCEDURES .....</b>	<b>61</b>
5.1	FINITE ELEMENT FORMULATION .....	61
5.2	FINITE .....	65
5.3	ALGORITHMS USED IN THE MATERIAL MODELS .....	66
5.3.1	INCORRECT STRESS PATH .....	67
5.3.2	FALSE LOAD REVERSALS .....	69
5.3.3	PROBLEMS WITH NEWTON-RAPHSON METHOD .....	71
5.4	FINITE ELEMENT MODEL .....	72
5.4.1	TYPES OF ELEMENT .....	72
5.4.2	SIZE OF FINITE ELEMENT MESH .....	74
5.4.3	LOADING ALGORITHMS .....	75
5.5	INCREMENTAL-ITERATIVE ALGORITHMS .....	78
5.5.1	NEWTON-RAPHSON ALGORITHMS .....	78
5.5.2	CONVERGENCE CRITERIA .....	80
<b>6.</b>	<b>PCA WALL TESTS .....</b>	<b>82</b>
6.1	PCA EXPERIMENTAL PROGRAM .....	83
6.2	FINITE ELEMENT MODEL .....	85
6.3	PARAMETRIC STUDY .....	86

6.3.1	PARAMETERS USED TO DEFINE NORMAL STRESSES .....	87
6.3.2	PARAMETERS USED TO DEFINES SHEAR STRESSES .....	89
6.4	EVALUATION OF THE FINITE ELEMENT RESULTS .....	91
6.4.1	LOAD VS. TOP DEFLECTION CURVE .....	92
6.4.2	LOAD VS. SHEAR DISTORTION CURVE .....	93
6.4.3	FAILURE MODES .....	94
	(a) BAR FRACTURE .....	95
	(b) INELASTIC BAR BUCKLING .....	95
	(c) INSTABILITY OF THE COMPRESSION ZONE .....	97
	(d) BOUNDARY ELEMENT CRUSHING .....	97
	(e) WEB CRUSHING .....	98
6.4.4	CRACK PATTERNS .....	100
6.5	TYPICAL CYCLIC BEHAVIOR OF R/C SHEAR WALLS .....	101
<b>7.</b>	<b>TESTS OF C-SHAPED WALLS .....</b>	<b>106</b>
7.1	EXPERIMENTAL PROGRAM .....	106
7.1.1	C-SHAPED WALL SPECIMENS .....	107
7.1.2	TESTING PROCEDURES .....	108
7.1.3	INSTRUMENTATION .....	109
7.2	OBSERVED RESPONSE OF THE WALLS .....	110
7.3	FINITE ELEMENT MODEL .....	111
7.3.1	CHOICE OF ELEMENT .....	111
7.3.2	WALL MODEL .....	112
7.4	EVALUATION OF THE FINITE ELEMENT RESULTS .....	114
<b>8.</b>	<b>APPLICATIONS OF THE FINITE ELEMENT METHOD .....</b>	<b>117</b>
8.1	ENERGY DISSIPATION CAPACITY OF R/C WALLS .....	117
8.1.1	ENERGY DISSIPATION MECHANISMS .....	118
8.1.2	REINFORCEMENT DETAILS .....	119
8.1.3	ANALYTICAL RESULTS .....	121
8.2	SHEAR WALLS WITH OPENINGS .....	124
8.2.1	PCA TESTS OF WALLS WITH AND WITHOUT OPENINGS .....	125
	8.2.1.1 EXPERIMENTAL RESULTS .....	126
	8.2.1.2 ANALYTICAL RESULTS .....	127
8.2.2	TESTS OF WALLS WITH STAGGERED OPENINGS .....	130
	8.2.2.1 EXPERIMENTAL RESULTS .....	131

8.2.2.2	ANALYTICAL RESULTS .....	131
8.3	EFFECTIVE WIDTH OF FLANGES IN C-SHAPED WALLS .....	134
8.3.1	ANALYTICAL PROGRAM .....	135
8.3.2	CALCULATED RESPONSE .....	136
8.4	SUMMARY .....	139
<b>9.</b>	<b>SUMMARY AND CONCLUSIONS .....</b>	<b>141</b>
9.1	OVERVIEW .....	141
9.2	CONCLUSIONS .....	146
9.3	RECOMMENDATIONS FOR FUTURE RESEARCH .....	148
9.3.1	EXPERIMENTAL PROGRAMS .....	148
9.3.2	ANALYTICAL MODELS .....	149
<b>TABLES</b>	.....	<b>151</b>
<b>FIGURES</b>	.....	<b>163</b>
<b>APPENDIX</b>		
A.	COMPRESSION STIFFENING AND COMPRESSION SOFTENING CURVES FOR THE CON- CRETE MODEL .....	348
A.1	COMPRESSION STIFFENING CURVE .....	348
A.2	COMPRESSION SOFTENING CURVE .....	349
B.	STRESS-STRAIN RELATIONSHIP FOR CONFINED CONCRETE .....	351
C.	RULES FOR CYCLIC STRESS-STRAIN RELATIONSHIP OF CONCRETE .....	353
D.	FINITE ELEMENT MESHES FOR WALLS .....	357
E.	MATERIAL PROPERTIES FOR PCA WALL TESTS .....	363
F.	MATERIAL PROPERTIES FOR C-SHAPED WALLS .....	365
G.	MATERIAL PROPERTIES FOR WALL C11 AND PW1 .....	366
H.	MATERIAL PROPERTIES OF WALLS W1, W2, W3, AND W4 .....	367
<b>LIST OF REFERENCES</b>	.....	<b>368</b>
<b>VITA</b>	.....	<b>385</b>

## LIST OF TABLES

Table 4.1	Parameters used to define the Reinforcing Steel Model (for Grade 60 Steel) .....	152
Table 5.1	Classifications of Nonlinear Analyses (from [13]) .....	153
Table 5.2	CPU Time Required in the Analyses of Wall R1 with Different Schemes for Updating Stiffness Matrix .....	153
Table 6.1	Properties of PCA Wall Specimens (from Oesterle [103]) .....	154
Table 6.2	Parameters used to define the Concrete Model for PCA Wall Specimen .....	155
Table 6.3	Observed Failure Modes in PCA Wall Specimens .....	156
Table 7.1	Comparisons between 2-D Plane Stress Elements and Shell Elements .....	159
Table 7.2	Failure Modes in Walls CLS and CMS .....	160
Table 8.1	Amount of Reinforcement in each Reinforcement Option .....	161
Table 8.2	Shear Forces and Nominal Shear Strengths in the East Piers of Wall W2, W3, and W4 .....	161
Table 8.3	Parametric Study of C-Shaped Walls .....	162
Table C.1	Loading and Unloading Rules for Unconfined Concrete .....	355
Table E.1	Measured Concrete Properties (from (104, 105)) .....	363
Table E.2	Measured Reinforcing Steel Properties (from (104, 105)) .....	364
Table F.1	Measured Concrete Properties .....	365
Table F.2	Measured Steel Properties .....	365
Table G.1	Measured Concrete Properties (from (125)) .....	366
Table G.2	Measured Steel Properties (from (125)) .....	366
Table H.1	Material Properties for Concrete (from (6)) .....	367
Table H.2	Material Properties for Reinforcing Steel (from (6)) .....	367





## LIST OF FIGURES

Fig. 2.1	Discrete Crack Models (from [136]) .....	164
Fig. 2.2	Smeared Crack Model .....	164
Fig. 2.3	Separation of Shear Strain .....	165
Fig. 3.1	Typical Normal Stress Function .....	166
Fig. 3.2	Tension Stiffening .....	166
Fig. 3.3	Scatter in Data Representing Tension Stiffening (from Vecchio and Collins [143]) .....	167
Fig. 3.4	Tension Stiffening Model .....	167
Fig. 3.5	Load vs. Deflection Curve of Wall B4 (from Oesterle [105]) .....	168
Fig. 3.6	Response of Concrete Subjected to Cyclic Tension .....	168
Fig. 3.7	Rules for Crack Closing ( $\Delta\varepsilon < 0$ ) .....	169
Fig. 3.8	Rules for Crack Opening ( $\Delta\varepsilon > 0$ ) .....	170
Fig. 3.9	Focal Points for Crack Closing and Opening .....	171
Fig. 3.10	Compression Softening Model .....	171
Fig. 3.11	Evaluation of Compression Softening Function (from Oesterle [105]) ..	172
Fig. 3.12	The Proposed Model for Confined Concrete (from Shiekh and Uzumeri [125]) .....	172
Fig. 3.13	Proposed Compressive Cyclic Stress–Strain Relationship .....	173
Fig. 3.14	Rules for Unloading and Reloading: Unconfined Concrete .....	173
Fig. 3.15	Comparison of Calculated and Experimental Data for Response of Concrete subjected to Cyclic Compression Loads (Sinha et al. [128]) .....	174
Fig. 3.16	Comparison of Calculated and Experimental Data for Response of Concrete subjected to Cyclic Compression Loads (Karsan and Jirsa [79]) .....	175
Fig. 3.17	Comparison of Calculated and Experimental Data for Response of Concrete subjected to Cyclic Compression Loads (Karsan and Jirsa [79]) .....	176
Fig. 3.18	Rules for Unloading and Reloading: Confined Concrete .....	177
Fig. 3.19	Calculated Cyclic Response for Unconfined and Confined Concrete ...	178
Fig. 3.20	Interface Shear Transfer .....	179

Fig. 3.21	Relationship between Shear Interface Transfer Stiffness and Normal Strain across Cracks .....	179
Fig. 3.22	The Mechanisms of Dowel Action (from Paulay et al.(115)) .....	180
Fig. 3.23	The Interaction between Cracked Concrete and a Reinforcing Bar .....	180
Fig. 3.24	Typical Characteristics of Dowel Action .....	181
Fig. 3.25	Relationship between Dowel Action Stiffness and Shear Strain .....	181
Fig. 3.26	Typical Cyclic Shear Response .....	182
Fig. 3.27	Cyclic Shear Model .....	185
Fig. 3.28	The Proposed Cyclic Shear Model .....	186
Fig. 3.29	Monotonic Loading Curve of Reinforcing Steel .....	187
Fig. 4.1	Typical Cyclic Stress–Strain Relationship for Reinforcing Steel (from Aktan [5]) .....	187
Fig. 4.2	Monotonic Loading Curve for Reinforcing Steel .....	187
Fig. 4.3	Enveloped Curves .....	188
Fig. 4.4	Equation for $s_o$ (From Aktan et al. [5]) .....	188
Fig. 4.5	Analytical Stress–Strain Relationship of Reinforcing Bars in R/C Shear Walls .....	189
Fig. 4.6	Common Points and Ultimate Points .....	190
Fig. 4.7	Typical Experimental Results of Load Reversals from the Yield Plateau .....	191
Fig. 4.8	Unloading from Yield Plateau (From Popov [118]) .....	192
Fig. 4.9	Evaluation of the Proposed Steel Model .....	193
Fig. 5.1	Solution Algorithm for each Load Step (from[49]) .....	201
Fig. 5.2	Solution Path of Incremental–iterative Algorithm (from [23]) .....	202
Fig. 5.3	Numerical Problem with Newton–Raphson Iteration Algorithm .....	202
Fig. 5.4	Relationship between Fracture Energy and Mesh Size .....	203
Fig. 5.5	Finite Element Mesh for Wall R1 .....	204
Fig. 5.6	Calculated Crack Patterns for Wall R1 .....	204
Fig. 5.7	Calculated Load–Deflection Curves for Wall R1 .....	205
Fig. 5.8	Newton–Raphson Iterative Algorithms .....	206
Fig. 5.9	Convergence Rate of Different Schemes for Updating Stiffness Matrix .....	207
Fig. 6.1	Nominal Dimensions of the PCA Wall Specimens (from [106]) .....	208
Fig. 6.2	Typical Loading Histories (from [103]) .....	209

Fig. 6.3	Finite Element Model for a PCA Wall Specimen .....	210
Fig. 6.4	Sensitivity of the Calculated Response of Wall B4 to the Choice of $\alpha$ ...	211
Fig. 6.5	Sensitivity of the Calculated Response of Wall R1 to the Choice of $\sigma_i$ in Boundary Elements .....	212
Fig. 6.6	Sensitivity of the Calculated Response of Wall B7 to the Choice of $\sigma_i$ in Boundary Elements .....	213
Fig. 6.7	Sensitivity of the Calculated Response of Wall R1 to the Choice of $\sigma_i$ in Web .....	214
Fig. 6.8	Sensitivity of the Calculated Response of Wall B7 to the Choice of $\sigma_i$ in Web .....	215
Fig. 6.9	Sensitivity of the Calculated Response of Wall R1 to the Choice of $\epsilon_i$ ..	216
Fig. 6.10	Sensitivity of the Calculated Response of Wall B7 to the Choice of $\epsilon_i$ ...	217
Fig. 6.11	Sensitivity of the Calculated Response of Wall R1 to the Choice of $\sigma_1$ ..	218
Fig. 6.12	Sensitivity of the Calculated Response of Wall B7 to the Choice of $\sigma_1$ ..	219
Fig. 6.13	Sensitivity of the Calculated Response of Wall B7 to the Choice of $\sigma_2$ ..	220
Fig. 6.14	Sensitivity of the Calculated Response of Wall B7 to the Choice of $\sigma_3$ ..	221
Fig. 6.15	Sensitivity of the Calculated Response of Wall B7 to the Choice of $\sigma_3$ and $\sigma_n$ .....	222
Fig. 6.16	Sensitivity of the Calculated Response of Wall B7 to the Choice of $\mu_1$ ..	223
Fig. 6.17	Sensitivity of the Calculated Response of Wall B7 to the Choice of $\mu_2$ ..	224
Fig. 6.18	Sensitivity of the Calculated Response of Wall B7 to the Choice of $\epsilon_{\min}$ ..	225
Fig. 6.19	Sensitivity of the Calculated Response of Wall B7 to the Choice of $\gamma_n$ ..	226
Fig. 6.20	Sensitivity of the Calculated Response of Wall B7 to the Choice of $\tau_{\text{slip}}$ ..	227
Fig. 6.21	Load vs. Deflection Curve for Wall R1 .....	228
Fig. 6.22	Load vs. Deflection Curve for Wall R2 .....	229
Fig. 6.23	Load vs. Deflection Curve for Wall R3 .....	230
Fig. 6.24	Load vs. Deflection Curve for Wall R4 .....	231
Fig. 6.25	Load vs. Deflection Curve for Wall B1 .....	232
Fig. 6.26	Load vs. Deflection Curve for Wall B2 .....	233
Fig. 6.27	Load vs. Deflection Curve for Wall B3 .....	234
Fig. 6.28	Load vs. Deflection Curve for Wall B4 .....	235
Fig. 6.29	Load vs. Deflection Curve for Wall B5 .....	236

Fig. 6.30	Load vs. Deflection Curve for Wall B6 .....	237
Fig. 6.31	Load vs. Deflection Curve for Wall B7 .....	238
Fig. 6.32	Load vs. Deflection Curve for Wall B8 .....	239
Fig. 6.33	Load vs. Deflection Curve for Wall B9 .....	240
Fig. 6.34	Estimation of Shear Distortion .....	241
Fig. 6.35	Load vs. Shear Distortion at 6-ft Level: Wall R1 .....	242
Fig. 6.36	Load vs. Shear Distortion at 6-ft Level: Wall R2 .....	243
Fig. 6.37	Load vs. Shear Distortion at 6-ft Level: Wall R3 .....	244
Fig. 6.38	Load vs. Shear Distortion at 6-ft Level: Wall R4 .....	245
Fig. 6.39	Load vs. Shear Distortion at 6-ft Level: Wall B1 .....	246
Fig. 6.40	Load vs. Shear Distortion at 6-ft Level: Wall B2 .....	247
Fig. 6.41	Load vs. Shear Distortion at 6-ft Level: Wall B3 .....	248
Fig. 6.42	Load vs. Shear Distortion at 6-ft Level: Wall B4 .....	249
Fig. 6.43	Load vs. Shear Distortion at 6-ft Level: Wall B5 .....	250
Fig. 6.44	Load vs. Shear Distortion at 6-ft Level: Wall B6 .....	251
Fig. 6.45	Load vs. Shear Distortion at 6-ft Level: Wall B7 .....	252
Fig. 6.46	Load vs. Shear Distortion at 6-ft Level: Wall B8 .....	253
Fig. 6.47	Load vs. Shear Distortion at 6-ft Level: Wall B9 .....	254
Fig. 6.48	Buckling Modes of Reinforcing Bars (from Gosain et al [61]) .....	255
Fig. 6.49	Effective Strength Factors vs. Normalized Shear Distortion for Shear Walls (from [103]) .....	255
Fig. 6.50	Typical Crack Patterns in PCA Wall Specimens .....	256
Fig. 6.51	Calculated Crack Patterns for Wall R1 at Different Top-Deflection Levels .....	257
Fig. 6.52	Calculated Crack Patterns for Wall B7 at Different Top-Deflection Levels .....	258
Fig. 6.53	Calculated Deformed Shape of Wall R1 at Different Top-Deflection Levels .....	259
Fig. 6.54	Calculated Shear Strain Distribution in Wall R1 at Different Top-Deflection Levels .....	260
Fig. 6.55	Calculated $\epsilon_{yy}$ Distribution in Wall R1 at Different Top-Deflection Levels .....	261
Fig. 6.56	Calculated $\sigma_{yy}$ Distribution in Wall R1 at Different Top-Deflection Levels .....	262

Fig. 6.57	Calculated Deformed Shape of Wall B7 at Different Top–Deflection Levels .....	263
Fig. 6.58	Calculated Shear Strain Distribution in Wall B7 at Different Top–Deflection Levels .....	264
Fig. 6.59	Calculated $\epsilon_{yy}$ Distribution in Wall B7 at Different Top–Deflection Levels .....	265
Fig. 6.60	Calculated $\sigma_{yy}$ Distribution in Wall B7 at Different Top–Deflection Levels .....	266
Fig. 6.61	Calculated Load vs. Strain in Flexural Reinforcement: Wall R1 .....	267
Fig. 6.62	Calculated Load vs. Strain in Flexural Reinforcement: Wall B7 .....	268
Fig. 6.63	Calculated Strain in Vertical Reinforcing Steel at Maximum Positive Loadings: Wall R1 .....	269
Fig. 6.64	Calculated Strain in Vertical Reinforcing Steel at Maximum Negative Loadings: Wall R1 .....	270
Fig. 6.65	Calculated Strain in Vertical Reinforcing Steel at Maximum Positive Loadings: Wall B7 .....	271
Fig. 6.66	Calculated Strain in Vertical Reinforcing Steel at Maximum Negative Loadings: Wall B7 .....	272
Fig. 6.67	Calculated Stress–Strain Relationship in Vertical Reinforcement for Wall R1 .....	273
Fig. 6.68	Calculated Stress–Strain Relationship in Vertical Reinforcement for Wall B7 .....	274
Fig. 7.1	Walls CLS and CMS .....	275
Fig. 7.2	Experimental Setup .....	276
Fig. 7.3	Imposed Displacement Histories during Stages II through V for Walls CLS and CMS .....	277
Fig. 7.4	Finite Element Model for Evaluating Differences between the Calculated Response using Plane Stress and Shell Elements .....	278
Fig. 7.5	Wall Model and the Calculated Vertical Displacements at the top of the Wall .....	279
Fig. 7.6	Calculated Deformed Shapes of the C–Shaped Walls .....	280
Fig. 7.7	Distribution of Calculated Axial Stress in the C–Shaped Wall Model ..	281
Fig. 7.8	Loading and Boundary Conditions for Finite Element Models of Walls CLS and CMS .....	282
Fig. 7.9	Load vs. Deflection Curves at Different Levels for Wall CLS .....	283

Fig. 7.10	Load vs. Deflection Curves at Different Levels for Wall CMS .....	284
Fig. 7.11	Load vs. Shear Distortion at 3-ft Level: Wall CLS .....	285
Fig. 7.12	Load vs. Shear Distortion at 3-ft Level: Wall CMS .....	286
Fig. 7.13	Calculated Deformed Shape of Wall CLS .....	287
Fig. 7.14	Calculated Vertical Stress Distribution in Wall CLS .....	288
Fig. 7.15	Calculated In-plane Shear Strain Distribution in Wall CLS .....	289
Fig. 7.16	Calculated Deformed Shape of Wall CMS .....	290
Fig. 7.17	Calculated Vertical Stress Distribution in Wall CMS .....	291
Fig. 7.18	Calculated In-plane Shear Strain Distribution in Wall CMS .....	292
Fig. 7.19	Calculated Crack Patterns for Wall CLS at Different Top-Deflection Levels .....	293
Fig. 7.20	Calculated Crack Patterns for Wall CMS at Different Top-Deflection Levels .....	294
Fig. 7.21	Calculated Stress-Strain Relationship in Vertical Reinforcement in South Flange for Wall CLS .....	295
Fig. 7.22	Calculated Stress-Strain Relationship in Vertical Reinforcement in South Flange for Wall CMS .....	296
Fig. 8.1	Calculation of the Accumulated Energy Dissipation Ratio .....	297
Fig. 8.2	Reinforcement Details Considered in the Finite Element Analyses ....	298
Fig. 8.3	Load vs. Top Deflection Curves for Wall B2 with Different Reinforcement Details .....	299
Fig. 8.4	Load vs. Shear Distortion Curves for Wall B2 with Different Reinforcement Details .....	300
Fig. 8.5	Load vs. Top Deflection Curves for Wall B7 with Different Reinforcement Details .....	301
Fig. 8.6	Load vs. Shear Distortion Curves for Wall B7 with Different Reinforcement Details .....	302
Fig. 8.7	Crack Patterns in Wall B2 with Different Reinforcement Details .....	303
Fig. 8.8	Crack Patterns in Wall B7 with Different Reinforcement Details .....	304
Fig. 8.9	Accumulated Energy Dissipation Ratio for Walls B2 and B7 .....	305
Fig. 8.10	Shear Wall Systems (from [125]) .....	306
Fig. 8.11	Overall Dimensions of Walls CI1 and PW1 .....	307
Fig. 8.12	Location and Dimensions of Openings in Wall PW1 .....	307

Fig. 8.13	Reinforcement Details in Wall CI1 .....	308
Fig. 8.14	Top–Deflection History for Walls CI1 and PW1 .....	309
Fig. 8.15	Specimens CI1 and PW1 after Failures .....	310
Fig. 8.16	Finite Element Meshes for Walls CI1 and PW1 .....	311
Fig. 8.17	Load vs. Top Deflection Curves for Wall CI1 .....	312
Fig. 8.18	Load vs. Top Deflection Curves for Wall PW1 .....	313
Fig. 8.19	Load vs. Shear Distortion for Wall CI1 .....	314
Fig. 8.20	Load vs. Shear Distortion for Wall PW1 .....	315
Fig. 8.21	Shear Strain Distribution and Crack Patterns for Walls CI1 and PW1 ...	316
Fig. 8.22	Diagonal Reinforcement in Wall PW1 .....	317
Fig. 8.23	Load vs. Top Deflection Curves for Wall PW1 .....	318
Fig. 8.24	Load vs. Shear Distortion Curves for Wall PW1 .....	319
Fig. 8.25	Crack Patterns in Wall PW1 .....	320
Fig. 8.26	Shear Strain Distribution in Wall PW1 .....	323
Fig. 8.27	Dimensions of Wall Specimens Tested at the University of Michigan ...	324
Fig. 8.28	Reinforcement Details for Wall W1: Cross Section .....	324
Fig. 8.29	Reinforcement Details for Wall Specimens: Elevation .....	325
Fig. 8.30	Typical Top–Deflection History for Walls W1, W2, W3, and W4 .....	326
Fig. 8.31	Crack Patterns in Wall W2 after Failure .....	327
Fig. 8.32	Diagonal Tension Shear Failure in Reinforced Concrete Beam (from [55]) .....	327
Fig. 8.33	Finite Element Meshes for Wall Specimens .....	328
Fig. 8.34	Load vs. Top Deflection Curve for Wall W1 .....	329
Fig. 8.35	Load vs. Top Deflection Curve for Wall W2 .....	330
Fig. 8.36	Load vs. Top Deflection Curve for Wall W3 .....	331
Fig. 8.37	Load vs. Top Deflection Curve for Wall W4 .....	332
Fig. 8.38	Crack Patterns in Wall W2: Original Reinforcement Details .....	333
Fig. 8.39	Shear Forces Distribution in Walls W2, W3, and W4 .....	334
Fig. 8.40	Diagonal Reinforcement in Walls W2, W3, and W4 .....	335
Fig. 8.41	Shear Forces in Walls W2, W3, and W4: with Diagonal Reinforcement .	336
Fig. 8.42	Crack Patterns in Wall W2: with Diagonal Reinforcement .....	337

Fig. 8.43	Influence of Diagonal Reinforcement on the Shear Stress Distribution in Walls W2, W3, and W4 .....	338
Fig. 8.44	Finite Element Meshes for C-Shaped Wall Models .....	339
Fig. 8.45	Top-Deflection History for C-Shaped Walls: Case D .....	340
Fig. 8.46	Effective Width of the South Flange for C-Shaped Walls .....	340
Fig. 8.47	Secant Stiffnesses of C-Shaped Walls at Different Deformation Levels .....	341
Fig. 8.48	Calculated Load vs. Top Deflection Curves for C-Shaped Walls: Case A .....	342
Fig. 8.49	Calculated Load vs. Top Deflection Curves for C-Shaped Walls: Cases B and C .....	343
Fig. 8.50	Distribution of Strain in Vertical Reinforcing Bars along the Base of the South Flange .....	344
Fig. 8.51	Calculated Results of C-Shaped Walls subjected to Cyclic Loadings ...	345
Fig. A.1	Compression Stiffening Curve .....	349
Fig. A.2	Compression Softening Curve .....	350
Fig. B.1	Stress-Strain Relationship for Confined Concrete .....	352
Fig. C.1	Stress-strain of Unconfined Concrete subjected to Cyclic Compressive Loading .....	356
Fig. C.2	Rules for Cyclic Compressive Loading .....	356
Fig. D.1	Finite Element Meshes for PCA Walls .....	357
Fig. D.2	Finite Element Meshes for Walls CLS and CMS .....	360
Fig. D.3	Finite Element Meshes for Walls CI1 and PW1 .....	361
Fig. D.4	Finite Element Meshes for Walls W1, W2, W3, and W4 .....	362



# 1. INTRODUCTION

## 1.1 OVERVIEW

During the past forty years, reinforced concrete shear walls have been widely used as the primary lateral-load resisting systems for both wind and earthquake loading in multi-story buildings throughout the world. Observations from previous earthquakes have shown that well-designed shear walls can be used to control both structural and nonstructural damage in the buildings (57). However, it is usually not economical to design tall reinforced concrete shear walls to remain elastic during severe earthquakes. As a result, the inelastic response of shear walls must be considered during the design process (48, 105). The inelastic behavior of shear walls is controlled by the inelastic response of both the concrete and reinforcing steel. Tension stiffening, compression softening, and crack closing and reopening are the major aspects of inelastic behavior in concrete, while yielding, strain-hardening, and Baushinger effects must be considered when modelling the reinforcing steel. These phenomena are the major sources of energy dissipation in reinforced concrete structures and are important factors in determining the failure modes of reinforced concrete shear walls. In order for shear wall structures to survive large seismic disturbances, sudden failures due to shear and local instabilities must be suppressed (112). Therefore, structural engineers must understand thoroughly the inelastic behavior of reinforced concrete shear walls. They also must be able to predict the correct failure mode in order to prevent the collapse of a structure due to a sudden failure of the primary load-carrying system under intense ground motion.

Since the 1970's, a number of research programs have investigated the inelastic behavior of slender reinforced concrete shear walls subjected to cyclic lateral loads (29, 105, 140). Most of this research has concentrated on experimental work rather than the development of analytical models for evaluating the cyclic behavior of shear walls. In the current design process, most structural engineers rely on the ACI Building Code provisions (2) to evaluate the strength of shear walls. However, these design provisions are not sufficient to identify the likely modes of failure in shear walls (149). The procedures used to calculate the nominal shear strength of walls in the ACI Building Code (2)

are based on the modified truss analogy and rely on data from reinforced concrete beams subjected to monotonically increasing loads (148). Consequently, these procedures are often unconservative when used to calculate the shear strength of reinforced concrete shear walls subjected to cyclic loading. Because of this lack of an appropriate analytical model for evaluating the cyclic response of shear walls, methods for assessing the strength, stiffness, and nonlinear deformation response of slender reinforced concrete walls subjected to cyclic loadings need to be developed. This is the overall goal of this investigation.

This research is part of an ongoing investigation of the cyclic behavior of slender reinforced concrete shear walls taking place in the Department of Civil Engineering at the University of Illinois, Urbana-Champaign. Reinforced concrete shear walls with different shapes, reinforcement ratios, and loading histories were tested. The major objective of this phase of the research is to develop the appropriate analytical models for modelling the inelastic hysteresis behavior of slender reinforced concrete shear walls. The finite element method was chosen as the numerical technique in this investigation because this method, when combined with the proper constitutive models for concrete and reinforcing steel, offers a very powerful tool to investigate the response of shear walls with different configurations subjected to generalized loadings. Furthermore, finite element analysis also yields important detailed information on the behavior of shear walls, including the stress-strain relationships in concrete and reinforcing steel, deflected shapes, and crack patterns, which cannot be obtained from other analytical methods such as truss models (103) and shear hysteresis models (108).

The major problems of the nonlinear finite element analysis of reinforced concrete structures are the large amount of CPU time required for the analysis due to the complicated material models and the difficulties encountered in the stability and accuracy of the solutions (15). Some material models for concrete include excessively refined analyses, such as fracture mechanics and detailed crack localizations, which cause unneeded expenses (71). Most previous models for the cyclic behavior of reinforced concrete (134, 151) were tested and verified successfully at the element level (the finite element model consists of one or few elements), but when these material models were used

in the structural level problems (the finite element model consists of a large number of elements, such as the modelling of actual reinforced concrete structures), numerical problems associated with the complex stress-strain relationships prevented the completion of most analyses (134, 151). Therefore, the need exists to develop new material models for concrete and reinforcing steel that can avoid these problems.

The analytical models for concrete and reinforcing steel, once developed and verified using experimental results, will play an important role in the ongoing research. With these analytical models, the finite element method can be used to explore in detail the behavior of reinforced concrete walls that have different configurations and reinforcement details, and are subjected to different loading histories from the wall specimens tested in the laboratory.

## **1.2 OBJECTIVE AND SCOPE**

The major objectives of this research are:

1) To develop finite element material models for concrete and reinforcing steel that are appropriate for modelling the response of slender reinforced concrete shear walls subjected to reversed cyclic loadings. The material models must be simple, stable, and reliable in order to make the analyses feasible and economical with respect to CPU time and the convergence of nonlinear solutions. However, these material models should include all phenomena that have a significant influence on the cyclic behavior of slender reinforced concrete shear walls.

2) To verify the material models by comparing the calculated results with experimental data from several large-scale tests of slender reinforced concrete shear walls subjected to cyclic loadings. The overall hysteresis response, deflected shapes, crack patterns, and observed failure modes will be considered.

3) To extend the investigation on the behavior of slender reinforced concrete shear walls by using finite element analysis in lieu of further large-scale tests. The investigation includes studies

of the energy dissipation capacity of shear walls, the response of shear walls with openings, and the contribution of flanges to the response of C-shaped shear walls.

This report first discusses the current status of the research on the finite element analysis of reinforced concrete members in Chapter 2. Then, the details of the proposed material models for concrete and reinforcing steel are described in Chapters 3 and 4, respectively. In Chapter 5, the finite element procedures and some important numerical techniques used in this research are briefly discussed. Two experimental programs on the cyclic responses of slender reinforced concrete shear walls—one was the test of thirteen slender reinforced concrete shear walls at the Construction Technology Laboratory, PCA and the other was the test of two C-shaped shear walls carried on at the Department of Civil Engineering, the University of Illinois, Urbana-Champaign—were used for testing and verifying the proposed material models. Several aspects of the test results from these two experimental programs, including the load vs. top deflection curves, the load vs. shear deformation curves, crack patterns, and failure modes, are compared with those of the calculated results. The experimental setup, the analytical models, and the comparisons between the calculated response and the experimental data for these two experimental programs are described in Chapters 6 and 7. After the material models have been satisfactorily verified, the finite element method is used to study three topics dealing with the response of slender reinforced concrete shear walls: 1) the energy dissipation capacity of shear walls, 2) the response of shear walls with openings, and 3) the contribution of flanges to the response of C-shaped walls. These studies are described in Chapter 8. Summary, conclusions, and recommendations for future research are given in Chapter 9.

## **2. FINITE ELEMENT ANALYSIS OF REINFORCED CONCRETE MEMBERS**

The finite element method is a powerful structural analysis tool that has been widely used in many different types of problems. The strength of the finite element method is based primarily on its fundamental concept of discretization, which models a structure as an assemblage of several finite elements. This concept simplifies the modelling of complex structures and allows the formulation of the problem to be written in a matrix form, which is appropriate to be incorporated into computer programs. The concept of discretization is also useful for the study of problems with material and geometric nonlinearities, because it allows a variety of material and element models to be installed at the element level. Finite element users can select or develop the material and the element models that have the proper kinematic and constitutive relationships for the problems under study. As a result, with the proper material and element models for concrete and reinforcing steel, the finite element method can be a very powerful analytical tool for studying the behavior of reinforced concrete structures.

In this chapter, a brief review of the previous work in the finite element analysis of reinforced concrete is presented. This review emphasizes three areas related to the major objectives of this investigation: the finite element analysis of shear walls, the cyclic response of reinforced concrete members, and the applications of the finite element method. The different approaches previously used to for modelling cracked concrete and reinforcing steel are then discussed. The proposed material models for concrete and reinforcing steel are described at the end of this chapter.

### **2.1 LITERATURE REVIEW**

#### **2.1.1 OVERVIEW**

The earliest publication of the finite element analysis of reinforced concrete was written by Ngo and Scordelis (99) in 1967. In this paper, simply supported reinforced concrete beams with predefined cracks were analyzed using the finite element method. Since then, a large number of works on the finite element analysis of reinforced concrete have been published. Most of the early

investigators limited their work to two-dimensional plane stress problems and used the finite element method to investigate the behavior of reinforced concrete beams tested in laboratories (32, 41, 70, 98, 99, 141). Jofriet and McNiece (78) used the finite element method to study behavior of reinforced concrete slabs by using plate bending elements and a modified stiffness approach. Subsequently, several other researchers successfully used plate and shell elements to investigate the behavior of slabs and reinforced concrete shell structures (12, 15, 23, 27, 65, 84, 71).

Although the two-dimensional plane stress elements, plate elements, and shell elements have been successfully and widely used in the finite element analysis of reinforced concrete, the use of the three-dimensional element is very limited. This is due both to the computational effort required in the analysis and to the lack of knowledge concerning the behavior of concrete in a three-dimensional state of stress (136). Suidan and Schnobrich (135) used three-dimensional isoparametric elements to model reinforced concrete beams. Meyer and Bathe (95) used three-dimensional elements and shell elements to model reinforced concrete nuclear reactors that were subjected to internal pressure and temperature loadings. Bathe and Ramaswamy (15) also used the three-dimensional finite elements to analyze prestressed concrete reactor vessels. The extensive summary of the previous work in the finite element analysis of reinforced concrete can be found in the State-of-the-Art report published by the American Society of Civil Engineers (136).

### **2.1.2 PREVIOUS WORK ON R/C SHEAR WALLS**

Although the finite element method has been used in the analyses of various types of reinforced concrete members, including beams, slabs, shells, and panels, its application in the analysis of reinforced concrete shear walls is quite limited. In 1972, Yuzugulla (157) used the finite element method to study the monotonic behavior of a shear wall-frame system which was tested at the University of Tokyo. This research is one of the earliest attempts to model reinforced concrete shear walls by the finite element model. Aktan and Hanson (4) analyzed the monotonic and cyclic responses of slender reinforced concrete shear walls by using a finite element model that separated the walls into subregions. In each of the subregions, the linear behavior was represented by elastic

plane stress elements, and the nonlinear behavior was represented by joint elements connected to the boundary of the subregion. Bolander and Wight (26, 25) developed the finite element program SNAC primarily for use as a tool to investigate the inelastic response of shear wall dominant buildings subjected to quasi-static loadings.

Research in the finite element analysis of reinforced concrete shear walls in Japan is much more active than that in the U.S. Most of the shear wall research in Japan deals with the behavior of low-rise shear walls (height/length less than 1.0), which represent the reinforced concrete walls used in the nuclear power plants. Yamaguchi and Nomura (153) used the finite element method that was based on the plastic-fracture theory proposed by Bazant and Kim (20) to analyze four reinforced concrete shear walls subjected to monotonic and cyclic loadings. Ueda and Kawai (139) used a finite element model which consisted of rigid elements and spring elements to model the monotonic response of shear walls. Sotomura and Marazumi (131) analyzed a series of reinforced concrete shear walls with openings by using a simple smeared crack model for concrete, and an elasto-plastic model for reinforcing steel. Inoue et al. (73) developed the reinforced concrete material model based on the results from Vecchio and Collins' panel tests (143), where thirty reinforced concrete panels subjected to different uniform stress conditions were tested, and used the model in the analysis of several shear walls that had different reinforcement ratios and different shear span ratios. In all these previous analyses of reinforced concrete walls, most of the reinforced concrete models were simple, and, regardless of the differences in the material and element models, most of the analytical results agreed with the experimental results.

### **2.1.3 PREVIOUS WORK ON CYCLIC RESPONSE OF R/C MEMBERS**

Although there has been a large amount of research in the past three decades on the finite element analysis of reinforced concrete members, there were few studies of the behavior of reinforced concrete members subjected to cyclic loadings. Some of the pioneer researchers who used finite element analysis to model the cyclic response of reinforced concrete members include Cervenka (34), Cervenka and Gerstle (36, 37), Darwin and Pecknold (45), Bergan and Holand (23), Aktan

and Hanson (4), and Agrawal et al. (3). Despite the promising results from some of these studies, none of these studies is truly successful in modelling the cyclic response of reinforced concrete members. This is due to the fact that the reinforced concrete members studied in all these analyses were subjected to only a few cycles of load reversals. As a result, the cyclic response of these reinforced concrete members did not demonstrate important hysteresis characteristics, such as the hinging effects in load vs. deflection curves, the effects of cyclic shear deformation, and the deterioration of concrete because of cyclic compressive loadings.

Two major obstacles that most researchers experienced in the development of cyclic models for reinforced concrete are: 1) the lack of understanding in the cyclic response of reinforced concrete and 2) the numerical problems associated with complex rules for load reversals and stress-strain relationships in material models (102, 134). In order to obtain a detailed understanding of the cyclic behavior of reinforced concrete element and to gather essential experimental data needed for the formulation of such behavior, Stevens et al. (134) conducted cyclic tests on three reinforced concrete panels. In these tests, two panels with different amounts of reinforcement were subjected to load reversals in pure shear, while one other panel was subjected to reversed cyclic shear combined with biaxial compression. The average stress-strain relationship for these panels was then used as a basis for the development of a material model for concrete. Stevens et al. (134) proposed a concrete model based on the modified compression field theory. Two other researchers also used the results from these panel tests to verify their concrete models. Xu (151) proposed the model using a smeared non-orthogonal cracking approach, and Izumo et al. (75) developed the hysteresis constitutive law for reinforced concrete by combining several existing constitutive laws developed in Japan. The analytical results at the element level (a finite element model consists of one element) of these three models agreed well with the results of the panel tests. However, because of the complexities of these models, numerical problems usually occurred in the analysis of problems at the structural level (a finite element model consists of several elements) and, hence, prevented the completion of most analyses. Such problems greatly reduced the usefulness of these models.



## 2.1.4 APPLICATIONS OF THE FINITE ELEMENT METHOD

Most of the previous work in the finite element analysis of the behavior of reinforced concrete members concentrated on the development of the material model that could reproduce experimental results. Surprisingly, few researchers used the finite element method to investigate behavior of reinforced concrete members other than that of the specimens tested in the laboratory. Valliappan (141) was one of the first researchers to apply the finite element method to the analysis of reinforced concrete members other than reinforced concrete beams. In his paper, a material model first developed using the experimental data from reinforced concrete beam tests was then used to investigate the behavior of reinforced concrete haunches and hinges. Lin and Scordelis (84) verified their layered reinforced concrete shell element with the experimental results of several slabs tested in the laboratory. They demonstrated the applicability of the model by using it to analyze the failure load of a hyperbolic paraboloid shell. In an attempt to verify the safety of a vessel for a high-temperature gas-cooled reactor, Meyer and Bathe (95) used the three-dimensional reinforced concrete model to analyze the prestressed concrete vessels subjected to several different loading conditions. Vecchio (142) used the finite element method to study the effects of a perforation and the reinforcement details on the behavior of reinforced concrete walls. He compared the computed response of three square reinforced concrete walls, the first was solid, the second was perforated and had reinforcement recommended by ACI, and the third was perforated but did not include the recommended reinforcement details (2).

During the past decade, some researchers used the finite element method to study the effects of different design parameters on the response of reinforced concrete members. Ueda and Kawai (139) conducted finite element analyses of reinforced concrete shear walls with different amounts of reinforcement and axial load. Mikame et al. (96) used the finite element method to conduct an extensive parametric study of reinforced concrete shear walls. The parameters studied included reinforcement ratio, axial stress, compressive strength of concrete, cross sections of columns, and presence of openings. Massicotte et al. (90, 91) used the finite element method to analyze five rein-

forced concrete panels which were tested under axial and lateral loadings at the University of Alberta. The finite element analyses were then extended to investigate the behavior of twenty six reinforced concrete panels with different aspect ratios, thickness, amount of reinforcement, magnitudes of in-plane load, in-plane and rotational edge restraints, and the loading sequence.

## **2.2 CRACK MODELLING**

Tensile cracking is one of the most important reasons for nonlinearities in reinforced concrete (38, 39, 47, 84, 151). Because concrete is weak in tension, tensile cracking can have a significant effect on the behavior of most reinforced concrete members, even at an early stage of loading. As a result, proper crack modelling is crucial to the success of the concrete model. In order to incorporate cracking into the material model, the following basic components of crack modelling must be defined (136):

- 1) Crack representation
- 2) Crack initiation and crack propagation
- 3) Constitutive relationship for cracked concrete

During the past three decades, researchers have proposed a number of different models to represent cracks in reinforced concrete. The following sections discuss the different approaches that have been used to define the three basic components of crack modelling.

### **2.2.1 CRACK REPRESENTATION**

In the finite element formulation, stress and strain are assumed to be continuous within one finite element. However, when concrete cracks, discontinuities in stress and strain occur in the concrete matrix. Crack representation is the way that these discontinuities are incorporated into the concrete model. In general, two different approaches have been used to represent cracks:

- 1) Discrete crack model
- 2) Smeared crack model

In the discrete crack model, cracks are represented as a separation of nodes along element boundaries (25) as shown in Fig. 2.1. The post-cracking behavior, such as tension stiffening, aggregate interlock, and dowel action, can be incorporated into the model by using linkage elements to connect the separated nodes. The discrete model was first introduced by Ngo and Scordelis (99) in 1968 and was then adopted in other early investigations (70, 100). Although this model realistically represents the discontinuities in stress and strain across cracks, three major drawbacks prevent the successful application of this model:

- Cracking can occur only along element boundaries. Such restriction introduces bias into the finite element solution (136).
- If cracks are not predefined, cracking will cause the redefinition of the nodes. This node redefinition will continuously change the topology of the finite element mesh and, hence, destroy the narrow bandwidth in the structural stiffness matrix.
- Once the separation of the nodes has occurred, crack closing and reopening needs to be considered as a contact problem. This greatly complicates the finite element procedure, especially in the problems that involve cyclic loading.

In the smeared crack model, concrete is assumed to remain continuous after cracking. The stress-strain discontinuities across the cracks are averaged over the element in the vicinity of the cracks; consequently, the stress-strain relationship of cracked concrete can still be described in a continuous manner. At each integration point in a concrete element, cracks are considered to be parallel and finely spaced over the area, and the average stress-strain relationship of cracked concrete is represented by a constitutive matrix (Fig. 2.2). The smeared crack model was first introduced by Rashid (120) in 1968. Since then, the model has been successfully used in a wide range of problems (136). The success and the popularity of the smeared crack model are the result of several practical advantages (25):

- Cracking can occur in any direction and multiple cracks are allowed at each integration point.
- Each crack is represented by simply adjusting the constitutive matrix at the integration point where the crack occurs. The topology of the finite element mesh remains the same throughout the analysis.
- Because cracks at each integration point are considered separately, the direction of each crack can be different, and partial cracking (cracking does not occur at every integration point in one element) is also allowed.

Because the smeared crack model represents cracks as being finely spaced or “smeared,” the model is suitable for modelling reinforced concrete members with a distributed crack pattern. However, for reinforced concrete members in which one or few large cracks dominate the response, the discrete crack model might be more appropriate than the smeared crack model. Recently, some researchers have used both crack models in the analysis of problems where the effects of both single cracks and distributed cracks are significant. For example, Okamura et al. (107) used the finite element model which used both smeared crack and discrete crack elements in the region where large cracks were likely to occur to analyze the behavior of reinforced concrete shear walls.

## **2.2.2 CRACK INITIATION AND CRACK PROPAGATION**

Most concrete models adopt a strength criterion for crack initiation. Cracking occurs at one integration point when the principal stress at that point exceeds the cracking stress. Some researchers simply used the uniaxial tensile strength or the modulus of rupture for the value of the cracking stress, while others used the tensile strength of concrete under the tension–tension or the tension–compression biaxial stress state, such as the biaxial strength envelop proposed by Kupfer et al. (81).

After a crack has formed, it will extend to the adjacent concrete element. Two criteria have been used for determining crack propagation:

- 1) Strength criterion
- 2) Fracture mechanics criterion

The strength criterion for crack propagation is similar to the strength criterion for crack initiation; the crack propagates when stress at the crack tip exceeds the cracking stress. Although the strength criterion seems logical, it is refuted by Bazant and Cedolin (17, 18, 30). They argue that when the finite element mesh is refined and the crack tip becomes sharpened, high stress concentration occurs at the crack tip even with a small applied load. If the strength criterion is used for crack propagation, such stress concentration will allow cracks to propagate even at an insignificant load level. Therefore, Bazant and Cedolin conclude that the strength criterion is not objective because the results depend on finite element size and do not converge as the element size is reduced to zero (30).

The fracture mechanics criterion for the smeared crack model was first proposed by Bazant and Cedolin (17, 30) as the solution to the “non-objectivity” of the strength criterion. In this approach, each crack is modelled by a one-element wide band of concrete elements (a blunt crack band). Based on the assumption that “the work consumed when the crack band is extended by a unit length is a constant” (17), the crack propagates to the next element at the tip of the crack band when the computed energy release rate of the crack band exceeds the critical value, which depends on the fracture energy ( $G_f$ ) of concrete (83). Although several researchers have adopted this fracture mechanics criterion (19, 43, 50, 59, 67, 152), the application of the fracture mechanics in the finite element analysis of reinforced concrete structures is still very limited.

Most of the previous researchers successfully used strength as a criterion for crack propagation in the finite element analyses of various types of reinforced concrete members, including beams, slabs, shells, and shear walls (151). The “non-objectivity” of the strength criterion did not have any effect on these analyses, because in most of these analyses, the size of a concrete element was much larger than the size of a crack, and a cracked element represented the average behavior of several cracks rather than the behavior of a single crack. Therefore, the strength criterion is sufficient for

crack propagation in the problems where cracks are distributed and the average response of cracked concrete dominates the behavior of the reinforced concrete members. However, for the crack propagation in the problems in which the behavior of reinforced concrete members is controlled by few dominant cracks, the fracture mechanics criterion might be required (122, 136). Examples of such problems are the analysis of shear crack propagation in a reinforced concrete nuclear vessel and the analysis of flexural crack propagation in a plain concrete notched beam.

### **2.2.3 CONSTITUTIVE MODELLING OF CRACKED CONCRETE**

The constitutive modelling of cracked concrete consists of two major components: the stress-strain relationship and the crack model. The first component represents an average stress-strain relationship of cracked concrete in the direction of the crack. For monotonic loading, the relationship usually includes the nonlinear behavior of concrete subjected to uniaxial or biaxial compressive stress with a simple unloading algorithm. This relationship is developed by fitting a curve to experimental data. Several stress-strain curves for concrete have been proposed (39, 119, 136), and some of them have been used successfully in the finite element analysis of reinforced concrete members (86, 157). For cyclic loading, the stress-strain relationship must also include the important aspects of the cyclic behavior of concrete, such as crack closing and reopening as well as the effects of cyclic compressive stress and cyclic shear stress. Currently, the experimental data for some of these aspects related to the cyclic behavior are still limited and few researchers have proposed the complete stress-strain relationship for finite element applications (134, 151).

The second component, the crack model, represents the relationship between strain (stress) in the global coordinate and strain (stress) in the direction of the crack (the crack coordinate). The formulation of the crack model is based primarily on the assumptions of the direction of the crack and on the transformation of strain (stress) in the global coordinate to strain (stress) in the direction of the crack. There are three major crack models that have been used successfully in the past: 1) the fixed crack model, 2) the rotating crack model, and 3) the non-orthogonal multi-crack model.

### 2.2.3.1 FIXED CRACK MODEL

In the fixed crack model, cracking occurs normal to the direction of the maximum principal stress when the maximum principal stress reaches the cracking stress. The cracked concrete is then assumed to be orthotropic, with the axis of orthotropy (the crack coordinate) parallel and normal to the crack. The crack direction is assumed to remain fixed throughout the analysis. The rotation of strain (stress) from the global coordinate to the crack coordinate can be done simply by using the conventional rotation matrix for strain (stress). The constitutive relationship of cracked concrete for two-dimensional plane stress problems can be written in the crack coordinate as follows:

$$\begin{bmatrix} \partial\sigma_1 \\ \partial\sigma_2 \\ \partial\tau_{12} \end{bmatrix} = \begin{bmatrix} E_1 & 0 & 0 \\ 0 & E_2 & 0 \\ 0 & 0 & \beta G \end{bmatrix} \begin{bmatrix} \partial\varepsilon_1 \\ \partial\varepsilon_2 \\ \partial\gamma_{12} \end{bmatrix} \quad (2.1)$$

$E_1$  and  $E_2$  are the tangent stiffnesses of cracked concrete normal and parallel to the first crack. The second crack is allowed to occur in the direction normal to the first crack by adjusting the value of  $E_2$ . The term  $\beta G$  represents the shear stiffness retained in the crack direction because of aggregate interlock and dowel action. In the problems with monotonic loadings, several researchers (11, 12, 21, 26, 39, 46, 65, 101, 151) reported that the term  $\beta G$  is necessary for the numerical stability of the solution; the exact value of  $\beta G$ , however, is not crucial to the solution, provided that the value is above the minimum value (65).

The fixed crack model has been successfully used by several investigators, such as Agrawal et al. (3), Balakrishnan and Murray (9, 10), Cervenka (35), Darwin and Pecknold (45), Hand et al. (65), Jofriet and McNiece (78), Lin and Scordelis (84), Sotomura et al. (131), Suidan and Schnobrich (135), and Yamaguchi et al. (153). Despite its success in the analyses of various types of reinforced concrete members, the fixed crack model has been unable to correctly model the response of some reinforced concrete panels tested by Vecchio and Collins (143). Several researchers (11, 42, 71, 90, 97) have reported that the fixed crack model yields a response that is too strong for the

panels with highly anisotropic reinforcement. This deficiency can be explained by Vecchio and Collins' test results (143), which indicate that cracks in the anisotropically reinforced panels, instead of remaining fixed, change their directions during the test. Hence, the assumption of fixed crack direction imposes an extra constraint on the finite element analysis which leads to an overestimation of the calculated stiffness of the panels with anisotropic reinforcement. As a result, some researchers, such as Milford (97) and Gupta and Akbar (63), considered the assumption of fixed crack to be incorrect, and adopted the model that allowed cracks to rotate, the rotating crack model.

### **2.2.3.2 ROTATING CRACK MODEL**

In the rotating crack model, cracked concrete is assumed to be orthotropic, as it is assumed in the fixed crack model. However, the axis of orthotropy, or the crack coordinate, does not remain fixed but is always aligned with the major principal strain direction. The transformations of the strain, stress, and the constitutive matrix of the rotating crack model from the crack coordinate to the global coordinate are similar to those of the fixed crack model except for the change in the crack direction.

The early researchers who adopted the rotating crack model include Milford (97), and Vecchio, Collins (144), and Gupta and Akbar (63). In 1983, Gupta and Akbar (63) proposed the rotating crack model and defined two parts to the constitutive matrix: 1) the conventional constitutive matrix (similar to what is used in the fixed crack model) and 2) a contribution which reflects the possible changes in crack direction. Milford (97) was the first to incorporate this model into a finite element program and used it to analyze a reinforced concrete cooling tower. Vecchio and Collins (144) proposed another rotating crack model based on the compression field theory, which assumes that the principal stress direction of concrete coincides with the principal strain direction. Several other researchers who adopted the rotating crack model in their concrete models are Hu and Schnobrich (71, 72), Crisfield and Wills (42), Balakrishnan and Murray (9, 10), Massicotte and McGregor (90), and Inoue et al. (73).



Results of the rotating crack model agree with the experimental results for panels with anisotropic reinforcement (143). However, the rotating crack model has suffered two major drawbacks:

- Some researchers, such as Bazant (16), De Borst and Nauta (47), and Noguchi (102), criticized the validity of the assumption of crack rotation. Bazant and Noguchi argue that the rotation of the axes of orthotropy means that damage in concrete is temporary and depends solely on the current strain state. This is not true of concrete in general.

- The crack rotation causes discontinuities in stress and strain in the crack direction. In the rotating crack model, stress and strain in the crack direction at the end of the last load step is different from stress and strain in the new crack direction at the beginning of the next load step (134). This complicates the rules defining the stress–strain relationship in a concrete model because, instead of using only one or a few curves to define a certain region in the stress–strain relationship (as used in the fixed crack model), a whole family of curves are required (134). Furthermore, the rotation of the direction of the crack can cause false unloading and stress overshooting at some integration points. This usually leads to numerical difficulties during the analysis, especially in the case of cyclic loadings.

The rotating crack models have been applied successfully in the analysis of reinforced concrete members under monotonic loadings. The only effort to incorporate the cyclic response into the rotating crack model has been done by Stevens et al. (134). This model is successful at the element level where the analytical results agree well with the cyclic response of reinforced concrete panels (134). However, the application of the model at the structural level is not as successful and is still very limited.

### **2.2.3.3 NON-ORTHOGONAL MULTI-CRACK MODEL**

The non-orthogonal multi-crack model was proposed by De Borst and Nauta (46, 47) in 1985 as a solution to the deficiencies of the fixed crack and the rotating crack models. The fundamental feature of this model is a decomposition of a total strain increment  $\Delta\varepsilon$  into a concrete strain

increment,  $\Delta\varepsilon^{co}$ , and a crack strain increment,  $\Delta\varepsilon^{cr}$ . The relationship between these strain increments can be written as the following:

$$\Delta\varepsilon = \Delta\varepsilon^{cr} + \Delta\varepsilon^{co} \quad (2.2)$$

Such strain decomposition allows intact concrete and cracks to be modelled separately. Because crack strain is separated from concrete strain and is the summation of the contributions from all cracks at that point, each crack is treated independently and multiple non-orthogonal cracks can occur at one integration point. Bolander and Wight (25, 26) used this model successfully in the analysis of the monotonic response of reinforced concrete shear walls. Xu (151) modified the model to include cyclic behavior. Xu's model was successful at the element level when it was used to model the cyclic response of reinforced concrete panels tested by Stevens et al. (134). However, it was not successful at the structural level because numerical difficulties usually prevented the completion of most analyses (151).

Although the model employs a useful concept of the strain decomposition, the application of the non-orthogonal multi-crack model is still limited (42, 151). The complexity of the model is one of the major factors that prevent the successful application of the model. For example, Crisfield and Wills (42), who considered this model to be most "hopeful," encountered significant numerical difficulties while attempting to implement this model, and ended up adopting the rotating crack model instead. Another difficulty of using this model lies in the amount of computational effort required in the calculation of the constitutive relationship. This calculation, at each integration point, involves matrix inversion, matrix addition, matrix subtraction, and several matrix multiplications. This problem becomes significant when a finite element model consists of a large number of concrete elements and is subjected to hundreds or even thousands of load steps.

## 2.3 MODELLING OF STEEL REINFORCEMENT

The strength and stiffness of reinforced concrete members depend greatly on the characteristics of reinforcing steel (95). Fortunately, the development of the reinforcing steel model is much more straightforward than the development of the concrete model because the behavior of reinforcing steel is essentially uniaxial and is well defined both for monotonic and cyclic loadings (95). The steel reinforcement model consists of two major components: 1) the steel reinforcement representation and 2) the stress–strain relationship.

### 2.3.1 STEEL REINFORCEMENT REPRESENTATION

Three major models of steel reinforcement have been used successfully in the finite element analysis of reinforced concrete:

- 1) Discrete steel model
- 2) Embedded steel model
- 3) Smeared steel model

In a discrete model, a reinforcing bar is represented by a one–dimensional bar element. The model was used in the first publication of the finite element analysis of reinforced concrete by Ngo and Scoredelis (99) and is still being widely used (136). The advantages of this model are its simplicity and its ability to include bond–slip relationships between concrete and steel by using a linkage element to connect the common nodes of a bar element and a concrete element. The bending stiffness and the shear stiffness of the reinforcing bar can be modelled by using a beam element instead of a bar element. The major disadvantage of the discrete model is its mesh dependency; the direction and location of bar elements depend on the mesh layout of the finite element model.

In an embedded model, a reinforcing bar is considered to be a uniaxial member, but it is represented by a two–dimensional or a three–dimensional isoparametric element. The stiffness of each layer of reinforcing bars is evaluated individually with an isoparametric shape function (54). The

model was proposed as a solution to the problem of mesh dependency in the discrete model. Perfect bond between concrete and reinforcing steel is assumed in this model.

In a smeared model, reinforcing steel is assumed to be uniformly distributed over a concrete element in a particular direction. The two-dimensional plane stress constitutive matrix for the smeared model can be written in the direction of the reinforcing bar as follows:

$$[D^s] = \begin{bmatrix} \rho E_s & 0 & 0 \\ 0 & 0 & 0 \\ 0 & 0 & 0 \end{bmatrix} \quad (2.3)$$

where  $\rho$  represents the reinforcement ratio and  $E_s$  represents the stiffness of the reinforcing steel.

After being rotated to the global direction, the constitutive matrix of reinforcing steel is superimposed on top of the constitutive matrix of concrete to obtain the total constitutive matrix of reinforced concrete. The perfect bond between reinforcing steel and concrete must also be assumed in this model.

### 2.3.2 STRESS–STRAIN RELATIONSHIP OF REINFORCING STEEL

The major characteristics of the cyclic stress–strain relationship of reinforcing steel include an initial elastic region, a yield plateau, a strain–hardening region, and the Bauschinger effect because of load reversals. Several different stress–strain relationships have been used successfully in the finite element analysis of reinforced concrete members, ranging from very simple models which assume the stress–strain relationship to be elasto–plastic to very complex models which include the inelastic cyclic behavior such as the Bauschinger effects. The degree of sophistication of the stress–strain relationship required in the analysis depends on the nature of the problems being analyzed. For reinforced concrete members subjected to monotonic loadings, a simple bilinear or trilinear model might be adequate (134). But when reinforced concrete members are subjected to cyclic loadings and have the behavior which is strongly influenced by the characteristics of reinforcing steel, a simple model is inadequate and a more realistic model is necessary (134).

## **2.4 PROPOSED MATERIAL MODELS**

One of the major objectives of this research is to develop material models for concrete and reinforcing steel that are appropriate for modelling the cyclic response of slender reinforced concrete walls. The models for cyclic behavior of reinforced concrete recently developed by Xu (151) and by Stevens et al. (134) were not successful in analyzing structural problems due to numerical difficulties associated with the complex stress-strain relationships (134, 151). Hence, the usefulness of these models is limited. In order to avoid these numerical problems and to be practical for structural problems regarding the computation time required in the analysis, the proposed models must have the following properties:

- 1) **Simplicity** – The models must be simple and should include only the aspects of behavior that have a significant effect on the cyclic behavior of slender reinforced concrete walls.
- 2) **Stability** – The models must be stable and have a good convergence rate during the iteration procedure of the nonlinear analysis, especially when the analysis is done at the structural level.
- 3) **Reliability** – The models must be reliable. They must be the correct representations of the cyclic behavior of concrete and reinforcing steel in slender reinforced concrete walls.

The proposed models for concrete and reinforcing steel are described in the following sections.

### **2.4.1 PROPOSED CONCRETE MODEL**

During the past decade, several researchers (10, 11, 35, 38, 42, 59, 64, 71, 72, 90, 142) used Vecchio and Collins' experimental results of thirty reinforced concrete panels tested under different uniform stress conditions (143) as the basis for their concrete model development. Although this approach seems reasonable and promising, it has one major drawback: the behavior of the reinforced concrete panels might not correctly represent the behavior of reinforced concrete in other types of reinforced concrete members. This is because the behavior of reinforced concrete depends greatly

on boundary conditions, loading history, and geometry of the member. Therefore, developing a concrete model based on the panel test results does not guarantee the success of the model in other structural problems. On the other hand, such an approach might result in an unnecessarily complicated model or in a model that lacks some of the essential aspects of the behavior of the reinforced concrete members being studied.

Because the cyclic response of slender reinforced concrete walls is the major topic of this research, the proposed concrete model must correctly represent the behavior of concrete in the walls. From the test results of isolated walls tested by Oesterle et al. (105, 106) and also the test results of C-shaped walls tested in this investigation, there are several important aspects of behavior of concrete that should be included in the concrete model:

- Cracks are distributed quite uniformly in the lower portion of the walls.
- Most of the cracks that developed when the wall was subjected to cyclic loading were nearly orthogonal to the cracks that developed during the first load cycle.
- The directions of most cracks did not change during testing.
- Shear deformations were concentrated in the lower portion of the walls in the direction parallel to the base of the walls.

Based on these observations, the smeared crack model with fixed orthogonal cracks using the strength criterion for crack initiation and propagation has been adopted in the proposed concrete model. However, the conventional fixed crack model cannot represent the large shear deformation in the lower portion of the wall correctly. After trying several different approaches, it was concluded that the best way to model the shear deformation in the walls was to separate shear strain from other strain components in the global coordinate system as shown in Fig. 2.3.

The separation of the shear strain from the global longitudinal and transverse strains leads to the separation of the shear stiffness in the global coordinate system from the normal stiffness in the crack coordinate system. The separation of shear strain also allows the lower portion of the wall to experience high shear deformation, as observed in the test results, without causing premature

crushing of concrete in the crack direction. The shear stiffness of the proposed model is controlled primarily by only one function,  $G_{cr}$ . Two functions must be defined in the concrete model: the normal stress function and the shear stress function. These two functions are described in Chapter 3.

## 2.4.2 PROPOSED STEEL MODEL

Although the smeared steel model has been used by several researchers recently, the discrete steel model was adopted in this investigation. The reasons for choosing the discrete steel model are as follows:

- A discrete bar element is a correct representation of each reinforcing bar in shear walls. The layout of bar elements in the finite element model can closely resemble the layout of reinforcing bars in shear walls.
- If necessary, the effect of bond–slip between concrete and reinforcing steel can be added by using linkage elements. This cannot be done in the smeared steel model.
- Because of the horizontal and vertical arrangement of the reinforcing bars in shear walls, and because of the layout of the finite element mesh, the discrete steel model does not suffer mesh dependency. Each group of reinforcing bars can be modelled correctly by a bar element without any difficulties.

There is only one function, the uniaxial stress–strain relationship, which has to be defined in the steel model. This function is described in Chapter 4.

### 3. MATERIAL MODEL FOR CONCRETE

The proposed material model for concrete, as described in Chapter 2, consists of two independent functions: the normal stress function and the shear stress function. The normal stress function represents the average relationship between stress and strain in the direction normal to the crack while the shear stress function represents the average relationship between shear stress and shear strain in the direction parallel to the base of the walls. Two important characteristics of these two functions are the material nonlinearity and the history dependency. The nonlinear behavior of concrete, which occurs when concrete cracks or is subjected to high compressive stress or cyclic loadings, has a significant effect on the response of reinforced concrete shear walls. To model these types of behavior, each stress function is composed of several equations and rules, each of which simulates an important aspect of the nonlinear behavior of concrete. The behavior of concrete also greatly depends on the loading history. Hence, these functions must be history-dependent; the current stress depends not only on the current strain but also on the stress-strain history. At every integration point in each concrete element, several parameters reflecting the loading history need to be kept and updated. Because these two stress functions govern the response of the concrete model, their behavior is crucial to the success of the finite element analysis. As a result, a large amount of effort was spent developing and evaluating these functions.

In this chapter, the normal stress function and the shear stress function are discussed. In each discussion, the related experimental data, the proposed function, and the evaluation of the function are presented. Because there is no single set of experimental data that represents the whole cyclic stress-strain relationship of concrete, each section of the proposed functions is evaluated separately with the appropriate set of the experimental data. In the situations where the proper experimental data are not available at the element level, the function is evaluated by comparing certain aspects of the experimental data with the corresponding calculated results from the finite element analyses. For example, experimental data on cyclic shear transfer do not exist at the element level; therefore,



the shear stress function is evaluated by comparing the calculated cyclic shear deformation in complete wall models with the experimental data.

### 3.1 NORMAL STRESS FUNCTION

The normal stress function represents the average stress-strain relationship in concrete in the direction normal to the crack. Because concrete is assumed to remain continuous after cracking, a stress-strain discontinuity across the crack is distributed over the entire concrete element. As a result, the normal stress function represents not only the average stress-strain relationship in intact concrete but also the discontinuity due to cracking. The normal stress function used in the proposed concrete model is based on two major assumptions: 1) Poisson's ratio of cracked concrete is zero and 2) the behavior of cracked concrete is uniaxial in the direction of the crack. In the first assumption, Poisson's ratio of cracked concrete is assumed to be zero because the interaction between the two orthogonal directions is greatly reduced after cracking. This assumption has been adopted in most smeared crack concrete models (136). Some researchers allow concrete to regain Poisson's effect when cracks have been closed (9, 44, 45, 86, 87). However, in this study, Poisson's effect was found to be insignificant in the analysis of reinforced concrete shear walls, and Poisson's ratio for cracked concrete is assumed to be zero throughout the analysis. In the second assumption, concrete is assumed to behave uniaxially in the direction of the crack; it is assumed that the stress in the crack direction depends solely on the strain in that direction. Although this assumption does not take into account the effect of biaxial stress or the reduction of the primary compressive strength due to the normal tensile strain as reported by Stevens et al. (134) and Belarbi and Hsu (22), it satisfactorily represents the average response of concrete in shear walls. The normal stress function is simplified because, based on this assumption, the normal stress function depends only on the stress and strain in one direction. In addition, it also allows the use of uniaxial test results of concrete to validate the concrete model.

In the analysis of the cyclic behavior of reinforced concrete members, the state of stress at an integration point in an individual element can change due to a change in the direction of the ap-

plied loading or to a redistribution of stress due to nonlinear response anywhere in the structure. Therefore, all elements will be subjected to loading, unloading, and reloading during a particular analysis, and the normal stress function must be able to define the stress–strain relationship of any loading sequence. The function must also simulate all the important aspects of behavior of concrete in reinforced concrete shear walls. From observations of the experimental results and comparisons between analytical and experimental results, the important aspects of behavior in reinforced concrete walls include:

- Tension stiffening
- Crack closing and crack reopening
- Compression softening
- Effects of steel confinement
- Degradation of concrete properties with cyclic loading.

All these aspects of behavior compose the complete stress–strain relationship in the direction normal to the crack (Fig. 3.1). Each of the aspects of behavior list above is discussed in the following sections.

### **3.1.1 TENSION STIFFENING**

When reinforced concrete cracks, the concrete between cracks still carries tensile stress which is transferred through bond between the steel bar and the surrounding concrete (Fig. 3.2) (9, 58, 85). Such behavior makes the average stiffness in tension of a reinforcing bar embedded in concrete greater than that of a plain bar (Fig. 3.2) and, hence, is called “tension stiffening.” The tension stiffening behavior is different from the tension softening behavior, which represents the average stress–strain response in the fracture zone of plain concrete after cracking (9, 85). Because the tension stiffening behavior is caused by the interaction between concrete and steel, its characteristics depend on properties of both concrete and steel, such as crack spacing, reinforcement ratio, and interface bond transfer (9). Researchers have used experimental data (22, 116, 130, 143) and mathematical models (58, 66) to study the tension stiffening behavior of reinforced concrete. The results

from these studies exhibit a large amount of scatter (Fig. 3.3). As a result, the stress-strain relationship for tension stiffening has not yet been well defined.

Two approaches have been used to represent the tension stiffening behavior in the finite element analysis of reinforced concrete. In the first approach, the tension stiffening effect is included in the behavior of a reinforcing bar. After cracking, concrete is assumed to carry no tensile stress normal to cracks, and the stress-strain relationship of a reinforcing bar is modified to include the effect of tension stiffening. This approach was first introduced by Gilbert and Warner (60) in the analysis of reinforced concrete slabs, but few other researchers have adopted this approach. In the second approach, the tension stiffening of concrete is included in a concrete element. After concrete cracks, the stress-strain relationship of a reinforcing bar remains the same as that of a plain bar while the tensile stress of concrete normal to the crack, instead of immediately decreasing to zero, gradually decreases to represent the effect of tension stiffening. This approach was first introduced by Scanlon and Murray (121) and has since been used by many other researchers (8, 9, 10, 11, 35, 38, 39, 42, 66, 72, 73, 78, 84, 90, 144, 153). Various types of descending branches of the post-cracking stress-strain curve, ranging from simple bilinear curves to curves combining complicated functions with several parameters, such as reinforcement ratios, crack direction, and bond stress, have been proposed. Despite the differences in their tension stiffening models, most of these researchers agree that the finite element analysis must include the effects of tension stiffening in order to accurately represent the load-deflection curve of the reinforced concrete members, especially when the members are lightly reinforced (35, 69).

In this investigation, the effect of tension stiffening is included in the concrete model. The stress-strain relationship of concrete after cracking is represented by a discontinuous linear unloading model shown in Fig. 3.4. In this model, tensile stress of in the concrete immediately drops from the cracking stress  $\sigma_{cr}$  to a smaller stress  $\alpha\sigma_{cr}$  after cracking. Then, as the tensile strain increases, the tensile stress decreases linearly to a lower-bound stress of  $\sigma_i$  at the tensile strain of  $\epsilon_i$ . The tensile stress then remains constant at  $\sigma_i$ . This discontinuous linear unloading model has been successfully

used by Yamaguchi and Nomura (153) and Inoue et al. (73) in the finite element analyses of reinforced concrete shear walls.

As can be seen in the experimental results of the reinforced concrete panels tested by Vecchio and Collins (143) in Fig. 3.3, the experimental data on tension stiffening behavior have varied widely. Therefore, in the evaluation of the proposed model, no attempt was made to evaluate the tension stiffening of concrete at the element level. The tension stiffening model was evaluated at the structural level by comparing the analytical results and the experimental data from reinforced concrete shear walls. The parameters that define the tension stiffening behavior ( $\alpha$ ,  $\epsilon_i$ , and  $\sigma_i$ ) were adjusted until the calculated load vs. top-deflection curves agreed the experimental data from the PCA wall tests (105,106). The parametric study used to determine the appropriate values for these parameters are discussed in Chapter 6. It can be seen from the finite element results (Fig. 3.5) that tension stiffening has a significant effect on the calculated load-deflection curve for the walls, especially at early stages of the monotonic loading. However, its effect is less significant after reinforcing steel starts yielding or after the walls have been subjected to a few cycles of cyclic loading.

### 3.1.2 CRACK CLOSING AND REOPENING

When reinforced concrete members are subjected to cyclic loading, cracks close and reopen throughout the loading history. As the crack status changes from fully open to fully closed, the stiffness of cracked concrete increases from a value near zero to a value close to the initial modulus of elasticity for concrete ( $E_c$ ). Several researchers (61, 92, 102, 110, 132, 134, 147, 154, 158) report that cracked concrete can transfer compressive stress across cracks even when the cracks remain open. The misalignment of the two opposite crack surfaces allow high spots to come into contact and, hence, start transferring compressive stress. The stiffness of cracked concrete gradually increases as the cracks close. In Fig. 3.6, a typical cyclic stress-strain relationship and a relationship between stress and crack width are presented. These curves have several common characteristics:

- The envelope curve of the cyclic tensile stress-strain relationship can be estimated by the monotonic curve for concrete in uniaxial tension, and the envelope curve of the cyclic compressive

stress-strain relationship can be estimated by the monotonic curve for concrete in uniaxial compression.

- The unloading curve in tension (when cracks are closing) consists of three major regions: the initially stiff region, the softened region, and the stiffened region as show in Fig. 3.6. The curve then merges with the envelope curve in compression at some point in the compressive strain range.

- The reloading curve in tension (when cracks are opening) starts with the same stiffness as the uncracked stiffness of concrete. Then, the curve gradually softens and merges with the envelope curve in tension at some point in the tensile strain range.

In the smeared crack model, most researchers use the strain normal to the crack as the criterion for defining crack closing and reopening. Early researchers, such as Cervenka (33) and Agrawal (3), consider a crack to be fully open when the strain normal to the crack is tensile (positive), and a crack to be fully closed when the strain normal to the crack is compressive (negative). In this approach, the sudden increase in the concrete stiffness as the crack status changes from fully open to fully closed usually causes numerical difficulties in the analysis. As a result, small load increments must be used in order to prevent excessive compressive strain caused by the zero stiffness used in the load step prior to crack closing (3, 33). Darwin and Pecknold (45) were the first to include a gradual increase in concrete stiffness as the cracks closed. However, such an increase in stiffness was not intended to represent the behavior of crack closing, but rather to prevent the numerical problems associated with a sudden increase in the stiffness of cracked concrete. Due to a lack of experimental data to define the cyclic response of cracked concrete, it was not until the late 1980s that the complete stress-strain relationships for cracked concrete were proposed. Researchers who proposed these relationships include Stevens et al. (134), Xu (151), Izumo et al. (75), and Yankelevsky and Reinhardt (155).

In this research, it was found that the simple crack closing and reopening models like the one proposed by Darwin and Pecknold (45) are not sufficient to model the cyclic response of reinforced concrete walls. As a result, the more realistic crack closing and reopening model must be included

in the normal stress function. The characteristics of crack closing and reopening in the proposed model are based on the characteristics of the cyclic response of concrete observed in the experimental data shown in Fig. 3.6 (134, 155).

Typical crack closing and opening rules are described in Fig. 3.7 and 3.8. Cracks are considered to be fully closed when the compressive strain exceeds  $\epsilon_n$  while cracks are considered to be partially open when the strain is between  $\epsilon_n$  and  $\epsilon_i$ . The cracks are considered to be fully open when the tensile strain exceeds  $\epsilon_i$  (Fig. 3.9). At each load step, the cracked concrete is considered to be opening if the incremental strain is tensile and to be closing if the incremental strain is compressive (the convention of positive strains or stresses corresponding to tension is used throughout this investigation). The schemes for defining the stress-strain relationship have been adopted from the Focal Point Model proposed by Yankelevsky and Reinhardt (155). In the proposed model, five focal points,  $(0, \sigma_1)$ ,  $(\epsilon_i, \sigma_2)$ ,  $(\epsilon_i, \sigma_i)$ ,  $(\epsilon_3, \sigma_3)$ ,  $(\epsilon_n, \sigma_n)$ , are used to define the cyclic tensile response of concrete (Fig. 3.9). All these points except  $(\epsilon_n, \sigma_n)$ , which depends on the history of cyclic compressive loadings, are constant throughout all loading cycles. The rules defining crack closing and crack opening in the  $i$  direction can be described as follows:

- $(\epsilon, \sigma)$  represents the strain and stress at the last load step
- $(\epsilon_c, \sigma_c)$  represents the strain and stress at the current load step
- $\epsilon_{\max}^i$  represents the previous maximum tensile strain in the  $i$ -th direction
- $\Delta\epsilon$  represents the incremental strain,  $\epsilon_c - \epsilon$

### **CRACK CLOSING ( $\Delta\epsilon < 0$ )**

The stress-strain curves for crack closing are shown in Fig. 3.7. Three major regions are defined:

**Region 1: Initially Stiff Region** [ when  $\sigma > \sigma_2$  ]: The stress-strain curve is defined by a line connecting  $(\epsilon, \sigma)$  and  $(0, \sigma_1)$ . This curve represents the initial response of concrete when the cracks begin to close. The stiffening becomes less pronounced when the crack closing starts at the larger strain. Region 1 ends when the compressive stress exceeds  $\sigma_2$ .

Region 2: Softened Region [ when  $\sigma = \sigma_2$  and  $\varepsilon > \varepsilon_i$  ]: The stress–strain curve is a horizontal line connecting  $(\varepsilon, \sigma)$  and  $(\varepsilon_i, \sigma_2)$ . In this zone, stress remains constant at  $\sigma_2$ , and the tangent stiffness is zero. This curve represents the closing of fully open cracks. Because the two opposite crack surfaces are widely separated, there is no resistance to closing of the cracks until the tensile strain is reduced to  $\varepsilon_i$  and contact occurs between the two surfaces.

Region 3: Stiffened Region [ when  $\sigma < \sigma_2$  and  $\varepsilon_n < \varepsilon < \varepsilon_i$  ]: The stress–strain curve is a curve connecting  $(\varepsilon, \sigma)$  and  $(\varepsilon_n, \sigma_n)$ . The curve is defined by Eq. (3.1)

$$\frac{\varepsilon_c - \varepsilon_n}{\varepsilon_{os}} = \frac{\sigma_c - \sigma_n}{\sigma_{os}} + \left( \frac{\sigma_c - \sigma_n}{\sigma_{os}} \right)^s \quad (3.1)$$

where

$$s = \left( \frac{E_c}{E_t} - 1 \right) \left( \frac{k_2}{k_1 E_c - k_2} \right)$$

$$\sigma_{os} = \frac{|k_2|^{\frac{s}{s-1}}}{|k_1 E_c - k_2|^{\frac{1}{s-1}}}$$

$$\varepsilon_{os} = \frac{\sigma_{os}}{E_c}$$

$$k_1 = \varepsilon_c - \varepsilon_n$$

$$k_2 = \sigma_c - \sigma_n$$

$E_t$  = the tangent stiffness at the beginning of the unloading curve

$E_c$  = the initial modulus of elasticity for concrete

The values of  $s$  and  $\sigma_{os}$  are defined such that the tangent stiffness at the starting point of the unloading curve (points E, F, and G in Fig. 3.7) is equal to  $E_t$  and the tangent stiffness at the point  $(\varepsilon_n, \sigma_n)$  is equal to  $E_c$ .  $E_t$  is the slope of the line connecting  $(\varepsilon, \sigma)$  and  $(\varepsilon_3, \sigma_3)$ , and  $E_c$  is the initial modulus of elasticity for concrete. This curve represents the gradual increase in the stiffness of cracked concrete that results from crack closing. The curve merges with the envelope curve for concrete under uniaxial compressive stress at  $(\varepsilon_n, \sigma_n)$ .

### **CRACK OPENING ( $\Delta\varepsilon > 0$ )**

The stress–strain curves for crack opening are shown in Fig. 3.8. Each curve consists of four major regions:

Region 1: Initially Stiff Region [ when  $\sigma < \sigma_4$  and  $\varepsilon_n < \varepsilon < \varepsilon_{max}^t$  ]: The stress–strain curve is defined by a line with a tangent stiffness equal to the initial modulus of elasticity for concrete ( $E_c$ ). This curve represents the initially stiff response of cracked concrete when the crack opening occurs.

Region 2: Linear Softening Region I [ when  $\sigma_2 > \sigma > \sigma_4$  and  $\varepsilon_n < \varepsilon < \varepsilon_{max}^t$  ]: The stress–strain curve is defined by a line connecting  $(\varepsilon, \sigma)$  and  $(\varepsilon_{max}^t/2, \sigma_2)$ .

Region 3: Linear Softening Region II [ when  $\sigma > \sigma_2$  and  $\varepsilon_n < \varepsilon < \varepsilon_{max}^t$  ]: The stress–strain curve is a straight line connecting  $(\varepsilon_{max}^t/2, \sigma_2)$  and  $(\varepsilon_{max}^t, \sigma_i)$ .

Region 4: Softened Region [ when  $\sigma = \sigma_i$  and  $\varepsilon_{max}^t < \varepsilon$  ]: The stress–strain curve is defined by a horizontal line where  $\sigma$  is equal to  $\sigma_i$  and the tangent stiffness is zero.

Although some experimental data related to the cyclic response of concrete in tension do exist, they are not in the appropriate form to be used to evaluate the proposed crack closing and reopening functions. For example, the experimental data by Reinhardt and Yankelevsky (155) are presented in term of stress and crack width instead of stress and strain and, hence, are not applicable to the evaluation of the proposed functions. As a result, the proposed crack closing and reopening functions have been evaluated at the structural level. The parameters that define the crack closing and reopening behavior,  $\sigma_1, \sigma_2, \sigma_3, \sigma_4$ , and  $\sigma_n$ , were adjusted so that the calculated response of reinforced concrete walls from the finite element analysis agree with the experimental data from the PCA wall tests (105, 106). The parametric study used to define the appropriate values of these parameters is described in Chapter 6.

### 3.1.3 COMPRESSION SOFTENING

Compression softening represents an observed softening of concrete when it is subjected to high compressive stress. The stress–strain relationship of concrete in uniaxial compression is essentially linear when the concrete is subjected to low compressive stress. As the compressive stress increases, the stress–strain curve of concrete begins to soften gradually until it reaches the compres-



sive strength at the apex of the curve (Fig. 3.10). The compressive stress then starts to decrease with increasing compressive strain. Such degradation in strength represents the accumulated damage in concrete due to large compressive strains (136). Compression softening was found to have a significant effect on the calculated response of reinforced concrete walls, especially when extensive concrete crushing occurs in the boundary elements. Hence, the compression softening behavior must be included in the normal stress function.

Several stress–strain relationships for compression softening behavior in concrete have been proposed during the last four decades. The summary of these relationships can be found in the paper by Popovics (119). In the proposed model, the relationship which was first proposed by Smith and Young (129) and was later used by several other researchers, such as Yankelevsky and Reinhardt (156) and Karsan and Jirsa (79), is adopted for describing the compression softening behavior. This relationship was chosen because it accurately represents the entire stress–strain curve of concrete under uniaxial compression, representing both the ascending and descending portions with one simple function. Furthermore, only concrete strength and the initial concrete stiffness need to be defined. The original relationship has been modified slightly so that the transition between the crack closing curve and the compression softening curve is smooth. Both the crack closing curve and the compression softening curve must have the same tangent stiffness, which is equal to the initial modulus of elasticity for concrete ( $E_c$ ), at the transition point ( $\epsilon_n, \sigma_n$ ) (Fig. 3.10). This relationship can be defined as follows:

$$\text{when } \epsilon > \epsilon_n \quad \sigma = E_c \epsilon \quad (3.2)$$

$$\text{when } \epsilon < \epsilon_n \quad \frac{\sigma - \sigma_n}{\sigma_{oc}} = \frac{\epsilon_c - \epsilon_n}{\epsilon_{oc}} e^{(1 - \frac{\epsilon - \epsilon_n}{\epsilon_{oc}})} \quad (3.3)$$

where

$$\sigma_{oc} = f_{cult} - \sigma_n$$

$$\epsilon_{oc} = \frac{\sigma_{oc} e}{E_c}$$

$f_{cult}$  = the compressive strength of concrete

$E_c$  = the initial modulus of elasticity for concrete

$e$  = the base of the natural logarithms

The terms  $\epsilon_n$  and  $\sigma_n$  are defined in the previous section. The two concrete properties needed to be defined are  $E_c$  and  $f_{cult}$ .

The comparison between the proposed function and experimental data is given in Fig. 3.11. The compression softening curve is used as an envelope curve for unconfined concrete. The rules for unloading and reloading in this region and the effect of cyclic loadings are described in Section 3.1.5.

### 3.1.4 CONFINED CONCRETE

Experimental data clearly indicate that “the strength and ductility of concrete are greatly increased under the condition of triaxial compression” (111). In reinforced concrete members, the condition of triaxial compression exists when concrete is confined by transverse reinforcement, which is usually provided in the form of a closely spaced spiral or tie reinforcement (111). Transverse reinforcement provides passive confinement. When the compressive stress is low, the transverse reinforcement is slightly stressed and, hence, does not provide any confinement for concrete. As a result, the concrete within the transverse reinforcement is unconfined when the compressive stress is low. As the compressive stress approaches the compressive strength of concrete, the transverse steel starts to provide confinement because the crushed concrete is pushed against the transverse steel. This, in turn, creates reaction pressure against the concrete. Experimental data from several investigation have indicated that the confinement provided by transverse reinforcement can significantly increase the strength and ductility of concrete at high compressive stresses (111).

According to the 1989 ACI Building Code (2), transverse reinforcement should be provided in the boundary elements of reinforced concrete shear walls. The transverse reinforcement can be either in the form of closed column ties or spiral reinforcement in accordance with Section 21.4.4 (2). These spirals and closely-spaced ties can provide confinement for concrete in the boundary elements. As a result, the behavior of confined concrete must be included in the normal stress function; otherwise, either the premature crushing of concrete in the confined boundary elements or numerical problems associated with concrete crushing will occur during the analysis.

The analytical model for confined concrete proposed by Shiekh and Uzumeri (125) was adopted in this research. The stress–strain curve for confined concrete is shown in Fig. 3.12. The curve consists of three sections: 1) the uncrushed section, 2) the crush plateau, and 3) the totally crushed section. The uncrushed section has a stress–strain curve that is similar to the compressive stress–strain curve of unconfined concrete prior to crushing. The stress–strain curve is linear with a tangent stiffness equal to the initial modulus of elasticity of concrete ( $E_c$ ) until it reaches the point  $(\epsilon_n, \sigma_n)$ . Then it follows the compression softening curve defined by Eq. 3.3 until the curve reaches the concrete compressive strength  $f_{cult}$ . The value of  $f_{cult}$  is equal to  $k_s f_c'$ , rather than  $f_c'$ , the unconfined compressive strength. The term  $k_s$  represents the increase in the compressive strength resulting from the confinement. After reaching  $f_{cult}$ , the stress–strain curve enters the crush plateau where the compressive stress remains constant at  $f_{cult}$  until the compressive strain reaches  $\epsilon_2$ . When the compressive strain exceeds  $\epsilon_2$ , the stress–strain curve is in the totally crushed section. The curve descends linearly from  $(\epsilon_2, f_{cult})$  to  $(\epsilon_{85}, 0.85 \cdot f_{cult})$  and remains on this line until the compressive stress reaches  $0.30 \cdot f_{cult}$ . For larger compressive strains, the compressive stress remains constant at  $0.30 \cdot f_{cult}$ .

In the proposed analytical model for confined concrete, three parameters ( $k_s$ ,  $\epsilon_2$ , and  $\epsilon_{85}$ ) have to be defined. The values of these parameters depend on several factors such as the volumetric transverse reinforcement ratio, tie spacing, characteristics of reinforcing steel, and the distribution of the longitudinal steel around the core concrete perimeter. The procedures for calculating these parameters are described in Appendix B.

### **3.1.5 DEGRADATION OF CONCRETE PROPERTIES UNDER CYCLIC LOADINGS**

Because the primary objective of this research is to study the cyclic response of reinforced concrete shear walls, the normal stress function must include the degradation of strength due to cyclic loading. The cyclic stress–strain relationship for concrete in the proposed model is based on the experimental work by Karsan and Jirsa (79) and Sinha et al. (128). Parts of the algorithm used

to define the cyclic stress–strain relationship in the proposed model are adopted from the model for cyclic behavior of concrete proposed by Yankelevsky and Reinhardt (156):

The typical compressive cyclic stress–strain relationship used in the proposed concrete model is shown in Fig. 3.13. The rules for defining this relationship are based on two curves: an envelope curve and a common point curve. The envelope curve defines the boundary of the permissible stress–strain loci; the stress–strain curve must always lie within the area enclosed by the envelope curve and the strain axis. The envelope curve is represented by the uniaxial stress–strain curve of concrete under monotonic compressive loading. Each point on the common point curve,  $(\epsilon_{cp}, \sigma_{cp})$ , represents the focal point of the reloading curve in compression whose previous maximum compressive strain at the beginning of the reloading curve was equal to  $\epsilon_{cp}$ . The common point curve is defined in Eq. 3.4.

$$\sigma_{cp} = \sigma_n + 0.85 * \left[ \sigma_{oc} \frac{\epsilon_{cp} - \epsilon_n}{\epsilon_{oc}} e^{1 - \frac{\epsilon_{cp} - \epsilon_n}{\epsilon_{oc}}} \right] \quad (3.4)$$

where

$(\epsilon_{cp}, \sigma_{cp})$  are strain and stress on the common point curve

$(\epsilon_n, \sigma_n)$  are parameters for the concrete model

$(\epsilon_{oc}, \sigma_{oc})$  are defined in Section 3.1.3.

The rules for loading and unloading in compression are shown in Fig. 3.14. The unloading curve consists of three major regions: the initial unloading (D–E), the softening unloading (E–F), and the zero–stress unloading (F–G). The initial unloading curve is a line with the slope  $E_c$ . The curve can start from any point on or below the envelope curve. It ends at the point where the compressive stress reaches  $0.30 f_{cult}$ . The softening unloading curve is a line connecting the end of the initial unloading curve and the point  $(\epsilon_p, 0)$  on the strain axis. Strain  $\epsilon_p$  represents the permanent compressive strain in the current load cycle. The value of  $\epsilon_p$  is calculated by using Eq. 3.5 and 3.6, which were proposed by Yankelevsky and Reinhardt (156).

$$\varepsilon_p = \frac{\varepsilon_{ult} [1.0 - 0.425e^{(1-s)}]}{1 - (s e^{(1-s)})} \quad (3.5)$$

$$\text{if } \varepsilon_p < 0.70 \cdot \varepsilon_{\max}^c \quad \varepsilon_p = 0.70 \cdot \varepsilon_{\max}^c \quad (3.6)$$

when  $s = \frac{\varepsilon_{\max}^c}{\varepsilon_{ult}}$   
 $\varepsilon_{ult} =$  the compressive strain at the compressive strength of concrete,  $f_{c,ult}$   
 $\varepsilon_{\max}^c =$  the previous maximum compressive strain

The zero-stress unloading curve starts from the point  $(\varepsilon_p, 0)$  and then follows the strain axis. Once the curve reaches the origin, it follows the unloading curve of concrete in tension.

The reloading curve in compression consists of three regions: the initial reloading (A–B, G–H), the softening reloading (B–C, H–I), and the envelope curve (C–D, I–J). The initial reloading curve is a line connecting the starting point of the reloading curve and the point on the common point curve with a strain equal to the previous maximum compressive strain,  $\varepsilon_{\max}^c$ . The curve ends when it intersects the common point curve. The softening reloading curve is a line that starts at the end of the initial reloading curve and has the slope of  $0.10 E_c$ . The softened reloading curve ends when it reaches the envelope curve. Then the reloading curve follows the envelope curve. The rules for these cyclic unloading and reloading curves are described in Appendix C. Comparisons between the proposed cyclic model and experimental results are shown in Fig. 3.15 through 3.17.

All previous experimental work on the cyclic compressive behavior of concrete applies to unconfined concrete. Information on the cyclic compressive response of confined concrete was not available in the literature. Therefore, the approach used to define the monotonic stress–strain relationship for confined concrete (Section 3.1.4 and Fig. 3.12) and the loading and unloading curves used to define the cyclic stress–strain relationship of unconfined concrete are used to define the cyclic stress–strain relationship for confined concrete.

As shown in Fig. 3.18, the reloading curve in compression for confined concrete consists of three regions: the initial reloading (E–F), the softening reloading (F–G), and the crush plateau (A–B,

G–H–I). The initial reloading curve and the softening reloading curve are the same as those for unconfined concrete. The initial reloading curve (E–F) is a line connecting the starting point of the reloading curve and the point on the common point curve with a strain equal to the previous maximum compressive strain,  $\varepsilon_{\max}^c$  (point F). The curve ends when it intersects the common point curve (the common point curve is defined in Eq. 3.4). The softening reloading curve is a line that starts at the end of the initial reloading curve and has the slope of  $0.10 E_c$  (point F). The softened reloading curve ends when it reaches the envelope curve (point G). Then, instead of following the enveloped curve as the stress–strain for unconfined concrete, the reloading curve remains horizontal until unloading occurs (point B) or until the strain reaches  $\varepsilon_2$  (point H). If the compressive strain exceeds  $\varepsilon_2$ , the curve descends linearly from  $(\varepsilon_2, \sigma_G)$  to  $(\varepsilon_{85}, 0.85 \cdot \sigma_G)$  ( $\sigma_G$  is the compressive stress when the compressive strain is equal to  $\varepsilon_2$ ) and remains on this line until the compressive stress reaches  $0.30 \cdot f_{\text{cult}}$ . For larger compressive strains, the compressive stress remains constant at  $0.30 \cdot f_{\text{cult}}$ . The reloading curve in this region is similar to the monotonic stress–strain relationship for confined concrete after concrete has crushed (Fig. 3.12).

The unloading curves for confined concrete are the same as those for unconfined concrete and consist of three regions: the initial unloading (B–C, I–J), the softening unloading (C–D, J–K), and the zero–stress unloading (D–E). The initial unloading curve starts with the tangent stiffness equal to the initial modulus of elasticity for concrete ( $E_c$ ) (B–C, I–J) and continues until the compressive stress reaches  $0.30 \cdot f_{\text{cult}}$ . Then, the curve is a line connecting the end of the initial unloading curve and the point  $(\varepsilon_p, 0)$  (points D and K), where  $\varepsilon_p$  is defined in Eq. 3.5. The zero–stress unloading curve starts from the point  $(\varepsilon_p, 0)$  and then follows the strain axis. Once the curve reaches the origin, it follows the unloading curve of concrete in tension. The cyclic stress–strain relationship of unconfined and confined concrete subjected to the same strain history is shown in Fig. 3.19.

It can be seen that confined concrete is more ductile than unconfined concrete, and, hence, has better energy dissipation characteristics.

In the analysis of reinforced concrete walls in this investigation, strength degradation due to compressive cyclic loadings has an insignificant influence on the overall behavior of the structure because only a few concrete elements experience crushing during a typical analysis. However, incorporation of the cyclic loading effect does facilitate identification of certain failure modes because progressive crushing of the concrete in the boundary elements and adjacent web elements can be modelled.

### **3.2 SHEAR STRESS FUNCTION**

The shear transfer mechanism in cracked concrete has been investigated by several researchers during the last three decades. Most of the early experimental work related to shear transfer investigated the behavior of both reinforced and unreinforced concrete specimens that had a single crack and were subjected to monotonic loadings. The results of this work were used to develop design equations for shear transfer in reinforced concrete structures. Therefore, the researchers concentrated on investigating the strength rather than the stiffness of the shear transfer mechanism. Few researchers investigated the cyclic shear transfer behavior of reinforced concrete members because such experimental work requires a very complicated test set-up. Recent research on the cyclic shear transfer behavior of reinforced concrete panels was conducted by Stevens et al. at the University of Toronto (134).

Most of the analytical models for shear transfer in reinforced concrete that were proposed during the 70s and the 80s were intended to simulate the shear transfer behavior of reinforced concrete specimens with single cracks. These models commonly used three parameters: the crack width, the shear slip, and the area of the reinforcing steel. In the finite element analysis of reinforced concrete, such an approach might be applicable for the discrete crack model because a crack in concrete is treated as a separation between nodes. However, the method is not directly applicable for the smeared crack model because cracks are considered to be uniformly distributed in the smeared crack model and concrete is assumed to remain continuous after cracking. Therefore, the normal

crack strain, the shear strain, and the steel reinforcement ratio are reasonable parameters for defining the shear stress function in a smeared cracking model.

In the smeared crack model, two approaches have been used to represent the shear stiffness of cracked concrete: the reduced shear stiffness approach and the varied shear stiffness approach. In the reduced shear stiffness approach, the value of the uncracked shear stiffness is reduced by a factor after concrete cracks to account for the remaining capacity of cracked concrete to carry shear stress by aggregate interlock. Most of the early investigators who used smeared crack models adopted this approach (3, 11, 15, 26, 38, 42, 44, 65, 71, 72, 84, 97, 135, 153), and reduction factors ranging from 0.0 to 0.50 were used. In the varied shear stiffness approach, the shear stiffness of cracked concrete is assumed to be a function of the strain normal to the crack direction. This approach was first introduced by Cedolin and Dei Poli (15) in 1977. In their model, Cedolin and Dei Poli assume that the cracked shear stiffness is assumed to decrease linearly with an increase in the normal crack strain. Subsequently, several other researchers, such as Al-Mahaidi (7), Balakrishnan and Murray (9), Sotomura and Murazumi (131), Ueda and Kawai (139), and Cervenka (35), also adopted this approach and proposed several different functions to represent the shear stiffness of cracked concrete. Both the reduced shear stiffness approach and the varied shear stiffness approach yield satisfactory results for most analyses of reinforced concrete members subjected to monotonic loading. However, they are inadequate for problems where cyclic shear deformations govern the response. The shear transfer mechanisms for cracked concrete in these problems are much more complicated than assumed in either of these approaches.

In order to model correctly the cyclic shear response of reinforced concrete walls, the shear stress function in the concrete model must include all the important characteristics of the cyclic shear behavior observed in the walls. The model must also be simple so that convergence of the solution can be obtained without requiring a large amount of computation time. This makes analysis of structural level problems both feasible and practical. In the proposed model, the shear stiffness of cracked concrete is divided into two components:



- 1)  $G_{ist}$ : Shear stiffness from the aggregate interlock or the interface shear transfer (IST)
- 2)  $G_{dow}$ : Shear stiffness from the dowel action

The total shear stiffness ( $G$ ) can be written as follows:

$$G = G_{ist} + G_{dow} \quad (3.7)$$

These two components of shear stiffness and the effect of cyclic shear loading are described in the following sections.

### 3.2.1 SHEAR STIFFNESS DUE TO INTERFACE SHEAR TRANSFER

The surfaces of concrete cracks are rough and produce resistance when moved against each other (Fig. 3.20). Several researchers (68, 77, 82, 94, 114, 137, 138, 145) have investigated interface shear transfer in concrete specimens with a single crack. Variables studied included initial crack width, concrete strength, aggregate size, normal restraining stiffness, shear stress intensity, and cyclic shear stress. Of all these variables, the initial crack width was identified as having the most influence on the interface shear transfer mechanism of cracked concrete. The shear stiffness from interface shear transfer increases when the crack width decreases. Although several empirical formulas for calculating interface shear stiffness were proposed in these investigations, they all describe the relationship between the applied shear stress and the slip at the crack, and hence are not directly applicable to the interface shear stiffness in the smeared crack model.

In the proposed concrete model,  $G_{ist}$  is defined as follows:

$$G_{ist} = 2.0 \cdot \left[ \frac{1}{G_{ist}^1} + \frac{1}{G_{ist}^2} \right]^{-1} \quad (3.8)$$

where

$G_{ist}^1$  is the interface shear transfer stiffness in crack direction 1

$G_{ist}^2$  is the interface shear transfer stiffness in crack direction 2

The interface shear transfer stiffness is represented in the form that was first introduced by Buyukozturk et al. (28, 55) and is described in Eq. 3.9. (Fig. 3.21)

$$\begin{aligned}
 G_{ist}^i &= \mu_1 G_{conc} & \varepsilon_{nn}^i < \varepsilon_{cr} \\
 G_{ist}^i &= \frac{\mu_1 [\varepsilon_{min} - \varepsilon_{nn}^i]}{[\varepsilon_{min} - \varepsilon_{cr}]} G_{conc} & \varepsilon_{cr} \leq \varepsilon_{nn}^i < \varepsilon_{min} \\
 G_{ist}^i &= G_{min} & \varepsilon_{min} \leq \varepsilon_{nn}^i
 \end{aligned} \tag{3.9}$$

where	$\mu_1$	=	Parameter used to relate interface shear transfer stiffness to shear stiffness of uncracked concrete
	$\varepsilon_{nn}^i$	=	The normal crack strain in $i$ direction
	$\varepsilon_{cr}$	=	The tensile strain when concrete cracks
	$\varepsilon_{min}$	=	The normal crack strain where $G_{ist}^i = G_{min}$
	$G_{min}$	=	The minimum value of $G_{ist}^i$
	$G_{conc}$	=	The shear stiffness of uncracked concrete $\left( \frac{E_c}{2 [1 + \nu]} \right)$
	$E_c$	=	The initial modulus of elasticity for concrete
	$\nu$	=	Poisson's ratio for uncracked concrete

In this model, two parameters need to be defined:  $\mu_1$  and  $\varepsilon_{min}$ .  $G_{min}$  is used to set a limit for the minimum value of  $G_{ist}$ , because numerical problems can occur if  $G_{ist}$  is set to 0. The value of 0.0005  $G_{conc}$  is used for  $G_{min}$  in the proposed model.

### 3.2.2 SHEAR STIFFNESS DUE TO DOWEL ACTION

Reinforcing bars that pass through cracks in concrete provide stiffness through dowel action by the combination of three mechanisms: flexure, shear, and kinking (115) as shown in Fig. 3.22. The dowel action mechanisms have been investigated by Dulacska (52), Mattock (93), Paulay et al. (115), Jimenez et al. (77), and Laible et al. (82). Some important observations from these experimental investigations are described as follows:

- Dowel action exhibits a hardening type behavior; shear stiffness from dowel action increases with increasing shear deformation. At small shear deformations, dowel stiffness depends mostly on the shear and the flexural stiffness of the bar, because the part of the bar near the crack does not yet fully push against the surrounding concrete. When the shear deformation increases, the reinforcing bar starts to push against the surrounding concrete and the dowel action stiffness increases (Fig. 3.23). This behavior can be observed in several experimental results as shown in Fig. 3.24.

- Most researchers studied the shear strength rather than the shear stiffness of the dowel action. There are a few analytical models proposed for the dowel action stiffness, most of which use a beam on the elastic foundation approach to model the dowel action. A linear relationship is usually assumed between the dowel action stiffness and the diameter of the reinforcing bar.

Based on these observations, the model for dowel action stiffness is proposed as follows:

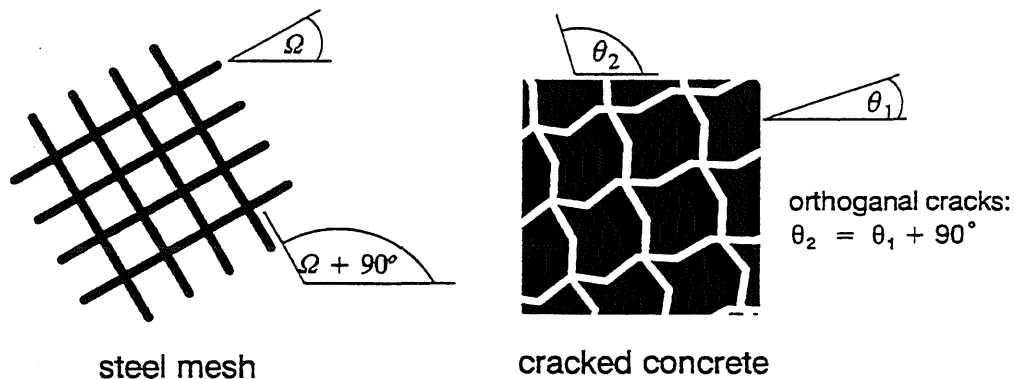
$$G_{dow} = 2.0 \cdot \left[ \frac{1}{G_{dow}^1} + \frac{1}{G_{dow}^2} \right]^{-1} \quad (3.10)$$

where  $G_{dow}^1$  is the dowel action stiffness in crack direction 1  
 $G_{dow}^2$  is the dowel action stiffness in crack direction 2

The model should include two important characteristics: an increase in dowel action stiffness as the shear strain increases and a linear relationship between the dowel action stiffness and the diameter of the reinforcing bar. The dowel action stiffness in crack direction  $i$ ,  $G_{dow}^i$ , is proposed in the following form (Fig. 3.25):

$$\begin{aligned}
 G_{dow}^i &= G_{\min} & |\gamma| < |\gamma_i| \\
 G_{dow}^i &= f(\theta_i, \Omega, r_1, r_2) \left| \frac{\gamma - \gamma_i}{\gamma_n} \right|^n & |\gamma_i| \leq |\gamma| < |\gamma_n + \gamma_i| \\
 G_{dow}^i &= f(\theta_i, \Omega, r_1, r_2) & |\gamma_n + \gamma_i| \leq |\gamma|
 \end{aligned} \tag{3.11}$$

- where
- $\gamma$  = shear strain
  - $\gamma_i$  = A parameter that includes influence of shear reversals and is defined in Section 3.2.3.
  - $\gamma_n, n$  = the constants to be defined
  - $f(\theta_i, \Omega, r_1, r_2)$  = the function representing the effects of the bar diameter and the directions of reinforcing bars
  - $\theta_i$  = the crack angle in  $i$  direction
  - $\Omega$  = the angle of steel reinforcement
  - $r_1 = \frac{\rho_{s1}}{\phi_{s1}}$  = the steel reinforcement ratio in direction 1 / bar diameter (in.)
  - $r_2 = \frac{\rho_{s2}}{\phi_{s2}}$  = the steel reinforcement ratio in direction 2 / bar diameter (in.)



$f(\theta_i, \Omega, r_1, r_2)$  is proposed in the following form:

$$f(\theta_i, \Omega, r_1, r_2) = (r_1 |\sin(\Omega - \theta_i)| + r_2 |\cos(\Omega - \theta_i)|) \mu_2 G_{conc} \quad (3.12)$$

where

$\mu_2$	=	Parameter used to relate dowel action stiffness to shear stiffness of uncracked concrete
$G_{conc}$	=	The shear stiffness of uncracked concrete $\left( \frac{E_c}{2[1 + \nu]} \right)$
$E_c$	=	The initial modulus of elasticity for concrete
$\nu$	=	Poisson's ratio for uncracked concrete

substituting Eq. 3.12 into Eq. 3.11 and 3.10 (for both crack directions  $i = 1, 2$ ) yields:

$$G_{dow} = G_{min} \quad |\gamma| < |\gamma_i|$$

$$G_{dow} = 2 \cdot \left[ \frac{[r_1^2 + r_2^2] sc + r_1 r_2}{(r_1 + r_2)(s + c)} \right] \mu_2 G_{conc} \left| \frac{\gamma - \gamma_i}{\gamma_n} \right|^n \quad |\gamma_i| \leq |\gamma| < |\gamma_n + \gamma_i| \quad (3.13)$$

$$G_{dow} = 2 \cdot \left[ \frac{[r_1^2 + r_2^2] sc + r_1 r_2}{(r_1 + r_2)(s + c)} \right] \mu_2 G_{conc} \quad |\gamma_n + \gamma_i| \leq |\gamma|$$

where

$s$	=	$ \sin(\Omega - \theta_1) $
$c$	=	$ \cos(\Omega - \theta_1) $

The use of  $\frac{\rho}{\phi}$  as a parameter in the dowel action stiffness is based on the analytical models proposed by Elliot (53) and Stanton (133), in which the dowel stiffness of a single bar varied linearly with its diameter. Therefore, the dowel action stiffness for a group of  $n$  bars should also vary linearly with  $n\Phi$  ( $\Phi$  = diameter of reinforcing bar). However,  $n\Phi$  is not an appropriate parameter because  $n$  cannot be defined at each crack in the smeared crack model. Hence, the value of  $\frac{\rho}{\phi}$ , which is direct-

ly related to  $n\Phi$  ( $\frac{\rho}{\phi} = \frac{n\pi\phi^2}{4A_c\phi} = \frac{\pi}{4A_c}n\phi$ ), is used instead.

In the dowel action stiffness model, three parameters must be defined:  $\mu_2$ ,  $\gamma_n$ , and  $n$ . The function of  $G_{min}$  is the same as that of  $G_{min}$  used for the interface shear transfer stiffness, and therefore the value of  $0.0005 G_{conc}$  is used again.

### 3.2.3 EFFECT OF CYCLIC LOADING

The shear transfer mechanisms for both reinforced and unreinforced concrete subjected to cyclic loadings have been investigated by several researchers: Paulay et al. (115), White and Holley (145), Laible et al. (82), Mattock (93), Paulay and Loeber (114), Jimenez et al. (76), and Stevens et al. (134). Most of these researchers investigated the cyclic shear transfer behavior of concrete specimens with a single crack. Only Stevens et al. (134) studied the behavior of reinforced concrete panels subjected to cyclic shear loadings. Although the detailed setup of each experimental test series was different, all research identified similar aspects of behavior for cyclic shear transfer in cracked concrete (Fig. 3.26):

- The load vs shear slip curves or shear stress vs shear strain curves consist of three parts: loading, unloading, and slip. (Fig. 3.26(a)).
- The unloading stiffness is higher than the loading stiffness. The unloading stiffness seems to be independent of the loading history and remains constant throughout the duration of the test.
- Permanent shear displacement or permanent shear strain increases as the number of cycles increases.

Although several researchers investigated the cyclic shear transfer behavior of reinforced concrete, few proposed analytical models for such behavior. In the model proposed by Stevens et al. (134), the cyclic shear transfer behavior is implicitly defined by the assumption that the direction of principal stress coincides with the direction of the principal strain. Xu (151) proposed a model in which shear transfer behavior is defined in the crack coordinate as shown in Fig. 3.27(a). Jimenez et al. (77) also proposed the hysteresis curve for the interface shear transfer mechanism that is shown in Fig. 3.27(b). The proposed model is qualitatively similar to Xu's model.

The proposed cyclic shear transfer model was based on observations from the experimental results and from the analytical models proposed by other researchers (Fig. 3.26 and 3.27). As shown in Fig. 3.28, the relationship between shear stress and shear strain consists of three regions: loading, unloading, and slip. In loading region (curves B–C and E–F), the relationship between shear stress and shear strain depends on the current total shear stiffness,  $G$ , which is based on the interface shear transfer stiffness and the dowel action stiffness as defined in Eq. 3.7. The unloading region (lines C–D and F–G) is defined by a line originating at the point where the incremental shear strain starts going in the opposite direction with a constant shear stiffness of  $G_{unl}$ . The unloading region ends when the unloading line intersects the strain axis (points A, D, and G). The slip region (lines D–E and A–B) connects the point where the unloading line intersects the strain axis and point  $(\beta \cdot \gamma_{max}^+, \tau_{slip})$  or point  $(\beta \cdot \gamma_{max}^-, -\tau_{slip})$  depending on the direction of loading.  $\gamma_{max}^+$  is the previous maximum positive shear strain where the previous unloading curves intersect the strain axis (point D) while  $\gamma_{max}^-$  is a previous maximum negative shear strain where the previous unloading curves intersect the strain axis (point A).

Two parameters for the cyclic shear behavior that need to be defined are  $\beta$  and  $\tau_{slip}$ .  $\beta$  and  $\tau_{slip}$  are used to define points  $(\beta \cdot \gamma_{max}^+, \tau_{slip})$  and  $(\beta \cdot \gamma_{max}^-, -\tau_{slip})$  which govern the stiffness of the slip region (lines A–B and D–E). A large value of  $\tau_{slip}$  results in a high shear stiffness in the slip region while a large value of  $\beta$  causes the slip region to be wide and the loading region (curves B–C and E–F) to start at larger shear strain. The parametric study used to define the appropriate values of these two parameters is described in Chapter 6.

### 3.3 SUMMARY

The material model for concrete consists of two functions: the normal stress function and the shear stress function. The normal stress function defines the stress–strain relationship of cracked concrete in the direction of the crack. The important aspects of the behavior of concrete that are included in the normal stress function are tension stiffening, crack closing and reopening, compression softening, effects of transverse reinforcement, and the strength and stiffness degradation due

to cyclic compressive loadings. The shear stress function represents the relationship between shear stress and shear strain of cracked concrete. The important aspects of the shear transfer mechanisms that are included in the shear stress function are the interface shear stiffness, the dowel action stiffness, and the loading and unloading rules for cyclic shear loadings.

Parameters for the normal stress function include  $\varepsilon_i$ ,  $\sigma_i$ ,  $\alpha$ ,  $\sigma_1$ ,  $\sigma_2$ ,  $\sigma_3$ ,  $\sigma_4$ , and,  $\sigma_n$  while parameters for the shear stress function include  $\mu_1$ ,  $\mu_2$ ,  $\varepsilon_{min}$ ,  $\gamma_n$ ,  $n$ ,  $\tau_{slip}$ ,  $G_{unl}$ ,  $\beta$ , and  $G_{min}$ . The parametric study used to define the appropriate values of these parameters is described in Chapter 6.



used other mathematical expressions to represent the cyclic response of reinforcing steel. Despite the differences in the formulations, all of these mathematical expressions have the two important characteristics of reinforcing steel in common: nonlinearity and history dependency.

## 4.2 PROPOSED STEEL MODEL

After trials with several different mathematical expressions, the Ramberg–Osgood equation was found to yield the most satisfactory results, based on both the accuracy of the model and the stability of the analysis. Therefore, the R–O equation was adopted to represent the cyclic stress–strain relationship of reinforcing steel in this research. The cyclic stress–strain relationship consists of three portions: the monotonic curve, the envelope curve, and the curve that controls load reversals from the yield plateau.

### 4.2.1 MONOTONIC CURVE

The monotonic curve consists of three regions as shown in Fig 4.2: the linear region (A–B), the yield plateau (B–C), and the strain–hardening region (C–D). The linear region and the yield plateau region represent the elasto–plastic behavior of reinforcing steel. The initial stress–strain curve is linear elastic with the slope  $E_s$  until it reaches the yield stress  $\sigma_y$ . Then, the curve becomes plastic until the strain reaches the strain–hardening region at  $\epsilon_{sh}$ . However, the zero stiffness of the yield plateau region usually causes numerical difficulties during the analysis; hence, a small value of the tangent stiffness ( $0.0001 \cdot E_s$ ) is used instead. The strain–hardening region starts at  $(\epsilon_{sh}, \sigma_y)$ . The R–O equation for the strain–hardening proposed by Aktan et al. (5) is adopted to represent the strain–hardening region of the proposed steel model (Eq. 4.2).

$$\frac{\epsilon}{\epsilon_{om}} = \frac{\sigma}{\sigma_{om}} + \left[ \frac{\sigma}{\sigma_{om}} \right]^m \quad (4.2)$$

$$\epsilon_{om} = \frac{\sigma_{om}}{E_s} \quad \sigma_{om}, m = \text{two parameters to be defined}$$

The values of  $\sigma_{om}$  and  $m$  can be taken from the values recommended in the report by Aktan et al. (5) or can be calculated such that the strain–hardening curve matches the available monotonic

The cyclic behavior of the reinforcing steel in the subsequent load cycles is greatly influenced by the previous strain history. As a result, an analytical model for the cyclic behavior of reinforcing steel must be able to represent the initial monotonic loading behavior, the nonlinear stress-strain relationship due to the Bauschinger effects, and the history dependent characteristics of the reinforcing steel.

The cyclic behavior of reinforcing steel was first studied experimentally by Singh et al. (127) in 1965, and several subsequent studies were conducted by Aktan et al. (5), Kent and Park (80), Seckin (124), and Ma et al. (89). The experimental results from these studies were later used by many researchers as the basis for the development of their reinforcing steel models. The approach that has been most widely used to represent the cyclic stress-strain relationship of reinforcing steel is based on the Ramberg-Osgood (R-O) equation. Although the equation was not originally intended to be applied for the cyclic behavior of reinforcing steel, it possesses the two important characteristics of the cyclic loading curve: the initially linear behavior with the slope  $E_s$  and the subsequently softening behavior with increasing strain. The R-O equation can be written in the following form (5):

$$\varepsilon - \varepsilon_i = \frac{\sigma - \sigma_i}{E_s} \left[ 1 + \left| \frac{\sigma - \sigma_i}{\sigma_o - \sigma_i} \right|^{\alpha-1} \right] \quad (4.1)$$

where

$(\varepsilon_i, \sigma_i)$	=	the strain and stress at the beginning of the curve
$E_s$	=	the initial modulus of elasticity of reinforcing steel
$\sigma_o, \alpha$	=	the parameters to be defined

Because the cyclic stress-strain relationship of reinforcing steel is strongly influenced by the strain history, the values of the parameters  $\sigma_o$  and  $\alpha$  depend not only on the initial properties of the reinforcing steel but also on the previous stress-strain history of the steel (80). With the proper values of these two parameters, the response of reinforcing steel calculated using the R-O equation is in good agreement with the experimental results (5, 80, 89, 109, 118). Besides the R-O equation, some researchers, such as Singh et al. (127), Xu (151), and Stevens et al. (134), have successfully

$$\frac{\varepsilon - \varepsilon_i}{\varepsilon_o} = \frac{\sigma - \sigma_i}{\sigma_o} + \left| \frac{\sigma - \sigma_i}{\sigma_o} \right|^\alpha \quad \text{when } (\sigma - \sigma_i) \geq 0 \quad (4.5)$$

$$\frac{\varepsilon - \varepsilon_i}{\varepsilon_o} = \frac{\sigma - \sigma_i}{\sigma_o} - \left| \frac{\sigma - \sigma_i}{\sigma_o} \right|^\alpha \quad \text{when } (\sigma - \sigma_i) < 0 \quad (4.6)$$

where

$$\varepsilon_o = \frac{\sigma_o}{E_s}$$

$(\varepsilon_i, \sigma_i)$  = strain and stress at the beginning of the current 1/2 cycle

$\sigma_o, \alpha$  = parameters to be defined

$E_s$  = the initial modulus of elasticity for the reinforcing bar

The parameters  $\sigma_o$  and  $\alpha$  reflect the history dependency of the cyclic behavior of reinforcing steel. The values of these two parameters depend on both the initial point of the current half cycle and the stress-strain history of the previous half cycles. Two different methods are used to calculate the parameters  $\sigma_o$  and  $\alpha$  of each half cycle depending on the location where the load reversal occurs on the current half cycle. The first method, which explicitly defines  $\sigma_o$  and  $\alpha$ , is used when the magnitude of the initial stress,  $\sigma_i$ , is greater than the magnitude of the previous maximum stress ( $\sigma_{\max}$ )<sup>1</sup>. The second method, which uses the concept of “a common point” and “an ultimate point,” is used when the magnitude of the initial stress,  $\sigma_i$ , is less than the magnitude of the previous maximum stress. The details of each method are described as follows:

#### Method 1: When $|\sigma_i| > |\sigma_{\max}|$

When the unloading curve occurs at an initial stress that is greater than the previous maximum tensile stress or is less than the previous maximum compressive stress,  $\sigma_o$  and  $\alpha$  for Grade 60 reinforcing bar maybe calculated explicitly using the following equation:

<sup>1</sup> The previous maximum stress ( $\sigma_{\max}$ ) is the previous maximum compressive stress when  $\sigma_i$  is in compression and is the previous maximum tensile stress when  $\sigma_i$  is in tension

test results for the particular reinforcing steel. For the latter approach, two points on the strain-hardening curve,  $(\epsilon_{sh}, \sigma_y)$  and  $(\epsilon_2, \sigma_2)$ , are used to calculate  $\sigma_{om}$  and  $m$  as follows:

$$m = \ln \left[ \frac{\epsilon_{sh} E_1 - \sigma_y}{\epsilon_2 E_2 - \sigma_2} \right] \frac{1}{\ln \frac{\sigma_y}{\sigma_2}} \quad (4.3)$$

$$\sigma_{om} = \frac{\sigma_y}{e^{\frac{\ln \left( \frac{\epsilon_{sh}}{\epsilon_2} - 1 \right)}{m-1}}} \quad (4.4)$$

where  $(\epsilon_{sh}, \sigma_y)$  is the starting point of the strain-hardening curve  
 $(\epsilon_2, \sigma_2)$  is an arbitrary point on the strain-hardening curve  
 $E_1$  and  $E_2$  are the tangent stiffnesses at  $(\epsilon_{sh}, \sigma_y)$  and  $(\epsilon_2, \sigma_2)$  respectively.

Aktan et al. (5) recommended values of  $m = 4.30$  and  $\sigma_{om} = 0.70 \cdot \sigma_y$  based on the observed properties of reinforcing steel with a modulus of elasticity of 29,000 ksi and the yield strength of 60 ksi. In the analysis of reinforced concrete shear walls in this research, the values of  $\sigma_{om}$  and  $m$  were calculated according to the available experimental data for each type of reinforcing bar.

## 4.2.2 ENVELOPE CURVES

Typical envelope curves for the cyclic stress-strain relationship of steel using the proposed model are shown in Fig. 4.3. A complete stress-strain cycle (A-B-C) consists of two half cycles: a half cycle from tension (A-B) and a half cycle from compression (B-C). Each half cycle starts with an initial point  $(\epsilon_i, \sigma_i)$  and with a stiffness equal to the initial modulus of elasticity for reinforcing steel ( $E_s$ ). The R-O equation is used to represent the stress-strain relationship of each half cycle (Eq. 4.5 and Eq. 4.6).

ments experience symmetrical load reversals. Therefore, their behavior is governed by envelope curves defined using this method (Fig. 4.5).

Method 2: When  $|\sigma_i| < |\sigma_{\max}|$

The values of  $\sigma_o$  and  $\alpha$  from Eq. 4.8 yield satisfactory cyclic response for reinforcing steel when the load cycles are symmetrical, and the strain gradually increases between subsequent cycles. However, when the load cycles are highly unsymmetrical, or when unloading occurs at a low initial stress, the use of  $\sigma_o$  and  $\alpha$  from Eq. 4.8 usually results in an incorrect representation of the cyclic response of a reinforcing bar. As a result, another algorithm for calculating  $\sigma_o$  and  $\alpha$  in those unsymmetrical unloading cases is required. Such an algorithm is based on the following observations from the cyclic response of the reinforcing bars tested by Aktan et al. (5).

- In a half cycle with an initial stress ( $\sigma_i$ ) that is less than the previous maximum stress ( $\sigma_{\max}$ ), a stress-strain curve will merge with and follow the previous half cycle of loading in the same direction.
- A cyclic stress-strain curve is bounded by the tensile and the compressive strength of the bar. When the stress in the half cycle approaches the strength of the steel, the stress-strain curve tends to flatten so that the stress does not exceed either of these two limits.

These two observations led to the concepts of “common points” and “ultimate points.” The definitions of common and ultimate points for a half cycle from tension are shown in Fig 4.6(a) while those for a half cycle from compression are shown in Fig. 4.6(b). In Fig. 4.6(a), a common point for a half cycle from tension (curve C-E) is defined by point D. D is the point on the curve defined during the previous half cycle from tension (curve A-B) at strain equal to  $\epsilon_B - 0.01$  ( $\epsilon_B$  is the strain at the end of half cycle A-B). In Fig. 4.6(b), a common point for a half cycle from compression (curve H-J) is defined by point I. I is the point on the curve defined during the previous half cycle from compression (curve F-G) at strain equal to  $\epsilon_G + 0.01$  ( $\epsilon_G$  is the strain at the end of half cycle F-G).

$$\sigma_0 = A + B(\sigma_{\max} - \sigma_{\min}) \quad (4.7)$$

where  $\alpha = 6$   $A = 0.7938$   $B = 0.55723$  for 1/2 cycle from compression

$\alpha = 7$   $A = 0.7735$   $B = 0.47989$  for 1/2 cycle from tension

$\sigma_{\max}$  = the maximum tensile stress prior to the current 1/2 cycle

$\sigma_{\min}$  = the maximum compressive stress prior to the current 1/2 cycle

Equation 4.7 was first proposed by Aktan et al. (5). The values of  $A$  and  $B$  were obtained from a least squares analysis (Fig. 4.4) of the cyclic response of Grade 60 reinforcing bars. In this research, Eq. 4.6 was modified slightly so that the value of  $\sigma_0$  was also appropriate to be used for modelling the cyclic response of reinforcing steel with yield stress other than 60 ksi. Such modification, which was based primarily on the observations of the cyclic response of reinforcing bars with different yield stresses (5, 124), is given in Eq. 4.8. The values of  $\sigma_0$  for Grade 75 steel calculated from this equation are shown in Fig. 4.4.

$$\sigma_0 = A \frac{f_y}{60.0} + B(\sigma_{\max} - \sigma_{\min}) \quad (4.8)$$

where  $A, B, \sigma_{\max}$ , and  $\sigma_{\min}$  are the parameters defined in Eq. 4.7.

$f_y$  is the yield stress of a reinforcing bar.

This method is used to define the cyclic behavior of the reinforcing steel that is subjected to symmetrical load cycles<sup>2</sup> where the maximum compressive stress and the maximum tensile stress gradually increase in subsequent cycles. In the analysis of shear walls with rectangular and barbell cross section, the main reinforcing bars in the boundary ele-

---

<sup>2</sup> A symmetrical load cycle is defined as a load cycle where both a half cycle from tension and a half cycle from compression experience the same magnitude of strain.

at the ultimate point is set equal to  $0.001 \cdot E_s$  ( $E_s$  is the initial modulus of elasticity for the reinforcing bar). For example, after the stress–strain relationship for the current half cycle from compression in Fig. 4.6(b) (curve H–J) has been defined, the stress at the ultimate point (point J) is evaluated. If the magnitude of  $\sigma_j$  is less than the magnitude of the tensile strength, curve H–J needs no adjustment. On the other hand, if the magnitude of  $\sigma_j$  is greater than the magnitude of the tensile strength, curve H–J is adjusted so that stress at point J is equal to the tensile strength and the tangent stiffness at point J is equal to  $0.001 \cdot E_s$ .

It can be seen that a stress–strain curve of a half cycle defined either by a common point or an ultimate point is limited by four constraints: 1) stress and strain at the initial point ( $\epsilon_i, \sigma_i$ ), 2) stress and strain at the common point or at the ultimate point ( $\epsilon_2, \sigma_2$ ), 3) the tangent stiffness at point ( $\epsilon_i, \sigma_i$ );  $E_s$ , and 4) the tangent stiffness at point ( $\epsilon_2, \sigma_2$ );  $E_t$ . The values of  $\sigma_0$  and  $\alpha$  that make the curve of a half cycle satisfy all these constraints can be calculated by using Eq. 4.9 and Eq. 4.10:

$$\alpha = \left( \frac{E_s}{E_t} - 1 \right) \left| \frac{k_2}{k_1 E_s - k_2} \right| \quad (4.9)$$

$$\sigma_0 = \frac{|k_2|^{\frac{\alpha}{\alpha-1}}}{|k_1 E_s - k_2|^{\frac{1}{\alpha-1}}} \quad (4.10)$$

where

- $(\epsilon_i, \sigma_i)$  = strain and stress at the beginning of the current 1/2 cycle
- $(\epsilon_2, \sigma_2)$  = strain and stress at the common or ultimate point
- $E_s$  = the initial modulus of elasticity for the reinforcing bar
- $E_t$  = tangent stiffness of a curve at point  $(\epsilon_2, \sigma_2)$
- $k_1 = \epsilon_2 - \epsilon_i$      $k_2 = \sigma_2 - \sigma_i$

The reinforcing steel in the web of a wall typically experiences highly unsymmetrical load reversals due to shifting of the neutral axis of the walls during the cyclic loadings. here-

An ultimate point for a half cycle from tension (curve C–E) is defined by point E in Fig. 4.6(a). E is the point on the curve defined during the current half cycle from tension (curve C–E) at strain equal to  $\varepsilon_C - 0.09$  ( $\varepsilon_C$  is the strain at the beginning of half cycle C–E). An ultimate point for a half cycle from compression (curve I–J) is defined by point J in Fig. 4.6(b). J is the point on the curve defined during the current half cycle from compression (curve H–J) at strain equal to  $\varepsilon_H + 0.09$  ( $\varepsilon_H$  is the strain at the beginning of half cycle H–J). It should be noted that the strain increments of  $\pm 0.01$  and  $\pm 0.09$  used to define the common point and the ultimate point are obtained from the observation of the experimental data and from trials of different values of strain increments.

By using common and ultimate points, the rules for defining the stress–strain relationship of each half cycle can be described as follows:

- In a half cycle with an initial stress that is less than the magnitude of the previous maximum stress in that direction, the values of  $\sigma_0$  and  $\alpha$ , which define the stress–strain relationship of the current half cycle (Eq. 4.5 and Eq. 4.6), are calculated so that the current half cycle will merge with the previous half cycle from the same direction at a common point. At a common point, the stress–strain curves of both cycles have the same stress, strain, and tangent stiffness. For example, the current half cycle in tension in Fig. 4.6(a) (curve C–E) merges with the previous half cycle in tension (curve A–B) at the common point (point D) because the magnitude of the initial stress ( $\sigma_C$ ) is less than the magnitude of the previous maximum tensile stress ( $\sigma_A$ ). At the common point, curves C–E and A–B have the same stress, strain, and tangent stiffness ( $E_t$ ). The tangent stiffness is defined by the stress–strain relationship of curve A–B, which is already known.

- After the stress–strain relationship of the current half cycle is defined, the stress at the ultimate point for the current half cycle is calculated. If the magnitude of the stress at the ultimate point exceeds the steel strength in that direction, the stress–strain relationship is adjusted so that stress at the ultimate point is equal to the strength. The tangent stiffness





fore, the calculated response of the reinforcing bars in the web are typically governed by the concept of a common point as shown in Fig. 4.5.

### 4.2.3 LOAD REVERSALS FROM YIELD PLATEAU

Another curve is required to define the cyclic response of the reinforcing steel in the proposed model, a curve to define the stress-strain relationship of the current half cycle when the previous half cycle starts from a yield plateau. This curve, which is based on the analytical model proposed by Ma et al. (89) and Popov (118), represents the typical behavior of a reinforcing bar observed in the experimental data (5, 89, 118, 124). As shown in Fig. 4.7, a typical load cycle for a reinforcing bar that is unloaded from the yield plateau can be divided into two types: a cycle with a small loop width (cycle A-B-C) and a cycle with a large loop width (cycle D-E-F). A reloading curve (curve B-C) of a load cycle with a small loop width is nearly straight with a tangent stiffness equal to  $E_s$  at the beginning and then experiences a well-defined yield plateau. A reloading curve (curve E-F) of a load cycle with a large loop width experiences a significant Bauschinger effect from the beginning. Then, it merges with a monotonic strain-hardening curve that is shifted to the point where a load reversal occurs on a yield plateau (point D).

Based on these observations, the steel model divides the load cycles that start unloading from the yield plateau into two cases based on the loop width ( $\Delta\epsilon_s'$ ) of the load cycle (Fig. 4.8). These two cases are discussed as follows.

Case 1:  $\Delta\epsilon_s' < 0.50 \cdot |\epsilon_{sh} - \epsilon_y|$  (Fig. 4.8 (a))

In a load cycle with a loop width ( $\Delta\epsilon_s'$ ) smaller than  $0.50 \cdot |\epsilon_{sh} - \epsilon_y|$  (A-B-C-D in Fig. 4.8(a))<sup>3</sup>, the reloading half-cycle (B-C-D) will be an elasto-plastic curve similar to the initial stress-strain curve under monotonic loading. If the loading continues in the same direction, the bar will experience strain-hardening at the same strain as defined for the monotonic case.

---

<sup>3</sup>  $\epsilon_{sh}$  is the strain at the beginning of the strain-hardening curve and  $\epsilon_y$  is the yield strain.

Case 2:  $\Delta\varepsilon_s' \geq 0.50 \cdot |\varepsilon_{sh} - \varepsilon_y|$  (Fig. 4.8 (b))

In a load cycle with a loop width ( $\Delta\varepsilon_s'$ ) equal to or greater than  $0.50 \cdot |\varepsilon_{sh} - \varepsilon_y|$  (E-F-G in Fig. 4.8(b)), the reloading half-cycle (F-G) will not exhibit elasto-plastic behavior. The stiffness of the bar will decrease before the yield level is reached. A revised monotonic strain-hardening curve is defined beginning at point E, the point on the yield plateau at which unloading began. The reloading half-cycle will merge with this shifted strain-hardening curve at the common point of load cycle E-F-G (point G), where the strain at point G is 0.01 larger than the strain at point E.

### 4.3 EVALUATION OF THE STEEL MODEL

The proposed material model for reinforcing steel has been evaluated using two sets of cyclic data for reinforcing bars (Aktan et al. (5) and Seckin (124)). Data are available from tests of reinforcing bars with three different yield stresses: 50 ksi, 60 ksi, and 75 ksi. A reinforcing bar is modelled by a single 2-node bar element. The bar element is subjected to prescribed displacement at one end which simulates the strain history used in the experiments. The values of all the parameters used in the stress-strain model (except the yield stress and the strain-hardening parameters) are the same for all the reinforcing steels being studied. The values of the yield stress and the strain-hardening parameters are adjusted according to the monotonic test results of each reinforcing bar. The comparisons between the analytical results and the experimental results are shown in Fig. 4.9 (a)-(h).

The calculated behavior of the reinforcing bars agree with the experimental result (Fig. 4.9). One advantage of the proposed steel model is that a single set of parameters can be used to predict the cyclic responses of reinforcing steel with different yield stresses. This makes the proposed steel model practical because the cyclic test data of reinforcing bars are not available in most situations. The only parameters required for the steel model are the yield stress,  $f_y$ , and the strain-hardening parameters,  $\varepsilon_{sh}$ ,  $\sigma_{0m}$ , and  $m$ , all of which can be obtained from the monotonic test of a reinforcing bar.

## 4.4 SUMMARY

The material model for reinforcing steel defines the stress–strain relationship in the axial direction for a reinforcing bar. This stress–strain relationship consists of three portions: 1) an elasto–plastic curve, 2) a strain–hardening curve, and 3) a load reversal curve. The elasto–plastic curve represents the initial elastic range and the yield plateau of a reinforcing bar and is governed by the initial modulus of elasticity ( $E_s$ ) and the yield stress ( $f_y$ ) of the reinforcing bar. The strain–hardening curve represents the hardening behavior of reinforcing steel in the post–yielding region and is described by the Ramberg–Osgood equation. Parameters for the strain–hardening curve are  $\epsilon_{sh}$ ,  $\sigma_{0m}$ , and  $m$ . The values of these parameters can be calculated according to the available experimental data for a particular reinforcing steel or the values recommended by Aktan et al. (5) can be adopted. The load reversal curve represents the loading and unloading regions for reinforcing steel and is also described by the Ramberg–Osgood equation. The parameters for a load reversal curve are  $\alpha$ ,  $A$ , and  $B$ . The values of these parameters recommended by Aktan et al. (5) lead to calculated response that agreed well with the experimental data. The values of these parameters are summarized in Table 4.1.

## 5. FINITE ELEMENT PROCEDURES

Besides the development and verification of the material models, several other aspects of the analytical procedures influence the results obtained from the finite element analyses of reinforced concrete walls. These aspects, which include the finite element formulation, the algorithms used in the material models, the finite element model, and the incremental–iterative algorithms, have significant effects on the accuracy, stability and convergence of the finite element solution. The proper selection of these procedures depends greatly on the nature of the problems being studied. Therefore, in order to obtain accurate and stable solutions with a good convergence rate, users have to select the finite element procedures that are suitable for their problems. This requires an understanding of the characteristics of the finite element procedures, as well as the nature of the problems to be analyzed.

The major objective of this chapter is to discuss some important characteristics of the finite element procedures used in the analyses of reinforced concrete shear walls in this investigation. The finite element formulation and the finite element program FINITE are first discussed. Then some important algorithms used in the material models are described. The procedures for modelling reinforced concrete shear walls and the incremental–iterative algorithms used to solve nonlinear equilibrium equations are given at the end of this chapter.

### 5.1 FINITE ELEMENT FORMULATION

The most widely used finite element formulation for engineering applications is the displacement–based finite element method (13). This formulation is based primarily on the use of the principle of virtual work (displacement) and uses a displacement interpolation function together with nodal displacements to estimate the displacement field within each finite element. The principle of virtual displacement states that “the equilibrium of the body requires that for any compatible, small virtual displacements (which satisfy the essential boundary conditions) imposed on the body, the total internal virtual work is equal to the total external virtual work” and can be written as shown in Eq. 5.1 (13):

$$\int_V \bar{\varepsilon}^T \sigma \, dV = \int_V \bar{U}_b^T f_b \, dV + \int_s \bar{U}_s^T f_s \, dS + \sum_i \bar{U}_i^T F_i \quad (5.1)$$

where  $\bar{U}$  = virtual displacements  
 $\bar{\varepsilon}$  = virtual strains  
 $f_b, f_s, F_i$  = body forces, surface tractions, and concentrated forces  
 $\bar{U}_b, \bar{U}_s, \bar{U}_i$  = virtual displacements corresponding to  $f_b, f_s, F_i$   
 $\sigma$  = actual stresses corresponding to actual strains  $\varepsilon$

A continuous displacement field,  $u^{(m)}$ , for element  $m$  is interpolated from the nodal displacements,  $U$ , by using a displacement interpolation matrix,  $H^{(m)}$ , as follows (13):

$$u^{(m)}(x, y, z) = H^{(m)}(x, y, z) U \quad (5.2)$$

where  $u^{(m)}$  = a continuous displacement field for element  $m$   
 $H^{(m)}$  = a displacement interpolation matrix for element  $m$   
 $U$  = a vector of global displacement components at all nodes

In linear system, strains in an element  $m$ ,  $\varepsilon^{(m)}$ , can be evaluated from the nodal displacements by using the strain-displacement matrix,  $B^{(m)}$  (13):

$$\varepsilon^{(m)} = B^{(m)} U \quad (5.3)$$

The strains in element  $m$ ,  $\varepsilon^{(m)}$ , can be related to the element stresses,  $\sigma^{(m)}$ , by using the constitutive matrix  $C$ :

$$\sigma^{(m)} = C^{(m)} \varepsilon^{(m)} \quad (5.4)$$

By substituting Eq. 5.2 through 5.4 for both real and virtual displacements and strains into Eq. 5.1 and rearranging the terms, the principle of virtual displacement (Eq. 5.1) can be rewritten as follows (13):

$$K U = R \quad (5.5)$$

where  $R = R_B + R_S + R_I + R_C$  (5.6)

The matrix  $K$  is the stiffness of the element assemblage,

$$K = \sum_m \int_{V^{(m)}} B^{(m)T} C^{(m)} B^{(m)} dV^{(m)} \quad (5.7)$$

The load vector  $R_B$  is the equivalent nodal load due to the element body forces,

$$R_B = \sum_m \int_{V^{(m)}} H^{(m)T} f_B^{(m)} dV^{(m)} \quad (5.8)$$

The load vector  $R_S$  is the equivalent nodal load due to the element surface forces,

$$R_S = \sum_m \int_{S^{(m)}} H^{S(m)T} f_B^{S(m)} dS^{(m)} \quad (5.9)$$

The load vector  $R_I$  is the equivalent nodal load due to the element initial stress  $\sigma^I$ ,

$$R_I = \sum_m \int_{V^{(m)}} B^{(m)T} \sigma^I dV^{(m)} \quad (5.10)$$

The load vector  $R_C$  is the vector of concentrated loads  $F$ ,

$$R_C = F \quad (5.11)$$

Although Eq. 5.1 is true for both linear and nonlinear materials, Eq. 5.5 is applicable only to problems with linear materials because it has been assumed that the stiffness matrix  $K$  is independent of the nodal displacements. This constant stiffness matrix,  $K$ , is in fact a result of the use of a constant constitutive matrix,  $C$ , and a constant strain-displacement matrix,  $B$ , both of which are used in the derivation of the stiffness matrix as shown in Eq. 5.7. As a result, the nodal displacements,  $U$ , corresponding to the load vector,  $R$ , can be calculated directly from Eq. 5.5. However, if the stress-strain relationship is nonlinear, or if the body experiences large displacements or strains, the constitutive matrix,  $C$ , or the strain-displacement matrix,  $B$ , will no longer be constant and will

depend on the current deformed configuration of the body. This will cause the stiffness matrix and the governing equilibrium equations to be nonlinear; therefore, incremental–iterative algorithms are required to solve the governing equilibrium equations.

The fundamental objective of the nonlinear finite element formulation is to search for the state of equilibrium of the body at time step (or load step)  $t + \Delta t$  corresponding to the applied load vector  ${}^{t+\Delta t}R$  (assuming that the state of equilibrium at time step  $t$  is already known) (13). The state of equilibrium at time step  $t + \Delta t$  is obtained when the applied nodal load,  ${}^{t+\Delta t}R$ , is equal to the equivalent nodal load corresponding to the element stress, as follows,  ${}^{t+\Delta t}F$  (13):

$${}^{t+\Delta t}R - {}^{t+\Delta t}F = 0 \quad (5.12)$$

where

$${}^{t+\Delta t}F = {}^tF + \Delta F \quad (5.13)$$

$${}^tF = \sum_m \int_{V^{(m)}} {}^tB^{(m)T} {}^t\sigma^{(m)} {}^t dV^{(m)} \quad (5.14)$$

$\Delta F$  = Vector of the incremental nodal forces corresponding to the changes in element stresses from time step  $t$  to  $t+\Delta t$

However, because the incremental nodal load corresponding to the element stress,  $\Delta F$ , also depends on the incremental displacements,  $\Delta U$ , the value of  $\Delta F$  is not known until the equilibrium state at time step  $t + \Delta t$  has been reached. As a result, the incremental nodal load corresponding to the incremental element stresses at time step  $t + \Delta t$ ,  $\Delta F$ , has to be approximated by using the stiffness matrix at time step  $t$ ,  ${}^tK$ , which is already known (13).

$$\Delta F \approx {}^tK \Delta U \quad (5.15)$$

The total nodal load corresponding to the element stress at time  $t+\Delta t$ ,  ${}^{t+\Delta t}F$ , can be approximated as follows:

$${}^{t+\Delta t}F \approx {}^tF + {}^tK \Delta U \quad (5.16)$$



Substituting Eq. 5.16 into Eq. 5.12 leads to:

$${}^tK \Delta U = {}^{t+\Delta t}R - {}^tF \quad (5.17)$$

The resulting nodal displacements at time step  $t + \Delta t$  can be approximated as follows:

$${}^{t+\Delta t}U \approx {}^tU + \Delta U \quad (5.18)$$

Equation 5.17 is the fundamental equation of equilibrium in the nonlinear finite element formulation. However, because of the assumption used in Eq. 5.15, the approximation of the nodal displacements in Eq. 5.18 may contain significant errors depending on the size of the time step used. Therefore, Eq. 5.17 needs to be solved iteratively so that the state of equilibrium in Eq. 5.12 is obtained with sufficient accuracy (13). This iterative process is discussed in Section 5.5.

In general, nonlinear analyses can be classified into three different types as shown in Table 5.1 (13). Because concrete cannot sustain large relative deformation, most analyses of reinforced concrete members can be considered as having only material nonlinearities (15). However, geometric nonlinearities can also have significant effects on the behavior of some types of reinforced concrete members, such as reinforced concrete plates and shells, which undergo large rigid body displacements and rotations (23). Only the material nonlinearity is included in the finite element formulation in this investigation because displacements and strains in most concrete and steel elements of the wall models remain small throughout the loading history and the major sources of nonlinearities in the analysis are the stress-strain relationships for steel and concrete.

## 5.2 FINITE

The finite element analysis program, FINITE, was used in the analysis of reinforced concrete walls in this investigation. FINITE, which was jointly developed by the Civil Engineering departments at the University of Illinois at Urbana-Champaign, the University of Kansas, the University

of Wyoming, and Carnegie–Mellon University, is “a general purpose computer system for the analysis of linear and nonlinear structures” (88). Nonlinear effects from strain–displacement relationships (geometric nonlinearities) and from material constitutive relationships (material nonlinearities) are both included in the finite element formulation. The total Lagrangian approach, which utilizes the second Piola–Kirchhoff stress and the Green engineering strain, is used in the formulation of the problems with geometric nonlinearity. The incremental–iterative Newton–Raphson algorithm is used for solving the nonlinear equilibrium equations (88).

One feature which makes FINITE suitable for this study is the ability to allow installation of new element models and new material models with minimal effort. The ease with which these models can be installed is due primarily to FINITE’s separation of the element and the material routines from the main system. The main system is responsible for most of the major tasks in the analysis such as solving the equilibrium equations, managing all memory and databases, computing the stiffness matrix, and printing the results. It provides the necessary data for and receives the computed results from the element and the material routines through the use of subroutine arguments. A typical computational procedure for each load step is illustrated in Fig. 5.1, where the blocks with a solid boundary represent the tasks performed by the main system and the blocks with a broken boundary represent the tasks performed by the material and element routines. Because all the element model routines, regardless of their type or complexity, have similar arguments (which is also true for material model routines), model developers can add a new element model or a new material model without having to modify the main system. As a result, model developers can focus their attention on the performance of the new models rather than on the formulation of the finite element procedures (51).

### **5.3 ALGORITHMS USED IN THE MATERIAL MODELS**

Besides the proper stress–strain relationships, another important aspect of the material model that greatly influences the accuracy and the stability of the finite element analysis is the algorithms used to update stresses and stiffnesses during the iterative procedures. Such algorithms determine

the stress path at each integration point with respect to the computed strain increments. Despite the correct constitutive stress-strain relationship, improper algorithms can cause stresses to follow an incorrect path which will result in the incorrect response or an unstable solution. In the analysis of reinforced concrete walls subjected to cyclic loading, inappropriate algorithms can lead to any one of these three problems: an incorrect stress path, false load reversals, or nonconvergence in the iterative procedures. Each of these problems is discussed below:

### 5.3.1 INCORRECT STRESS PATH

A typical iterative procedure to find equilibrium solutions for load steps A-B is shown in Fig. 5.2. In this figure, the iterative solutions follow path A-1-...-5-B while the true solutions follow a path which is a solid curve connecting points A and B. The intermediate solutions at point 1,2,...,5 are incorrect because they do not satisfy the governing equilibrium equations; therefore, they should not cause any artificial damage to the finite element model (23). This is very important to both concrete and reinforcing steel because the behavior of these two materials depend on the loading history(23).

In the nonlinear finite element analysis, there are two different methods for calculating incremental strains and updating stresses at each iteration: the path dependent method and the path independent method. As the solution is advancing from step n to step n+1, strain increments for updating stresses in these two methods can be written as follows (88):

$$\text{Path dependent method} \quad \Delta \varepsilon_{PD}^i = \varepsilon_{n+1}^i - \varepsilon_{n+1}^{i-1} \quad (5.19)$$

$$\text{Path independent method} \quad \Delta \varepsilon_{PI}^i = \varepsilon_{n+1}^i - \varepsilon_n \quad (5.20)$$

where  $\varepsilon_n$  = converged strains from the last load step n  
 $\varepsilon_{n+1}^i$  = total strains at iteration i of load step n+1  
 $i$  = iteration number

In the path dependent method, the stress at iteration  $i$  is calculated from the iterative strain increment at iteration  $i$  and uses the non-converged stress and strain at iteration  $i-1$  as the initial condition. This method assumes that the iterative solution path (A-1-...-5-B in Fig. 5.2) is correct; therefore, any nonlinear behavior or damage that occurs along this path will affect the converged solution of this load step. In the path independent method, the stress at iteration  $i$  is calculated from the total strain increment and uses the converged stress and strain from the last load step as the initial condition. Since the stresses are always calculated from the converged stresses and strains of the last load step, the converged solution of the current load step will not be affected by the incorrect path of the iterative solution. Theoretically, the path independent method should be used in the numerical algorithms of the proposed material models because it does not introduce any errors caused by the incorrect path of the iterative solution (14, 23, 88, 95). However, in some situations such as the cracking of concrete, using the path independent method usually leads to a much slower convergence rate than using the path dependent method (88).

The path independent method is used in most of the solution algorithms for the proposed concrete and reinforcing steel models. The converged stresses and strains from the last load step are used as the initial condition for updating stresses at every iteration of the current load step. In the analysis of reinforced concrete walls, this method yields both a satisfactory convergence rate and a stable solution in most situations. However, in load steps where concrete cracking occurs at several integration points, the path independent method usually yields very a slow convergence rate or, sometimes, even leads to a divergent solution. This is due to the fact that when concrete at one integration point cracks, it releases a large amount of strain energy. This usually causes concrete at the adjacent integration points, which has been cracked during the previous iteration to become uncracked. Because the tensile stress of concrete changes abruptly as concrete's status changes, the repeated changing of concrete's status from cracked to uncracked and vice versa, which occurs when the path independent method is used, usually leads to a very slow convergence rate or even a divergent solution. To avoid such problem, the path dependent method is used for concrete cracking; the stresses and strains of concrete at the iteration where cracking occurs are used as the initial condition

for updating stresses in the following iteration. In order to prevent incorrect cracking introduced by an incorrect path of the iterative solutions, the load step size in the analysis should be small so that the iterative solution path remains close to the true solution path. This method, which was also recommended in the analysis of reinforced concrete members by other researchers (88), was found to yield satisfactory results for the analysis of reinforced concrete walls in this investigation.

### **5.3.2 FALSE LOAD REVERSALS**

In the analysis of reinforced concrete members subjected to cyclic loading, load reversals in concrete and reinforcing steel are caused by the changes in the direction of applied load or by the load redistribution due to material nonlinearity. As a result, these load reversals can occur throughout the loading history and have significant effects on the cyclic response of the members. For the purpose of this investigation, load reversals were divided into two categories: true load reversals and false load reversals. A true load reversal is defined as a load reversal that occurs with a large strain increment (compared with the strain increments of previous load steps), continues for several load steps, and has a significant effect on the response of the wall. A false load reversal is defined as a load reversal that occurs with a small strain increment and continues for only one or two steps before the load is again reversed to the original direction. The false load reversal does not have any significant effect on the response of the wall except that numerical problems such as a slow convergence rate or the non-convergence of the solutions may result. Therefore, the solution algorithm must have the ability to prevent the occurrence of these false load reversals. Criteria for avoiding false load reversals are crucial to the success of the cyclic analysis. If the criteria are too relaxed and allow false load reversals to occur repeatedly, the finite element solution will converge very slowly or, sometimes, diverge. On the other hand, if the criteria for identifying false load reversals are too strict, they may prevent the actual load reversals from occurring and cause the solution to follow an incorrect path.

In the proposed concrete and steel models, several criteria are used to prevent false load reversals and to improve the convergence rate of the solutions with load reversals. These criteria are described as follows:

- The total strain increments: The total, rather than iterative, strain increments are used to evaluate the load reversals for each component of strain. This is in fact the path independent method, which is described in Section 5.3.1. A reverse in the direction of the total strain increment correctly indicates that a load reversal has occurred because the total strain increments are calculated from the converged strains of the last load step. On the other hand, a reverse in a direction of the iterative strain increment is not a correct indication of a load reversal because the iterative strain increments are calculated from the strains of the last iteration which are intermediate solutions that do not satisfy the equilibrium conditions. In each load step, the iterative strain increments might change directions several times depending on the corrective strain increments at each iteration, even when the solutions continue on the loading path of the stress-strain curve and the total strain increments do not change directions at any iteration.

- Maximum iteration number: In both the concrete and the steel models, load reversals are allowed to occur only when they start in the first five iterations of the current load step. Load reversals that start after the fifth iteration are not allowed and are treated as if they were on the current loading path. This criterion is based on the analytical results which show that most of the major load reversals and changes in stiffness occur in the first few iterations. Such behavior was also observed in the analysis of reinforced concrete shear walls by Okamura et. al. (107). Load reversals that take place in later iterations are likely to be false load reversals and, therefore, should be prevented. If true load reversals do occur after the fifth iteration, this criterion will simply postpone the occurrences of these load reversals until the next load step.

- Magnitude of reversing strain: In the steel model, load reversals are allowed to occur only when the magnitude of the current reversing strain increment is greater than 25% of the magnitude of the total strain increment from the previous load step. The purpose of this criterion is to delay until the next load step the occurrence of load reversals that are small and likely to be false load reversals. If these load reversals are true, their magnitudes in the next load step will be large enough for load reversals to occur. If these load reversals are false, the directions of the strain increments in the next load step will reverse back to the original directions and the solution will continue on the loading path. This algorithm is implemented only in the reinforcing steel model because the small loops of false load reversals usually cause numerical problems in evaluating parameters for the Ramberg–Osgood functions.

It should be noted that these criteria are based primarily on trials of different ways to improve the convergence and the stability of the solutions. Such criteria depend greatly on the nature of the problems being studied; therefore, they might need some adjustments if applied to other types of reinforced concrete members or loading conditions.

### **5.3.3 PROBLEMS WITH NEWTON–RAPHSON METHOD**

In the analysis of reinforced concrete walls, the problem that usually causes nonconvergence in the Newton–Raphson algorithm, as shown in Fig. 5.3, occurs when the iterative solutions alternate between two points, A and C, on the solution path without converging to an equilibrium position at point E. This problem usually occurs when the stress–strain curve for the material model softens and then stiffens again such as yielding followed by strain–hardening in reinforcing steel. Because either point A or point C in Fig. 5.3 corresponds to an equilibrium position, the finite element solution will not converge and continues to alternate between these two points. In order to improve the convergence rate of the solution, special numerical techniques were implemented in both concrete and steel material models. If an alternating solution is detected during the iterative procedure, the solution path will be allowed to converge to point B and the solution will be corrected to point C

in the next load step. Although, point B is not on the true solution path, the selection of point B during the current load step does not have a significant effect on the accuracy of the finite element solution because the solution is corrected in the following load step.

## **5.4 FINITE ELEMENT MODEL**

Another important aspect of the finite element procedures is the choice of the element model. In this investigation, the finite element model must correctly represent the geometry, boundary conditions, and loading history of the walls under study. The following sections discuss several aspects of the finite element model for shear walls, including the types of elements, the size of the finite element mesh, the load step size, and the loading algorithm.

### **5.4.1 TYPES OF ELEMENT**

The first question that arose in the modelling phase of the finite element analysis was what types of elements were most suitable for the concrete and reinforcing steel. There are two different methods for selecting the most suitable element. The first method advocates the use of a small number of elements with a high order interpolation function. For example, Stevens et al. (134) used elements with a cubic displacement interpolation function and, hence, a quadratic strain distribution for concrete elements because they believed that this type of element would “take full advantage of the smeared nature of the constitutive laws”(134). The second method advocates the use of a large number of elements with a low order interpolation function such as linear displacement or quadratic displacement elements. Bergan and Holand (23) adopted this method because “it seems illogical to use high order interpolation which implies artificial differentiability and smoothness of the displacement functions. Very simple types of elements are therefore usually preferable.”

When a reinforced concrete wall is subjected to cyclic loading, extensive cracking of the concrete occurs in the lower portion of the wall. Therefore, the strain distribution in concrete is highly discontinuous; concrete strains at each point are governed only by the displacement of concrete in the vicinity and are not likely to be affected by the displacement of concrete at distant locations.



As a result, the use of several small linear elements, in which strains are calculated from displacements at four close nodes, is more appropriate for representing the discontinuous displacement field in cracked walls than the use of a few large elements with a high order interpolation function, in which strains are influenced by displacements at distant nodes. In the finite element models used for the walls in this investigation, linear isoparametric 4-node elements with a 2x2 integration rule and 2-node bar elements are used to represent the concrete and reinforcing steel, respectively.

Another advantage of the linear element with a 2x2 integration rule is that the linear element performs well and remains stable even when cracking has occurred at all four integration points in the element (8, 50). The stiffness of a cracked linear element with a 2x2 integration rule has three zero energy modes, all of which represent the required rigid body motions of the element. Other types of elements might have several additional zero energy modes when cracked. For example, the stiffness of a cracked quadratic element with a 2x2 integration rule has eight zero energy modes, three of which are the required rigid body modes while the other five are non-rigid body zero energy modes (50, 83). These additional zero energy modes allow the element to deform with no strain and, therefore, can cause unpredictable deformed shapes of the element in the solution (50, 83).

In the cyclic analysis of reinforced concrete walls, the problem of the additional zero energy modes is very important because the whole analysis consists of several thousand iterative solutions and, therefore, opens up the possibility of the non-rigid body zero energy modes interfering with the results. Another element that has the same stability as the linear element with a 2x2 integration rule is a quadratic element with a 3x3 integration rule. However, this element requires much greater computational effort than the linear element. Some researchers also reported that the quadratic element did not yield more accurate analytical results than the linear element (50). Consequently, the linear element was chosen in this investigation. After the element for concrete had been chosen, the selection of the element for reinforcing steel was straightforward. A 2-node bar element was selected because its displacement is compatible with the displacement along the boundary of the 4-node linear element. The 2-node bar elements can also use the same finite element mesh as the concrete elements without the need to create extra nodes.

## 5.4.2 SIZE OF FINITE ELEMENT MESH

The size of the finite element mesh also has a significant effect on the results of the analysis of reinforced concrete walls. The model with an unnecessarily fine mesh requires an extra amount of computation time while the model with a mesh that is too coarse might not be adequate to represent the behavior of the wall correctly. The proper size of the finite element mesh for reinforced concrete members depends greatly on the nature of the problem being studied. Because there are no definite rules for selecting the proper mesh size for the analysis of reinforced concrete members, testing of finite element models with different mesh sizes is usually a good way to gain an initial understanding about the proper mesh size and the sensitivity of the results to different mesh sizes. In this investigation, the layout of the finite element mesh was also governed by the locations of reinforcing bars. Because the reinforcing steel was modelled using bar elements, the mesh layout was designed such that the location of the steel elements were close to the actual locations of reinforcing bars in the wall. The details of the mesh layouts for specific wall specimens are given in Chapter 6 and Chapter 7.

Another aspect of the mesh size that must be considered is the effect of mesh refinement on the convergence of the solution. This is also related to the evaluation of the proposed material models because an acceptable finite element model must yield solutions that converge as the mesh is refined (50). In the analytical models that are based on the fracture mechanics approach, a crack in concrete is modeled by a band of concrete elements and the fracture energy ( $G_f$ ), which represents work done in generating the unit area of a crack surface, is assumed to be constant (50). As a result, the stress-strain relationship of cracked concrete is also a function of an element size and must be adjusted as the finite element mesh is refined so that the fracture energy ( $G_f$ ) of the crack band remains constant as shown in Fig. 5.4(a) (50). In the analytical models that are based on the strength criterion, each cracked element represents the average behavior of several cracks. If the same assumption of constant fracture energy is used, it can be shown (Fig. 5.4(b)) that the stress-strain relationship of cracked concrete depends only on crack spacings and is independent of the mesh size.

As a result, the proposed concrete model used in this investigation, which is based on the strength criterion, should be applicable to any mesh size as long as the size of the concrete element is not of the same order of magnitude as or smaller than the size of the crack.

In order to investigate the performance of the proposed model with respect to mesh refinement, a reinforced concrete shear wall subjected to monotonic loading was analyzed using two different finite element models: one with a fine mesh and the other with a coarse mesh. The configuration and the reinforcing steel of the wall model resembled those of wall R1<sup>1</sup>. The model with a fine mesh consisted of 570 concrete elements and 993 steel elements while the model with a coarse mesh consisted of 180 concrete elements and 378 steel elements. The mesh layouts, the crack patterns, and the load–deflection curves of these two models are shown in Fig. 5.5, 5.6, and 5.7, respectively. It can be seen that both models yielded similar analytical results. Therefore, the proposed material models are considered to be objective with respect to mesh refinement. Another important observation from these analyses is that, although the two models yielded similar analytical results, the model with a fine mesh required six times as much CPU time as the model with a coarse mesh. This emphasizes the importance of the proper mesh size especially when the analysis consists of several hundred load steps and the CPU time becomes a major concern in the analysis.

### 5.4.3 LOADING ALGORITHMS

In the analysis of reinforced concrete members, there are two different loading algorithms: a load–control algorithm and a displacement–control algorithm. In the load–control algorithm, loads are applied incrementally at each load step while, in the displacement–control algorithm, displacements at particular nodes are prescribed incrementally at each load step. Darwin and Pecknold (44) reported that the displacement–control algorithm gave more accurate analytical results for the cyclic responses of reinforced concrete members than the load–control algorithm. This is due to the fact that most reinforced concrete members experience softening behavior after the longitudinal reinforcement has yielded or as the cyclic loading intensifies. Because the location where the soften-

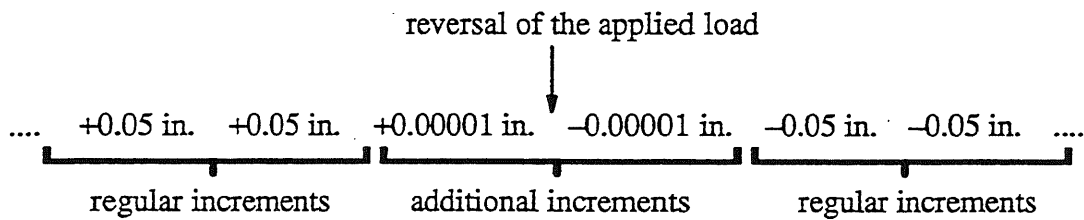
---

<sup>1</sup> The details of wall R1 are given in Chapter 6.

ing behavior starts and the strength of the reinforced concrete member is not known before the analysis, it is difficult to prescribe the proper load increments for the whole loading history. Too large load increments might exceed the strength of the member and cause the solution to diverge while too small load increments will require a large amount of CPU time in the analysis. The displacement-control algorithm usually yields a more stable solution than the load-control algorithm because the prescribed displacements are not likely to exceed the deformation capacity of the specimen except at the very end of the loading history. As a result, the displacement-control algorithm was used for loading the wall models in this investigation.

Similarly to the selection of mesh size, the selection of the incremental displacement size also depends greatly on the nature of the problem being studied and can be estimated by initially trying several analyses with different sizes of incremental displacement. In the analysis of reinforced concrete walls considered in this investigation, in which the displacement at the top corner node of each wall was prescribed, an incremental displacement equal to half of the top displacement that caused initial cracking in the walls was found to yield good results for the first few cycles. In later cycles, when most of the steel elements in the lower 3 ft. of the wall had yielded and most of the concrete elements in the lower portion of the wall had cracked, the incremental displacements could be doubled. This increase in the size of the incremental displacements did not lead to numerical problems because the two major causes of material nonlinearity (yielding of the steel and cracking of the concrete) had already occurred.

Another important aspect of the loading algorithm used for the cyclic analysis of reinforced concrete walls is the technique used to prescribe incremental displacements when the applied load is reversed. Instead of abruptly reversing direction, a gradual change in the direction of the incremental displacements was used when the direction of the applied load changed. This is done by adding two additional displacement increments between the load steps where the direction of loading is reversed. The magnitude of these two increments is very small compared to those of the regular increments. The typical displacement increments at the reversal of the applied load can be written as follows:



In each of these two additional displacement increments, only one iteration is allowed and the analysis then proceeds to the next step. The numerical problems usually occur if a regular load increment is used in the load step in which the reversal of the applied load occurs. At the first iteration of that load step, the finite element program does not know that the applied load is reversed; therefore, the current loading stiffness is used to find the solution for this iteration. The program realizes that the applied load has been reversed when the stresses are updated and the residual load is calculated at the end of the first iteration. Then, the unloading stiffness is used instead for solving the equilibrium equation in the second iteration. If local load reversals in the stress-strain relationship occur at a large number of integration points, the loading stiffness and the unloading stiffness of the model will differ greatly. This difference might cause the solution calculated during the first iteration to deviate greatly from the true solution path and cause numerical problems in the solution. Therefore, the small displacement increments are added at the load step where the applied load is reversed. Because these two increments are very small, using only one iteration does not affect the equilibrium condition of the model and allows load reversals to occur in these additional steps while the iterative solution remains close to the true solution path. Because load reversals have already occurred at most integration points in the previous load step, the correct unloading stiffness will be used in the first iteration and a much more stable solution is obtained when the regular displacement increment is used in the next step.

## 5.5 INCREMENTAL – ITERATIVE ALGORITHMS

In the nonlinear analysis of reinforced concrete members, most of the computation time is spent solving the nonlinear equilibrium equations that govern the response of the finite element model (14). As a result, the appropriate strategy for solving these equations with good stability and proper accuracy is essential to the success of the finite element analysis. The incremental–iterative algorithms used for solving nonlinear equations in this investigation consist of two major elements: the Newton–Raphson algorithms and the convergence criteria. Each these elements is discussed below.

### 5.5.1 NEWTON – RAPHSON ALGORITHMS

The widely used iteration schemes for the solution of the nonlinear finite element equations are based on the Newton–Raphson (N–R) iteration algorithm. In this algorithm, the displacement vector  $U$  that satisfies the equilibrium condition at time  $t+\Delta t$  can be found by successive approximations in the following form (95):

$${}^{t+\Delta t}K^{i-1} \Delta U^i = {}^{t+\Delta t}R - {}^{t+\Delta t}F^{i-1} \quad (5.21)$$

where

- ${}^{t+\Delta t}K^{i-1}$  = the tangent stiffness matrix at iteration  $i-1$  of load step  $t+\Delta t$
- $\Delta U^i$  = the incremental displacement vector at iteration  $i$
- ${}^{t+\Delta t}R$  = the externally applied load vector at load step  $t+\Delta t$
- ${}^{t+\Delta t}F^{i-1}$  = the load vector corresponding to the element stress at iteration  $i-1$  of load step  $t+\Delta t$

The total displacement can be calculated as follows:

$${}^{t+\Delta t}U^i = {}^{t+\Delta t}U^{i-1} + \Delta U^i \quad (5.22)$$

where  ${}^{t+\Delta t}U^i$  is the total displacement at iteration  $i$  of load step  $t+\Delta t$

The initial condition for Eq. 5.21 and 5.22 are as follows:

$${}^{t+\Delta t}U^0 = {}^tU \quad (5.23)$$

$${}^{t+\Delta t}F^0 = {}^tF \quad (5.24)$$

In this algorithm—the full N–R iteration—the stiffness matrix of the model,  $K$ , is updated in every iteration as shown in Eq. 5.21. Updating the stiffness matrix at every iteration is computationally expensive, therefore the full N–R iteration might not be efficient nor necessary for some types of problems (13, 14, 95). This led to the development of the modified N–R iteration, in which, instead of being updated in every iteration, the new stiffness matrix is updated only at certain iterations. This method involves fewer calculations of the stiffness matrix than the full N–R iteration. Although, the modified N–R iteration usually requires more iterations for the solution to converge than the full N–R iteration, the total computation time required by the modified N–R iteration may be less than that required by the full N–R iteration because the stiffness matrix is updated less often. These two iteration algorithms are illustrated by a single degree of freedom system as shown in Fig. 5.8.

For the finite element analysis of reinforced concrete members, many researchers (10, 31, 32, 44, 45, 110) reported that the full N–R iteration yielded better results than the modified N–R iteration. This is due to the fact that the behavior of both concrete and steel are strongly path dependent and the stiffnesses of concrete and steel at different stages (such as cracked vs. uncracked concrete or yielding vs. linear reinforcing steel) differ greatly. As a result, solving the equilibrium equations using a tangent stiffness that does not correspond to the current status of the material may cause the solution to deviate greatly from the true solution path and result in a slow convergence rate or a divergent solution. In this investigation, the full N–R iteration was found to yield solutions with good stability and a good convergence rate. The convergence characteristics of the full N–R iteration and that of the modified N–R iteration are illustrated in Fig. 5.9. This figure shows the convergence parameters at four arbitrarily selected load steps from the analysis of wall B4<sup>2</sup> with three different frequencies of updating the stiffness matrix: updating every iteration (the full N–R iteration),

---

<sup>2</sup> The details of wall B4 are given in Chapter 6.

updating every three iterations, and updating every five iterations. It can be seen that, among all these updating stiffness schemes, the full N-R iteration required the fewest iterations for the convergence of the solution in all load steps. Furthermore, in the later load steps, which are not shown in Fig. 5.9, both of the analyses with the modified N-R iteration diverged and, therefore, had to be terminated early. In fact, it was the unstable characteristics of the modified N-R iteration, rather than the computation time required in the analysis, that governed the selection of the stiffness updating schemes. Despite the fewer iterations required by the full N-R iteration, the total computation time of the full N-R iteration and the modified N-R iteration, as shown in Table 5.2, are not significantly different because the fewer iterations were obtained at the expense of updating the stiffness matrix more often.

## 5.5.2 CONVERGENCE CRITERIA

Besides the selection of the proper numerical techniques and the proper algorithms for updating stiffness, the success and accuracy of the incremental-iterative procedures also depend greatly on the convergence criteria, which define the conditions that must be satisfied for termination of the iteration (14, 95). At the end of each iteration, some forms of the analytical solutions are checked with the convergence tolerance to see whether the analysis can proceed to the next load step or more iterations are needed for the current load step. If the convergence tolerance is too relaxed, the solution might be inaccurate and follow an incorrect solution path. On the other hand, if the convergence tolerance is too strict, a large amount of computational effort will be spent obtaining solutions with unnecessary accuracy (14). In general, there are three different solution variables that have been used as convergence criteria: the displacement, the residual loads, and the internal energy (14, 95). Each criterion uses some form (e.g. the Euclidean norm of the incremental displacements or the maximum entry of the residual load vector) of the corresponding solution variables to check the convergence of the iterative solutions. The proper selection of these criteria depend greatly on the nature of the problems being studied. For example, the internal energy criterion is suitable for the problems



in which the units of the load vector are inconsistent, such as a load vector that consists of both forces and moments.

In this investigation, the ratio of the norm of the residual load vector to the norm of the applied load increment is used as the criterion for termination of the iteration. The iterative solution of the current step is considered to converge if the following condition has been satisfied (88).

$$\|R\| \leq \|\Delta P\| * \frac{TOL}{100} \quad (5.25)$$

where

- $\|x_i\|$  = the Euclidean norm of vector  $x = \sqrt{\sum x_i^2}$
- R = the total residual load vector
- $\Delta P$  = the applied load increment
- TOL = the convergence tolerance

The residual load was chosen as the convergence criterion because it represented the current equilibrium condition of the solution. In addition, all entries of the residual load vector have the same units; therefore, there is no inconsistency when the norm of the residual load is calculated. It should be noted that the residual load vector, R, is computed from the total, rather than incremental, equilibrium conditions. Therefore, errors do not accumulate in the solutions between load steps. Also, because the residual loads are computed from the total equilibrium conditions, the loads steps that converge will yield correct results even when the prior load steps did not converge (88).

The convergence tolerance of 5% was used in all the analyses of reinforced concrete walls in this investigation. This value yielded the solution with satisfactory accuracy and in reasonable computation time.

## 6. PCA WALL TESTS

As mentioned in Chapter 1, a reinforced concrete shear wall is an effective and economical structural component in tall buildings for resisting lateral load caused either by wind or by earthquake. However, it is usually impractical and uneconomical to design shear walls to remain elastic during strong ground motion (103). In a severe earthquake, the inelastic behavior of reinforced concrete shear walls, such as yielding of flexural reinforcement and cracking of concrete, are anticipated and desirable because these types of behavior help dissipate energy and, therefore, prevent a sudden collapse of the building. This concept leads to the need for the understanding of the inelastic cyclic behavior of reinforced concrete shear walls (103). Prior to the 1970s, despite a large number of buildings with shear walls having been built, the information about the inelastic ductility, energy dissipation, and other important aspects of inelastic behavior of reinforced concrete shear walls was quite limited. In order to provide this needed information, the Portland Cement Association (PCA) conducted an extensive experimental program to investigate the inelastic behavior of reinforced concrete structural walls. A variety of large-scale isolated structural walls with different design parameters, such as cross sections, reinforcing steel, axial stress, and shear reinforcement, were tested under in-plane cyclic lateral load. This experimental study was one of the most elaborate and extensive research programs on reinforced concrete shear walls carried on in the US. It has provided valuable detailed information on the cyclic response of shear walls.

The PCA test program was designed to investigate the important inelastic aspects of behavior in reinforced concrete walls. Its experimental results contain information on most of the significant inelastic types of response. As a result, these experimental data are appropriate to be used as the basis for evaluating the analytical models developed in this research. A successful finite element model must be able to simulate the important nonlinear characteristics of all the wall specimens. One of the objectives of this evaluation is to use a single set of model parameters (except the parameters that are design variables, such as ratio of steel reinforcement) in the analyses of all the wall specimens. If the analytical model can reproduce the behavior of several shear walls with different design

variables, the model will be considered successful and can then be used to investigate of the behavior of walls that are different from the wall specimens tested in the laboratory.

In this chapter, the PCA experimental program and the details of the wall specimens are discussed briefly. Then the finite element models, the analytical procedures, and the values of the parameters used in the material models are described. Comparisons between different aspects of the experimental results and the calculated response are discussed at the end of this chapter.

## 6.1 PCA EXPERIMENTAL PROGRAM

The primary objectives of the PCA experimental program were to determine the load-deflection characteristics, the ductility, the energy dissipation capacity, and the flexural and shear strengths of the structural walls (105). In order to accomplish these objectives, a series of reinforced concrete structural walls were tested under the in-plane, lateral, cyclic loading. The detailed description of the test program can be found in the PCA reports on tests of isolated walls (105, 106).

The nominal dimensions of the wall specimens and a typical steel reinforcement arrangement are shown in Fig. 6.1. Walls with two different cross sections—rectangular and barbell shaped—were selected for the evaluation of the proposed analytical models. The details of the thirteen wall specimens that were analyzed in this research are summarized in Table 6.1. These walls were identified as R1, R2, R3, R4, B1, B2, B3, B4, B5, B6, B7, B8, and B9. In addition to the wall cross section, the primary experimental parameters were:

- the amount of the flexural reinforcement
- the amount of the horizontal shear reinforcement
- the amount of the transverse reinforcement in the boundary elements
- the axial compressive stress
- the loading history
- the compressive strength of concrete

The flexural reinforcement in each wall specimen was selected based on the flexural provisions of the 1977 ACI Building Code (1). The design compressive strength of concrete was 3000 psi for wall B6 and 6000 psi for all other walls. The design yield stress of the flexural reinforcement was 60 ksi and the strain-hardening effect was neglected (103).

Several criteria were used to select the horizontal web reinforcement in each wall specimen. In specimens R1, R2, R4, B1, B3, and B4, the minimum web reinforcement allowed in the 1977 ACI Building Code (1) was used. In specimens B2 and B5, the web reinforcement was selected such that the nominal shear strength was equal to the nominal flexural strength. The amount of the web reinforcement provided in specimens B2 and B5 was also provided in specimens B6, B7, and B9. The horizontal web reinforcement in wall B8 was selected such that the nominal shear strength was equal to the nominal flexural strength which took into account the increase in the strength of the flexural reinforcement due to the strain-hardening effect (106).

Two methods were used to design the transverse reinforcement in the boundary elements. In the first method, the transverse reinforcement was selected to comply with the provisions in Section 7.10 of the 1977 ACI Building Code (1) for ordinary column ties. This amount of transverse reinforcement, which provided little, if any, confining pressure to concrete in the boundary elements, was used in the specimens R1, B1, and B2. In the second method, which was used for all other specimens, the transverse reinforcement was designed as confinement reinforcement (103). Such reinforcement, which provides a significant amount of confining pressure for concrete in the boundary elements, was fabricated in the form of rectangular hoops and cross-tie reinforcement in accordance with the Appendix A of the 1977 ACI Building Code (1). This confinement was provided only in the lower 6 ft. of the boundary element, and the ordinary column ties were used over the remaining 9 ft. of the specimen.

Specimens R1, R2, and B1 through B5 were tested without any applied axial load. In specimens R3, R4, and B6 through B9, constant axial compressive loads were maintained throughout the loading history. The axial loading system was designed such that the lower reaction beams for axial

load translated with the top displacement of the wall. The resultant axial force remained vertical during the horizontal loading cycles.

For lateral loading, a horizontal force was applied through the top slab such that each wall was loaded as a cantilever beam with a point load at the end (103). Three different loading histories were used: monotonic loading, increasing incremental loading (IR), and modified reversing loading (MR). In the monotonic loading, a wall specimen was subjected to a monotonically increasing load to failure. In the IR loading, the amplitude of the applied displacement cycles was increased incrementally. During each increment, the specimen was subjected to three complete loading cycles. Before yielding occurred, the walls were cycled at three force levels. After initial yielding, deflections were increased by 1 in. during each increment (103). In MR loading, the loading history was determined from "a statistical investigation of the dynamic response of isolated walls to various earthquake motions" (106). The typical IR and MR loading histories are shown in Fig. 6.2. Specimen B4 was subjected to the monotonic loading while specimens R3 and B9 were subjected to MR loading. All other walls were subjected to IR loading.

## 6.2 FINITE ELEMENT MODEL

A typical finite element model of the PCA wall specimens with rectangular and barbell cross sections is shown in Fig. 6.3. Concrete elements are modeled using 4-node isoparametric plane stress elements while reinforcing bars are modeled using 2-node truss elements. The concrete elements can be divided into two groups: the concrete elements in the boundary elements and the concrete elements in the web. Some parameters used to define the material model for these two groups of concrete elements are different because different amounts of flexural and transverse reinforcement influence the behavior of concrete. Each concrete element is surrounded by four steel elements as shown in Fig. 6.3. Horizontal steel elements represent the horizontal web reinforcement and transverse reinforcement in the boundary elements while vertical steel elements represent the longitudinal reinforcement in the boundary elements and the vertical reinforcement in the web. The mesh layout for the analytical model of the wall is governed by the location of the reinforcing bars and

by the size of the boundary elements. Four different mesh layouts were used to model the PCA wall specimens. The details of the mesh layouts are described in Appendix D.

The wall model is fixed at its base. Both translational degrees of freedom ( $u$  and  $v$ ) of all nodes at the base of the wall are constrained. The model is loaded using a displacement-control algorithm. The displacement at the top corner node of the wall is prescribed incrementally to simulate the loading history of the wall specimens. The analysis is terminated when a major failure has been observed in the analytical results. Details of the loading algorithm and the selection of a size of a load step are described in Chapter 5. A layer of elastic elements is placed at the top of the wall model to represent the top slab in a wall specimen. This layer of elastic elements helps distribute lateral load from the corner node to the lower portion of the wall. It also helps prevent excessive cracking of concrete and yielding of steel reinforcement caused by the large concentrated load at the corner node. In the walls with applied axial load, vertical point loads are applied at the top nodes of the boundary elements (Fig. 6.3). The magnitude of the point loads remain constant throughout the analysis.

### 6.3 PARAMETRIC STUDY

As described in Chapter 3, seventeen parameters that are required to define the proposed concrete model include  $\epsilon_i$ ,  $\sigma_i$ ,  $\alpha$ ,  $\sigma_1$ ,  $\sigma_2$ ,  $\sigma_3$ ,  $\sigma_4$ , and  $\sigma_n$  for the normal-stress function and  $\mu_1$ ,  $\mu_2$ ,  $\epsilon_{\min}$ ,  $\gamma_n$ ,  $n$ ,  $\tau_{\text{slip}}$ ,  $G_{\text{unl}}$ ,  $\beta$ , and  $G_{\min}$  for the shear-stress function. Unlike the steel model, where the experimental data on the cyclic response of reinforcing bars are available and can be used for evaluating values of the material model parameters, the experimental data for several important aspects of cyclic behavior of concrete, such as a cyclic shear stress-strain relationship, do not exist. Therefore, a parametric study was required to determine appropriate values for the parameters that define the concrete model. Complete walls were chosen to evaluate the sensitivity of the structural response to the choice of each parameter. An objective of such study was to find one set of parameters that yielded satisfactory calculated responses for all walls. The parameters that define the concrete model were adjusted until several important aspects of the calculated results, such as load vs. deflection

relationship, load vs. shear distortion relationship, crack patterns, and failure modes, agreed with the experimental data from reinforced concrete walls.

The following section describes the parametric study of the concrete model's parameters. The calculated results of walls R1 and B7 were selected to illustrate the sensitivity of the parameters because the behavior of these two walls represent the typical cyclic responses of reinforced concrete shear walls subjected to low and high nominal shear stress. Wall R1 is a representative of the walls that are subjected to low nominal shear stress while wall B7 is a representative of the walls that were subjected to high nominal shear stress. The calculated response of other walls is described in Section 6.4.

### 6.3.1 PARAMETERS USED TO DEFINE NORMAL STRESSES

Eight parameters,  $\epsilon_i$ ,  $\sigma_i$ ,  $\alpha$ ,  $\sigma_1$ ,  $\sigma_2$ ,  $\sigma_3$ ,  $\sigma_4$ , and  $\sigma_n$ , are used to define the stress-strain relationship of cracked concrete in the direction normal to the crack. These parameters control several important aspects of the cyclic behavior of concrete, such as tension stiffening, crack closing, and crack reopening. The sensitivity of the calculated response of wall models to the choice of different values of normal-stress parameters are shown in Fig. 6.4 through 6.15.

$\alpha$  :  $\alpha$  is the parameter that determines the amount of tensile stress retained by concrete immediately after cracking (Fig. 3.4). Figure 6.4 shows the calculated load vs. top deflection curves for wall B4 with different values of  $\alpha$ . It can be seen that too large a value of  $\alpha$  causes sudden drop in the load-carrying capacity of wall B4 while too small a value of  $\alpha$  causes the load-carrying capacity of wall B4 to be significantly lower than the measured response. The value of  $\alpha$  is important for the behavior of the walls subjected to monotonic loading; however, it does not have significant influence on the calculated response of the walls subjected to cyclic loading.

$\sigma_i$  :  $\sigma_i$  defines the tensile stress that cracked concrete is able to sustain after the tensile strain of concrete exceeds  $\epsilon_i$  (Fig. 3.4). Figures 6.5 through 6.8 show the load vs. top deflec-

tion curves and the load vs. shear distortion curves<sup>1</sup> for walls R1 and B7 with different values of  $\sigma_i$  in the boundary elements and web. The different values of  $\sigma_i$  do not have any effect on the shear distortion but have some influence on the calculated strength of the walls. Larger values of  $\sigma_i$  increase the load-carrying capacity of the walls in each cycle because the cracked concrete can sustain higher tensile stress and, therefore, helps the flexural steel to resist the overturning moment. The effects of different values of  $\sigma_i$  are more evident in wall R1 than in wall B7 because wall R1 has smaller reinforcement ratio and, therefore, the contribution of concrete is more important.

$\varepsilon_i$  :  $\varepsilon_i$  defines the strain at which the cracks begin to close (Fig. 3.9).  $\varepsilon_i$  also controls the initial tangent during crack closing (the slope of a line connecting  $[\sigma_2, \varepsilon_i]$  and  $[\sigma_3, \varepsilon_3]$ ). A small value of  $\varepsilon_i$  delays crack closing until tensile strain is small and leads to a large initial tangent stiffness. This causes the tangent stiffness of the load-deflection curve of the wall with a small value for  $\varepsilon_i$  to change abruptly as the majority of the cracks are closing simultaneously. A large value of  $\varepsilon_i$  causes the cracked concrete to start resisting compressive stress at higher tensile strains and, therefore, results in higher flexural stiffness of the wall as the cracks begin to close. As a result, a wall model with high value of  $\varepsilon_i$  tends to have larger shear distortion than a wall model with low value of  $\varepsilon_i$ . This behavior can be observed in the calculated results for walls R1 and B7 shown in Fig. 6.9 and 6.10.

$\sigma_1$  :  $\sigma_1$  determines the initial stiffness of concrete when unloading from tension (Fig. 3.9). A large value of  $\sigma_1$  results in a high unloading stiffness of the wall when a load reversal occurs. However,  $\sigma_1$  effects only the initial unloading stiffness of the load-deflection curve because, once the stress in the cracked concrete reaches  $\sigma_2$ , the stiffness is controlled by other parameters. Figures. 6.11 and 6.12 show the calculated results for walls R1 and B7 with different values of  $\sigma_1$ . Wall R1 is more sensitive to the increase in the unloading stiffness than wall B7, because wall R1 has less flexural reinforcement.

---

<sup>1</sup> Calculation of the shear distortion is described in Section 6.4.2



$\sigma_2$ ,  $\sigma_3$ , and  $\sigma_n$ :  $\sigma_2$ ,  $\sigma_3$ , and  $\sigma_n$  are the parameters that control the stress–strain curve for concrete when cracks are closing.  $\sigma_2$  is the compressive stress at which crack closing is initiated,  $\sigma_3$  defines the initial stiffness of the crack closing curve, and  $\sigma_n$  is the compressive stress at which the cracks are fully closed and the reloading curve merges with the uniaxial compressive curve. The effects of changing the values of these parameters on the calculated response of wall B7 are shown in Fig. 6.13 through 6.15. If the values of these three parameters are adjusted such that the cracked concrete can resist compressive stresses at high tensile strains (for example, large values for  $\sigma_2$ ,  $\sigma_3$ , and  $\sigma_n$ ), the strength of the wall will be greatly reduced because the cracked concrete in the web is capable of resisting compressive stress, even when cracks are open. This reduces the moment arm between the resultant of the compressive and tensile forces and, hence, reduces the flexural capacity of the wall.

It can be seen that the calculated behavior of the wall models is not very sensitive to the values of the normal stress parameters. Small changes in each parameter do not have significant influence on the analytical results. The values of the normal stress parameters used in the analysis of PCA wall tests are given in Table 6.2(a).

### 6.3.2 PARAMETERS USED TO DEFINES SHEAR STRESSES

Nine parameters,  $\mu_1$ ,  $\mu_2$ ,  $\epsilon_{min}$ ,  $\gamma_n$ ,  $n$ ,  $\tau_{slip}$ ,  $G_{unl}$ ,  $\beta$ , and  $G_{min}$ , are used to defined the cyclic shear stress–strain relationship of cracked concrete. The calculated response of wall B7 was used to study the sensitivity of the shear–stress parameters because wall B7 was subjected to high nominal shear stress and experienced large inelastic shear distortion. Therefore, the sensitivity of the shear–stress parameters can be observed in the calculated response of wall B7 better than in the calculated response of other walls, such as wall R1, that were subjected to low nominal shear stress and experienced small inelastic shear distortion. The sensitivity of the calculated response of wall B7 to the choice of different values of the shear–stress parameters are shown in Fig. 6.16 through 6.20.

$\mu_1$  :  $\mu_1$  is a coefficient which defines the interface shear stiffness (Eq. 3.9). It is used to adjust the contribution of the interface shear transfer mechanism to the total shear stiffness

of cracked concrete. Figure 6.16 shows the calculated results for wall B7 with different values of  $\mu_1$ . A small value of  $\mu_1$  causes the load-top deflection curve to experience pinching due to the domination of the shear deformation mode. The load vs. shear distortion curve for the wall with a small value of  $\mu_1$  is controlled mostly by the dowel shear stiffness. A large value of  $\mu_1$  leads to a load deflection curve with less pinching and with smaller shear distortion because the shear stiffness of the wall is large and the wall tends to deform in flexure rather than shear.

$\mu_2$  :  $\mu_2$  is a coefficient which defines the dowel shear stiffness (Eq. 3.11). It is used to adjust the contribution of the dowel mechanism to the total shear stiffness of cracked concrete. Figure 6.17 shows the calculated results for wall B7 with different values of  $\mu_2$ . The effects of different values of  $\mu_2$  have similar trends as that of  $\mu_1$ ; large values of  $\mu_2$  result in well-rounded load-deflection curves with small shear distortions. However, the effect of small values of  $\mu_2$  is less significant than the effect of small values of  $\mu_1$ . This shows that the interface shear transfer is the major shear transfer mechanism in the cyclic response of reinforced concrete shear walls.

$\epsilon_{min}$  :  $\epsilon_{min}$  is the tensile strain at which concrete can no longer provide any interface shear resistance (Eq. 3.9). The interface shear stiffness decreases linearly from the initial value at the cracking strain ( $\epsilon_{cr}$ ) to  $G_{min}$  at  $\epsilon_{min}$  (Fig. 3.21). The calculated results for wall B7 with different values of  $\epsilon_{min}$  are shown in Fig. 6.18. A small value of  $\epsilon_{min}$  results in a load-deflection curve with significant pinching and with large shear distortions because the concrete cannot provide the necessary interface shear stiffness even when cracks are nearly closed. A large value of  $\epsilon_{min}$  leads to a well-rounded load-deflection curve with small shear distortion.

$\gamma_n$  :  $\gamma_n$  is the parameter used in the calculation of the dowel shear stiffness (Eq. 3.14). The calculated results for wall B7 with different values of  $\gamma_n$  are shown in Fig. 6.19.  $\gamma_n$  has a significant effect on the shear distortion of the wall because the dowel shear stiffness is

proportional to  $(1/\gamma_n)^3$ . A small value of  $\gamma_n$  leads to a large dowel shear stiffness, greatly reduces the shear distortion of the wall, and results in a well-rounded load-deflection curve. A large value of  $\gamma_n$  significantly reduces the dowel shear stiffness and results in a load-deflection curve with significant pinching.

$\tau_{slip}$ :  $\tau_{slip}$  defines the shear stress where the shear stiffness increases after the concrete has experienced slip near zero load (Fig. 3.27). The calculated results for wall B7 with different values of  $\tau_{slip}$  are shown in Fig. 6.20. It can be seen that  $\tau_{slip}$  controls the shape of the hysteresis curve near the origin in both the load-deflection and the load-shear distortion curves. A small value of  $\tau_{slip}$  causes significant pinching while a large value of  $\tau_{slip}$  leads to curves with a well-rounded shape.

The calculated response of the walls are more sensitive to the choice of the shear-stress parameters than to the choice of the normal-stress parameters. Small changes in each of the shear-stress parameter may have significant effect on the calculated behavior of the wall. The values of the shear-stress parameters used in the analysis of PCA walls are given in Table 6.2(b).

## 6.4 EVALUATION OF THE FINITE ELEMENT RESULTS

The analytical results from the finite element analysis of reinforced concrete walls contain a variety of information, including nodal reactions, nodal displacements, and stress and strain at all Gauss points. This information is essential to the development and evaluation of the proposed concrete and steel models because it allows different aspects of the results to be compared with the experimental data. The finite element results also provide the opportunity to inexpensively evaluate the behavior of a large number of walls with different configurations and reinforcement details. This information helps researchers gain a better understanding of the cyclic behavior of reinforced concrete walls, which will lead to an improvement in the design provisions for better cyclic inelastic performance of the walls.

In the following sections, several important aspects of the finite element results are compared with the experimental data. The comparisons include load vs. top-deflection curves, load vs. shear distortion curves, failure modes, and crack patterns.

### 6.4.1 LOAD VS. TOP DEFLECTION CURVE

The major function of reinforced concrete shear walls in tall buildings is to provide lateral stiffness. The design of shear walls is usually governed either by strength or lateral-stiffness requirements. For the design of reinforced concrete walls in a seismic zone, the energy dissipation characteristics of the wall are also a major concern. All the important aspects of the cyclic behavior, which include the strength, the lateral stiffness, and the energy dissipation characteristics, are illustrated in the load vs. top-deflection ( $P-\Delta$ ) curve of the walls. As a result, the  $P-\Delta$  curve is the primary focus in the evaluation of the results of the finite element analyses. A successful finite element model must be able to reproduce the  $P-\Delta$  curve from the experimental results accurately.

Calculated and measured  $P-\Delta$  curves for the PCA walls are shown in Fig. 6.21 through 6.33. The calculated response of all thirteen walls are in good agreement with the measured data. In general, these walls can be divided into two groups according to the magnitude of the maximum applied shear stress (103). The first group includes walls R1, R2, R4, B1, B3, and B4 that were subjected to low nominal shear stress (less than  $6.0\sqrt{f'_c}$ ). The second group comprises walls R3, B2, B5, B6, B7, B8, and B9 that were subjected to high nominal shear stress (greater than  $6.0\sqrt{f'_c}$ ).

The cyclic  $P-\Delta$  curves are generally governed by two deformation modes: flexural and shear. In the flexural mode, a wall deforms by changing its curvature along the length of the wall. This mode of deformation is governed by the flexural stiffness of the wall. Under cyclic loading, the walls that deform in the flexural mode dissipate energy through yielding of flexural reinforcement and, therefore, display good energy dissipation characteristics. The shear mode of deformation occurs when the wall deforms primarily by changing the shear distortion in the lower part of the wall. This mode of deformation is governed by the shear stiffness of the wall and is usually less desirable than the flexural mode because the shear mode can cause "pinching" in the  $P-\Delta$  curve which leads

to poor energy dissipation characteristics. Sudden shear failure or web crushing can also occur in the walls that deform primarily in the shear mode.

Each section of the  $P-\Delta$  curve is dominated either by the flexural or shear mode. A wall will deform in the shape that has the minimum strain energy; therefore, it will deform in the mode that has the smaller stiffness. For example, when the applied lateral load is near zero, the majority of the cracks in the lower portion of the wall are open. This results in a low shear stiffness in that portion of the wall. Therefore, in this region of the  $P-\Delta$  curve, the wall deforms primarily in the shear mode. As unloading continues, cracks in the compression zone start to close and reinforcing bars start to provide resisting force through dowel action. The shear stiffness increases and the behavior of the wall is dominated by flexure. In the walls that are subjected to low nominal shear stresses, the flexural stiffness is low due to the low reinforcement ratio in the boundary elements. Consequently, no pinching was observed in the  $P-\Delta$  curve, and the response was dominated by flexure. In the walls that are subjected to large nominal shear stress, the flexural stiffness is large because of the high reinforcement ratio in the boundary elements, and the  $P-\Delta$  curve experience significant pinching or stiffening behavior as the deformation mode changes from shear to flexure.

#### **6.4.2 LOAD VS. SHEAR DISTORTION CURVE**

Average shear distortion in the lower portion of the wall can be estimated from the displacements at four corner points of a rectangular region which is located on a web of the wall (Fig. 6.34). In the experiments, these displacements were obtained from LVDT readings, while in the finite element analysis, they were obtained from the displacements of the corresponding nodes. This shear distortion is an approximation because the calculation is based on several assumptions such as plane section of the wall remains plane and shear strain is uniformly distributed in the web of the wall. However, it provides a reasonable estimate of the cyclic shear distortion in each wall specimen. Because this shear distortion is directly related to the shear transfer mechanisms of reinforced concrete in the web, evaluation of shear distortions is useful in the development and verification of the proposed shear-stress function for the concrete model. The parameters required to define the shear

stress function were adjusted such that the load–shear distortion ( $P-\gamma$ ) curves of the finite element results agree with those of the experimental results.

The comparisons between the measured and calculated  $P-\gamma$  curves are shown in Fig. 6.35 through 6.47. All comparisons show good agreement between the calculated results and the measured data. The  $P-\gamma$  curves can be divided into two groups according to the magnitude of the maximum applied shear stress. The  $P-\gamma$  curves for the walls that were subjected to low nominal shear stress (walls R1, R2, R4, B1, and B3) experienced small, if any, pinching. On the other hand, the  $P-\gamma$  curves for the walls that were subjected to high nominal shear stress (walls R3, B2, and B5 to B9) experienced significant pinching and degradation of shear stiffness in the later cycles.

### 6.4.3 FAILURE MODES

Studying failure modes of the slender reinforced concrete structural walls under cyclic loadings is also another objective of this research. Five different failure modes that were observed in the thirteen wall specimens are (105, 106):

- a) Bar fracture,
- b) Inelastic bar buckling,
- c) Instability of the compression zone,
- d) Web crushing,
- e) Boundary element crushing.

The finite element models developed in this research should also be able to reproduce the mode of failure for each wall and to estimate the deformation level at which the failure occurs. The post–failure behavior of the wall is not incorporated into the proposed model because such behavior is usually unstable and depends greatly on the loading technique used in the experimental work. Furthermore, some failure modes involve a sudden release of a large amount of strain energy which causes numerical problems in the analysis.

The criteria for defining each failure mode are described in the following sections. Comparisons between the calculated and observed failure modes are summarized in Table 6.3.

### **(a) BAR FRACTURE**

Wall B4, which was subjected to monotonic loading, lost its load-carrying capacity because the main reinforcement fractured. Bar fracture was also observed in several other walls, such as R1, B1 and B3. However the bars in these walls had buckled previously which led to the premature rupture of the reinforcing bars.

The proposed steel model incorporates bar fracture by evaluating the calculated axial strain in each steel element. If the strain exceeds the ultimate tensile strain, which is an input parameter for the steel, bar fracture has occurred.

### **(b) INELASTIC BAR BUCKLING**

Inelastic bar buckling was observed in wall R1, B1, and B3. In these walls, longitudinal reinforcement buckled within the lower 3' of the boundary elements. There were three major factors that influenced buckling of the flexural reinforcement:

- The loss of surrounding concrete, which acted as a lateral support for reinforcing bar, caused by alternating tensile and compressive stresses (103, 110).
- The reduction in tangent modulus of steel due to tensile or compressive yielding and the Bauschinger effect (80, 103, 109, 118).
- The eccentric compressive force on the reinforcing bar caused by increasing shear distortion (103, 106).

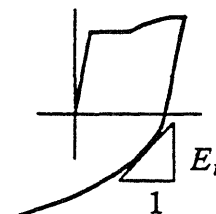
Although, buckling of reinforcing bar did not result in a sudden loss of load carrying capacity in the structural walls, it did lead to bar fracture after several cycles of alternating tensile and compressive stress.

Few researchers have investigated the inelastic bar buckling in reinforced concrete members. Gosain, et al. (62) studied shear requirements for load reversals on reinforced concrete mem-

bers from the experimental results of several other researchers. They reported that loss of concrete cover and reduction of stiffness of reinforcing bars (Bauschinger effect) significantly reduced the buckling capacity of a reinforcing bar. Bertero and Collins (24) investigated inelastic bar buckling in the failure of the Olive View stair towers during the San Fernando earthquake and proposed equations for calculating spacing of steel confinement required to prevent inelastic bar buckling. In both studies, the tangent modulus theory was used to calculate the buckling stress of the reinforcing bar. The equation is similar to the well-known Euler equation except that a tangent modulus ( $E_t$ ) was used instead of Young's modulus (Eq. 6.1).

$$\sigma_{cr} = \frac{\pi^2 E_t}{\left[ \frac{kl}{r} \right]^2} \quad (6.1)$$

- where
- $\sigma_{cr}$  = Buckling stress
  - $E_t$  = Tangent modulus of a reinforcing bar
  - $l$  = Unsupported length of a reinforcing bar (spacing between steel confinement)
  - $k$  = Factor for an effective length of a reinforcing bar
  - $r$  = Radius of gyration of a bar



The value of  $k$  depends on the buckling mode shape of the bar. Gosain et al. (62) and Bertero and Collins (24) recommended the values of  $k$  between 1/2 and 1 based on the buckling mode shape as shown in Fig. 6.48. In this research, the value of 1/2 is used.

In the analysis, the buckling stress of the bars that have potential to buckle (bars at the face of the boundary elements in the lower 3 ft. of the wall) is calculated at the beginning of each load step. If the concrete adjacent to that bar has already spalled and the compressive stress of that bar exceeds the current buckling stress, the bar is considered to buckle. Concrete is considered to have spalled when the following criteria have been met:



- Concrete at that Gauss point has been totally crushed (as described in Section 3.1.4).
- After crushing, the concrete at that Gauss point must have been subjected to alternating tensile and compressive stress for at least four cycles.

The second criterion is based on the observation from the experimental work that concrete does not spall immediately after it has been crushed (110). The crushed concrete starts spalling after it has been subjected to a few cycles of alternating tensile and compressive stress. In the proposed model, a reinforcing bar is considered to lose its lateral support when concrete at the closest two Gauss points has spalled.

### **(c) INSTABILITY OF THE COMPRESSION ZONE**

In this mode of failure, an out-of-plane instability of the compression zone occurred in the lower 3 ft. of the wall. It was observed only in wall R2. The wall lost its load-carrying capacity when a large out-of-plane displacement occurred in the lower portion of the wall following several large load reversals. This failure mode cannot be detected by the proposed model. In order to detect this mode of failure, buckling capacity of the wall needs to be investigated, which is beyond the scope of this investigation.

### **(d) BOUNDARY ELEMENT CRUSHING**

Specimens R3 and R4, both of which were rectangular walls with applied axial loads, failed because the concrete in the boundary elements was crushed completely. The criteria for concrete crushing are discussed in Chapter 3. For confined concrete, the compressive stress-strain relationship can be divided into three regions: uncrushed, crushed plateau, and totally crushed (Fig. 3.12). Confined concrete is considered to be crushed when the compressive stress-strain curve reaches the totally crushed region ( $\epsilon < \epsilon_2$ )<sup>2</sup>. The value of  $\epsilon_2$  depends on the amount and the arrangement of steel reinforcement as described in Appendix B. For unconfined concrete (Fig. 3.10), the compres-

---

<sup>2</sup> Compressive strain is considered to be negative while tensile strain is considered to be positive.

sive stress–strain relationship does not have the crush plateau. Concrete changes directly from uncrushed to totally crushed. To check crushing of concrete, the calculated compressive strain at every Gauss point is checked at the beginning of each new load step. If the compressive strain is less than  $\epsilon_2$  for confined concrete or is less than  $\epsilon_{ult}$  for unconfined concrete (Fig 3.10 and 3.12), concrete at that Gauss point is considered to be crushed.

### (e) WEB CRUSHING

Web crushing is a common failure mode in beams or walls “with large flanges and relatively thin web subjected to high shear stress” (103). The PCA wall specimens that experienced web crushing are B2, B5, B6, B7, B8, and B9. As reported by Oesterle et al. (103), web crushing strength of structural wall depends on deformation history, concrete strength, applied axial load, and applied lateral load. They also reported that the compressive strength of concrete struts in the web decreased due to the deformation history. Such decrease in compressive strength led to the web crushing in concrete struts at a stress level that is much lower than the compressive strength of concrete.

Several researchers have proposed analytical models for calculating the effective strength of concrete struts as described in Eq. 6.2 through 6.4.

$f_d$  = Effective compressive strength of concrete struts

$$\text{Placas and Regan (117): } f_d = (25 + 500 \rho_h) \sqrt{f'_c} \quad (6.2)$$

$\rho_h$  = Horizontal shear reinforcement ratio

$$\text{Collins (40): } f_d = k_d f'_c \quad (6.3)$$

$$k_d = \frac{3.60}{1 + \frac{2\gamma}{\epsilon_0}}$$

$\gamma$  = Average value of maximum shear strain  
 $\epsilon_0$  = Axial strain at peak compressive stress of concrete cylinder

$$\begin{aligned}
\text{Stevens et al. (134):} \quad f_d &= k_d f'_c && (6.4) \\
k_d &= \frac{1}{0.80 + 0.34 \left[ \frac{\varepsilon_1}{\varepsilon_0} \right]} \\
\varepsilon_1 &= \text{Principal tensile strain } \perp \text{ to crack} \\
\varepsilon_0 &= \text{Axial strain at peak compressive stress} \\
&\quad \text{of concrete cylinder}
\end{aligned}$$

Oesterle et al. (104) compared the effective strength calculated from Eq. 6.3 with the experimental results from the PCA tests of isolated walls. The calculated results agree with the experimental data as shown in Fig. 6.49.

During the experimental tests, it was observed that crushing of concrete struts started in the lower 3 ft of the compression zone in the walls that failed in the web crushing mode. These sections of the webs experienced high shear distortions prior to the crushing (0.010–0.030 radian). Therefore, it is reasonable to assume that the reduction in compressive strength of concrete struts in slender reinforced concrete walls is related to shear distortion in the lower portion of the walls. The equation proposed by Collins (Eq. 6.3), which uses shear distortion as a measure of strain condition, was adopted in this research as a means of calculating the effective compressive strength of the concrete struts. Although Eq. 6.4, which was proposed by Stevens et al., is a refined version of Eq. 6.3, it is not appropriate for the analysis considered in this study because principal tensile strain is used as the measure of the strain condition. If Eq. 6.4 is used to calculate web crushing in shear walls, web crushing would be calculated to occur in the tensile boundary element, where the principal tensile strain is highest, rather than in the compression zone as observed in the PCA wall tests.

In the proposed model, the compressive stress in the direction of the crack and the effective compressive strength are calculated at every Gauss point. If the compressive stress exceeds the effective compressive strength at any location, the concrete at that point is considered crushed. Because the effective strength of concrete calculated from Eq. 6.3 is approximate, the proposed model can only indicate the possibility of a web crushing mode of failure in an approximate manner. During the analyses, web crushing was evaluated at the peak positive and negative displacement of each

load cycle. If the effective compressive strength of the concrete was exceeded at more than eight Gauss points in the web, web crushing was considered to have occurred during that load cycle.

#### 6.4.4 CRACK PATTERNS

Crack patterns of the wall specimens can also be divided into two groups according to the level of the maximum nominal shear stress applied to the walls (103). Crack patterns of the walls that were subjected to low nominal shear stresses (walls R1, R2, R4, B1, and B3) consist of large horizontal cracks in the lower 3 ft. of the walls and some inclined cracks in the upper portion of the walls (Fig. 6.50[a]). These horizontal cracks, which are the result of large tensile strain in the boundary elements, governed the cyclic response of the walls after a few inelastic cycles. The shear stresses were transferred primarily by aggregate interlock and dowel action mechanisms. Because of the low flexural strength of the walls, these shear transfer mechanisms were adequate to prevent a brittle shear failure mode and to develop the flexural failure mode instead. Crack patterns of the walls that were subjected to high nominal shear stresses (walls R3, B2, B4 through B9) were dominated by the inclined cracks "crisscrossing" the web (106) (Fig. 6.50[b]). Shear stress was transferred primarily by truss action of the concrete struts along these inclined cracks. Because of their high flexural strength which resulted in high compressive stress in the concrete struts, these walls failed by crushing of concrete in the web.

The typical calculated crack patterns in a wall that was subjected to low nominal shear stress (wall R1) and in a wall that was subjected to high nominal shear stress (wall B7) are shown in Fig. 6.51 and 6.52. Crack patterns are shown at seven load steps, each of which is the load step corresponding to a maximum or minimum displacement during the loading cycle. The thickness of each crack represents the magnitude of the tensile strain normal to the crack. The calculated crack pattern for wall R1 is dominated by horizontal cracks in the lower portion of the wall from the early stages of loading. Inclined cracks occur in the upper portion of the web during the later stages of loading. However, the crack widths of the horizontal cracks are larger than those of the inclined cracks. The calculated crack pattern for wall B7 includes both inclined cracks in the web and horizontal cracks

in the boundary elements. The steep angles of cracks in the web reflect the presence of high shear stresses. This shear stress, which is a result of the applied compressive axial stress and a large amount of flexural reinforcement in the boundary elements, caused the principal stress direction to rotate from the vertical direction and resulted in the inclined crack angles. As the load reversal continues, the widths of both the inclined and horizontal cracks increase. This reflects the combination of both the flexural and shear modes of deformation. The calculated crack angles in the web for wall B7 (Fig. 6.52), most of which are close to 45 degrees, are more uniform than those for wall R1, which are more scattered. Such behavior was also observed in the experimental results (Fig. 6.50).

Another important observation from the calculated crack pattern is that the majority of the cracks remained open throughout the loading cycles in the lower portion of both walls R1 and B7. Only a small number of cracks, most of which were in the compression zone, closed. Because the concrete with wide-open cracks could provide little compressive and tensile resistance, the major force resistance in the lower portion of the wall was provided mainly by the reinforcing steel. This behavior confirms the important role of reinforcing steel in governing the cyclic response of reinforced concrete shear walls.

## **6.5 TYPICAL CYCLIC BEHAVIOR OF R/C SHEAR WALLS**

As mention in Section 6.2, the results of the finite element analysis contain a variety of information, some of which cannot be measured directly and are useful for understanding of the cyclic response of reinforced concrete shear walls. It is important for the finite element users to realize that despite the several digits of precision obtained from the calculations, the finite element results cannot be more accurate or better than the assumptions used in the material models. The finite element method can provide valuable information as long as the users are aware of all the important assumptions made in the material models and the limitations of finite element analysis, in general.

In the following section, detailed results from the analysis of two wall specimens, R1 and B7, are examined. R1 is representative of the walls that were subjected to low nominal shear stress while B7 represents the walls that were subjected to high nominal shear stress. The analytical results

include deformed shapes, stress and strain distributions in the concrete, and stress–strain relationship in the reinforcing steel.

The deformed shapes, shear strain distribution, axial strain ( $\epsilon_y$ ) distribution, and axial stress ( $\sigma_y$ ) distribution for walls R1 and B7 at several load steps are shown in Fig. 6.53 through 6.60. The load vs. strain curves for the longitudinal reinforcement are given in Fig. 6.61 and 6.62. The distributions of strain in the vertical reinforcement at different heights above the base are shown in Fig. 6.63 through 6.66. The complete stress–strain relationships for vertical reinforcing bars in the lower 3 ft of walls R1 and B7 are shown in Fig. 6.67 and 6.68. Some important aspects of the cyclic behavior of the walls are summarized below:

- Although wall R1 has a well–rounded force–deformation curve indicating good energy dissipation characteristics, the shear strain in the lower portion of wall R1 is as large as that of wall B7 (Fig. 6.54 and Fig. 6.58). This shows that the well–rounded P– $\Delta$  curve of wall R1 is not caused by the domination of the flexural mode of deformation but rather is caused by the low flexural stiffness of the wall. As a result, no pinching or increase in lateral stiffness is observed in the load–deflection curve as the mode of deformation changes from the shear mode to the flexural mode. In spite of the large shear distortion, wall R1 does not experience web crushing because the strength of the wall is governed by the low flexural capacity.

- Shear distortions in both wall R1 and B7 are concentrated in the lower 6 ft of the walls. When the vertical steel yields, the crack widths increase. The increase in crack width greatly reduces the ability of concrete to transfer shear stress by aggregate interlock. The concentration of the shear distortion occurs in the area where the vertical steel has yielded (Fig. 6.54, 6.55, 6.58, and 6.59). Therefore, one possible way to decrease shear distortion of the wall is to provide additional reinforcement in the lower portion of the wall to help minimize the crack width of concrete in the web and, therefore, improve the shear transfer mechanism by aggregate interlock. This approach is discussed in Chapter 8.

- The distribution of vertical stress and strain in walls R1 and B7 (Fig. 6.55, 6.56, 6.59, and 6.60) indicates that compressive stresses exceed  $0.20 f'_c$  in the lower 8 ft of the boundary element in wall R1 while at least 12 ft of the boundary element in wall B7 is subjected to the same level of compressive stress. According to Section 21.5.3 of the 1989 ACI Building Code (2), which requires transverse reinforcement to be provided in the boundary elements with the stress<sup>3</sup> at the extreme fiber exceeding  $0.20 f'_c$ , the transverse reinforcement should be provided in the boundary elements of wall R1 up to the height of 7 ft and in the boundary elements of wall B7 up to the height of 12 ft. Based on the calculated results, the code provisions can estimate the location where the transverse reinforcement is needed in the boundary elements fairly accurately despite the simple method used in the calculation. However, if the configurations of the wall are more complicated or the wall is subjected to different types of loadings, these simple code provisions are not likely to be able to estimate correctly the location where the transverse reinforcement is needed. In such situation, finite element analysis can be used to estimate the level of compressive stress in the boundary elements for a proper design of the transverse reinforcement.

- The distribution of strain in vertical reinforcement at different sections of the walls are shown in Fig. 6.63 through 6.66. In both walls, the vertical strain distribution is not linear as usually assumed in the design process. A large strain gradient occurs in the compression zone. Because the compression zone is relatively small compared with the depth of the wall and the stress in reinforcing steel does not vary much after the steel has yielded, the assumption of linear strain distribution still provides a reasonable approximation of the flexural strength of the walls. However, such assumption is inadequate to estimate the stiffness of the wall especially when the wall is subjected to several large load reversals. In order to more closely estimate the deformation characteristics of the walls, the nonlinear distribution of vertical reinforcement at different sections must be considered.

---

<sup>3</sup> Stress is calculated from the factored force using a linear model and gross-section properties.

- The plots of load vs. strain in the main flexural reinforcement of walls R1 and B7 are shown in Fig. 6.61 and 6.62. This curve together with the  $P-\Delta$  curves (Fig. 6.21 and Fig. 6.31) and the  $P-\gamma$  curves (Fig. 6.35 and Fig. 6.45) illustrate the load resisting mechanisms in shear walls. Each half cycle of a  $P-\Delta$  curve consists of three major regions: 1) stiff unloading region, 2) shear dominated region, and 3) flexural dominated region. The stiff unloading region is a result of the initially high flexural and shear stiffness at the beginning of a load reversal. The shear dominated region is the section of the curve where a large increase in shear distortion occurs in the lower portion of the wall, while the flexural dominated region is the section of the curve where there is a large change in a curvature of the wall. For example, in the last load reversal of wall R1 (+4.00 in. to -4.00 in. in Fig. 6.21), the stiff unloading region is section A-B. Because of high shear and flexural stiffnesses at the beginning of unloading, there are small changes in the strain in longitudinal reinforcement (Fig. 6.61) and in the shear distortion (Fig. 6.35) in this region. The next region, which is the section of the curve from point B to point C (Fig. 6.21), is dominated by shear distortion. In this region, the top of the wall travels 3.0 in. with a large increase in shear distortion in the lower portion of the wall (Fig. 6.35) but with a small increase in compressive strain of the flexural reinforcement (Fig. 6.61). This shows that the wall deforms more in the shear mode than in the flexural mode. The next region, which is the section of the curve from point C to point D (Fig. 6.21), represents the flexural dominated region. In this region, the top of the wall travels 3.8 in. with a much smaller increase in shear distortion than that in the previous region (Fig. 6.35) but with large increase in the compressive strain in the flexural reinforcement (Fig. 6.61). This shows that, in this region, wall R1 deforms primarily in the flexural mode. Wall B7 also exhibits similar behavior. The only difference is that the flexural stiffness of wall B7 is much greater than that of wall R1. This results in pinching of the  $P-\Delta$  curve as the curve changes from the shear dominated region to the flexural dominated region.

- The typical stress-strain relationship for vertical reinforcing steel in the lower 3 ft of walls R1 and B7 are shown in Fig. 6.67 and 6.68. All the reinforcing steel in this region



started yielding at the early stage of loading. Reinforcing bars that were located near and in the boundary elements experienced large load reversals and a significant Bauschinger effect. Tensile stress in the longitudinal bars at the base of both boundary elements could be as high as 140% of the yield stress. This high stress had a significant effect on the ultimate capacity of the walls and must be considered when the ultimate strength of the walls was evaluated. It can also be seen that most of the reinforcing bars in the lower portion of both walls R1 and B7 experienced tensile strain during most of the loading history. This indicates that the majority of the cracks in the lower portion of the walls remained open throughout the loading history and the major force resistance was provided by reinforcing steel.

All these calculated results illustrate the variety of information that can be obtained from the finite element analysis. Such information can be useful both in the design process to check the inelastic response of shear walls and in the research to obtain better understanding in the behavior of shear walls. Applications of the finite element method in the analysis of reinforced concrete shear walls are discussed in Chapter 8.

## 7. TESTS OF C-SHAPED WALLS

When reinforced concrete shear walls are used as lateral load resisting systems in tall buildings, they are commonly constructed as elevator cores or stair wells. Such practices result in shear walls with intersecting flanges in the orthogonal direction. Although these intersecting flanges have a significant influence on the behavior of the wall when subjected to lateral loads, the flange contribution to the overall, load resisting capacity of the walls is not explicitly defined. For the design of structural walls, the current 1989 ACI Building Code (2) does not have any provision for evaluating the effective width of intersecting flanges. Provisions for evaluating the effective width of T-beams are typically used. The definition of effective width for T-beams provides a conservative estimate of the strength of a wall under monotonic loadings; however, it is inadequate for calculating the behavior of the wall when subjected to cyclic loading. As a result, a better understanding of the contributions of intersecting flanges to the overall behavior of a wall is needed.

There are also several other aspects of the behavior of intersecting legs that need further study, such as influence of vertical and horizontal web reinforcement and effects of confinement reinforcement in the boundary elements. In order to provide some of the needed information, an experimental program was undertaken to investigate the strength and stiffness characteristics of walls with intersecting flanges subjected to cyclic loadings. Two isolated, C-shaped wall specimens were tested under lateral load reversals at the University of Illinois.

In this chapter, the experimental program is discussed briefly, the experimental results are summarized, and the proposed analytical models are used to calculate the cyclic response of the two wall specimens.

### 7.1 EXPERIMENTAL PROGRAM

The major objectives of the experimental program were:

- 1) to investigate the inelastic cyclic response and energy dissipation characteristics of walls with intersecting flanges;

- 2) to determine the effective stiffness of walls with intersecting flanges at various levels of displacement;
- 3) to determine the influence of the amount of web reinforcement on the behavior of the walls;
- 4) to provide experimental data to verify the results from finite element models of walls with intersecting flanges.

In order to accomplish these objectives, two C-shaped, reinforced concrete walls were constructed and subjected to cyclic loadings. The details of the specimens and the testing procedures are described as follows.

### **7.1.1 C-SHAPED WALL SPECIMENS**

Both of the wall specimens (walls CMS and CLS) had a C-shaped cross section. Each section consisted of two 36-in. long parallel webs and a 60-in. long connecting flange as shown in Fig. 7.1. Both walls were 9-ft. tall and 3-in. thick. The 60-in. flange width was chosen to be longer than the effective width defined for a T-beam with a 3-in. flange in Sections 8.10.2 and 8.10.4 of the 1989 ACI Building Code (2). Each wall was cast on a base girder which was later anchored to the testing floor.

Both walls had the same amount of flexural reinforcement. The main longitudinal reinforcement in each web consisted of ten #3 bars, four of which were placed in the boundary element at the intersection between the flange and the web while the other six bars were placed in the boundary element at the north end of the web (Fig. 7.1). The transverse reinforcement in the boundary element was made from No.10 gage wire. Square spirals were used in the boundary elements with four longitudinal reinforcing bars while rectangular spirals with cross-ties were used in the boundary elements with six longitudinal reinforcing bars (Fig. 7.1). The vertical spacing of all transverse reinforcement was 2 in. The amount of transverse reinforcement provided in the boundary elements was equal to

approximately two-thirds of the amount required in the 1989 ACI Building Code (2) for walls with high axial stresses.

The difference between walls CLS and CMS was the amount of web reinforcement. Wall CLS was designed to have a web reinforcement ratio of 0.0025, the minimum allowed in the 1989 ACI Building Code (2), while wall CMS had twice as much web reinforcement. Web reinforcement ratios in the vertical and horizontal directions are equal. A single layer of #2 deformed bars were used as the web reinforcement. The nominal spacing of the bars was 6 in. in wall CLS and 3 in. in wall CMS (Fig. 7.1). Measured material properties for these two walls are given in Appendix F.

Both walls were subjected to static load reversals with the lateral force applied at the top of the wall. Reinforcement was selected such that the nominal flexural capacity of each wall was less than the nominal shear capacity. According to the 1989 ACI Building Code (2), the nominal shear capacity of wall CLS was 63.3 kips and the nominal shear capacity of wall CMS was 99.4 kips. The nominal flexural capacity of wall CLS was between 44.6 kips and 51.8 kips while the nominal flexural capacity of wall CMS was between 53.2 kips and 64.4 kips. The lower bound of the nominal flexural capacity was obtained using an elasto-plastic stress-strain relationship for the reinforcing steel while the upper bound estimate included the strain-hardening behavior.

### **7.1.2 TESTING PROCEDURES**

Both wall specimens were subjected to lateral load reversals in the north-south direction. The lateral load was applied by a single ram with a capacity of 100 kips located on the top of the wall (Fig. 7.2). The ram was attached to a 2-in. thick steel plate which transferred load from the ram to the wall specimen. All vertical reinforcing bars extended through the steel plate. The longitudinal steel and vertical web steel had been threaded at the top prior to construction. Nuts were used to clamp the steel plate in place. The slip along this joint was measured to be less than 0.005 in. throughout the entire series of tests.

An axial load of 100 kips was applied to both wall specimens. The load was applied by eight center hole jacks which were placed on the top steel plate as shown in Fig. 7.2. The locations of these

jacks were selected such that the axial load was evenly distributed over the cross section. The axial load, which resulted in a nominal axial stress of 265 psi, was maintained throughout the test.

Each wall specimen was subjected to five stages of lateral load reversals. In stage I, a load of  $\pm 10$  kips<sup>1</sup>, which was approximately half of the initial cracking load, was gradually applied to the wall specimen. This load cycle was used to evaluate the uncracked stiffness of the wall specimen and to check whether all the instruments were working properly. In stage II, the wall specimen was loaded to top deflection of  $\pm 1$  in. In stage III, the wall specimen was again loaded to  $\pm 1$ -in. top deflection for two more cycles. This stage caused further yielding of the flexural reinforcement. In stage IV, the wall specimen was loaded for three cycles at  $\pm 1.5$ -in. top deflection. Finally, in stage V, the wall specimen was loaded until it failed. In this stage, the wall specimen was loaded to a top deflection greater than 2 in. The exact deflection was determined during the test according to the performance of the wall. The objective of this stage was to allow the wall specimen to experience a top deflection greater than 2 in. for several cycles. The displacement histories for stages II to V for walls CLS and CMS are shown in Fig. 7.3.

### 7.1.3 INSTRUMENTATION

Three types of displacement measuring instruments were used during the tests: Linear Voltage Displacement Transducers (LVDTs), dial gages, and mechanical strain gages. Thirty-seven LVDT's were used to monitor the response of specimen CLS and 45 LVDT's were used for specimen CMS. Twelve of these LVDTs measured the horizontal displacements, 9 ft, 6 ft, and 3 ft above the base girder along the north and south sides of both webs. Twelve other LVDTs measured the relative displacements in the diagonal, horizontal, and vertical directions of four points that were located in a 30-in. square in the lower, interior panel of both webs (points A,B,C, and D in Fig. 7.1(a)). These displacements were used to calculate shear distortion in the lower portion of the web. Thirteen other LVDTs measured the vertical displacement of the wall at 3 in. above the base. Four of these LVDTs were located at each of the four corners while the other nine were located along the base of the flange.

---

<sup>1</sup> Positive loadings cause the transverse flange to be in compression while negative loadings cause the transverse flange to be in tension.

In wall CMS, eight LVDTs were added to measure the vertical movement of the base girder. Some of the measurement from these LVDTs were later compared with the calculated nodal displacements from the finite element result. Such comparison is discussed in Section 7.4. A total of 26 dial gages were attached to each wall specimen. These dial gages were used to measure the displacements and rotations of the base girder, to measure slip along the construction joints, and to provide backup measurements for some of the LVDTs.

Two other types of instruments that were used to collect data during the tests were strain gages and load cells. Strain gages were attached to some of the vertical web reinforcement and main flexural reinforcement near the base of the wall specimen. Load cells were used to measure the applied axial load in each jack. Data from LVDTs, strain gages, and load cells were collected by the data acquisition system and recorded digitally using a personal computer.

## 7.2 OBSERVED RESPONSE OF THE WALLS

Both walls remained uncracked during stage I. During stage II and III, cracking of the concrete was observed in the lower portion of the wall and yielding of the longitudinal reinforcement in the boundary elements and vertical web reinforcement in the transverse wall was observed. Significant horizontal cracks and inclined cracks were also observed in the webs of the specimens. Concrete in the north boundary elements started spalling in this stage of the loading history. In stage IV, at  $\pm 1.5$ -in. top deflection, all cover concrete in the north boundary elements spalled. The main flexural reinforcing bars in the north boundary elements were observed to buckle slightly. However, such buckling did not progress because the bars were still restrained by the confinement reinforcement.

Failures of both wall specimens occurred in load stage V following crushing of the concrete in the north boundary elements. Specimen CLS lost its load-carrying capacity when the rectangular spiral reinforcement in the lower portion of the north-west boundary element suddenly fractured and several longitudinal reinforcing bars buckled. This spiral reinforcement fractured because the adjacent longitudinal bars in the lower portion of the boundary element buckled in opposite direc-

tions. Specimen CMS lost its load-carrying capacity at the second cycle approaching -2.50-in. top deflection when extensive buckling of the longitudinal bars occurred in the north boundary elements. However, no fracture of the spiral reinforcement was observed in wall CMS because the adjacent longitudinal bars in the lower portion of the boundary element buckled in the same direction. After the failure, the region of crushed concrete extended nearly the entire length of the web in both wall specimens.

## **7.3 FINITE ELEMENT MODEL**

After the completion of the experimental program, the analytical models were developed to study the behavior of the walls. The selection of the finite element model and the analytical procedures are described below.

### **7.3.1 CHOICE OF ELEMENT**

The material model for concrete described in Chapter 3 was developed for two-dimensional plane stress elements. The model yielded satisfactory results for the analysis of reinforced concrete shear walls with rectangular and barbell cross sections. Because of the configuration of the intersecting flanges in the C-shaped walls, the original plan was to modify the concrete material model to be used with shell elements and use the shell elements to model the three-dimensional wall specimens. But when the problem was considered carefully, it was found that it might be possible to use two-dimensional plane stress elements to model the C-shaped wall instead of shell elements without a loss in the accuracy of the solution.

A shell element incorporates two types of stiffness: bending stiffness and in-plane stiffness. Without the bending stiffness, the shell element will behave in the same manner as a two-dimensional plane stress element. The C-shaped walls tested in this investigation had a long, thin flange (the span-to-depth ratio was about 36). Therefore, the bending stiffness of the flange will contribute little to the total stiffness of the wall (especially when the concrete in the flange cracks and the flexu-

ral stiffness of the flange is greatly reduced) and the flange in the C-shaped wall can be modelled by using two-dimensional plane stress elements.

Two linear finite element analyses of a C-shaped wall with the same dimensions as those of the walls tested in this research program were conducted to evaluate differences in the calculated results when the two-dimensional and the shell elements were used (Fig. 7.4). In the first analysis, two-dimensional plane stress elements were used to model the wall while the shell elements were used in the second analysis. In both cases, the top corner node of the wall was subjected to a prescribed displacement of +1 in. (positive top displacement causes the intersecting flange to be in compression). The results of the two analyses are compared in Fig. 7.5 through 7.7 and in Table 7.1. Several aspects of the calculated results are compared in these figures, including the distribution of vertical displacement along the top of the wall (Fig. 7.5), the deformed shape (Fig. 7.6), the vertical stress distribution in the wall (Fig. 7.7), the reaction at the corner node (Table 7.1), and the CPU time required in the analysis (Table 7.1). The distribution of the vertical displacement at the top of the wall was selected for comparison because it represents the sum of the vertical strains distributed along the vertical axis of the web and flange and, hence, represents the overall contribution of the web and flange in resisting the applied horizontal load. It can be seen that all these aspects of the calculated results using two-dimensional plane stress elements are nearly the same as those using shell elements. But using two-dimensional elements requires only about 1/7 of the CPU time required when using shell elements (Table 7.1). Therefore, two-dimensional plane stress elements were used to model the C-shaped shear wall in this investigation.

### **7.3.2 WALL MODEL**

Two-dimensional plane stress elements were used to model concrete elements in the walls. The same model was used for both walls CLS and CMS and, because of the symmetry, only half of each wall was modelled. The only difference between the finite element model of the two walls is the amount of web reinforcement. The model comprises 266 concrete elements and 536 steel elements. All nodes at the base of the wall were fixed in the horizontal and vertical directions (Fig.



7.8). The axial load was applied by vertical nodal loads at 2 nodes in the web and 6 nodes along the south flange of the wall (Fig. 7.8). The horizontal displacement in the direction of loading at top corner node (Fig. 7.8) was specified to be the same as the displacement history used in the experimental program (Fig. 7.3).

In the analyses of walls CLS and CMS, the values of all parameter used in the material models are the same as those used in the analyses of the PCA walls in Chapter 6 with two exceptions indicated below:

- For  $\epsilon_0$ , which controls the shear stiffness caused by aggregate interlock, a value of  $25.0 \cdot \epsilon_{cr}$  was used instead of  $12.50 \cdot \epsilon_{cr}$ . This change did not have influence the calculated load vs. top deflection response of the walls. However, it reduced the shear deformation in the lower 3 ft of the wall to a level which was consistent with the experimental results. The difference between the value of  $\epsilon_0$  used in the PCA walls and that used in the C-shaped walls might be attributed to two factors: the difference in the magnitude of the applied axial stress and the difference in the type of gravel used in the concrete mix of the wall specimens. These two factors have significant influence on the interface shear transfer stiffness of cracked concrete. The adjustment of the material model parameters indicates that the finite element analysis cannot completely replace the experimental work and the experiment results are still needed for calibrating the material model. However, once the material model has been calibrated for a certain type of reinforced concrete member, the finite element method can be used to extend the investigation on the response of that reinforced concrete member with different configurations, reinforcement details, and loading histories.

- The concrete elements in the south flange (which were modelled by using two-dimensional plane stress elements in the Y-Z plane) provided no shear stiffness in the direction of loading. Therefore, some of the shear stiffness parameters in the concrete elements in the south boundary elements ( $\mu_1$ ,  $\mu_2$ ,  $G_{min}$ ,  $\tau_{slip}$ , and  $G_{unl}$ ) were increased by a

factor of 10 to take into account the increased shear stiffness of the south flange. The factor was determined by dividing the width of the south flange by the thickness of the boundary element. The other shear stiffness parameters ( $\epsilon_{\min}$ ,  $\gamma_n$ ,  $n$ , and  $\beta$ ) were not changed because they are not effected by the difference in the thickness of the concrete element.

## 7.4 EVALUATION OF THE FINITE ELEMENT RESULTS

The comparisons between the calculated load vs. deflection at 3-ft, 6-ft, and 9-ft levels and the experimental data for walls CLS and CMS are shown in Fig. 7.9 and 7.10. The comparisons between the calculated load vs. shear distortion in the lower 3 ft of the web and the experimental data are shown in Fig. 7.11 and 7.12. The calculated responses of both walls are in good agreement with the experimental data.

The criteria for evaluating the failure modes in the analyses of the PCA walls (Section 6.4.3) were also used in the analyses of the C-shaped walls. The comparisons between the calculated failure modes and the observed failure modes are given in Table 7.2. The calculated results indicated that extensive crushing of concrete and inelastic bar buckling occurred in the north boundary elements of both walls in load stage V. Extensive web crushing in the lower portion of both walls was also observed during the last load cycle of the calculated response. These calculated failure modes agreed with the experiment results. In the experiments, both walls lost their load-carrying capacity after the north longitudinal reinforcement had buckled and the concrete in the north boundary elements had been crushed. Crushing of concrete along almost the entire length of the web was also observed in both walls at the end of the tests.

Several aspects of the calculated responses of wall CLS and CMS are shown in Fig. 7.13 through 7.22. Figures 7.13 through 7.18 show the calculated deformed shapes, the calculated vertical stress distribution, and the calculated shear strain distribution at different top-deflection levels for walls CLS and CMS. Figures 7.19 and 7.20 show the calculated crack patterns of both walls at different top-deflection levels. Figures 7.21 and 7.22 show the plots of the stress-strain relationship

of vertical reinforcement in the south flange at 3 in., 9 in., and 15 in. above the base. The following describes several important aspects of the calculated cyclic behavior of the C-shaped walls:

- Inelastic shear strain was concentrated in the lower 3 ft. of both walls (Fig. 7.15 and 7.18). The south flange did not significantly increase the inelastic shear stiffness of the walls. This is due to the fact that the thickness of the flange was much less than the depth of the web, and cracks in the lower portion of the flange remained open during most of the loading history. As a result, the shear stiffness of the flange in the N-S direction was much smaller than the shear stiffness of the web. Although wall CMS had twice the amount of web reinforcement provided in wall CLS, both walls experienced the same magnitude of shear distortion in the lower 3 ft of the walls. This indicates that the vertical and horizontal web reinforcement did not significantly improve the inelastic shear transfer capacity of the wall. The influence of different reinforcement details on the inelastic shear stiffness of walls is discussed in Section 9.1.

- As can be seen in Fig. 7.21 and 7.22, all the vertical steel at the base of the flange was effective in providing tensile resistance when the flange was in tension. All vertical reinforcement at the base of the south flange experienced similar stress-strain histories. This indicates that the effective width of the flange when it was in tension could be as high as ten times the thickness of the flange. The use of a too small effective width can lead to a significant underestimation of the strength of the wall. This might result in the selection of inadequate transverse reinforcement and unexpected crushing of the concrete in the boundary elements opposite the intersecting flange.

- When the flange is in compression, the concrete in the flange helps the south boundary elements provide the compression resistance. Figures 7.14 and 7.17 show that the compressive stress in the flange and in the south boundary element was quite uniform and remained low (less than  $0.3 f_c'$ ) throughout the analyses. This indicates that concrete in the entire flange was effective in providing the compression resistance for the wall. However,

the effective width of the flange at its capacity cannot be concluded from the calculated response because the amount of reinforcement in the north boundary element was not enough to cause crushing of the concrete in the south boundary elements and in the intersecting flange.

Because only two walls were analyzed, no major conclusions on the general cyclic behavior of C-shaped walls could be drawn from the calculated response. However, the proposed finite element models successfully simulated several important aspects of the cyclic behavior of C-shaped walls. Therefore, the finite element method can be used to extend the investigation on the behavior of C-shaped walls with different configurations. Such an investigation is discussed in Section 9.3.

## 8. APPLICATIONS OF THE FINITE ELEMENT METHOD

The material models for concrete and reinforcing steel that were presented in Chapters 3 and 4 and verified in Chapters 6 and 7 can now be used to investigate behavior of reinforced concrete walls with different configurations and loading histories. Finite element analysis of reinforced concrete members is useful both in research and in practice. In research, finite element analyses may be used to expand the scope of an experimental program. Because experimental testing is usually expensive and time-consuming, only a limited number of parameters can be studied. The finite element method can be a powerful tool for extending an investigation on the behavior of reinforced concrete members, provided that the finite element analysis is able to simulate all the important aspects of the experimental results. Finite element analysis also helps researchers to understand experimental results better by providing some important information (such as distribution of curvature and strain) which cannot be obtained from the experimental results. In design offices, the finite element method can be used to check the load distribution within each component of a structure, to check the behavior of a structure subjected to different types of loadings, and to improve the behavior of a structure by changing the reinforcement details.

This chapter illustrates three applications of finite element analysis to investigate the behavior of reinforced concrete shear walls. In the first application, finite element analysis is used to investigate the energy dissipation capacity of shear walls with different reinforcement details. The second application involves using the finite element method to study and to improve the behavior of reinforced concrete shear walls with openings. The third application studies the effective widths of C-shaped shear walls.

### 8.1 ENERGY DISSIPATION CAPACITY OF R/C WALLS

The two major objectives in the design of earthquake-resisting structures are: 1) to minimize structural damage in structures subjected to low-intensity earthquakes and 2) to prevent the collapse of but allow some structural damage in structures subjected to high-intensity earthquakes (123). Because of the large inherent lateral stiffness, a reinforced concrete shear wall is suitable for the first

objective. It can be designed to remain nearly elastic during a low-intensity earthquake and, hence, helps prevent structural damage to other components of the building. However, it is usually not economical to design a reinforced concrete shear wall to remain elastic during a strong earthquake. As a result, in order to accomplish the second objective, designers must ensure that shear walls have adequate energy dissipation capacity in the inelastic range to survive a strong ground motion.

### 8.1.1 ENERGY DISSIPATION MECHANISMS

Concrete experiences significant degradation of strength and stiffness when subjected to large-amplitude cyclic loads. Therefore, the major energy dissipation in reinforced concrete shear walls must be provided by the inelastic behavior of reinforcing steel (113). Appropriate detailed steel reinforcement can improve the energy dissipation capacity of the walls by 1) dissipating energy through yielding of the reinforcement itself and 2) reducing the strength and stiffness degradation of concrete and, hence, improving the energy dissipation capacity of concrete. The energy dissipated by a wall during a loading cycle can be represented by the area of the load vs. top deflection curve for that cycle. Reinforced concrete shear walls that deform primarily in a flexural mode and have small inelastic shear deformation will have a well-rounded load vs. deflection curve because the response of the wall is governed by the hysteresis behavior of the reinforcing steel. On the other hand, reinforced concrete shear walls that deform primarily in a shear mode and experience large inelastic shear deformation have load vs. top deflection curves with a significant pinching because the response of the wall is governed by the cyclic shear transfer mechanisms of cracked concrete. As a result, walls that deform mainly in a flexural mode have larger energy dissipation capacities and, hence, are more desirable in the design of earthquake-resistant structures than walls that deform mainly in a shear mode (113).

In this investigation, the calculated energy dissipation of each wall model was evaluated by using the accumulated energy dissipation ratio, which is an accumulated ratio between the energy dissipated by the wall model in each cycle and the energy dissipated by an equivalent elasto-plastic system (Fig. 8.1). The elasto-plastic system was chosen for comparison because it was the system

that had the best energy dissipation capacity (113). The initial stiffness of the elasto-plastic system is equal to the uncracked stiffness of the wall under study. As shown in Fig. 8.1, the energy dissipated by a wall model in each cycle is represented by the area of the calculated load vs. top-deflection curve for that cycle ( $A_1$  and  $A_2$  in Fig. 8.1) while the energy dissipated by an elasto-plastic system is represented by the area of the elasto-plastic load vs. top-deflection curve for that cycle ( $B_1$  and  $B_2$  in Fig. 8.1). An energy dissipation ratio close to one reflects a wall with good energy dissipation capacity while a ratio close to zero reflects a wall with poor energy dissipation capacity.

### 8.1.2 REINFORCEMENT DETAILS

In order to improve the energy dissipation capacity of shear walls, designers must try to reduce the inelastic shear deformation (or increase inelastic shear stiffness) in the lower portion of the wall, allowing the wall to deform mostly in the flexural mode. One possible way to reduce the inelastic shear deformation and, hence, increase the energy dissipation capacity of the wall is to provide appropriate reinforcement details in the lower portion of the wall. The finite element method was used to study the effects of different arrangements of reinforcement on the inelastic shear deformation and on the energy dissipation capacity of shear walls B2 and B7 which were tested at the PCA and described in Chapter 6. The eight arrangements of reinforcement considered are shown in Fig. 8.2 and the amount of reinforcement in each option is given in Table 8.1. Each of the reinforcement options is described below.

Option #1: Reinforcement details were the same as the original reinforcement details used in the PCA tests. The vertical web reinforcement ratio was 0.3% and the horizontal web reinforcement ratio was 0.6%. No diagonal reinforcement was used.

Option #2: The amount of horizontal web reinforcement was doubled in the lower 5 ft of the web. This option was chosen to investigate the effectiveness of horizontal web reinforcement in limiting the inelastic shear deformation of the wall.

Option #3: Vertical web reinforcement with a reinforcement ratio of 0.6% was added to the lower 5 ft of the web. This additional reinforcement was embedded in the base

girder in the same way as a conventional vertical web reinforcement. This option was used to investigate the effects of varying amounts of vertical web reinforcement on the energy dissipation capacity of the wall.

Option #4: Vertical web reinforcement with a reinforcement ratio of 0.6% was added in the lower 5 ft of the web. Unlike option #3, the additional vertical web reinforcement was not embedded in the base girder. This option was used to investigate the effectiveness of unanchored vertical web reinforcement in increasing the interface shear transfer stiffness of the web.

Option #5: Distributed diagonal reinforcement with a ratio of 0.4% (in each direction) was added to the lower 5 ft of the web. The diagonal reinforcement was anchored in the base girder. This option was used to investigate the effectiveness of the distributed diagonal reinforcement in reducing the inelastic shear deformation and in increasing the energy dissipation capacity of the wall.

Option #6: The reinforcement in this option is similar to that of option #5 except that the ratio of the additional diagonal reinforcement was 0.2% instead of 0.4%. This option, together with option #5, was used to test the effectiveness of different amounts of diagonal reinforcement in reducing inelastic shear deformation of the wall.

Option #7: Four diagonal #5 bars (two in each direction) were added to the web. This option, together with option #5, was used to compare the effectiveness of distributed diagonal reinforcing bars to the effectiveness of concentrated reinforcing bars in improving the energy dissipation capacity of the wall.

Option #8: Four diagonal #5 bars (two in each direction) were added to the web. The location of these bars was lower than the location of the bars in option #7 as shown in Fig. 8.2. This option was used to investigate the effect of the location of the bars on their capacity to limit the inelastic shear deformation of the wall.



A finite element mesh for each wall model was the same as that used in the analyses of the PCA walls in Chapter 6. Each wall model has the same boundary conditions, loading history, and the arrangement of horizontal and vertical reinforcing bar elements as the PCA wall models in Chapter 6 (Fig. 6.2 and 6.3). The area of the bar elements in the web was adjusted to represent the additional web reinforcement in each reinforcement option. Diagonal reinforcement was incorporated into the wall model using a 2-node bar element connecting the two diagonally opposite nodes in each concrete element. The material model parameters used in the analyses were the same as those used in the analyses of the PCA walls in Chapter 6 (Table 6.2).

### 8.1.3 ANALYTICAL RESULTS

Figures 8.3 through 8.9 show the calculated response of walls B2 and B7 with the eight different types of web reinforcement. Figures 8.3 and 8.5 show the load vs. top deflection curves while Fig. 8.4 and 8.6 show the load vs. shear distortion curves. Calculated crack patterns for walls B2 and B7 are shown in Fig. 8.7 and Fig. 8.8. Figure 8.9 gives the plots of the accumulated energy dissipation ratio vs. the cycle number for walls B2 and B7 using the different reinforcement details. The calculated results for each reinforcement option are discussed below:

Options #1, #2, and #3: As shown in Fig. 8.3 through 8.9, the wall models with reinforcement options #1, #2, and #3 yield similar analytical results for load vs. top deflection curves, load vs. shear distortion curves, crack patterns, and energy dissipation capacity. The load-deflection curves experience significant pinching because of large inelastic shear deformation in the lower portion of the walls. Of the eight reinforcement options analyzed, these three options have the lowest energy dissipation capacities (Fig. 8.9). These analytical results show that increasing the amount of horizontal (option #2) and vertical (option #3) web reinforcement improves neither the energy dissipation capacity nor the strength of the walls. Extensive web crushing was also observed in the calculated response of both walls B2 and B7 with reinforcement options #1, #2, and #3.

As observed from the calculated response of the PCA wall tests described in Chapter 6, the interface shear transfer stiffness is a major component in the total shear stiffness of the reinforced concrete in the web. In order to reduce the inelastic shear deformation in the lower portion of the wall, the web reinforcement must be designed to minimize the crack width of concrete in the web because the magnitude of the interface shear transfer stiffness depends greatly on the crack width. The widths of cracks in the web are governed primarily by the flexural behavior of the wall; therefore, increasing the horizontal web reinforcement does not have a significant effect on the crack widths as can be seen in Fig. 8.7 and 8.8. Increasing the vertical web reinforcement does not reduce the crack width either because, after yielding, the additional vertical reinforcement is not effective in holding the cracks together (Fig. 8.7 and 8.8). The dowel stiffness of the additional vertical reinforcement is also insignificant because it is much less than the dowel stiffness provided by the longitudinal reinforcement in the boundary elements. Moreover, the dowel stiffness does not contribute much to the overall shear stiffness of reinforced concrete shear walls. As a result, increasing the amount of conventional web reinforcement will not limit inelastic shear distortion nor increase the energy dissipation capacity of the walls. Because the additional web reinforcement does not decrease the inelastic shear distortion in a wall, it cannot help prevent web crushing failure or increase the strength of the wall. This is due to the fact that the reduction in the compressive strength of concrete struts, which leads to the web crushing failure, is governed primarily by the magnitude of shear distortion in the lower portion of the wall (Eq. 6.3).

Option #4: The energy dissipation capacity of wall models with reinforcement option #4 is significantly better than the energy dissipation capacities of wall models with reinforcement options #1, #2, or #3. The load vs. top deflection curve displays much less pinching while the inelastic shear distortion in the lower 3 ft of both walls is reduced by nearly 50% (Fig. 8.3 through Fig. 8.6). The only difference between reinforcement in option #4 and #3 is that the additional vertical web reinforcement in option #4 was not embedded in the base girder. This forced the vertical web reinforcement to yield primarily at the base level of the

wall. Most of the vertical web reinforcement above the base level remained elastic and, therefore, was able to hold together the cracked concrete in the web. This resulted in smaller crack widths in the web, although the crack at the base of the wall was larger (Fig. 8.7 and 8.8). The smaller crack widths in the web caused the increase in the interface shear stiffness of the cracked concrete and helped reduce the inelastic shear deformation, thereby improving the energy dissipation capacity of the walls.

Options #5 and #6: The energy dissipation capacities of wall models with reinforcement options #5 and #6 are greatly improved from those of options #1, #2, #3, and #4. Both load vs. top deflection curves and load vs. shear distortion curves have well rounded shapes (Fig. 8.3 through 8.6). The magnitude of the calculated shear distortion in the wall models with reinforcement options #5 and #6 is significantly smaller than that in the wall models with reinforcement options #1, #2, #3, and #4 (Fig. 8.4 and 8.6). These results show that the diagonal reinforcement is very effective in limiting the shear distortion and in improving the energy dissipation capacities of the walls. While vertical and horizontal web reinforcement indirectly helps transfer shear force through the dowel action and by transferring shear force to the diagonal concrete struts, the diagonal shear reinforcement directly transfers shear force to the base in the form of axial force, both tension and compression. Because the cyclic response of a reinforcing bar in the axial direction has good energy dissipation capacity, the cyclic shear transfer mechanisms developed using diagonal reinforcement have much better energy dissipation capacities than the conventional shear transfer mechanisms which use interface shear transfer and dowel actions. Reinforcement option #5 has better energy dissipation capacity than option # 6 because of the larger amount of diagonal reinforcement. Determining the optimal amount of diagonal reinforcement requires a more detailed investigation including both experimental and analytical tests, which is beyond the scope of this study.

Options #7 and #8: The improvements in the energy dissipation capacities of these two reinforcement options are close to those of options #5 and #6. This shows that both dis-

tributed diagonal reinforcement and concentrated diagonal reinforcement are effective in improving the energy dissipation capacity of the walls. Although option #5, which used distributed diagonal reinforcement, has more energy dissipation capacity than option #7, which used concentrated diagonal reinforcement, option #7 might be more economical and more practical. This is due to the fact that option #5 requires nearly twice as much reinforcing steel as option #7. Furthermore, option #5 requires a large number of reinforcing bars with different lengths. Therefore, it is more difficult to place the reinforcement for option #5 than for option #7, which requires only a few reinforcing bars with one or two different lengths. However, it should also be noted that the finite element analysis did not take into account bond-slip of the reinforcing bars and assumed a perfect bond between the concrete and reinforcing steel. Bond-slip might be important when a single large bar is used to transfer a large shear force.

From these analytical results, it can be seen that diagonal bars are the most effective form of reinforcement for improving the energy dissipation capacity of shear walls. In order for the diagonal bars to be effective in transferring the shear force to the base, the bars should remain elastic throughout the loading history. To prevent the yielding of the diagonal reinforcement, engineers can simply assume that all the applied shear force is transferred by the diagonal reinforcement and provide the amount of the diagonal reinforcement accordingly. Although diagonal reinforcement was used in the design of some shear walls in Chile (150), such practice is very limited in the U.S. and is not mentioned in the current ACI Building Code (2). More experimental programs are needed to study the cyclic response of reinforced concrete shear walls with diagonal reinforcement.

## **8.2 SHEAR WALLS WITH OPENINGS**

Solid, isolated reinforced concrete shear walls are not commonly used as the lateral-load resisting systems in tall buildings due to architectural constraints. Shear walls usually contain some openings or are connected with other structural members to form a lateral-load resisting system. As shown in Fig. 8.10, the shear wall systems generally used in tall buildings can be divided into

three types: coupled shear walls, wall-frame systems, and pierced shear walls (6, 126). Most previous investigations of shear wall systems have concentrated on the behavior of wall-frame systems and coupled shear walls. The study of the response of pierced shear walls, especially the inelastic cyclic response, is quite limited (126). A pierced shear wall is usually designed as a solid wall and the effect of openings is often neglected. Reinforcement interrupted by the openings is simply moved to the sides of the openings. Such practice may be adequate in walls subjected to monotonically increasing loads because the forces within the wall are not redistributed significantly and forces in each wall pier can be estimated using a conventional design method. However, when pierced walls are subjected to several cycles of post-yield load reversals, conventional design methods or a linear finite element analysis might not be able to estimate correctly the shear forces carried in each wall pier. This can result in inadequate distribution of shear reinforcement which can lead to a premature failure of the structure.

In this section, the finite element method is used to study the behavior of pierced shear walls. Experimental data from tests of pierced shear walls conducted at the Construction Technology Laboratory of PCA (126) and at the Department of Civil Engineering, the University of Michigan (6) were used in this study. The major objectives of this study are: 1) to identify differences in the general behavior of pierced shear walls and companion solid walls; 2) to study shear force redistribution in wall piers when the wall is subjected to severe cyclic loadings; and 3) to develop improved reinforcement details for pierced shear walls.

### **8.2.1 PCA TESTS OF WALLS WITH AND WITHOUT OPENINGS**

Two wall specimens, a solid isolated wall (wall CI1) and a companion wall with openings (wall PW1), were tested at the Construction Technology Laboratory of PCA in 1981 (126). As shown in Fig. 8.11, both specimens, which represented 1/3-scale, six-story shear walls, had a total height of 18 ft, a horizontal length of 6 ft-3 in., and a uniform web thickness of 4 in. Every 3 ft over the height of the wall, a 2.5-in. thick stub representing a floor slab ran along both sides of the specimens. In wall PW1, an opening of 12.5 in. by 18.0 in. was located at the center of the wall panel

in each story (Fig. 8.12). Reinforcement details for wall CI1 are shown in Fig. 8.13. Reinforcement details for wall PW1 were similar to those of wall CI1 except that the reinforcement interrupted by the openings was moved to the side of the openings. Both specimens were loaded as vertical cantilevers using horizontal forces applied through the top slab (126). The loading history for each wall, which was derived from the dynamic response of a 6-story building subjected to an input ground motion of two actual earthquake records, is shown in Fig. 8.14. Material properties for both walls are given in Appendix G. Detailed descriptions of the test setup and the wall construction can be found in Ref. 126.

### 8.2.1.1 EXPERIMENTAL RESULTS

Specimen CI1 was able to sustain 22 load cycles with a maximum applied load of 76.1 kips while specimen PW1 was able to sustain 23 load cycles with a maximum applied load of 65.7 kips before failure. The difference in the maximum applied loads can be attributed partly to the difference in the material properties of the two specimens, especially the yield stresses of the longitudinal reinforcement (Table G.2). The experimental results indicated that openings had little effect on the response of the wall specimens (126). Both specimens experienced similar deformation characteristics. Extensive yielding of vertical reinforcement and large inelastic shear deformation were concentrated in the lower 3 ft of the specimens. Significant pinching was observed in the load vs. shear distortion curves for both specimens.

Although these two walls had similar deformation characteristics, their failure modes were different. Wall CI1 failed in a “shear sliding” mode (126). During load cycle #22 (Fig. 8.14(a)), a large horizontal crack at mid-height of the first story remained open across the full length of the specimen and the resistance to the applied shear force was provided solely by the dowel action of the vertical reinforcement across the crack. The specimen failed when concrete in the vicinity of this horizontal crack was severely distressed and could no longer provide the reaction to the dowel forces. Wall PW1 failed in a shear-compression mode when diagonal cracks, which formed compression struts in both piers, spread into the boundary elements during load cycles 23 and 24 (Fig.

8.14(b)). Because the diagonal compression struts in the web were interrupted by the openings, shear stress had to be transferred through diagonal compression struts in the wall piers. This led to a concentration of shear force and shear deformation in the wall piers. Figure 8.15 illustrates the crack patterns in the the first story of walls CI1 and PW1 after failure.

### 8.2.1.2 ANALYTICAL RESULTS

Both wall specimens were modelled using 4-node two-dimensional plane stress elements for concrete and 2-node bar elements for reinforcing steel. Finite element meshes for these models are shown in Fig. 8.16. A strip of 4-in. thick linear elements with a modulus of elasticity equal to the modulus of elasticity of concrete was used to model a floor slab at each story and at the top of the specimens. All nodes at the base of the wall were fixed in the horizontal and vertical directions. The horizontal displacement of the node at the upper left corner (Fig. 8.16) was specified to be the same as the displacement history used in the experimental program (Fig. 8.14). The material model parameters used in the analyses were the same as those used in the analyses of the PCA walls in Chapter 6 (Table 6.2).

Figures 8.17 through 8.20 compare the calculated response with the experimental results for walls CI1 and PW1. Load vs. top deflection curves are shown in Fig. 8.17 and 8.18 and the load vs. shear distortion in the first two stories are presented in Fig. 8.19 and 8.20. These comparisons show fair agreement between the calculated response and the experimental results. Calculated load vs. top deflection curves for both walls are significantly different from the experimental results during the first cycle of response. Such differences might be attributed to several factors such as the difference between the assumed material properties and the actual material properties and the pre-existing shrinkage cracks in the walls before the test. The calculated response provides a good approximation of the measured response in later load cycles.

The calculated load vs. top deflection curves and the calculated load vs. shear distortion curves for both walls during the low-amplitude, post-yield cycles also deviate significantly from

the experimental data. During these cycles, both wall models experience larger shear distortion than that observed in the experimental results.

Besides the top deflection and the shear distortion, another important aspect of the experimental results is the failure mode. The current version of the concrete model cannot predict the sliding shear failure mode because the upper bound of the dowel force is not included in the model. However, a careful study of the analytical results indicates the potential failure mode of wall CI1. Crack patterns from the analytical results of wall CI1 at the end of load cycle #21 (Fig. 8.21(a)) show that horizontal cracks at the middle of the first story remained open across the full length of the wall. As a result, the shear force in the first story had to be transferred to the base through the dowel action of the vertical reinforcement. Figure 8.21(a) also shows that wall CI1 experienced large inelastic shear strains in the first story. This large inelastic cyclic shear strain damaged the concrete, making it unable to resist the large dowel forces in the reinforcing bars. This finally led to a sliding shear failure along the horizontal crack in the first story of wall CI1.

Extensive web crushing was calculated in both piers of wall PW1 in load cycles 20 through 24. This agrees with the shear-compression failure mode observed in the experimental results. Two factors contribute to this mode of failure: 1) a reduction of the compressive strength of the concrete because of the large inelastic shear strain in each pier; and 2) a large shear stress in each pier. Figure 8.21(b) shows that specimen PW1 experienced large shear strains in both the first-story piers. These large shear strains caused a reduction in the compressive strength of the concrete as discussed in Section 6.4.3.5. The crack patterns for wall PW1 (Fig. 8.21 (b)) also show that most of the diagonal compressive struts in web were interrupted by the openings and, therefore, were ineffective in transferring shear force. As a result, the shear force had to be transferred through the diagonal compressive struts in each pier. This resulted in high shear stresses in the compression pier. This high shear stress, together with the reduction in the compressive strength of the concrete in the wall piers, led to the shear-compression failure of wall PW1.



As can be seen from both the experimental and calculated results, the conventional design of shear reinforcement in pierced shear walls may be inadequate to control large inelastic shear deformation or to prevent shear-compression failure in wall piers. In order to improve the performance of pierced shear walls, especially when subjected to severe cyclic loadings, engineers must try to minimize the inelastic shear deformation in the lower portion of the wall piers. This can be done by increasing the inelastic shear stiffness of the wall piers. As discussed in Section 8.1 where the influence of several different reinforcement layouts were studied, diagonal web reinforcement is most effective in increasing the inelastic shear stiffness of the walls. To study the effects of diagonal reinforcement on the behavior of pierced walls, two wall models containing diagonal web reinforcement in the lower portion of the walls were analyzed using the finite element method. Both wall models had the same configuration as wall PW1, but wall PW1-A had diagonal reinforcement in the first story while wall PW1-B had diagonal reinforcement in both the first and the second stories (Fig. 8.22). The diagonal reinforcement ratio was 0.35% in each direction.

Figures 8.23 through 8.26 compare the calculated response of walls PW1, PW1-A, and PW1-B. The results include load vs. top deflection curves (Fig. 8.23), load vs. shear distortion curves (Fig. 8.24), crack patterns (Fig. 8.25), and shear strain distributions (Fig. 8.26). Comparisons of these results indicate that, among the three walls being studied, wall PW1-B had the most satisfactory inelastic response. Wall PW1-B had a well-rounded load vs. top deflection curve (Fig. 8.23(c)) and experienced small shear distortion in the first two stories (Fig. 8.24(c)). Inelastic shear strain in every story of wall PW1-B remained small, even during the last load cycle (Fig. 8.26(c)). Web crushing was not observed in either wall pier and wall PW1-B remained in a good condition after load cycle 23.

The inelastic response of wall PW1-A was not much improved from the inelastic response of wall PW1 despite the presence of the diagonal reinforcement in the first story. The load vs. top deflection curve of wall PW1-A experienced some pinching, similar to that of wall PW1. Although the inelastic shear distortion was small in the first story of wall PW1-A, it was concentrated in the second story (Fig. 8.24(b) and Fig. 8.26(b)). The calculated results show extensive web crushing

of concrete in both wall piers at the second story of wall PW1-A during load cycles 20 through 24. Unlike the response of wall PW1 where the flexural yielding was concentrated in the first story, the flexural yielding of wall PW1-A was concentrated in the second story because the diagonal web reinforcement increased the flexural stiffness of the first story. This flexural yielding, which caused wide cracks in the second story (Fig. 8.25(b)), greatly reduced the interface shear transfer capacity of the concrete in the second story of wall PW1-A. With a small interface shear transfer capacity and without the diagonal web reinforcement, the second story of wall PW1-A had inadequate inelastic shear stiffness to resist the applied cyclic loadings. This resulted in a shear-compression failure of the wall piers in the second story. The mode of failure in the second story of wall PW1-A was similar to that in the first story of wall PW1.

In wall PW1-B, where diagonal reinforcement was provided in both the first and the second stories, flexural yielding concentrated in the first story rather than in the third story (Fig. 8.24(c)). This occurred despite the higher flexural stiffness of the first story because yielding of the longitudinal reinforcement in the first story required less applied load than yielding of the flexural reinforcement in the third story due to the larger applied moment in the first story. Unlike wall PW1-A where the inelastic shear stiffness of the second story was reduced significantly following flexural yielding, the inelastic shear stiffness in the first story of wall PW1-B did not degrade significantly due to the presence of the diagonal web reinforcement.

## 8.2.2 TESTS OF WALLS WITH STAGGERED OPENINGS

Four isolated wall specimens with staggered openings tested at the University of Michigan (6), were also studied in this investigation. Each wall specimen had a barbell cross section, represented a 1/5-scale five-story wall, and was tested under reversed cyclic loadings. Wall W1 was a solid wall while walls W2, W3, and W4 had three different configurations of staggered door openings (Fig. 8.27). Reinforcement in each specimen was designed to represent the reinforcement commonly used in walls in Chilean buildings. The amount of the transverse reinforcement in the boundary elements was about 50% of that required in Section 2625(e)4 of the 1988 UBC (74). The vertical

and horizontal web reinforcement ratios were 0.27%. The longitudinal reinforcement in the boundary elements was similar in all four specimens (Fig. 8.28). However, the web reinforcement in the walls with openings differed from that used in the solid wall (Fig. 8.29). Web reinforcement interrupted by the openings was moved to the side of the openings. Following reinforcement details commonly used in Chile (6), diagonal reinforcement was placed near each corner of the door openings (Fig. 8.29(b)).

Each wall was subjected to two load cycles at overall drift levels of 0.25, 0.5, 0.75, 1.0, 1.5, and 2.0 % of the height of the wall (Fig. 8.30). An axial load of 60 kips was also applied throughout the tests. The material properties for wall W1, W2, W3, and W3 are given in Appendix H. More details on the experimental program can be found in Ref. 6.

### **8.2.2.1 EXPERIMENTAL RESULTS**

Wall W1 sustained 15 load cycles and a peak load of 36 kips when the test had to be terminated because the maximum displacement of the actuator had been reached. Moderate damage which included minor crushing and spalling of the cover concrete in the boundary elements, was observed. Walls W2, W3, and W4 were able to sustain 11 load cycles with peak loads between 34 kips and 36 kips before failure. A drift of 1% was achieved in these specimens without causing any significant damage to the specimens. The specimens suddenly lost their load resisting capacities when an inclined crack originating from the top corner of the first-story opening penetrated into the east pier and caused extensive crushing in the east boundary element. A typical crack pattern of the specimens after failure is shown in Fig. 8.31. It can be seen that the large inclined cracks observed in the east piers of walls W2, W3, and W4 are similar to the diagonal crack that develops in a reinforced concrete beam without stirrups which failed in shear (Fig. 8.32).

### **8.2.2.2 ANALYTICAL RESULTS**

All wall specimens were modelled by using 4-node, two-dimensional plane stress elements for concrete and 2-node bar elements for reinforcing steel. The finite element meshes of the wall

models are shown in Fig. 8.33. A row of elastic, plane stress elements was placed at the top of each wall model to represent the top slab. Both horizontal and vertical degrees of freedom of all nodes at the base of the wall were fixed. A constant vertical nodal load of 15 kips was applied at each of the four nodes at the top of the wall above the boundary elements. The horizontal displacement of the node at the upper west corner of each wall was specified to be the same as the displacement history used in the experimental tests (Fig. 8.30). The material model parameters used in the analyses were the same as those used in the analyses of the PCA walls in Chapter 6 (Table 6.2).

Measured load vs. top deflection curves are compared with the calculated response of walls W1, W2, W3, and W4 in Fig. 8.34 through 8.37. The calculated response of wall W1 agrees well with the experimental data. After 15 load cycle minor crushing of the concrete in the boundary elements was calculated but the wall model still remained in a good condition. The calculated response of walls W2, W3, and W4 before the diagonal tension crack and the shear-compression failure occurred in the experimental tests also agreed well with the experimental data. However, the concrete model adopted in this study used the concept of a smeared crack; therefore, it could not reproduce the large diagonal tension crack that led to the shear-compression failure of the east piers. As a result, the analytical model did not indicate the occurrence of the shear-compression failure in walls W2, W3, and W4. The analyses of these walls were terminated at the load cycle where the shear-compression failure occurred in the tests.

Despite the inability of the current concrete model to reproduce the large diagonal tension crack and the shear-compression failure in the wall piers, the finite element method can still be used to explain the cause of such a failure and to study ways to improve the behavior of pierced walls. The shear-compression failure that occurred in walls W2, W3, and W4 was the result of a large shear force carried by the east piers of the walls. This developed following a force redistribution in the lower portion of the walls after several cycles of inelastic response. When the walls were loaded in the east direction (the positive direction in Fig. 8.34 through 8.37), the compressive struts in the web were not capable of transferring the shear force to the base of the wall because they were interrupted by the openings. Furthermore, the tensile strain and the wide cracks in the lower west pier

(Fig. 8.38) made that pier ineffective in transferring the shear force. As a result, the east pier had to transfer the major portion of the applied shear force. Figure 8.39 shows the comparison between the total applied shear force and the shear forces carried by the east piers in walls W2, W3, and W4. The horizontal lines indicate the nominal shear strength of the east piers according to the 1989 ACI Building Code (2). In some cases, the shear forces carried by the east pier were calculated to be as high as 60% of the total applied shear force, thereby exceeding the nominal shear strength of the piers during most of the loading history. This high shear force was the reason for the shear-compression failure in the wall piers. Table 8.2 summarizes the nominal shear strengths of the east piers in walls W2, W3, and W4, and the calculated shear forces in the east piers during the last load cycle for both a linear and a nonlinear finite element analysis. It can be seen that the use of the conventional design method or even the linear finite element analysis can lead to an underestimation of the shear force in the critical pier and inadequate shear reinforcement.

Because the shear-compression failure in the wall specimens was caused by excessive shear force in the east pier, two possible ways to prevent this mode of failure as well as to improve the performance of a pierced wall were developed: 1) to provide adequate shear reinforcement in the east pier and 2) to reduce the magnitude of the shear force in the east pier.

In the first approach, the result of a nonlinear finite element analysis can be used to estimate the magnitude of shear force that each wall pier must carry. This shear force can then be used to select the web reinforcement in the pier. The results of this analysis indicated that the horizontal web reinforcement ratio in the east piers of walls W2, W3, and W4 should have been approximately 1%, rather than 0.3%. This calculation is based on an applied load of 20 kips in the wall pier and the assumption that the concrete does not contribute to normal shear strength under cyclic loading (2).

In the second approach, engineers must try to increase the shear transfer capacity of the west pier so that it helps carry some of the shear force. As demonstrated in Sections 8.1 and 8.2.1.2, diagonal web reinforcement is quite effective in increasing the inelastic shear transfer capacity, and, there-

fore, might be applicable in this situation. Walls W2, W3, and W4 were analyzed with diagonal reinforcement in the lower 28 in. of the west piers (Fig. 8.40) in order to observe the effects of diagonal web reinforcement on the shear force distribution in the lower portion of the pierced walls. The diagonal reinforcement ratio was 0.3% in each direction. Figure 8.41 shows the comparisons between the total applied shear and the shear force carried by the east piers when the diagonal reinforcement was used. Comparing Fig. 8.41 with Fig. 8.39, it can be seen that diagonal reinforcement in the web can reduce the magnitude of the shear force in the east pier by as much as 50%. Fig 8.43 shows the calculated shear stress distribution for walls W2, W3, and W4 with and without diagonal reinforcement in the west piers at the end of load cycle 11. This figure shows that the calculated shear stresses in the east piers of walls W2, W3, and W4 were significantly reduced when the diagonal shear reinforcement was provided in the west piers.

It should be noted that most of the previous research on the response of pierced shear walls has considered the stress concentration around the openings to be the major detrimental effect of the openings in shear walls (126, 6). This conclusion resulted in the reinforcement details around the openings which were used to prevent the crushing of concrete due to stress concentration. However, the finite element analyses of pierced shear walls subjected to cyclic loads shows that the major problem caused by openings in shear walls is not the stress concentration, but rather the reduction in the inelastic shear transfer capacity of wall piers. The 1989 ACI Building Code (2) in Section 21.7.3.6 mentioned briefly the maximum nominal shear strength of each wall pier. However, the code does not address the effect of openings on the shear transfer mechanisms of pierced walls.

### **8.3 EFFECTIVE WIDTH OF FLANGES IN C-SHAPED WALLS**

Besides functioning as a lateral-load resisting system, reinforced concrete shear walls in tall buildings are often designed to function as elevator cores or stair wells. This results in walls which have cross-sections with intersecting legs. Despite the common uses of shear walls with intersecting flanges in tall buildings, the current ACI Building Code (2) does not address the contribution of the intersecting flanges to the total response of shear walls. In practice, the provisions for the effective

width of T-beams are usually used in determining the effective width of shear walls with intersecting flanges. Although such provisions might yield satisfactory results when shear walls are subjected to small or moderate earthquake loading, they do not represent the observed behavior of intersecting walls, especially at forces near the capacity. This can lead to an unexpected mode of failure in a wall that is subjected to a strong earthquake.

### 8.3.1 ANALYTICAL PROGRAM

In this section, the finite element method was used to study the contribution of a transverse flange to the response of C-shaped reinforced concrete shear walls. The twelve wall models analyzed had the same configurations and material properties as wall CLS as described in Chapter 7 except that the width of the south flange was varied in this series of analysis. In some cases, the amount of longitudinal reinforcement in the north boundary elements was also increased. The width of the south flanges in these models varied from 0 in. in wall C0 to 140 in. in wall C140 as shown in Fig. 8.44. Because each wall was symmetric, only half of each wall was modelled. The material model parameters used in these analyses were the same as those used in the analyses of C-shaped walls as discussed in Chapter 7. In order to take into account the shear stiffness in the N-S direction of the intersecting flange, the shear stiffness parameters of the concrete element in the south boundary elements that are influenced by the stiffness of the flange, which included  $\mu_1$ ,  $\mu_2$ ,  $G_{\min}$ ,  $\tau_{\text{slip}}$ , and  $G_{\text{uni}}$ , were multiplied by the ratio of the width of the south flange to the thickness of the boundary element.

Each wall was analyzed using four different combinations of loading history and reinforcement ratio (Table 8.3). In these analyses, the south flange is compressed under positive displacements and the south flange is in tension under negative displacements. In case A, each wall model was initially loaded to a top deflection of +0.15 in., then each wall was loaded to the top deflection of -2.50 in. In case B, each wall model was initially loaded to the top deflection of -0.15 in., then each wall was loaded to the top deflection of +2.50 in. The walls were initially loaded to the 0.15-in. level so that the initial stiffness of the walls could be determined in both directions. In both cases

A and B, wall models had the same reinforcement as wall CLS. In case C, each wall model had five times as much longitudinal reinforcement in the north boundary elements as wall CLS. Each wall model in case C was subjected to the same loading history as walls in case B. In case D, each wall model, which had the same reinforcement as wall CLS, was loaded for two cycles at each of the following top displacement levels:  $\pm 0.1$  in.,  $\pm 0.2$  in.,  $\pm 1.0$  in.,  $\pm 2.0$  in. and  $\pm 3.0$  in (Fig. 8.45).

### 8.3.2 CALCULATED RESPONSE

Fig. 8.46 shows the effective width of the south flange in the C-Shaped wall models calculated using the provisions for the effective width of T-beams in Section 8.10.3 of the 1989 ACI Building Code (2). Based on these provisions, the effective flange width for each web of the wall model should not exceed six times the flange thickness (18 in.). The calculated response of the wall models are shown in Fig. 8.47 through 8.50. The secant stiffnesses of the wall models at different deflection levels in the north and south directions are shown in Fig. 8.47. The curve with a broken line in Fig. 8.47 illustrates the stiffness of uncracked C-shaped walls with different flange widths calculated using simple beam theory. The maximum flange width used in the stiffness calculation was governed by the effective width of a T-beam recommended in Section 8.10.3 of the ACI Building Code (2). This curve correctly represents the uncracked stiffness of the C-shaped walls when the actual flange width does not exceed the effective flange width for T-beams recommended in the ACI Building Code (2). However, the uncracked stiffness of the wall is underestimated when the actual flange width is much larger than the effective flange width recommended for T-beams in the ACI Building Code (2). It can also be seen from this figure that the presence of the south flange significantly increased the uncracked stiffness of the walls. However, the effectiveness of the flange in providing the the stiffness decreased as the width of the flange increased. This can be explained by examining at the strain in the vertical reinforcement in the south flange of uncracked walls (Fig. 8.50(a)). The magnitude of compressive strain in the south flange decreased as the distance from the web increased. This indicates that the portion of the south flange closest to the web is more effective in providing the wall stiffness than the portion farther from the web. The stiffness of the walls



drastically decreased when the concrete started cracking. As can be seen in Fig. 8.47(b), at the deflection level +0.15 in., the south flange did not provide the wall with significant stiffness when acting in compression. This is due to that fact that the neutral axis of the wall was shifted close to the flange. As a result, the moment of inertia of the cracked wall depended on reinforcing steel in the north boundary elements and in the web (which were farther from the neutral axis) rather than on the concrete and reinforcing steel in the south flange (which were closer to the neutral axis). When the wall was loaded to the north (the flange is in tension), the flange was more effective in providing the stiffness since the neutral axis was shifted closer to the north boundary elements (Fig. 8.47(a)). Therefore, reinforcing steel in the flange was far away from the neutral axis and was able to help increase the moment of inertia of the cracked wall.

Figure 8.48 shows the load vs. top deflection curves for wall models subjected to monotonically increasing loads in the north direction (case A). It can be seen that the capacity of the wall model increased with an increase in the width of the south flange. The increase in the strength of the walls can be explained by examining the strain distribution in the vertical reinforcement at the base of the south flange (Fig. 8.50(b)). It can be seen that at the top deflection of -2.50 in., all vertical reinforcing steel in the south flange of every wall model experienced a tensile strain which was much higher than the yield strain. This indicates that reinforcing steel in a flange width as high as 25 times the thickness of the web can effectively help the wall resist overturning moment. Although, the presence of the south flange acted to increase the strength of the walls, it also led to extensive crushing of the concrete in the north boundary elements and in the web because of the higher strength. At the displacement level -2.50 in., wall C0 experienced minor crushing in the north boundary elements while wall C140 experienced extensive crushing of the concrete in the north boundary elements and in the adjacent web after reaching a top deflection level of -1.50 in. As a result, neglecting the effect of vertical steel in the flange might cause a significant underestimation of the strength of the walls, and possibly leads to the selection of an inadequate amount of transverse reinforcement in the north boundary elements.

The calculated load vs. top deflection curves for wall models subjected to monotonically increasing load in the south direction (the south flange was in compression) are shown in Fig. 8.49. Wall models in case C (Fig. 8.49(b)) had five times as much reinforcement in the north boundary elements as the wall models in case B (Fig. 8.49(a)). All load vs. top deflection curves for wall models with different flange widths in case B were similar, except for walls C0 and C10. This is due to the fact that the amount of reinforcement in the north boundary elements was not enough to cause extensive crushing of the concrete in the south boundary elements of the wall models except in walls C0 and C10. The strain distribution in the vertical reinforcing bars along the base of the south flange in Fig. 8.50(c) shows that, at the displacement level of +2.50 in., extensive crushing of the concrete occurred only in walls C0 and C10. (Because of the assumption of perfect bond between concrete and reinforcing bars in the analysis, this vertical strain in reinforcing bars also represented the vertical strain in the concrete elements along the base of the south flange.)

The contribution of concrete in the south flange was more evident when the reinforcing steel in the north boundary elements was increased (case C), as shown in Fig. 8.49(b). Wall C0, C10, C20, C30, and C40 had significantly less strength than walls C50–C140 because of the extensive crushing of concrete in the south flange. Figure 8.50(d), which shows the vertical strain distribution along the south flange at the displacement level of +2.50 in., indicates that extensive crushing of concrete occurred in walls C0, C10, C20, C30, and C40 while concrete in other walls remained in a good condition. At the displacement level of +2.50 in., the strain distribution of concrete in the south flange (Fig. 8.50(d)) was much more uniform than the strain distribution of concrete in the south flange when the wall remained uncracked (Fig. 8.50(a)). This indicates that, when the walls are loaded to their capacity, the real effective width of the flange is much larger than the effective width of the wall obtained from a linear analysis. Although the calculated results show that the effective width of the flange in C-shaped walls when the flange is in compression can be significantly larger than the effective width of the flange recommended in the provisions for T-beams in the ACI Building Codes (2) (Fig. 8.46), the use of a conservative value for the effective width is still preferable.

The extra effective width will provide greater safety in the structure and prevent extensive crushing of the concrete in the boundary elements.

The calculated cyclic response of the wall models are shown in Fig. 8.51. Similarly to the calculated results for the walls subjected to monotonic loading, the capacity of the walls loaded in the south direction (south flange was in compression) was not increased much by the presence of the south flange while the capacity of the walls loaded in the north direction (south flange was in tension) was increased significantly as the width of the flange increased. Crushing of concrete in the south boundary elements was observed only in wall C0 and wall C10. Crushing of concrete in the north boundary elements and in the web was observed in walls C70, C80, C100, C120, and C140 while no sign of concrete crushing was observed in the north boundary elements of walls C0–C60. This observation indicates that although the presence of an intersecting flange along the south end of a wall increases the strength and helps prevent the crushing of concrete in the south boundary elements, it can cause extensive concrete crushing in the north boundary elements. As a result, extra transverse reinforcement should be provided in the boundary elements that are opposite the flange, especially when the flange is much wider than the thickness of the web. Fig. 8.51 also shows that the south flange did not have significant influence on the inelastic shear deformation of the C-shaped walls. Walls C0–C140 experienced the same magnitude of inelastic shear deformation in the lower 3 ft despite the difference in the width of the south flange in each wall model.

## 8.4 SUMMARY

This chapter illustrates the use of the finite element method to investigate the behavior of reinforced concrete walls with different configurations and design parameters. Several important findings from this investigation are summarized below:

- 1) Diagonal web reinforcement is an effective means of limiting inelastic shear distortion in the lower portion of the walls. It also significantly improves the energy dissipation capacity of the walls.

2) Openings in reinforced concrete walls can significantly reduce the inelastic shear transfer capacity and may cause premature failures of the wall piers. Diagonal web reinforcement can help increase the shear transfer capacity of the wall piers and, hence, improve the performance of the wall with openings.

3) The effective width of a flange in a C-shaped wall calculated according to the ACI provisions for the effective width of a T-beam in Section 8.10 (2) is conservative when used to evaluate the uncracked stiffness of the wall or to evaluate the strength of the wall when the flange is in compression. However, this effective width can significantly underestimate the strength of the wall when the flange is in tension. This can lead to inadequate transverse reinforcement and premature crushing of concrete in the boundary elements opposite the flange.

Although the proposed material models in this investigation are not capable of reproducing all observed aspects in reinforced concrete walls, such as sliding shear failures, the finite element analysis can still provide a wide-range of information that is useful for the study of the behavior of reinforced concrete walls. In order to successfully use the finite element method to study the response of reinforced concrete members, finite element users must realize the capability and limitations of the material models used in the analysis and understand the nature of the problems under study. This will help the users to select the appropriate calculated results that represents the important behavior of the reinforced concrete member and to interpret those results correctly.

## 9. SUMMARY AND CONCLUSIONS

The major objective of this study was to use the finite element method to study the cyclic response of slender, reinforced concrete shear walls. Because appropriate concrete and reinforcing steel models were not available, new material models which represent the cyclic response of reinforced concrete in shear walls were developed in this investigation. These material models were verified both at the element and structural levels: the results of the finite element analyses were compared with the experimental data from several experimental programs. After the material models had been satisfactorily tested and verified, the finite element method was used to extend the scope of the investigation of the response of slender reinforced concrete shear walls with different configurations, reinforcement details, and loading histories.

### 9.1 OVERVIEW

In this study, the finite element method was used to model the cyclic response of slender reinforced concrete shear walls. The finite element method was chosen as the analytical tool in this research because it was a powerful and versatile numerical method capable of analyzing a wide range of both linear and nonlinear structural problems. With the proper material models for concrete and reinforcing steel, the finite element method can be used to study the response of reinforced concrete shear walls with various configurations and reinforcement details, subjected to different loading histories.

Although, some researchers (Xu (151) and Stevens et al. (134)) have recently proposed material models for the cyclic response of reinforced concrete, these models were not successful when used to calculate response of complete structures due to numerical difficulties associated with the complicated stress-strain relationships. Most analyses diverged prior to completion (134, 151). Therefore, this research focused on developing new material models that can avoid these numerical difficulties and were appropriate for modeling the cyclic response of reinforced concrete shear walls. In order for the material models to be applicable in structural level problems and efficient

in terms of computation time, these new material models were required to be simple, stable, and reliable.

Because the major objective of this research is to study the cyclic response of slender reinforced concrete shear walls, the proposed concrete model must accurately represent the behavior of concrete in shear walls. Several important aspects of the behavior of concrete were observed from the measured response of walls tested in the laboratory: 1) cracks in the concrete tended to be distributed uniformly in the lower portion of the wall, 2) most of the cracks that developed when the wall was subjected to cyclic loading were nearly orthogonal to the cracks that developed during the first load cycle, and 3) most cracks did not rotate during the tests. Based on these observations, the proposed concrete model adopts the concept of a smeared crack model with fixed orthogonal cracks and uses a strength criterion for crack initiation and crack propagation. Cracks in concrete are assumed to be parallel and finely spaced. A crack occurs at an integration point when the maximum principal stress at that point exceeds the tensile strength of the concrete. A second crack at that integration point is allowed to form only in the direction perpendicular to the first crack. Once a crack forms, its direction is fixed throughout the analysis.

Inelastic shear distortion in the lower portion of the wall was observed to have a significant effect on the cyclic response of shear walls. In order for the proposed concrete model to be able to model this inelastic shear deformation, the shear strain component is separated from other strain components. This separation allows the concrete element to experience large inelastic shear strain without causing premature crushing of the concrete in the direction of the crack. As a result, the proposed concrete model defines two functions: the normal stress function and the shear stress function.

The normal stress function defines the stress-strain relationship of cracked concrete in the direction of the crack. The typical normal stress function is shown in Fig. 3.1. The important aspects of behavior of concrete that are included in the normal stress function are 1) tension stiffening, 2) crack closing and crack reopening, 3) compression softening, 4) the effect of steel confinement, and

5) the stiffness degradation due to cyclic loading. The basis for modelling these aspects of behavior is found in experimental data and previous analytical studies.

The shear stress function defines the relationship between shear stress and shear strain in the global coordinate system. The typical shear stress function is shown in Fig. 3.25(a). The shear stress function consists of three major components: 1) the shear stiffness from the interface shear transfer, 2) the shear stiffness from the dowel action, and 3) the rules for cyclic loading.

It was reported by several researchers (5, 80, 109, 118, 127) that the cyclic response of reinforced concrete members was greatly influenced by the cyclic response of reinforcing steel. This is also true for the cyclic response of slender reinforced concrete walls. In order to model the cyclic response of the walls correctly, the analysis must use a realistic reinforcing steel model that includes all important aspects of nonlinear behavior such as yielding, strain-hardening, and the Bauschinger effects. The reinforcing steel model in this research adopted the cyclic stress-strain relationship for reinforcing steel proposed by Aktan et al. (5) in the form of a Ramberg-Osgood equation. Several important modifications were made to the original relationship to increase the stability of the model and to improve the accuracy of the solution. The proposed reinforcing steel model was verified at the elemental level by using two sets of the cyclic response of a reinforcing bar: one by Aktan and et al. (5) and the other by Seckin (124). The calculated behavior was in excellent agreement with the experimental data.

The finite element program used in this research is FINITE. The unique feature of FINITE which made it suitable for this research is that new material models can be installed with minimal effort. As a result, developers can focus their attentions on the performance of the new material models rather than on modifying the existing finite element program (51). Although FINITE is capable of analyzing both geometrically nonlinear and materially nonlinear problems, only material nonlinearity was included in the analyses of reinforced concrete walls in this study. This is due to the fact that the displacement and strain in most concrete and reinforcing steel elements remained infinitesimal throughout the analysis and the major sources of nonlinearities in the analysis were the nonlinear

stress-strain relationships of concrete and reinforcing steel. The full Newton-Raphson iteration algorithm, in which the stiffness matrix is updated every iteration, was used as the iteration scheme for solving the nonlinear finite element equations. The ratio between the norm of the residual load and the norm of the applied load was used as a convergence criterion. A convergence tolerance of 5% was found to yield analytical results with satisfactory accuracy within a reasonable computation time.

In order to verify and calibrate the proposed material models, the finite element method was used to model the cyclic responses of thirteen slender reinforced concrete shear walls tested at the Construction Technology Laboratory (105, 106). The design variables of these walls were: the shape of the cross section, the amount of longitudinal reinforcement, the amount of horizontal web reinforcement, the amount of transverse steel in the boundary elements, the axial compressive stress, the loading histories, and the compressive strength of the concrete. Several types of data from the tests including load vs. top deflection curves, load vs. inelastic shear deformation curves, crack patterns, and failure modes, were compared with the results of the finite element analyses. The parameters used to define the normal stress and shear stress functions of the concrete model were adjusted so that the calculated response closely resembled the experimental results. After several trials, the optimum values of the parameters were determined. Using one set of parameters in the all analyses, the calculated response of all thirteen walls agreed well with the experimental data.

Another experimental program that was used to verify the proposed material models was the tests of C-shaped walls carried on as part of this research. Two C-shaped, reinforced concrete shear walls representing one-quarter scale models of reinforced concrete core walls were tested under cyclic loadings. Two-dimensional plane stress elements were used to model both the web and flange of the test specimens. The bending stiffness of the flange was neglected because its contribution to the overall stiffness of the walls was insignificant, especially after the concrete in the flange had cracked and the vertical steel reinforcement in the flange had yielded. The major contribution of the flange was provided by its in-plane force, which can be modelled by using two-dimensional



plane stress elements. The calculated response of both C-shaped wall specimens also agreed well with the experimental data.

After the material models for concrete and reinforcing steel had been thoroughly tested and satisfactorily verified, the finite element method was used to investigate three topics involving the response of slender reinforced concrete shear walls: 1) the energy dissipation capacity of shear walls, 2) the response of shear walls with openings, and 3) the contribution of flanges to the response of C-shaped shear walls.

In order for reinforced concrete shear walls to survive a strong earthquake, designers must ensure that the walls can dissipate energy when the wall is pushed into the inelastic range of response. In this study, the cyclic response of reinforced concrete shear walls with eight different web reinforcement patterns were analyzed using the finite element method. The energy dissipation capacity of each wall was evaluated and compared. It was found that merely increasing the amount of conventional vertical or horizontal web reinforcement did not improve the energy dissipation capacity of the walls. However, additional vertical reinforcement in the web, when it was stopped above the base of the wall and not embedded into the foundation, significantly improved the energy dissipation capacity of the wall. Among all the reinforcement options studied in this research, distributed diagonal web reinforcement in the lower portion of the wall was most effective in increasing the energy dissipation capacity of the walls. Concentrated diagonal shear reinforcement was less effective than distributed diagonal shear reinforcement; however, the former might be more desirable in practice because it requires fewer reinforcing bars and, therefore, is easier to place and arrange during construction.

To study the cyclic response of shear walls with openings, the finite element method was used to model the cyclic response of pierced shear walls tested at the Construction Technology Laboratory of PCA (126) and at the University of Michigan (6). The objectives of this study were 1) to use the finite element method to study the general behavior of walls with openings and 2) to study ways to improve the cyclic response of these walls. The analytical results showed that the major

problem caused by the openings in shear walls was the reduction in the inelastic shear transfer capacity of the walls. The presence of the openings significantly reduced the ability of diagonal compression struts in the web to transfer shear force and could result in a shear compression failure of concrete in the wall piers. The finite element analysis showed that diagonal reinforcement in the wall piers could significantly improve the inelastic shear transfer capacity of the wall piers, thereby helping to prevent shear-compression failures of the boundary elements. The finite element method can also be used to estimate the magnitude of shear force in each wall pier after forces were redistributed so that the proper amount of transverse reinforcement can be provided.

To study the contribution of flanges to the response of C-shaped walls, twelve C-shaped wall models with different flange widths, ranging from 0 in. to 140 in., were analyzed. The analytical results show that the effective width of a flange in C-shaped walls, both when the flange is in tension and when the flange is in compression, can be much larger than the effective width recommended in the provisions for T-beams in the 1989 ACI Building Code (2). When the flange is in compression, the ACI provisions for the effective width of T-beams yield a conservative value (six times the flange thickness), which is desirable. However, when the flange is in tension, the width of the flange where vertical steel reinforcement effectively provides tensile forces for resisting the overturning moment can be as high as 25 times the thickness of the web. The use of a too small an effective flange width can lead to a significant underestimation of the strength of the wall which can cause unexpected crushing of the concrete in the boundary elements opposite the flange.

## 9.2 CONCLUSIONS

The following conclusions are drawn from this study.

- 1) With the proper material models for concrete and reinforcing steel, the finite element method can be a powerful and versatile analytical tool for studying the cyclic response of reinforced concrete shear walls.

- 2) In order for the analysis of the cyclic response of reinforced concrete shear walls to be feasible and efficient in terms of computation time, the material models must be simple, stable, and reliable.
- 3) The concrete model used in this study adopted the concept of a smeared crack model with fixed-orthogonal cracks and used a strength criterion for crack initiation and for crack propagation. Satisfactory results were obtained using this approach.
- 4) The separation of the shear strain from other strain components allowed the concrete model to successfully simulate the inelastic shear deformation of shear wall.
- 5) Because the cyclic response of reinforcing steel has a significant effect on the cyclic response of shear walls, the analysis of shear walls requires a realistic steel model which takes into account yielding, strain-hardening, and the Bauschinger effects. In this study, the cyclic stress-strain relationship of reinforcing steel expressed in the form of the Ramberg-Osgood equation was found to yield good analytical results.
- 6) In the analysis of reinforced concrete shear walls, the full Newton-Raphson iteration algorithm, which updates the stiffness matrix every iteration, yields stable solutions with good convergence rate.
- 7) Adding conventional vertical or horizontal web reinforcement does not improve the energy dissipation capacity of shear walls. Among all the reinforcement details studied in this research, distributed diagonal shear reinforcement in the lower portion of the web is most effective in improving the energy dissipation capacity of shear walls.
- 8) The presence of openings in shear walls can have a significant influence on the inelastic shear transfer capacity of the walls. The calculated results show that diagonal shear reinforcement in the wall piers can improve significantly the shear transfer capacity of the wall piers. The finite element method can also be used to estimate the magnitude of the shear force in each wall pier so that the proper amount of transverse reinforcement can be provided.

- 9) The effective width of the flange in C-shaped walls, both when the flange is in compression and when it is in tension, can be much larger than the effective width recommended in the provisions for T-beams in the 1989 ACI Building Codes (2). When the flange is in compression, using an effective flange width which is smaller than the actual effective flange width yields a conservative value of the wall's strength. However, when the flange is in tension, using a too small effective width can lead to a significant underestimation of the strength of the wall, possibly resulting in unexpected crushing of the concrete in the boundary elements opposite the flange.

### **9.3 RECOMMENDATIONS FOR FUTURE RESEARCH**

Several other subjects related to this research have been identified that need further investigation. Experimental and analytical research needs are summarized below.

#### **9.3.1 EXPERIMENTAL PROGRAMS**

- 1) More experimental data on the cyclic behavior of reinforced concrete at the element level are needed. The types of behavior include the cyclic response of concrete under biaxial states of stress, the cyclic shear stress–shear strain relationship, and the upper bounds of the interface shear transfer mechanism and the dowel action mechanism.
- 2) More experimental data are needed on the interaction between concrete and reinforcing bars, especially under cyclic loadings. These data are essential in the development of the linkage elements, which may be used to connect the reinforcing bar elements to the concrete elements at the locations where bond–slip is important such as at the base of the walls.
- 3) The effectiveness of the diagonal shear reinforcement for improving the energy dissipation capacity of both solid walls and pierced walls should be investigated. This is necessary to verify the finite element results which indicate that the diagonal reinforcement is the most effective means of improving the energy dissipation capacity.

- 4) The cyclic response of C-shaped walls with different flange widths should be investigated. Although this type of shear wall is widely used as a major lateral load resisting system in tall buildings, there are no design provisions for such walls in the current 1989 ACI Building Codes (2). Experimental data will be useful in the development of design provisions for such walls.

### 9.3.2 ANALYTICAL MODELS

Several aspects of the proposed material models for concrete and reinforcing steel can be improved to increase the capacity of the models. Some of the possible improvements are listed as follows.

- 1) The reinforcing steel model can be included in the concrete model as a layer of reinforcement. This will allow the arrangement of reinforcing steel in the finite element model to be mesh-independent. Several layers of reinforcing steel with different angles can be included in one concrete element.
- 2) The rotating crack model should be added to the current proposed model as an option (i.e., finite element users can choose either the fixed crack model or the rotating crack model). This will allow the concrete model to be able to simulate the response of the reinforced concrete member where crack rotation is important. An example of such member is the reinforced concrete panel tested by Stevens et al. (134) where crack rotations were observed during the load reversals and had a significant effect on the cycle response of the panel.
- 3) A concrete element with a discrete crack model should be developed. This element can be used where a single large crack is likely to occur such as the area at the base of the wall.
- 4) A linkage element which models bond-slippage between concrete and reinforcing bars should be developed. Such an element can be used to connect concrete elements and reinforcing steel elements in the location where bond-slippage is critical.

5) Improvements need to be made in the current shear stress function of the proposed concrete model. Limiting strengths for both the interface shear transfer mechanism and the dowel action mechanism need to be added to the model. This must be done in conjunction with an experimental program because such information is not available at the present time.

**TABLES**

Table 4.1 Parameters used to define the Reinforcing Steel Model  
(for Grade 60 Steel)

Type of Curve	Parameter	Value
a strain hardening curve	m	4.30
	$\sigma_{om}$	42.0 ksi
a 1/2 cycle from compression	$\alpha$	6.0
	A	0.7938
	B	0.55723
a 1/2 cycle from tension	$\alpha$	7.0
	A	0.7735
	B	0.47989



Table 5.1 Classifications of Nonlinear Analyses (from [13])














Type of analysis	Description	Type of formulation
Materially–nonlinear only	Infinitesimal displacements and strains Nonlinear stress–strain relationship	Material nonlinearity
Large displacements, large rotations, but small strains	Displacements and rotations are large, but strains in fibers are small Stress–strain relationship may be linear or nonlinear.	Geometric nonlinearity with or without material nonlinearity
Large displacements, large rotations, and large strains	Strains in fibers are large. Displacements and rotations may be large. Stress–strain relationship may be linear or nonlinear	Geometric nonlinearity with or without material nonlinearity

Table 5.2 CPU Time Required in the Analyses of Wall R1 with Different Schemes for Updating Stiffness Matrix

Step	CPU Time required in the analysis (seconds) <sup>†</sup>		
	Updating [K] every iteration	Updating [K] every 3 iterations	Updating [K] every 5 iterations
13	31.20	34.23	34.16
14	12.92	13.93	19.21
15	31.75	34.45	50.41
16	17.64	24.14	19.29
Total	93.51 (100%)	106.75(114.2%)	123.0 (131.5%)

<sup>†</sup>HP 700 Machines

Table 6.1 Properties of PCA Wall Specimens (from Oesterle [103])

Specimen	Shape	Axial Load psi	Loading type *	$f_c'$ psi	$f_y$ (for gv) ksi	Reinforcement (%)			
						$Q_v$	$Q_h$	$Q_n$	$Q_s'$
R1		0.0	IR	6490	74.2	1.47	0.31	0.25	0.00
R2		0.0	IR	6735	65.3	4.00	0.31	0.25	2.07
R3		220.0	MR	3535	78.3	6.00	0.42	0.22	1.33
R4		220.0	IR	3285	71.2	3.50	0.31	0.28	1.07
B1		0.0	IR	7685	65.2	1.11	0.31	0.29	0.00
B2		0.0	IR	7775	59.6	3.67	0.63	0.29	0.00
B3		0.0	IR	6860	63.5	1.11	0.31	0.29	1.28
B4		0.0	MN	6530	65.3	1.11	0.31	0.29	1.28
B5		0.0	IR	6570	64.4	3.67	0.63	0.29	1.35
B6		425.0	IR	3165	63.9	3.67	0.63	0.29	0.81
B7		545.0	IR	7155	66.4	3.67	0.63	0.29	1.35
B8		545.0	IR	6085	64.9	3.67	1.28	0.29	1.35
B9		545.0	MR	6395	62.3	3.67	0.63	0.29	1.35

- \* IR = Increasing incremental loading
- MN = Monotonic loading
- MR = Modified reversing loading
- $Q_v$  = Ratio of area of longitudinal reinforcement to gross area of the boundary element
- $Q_h$  = Ratio of area of horizontal web reinforcement to gross area of vertical section through the web
- $Q_n$  = Ratio of area of vertical web reinforcement to gross area of horizontal section through the web
- $Q_s'$  = Ratio of volume of confinement reinforcement to the volume of core in accordance with Eq. A.4 of ACI 318-71

Table 6.2 Parameters used to define the Concrete Model for PCA Wall Specimens

a) Normal Stress Function

Parameter	Value
$\varepsilon_i$	50.0 $\varepsilon_{cr}$
$\sigma_i$	0.1 $\sigma_{cr}$
$\alpha$	0.2
$\sigma_1$	3.0 $\sigma_{cr}$
$\sigma_2$	0.2 $\sigma_{cr}$
$\sigma_3$	0.8 $\sigma_{cr}$
$\sigma_4$	0.2 $\sigma_{cr}$
$\sigma_n$	3.0 $\sigma_{cr}$

Concrete in Web

Parameter	Value
$\varepsilon_i$	50.0 $\varepsilon_{cr}$
$\sigma_i$	0.2 $\sigma_{cr}$
$\alpha$	0.3
$\sigma_1$	3.0 $\sigma_{cr}$
$\sigma_2$	0.2 $\sigma_{cr}$
$\sigma_3$	0.8 $\sigma_{cr}$
$\sigma_4$	0.2 $\sigma_{cr}$
$\sigma_n$	3.0 $\sigma_{cr}$

Concrete in Boundary Elements

b) Shear Stress Function

	Parameter	Value
$G_{ist}$	$\mu_1$	0.20
	$\varepsilon_{min}$	12.50 $\varepsilon_{cr}$
$G_{dow}$	$\mu_2$	0.20
	$\gamma_n$	0.015
	$n$	3
Cyclic	$\tau_{slip}$	0.04 ksi
	$G_{unl}$	0.10 $G_{conc}$
	$\beta$	0.70
	$G_{min}$	0.0005 $G_{conc}$

Table 6.3 Observed Failure Modes in PCA Wall Specimens

Specimen	Experimental Results		Analytical Results	
	Failure mode <sup>†</sup>	Description	Failure mode <sup>†</sup>	Description
R1	IB	First buckling of the main flexural reinforcement was observed in Cycle 20, the second cycle at +3 in. deflection. First bar fracture occurred at Cycle 26, the second cycle at +4 in. The specimen lost load carrying capacity when the bar fractured. No concrete crushing was observed.	IB	First bar buckling was observed in bar # 207 at load step 412, the second cycle at +3-in. deflection. Four more bars buckled in the later steps (#208, #209, #153, #154). Concrete at the face of the boundary element crushed
R2	IC	Instability in the compression zone due to large out of plane displacement was observed in Cycle 32, the second cycle at +4 in. The wall failed because of buckling of the compression zone in Cycle 35, the second cycle at +5 in.	BC	No bars buckled in Wall R2. Concrete in both boundary elements were extensively crushed after load step 425, the second cycle at +3-in deflection.
R3	BC	Apparent crushing was observed in both boundary regions in Cycle 2, the first cycle at 3-in. deflection but there was no drop in load associated with this crushing. The wall lost load carrying capacity in Cycle 8, at 3 in.-deflection due to extensive crushing in boundary elements.	BC	No bars buckled in Wall R3. Concrete in the boundary elements started crushing at load step 105, +1.85-in. deflection in the first cycle. Extensive concrete crushing in boundary elements started at load step 405, +2.90-in.deflection.
R4	BC	Crushing of the outer cover of the compression face was observed in Cycle 10 at a top deflection of 2 in. Further crushing of both boundary elements occurred during Cycles 13, 14, and 15 at peak to deflection of 3 in. Significant drop in load-carrying capacity of the wall occurred in Cycle 16 at 4-in. deflection due to extensive crushing of boundary elements	BC	No bars buckled in Wall R4. Concrete in the boundary elements started crushing at load step 174, +2-in.deflection. Extensive crushing of concrete in the boundary elements occurred at load steps 465 and 508, +4- and -4-in. deflection.

<sup>†</sup> IB = Inelastic Bar Buckling BC = Boundary Element Crushing IC = Instability in the Compression Zone BF = Bar Fracture WC = Web Crushing

Table 6.3 (Cont.) Observed Failure Modes in PCA Wall Specimens

Specimen	Experimental Results		Analytical Results	
	Failure mode <sup>†</sup>	Description	Failure mode <sup>†</sup>	Description
B1	IB	The first flexural bar was observed to buckle during Cycle 22, the first 3-in. deflection. In subsequent cycles, 13 other bars buckled. After the first bar buckled, the boundary elements started to deteriorate. The wall lost load-carrying capacity in Cycle 31, the first 5-in. deflection, due to bar fracture.	IB	First bar buckling occurred in bar # 220 at load step 263, the second cycle at +2.0-in. deflection. Three more bars buckled in later steps (#221, #222, and #145). Crushing of concrete in the boundary element was not extensive.
B2	WC IB	Crushing of concrete in the boundary element was first observed in Cycle 22, at 3-in. deflection. First two bars buckled during Cycle 26 at 4-in. deflection. Sudden web failure occurred in Cycle 28 at -5-in. deflection.	WC	First bar buckling occurred in bar # 136 at load step 717, the second cycle at +5.0-in. deflection. Few concrete elements in web started crushing at load step 671, the second cycle at -4.0 in. Extensive web crushing occurred at load steps 718 and 770, the first cycle at ±5.0-in. deflection
B3	BF	Significant crushing and grinding of web concrete was observed after Cycle 28, +4-in. deflection. Confinement hoops in the boundary elements helped to contain concrete and prevent bar buckling. The specimen lost load-carrying capacity in Cycle 39, at 7-in. deflection, when a vertical bar fractured. The fractured bar still had concrete cover and no evidence of previous buckling was observed.	BC	No bars buckled in wall B3. Crushing of concrete in the boundary elements occurred at load step 399, the second cycle at +3-in. deflection. Concrete crushing of the boundary elements became extensive at load steps 699 and 731, the first cycle at ±6-in. deflection.
B4	BF	Crushing in the compression boundary element started at Load stage 9 (2-in. deflection) and progressively increased throughout the test. The wall started losing its load-carrying capacity at Load stage 15 (8.5-in. deflection) when vertical bars fractured.	BF	Concrete in the compression boundary element started crushing at load step 25, +0.50-in. deflection. Bar # 145 fractured at load step 115, +7.80-in. deflection. Three more bars fractured at later load steps (#160, #175, and #235).

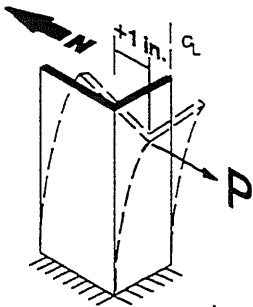
<sup>†</sup> IB = Inelastic Bar Buckling BC = Boundary Element Crushing IC = Instability in the Compression Zone BF = Bar Fracture WC = Web Crushing

Table 6.3 (Cont.) Observed Failure Modes in PCA Wall Specimens

Specimen	Experimental Results		Analytical Results	
	Failure mode <sup>†</sup>	Description	Failure mode <sup>†</sup>	Description
B5	WC	Crushing of concrete in the boundary elements was first observed in Cycle 19, at +2-in.deflection. The wall suddenly lost its load-carrying capacity in Cycle 28, at -5-in.deflection, when web crushing occurred.	WC	No bars buckled in Wall B5. Few concrete elements in web started crushing at load steps 629 and 671, the second cycle at ±4-in.deflection. Extensive web crushing occurred at load steps 718 and 770, the first cycle at ±5-in. deflection.
B6	WC	Crushing of concrete in the boundary elements was first observed in Cycle 16, at +1-in.deflection. The wall suddenly lost its load-carrying capacity in Cycle 26, at +3-in.deflection, when several compression struts crushed simultaneously.	WC BC	Crushing of concrete in the boundary elements started at load step 150, +2-in.deflection. Web crushing and extensive crushing in the boundary elements occurred at load steps 360 and 390, ±3-in.deflection.
B7	WC	Crushing of concrete in the boundary elements was first observed in Cycle 19, at 2-in.deflection. The wall suddenly lost its load-carrying capacity in Cycle 31, at +6-in.deflection, when several compression struts crushed simultaneously.	WC	Few concrete elements in web started crushing at load step 599, the second cycle at -4-in. deflection. Web crushing occurred extensively at load steps 698 and 750, the second cycle at ±5-in.deflection.
B8	WC	Crushing of concrete in the boundary elements was first observed in Cycle 14, at 2-in.deflection. The wall suddenly lost its load-carrying capacity in Cycle 31, at +6-in.deflection, when several compression struts crushed simultaneously.	WC	Few concrete elements in web started crushing at load steps 646, the first cycle at +5 in.deflection. Web crushing occurred extensively at load steps 698 and 750, the second cycle at ±5-in. deflection.
B9	WC	Crushing of concrete in the boundary elements was first observed in Cycle 2, at +5.3-in.deflection. The wall suddenly lost its load-carrying capacity in Cycle 4, at -4-in.deflection, when several compression struts in the lower left region of the web crushed.	BC WC	Crushing of concrete in the boundary elements occurred at load step 60, the second cycle at +5.30-in. and became extensive at load step 320 and 380 (+4.7-and -5.1-in. deflection). Web crushing of concrete occurred extensively at load step 380 (-5.1-in. deflection).

<sup>†</sup> IB = Inelastic Bar Buckling BC = Boundary Element Crushing IC = Instability in the Compression Zone BF = Bar Fracture WC = Web Crushing

Table 7.1 Comparisons between 2-D Plane Stress Elements and Shell Elements



Type of Elements	Horizontal Force (P) at the Corner Node <sup>†</sup>	CPU time required for the analysis (HP 700)
8-Node Plane Stress (2-D)	198.2 kips	5.6 seconds
8-Node Shell (3D)	200.0 kips	38.3 seconds

<sup>†</sup>This force results in a 1-in horizontal displacement in the south direction at the corner node.

Table 7.2 Failure Modes in Walls CLS and CMS

Specimen	Experimental Results		Analytical Results	
	Failure mode <sup>†</sup>	Description	Failure mode <sup>†</sup>	Description
CLS	IB BC	<p>Minor spalling was observed at the north end of the wall at a top deflection of -1.0 in. (1.0% drift) During the top displacement cycles to -1.65 in. (1.5% drift), all the concrete cover surrounding the north boundary elements spalled. The longitudinal reinforcing bars were observed to buckle slightly.</p> <p>Significant buckling of the north longitudinal reinforcement was observed during the 2.0 in. cycles (2% drift). Wall CLS failed in the third cycle approaching -2.25 in. top displacement. The failure followed crushing of the north boundary elements</p>	IB BC WC	<p>Concrete at the outer face of the north boundary elements started crushing in the first cycle at -1.0 in. top displacement. The north boundary element became extensively crushed in the first cycle at -2.35 in. top displacement. Buckling was observed in the bar at the bottom of the north boundary element in the last cycle at -2.90 in. top displacement.</p> <p>Extensive web crushing in the web elements adjacent to the north boundary elements was also observed in the last cycle at -2.90 in. top displacement.</p>
CMS	IB BC	<p>Minor spalling was observed at the north end of the wall at a top deflection of -1.0 in. (1.0% drift) During the top displacement cycles to -1.65 in. (1.5% drift), all the concrete cover surrounding the north boundary elements spalled. The longitudinal reinforcing bars were observed to buckle slightly.</p> <p>Significant buckling of the north longitudinal reinforcement was observed during the 2.0 in. cycles (2% drift). Wall CMS failed in the second cycle approaching -2.50 in. top displacement. The failure followed crushing of the north boundary elements</p>	IB BC WC	<p>Concrete at the outer face of the north boundary elements started crushing in the first cycle at -0.5 in. top displacement. The north boundary element became extensively crushed in the first cycle at -1.0 in. top displacement. The crushing of the north boundary element in wall CMS was much more extensive than that of wall CLS. Buckling was observed in the bar at the bottom of the north boundary element in the last cycle at -2.20 in. top displacement.</p> <p>Extensive web crushing in the web elements adjacent to the north boundary elements was also observed in the last cycle at -2.20 in. top displacement.</p>

<sup>†</sup> IB = Inelastic Bar Buckling BC = Boundary Element Crushing IC = Instability in the Compression Zone BF = Bar Fracture WC = Web Crushing



Table 8.1 Amount of Reinforcement in each Reinforcement Option

Reinforcement Details	Horizontal Web Reinforcement $\rho_h$ (%)	Vertical Web Reinforcement $\rho_v$ (%)	Diagonal Reinforcement
Option # 1	0.60	0.30	none
Option # 2	1.20	0.30	none
Option # 3	0.60	0.90 (embedded)	none
Option # 4	0.60	0.30 (embedded) 0.60 (not embedded)	none
Option # 5	0.60	0.30	distributed $\rho_d = 0.60$
Option # 6	0.60	0.30	distributed $\rho_d = 0.30$
Option # 7	0.60	0.30	4 # 5 bars
Option # 8	0.60	0.30	4 # 5 bars

Table 8.2 Shear Forces and Nominal Shear Strengths in the East Piers of Wall W2, W3, and W4

WALL	TOTAL APPLIED FORCE (kips)	SHEAR FORCE IN THE EAST PIER (kips)		NOMINAL SHEAR STRENGTH OF THE EAST PIER (KIPS)
		LINEAR FINITE ELEMENT ANALYSIS	NONLINEAR FINITE ELEMENT ANALYSIS	
W2	37.2	6.1	16.0	5.5
W3	37.1	9.7	21.1	8.1
W4	36.3	10.8	21.7	9.1

Table 8.3 Parametric Study of C-Shaped Walls

Case	Loading <sup>†</sup>		Reinforcement
	cycle 1	cycle 2	
A	+0.15 in.	-2.5 in.	Same as CLS
B	-0.15 in.	+2.5 in.	Same as CLS
C	-0.15 in.	+2.5 in.	Longitudinal reinforcement in the north boundary element was increased to five times that in CLS
D	Two cycles at $\pm 0.1$ , $\pm 0.2$ , $\pm 1.0$ , $\pm 2.0$ , and $\pm 3.0$ in.		Same as CLS

<sup>†</sup>Positive loading places the transverse flange in compression and negative loading places the transverse flange in tension.

**FIGURES**

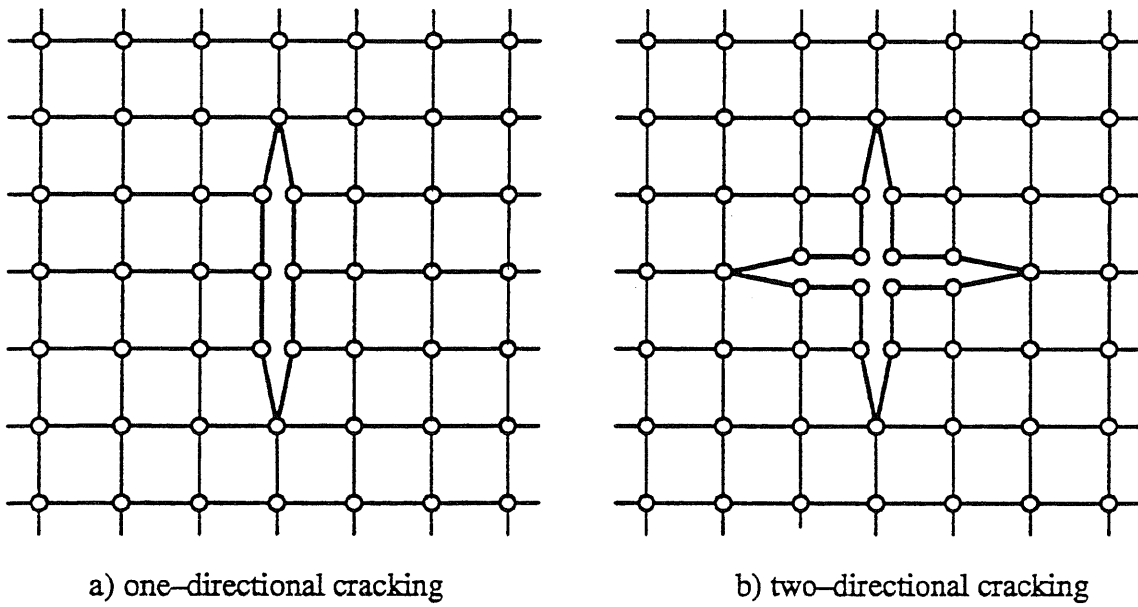
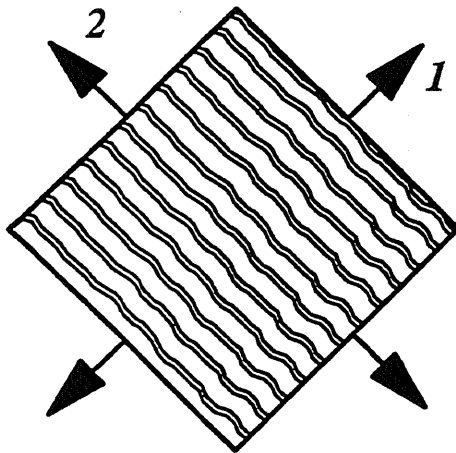


Fig. 2.1 Discrete Crack Models (from [136])



a) one-directional cracking

$$\begin{bmatrix} \partial\sigma_1 \\ \partial\sigma_2 \\ \partial\tau_{12} \end{bmatrix} = \begin{bmatrix} E_1 & 0 & 0 \\ 0 & E_2 & 0 \\ 0 & 0 & \beta G \end{bmatrix} \begin{bmatrix} \partial\varepsilon_1 \\ \partial\varepsilon_2 \\ \partial\gamma_{12} \end{bmatrix}$$

b) constitutive matrix in crack direction

Fig. 2.2 Smeared Crack Model

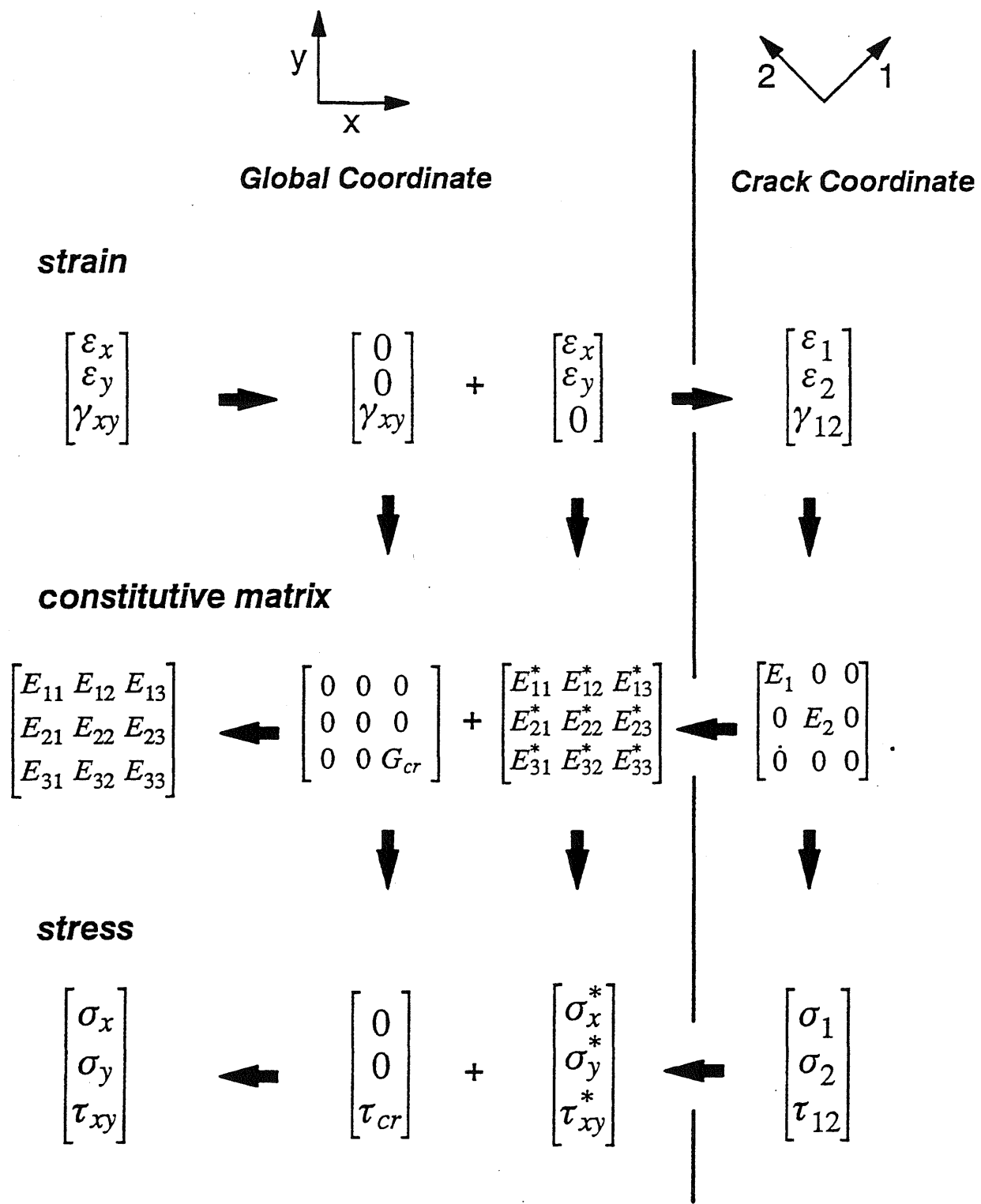


Fig. 2.3 Separation of Shear Strain

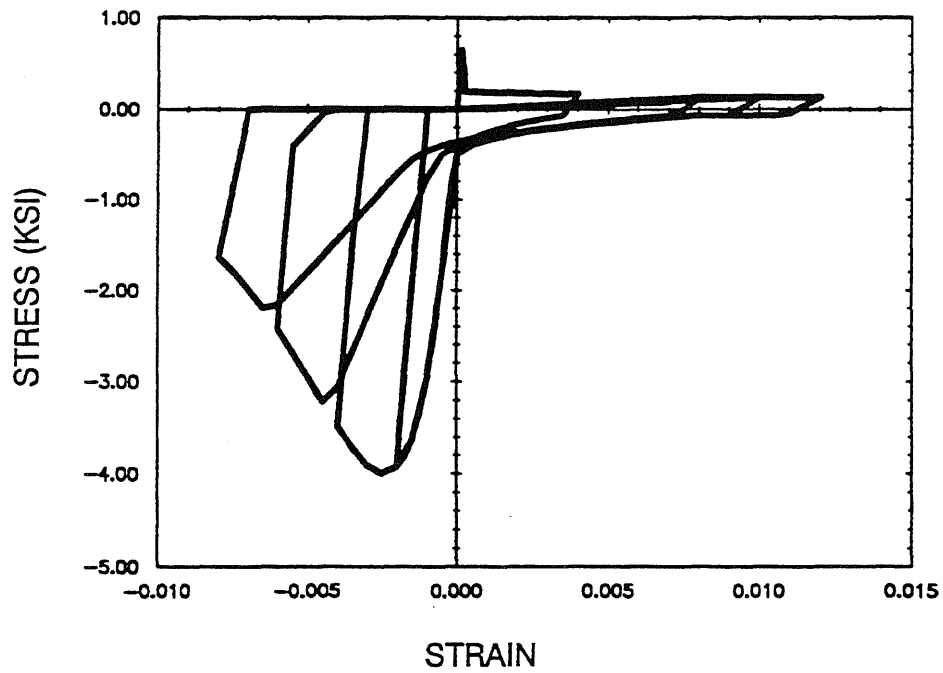
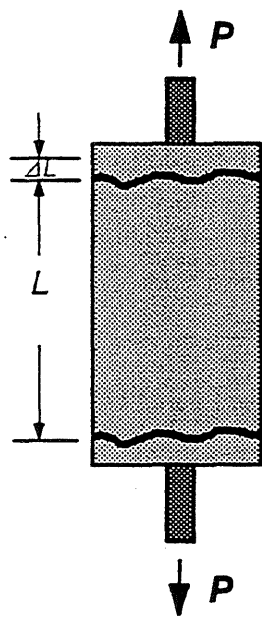


Fig. 3.1 Typical Normal Stress Function



$$\epsilon_{av} = \frac{\Delta L}{L}$$

$$\sigma_{av} = E_s \Delta \epsilon_{av}$$

	NO BOND		WITH BOND	
	Steel	Concrete	Steel	Concrete
STRAIN				
STRESS				
P	$\sigma_{av} A_s$	<	$(\sigma_{av} + \Delta \sigma) A_s$	

Fig. 3.2 Tension Stiffening

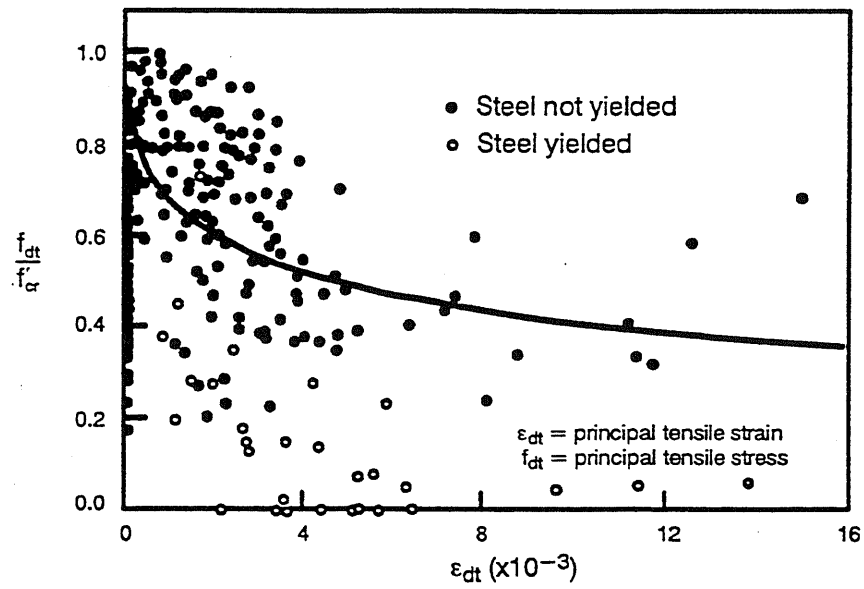


Fig. 3.3 Scatter in Data Representing Tension Stiffening (from Vecchio and Collins [143])

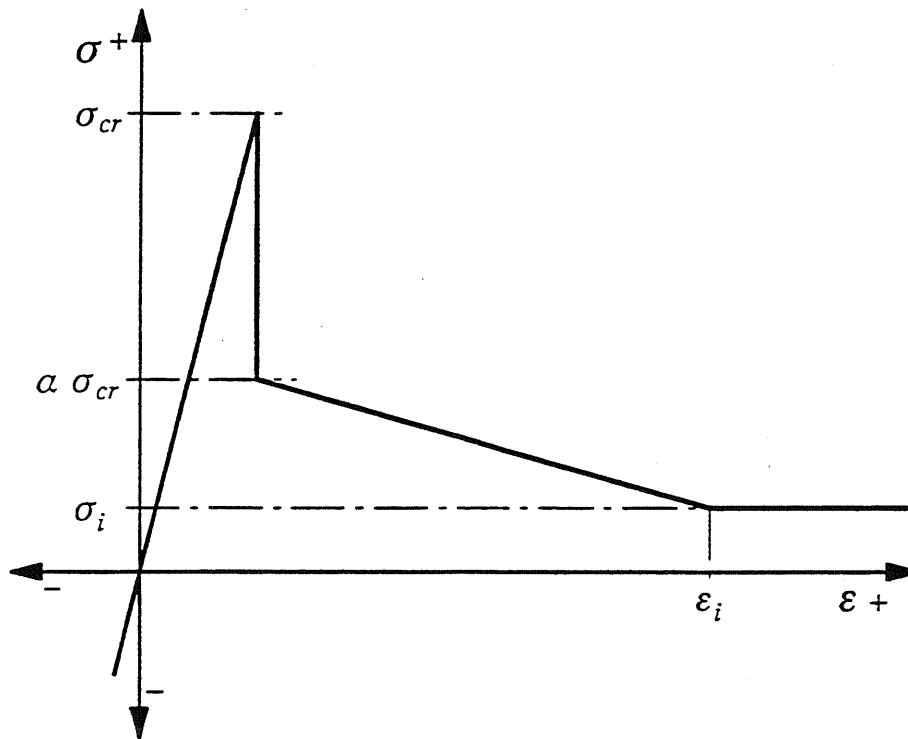


Fig. 3.4 Tension Stiffening Model

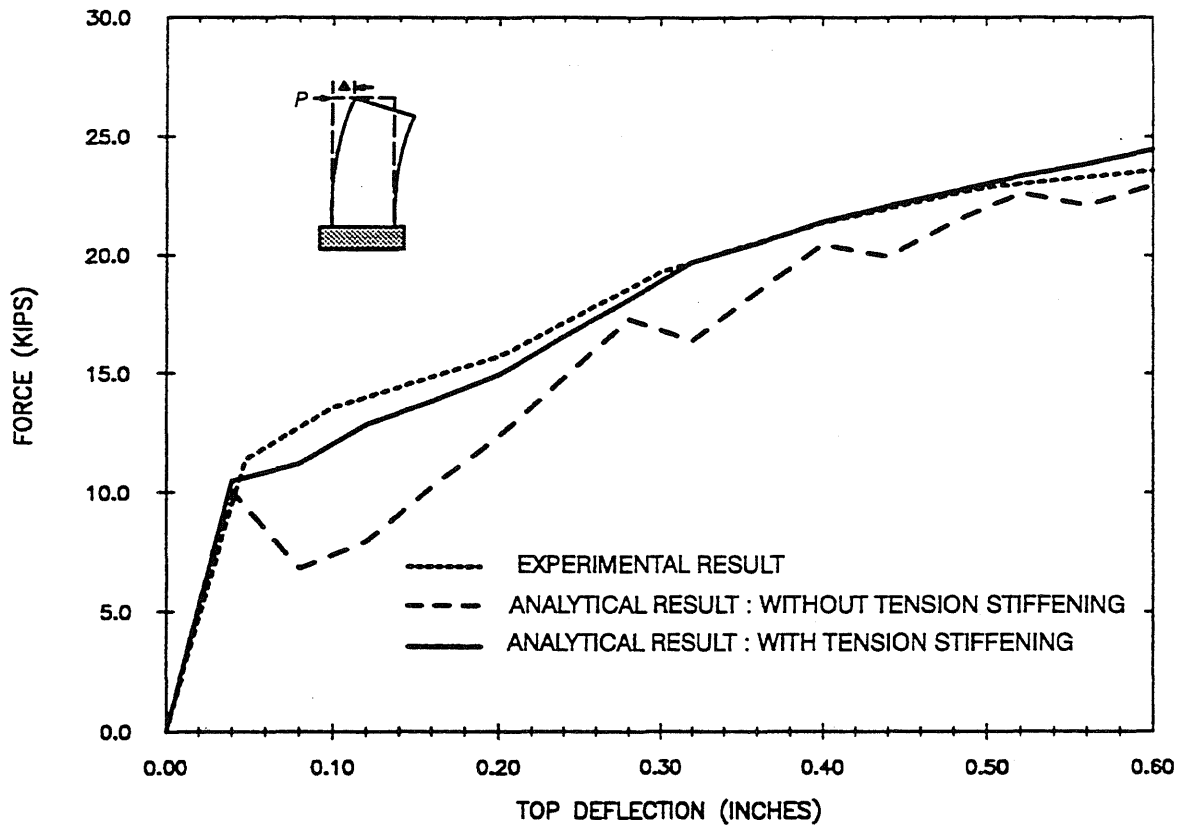
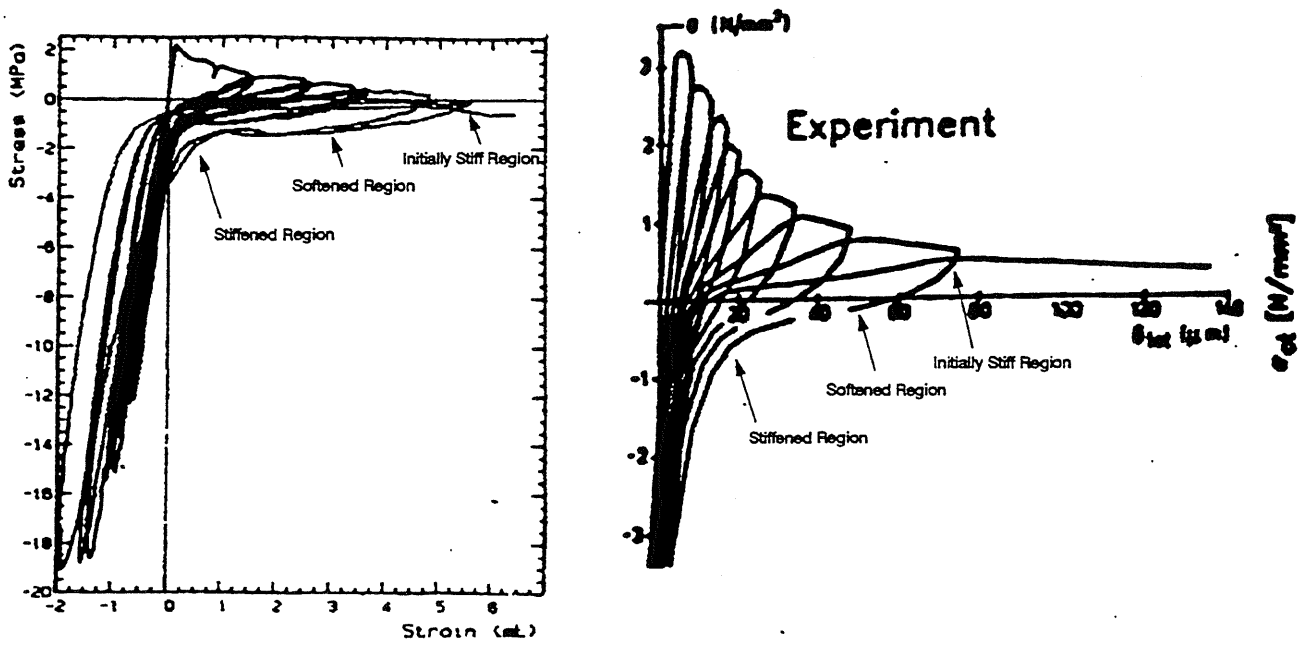


Fig. 3.5 Load vs. Deflection Curve of Wall B4 (from Oesterle [105])



a) Stress vs. Strain  
(from Stevens et al. (134))

b) Stress vs. Crack Width  
(from Yankelevsky and Reinhardt (155))

Fig. 3.6 Response of Concrete Subjected to Cyclic Tension



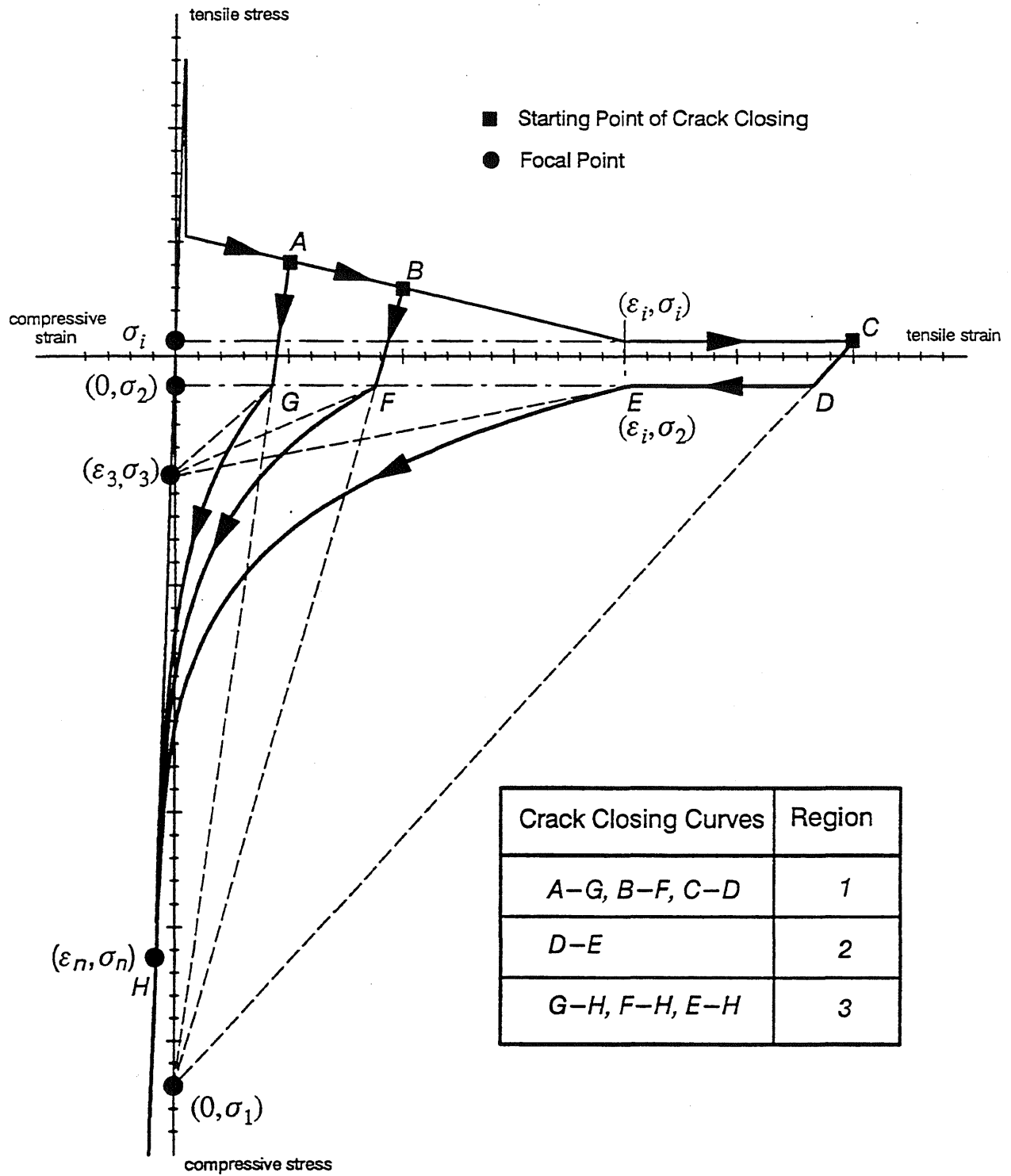


Fig. 3.7 Rules for Crack Closing ( $\Delta\varepsilon < 0$ )

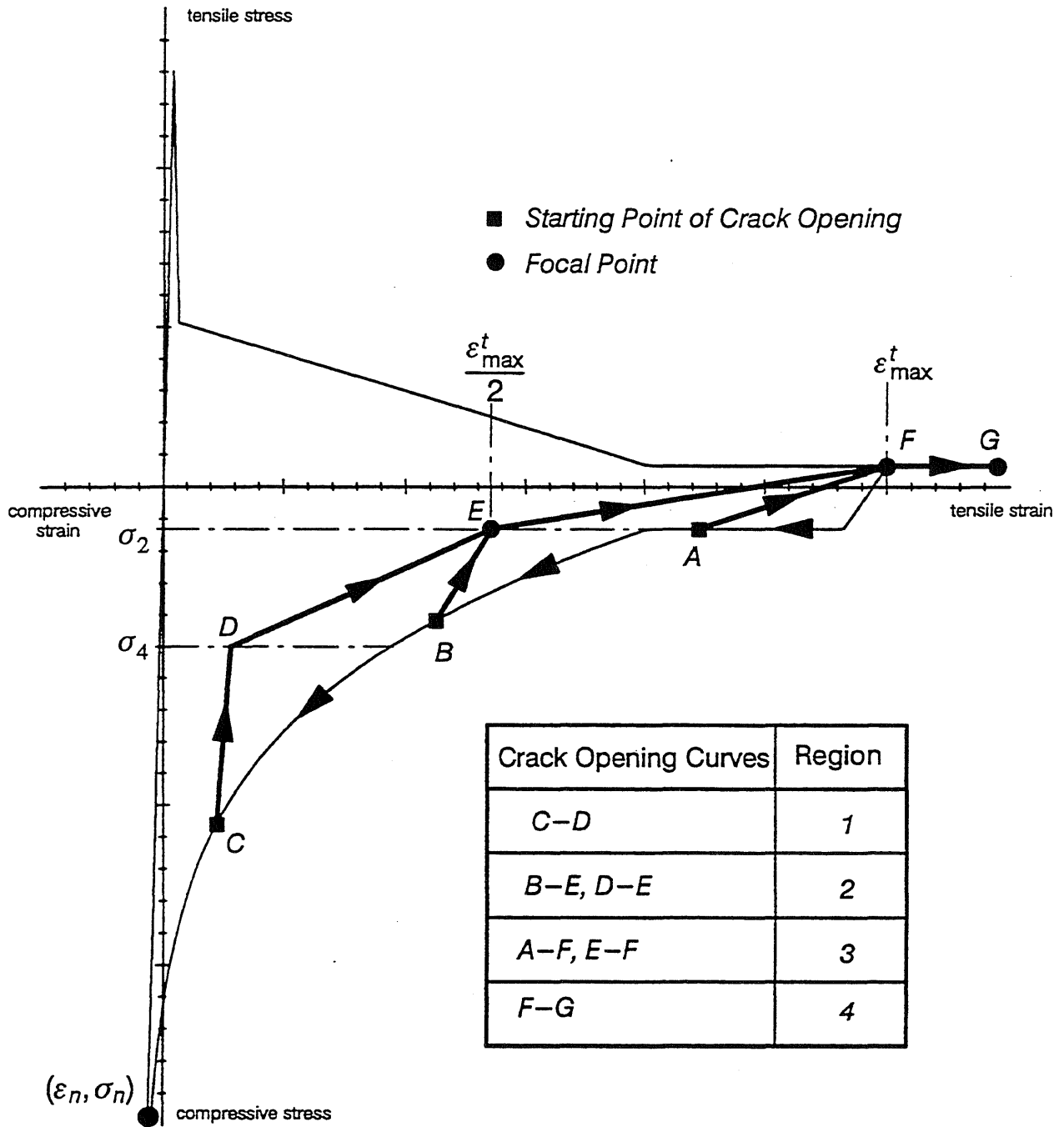


Fig. 3.8 Rules for Crack Opening ( $\Delta\epsilon > 0$ )

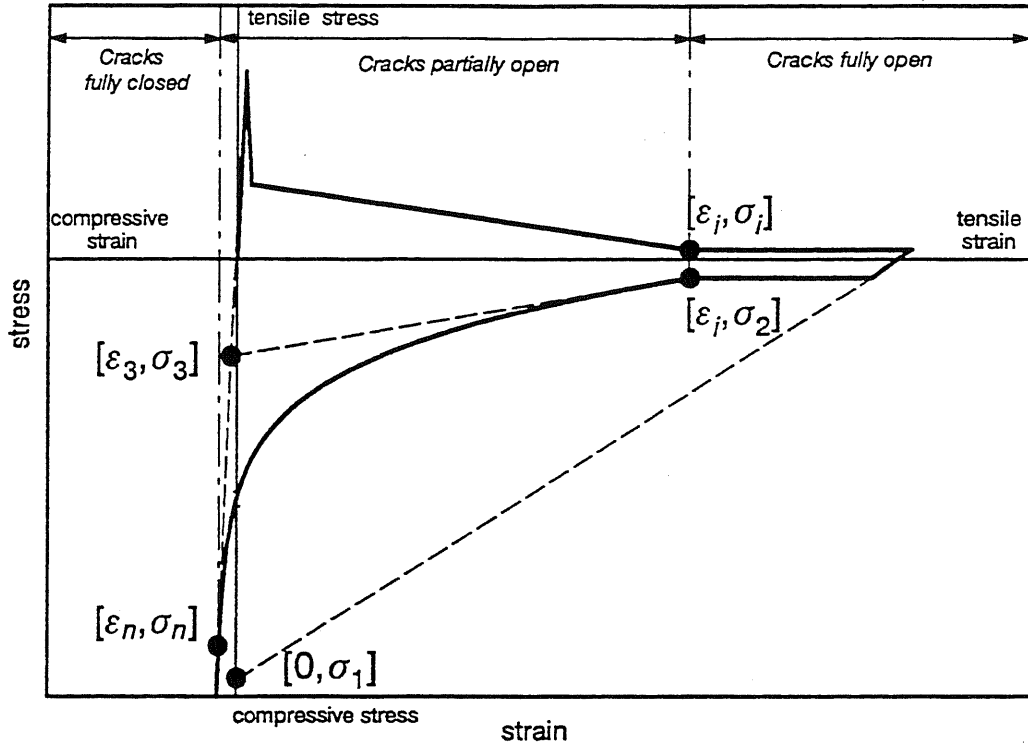


Fig. 3.9 Focal Points for Crack Closing and Opening

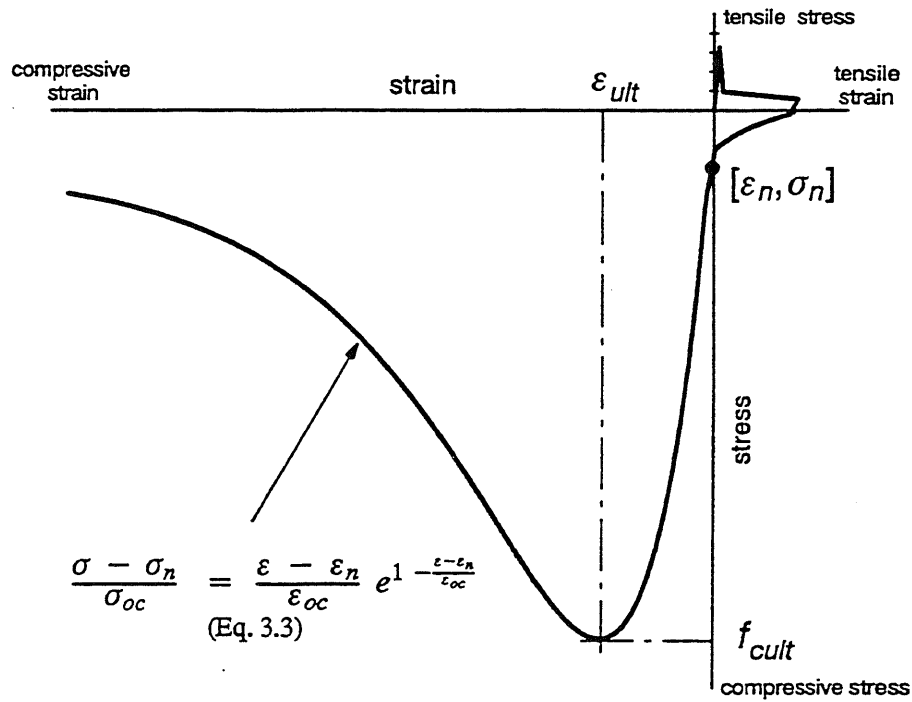


Fig. 3.10 Compression Softening Model

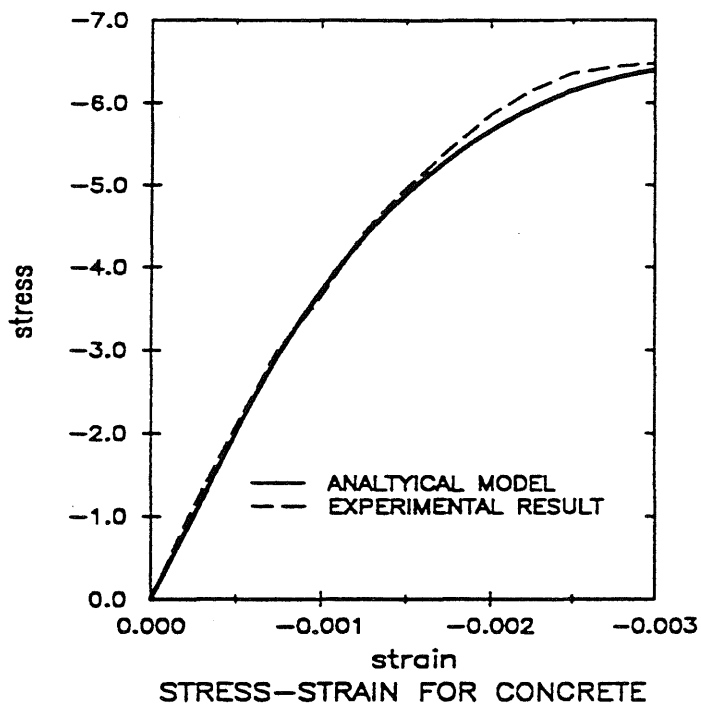


Fig. 3.11 Evaluation of Compression Softening Function (from Oesterle [105])

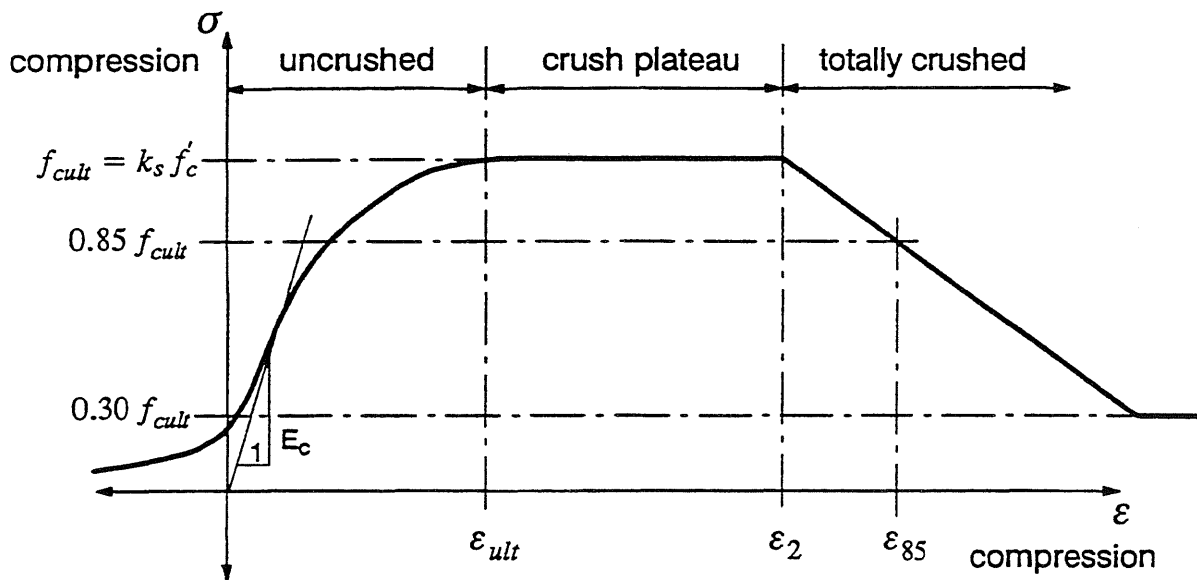


Fig. 3.12 The Proposed Model for Confined Concrete (from Shiekh and Uzumeri [125])

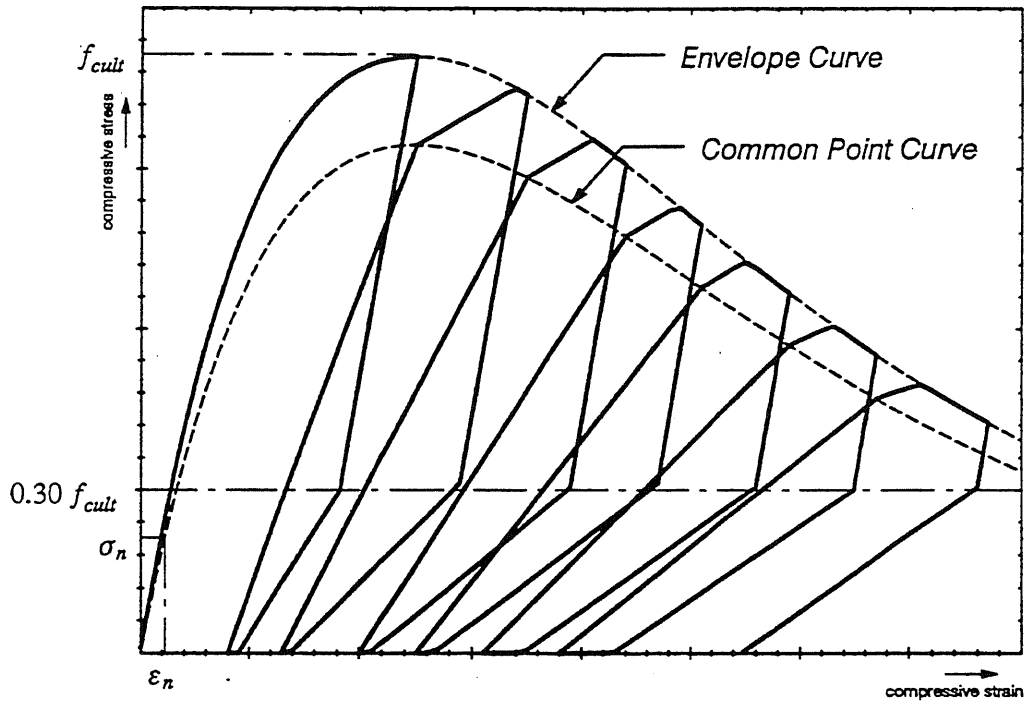


Fig. 3.13 Proposed Compressive Cyclic Stress-Strain Relationship

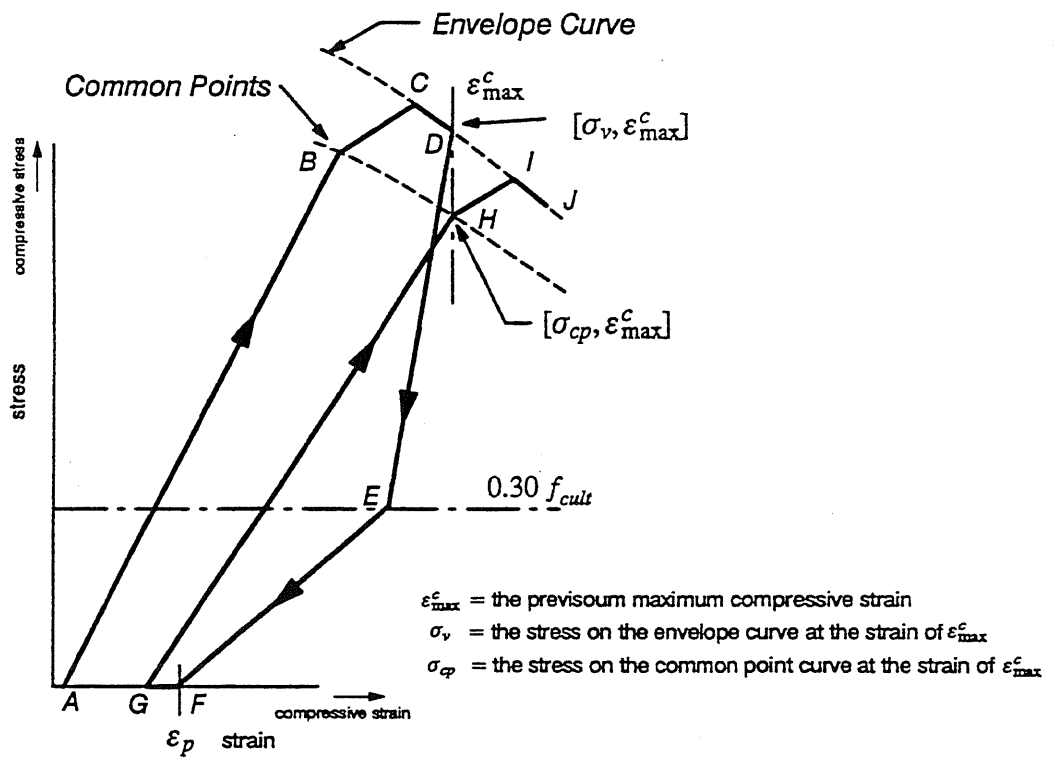


Fig. 3.14 Rules for Unloading and Reloading: Unconfined Concrete

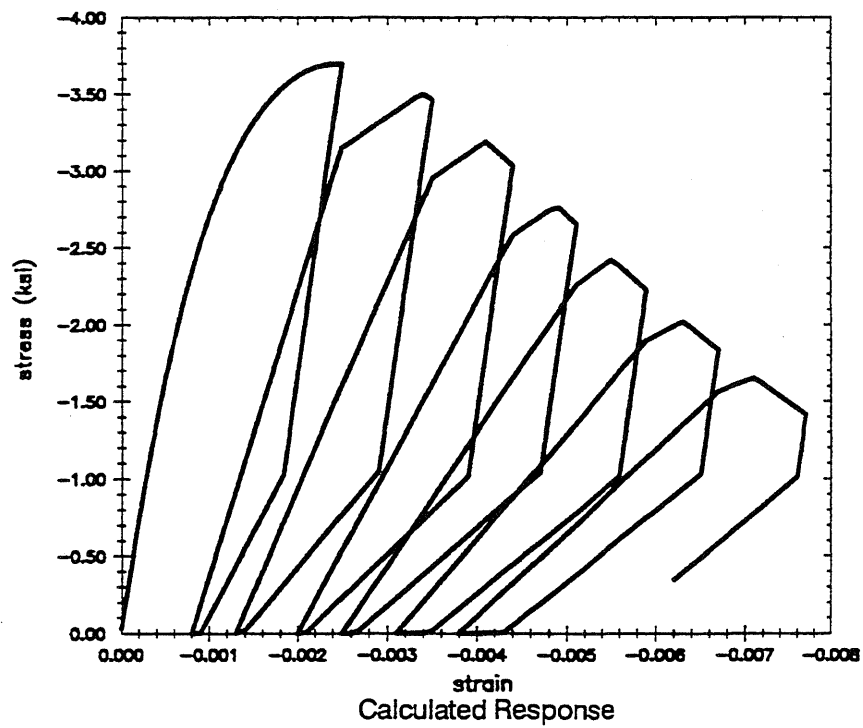
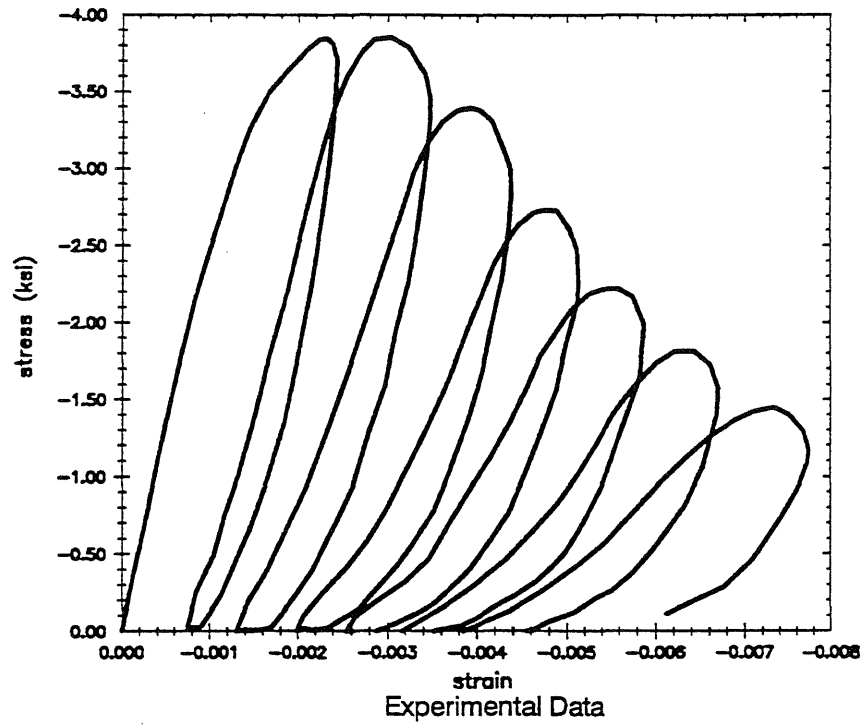


Fig. 3.15 Comparison of Calculated and Experimental Data for Response of Concrete subjected to Cyclic Compression Loads (Sinha et al. [128])

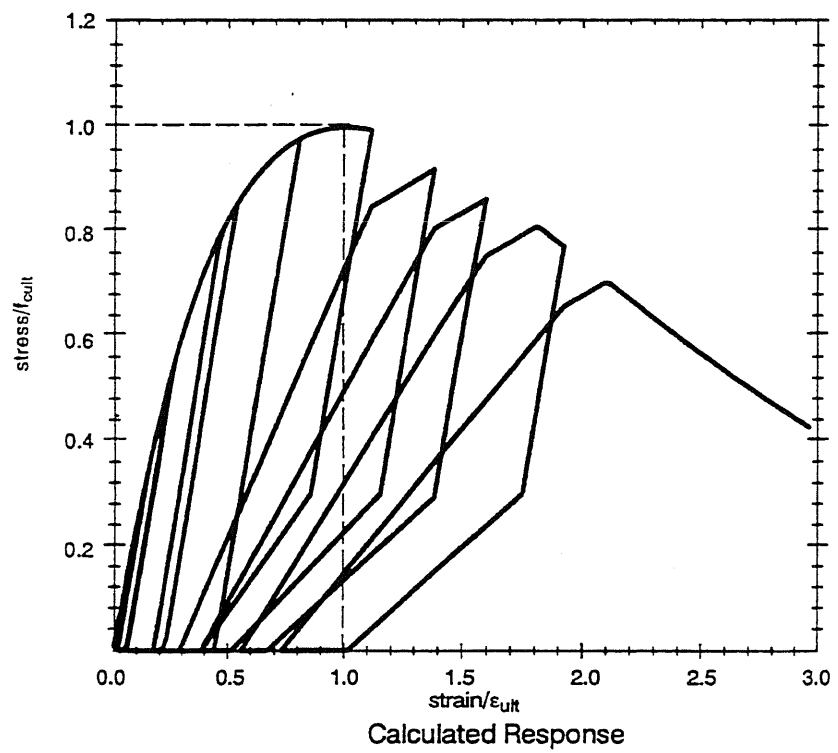
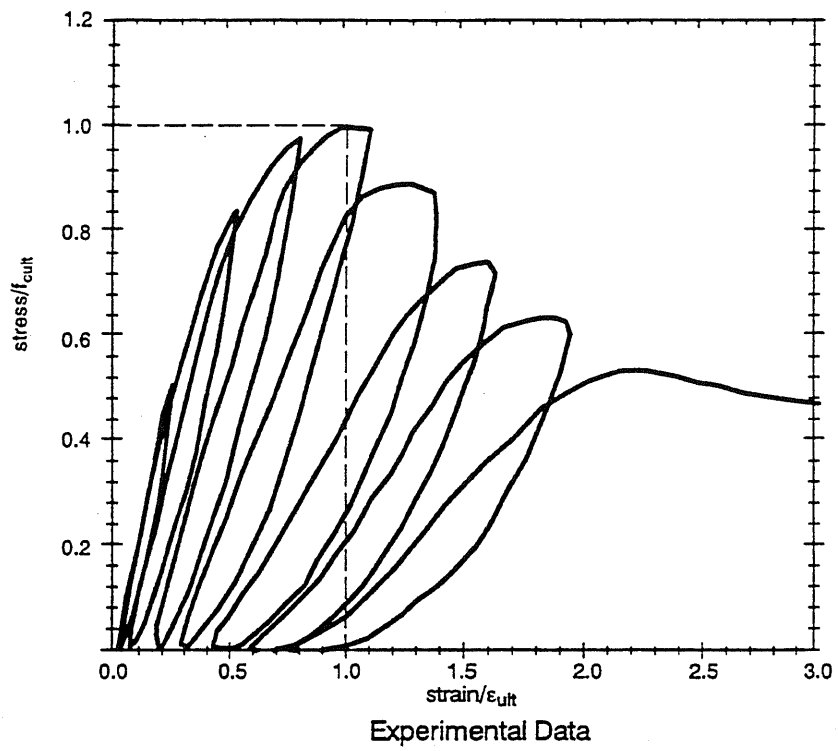


Fig. 3.16 Comparison of Calculated and Experimental Data for Response of Concrete subjected to Cyclic Compression Loads (Karsan and Jirsa [79])

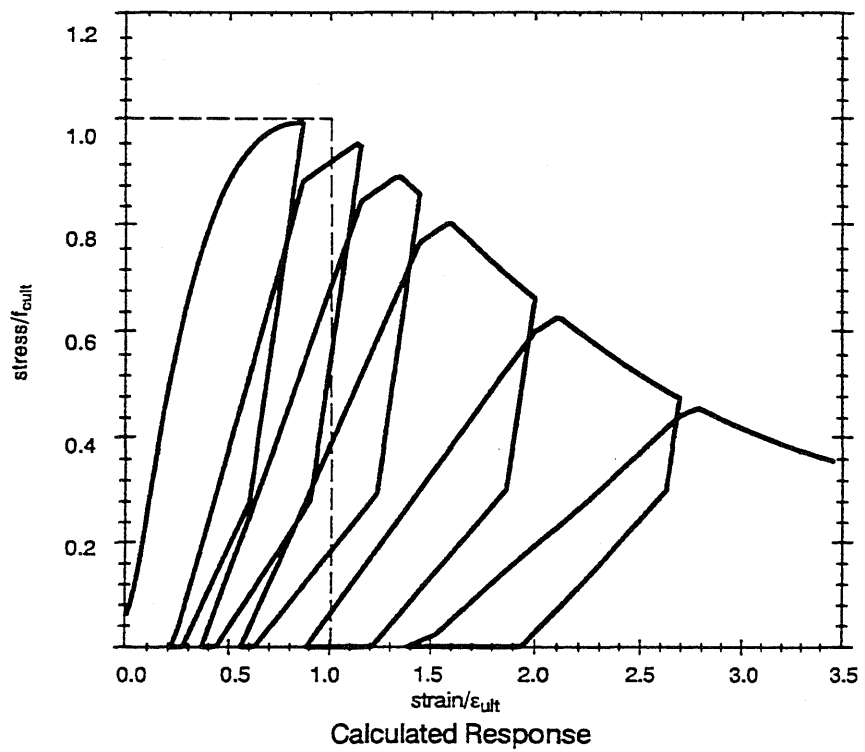
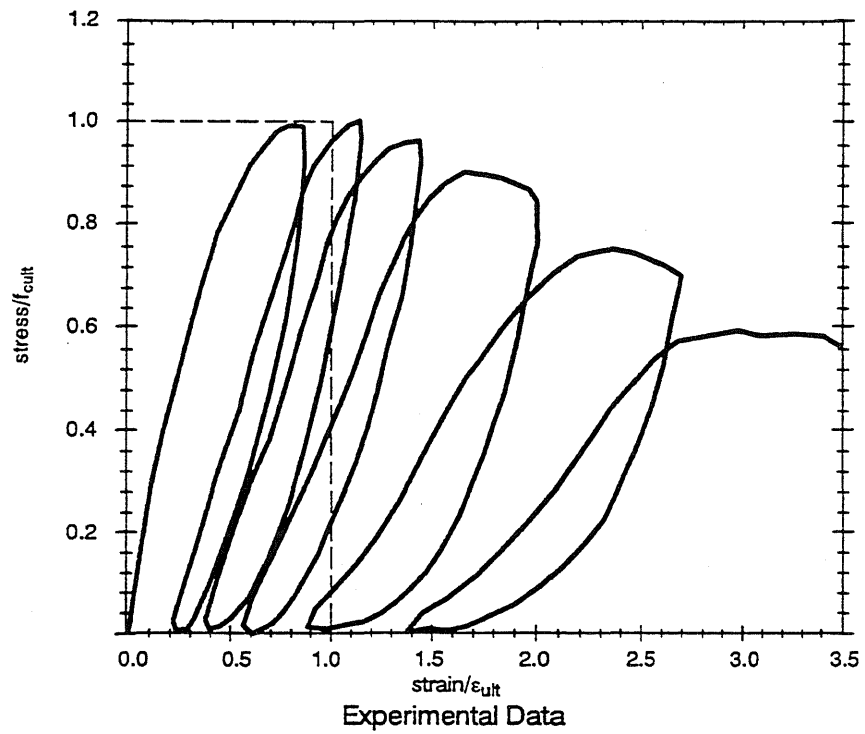


Fig. 3.17 Comparison of Calculated and Experimental Data for Response of Concrete subjected to Cyclic Compression Loads (Karsan and Jirsa [79])



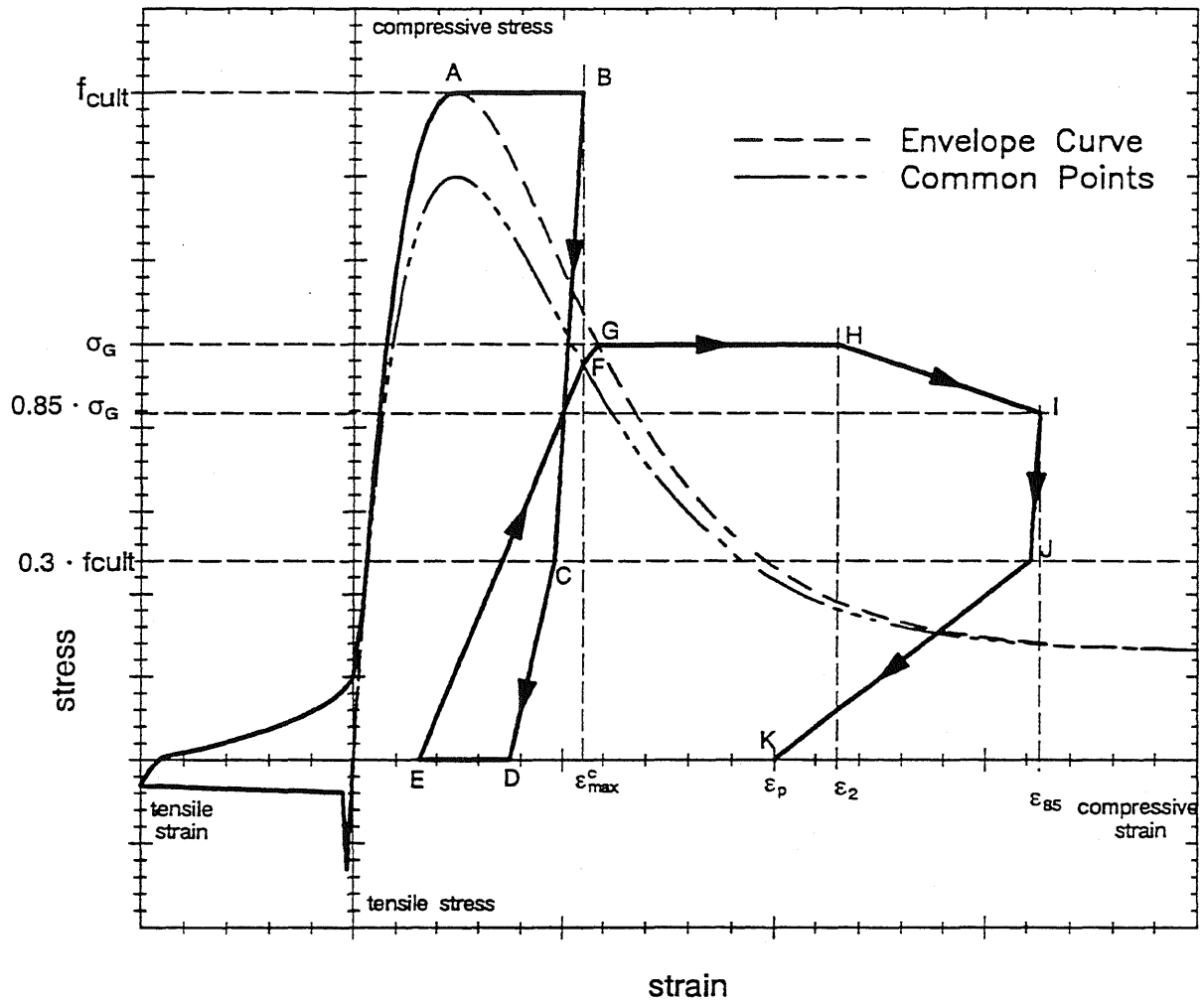
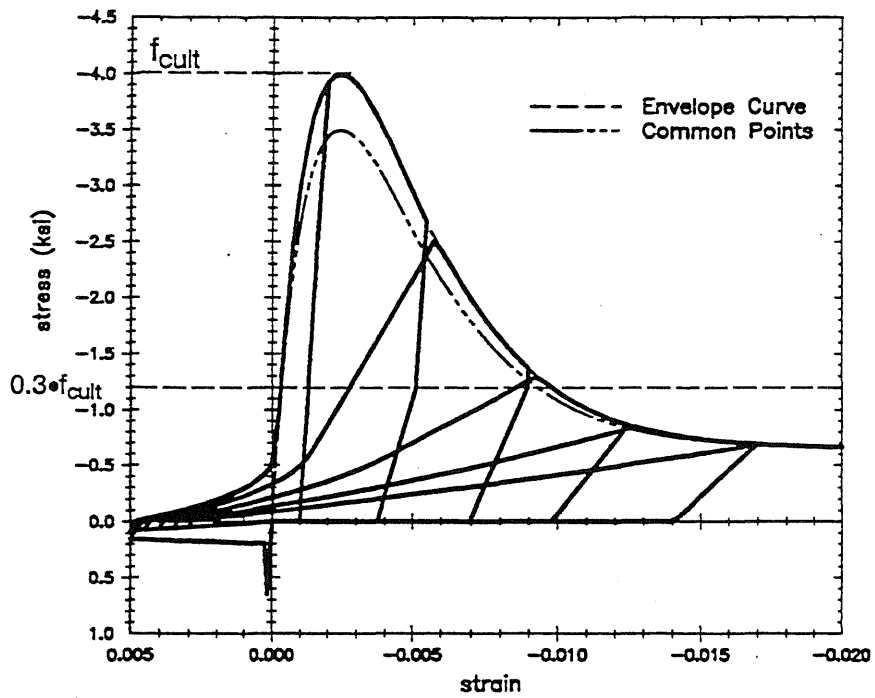
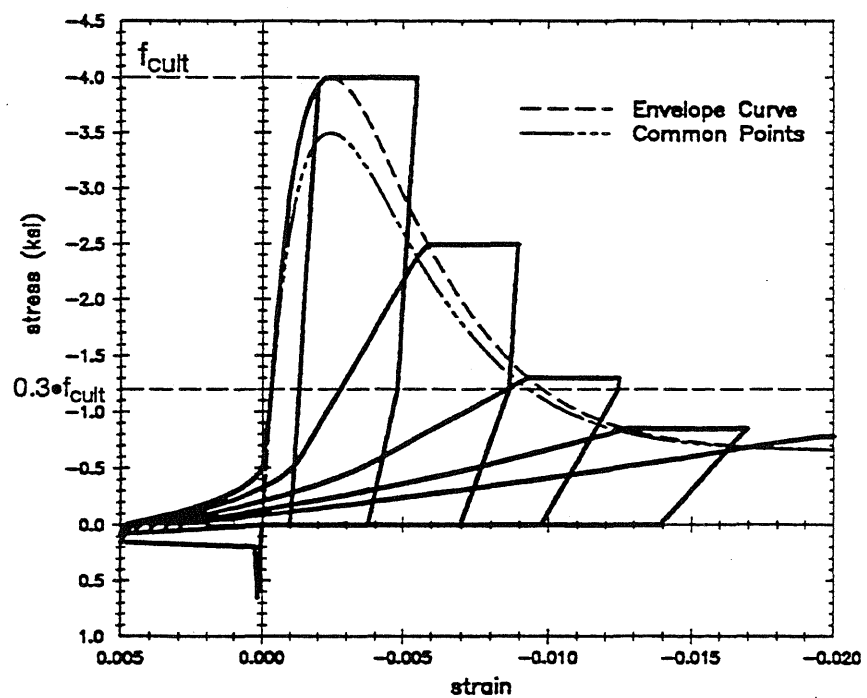


Fig. 3.18 Rules for Unloading and Reloading: Confined Concrete



a) Unconfined concrete



b) Confined concrete

Fig. 3.19 Calculated Cyclic Response for Unconfined and Confined Concrete

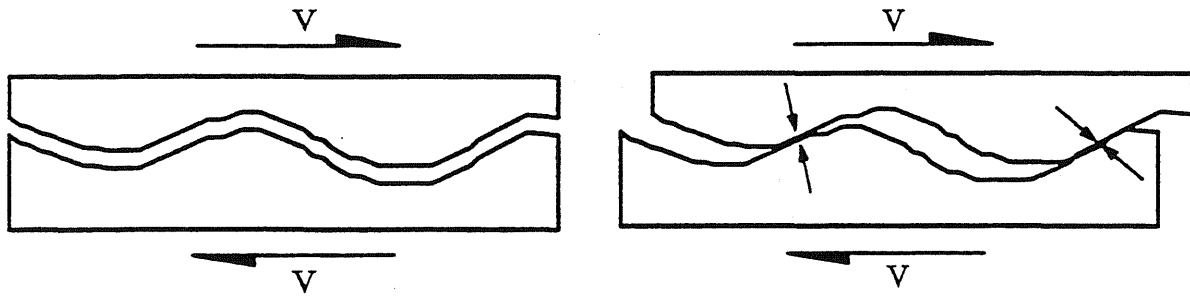


Fig. 3.20 Interface Shear Transfer

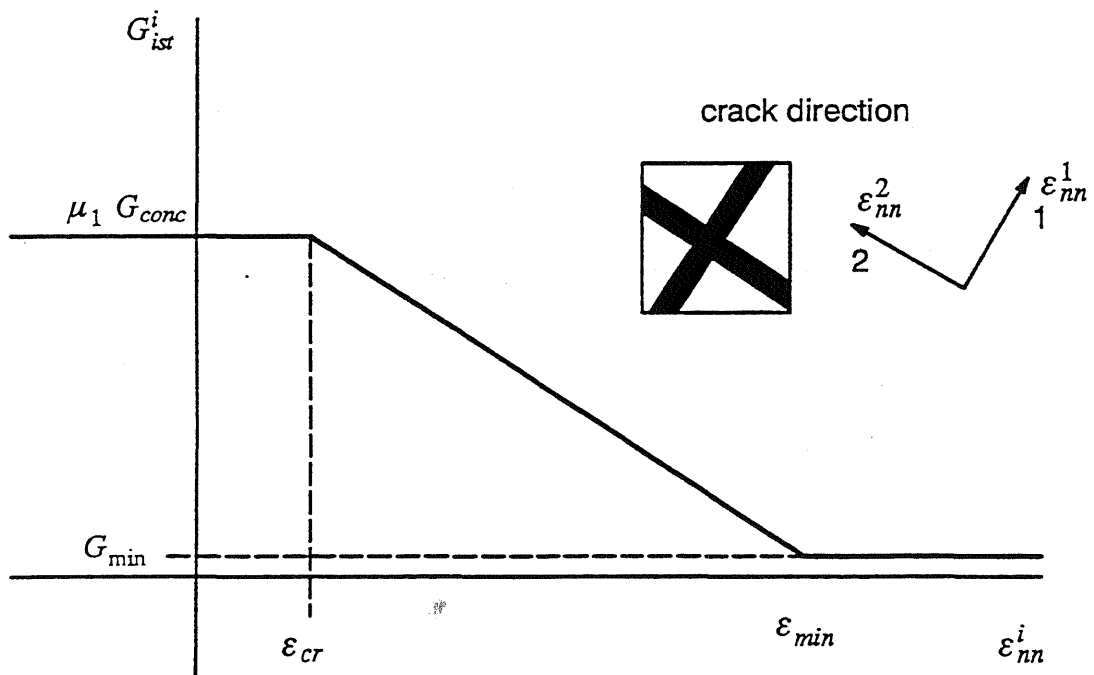


Fig. 3.21 Relationship between Shear Interface Transfer Stiffness and Normal Strain across Cracks

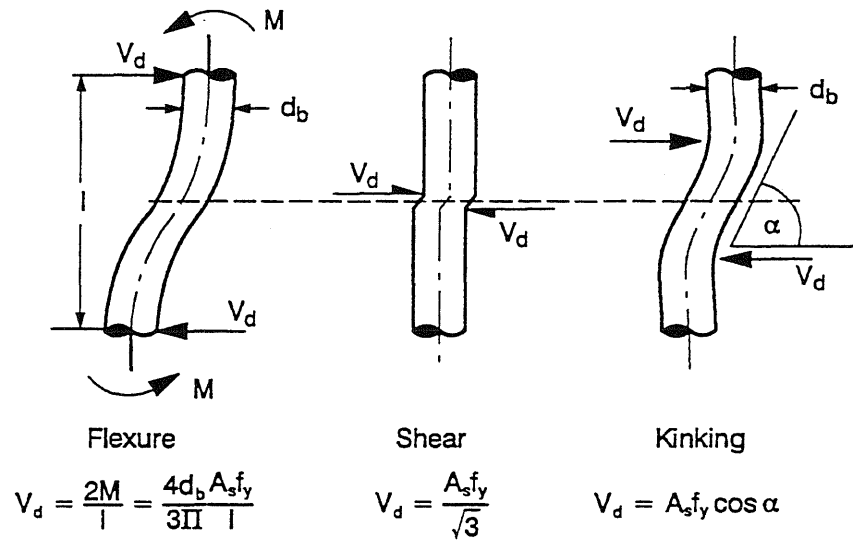


Fig. 3.22 The Mechanisms of Dowel Action (from Paulay et al.(115))

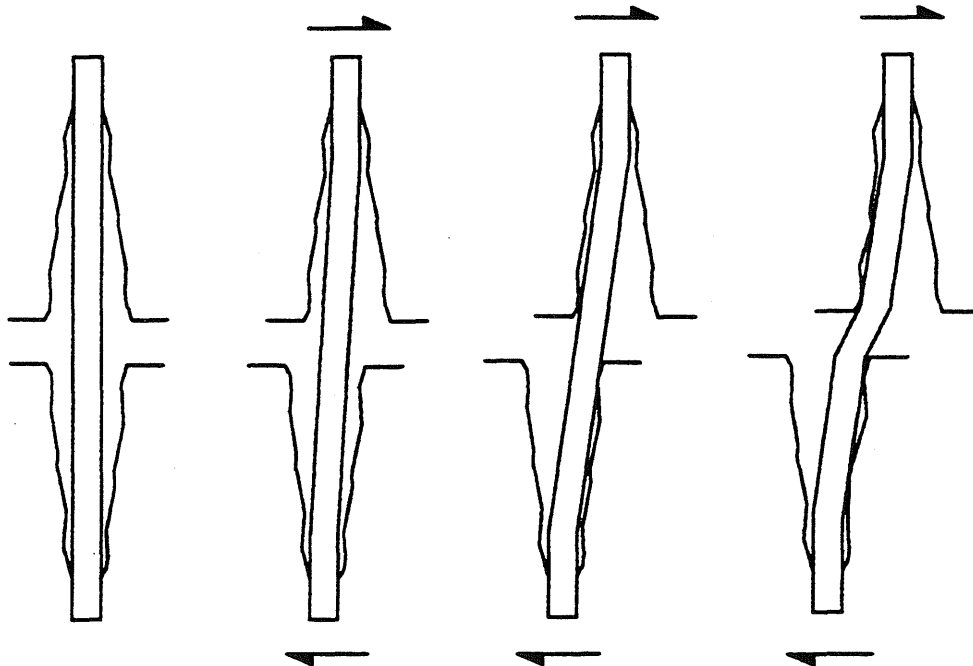
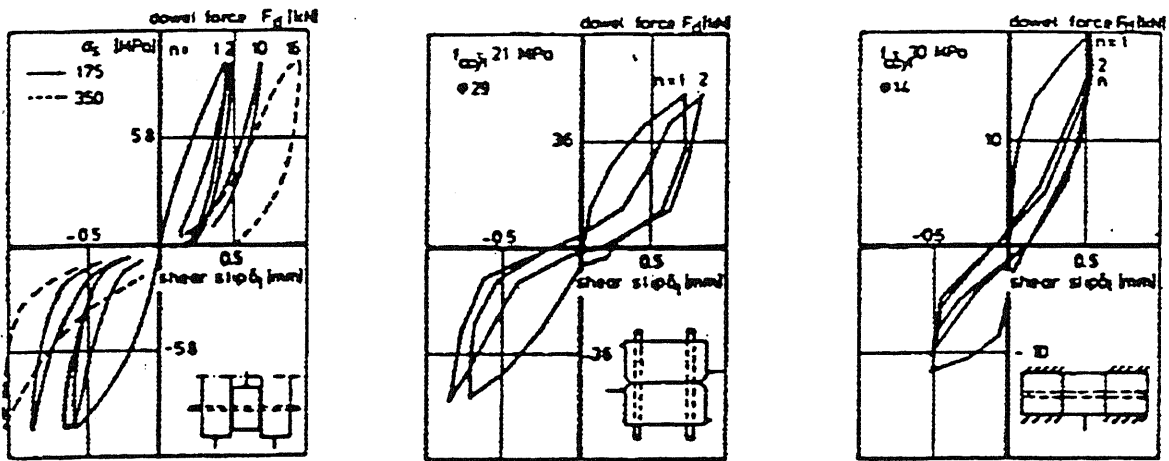


Fig. 3.23 The Interaction between Cracked Concrete and a Reinforcing Bar



a) Experiment of Elliot (53)

b) Experiment of Jimenez (76)

c) Experiment of Vintzeleou (145)

Fig. 3.24 Typical Characteristics of Dowel Action

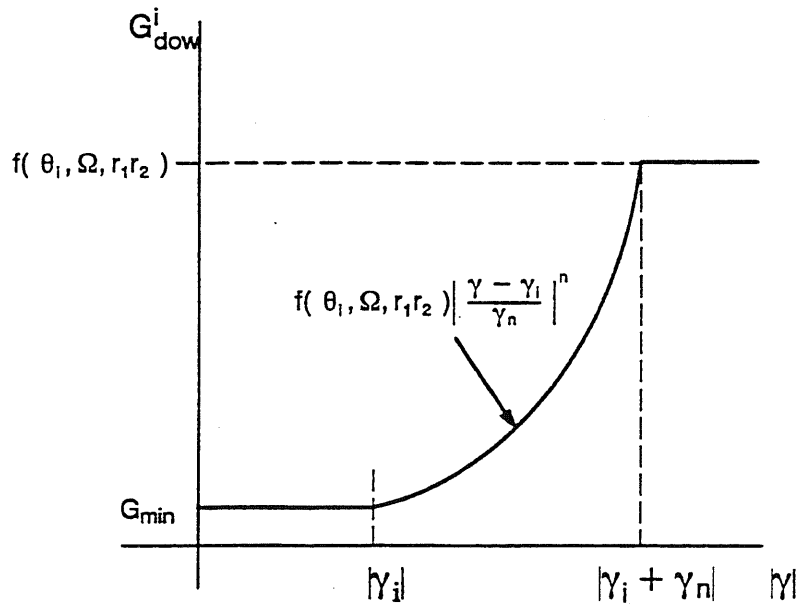
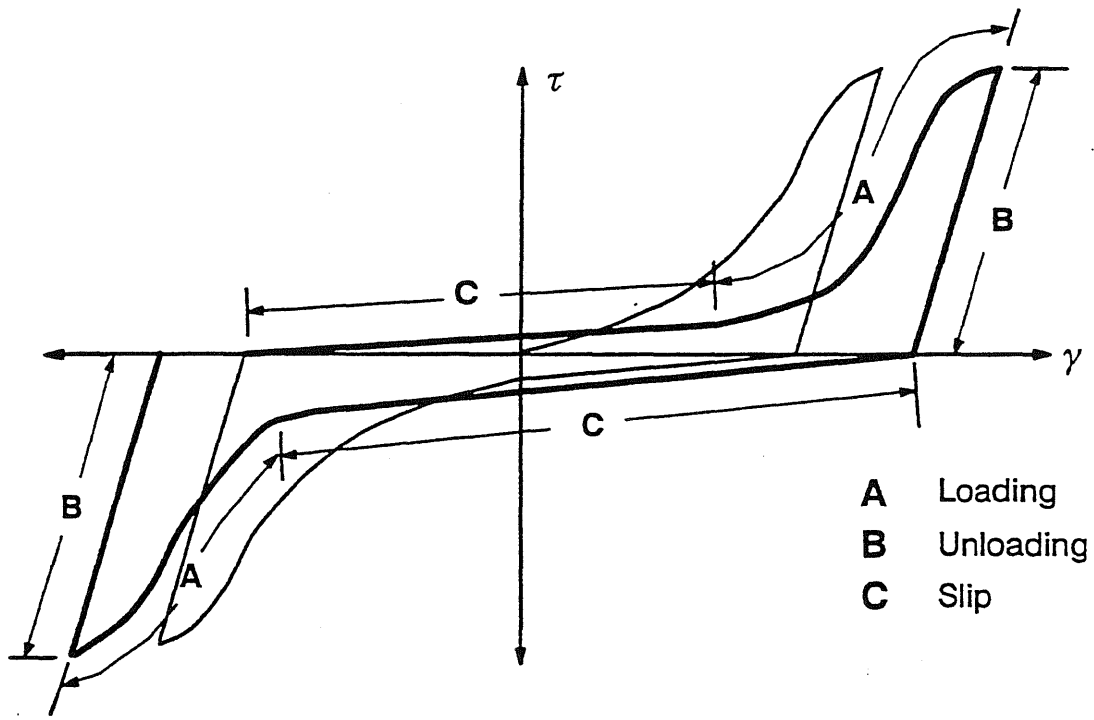
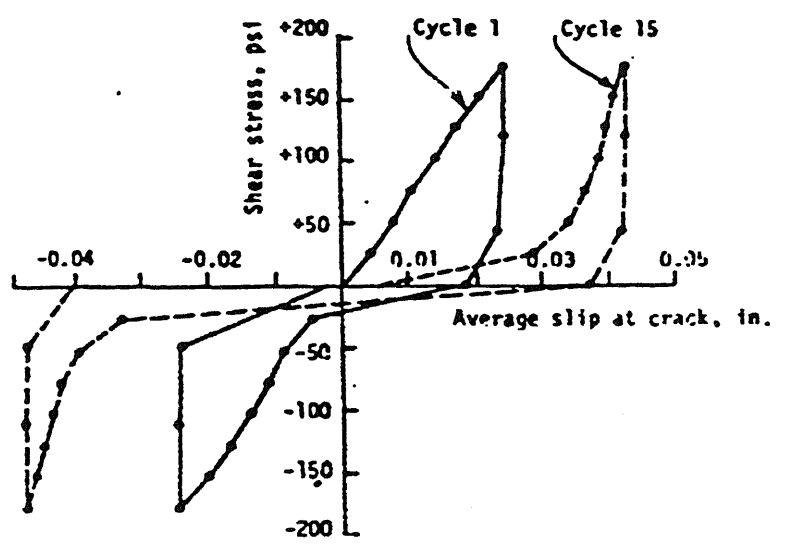


Fig. 3.25 Relationship between Dowel Action Stiffness and Shear Strain



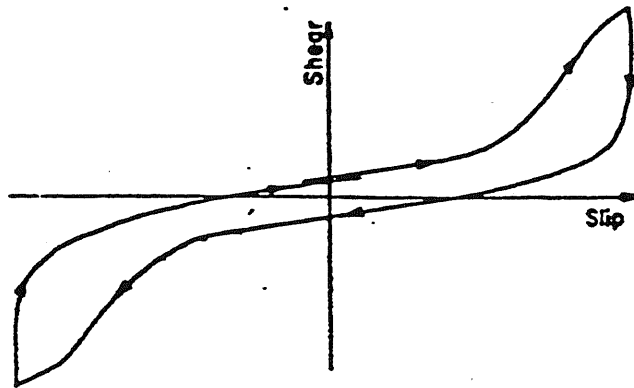
- A Loading
- B Unloading
- C Slip

a) Typical Cyclic Shear Response

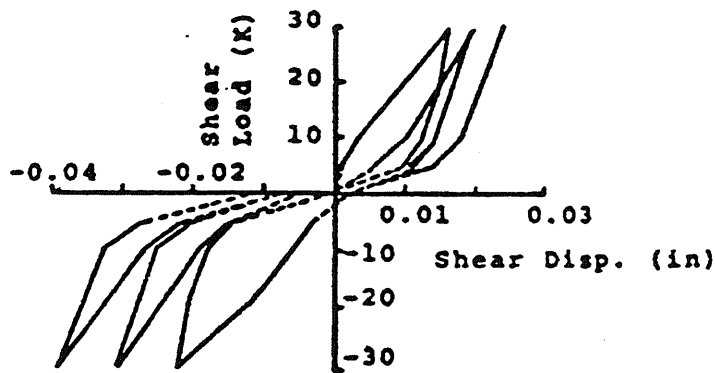


b) Shear Stress-Slip Curve (From Liable et al. [82])

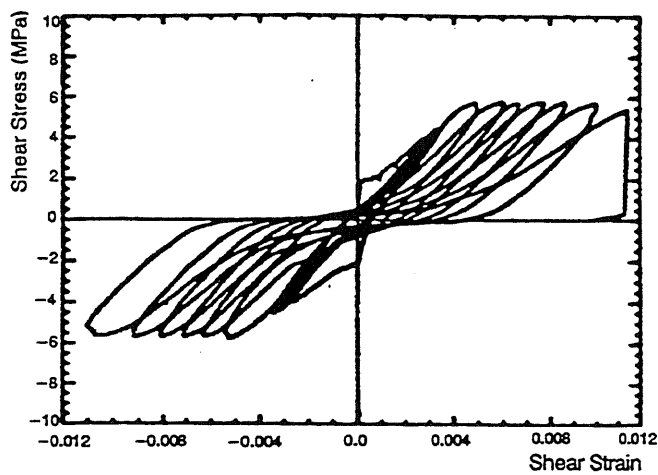
Fig. 3.26 Typical Cyclic Shear Response



c) Shear Stress-Slip Curve (From Mattock [93])

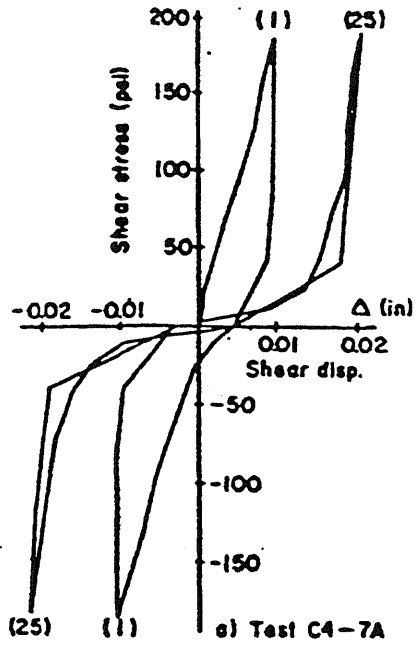


d) Shear Load vs. Shear Displacement Curve (From Stanton [133])

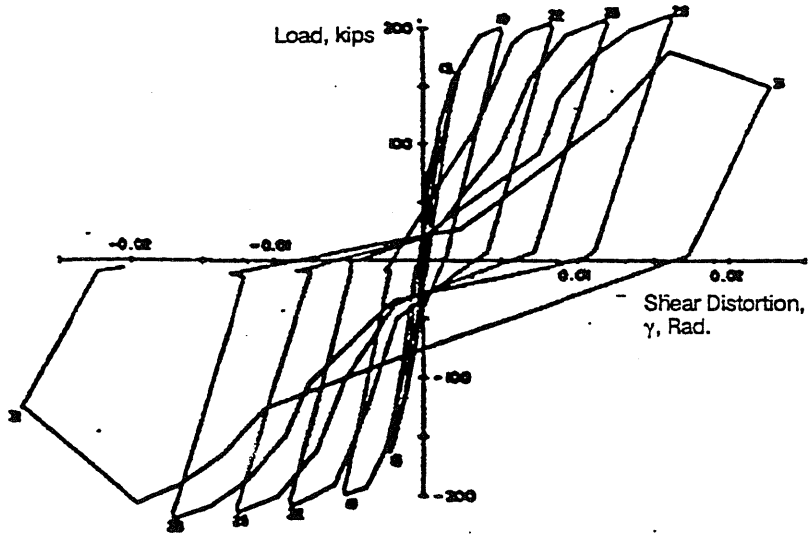


e) Shear Stress vs. Shear Strain Curve (From Steven et al. [134])

Fig. 3.26 Typical Cyclic Shear Response (Cont.)



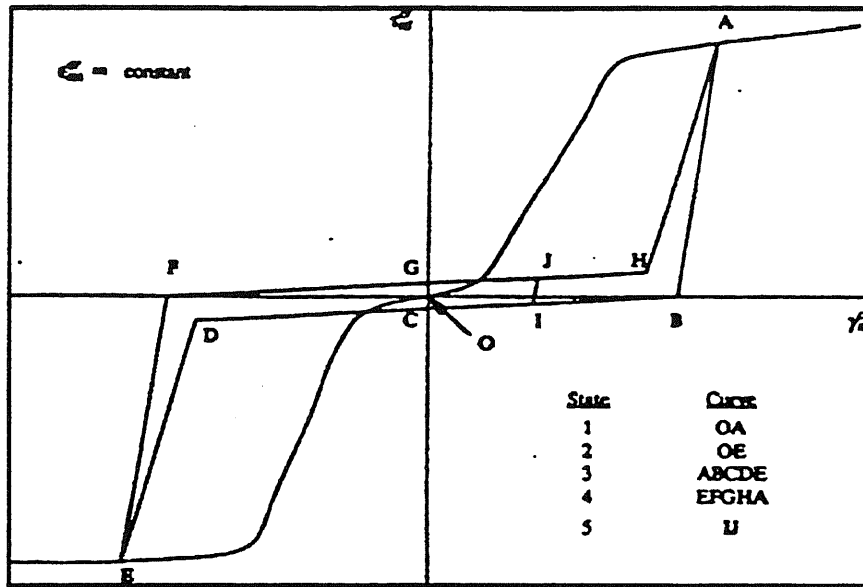
f) Shear Stress vs. Shear Displacement Curve (From Jimenez et al. [76])



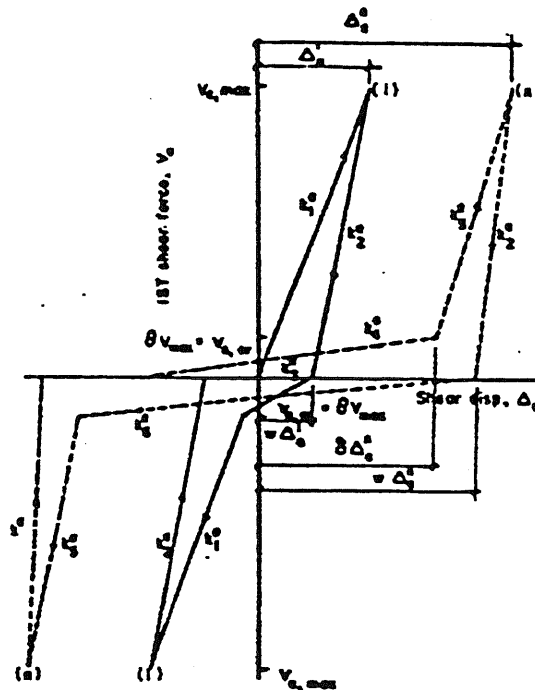
g) Load vs. Shear Deformation in Shear Walls (From Oesterle et al. [105])

Fig. 3.26 Typical Cyclic Shear Response (Cont.)



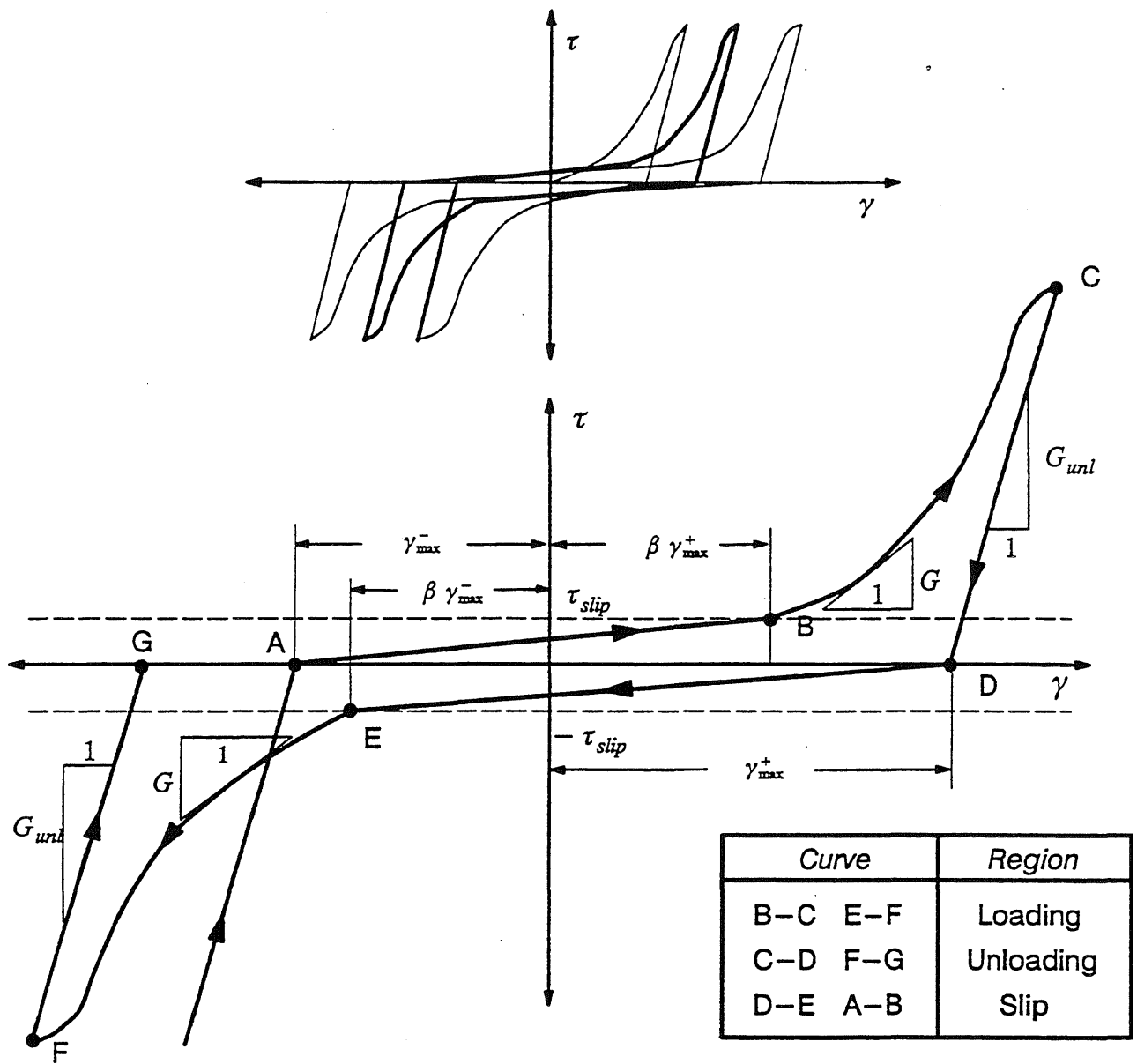


a) Model for Cyclic Shear Stress vs Shear Strain by Xu (151)



b) Model for Cyclic Shear Force vs. Shear Displacement by Jimenez et al. (77)

Fig. 3.27 Cyclic Shear Model



$\gamma_{\max}^-$  = max. negative shear strain intercept in the previous cycles

$\gamma_{\max}^+$  = max. positive shear strain intercept in the previous cycles

Fig. 3.28 The Proposed Cyclic Shear Model

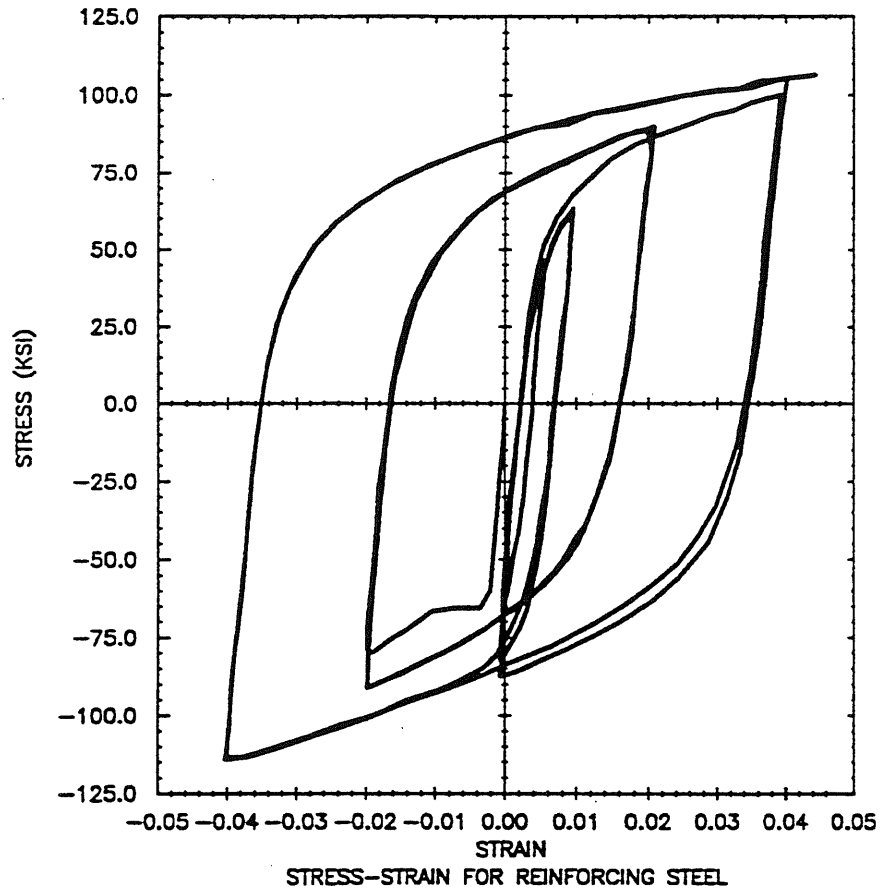


Fig. 4.1 Typical Cyclic Stress–Strain Relationship for Reinforcing Steel (from Aktan [5])

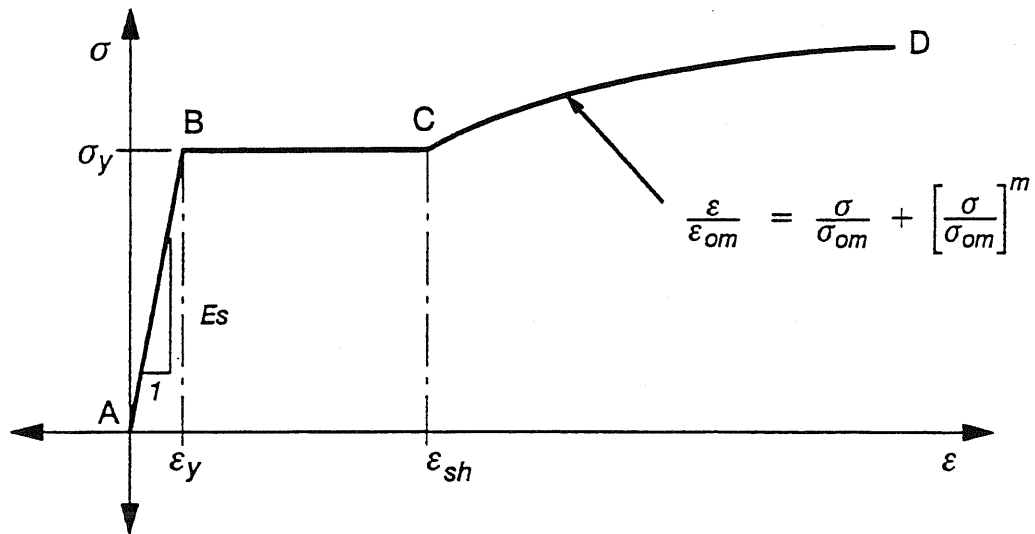


Fig. 4.2 Monotonic Loading Curve for Reinforcing Steel

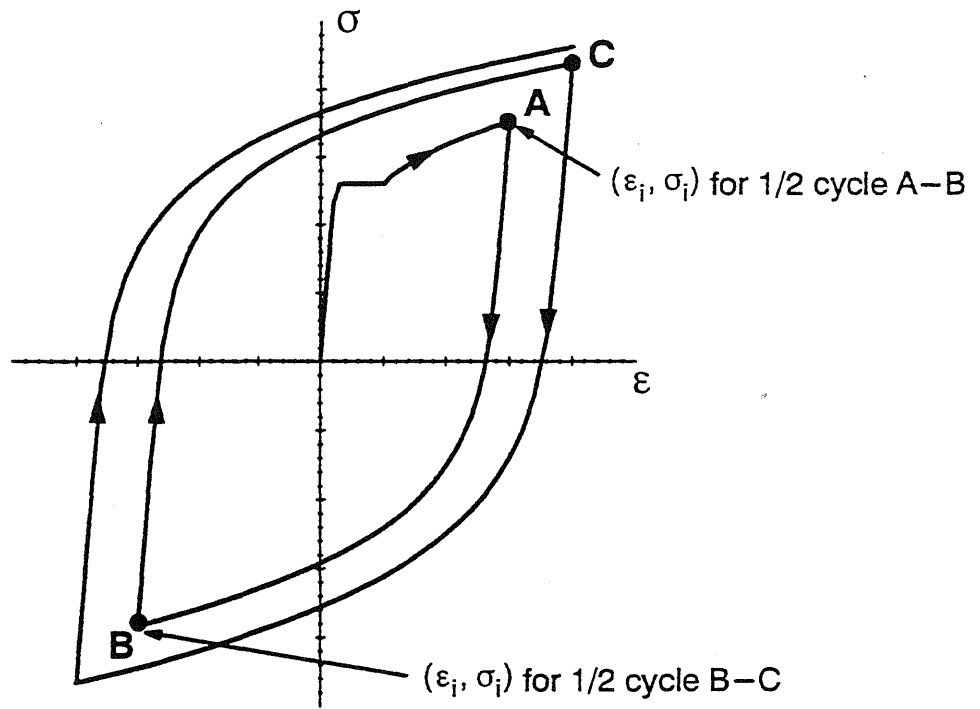


Fig. 4.3 Envelope Curves

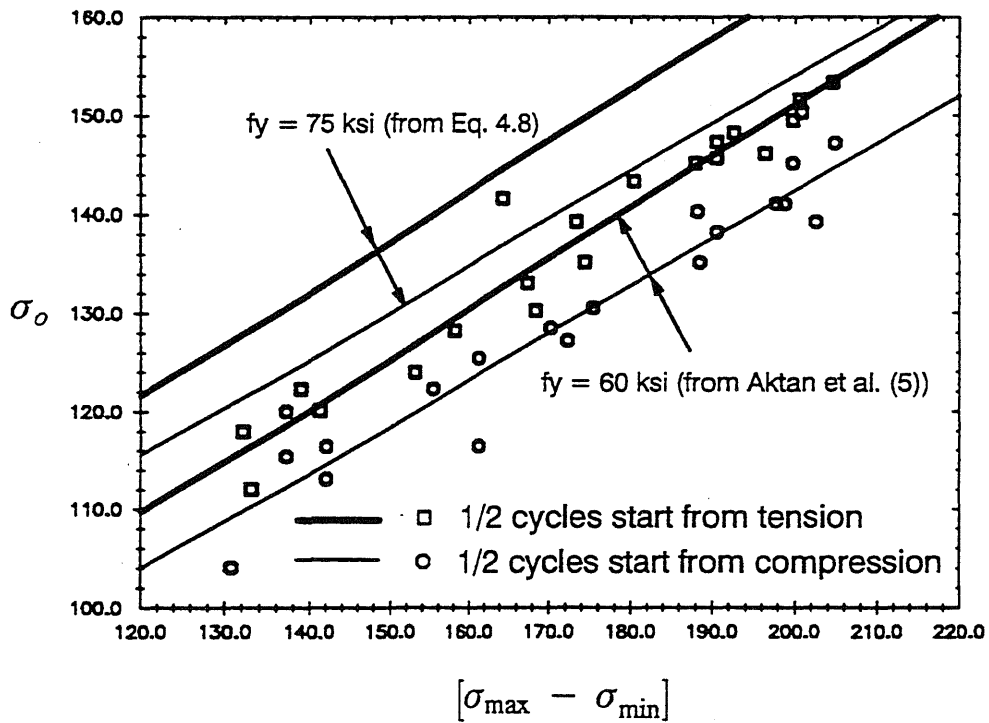
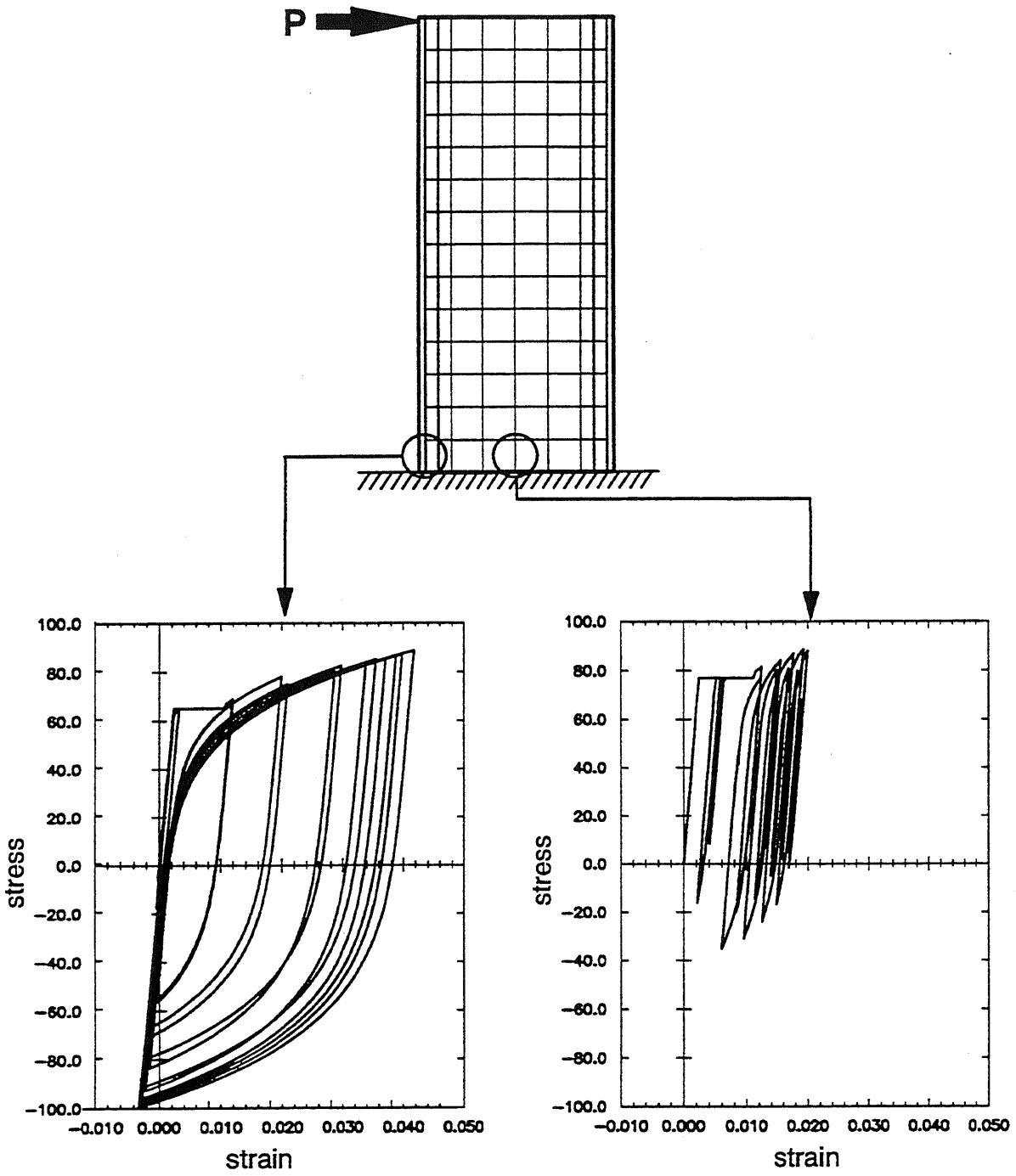


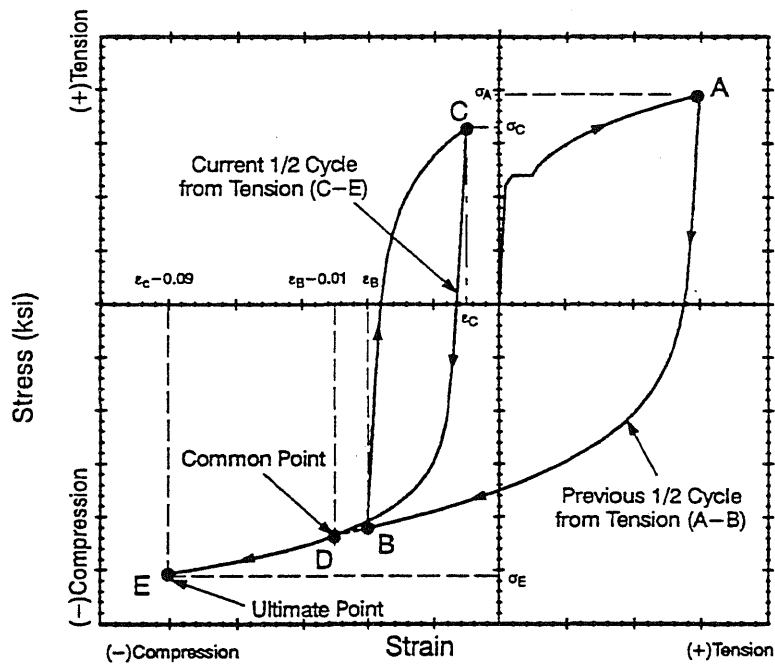
Fig. 4.4 Equation for  $\sigma_o$  (From Aktan et al. [5])



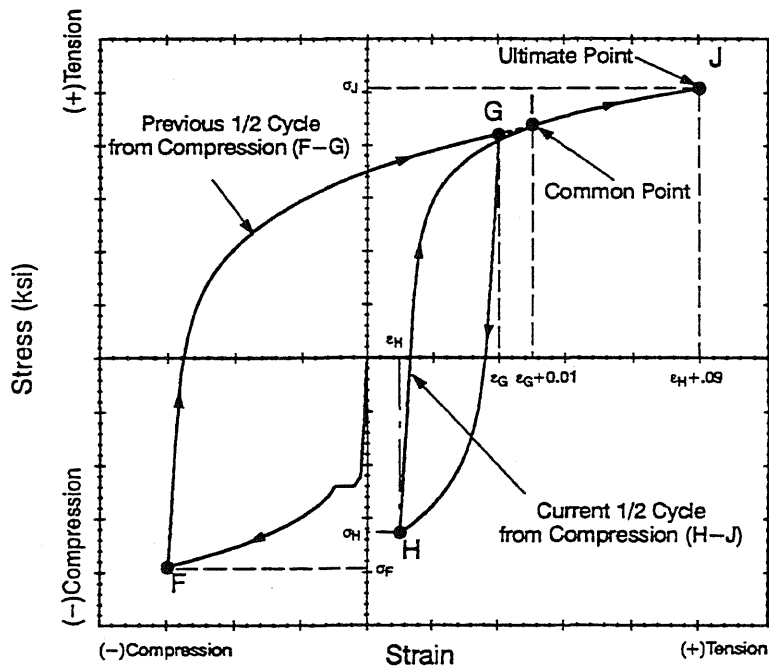
a) Reinforcing bar in the boundary element

b) Reinforcing bar in the web

Fig. 4.5 Analytical Stress-Strain Relationship of Reinforcing Bars in R/C Shear Walls



a) 1/2 Cycle from Tension



b) 1/2 Cycle from Compression

Fig. 4.6 Common Points and Ultimate Points

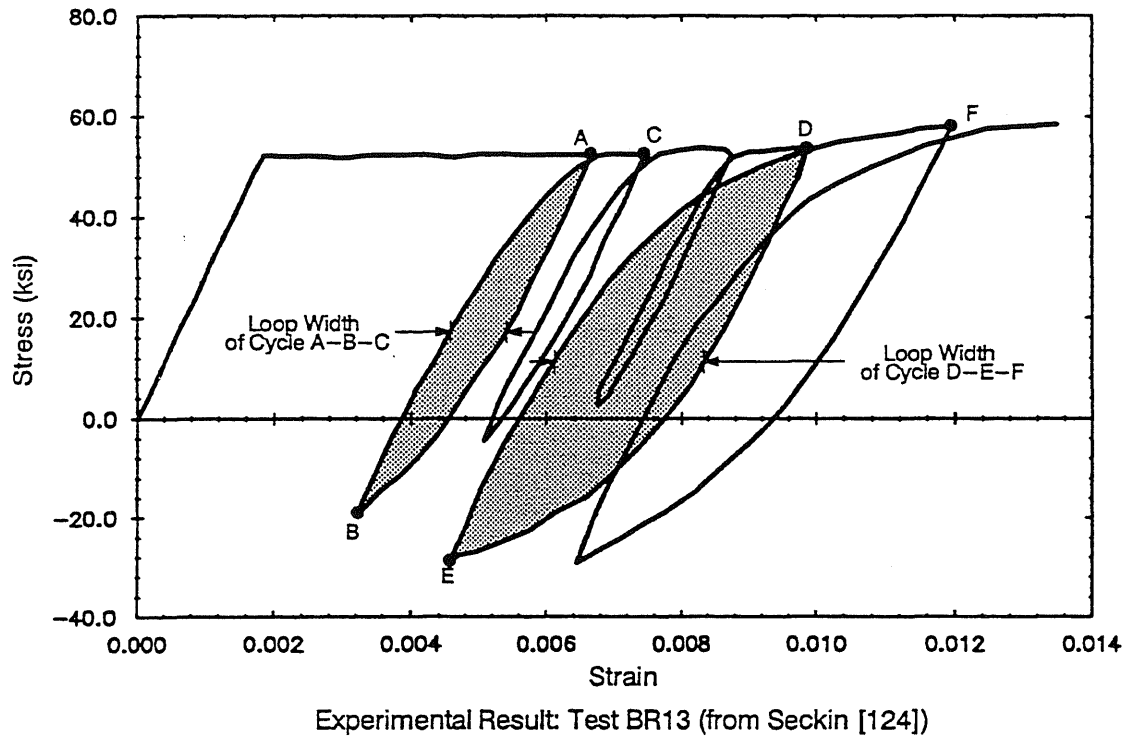
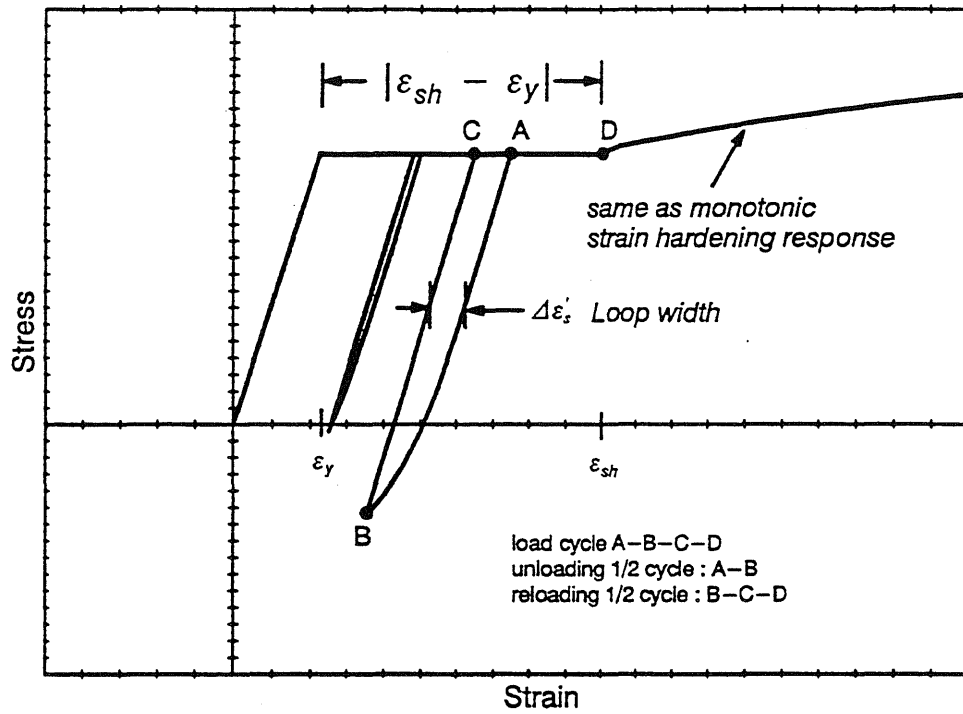
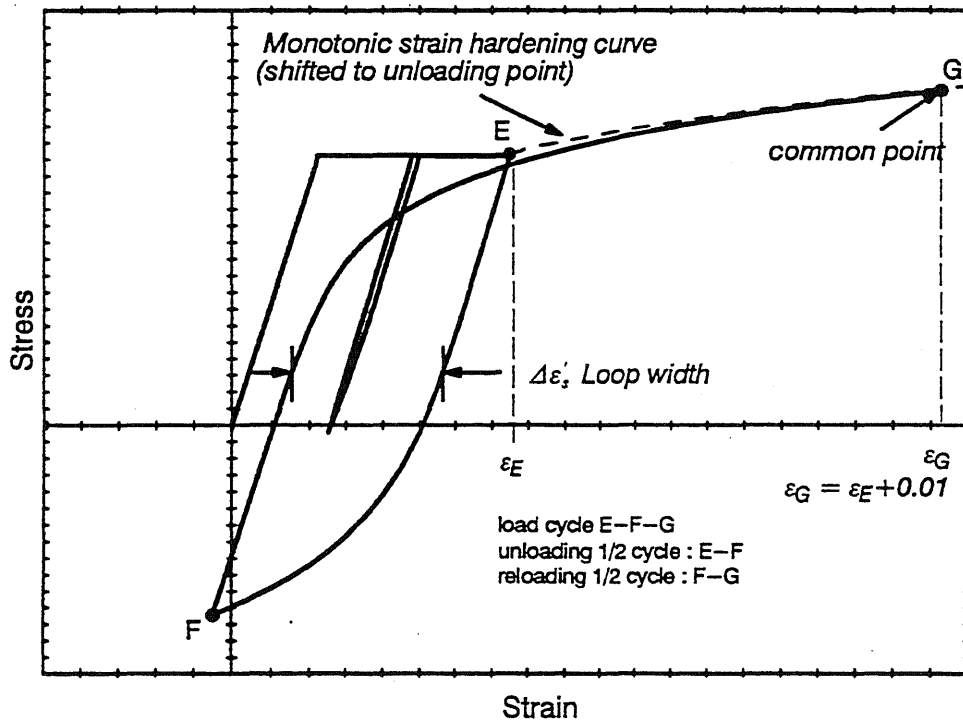


Fig. 4.7 Typical Experimental Results of Load Reversals from the Yield Plateau



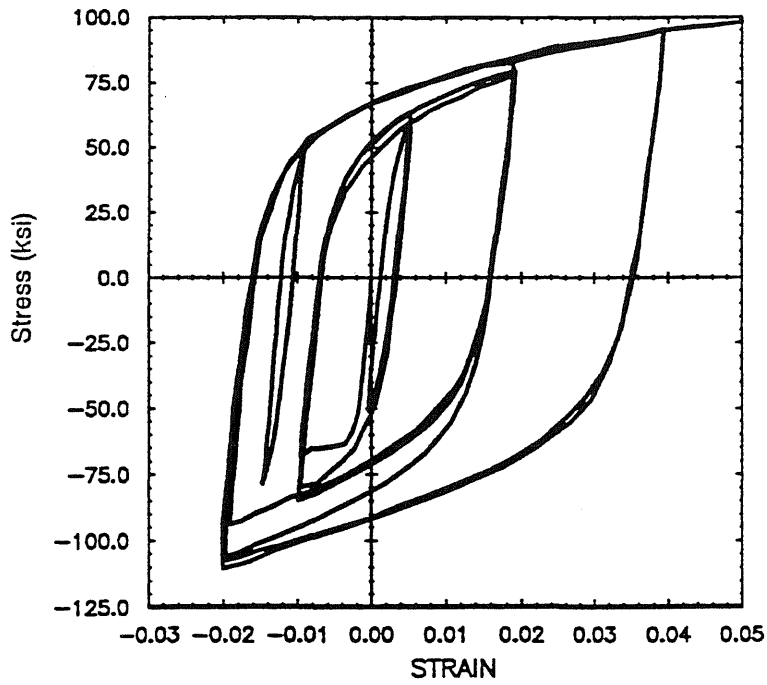
a)  $\Delta\varepsilon_s' < 1/2 |\varepsilon_{sh} - \varepsilon_y|$



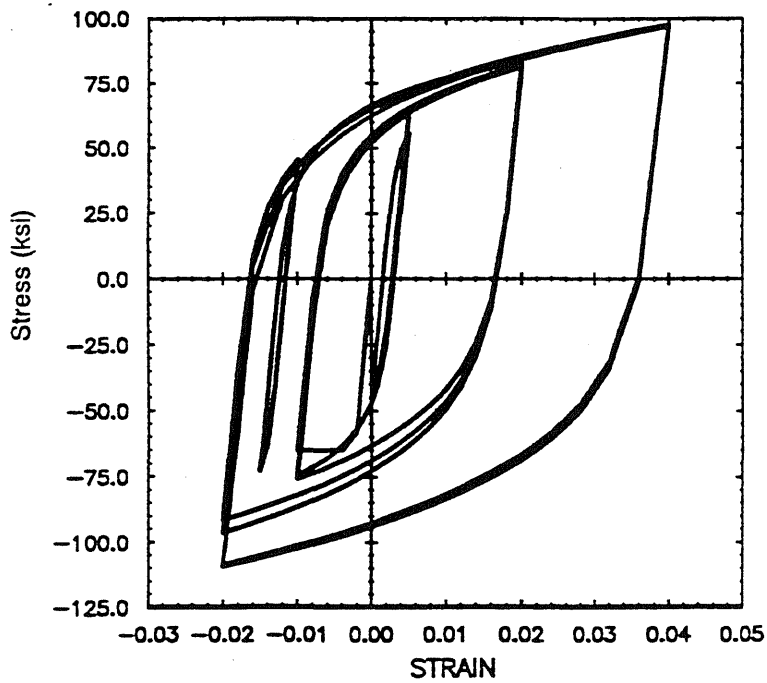
b)  $\Delta\varepsilon_s' \geq 1/2 |\varepsilon_{sh} - \varepsilon_y|$

Fig. 4.8 Unloading from Yield Plateau (From Popov [118])





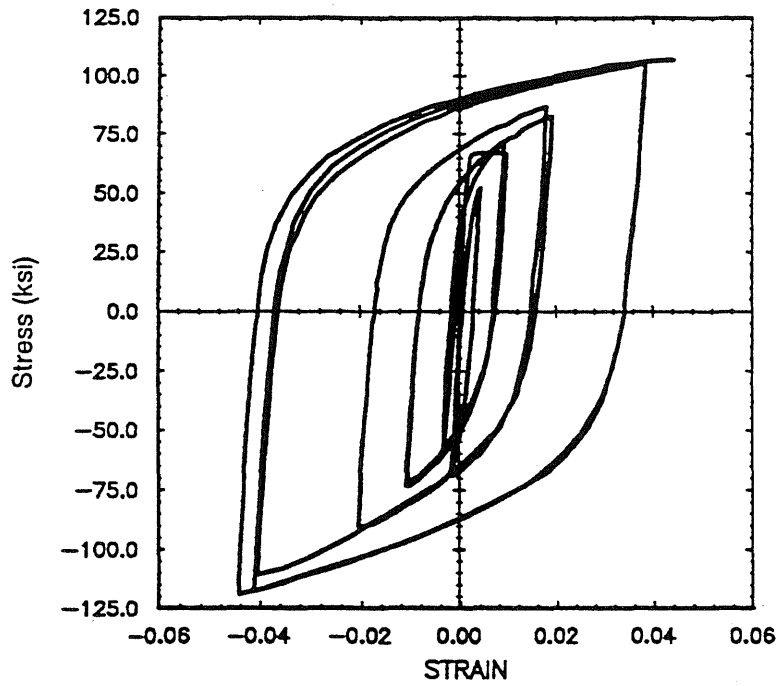
EXPERIMENTAL RESULT : TEST 1 #9 COUPON SRS397



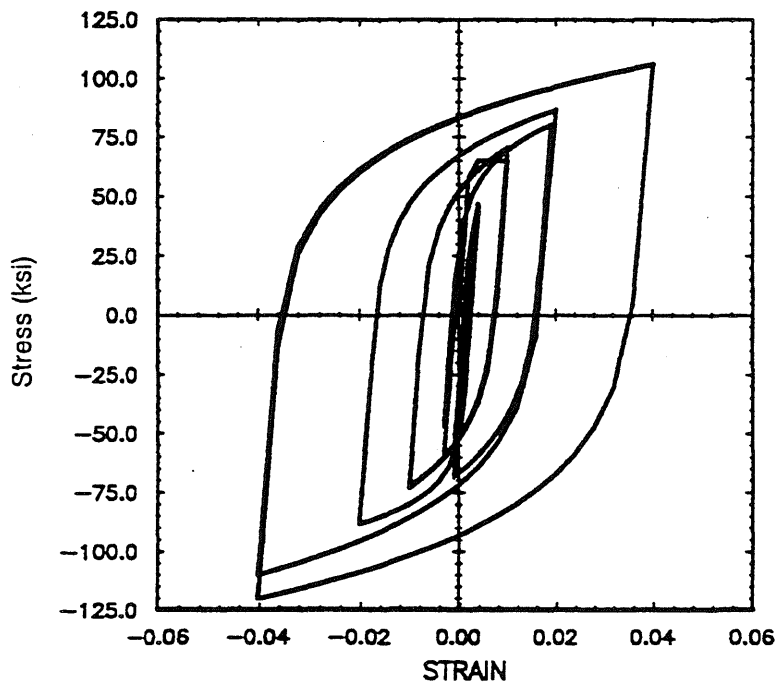
ANALYTICAL RESULT : TEST 1 #9 COUPON SRS397

a) Test 1 # 9 coupon (from Aktan et al. [5])

Fig. 4.9 Evaluation of the Proposed Steel Model



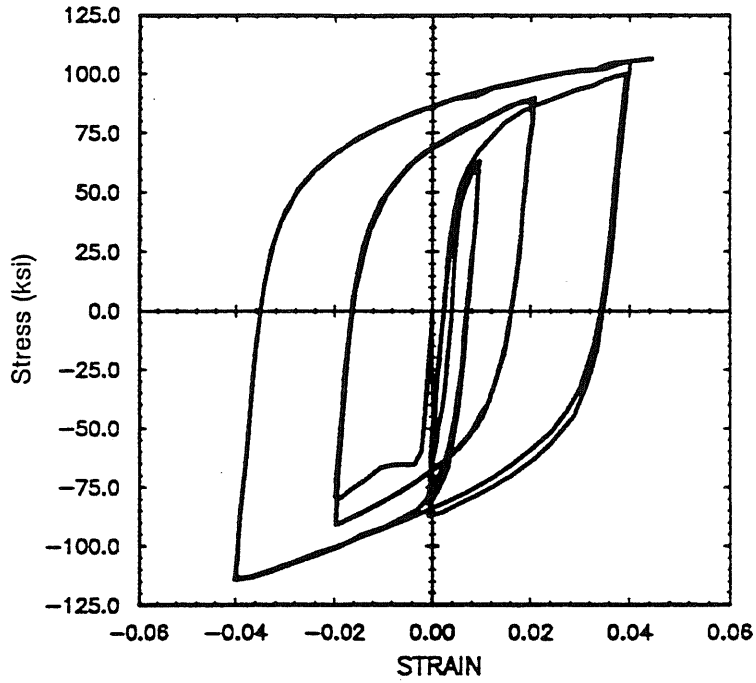
EXPERIMENTAL RESULT : TEST 3 #9 COUPON SRS397



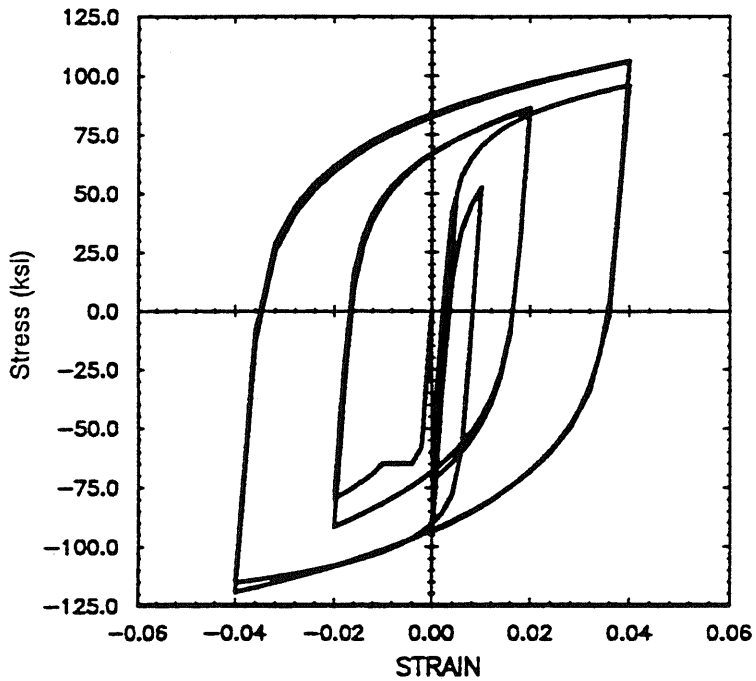
ANALYTICAL RESULT : TEST 3 #9 COUPON SRS397

b) Test 3 # 9 coupon (from Aktan et al. [5])

Fig. 4.9 Evaluation of the Proposed Steel Model (Cont.)



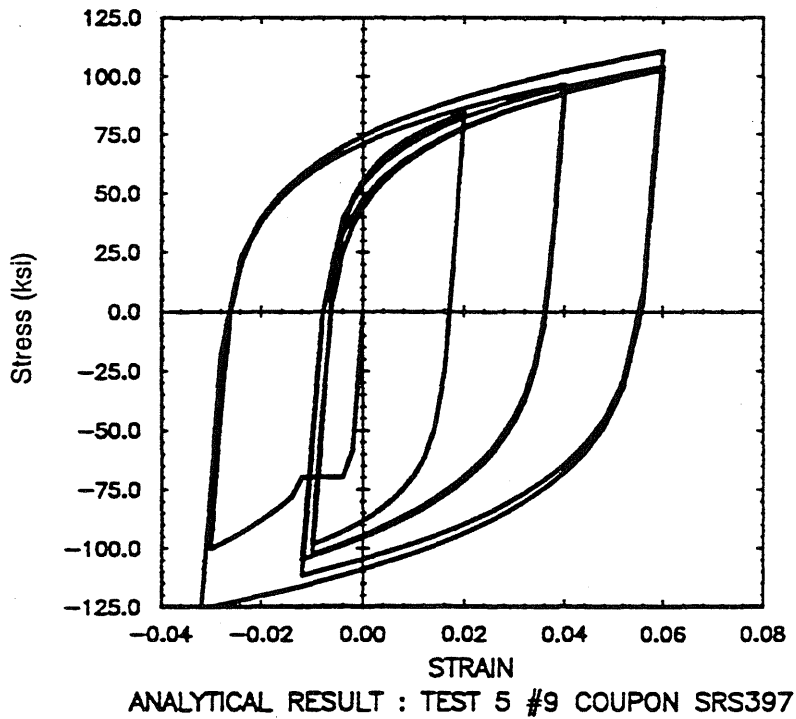
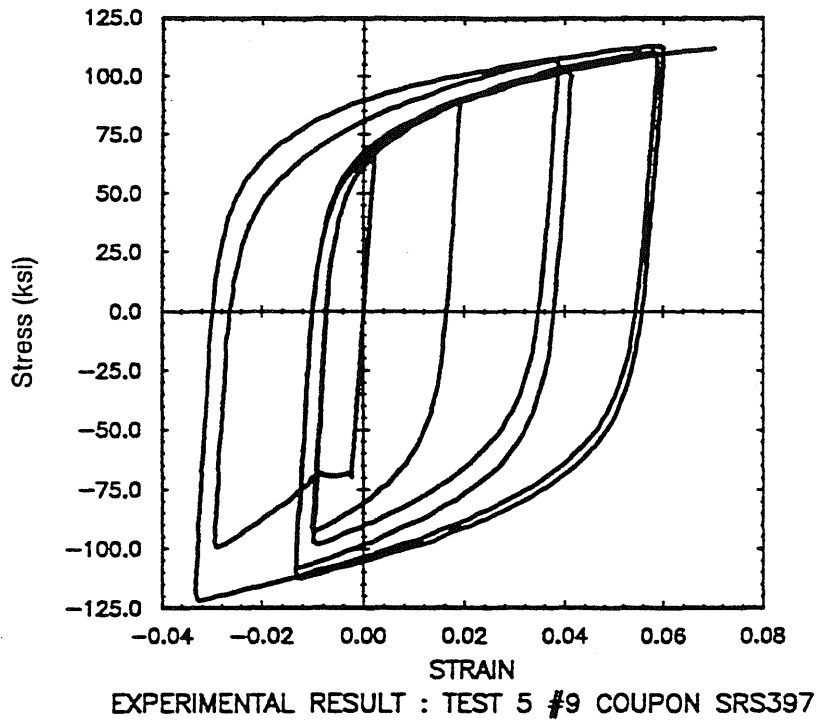
EXPERIMENTAL RESULT : TEST 4 #9 COUPON SRS397



ANALYTICAL RESULT : TEST 4 #9 COUPON SRS397

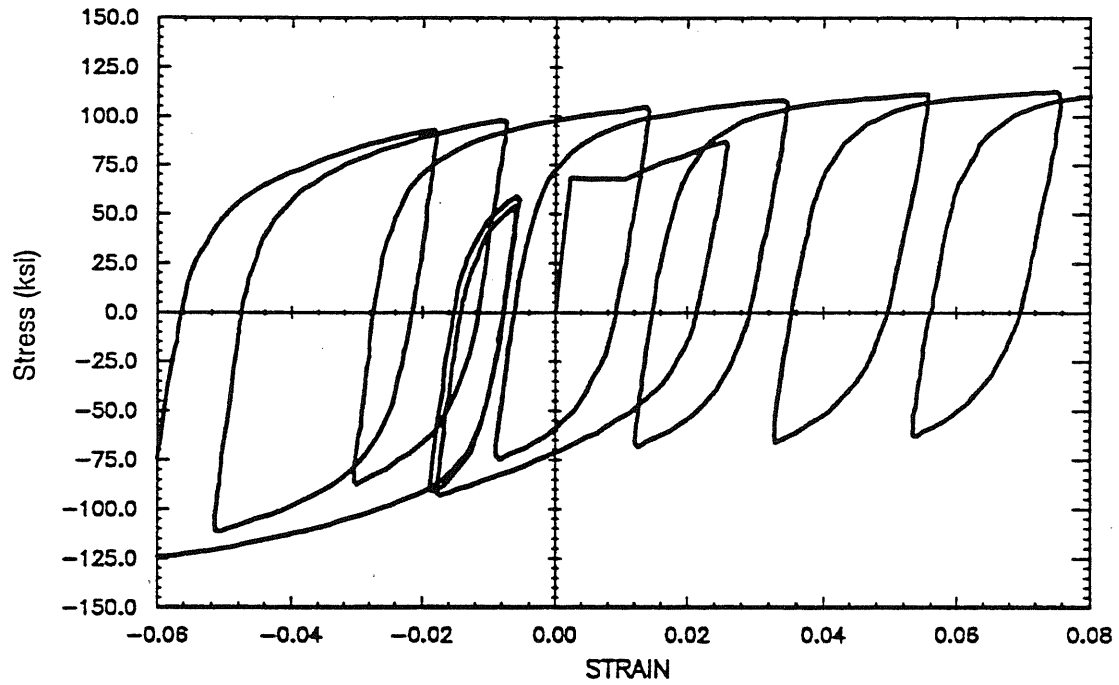
c) Test 4 # 9 coupon (from Aktan et al. [5])

Fig. 4.9 Evaluation of the Proposed Steel Model (Cont.)

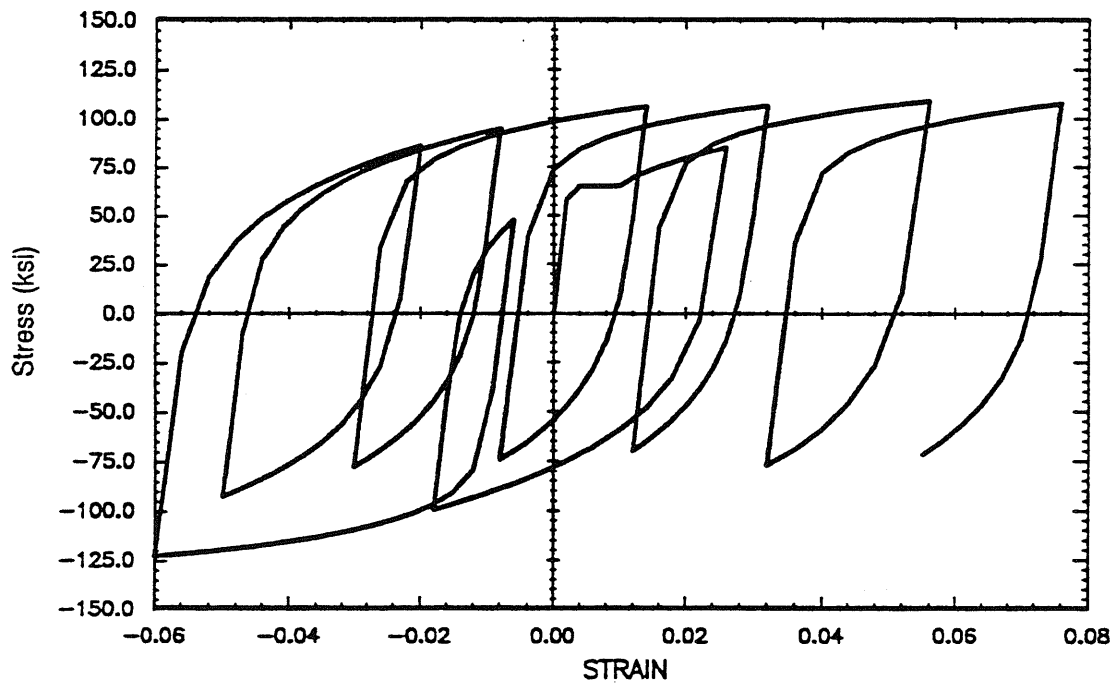


d) Test 5 # 9 coupon (from Aktan et al. [5])

Fig. 4.9 Evaluation of the Proposed Steel Model (Cont.)



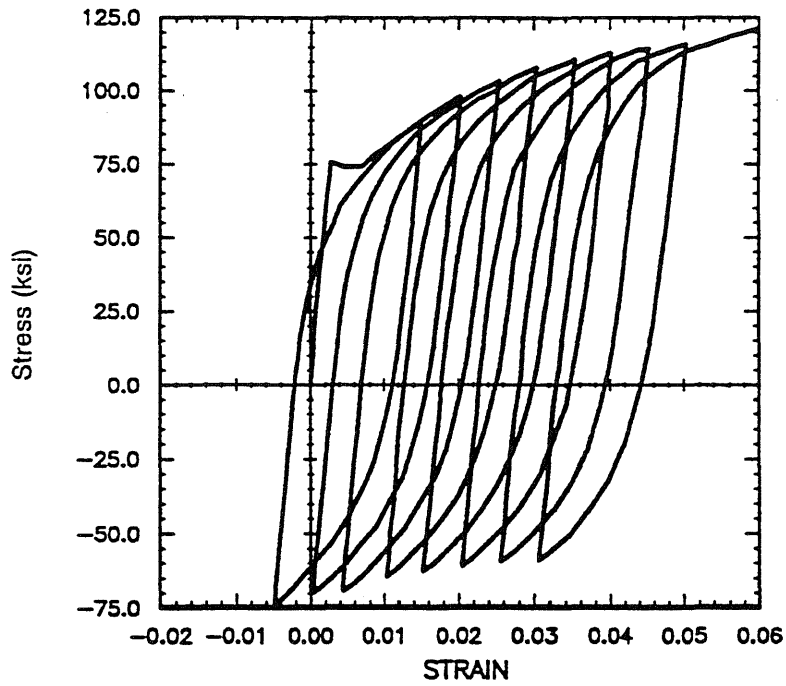
EXPERIMENTAL RESULT : TEST 6 #9 COUPON SRS397



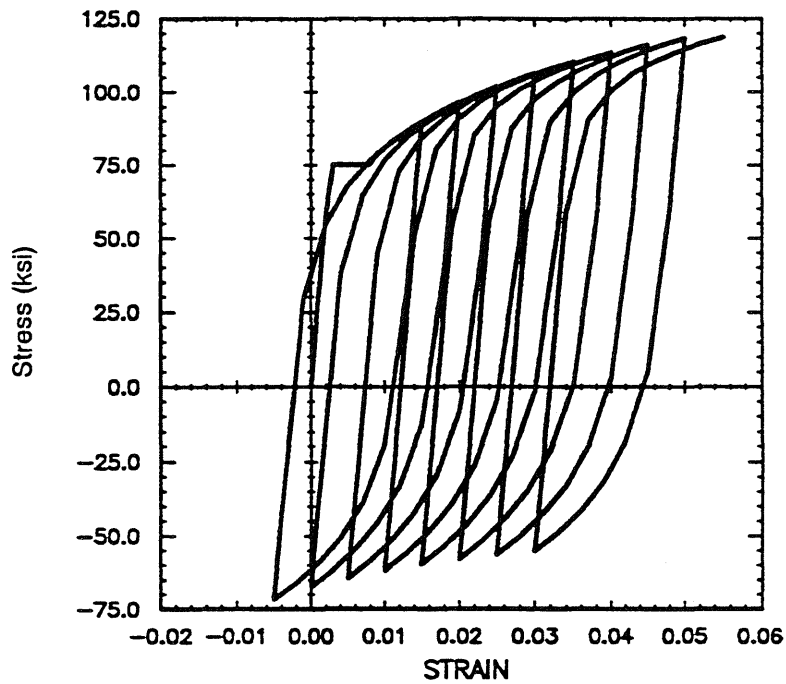
ANALYTICAL RESULT : TEST 6 #9 COUPON SRS397

e) Test 6 # 9 coupon (from Aktan et al. [5])

Fig. 4.9 Evaluation of the Proposed Steel Model (Cont.)



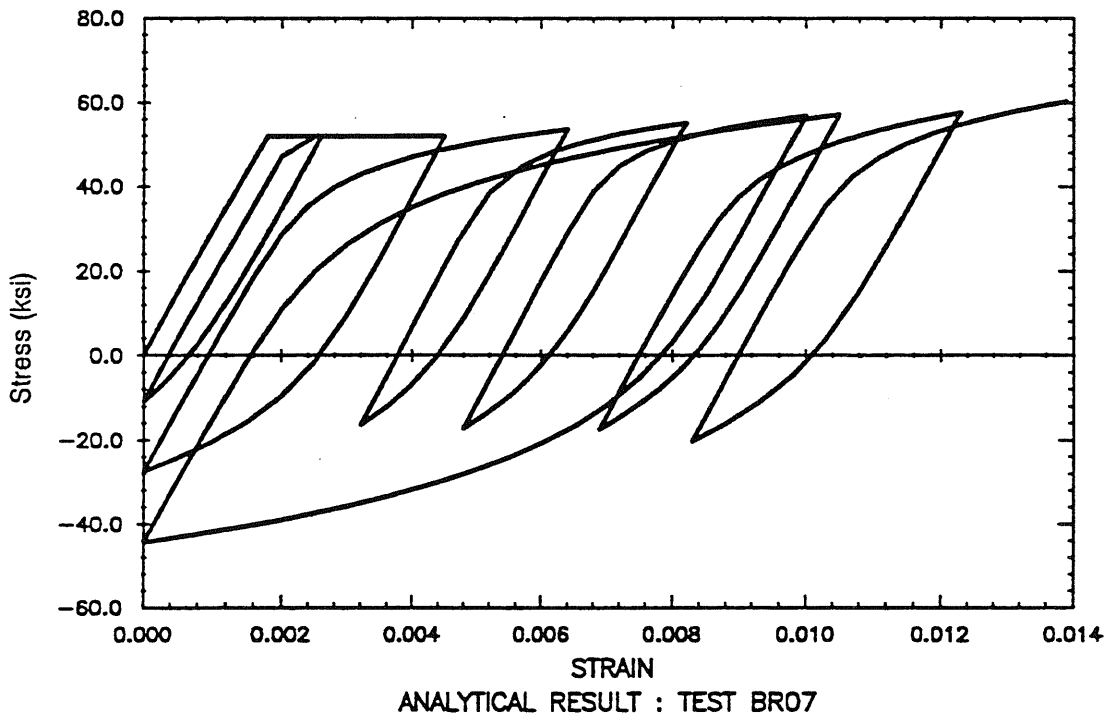
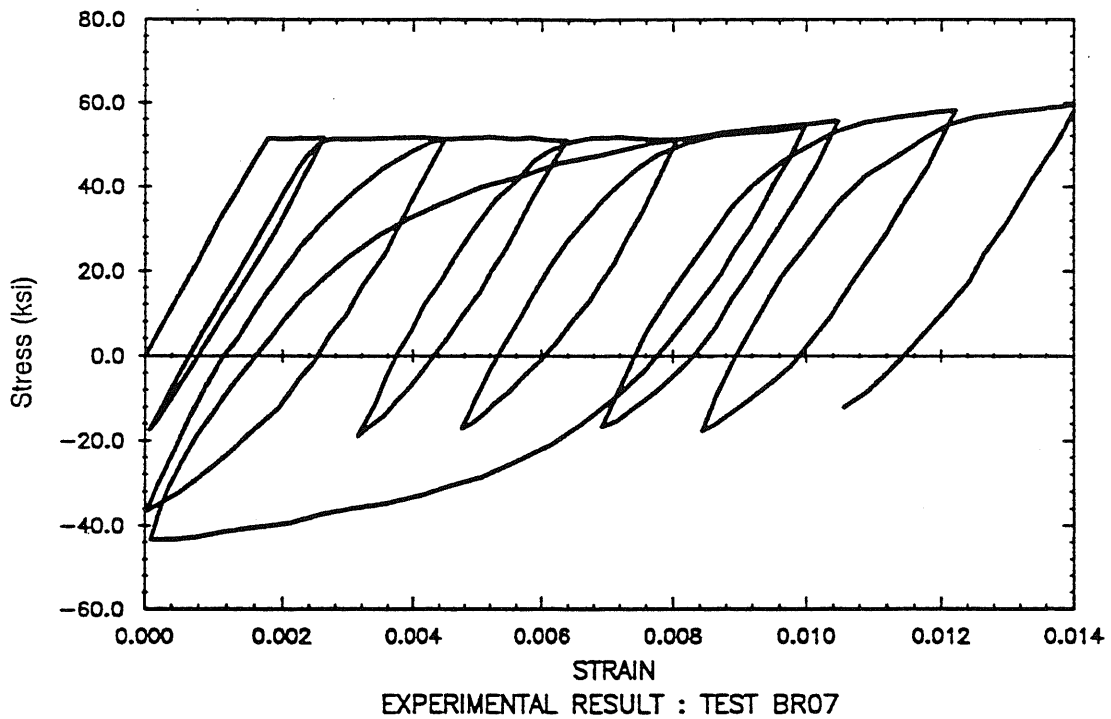
EXPERIMENTAL RESULT : TEST 8 #6 COUPON SRS397



ANALYTICAL RESULT : TEST 8 #6 COUPON SRS397

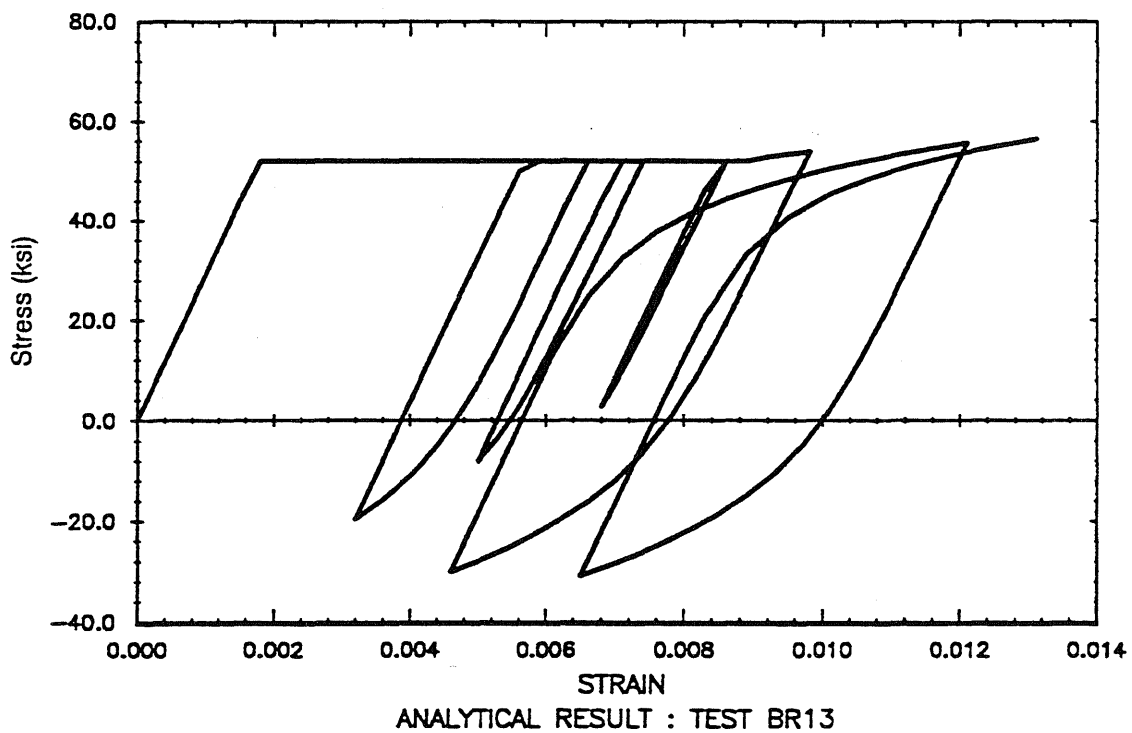
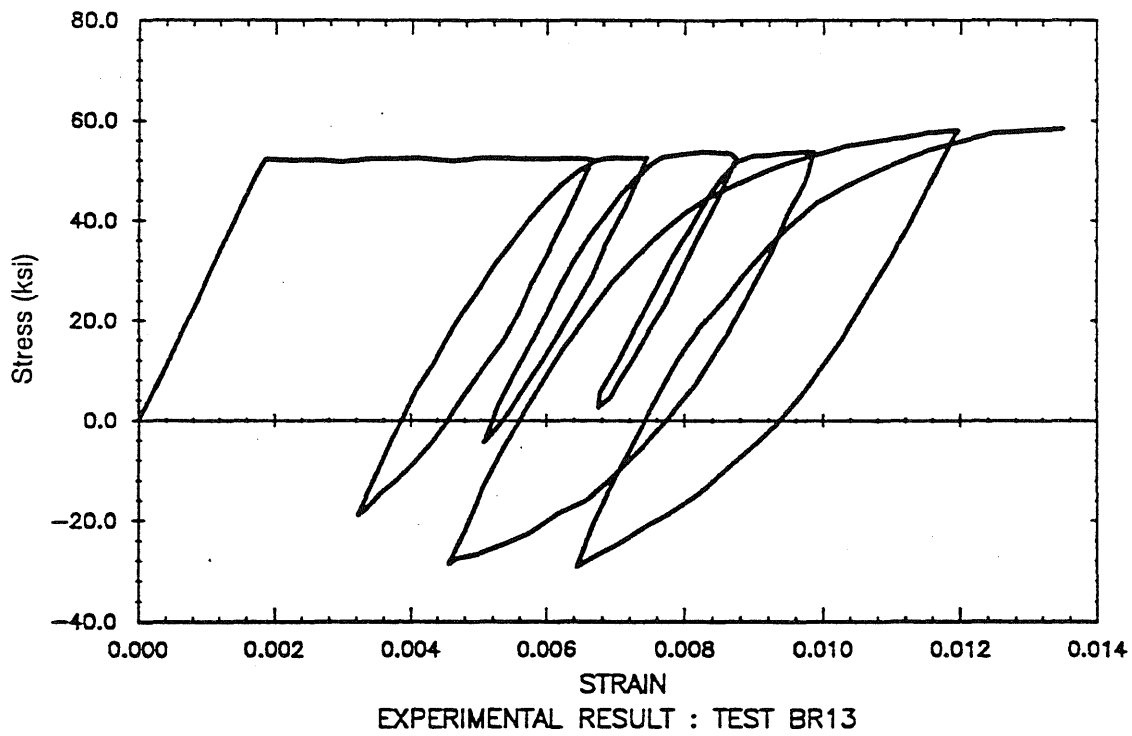
f) Test 8 # 6 coupon (from Aktan et al. [5])

Fig. 4.9 Evaluation of the Proposed Steel Model (Cont.)



g) Test BR07 (from Seckin [124])

Fig. 4.9 Evaluation of the Proposed Steel Model (Cont.)



h) Test BR13 (from Seckin [124])

Fig. 4.9 Evaluation of the Proposed Steel Model (Cont.)



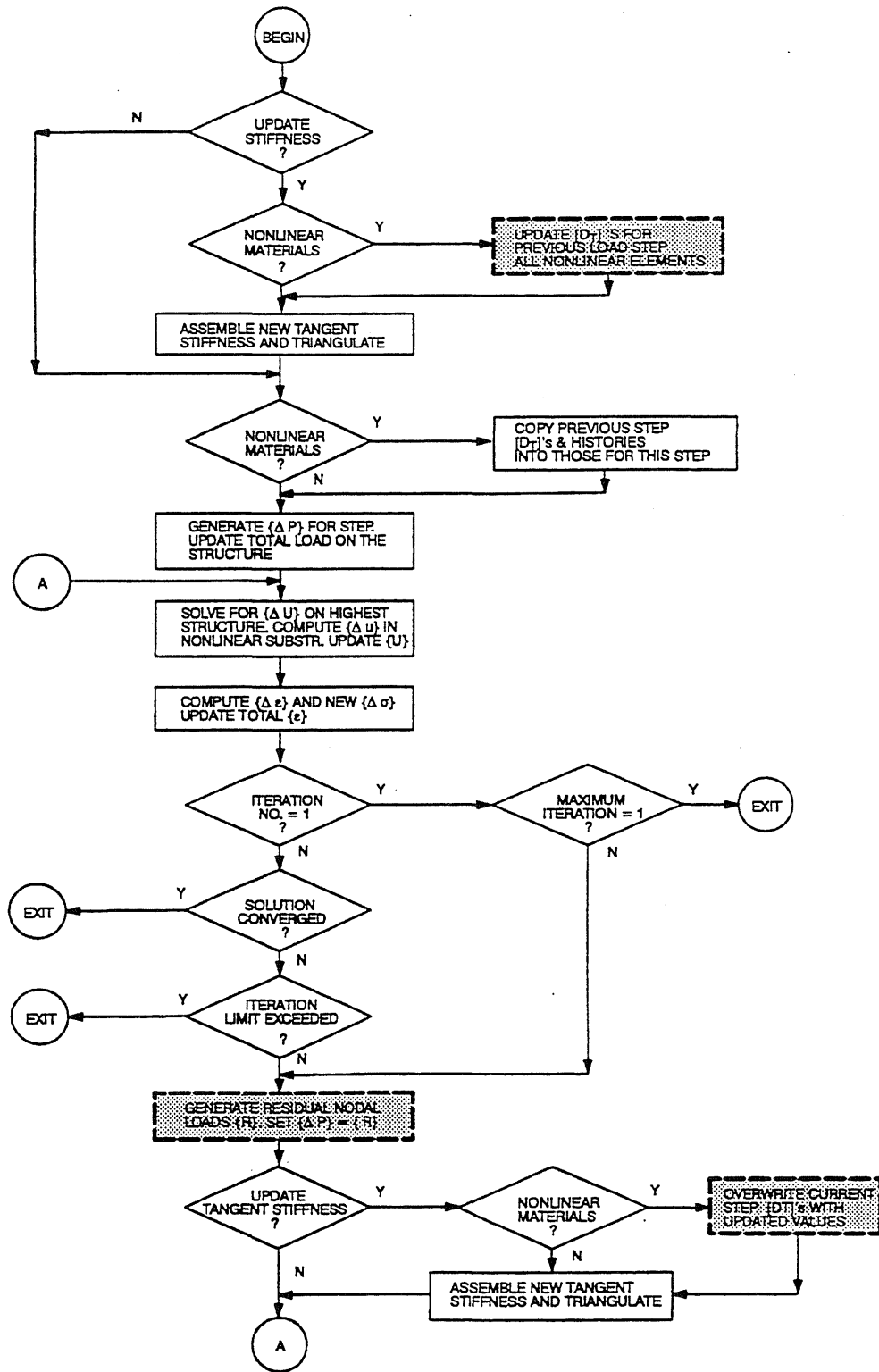


Fig. 5.1 Solution Algorithm for each Load Step (from[49])

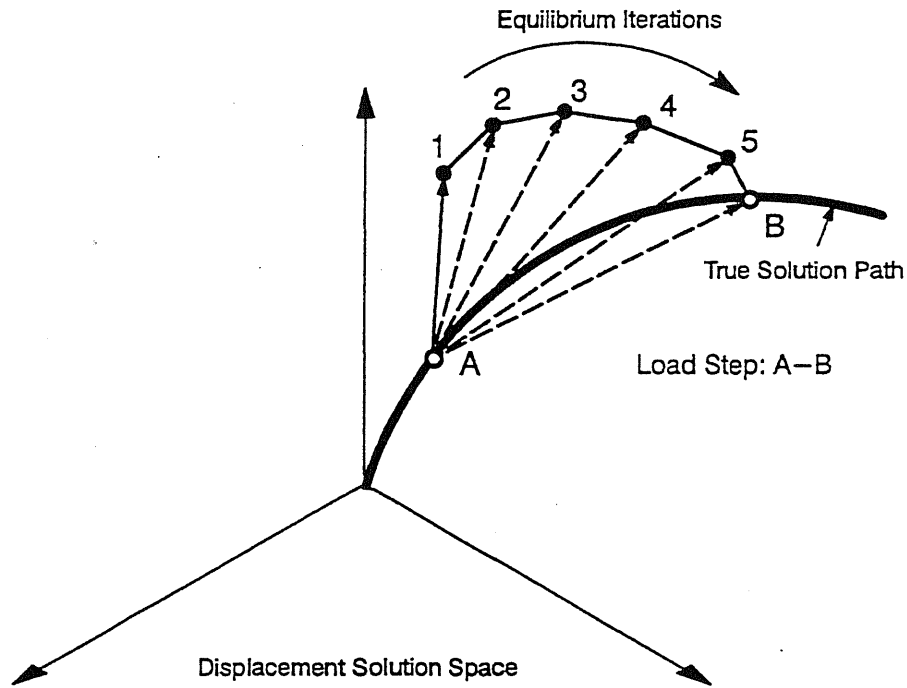


Fig. 5.2 Solution Path of Incremental-iterative Algorithm (from [23])

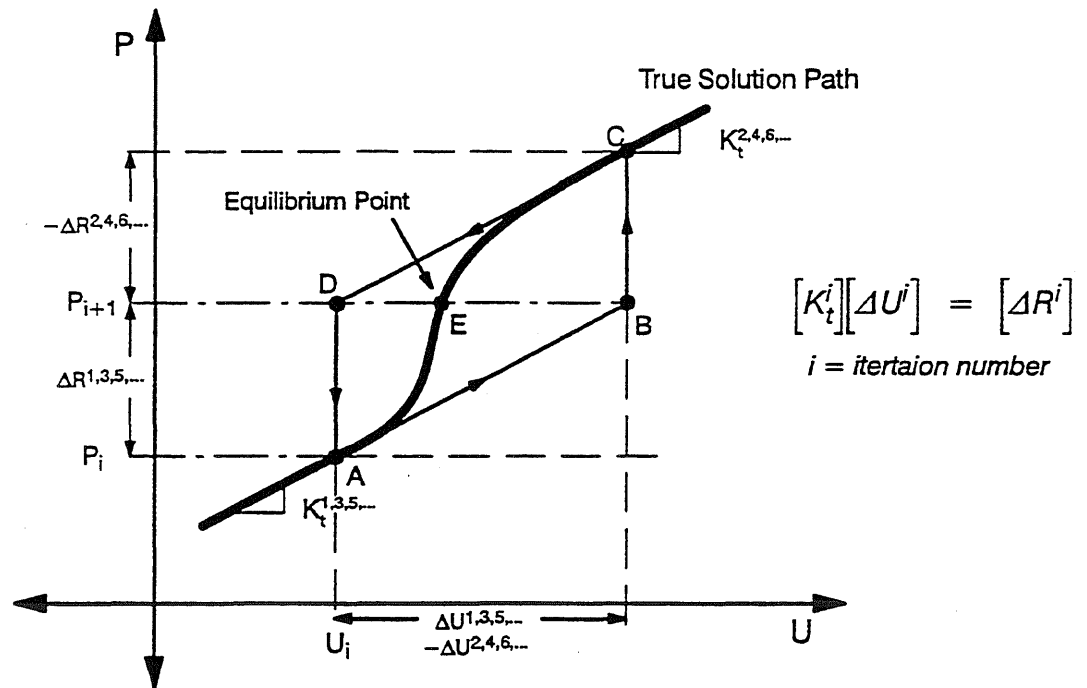
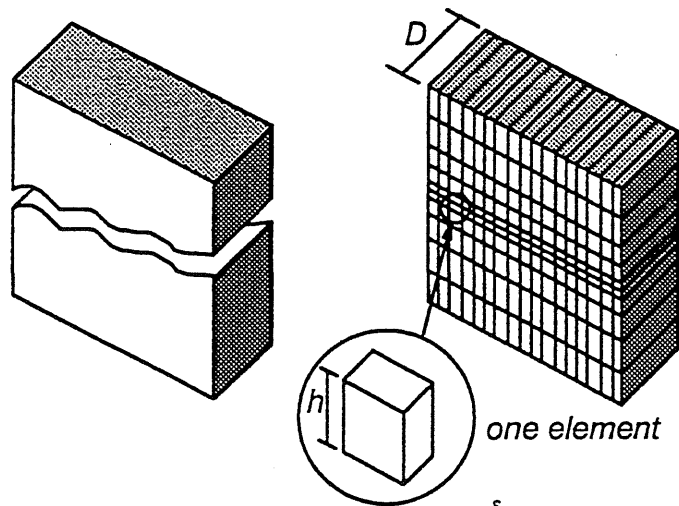


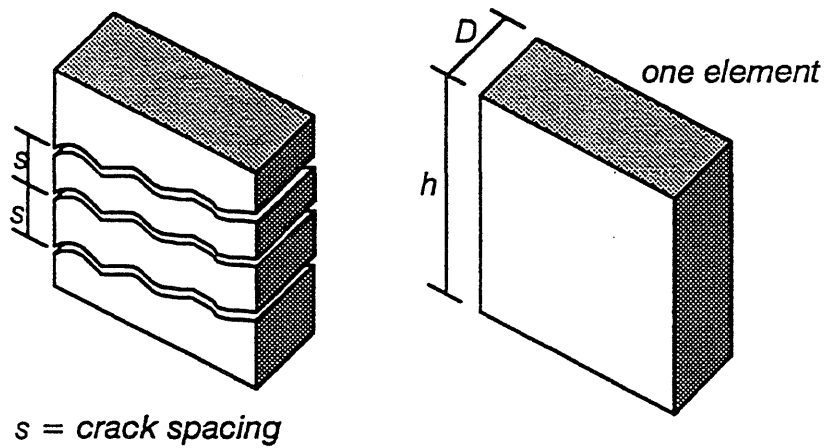
Fig. 5.3 Numerical Problem with Newton-Raphson Iteration Algorithm



$$G_f * h * b * D = h * b * D * \int_0^{\epsilon_0} \sigma d\epsilon$$

$$G_f = h * \int_0^{\epsilon_0} \sigma d\epsilon$$

a) Fracture Mechanics Approach

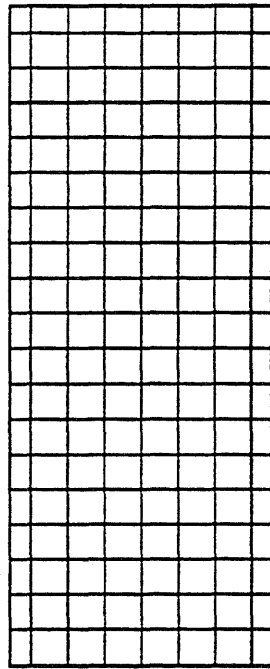


$$G_f * \frac{h}{s} * b * D = h * b * D * \int_0^{\epsilon_0} \sigma d\epsilon$$

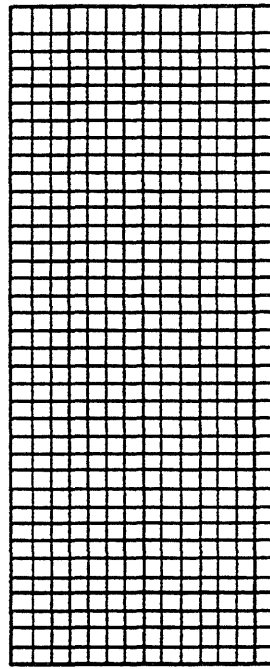
$$G_f = s * \int_0^{\epsilon_0} \sigma d\epsilon$$

b) Strength Criterion Approach

Fig. 5.4 Relationship between Fracture Energy and Mesh Size

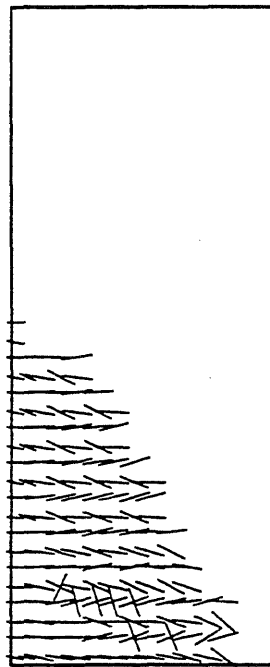


a) Coarse Mesh

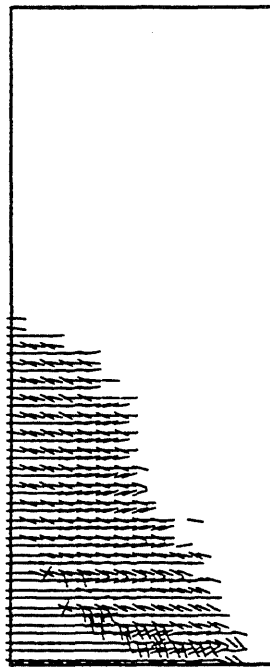


b) Fine Mesh

Fig. 5.5 Finite Element Mesh for Wall R1



a) Coarse Mesh



b) Fine Mesh

Fig. 5.6 Calculated Crack Patterns for Wall R1

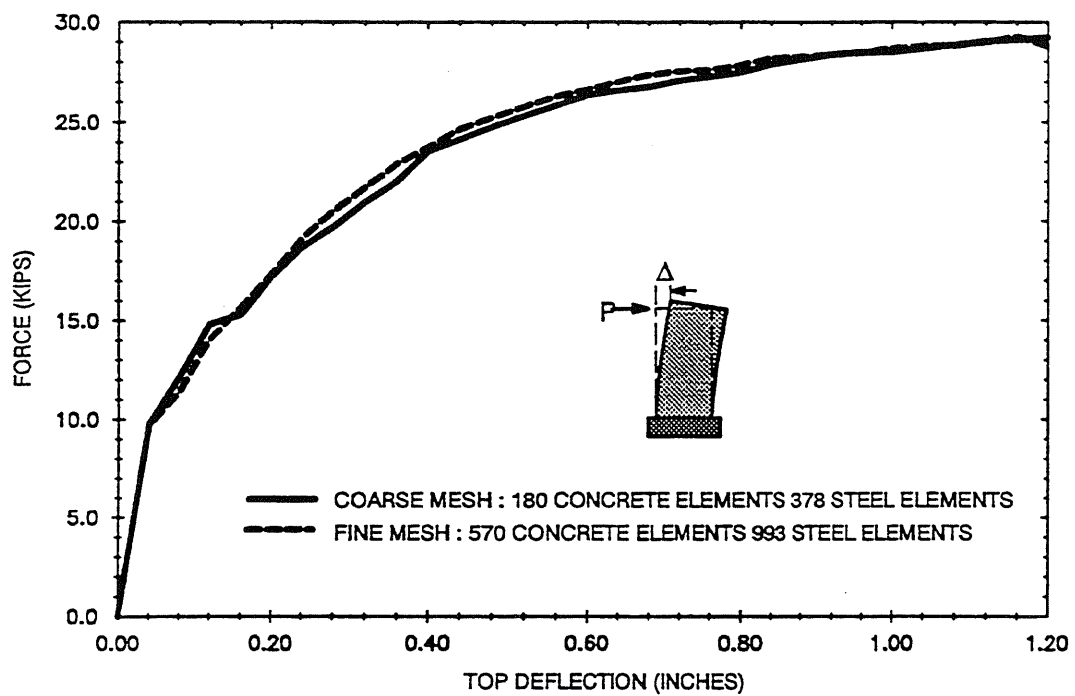
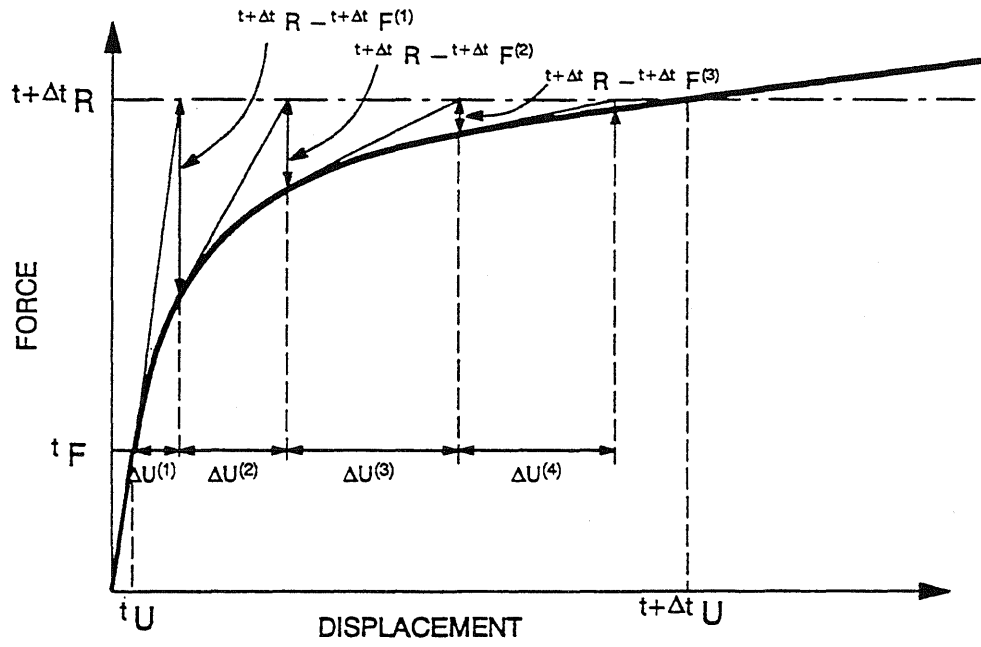
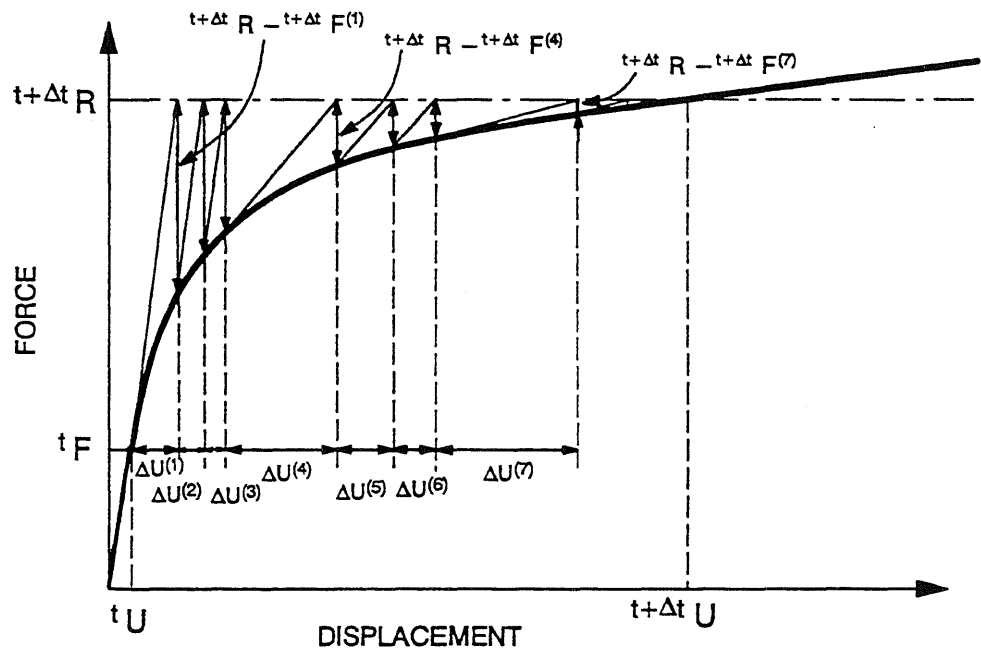


Fig. 5.7 Calculated Load-Deflection Curves for Wall R1

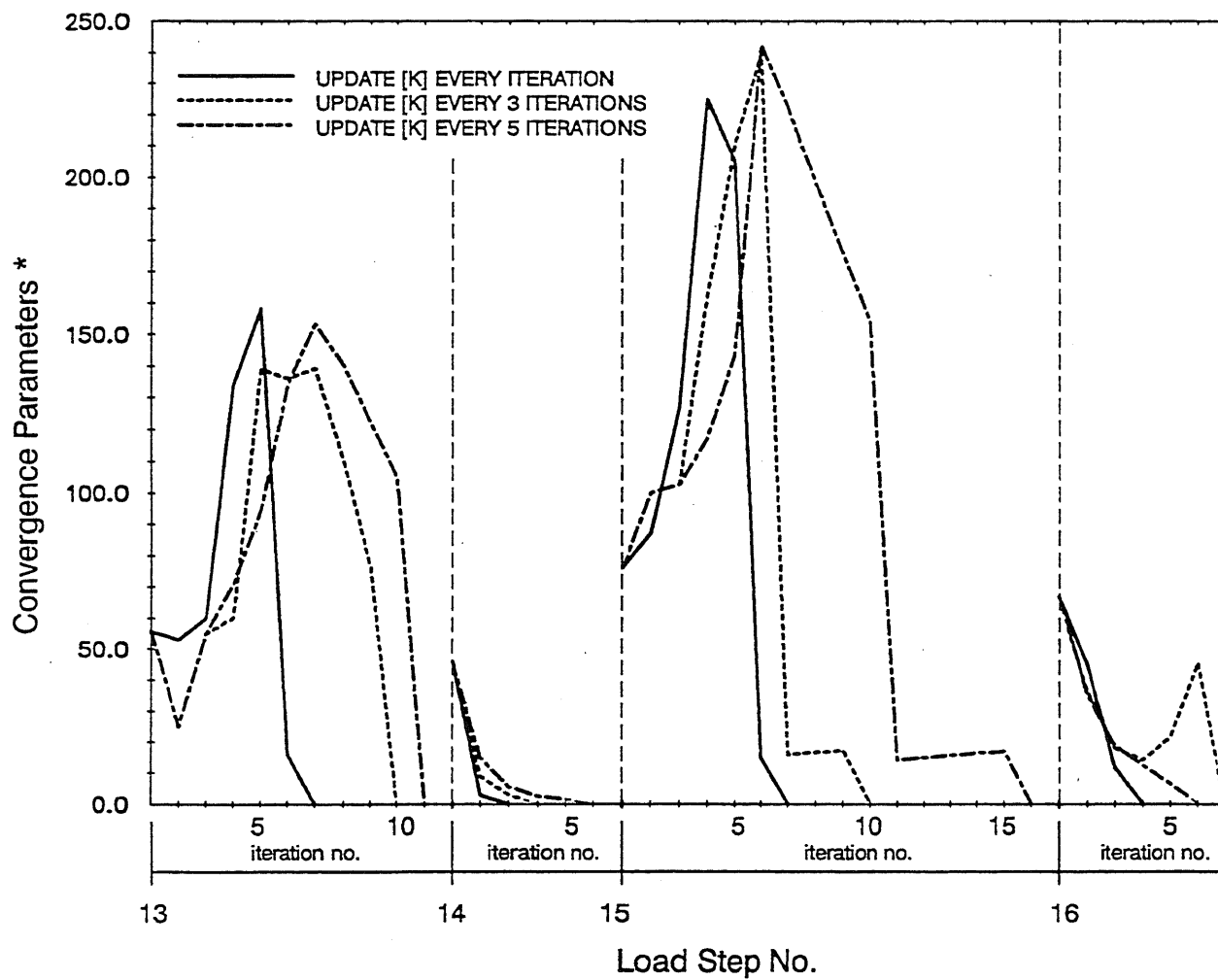


a) Full Newton-Raphson Algorithm



b) Modified Newton-Raphson Algorithm

Fig. 5.8 Newton-Raphson Iterative Algorithms



\* Convergence Parameter =  $\frac{\|R\|}{\|\Delta P\|} * 100$

Fig. 5.9 Convergence Rate of Different Schemes for Updating Stiffness Matrix

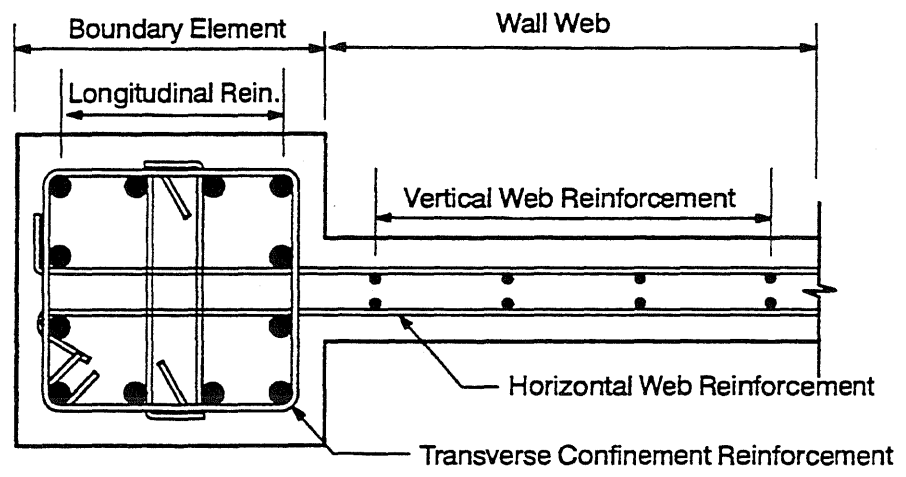
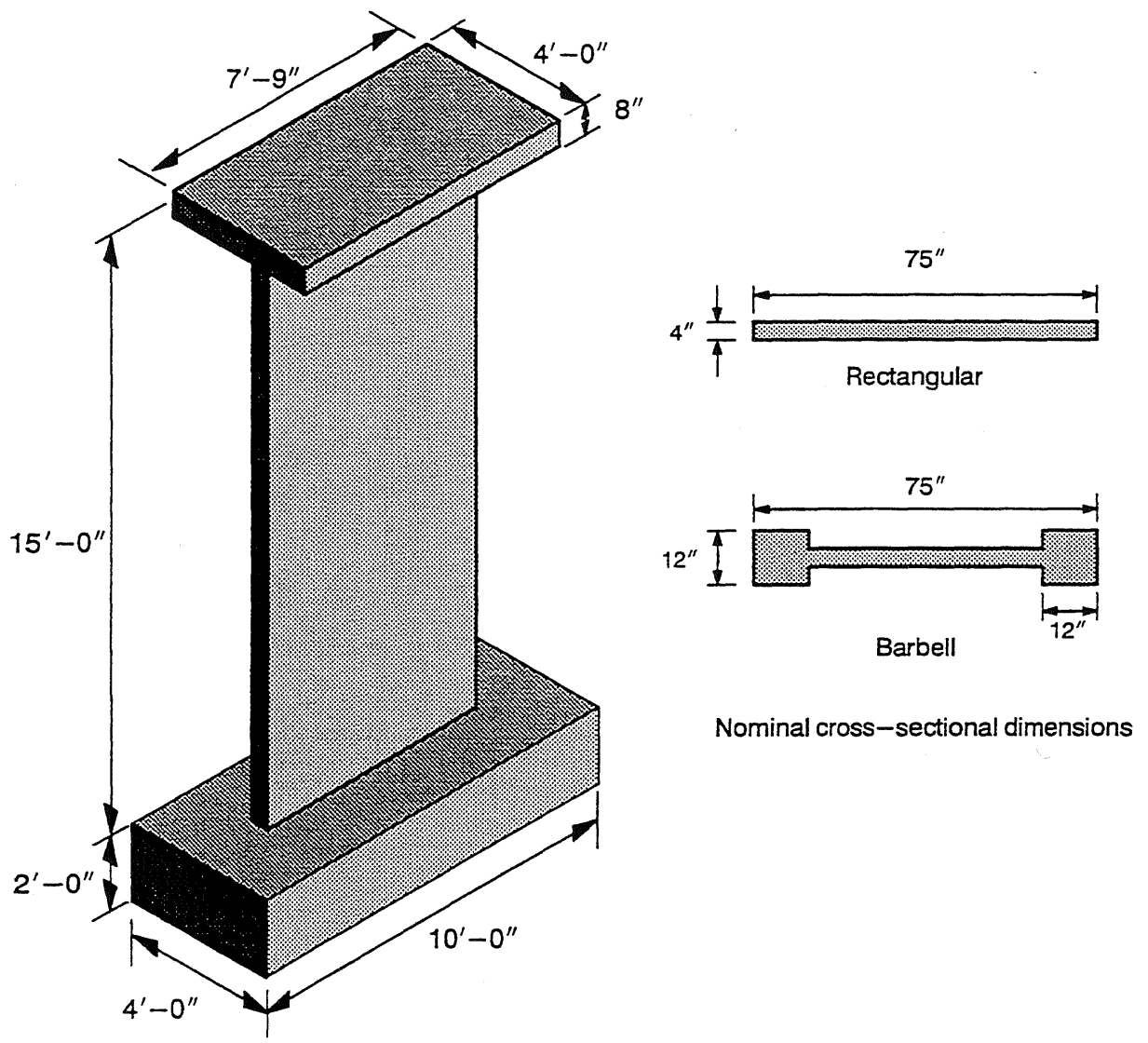
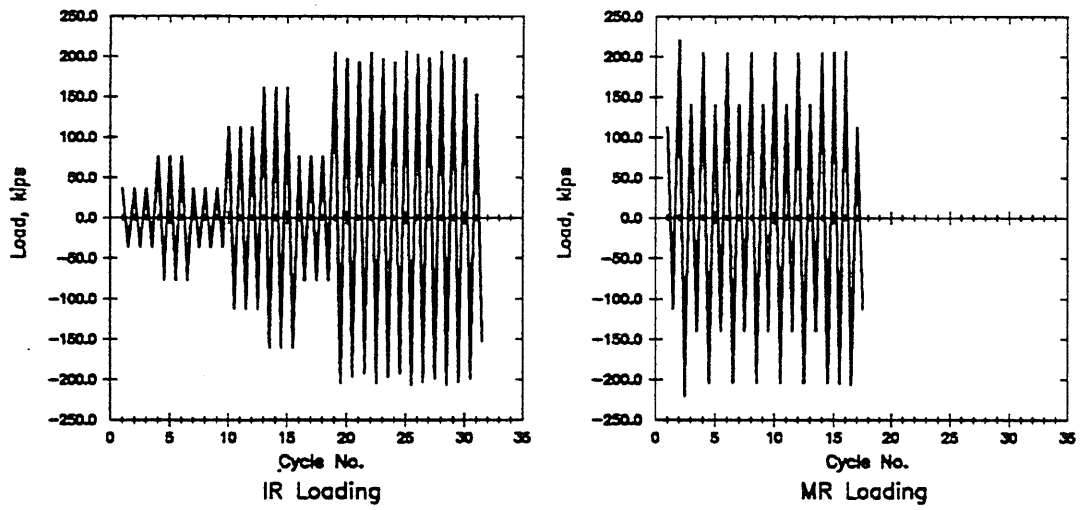
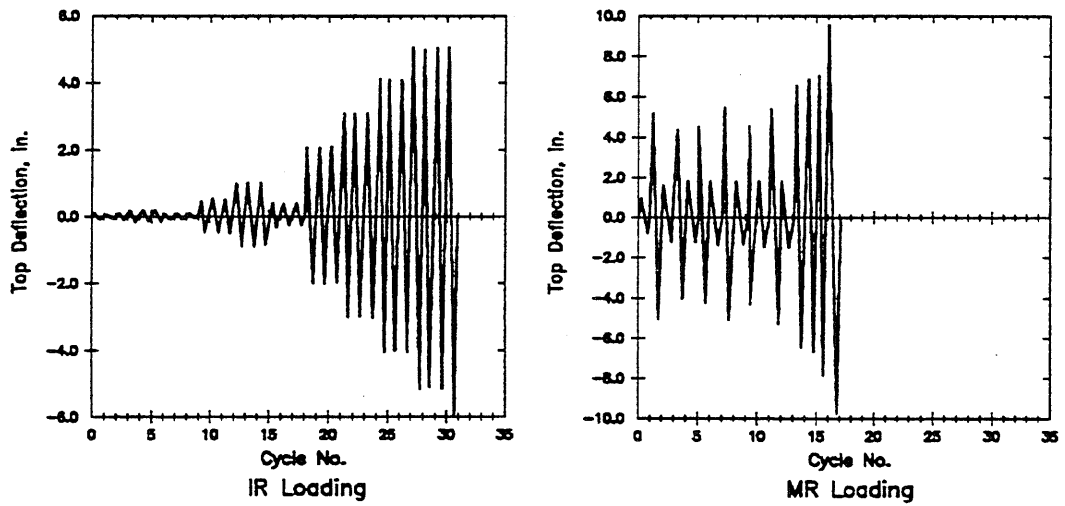


Fig. 6.1 Nominal Dimensions of the PCA Wall Specimens (from [106])





a) Load History



b) Deflection History

Fig. 6.2 Typical Loading Histories (from [103])

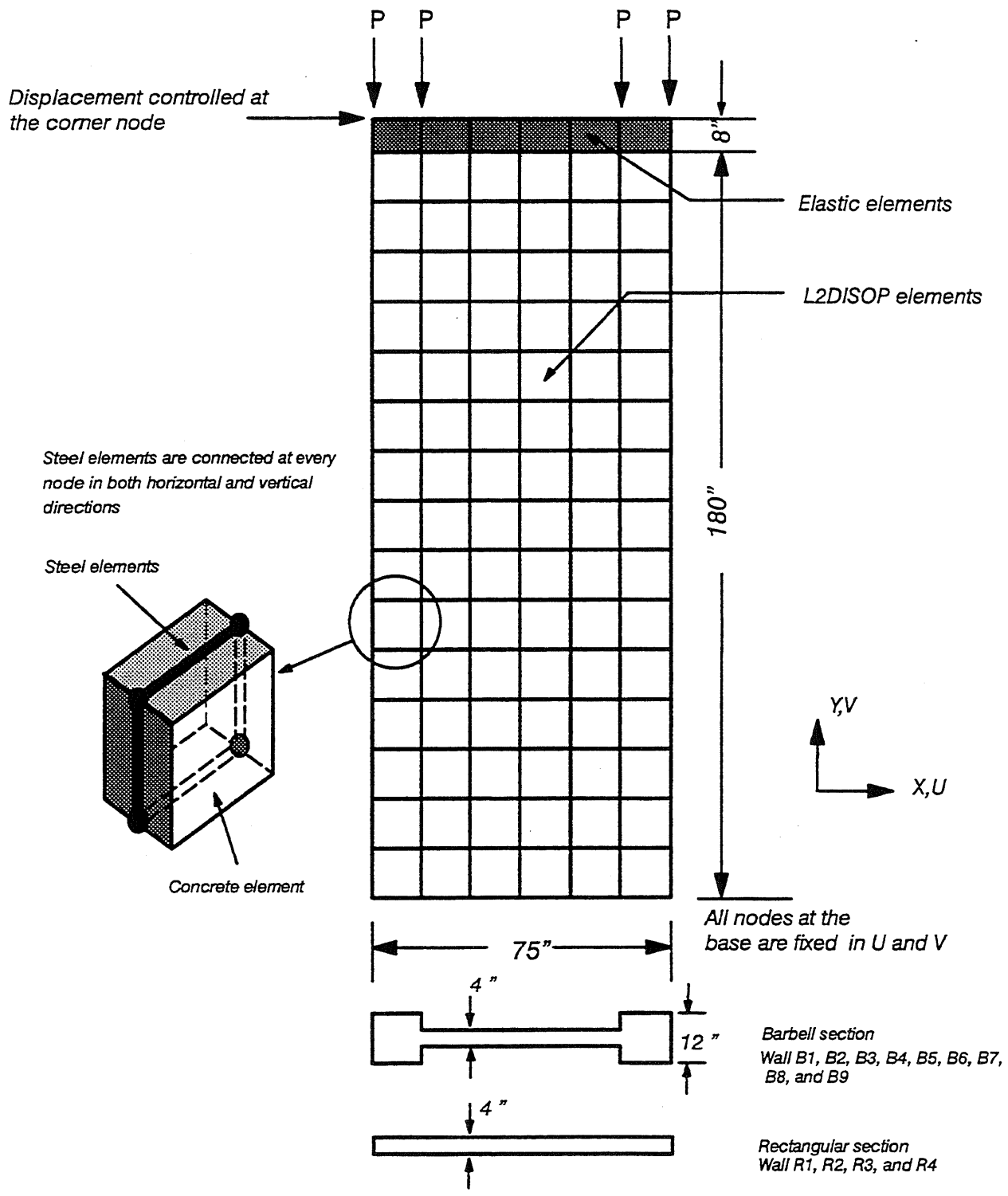


Fig. 6.3 Finite Element Model for a PCA Wall Specimen

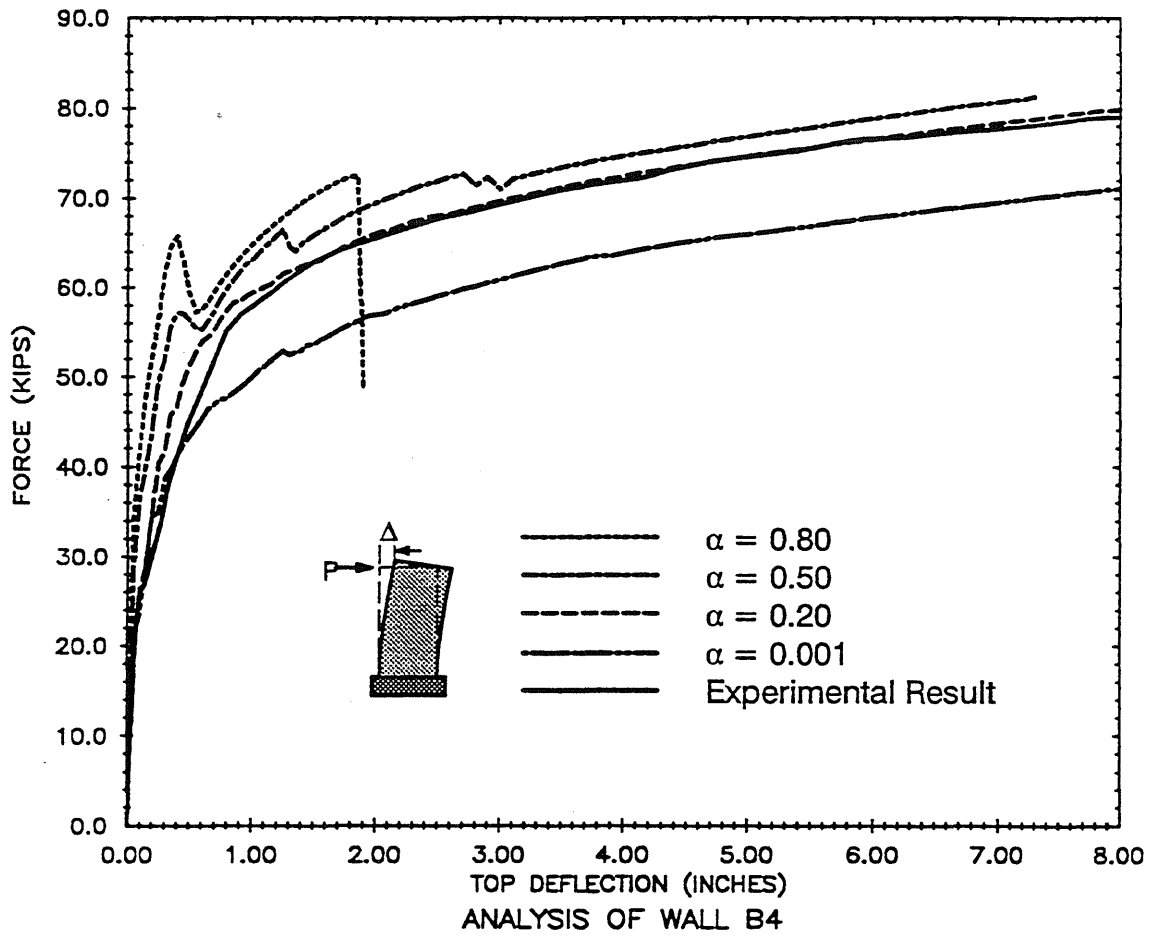


Fig. 6.4 Sensitivity of the Calculated Response of Wall B4 to the Choice of  $\alpha$

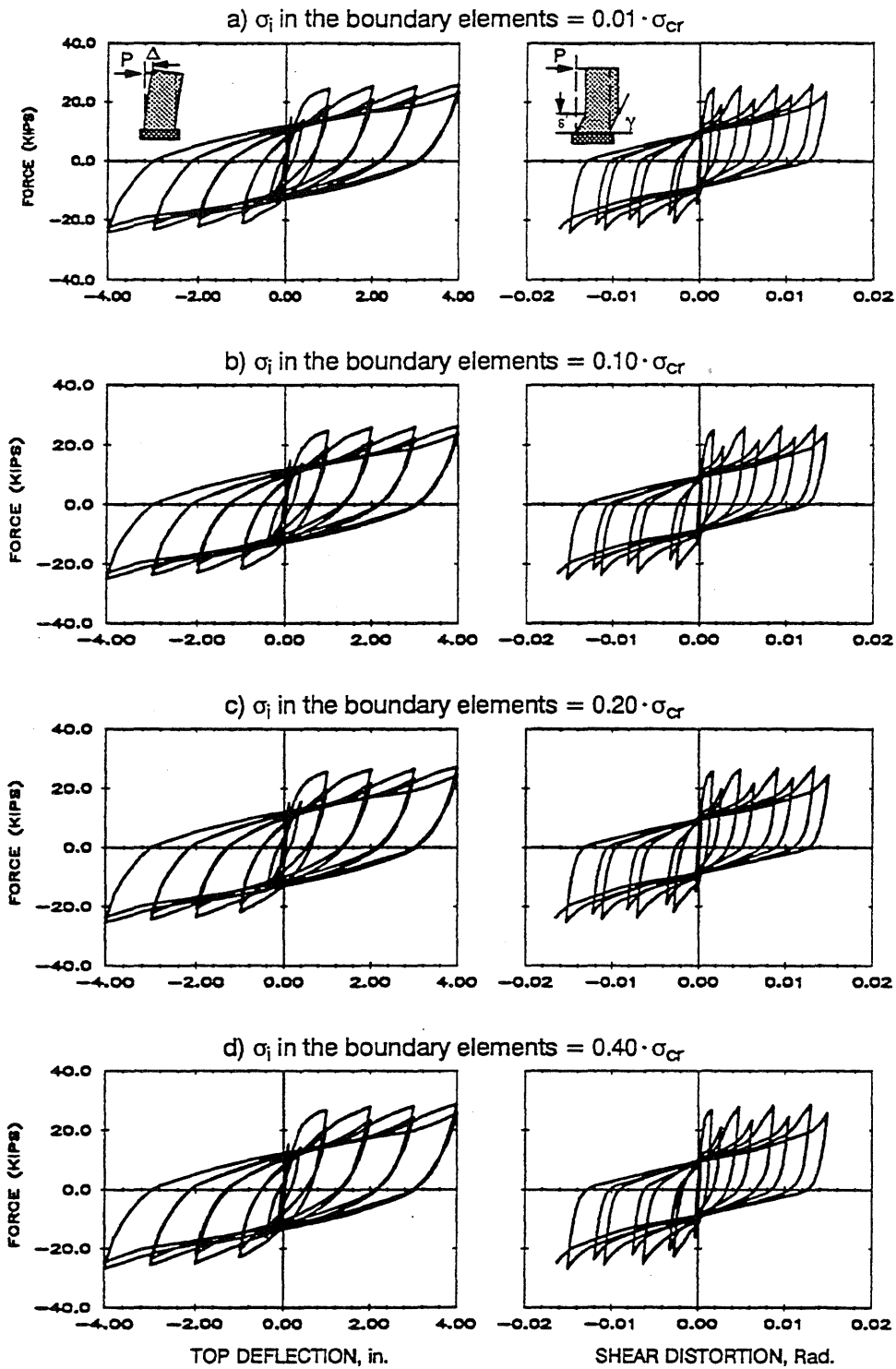


Fig. 6.5 Sensitivity of the Calculated Response of Wall R1 to the Choice of  $\sigma_i$  in Boundary Elements

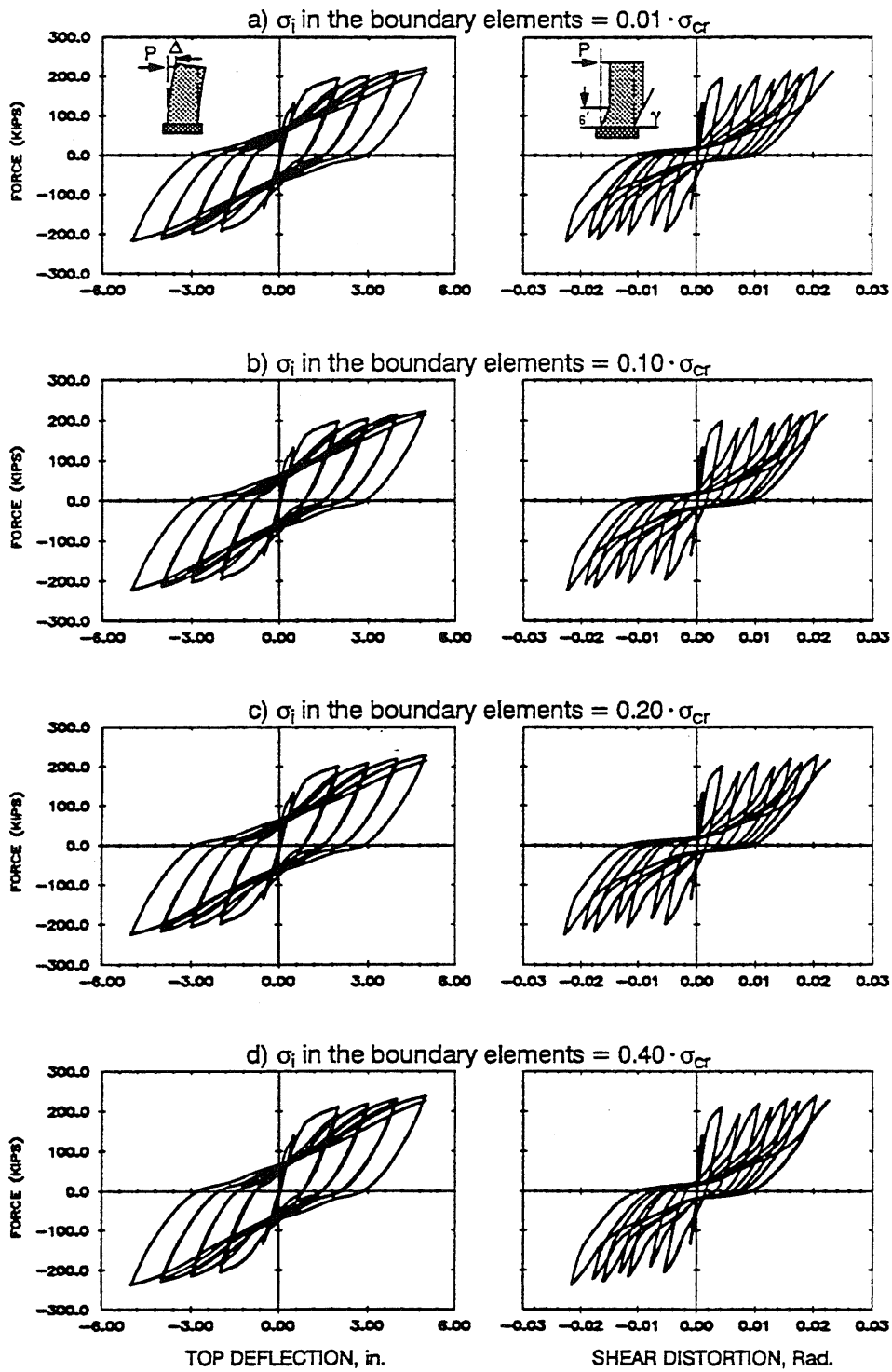


Fig. 6.6 Sensitivity of the Calculated Response of Wall B7 to the Choice of  $\sigma_i$  in Boundary Elements

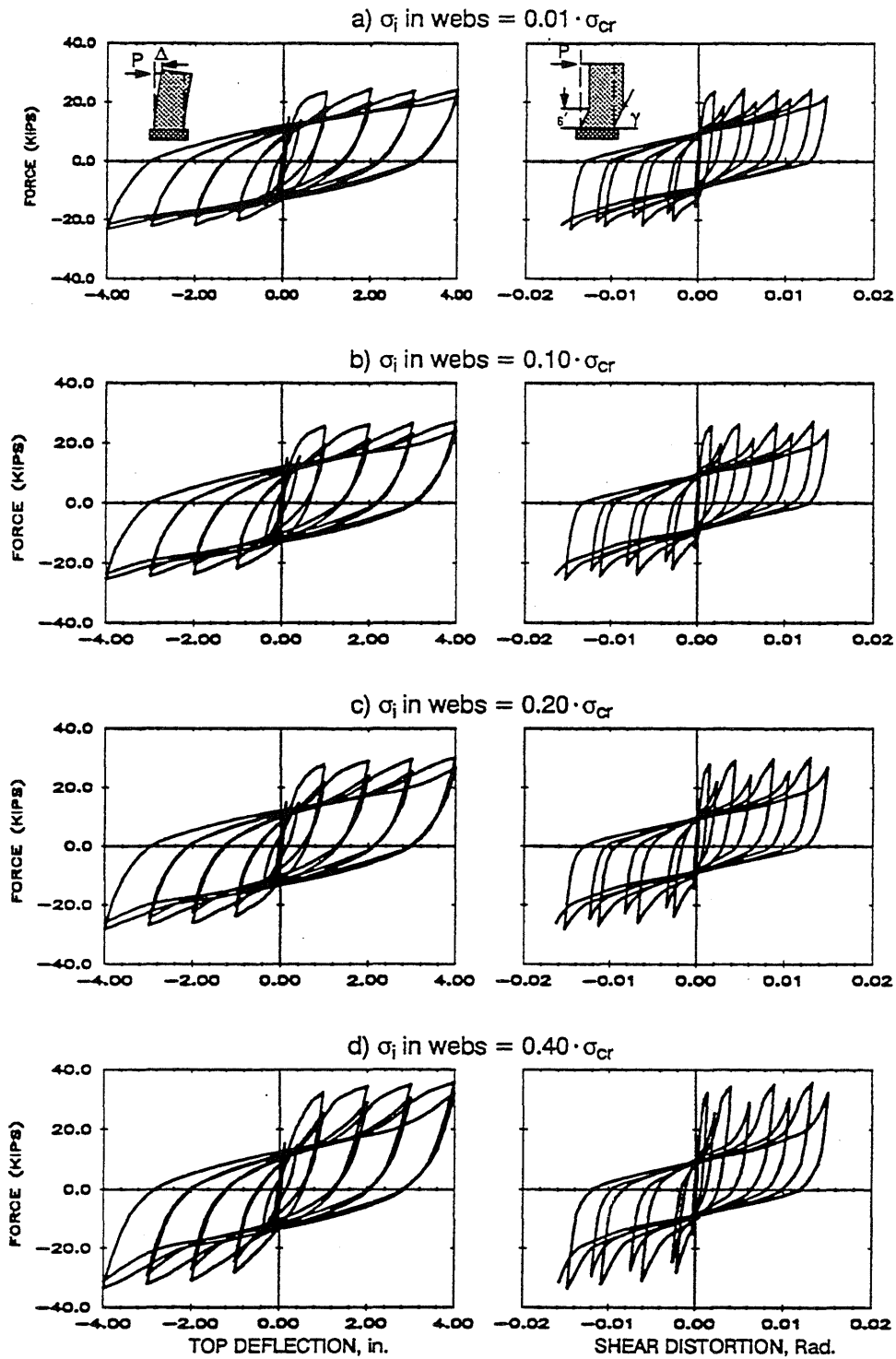


Fig. 6.7 Sensitivity of the Calculated Response of Wall R1 to the Choice of  $\sigma_i$  in Web

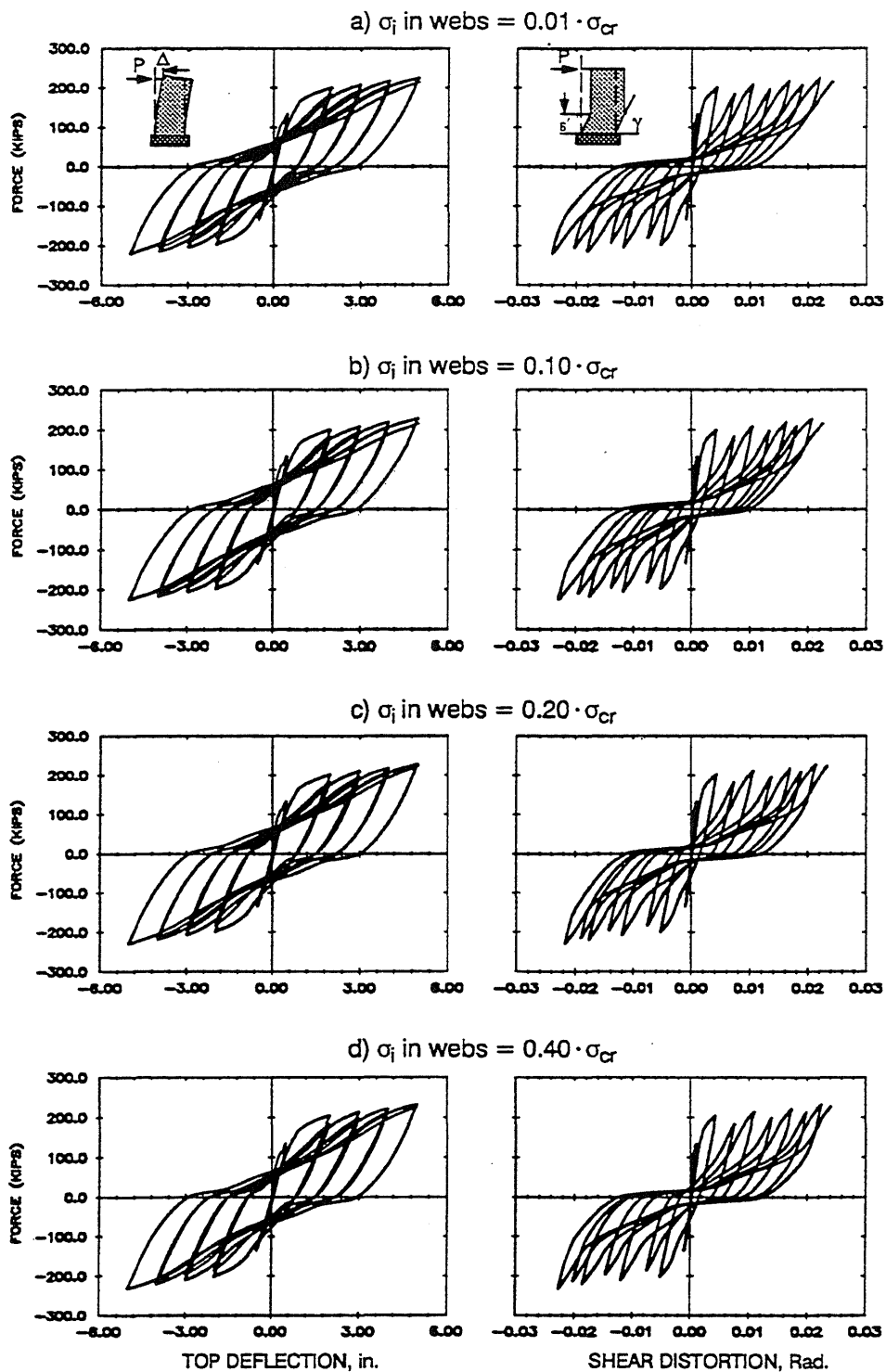


Fig. 6.8 Sensitivity of the Calculated Response of Wall B7 to the Choice of  $\sigma_i$  in Web

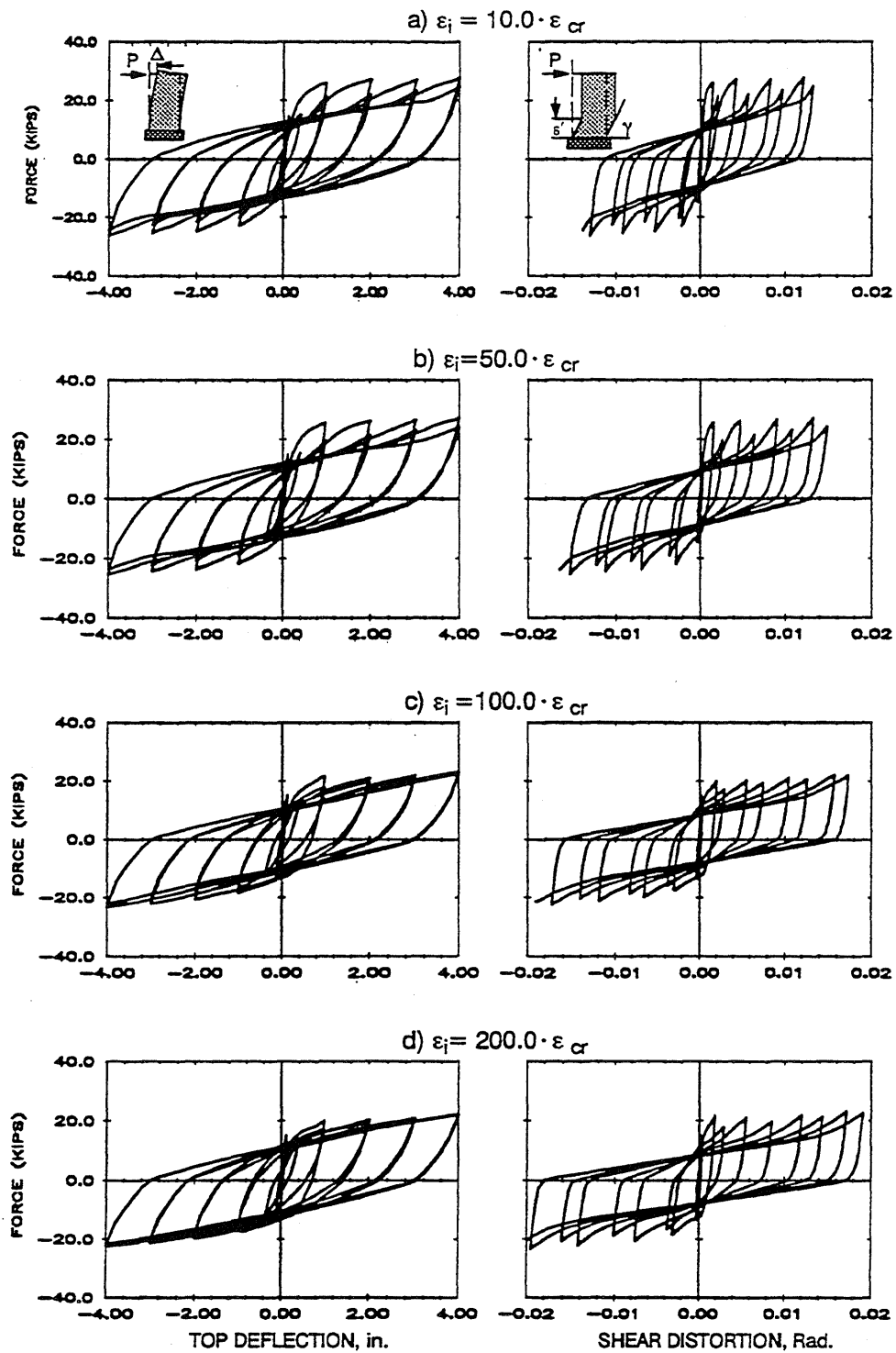


Fig. 6.9 Sensitivity of the Calculated Response of Wall R1 to the Choice of  $\epsilon_i$



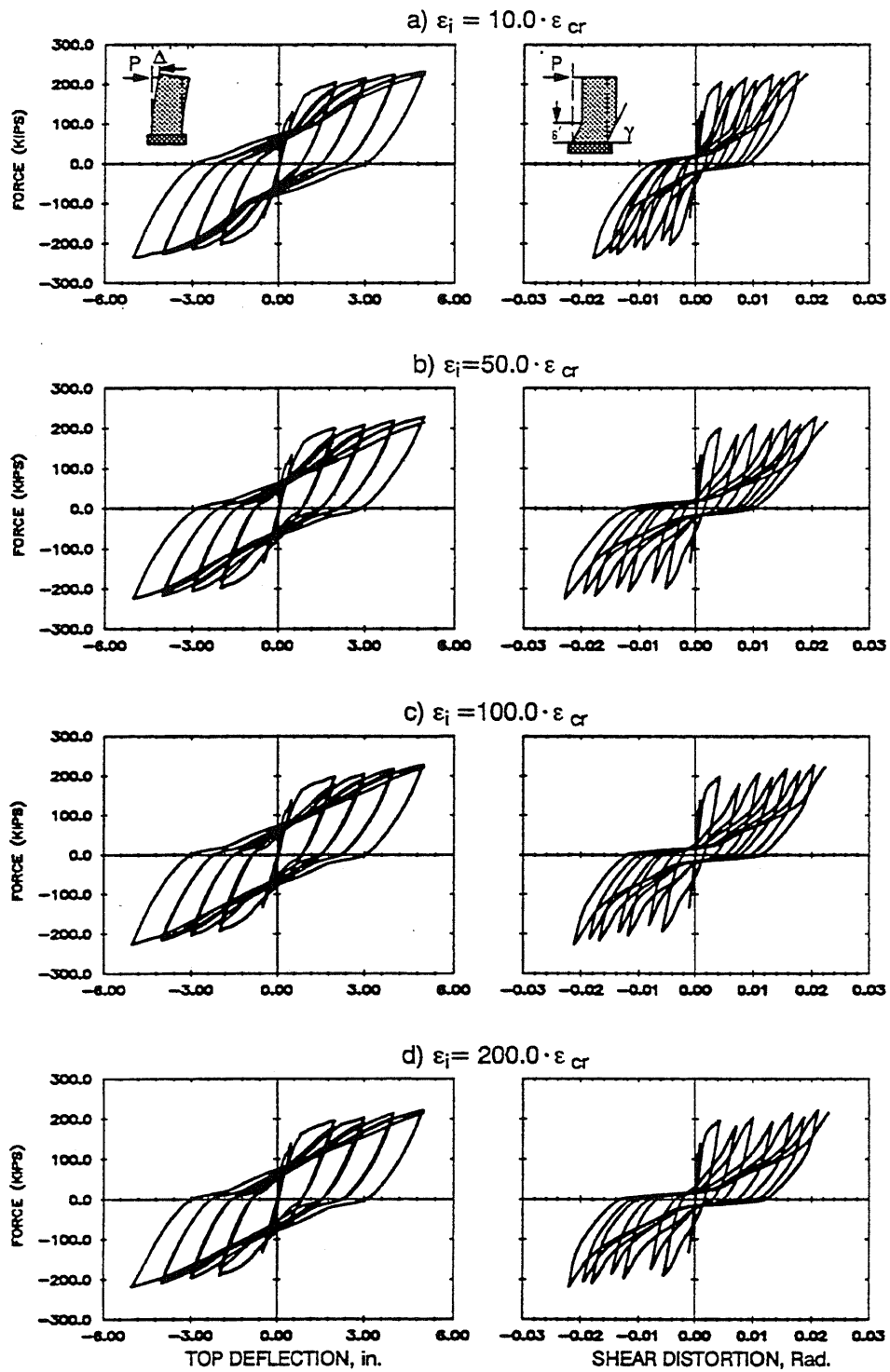


Fig. 6.10 Sensitivity of the Calculated Response of Wall B7 to the Choice of  $\epsilon_i$

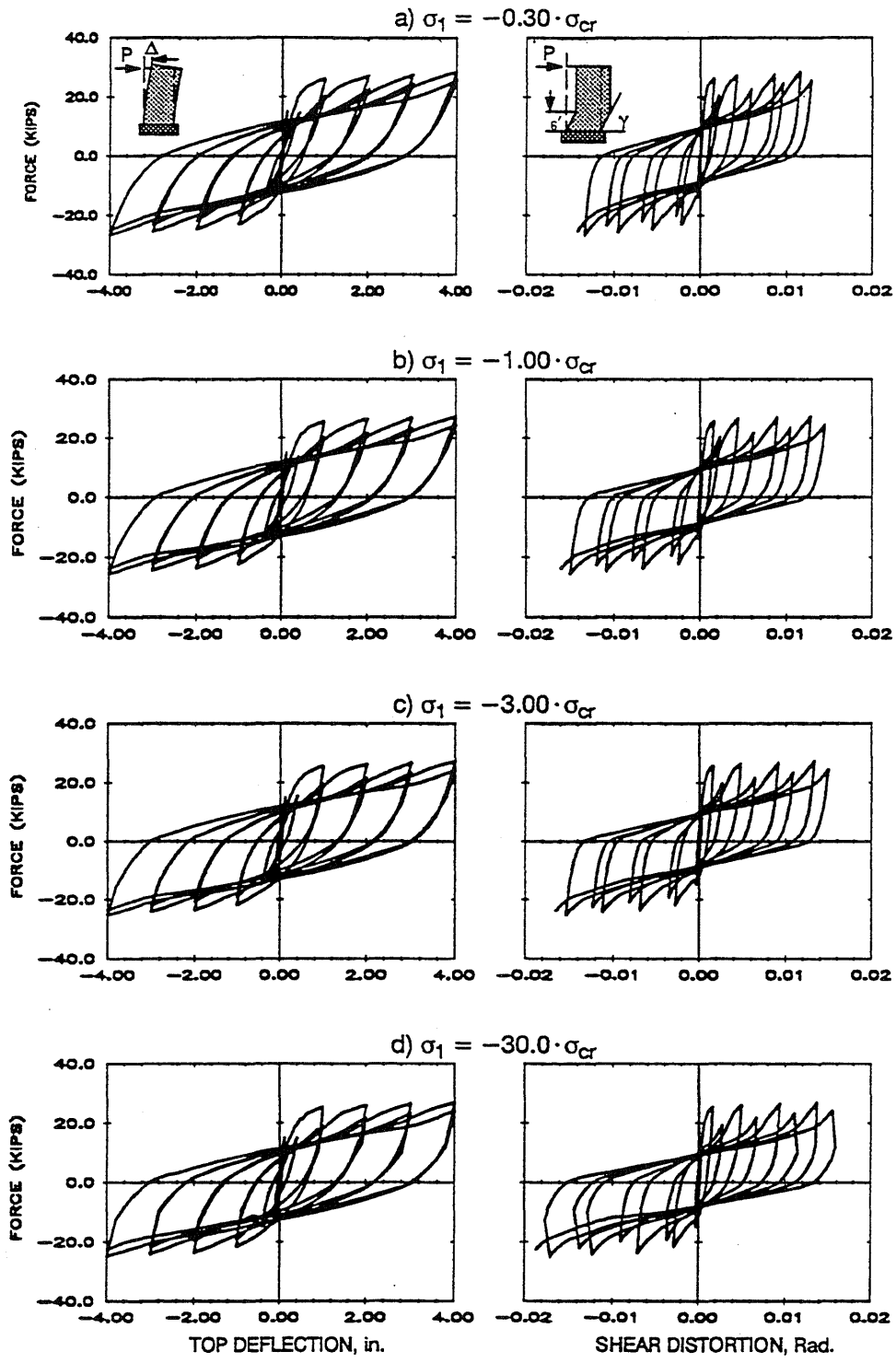


Fig. 6.11 Sensitivity of the Calculated Response of Wall R1 to the Choice of  $\sigma_1$

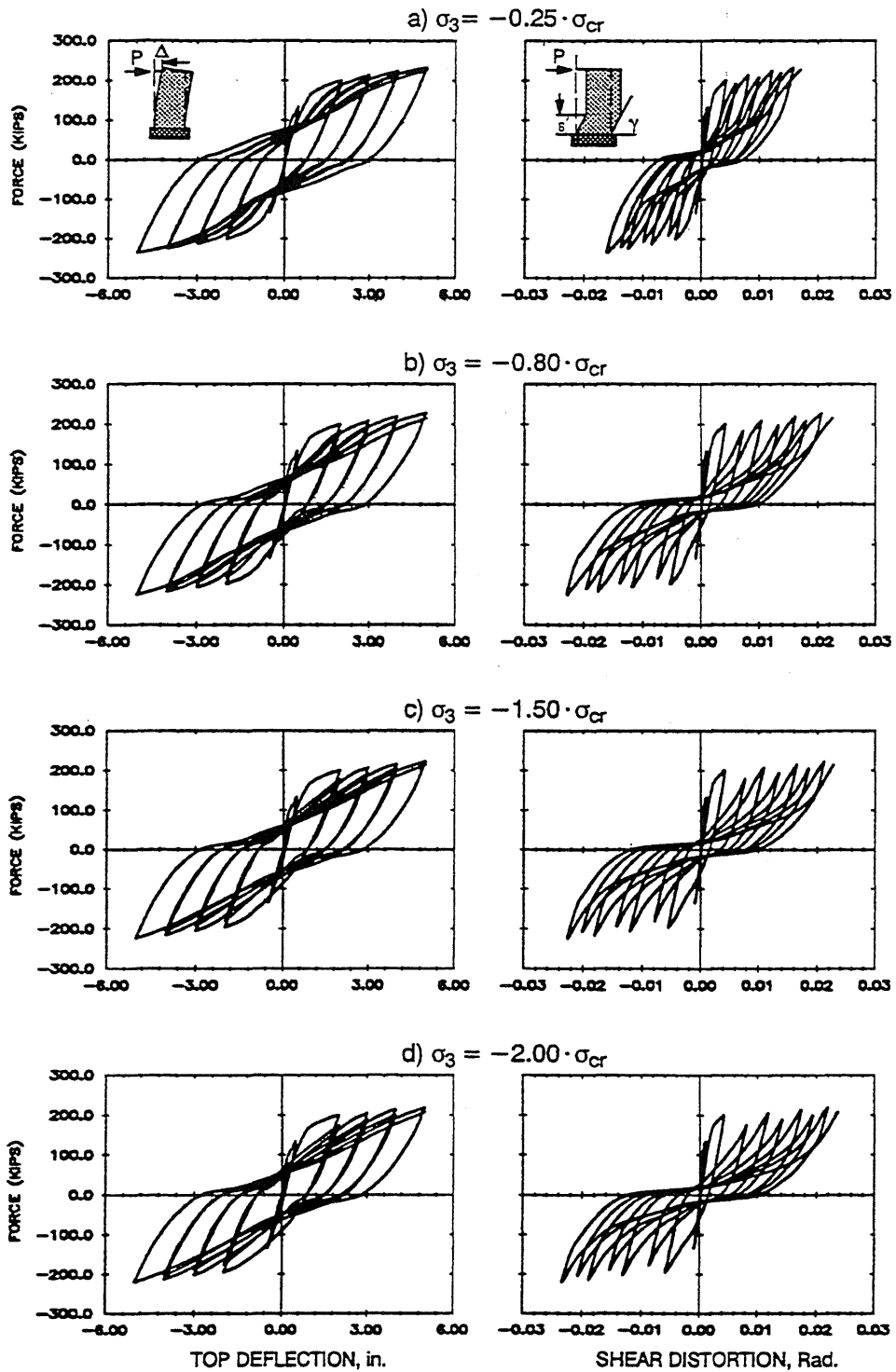


Fig. 6.14 Sensitivity of the Calculated Response of Wall B7 to the Choice of  $\sigma_3$

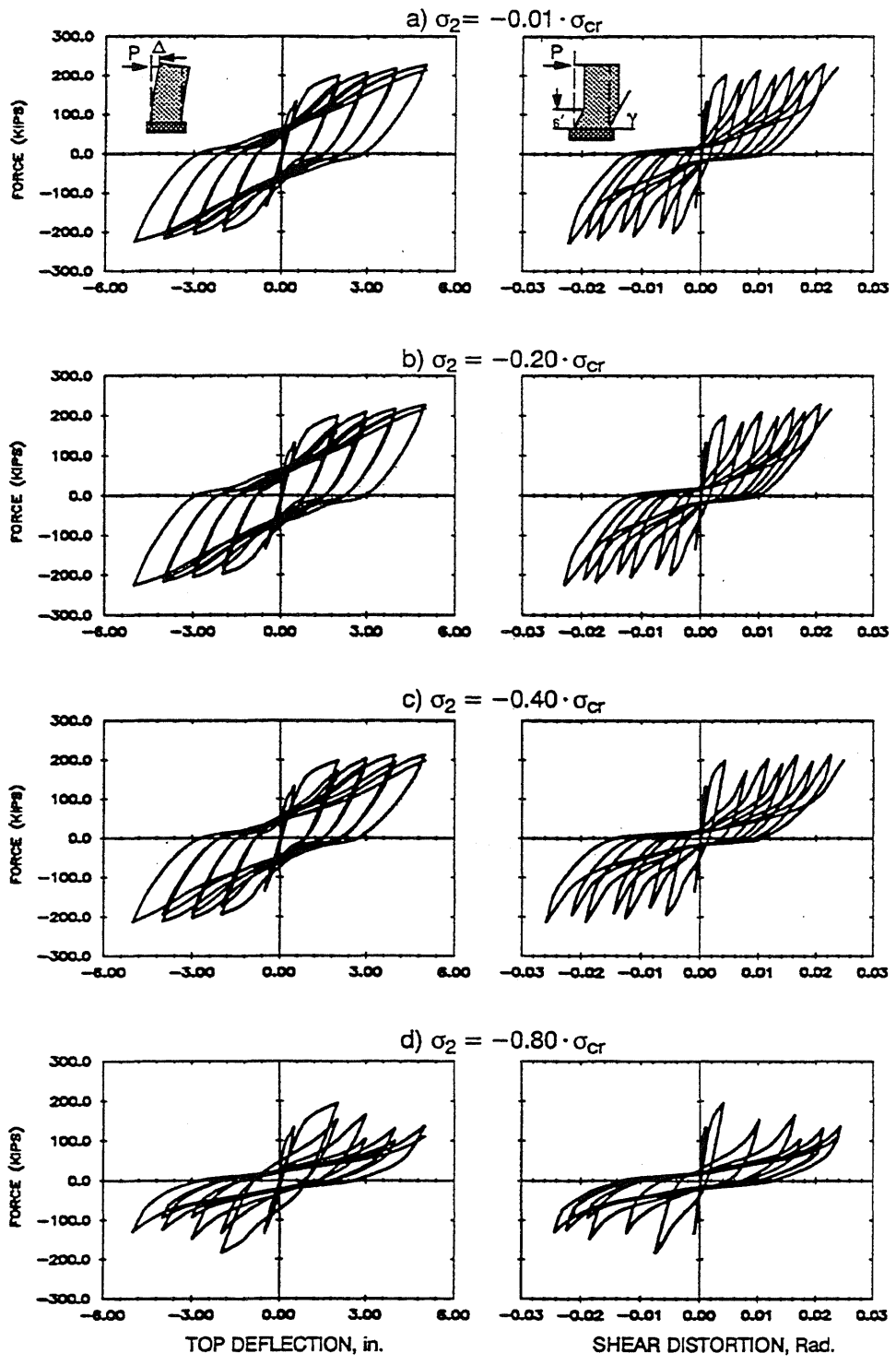


Fig. 6.13 Sensitivity of the Calculated Response of Wall B7 to the Choice of  $\sigma_2$

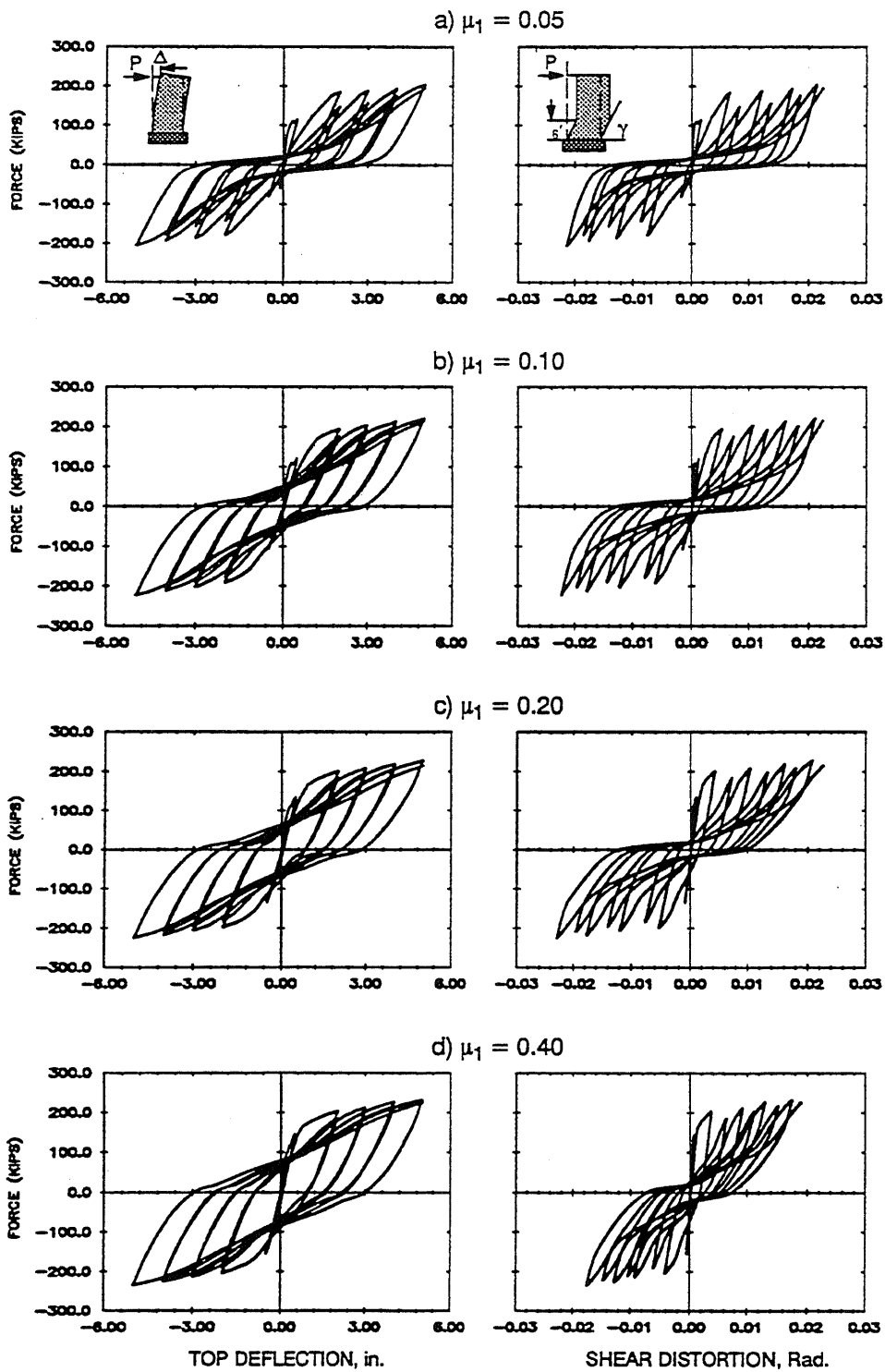


Fig. 6.16 Sensitivity of the Calculated Response of Wall B7 to the Choice of  $\mu_1$

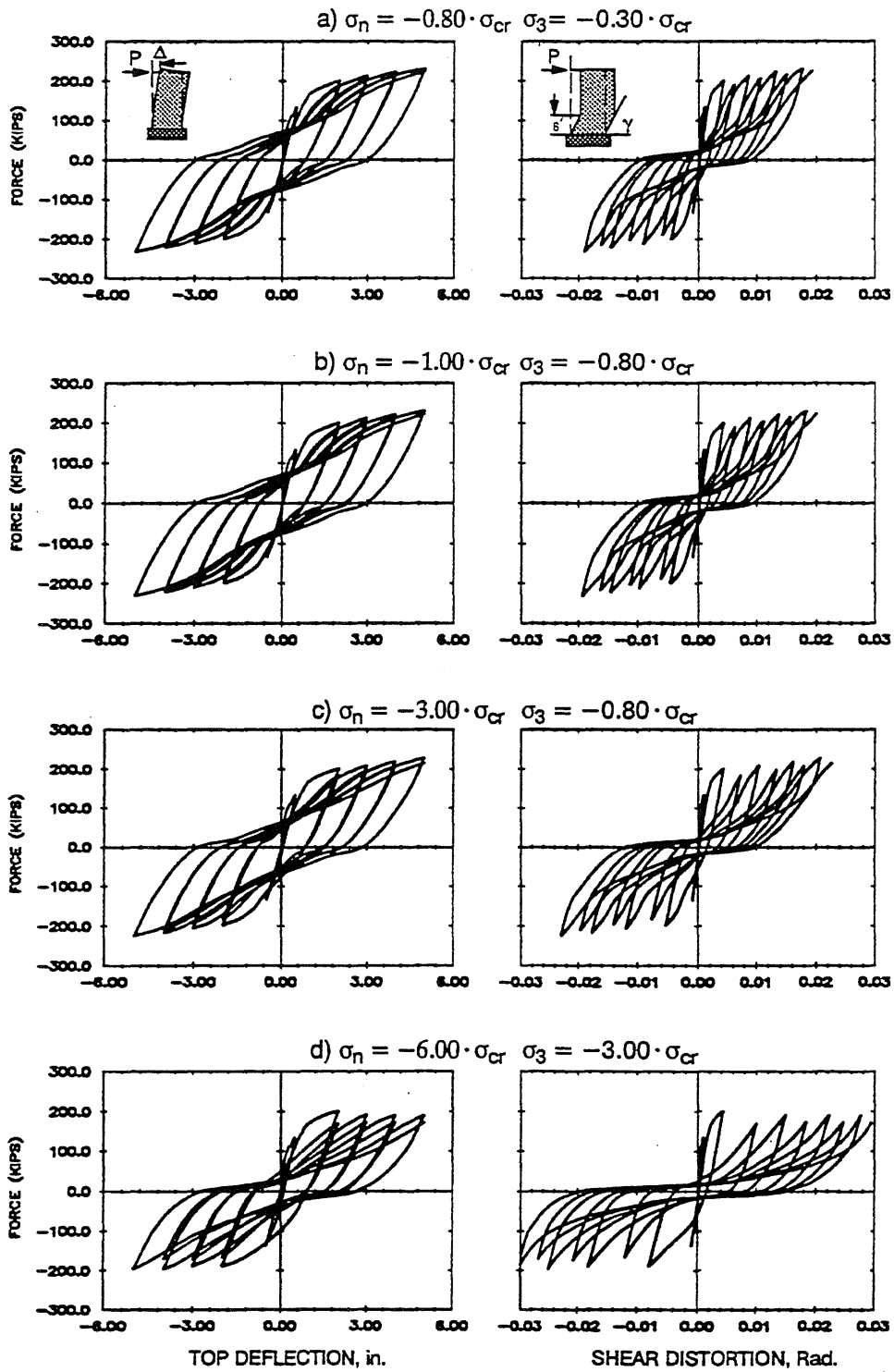


Fig. 6.15 Sensitivity of the Calculated Response of Wall B7 to the Choice of  $\sigma_3$  and  $\sigma_n$



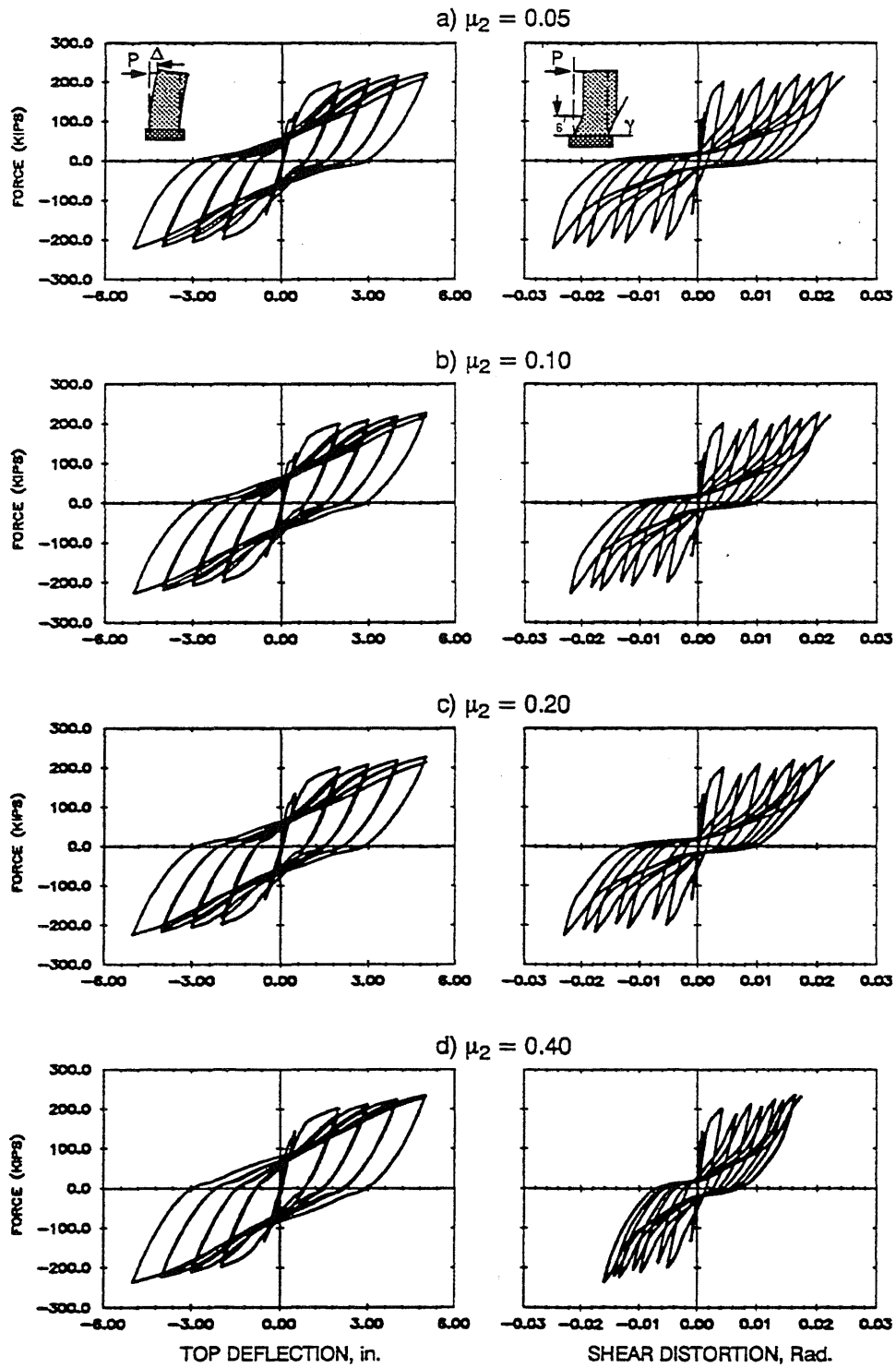


Fig. 6.17 Sensitivity of the Calculated Response of Wall B7 to the Choice of  $\mu_2$



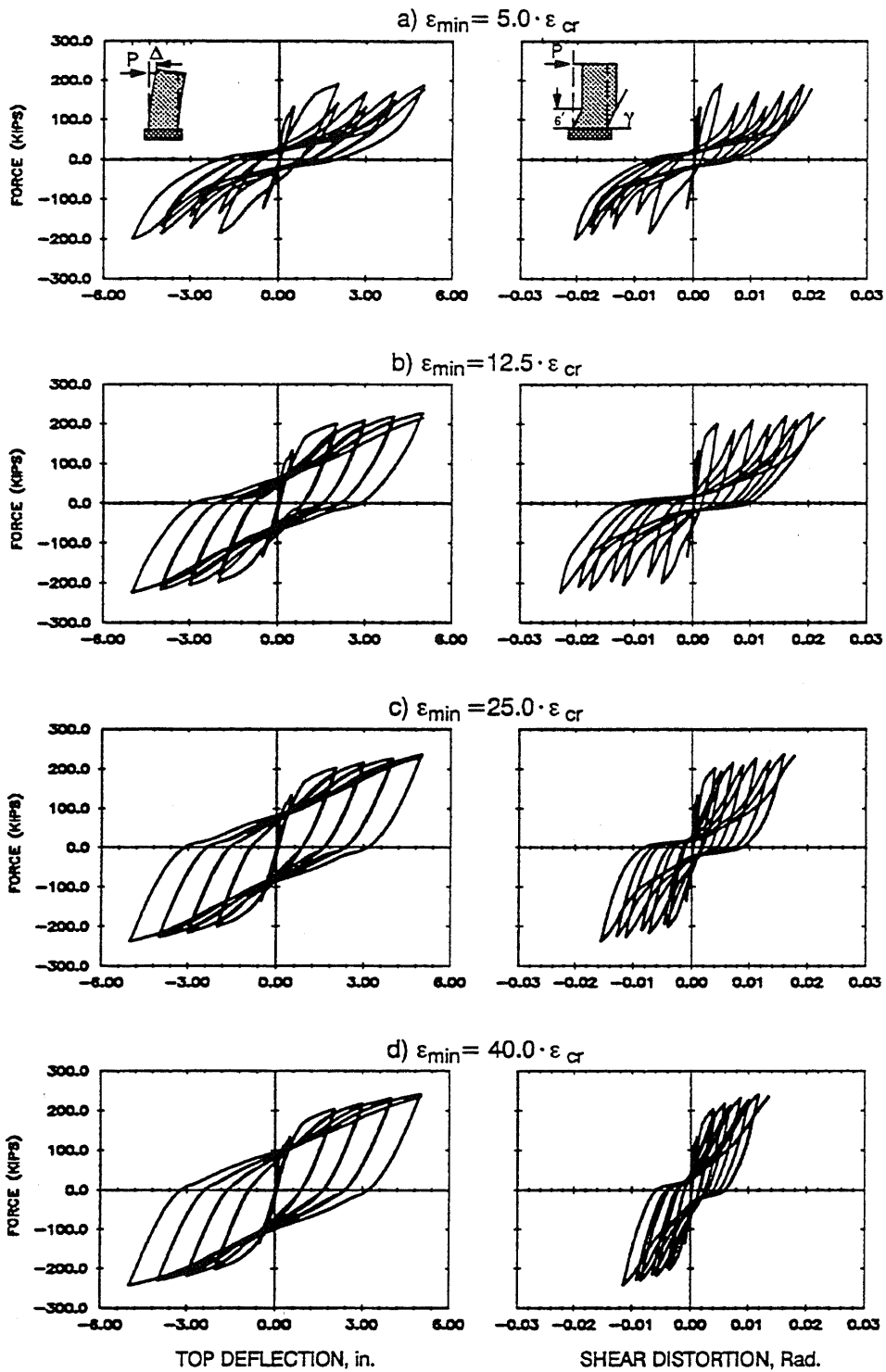


Fig. 6.18 Sensitivity of the Calculated Response of Wall B7 to the Choice of  $\epsilon_{min}$

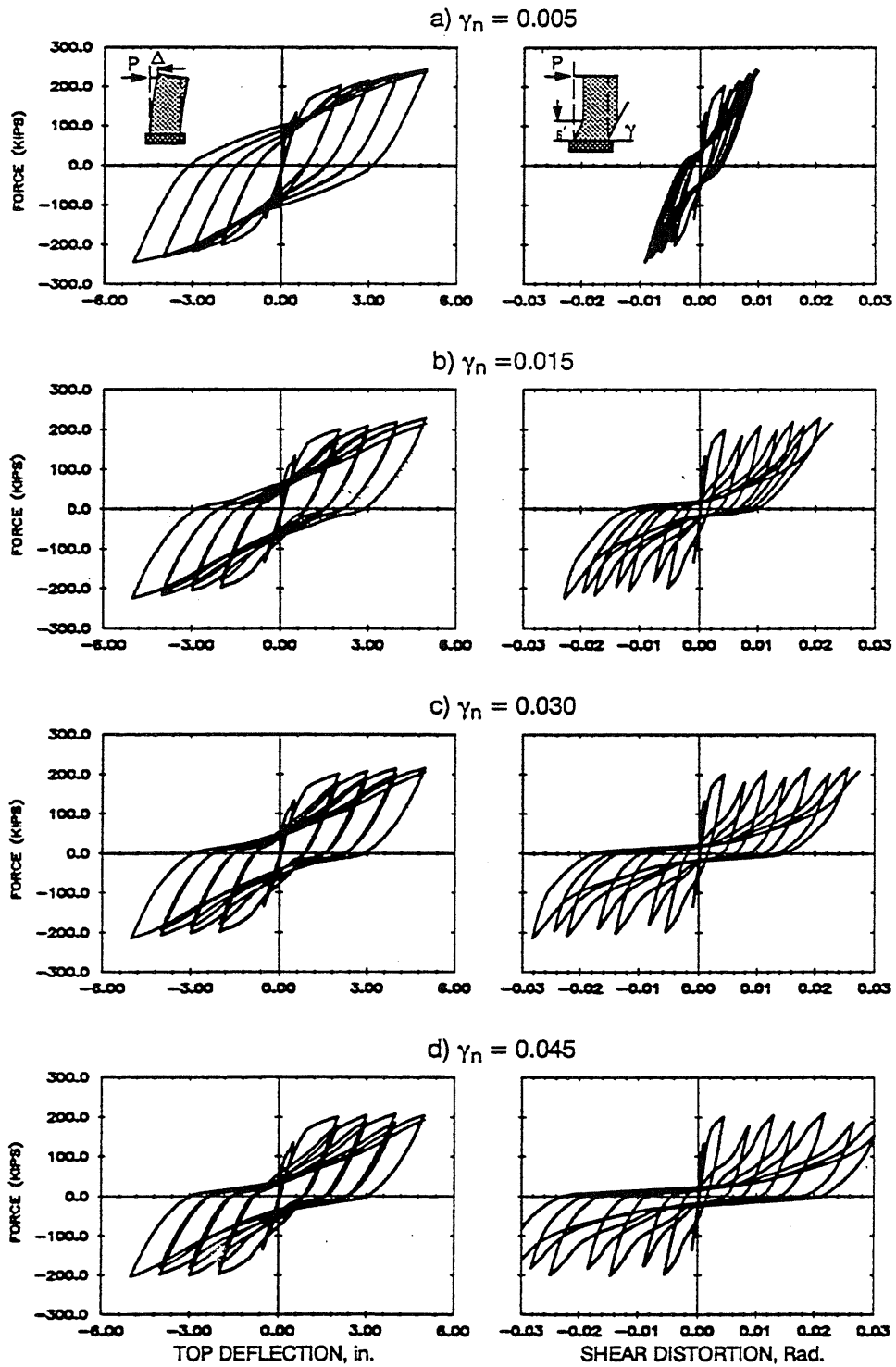


Fig. 6.19 Sensitivity of the Calculated Response of Wall B7 to the Choice of  $\gamma_n$

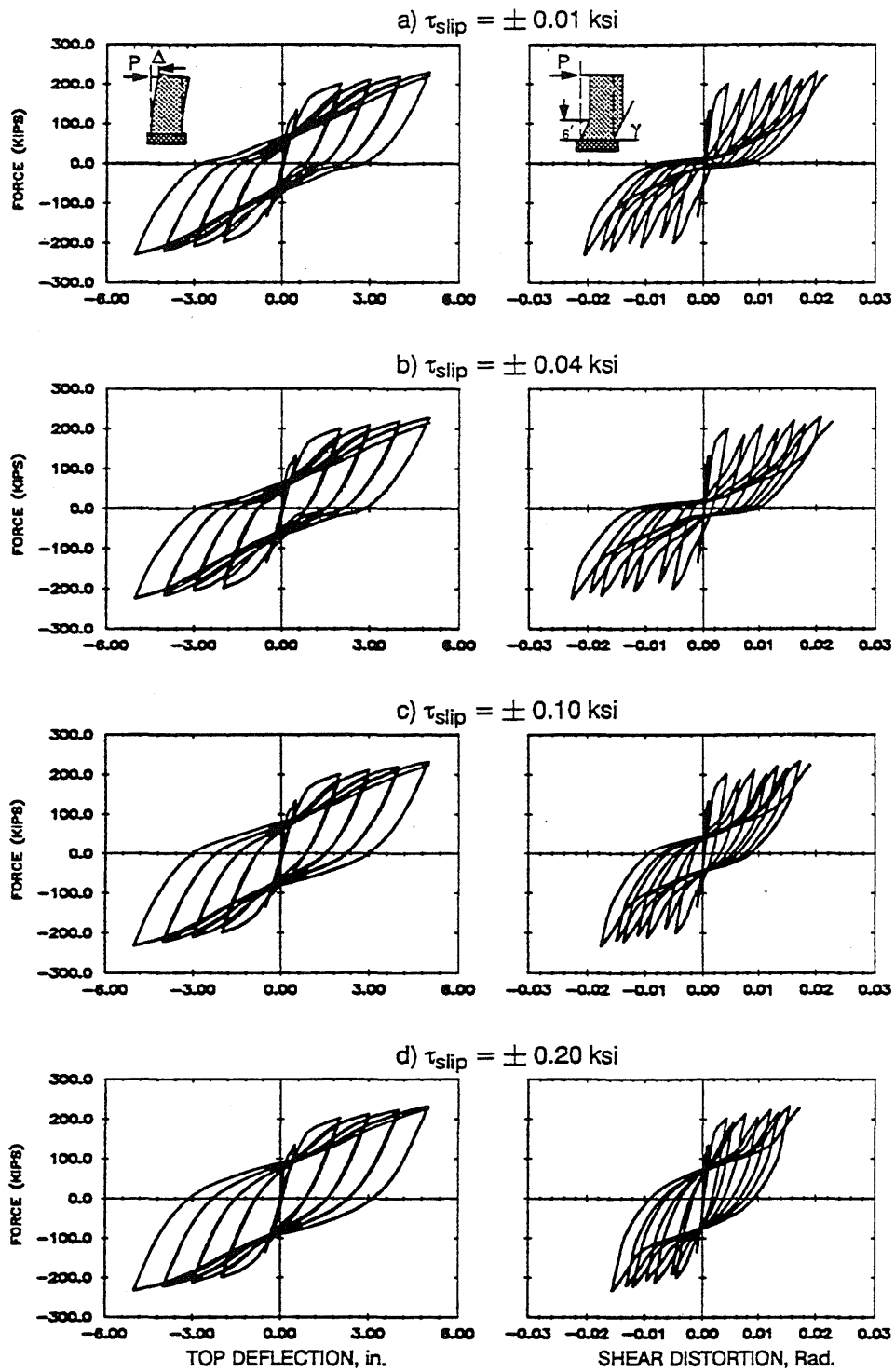


Fig. 6.20 Sensitivity of the Calculated Response of Wall B7 to the Choice of  $\tau_{slip}$

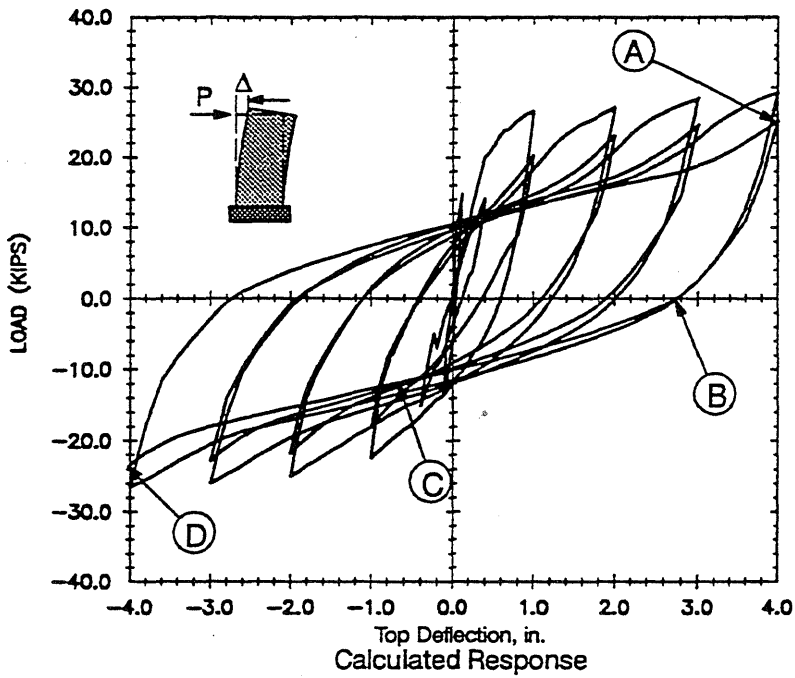
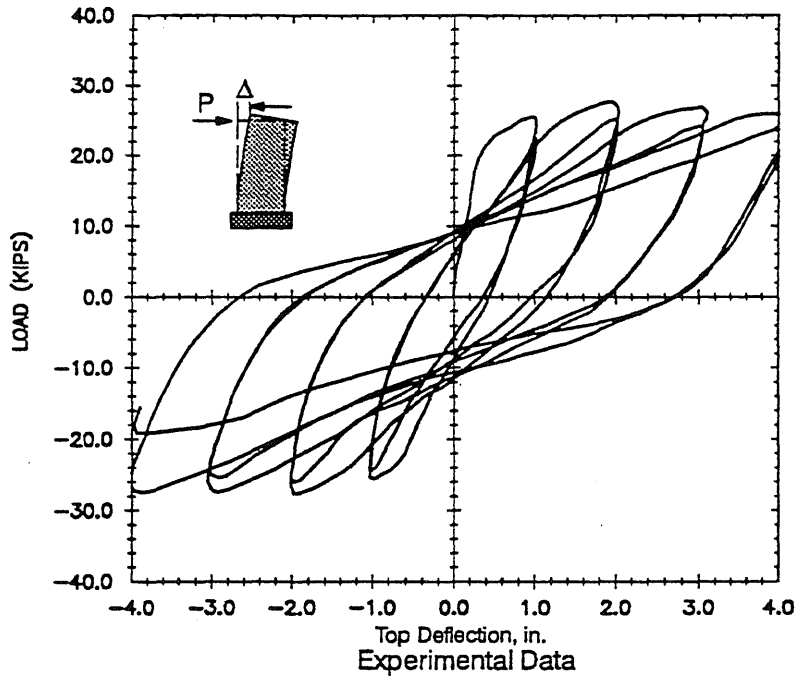


Fig. 6.21 Load vs. Deflection Curve for Wall R1

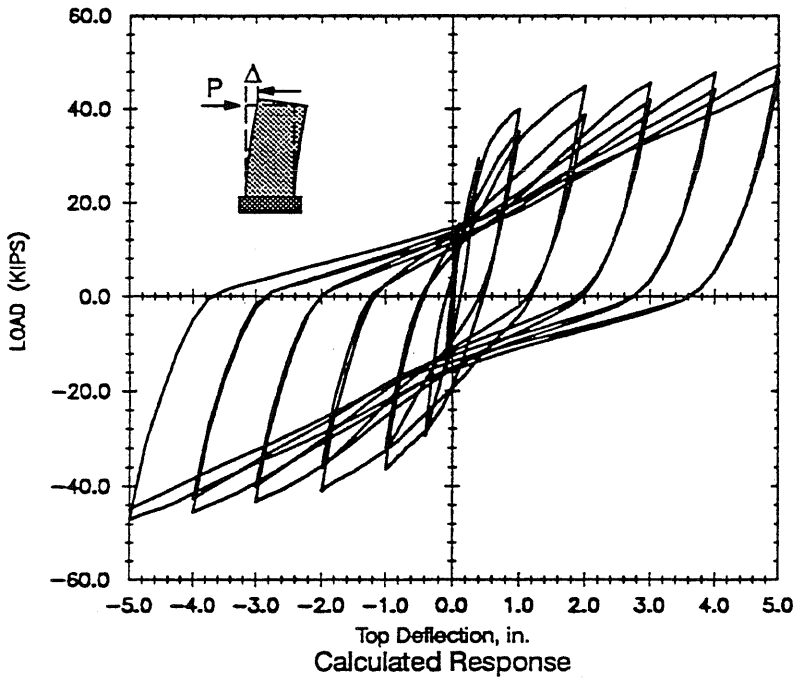
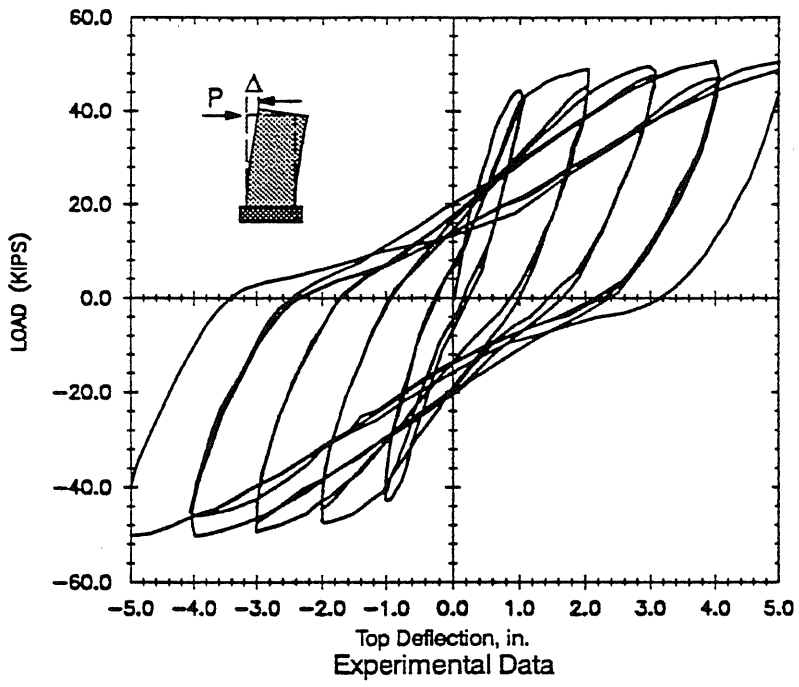


Fig. 6.22 Load vs. Deflection Curve for Wall R2

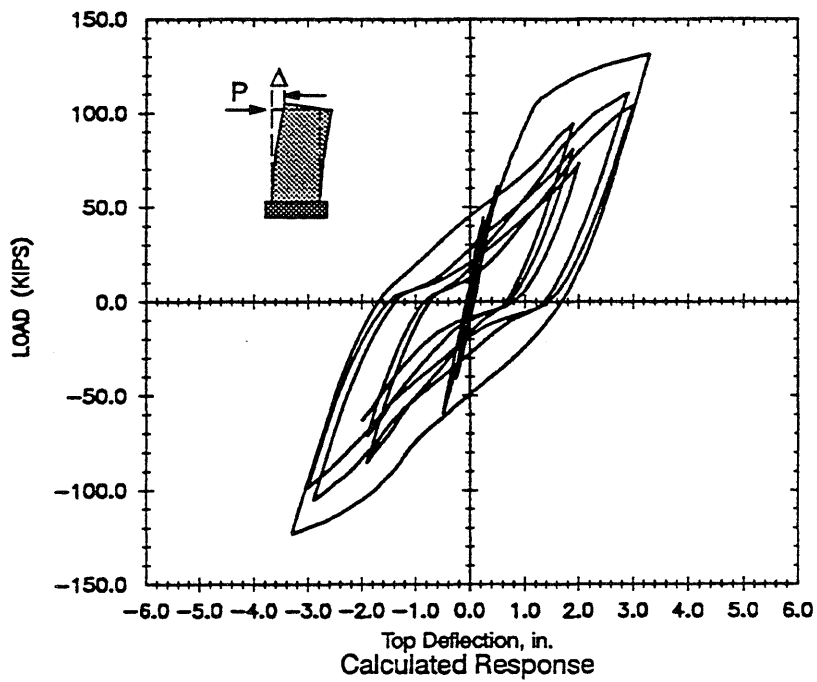
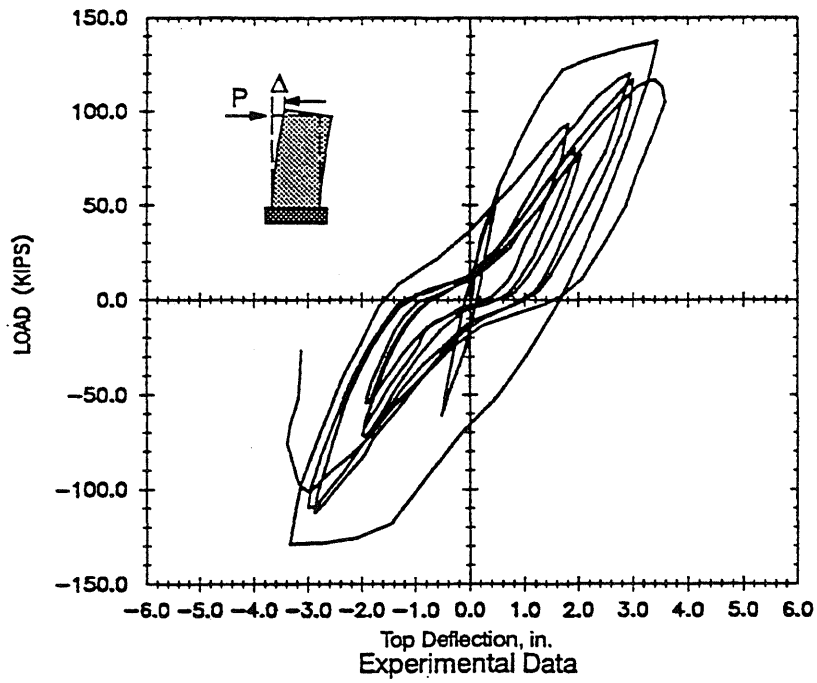


Fig. 6.23 Load vs. Deflection Curve for Wall R3

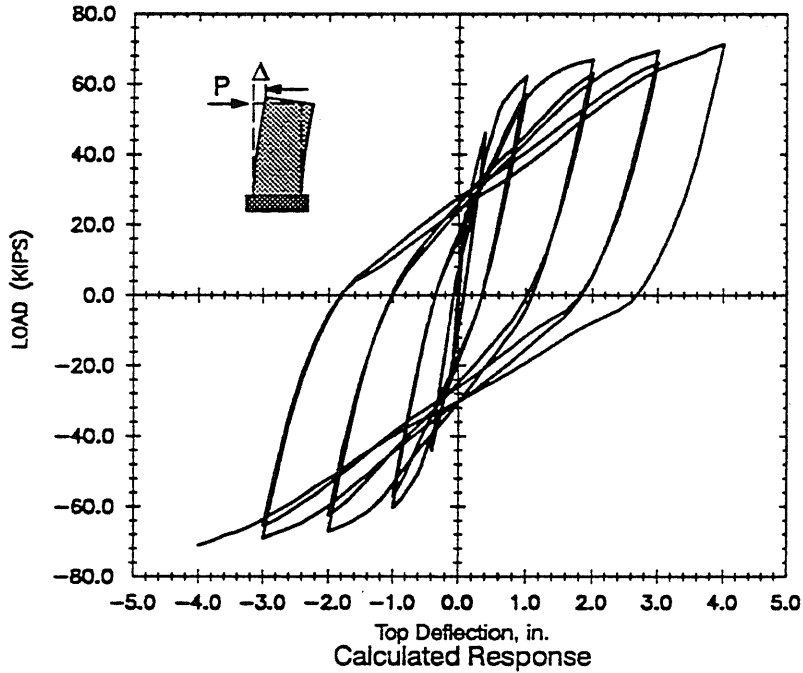
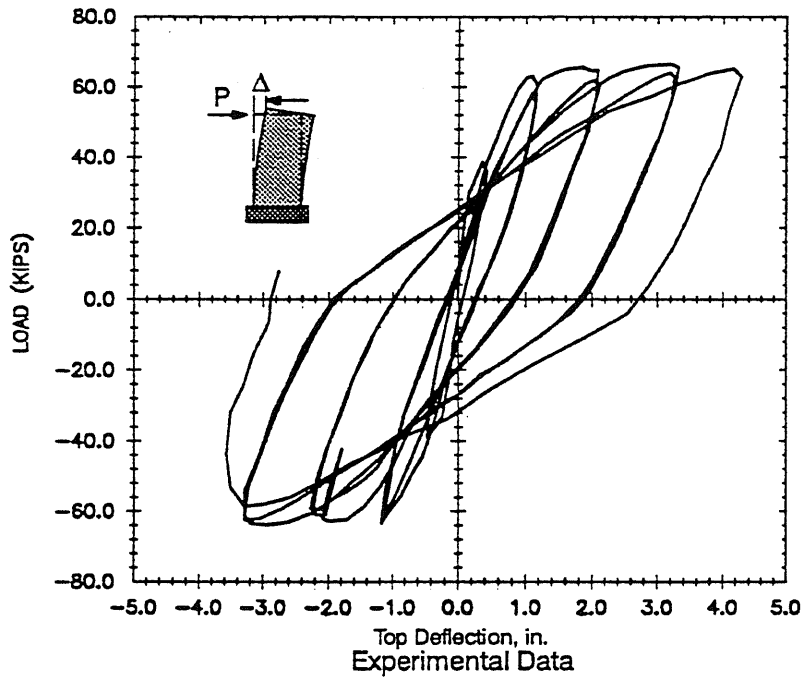


Fig. 6.24 Load vs. Deflection Curve for Wall R4

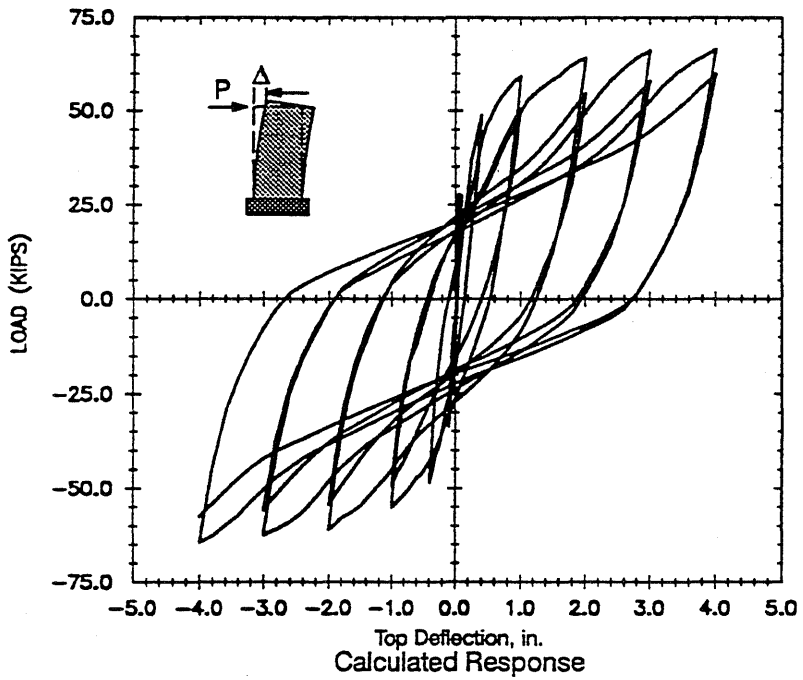
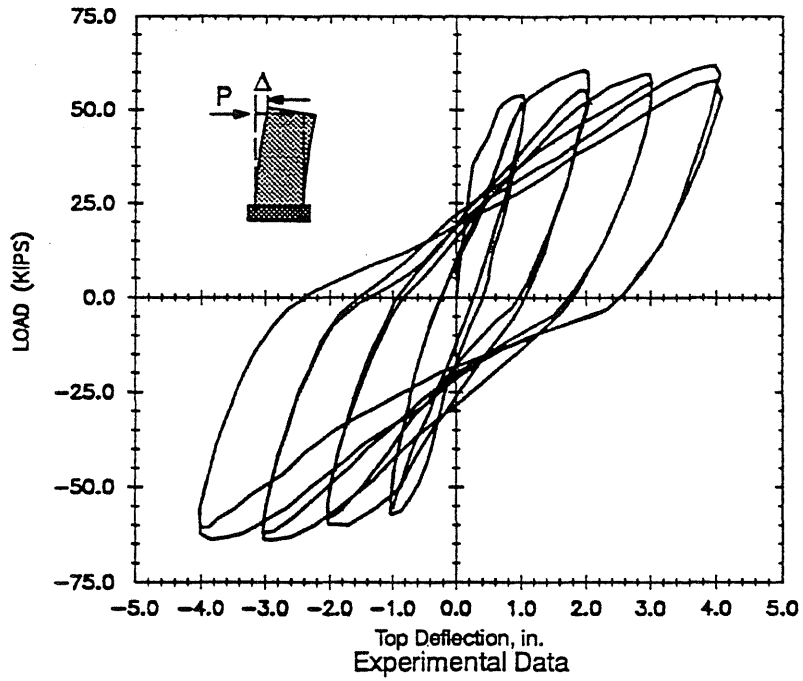


Fig. 6.25 Load vs. Deflection Curve for Wall B1



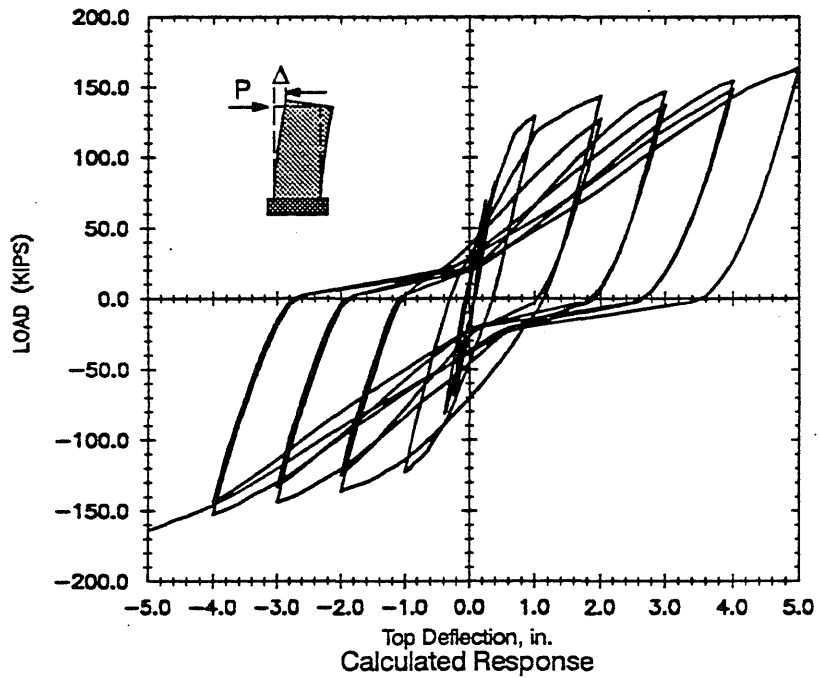
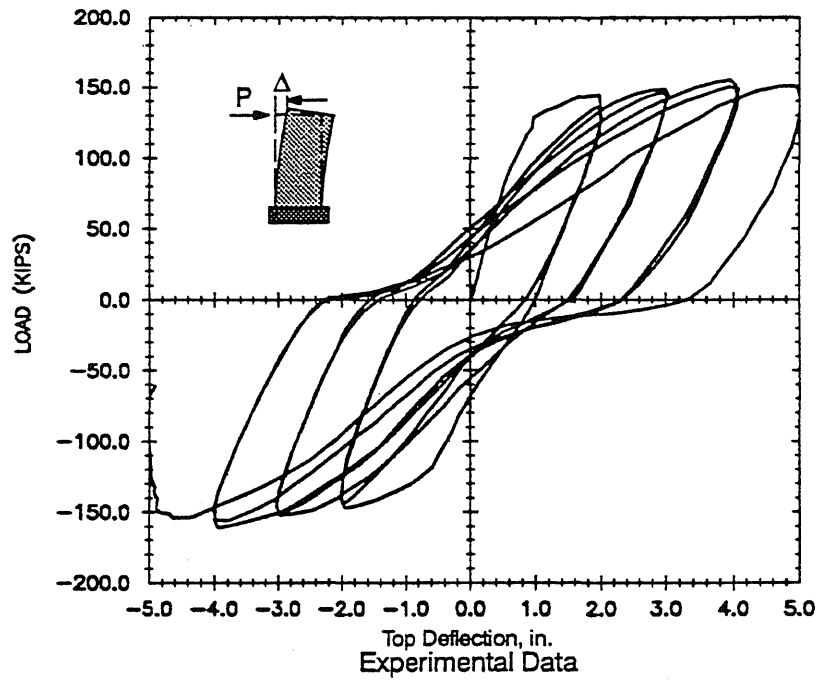


Fig. 6.26 Load vs. Deflection Curve for Wall B2

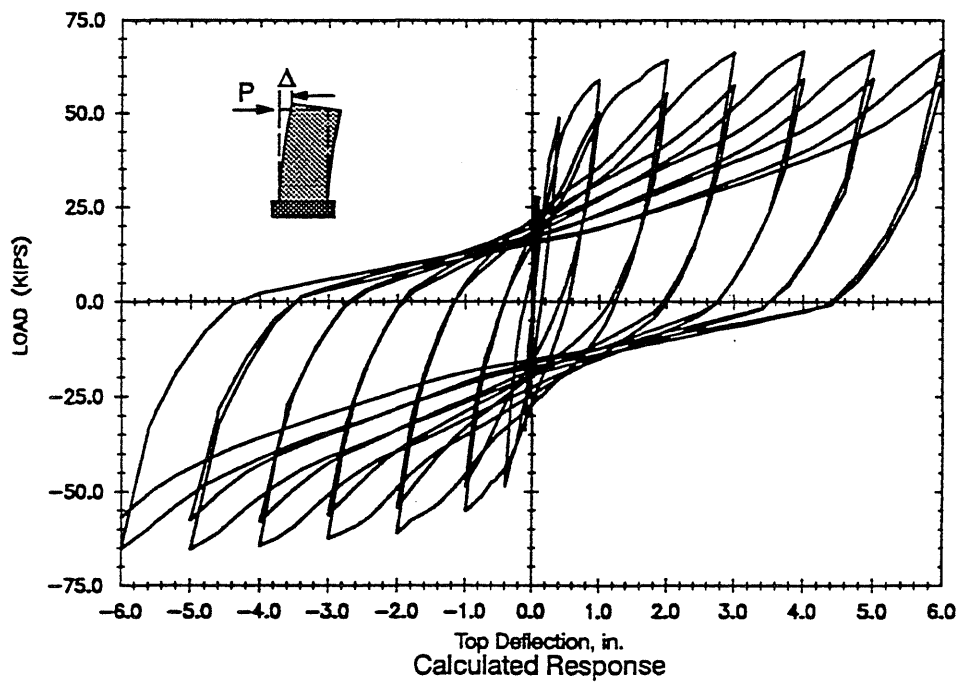
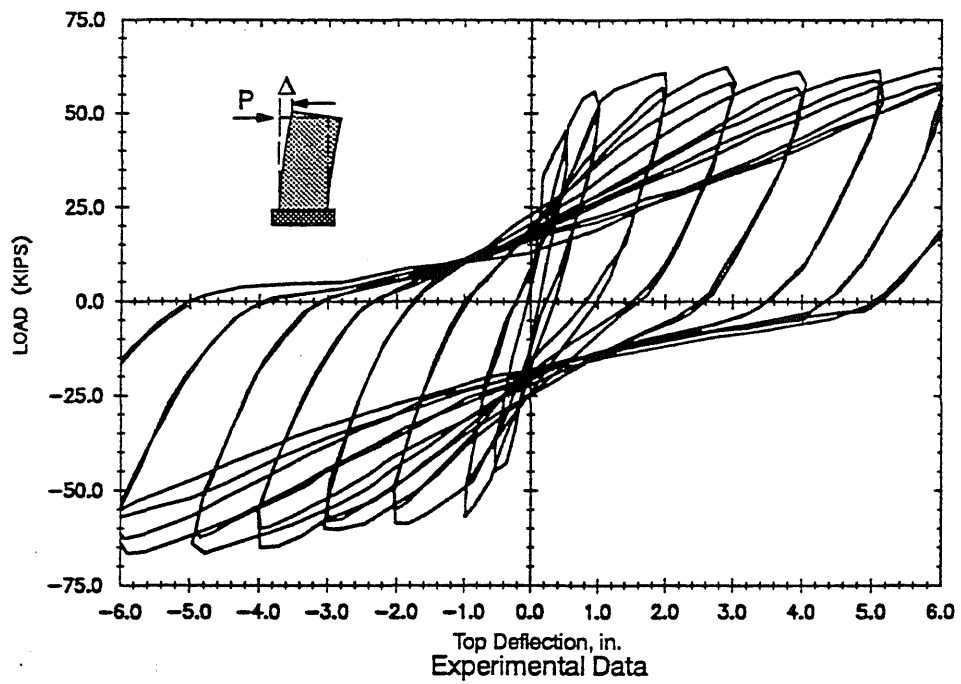


Fig. 6.27 Load vs. Deflection Curve for Wall B3

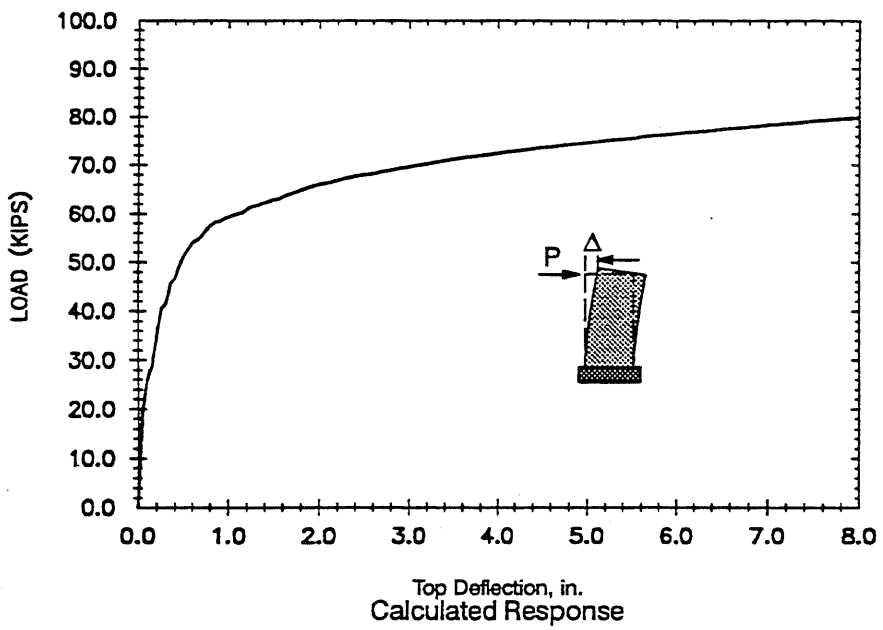
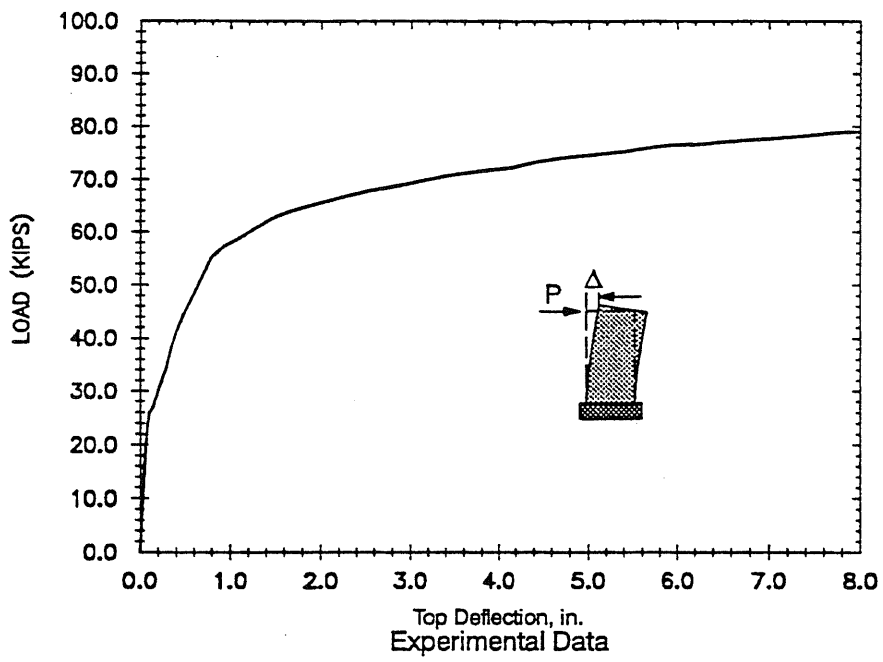


Fig. 6.28 Load vs. Deflection Curve for Wall B4

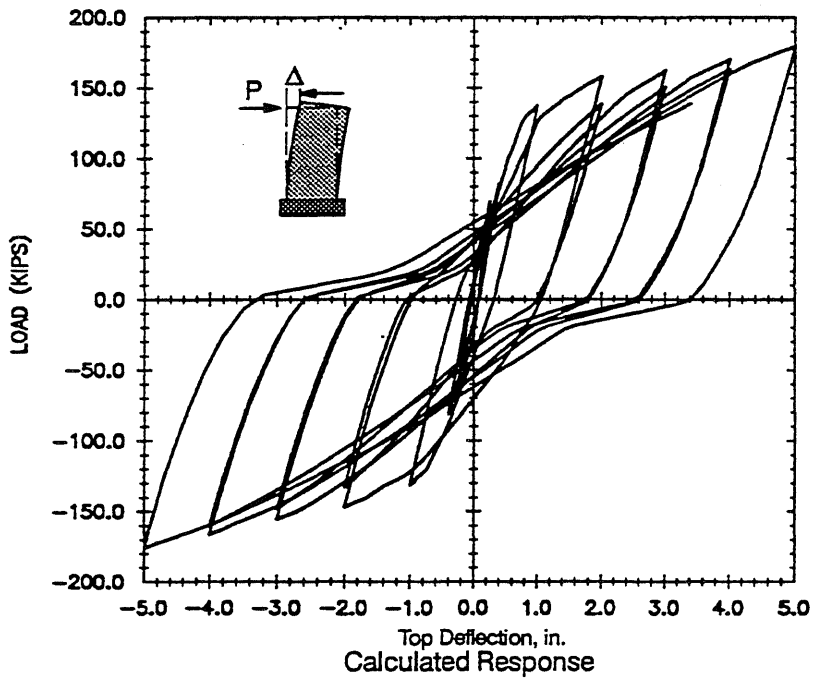
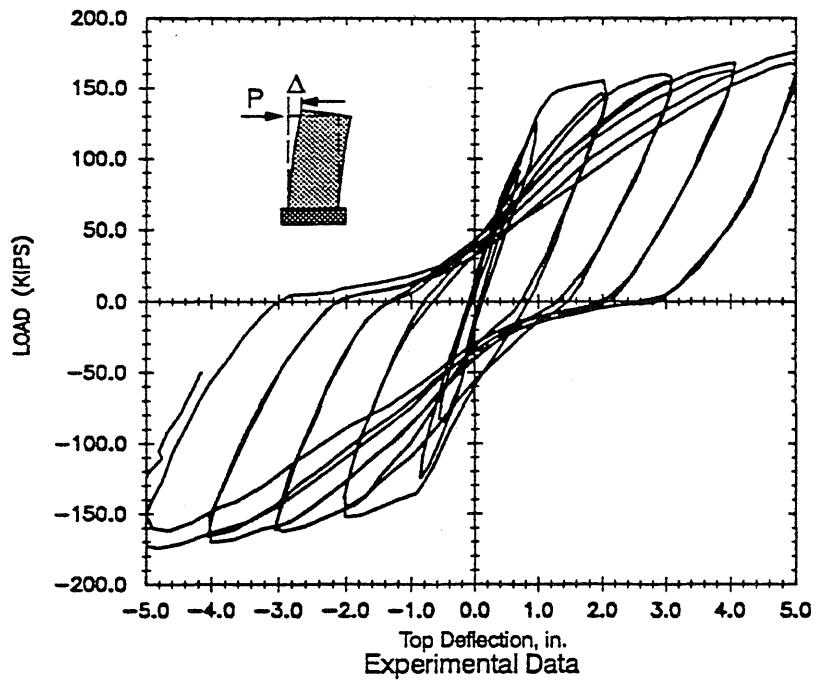


Fig. 6.29 Load vs. Deflection Curve for Wall B5

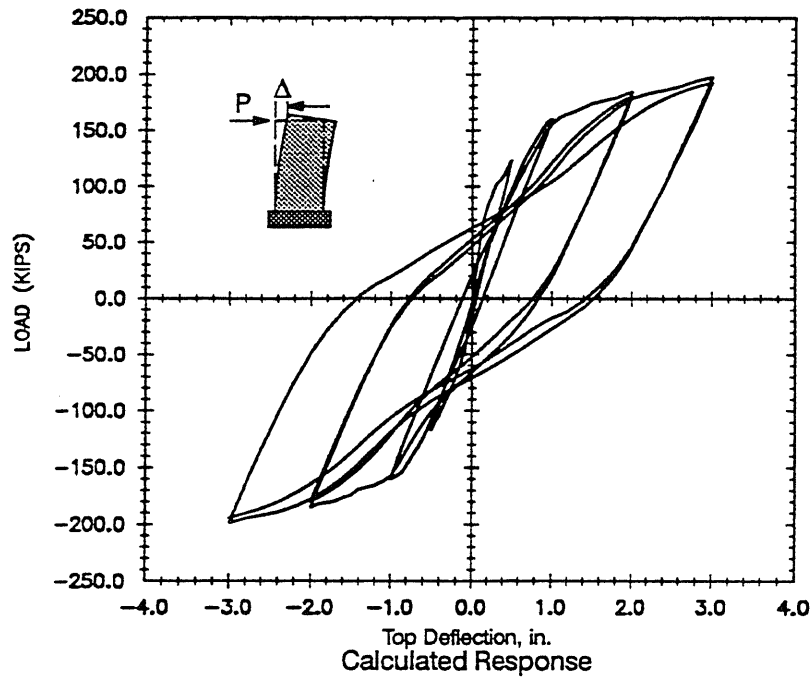
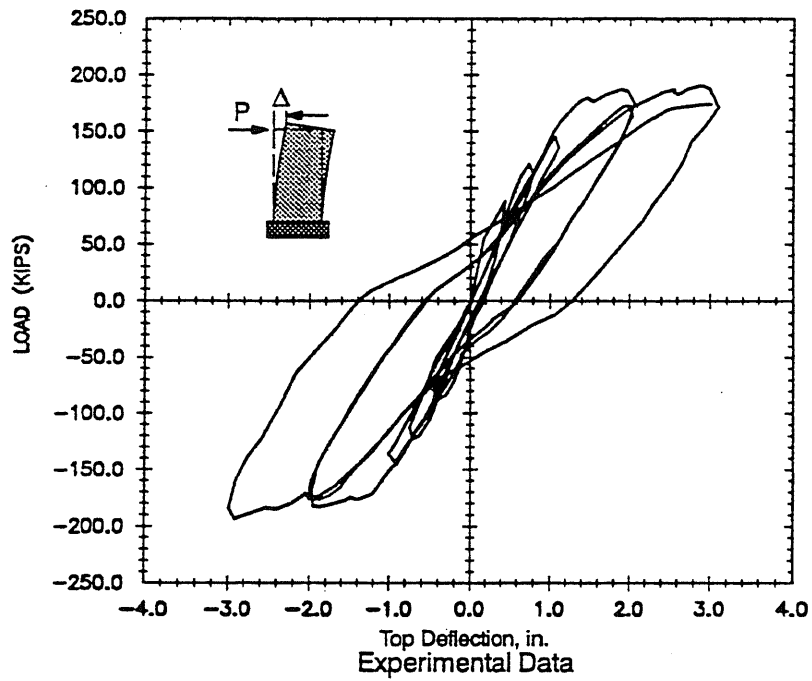


Fig. 6.30 Load vs. Deflection Curve for Wall B6

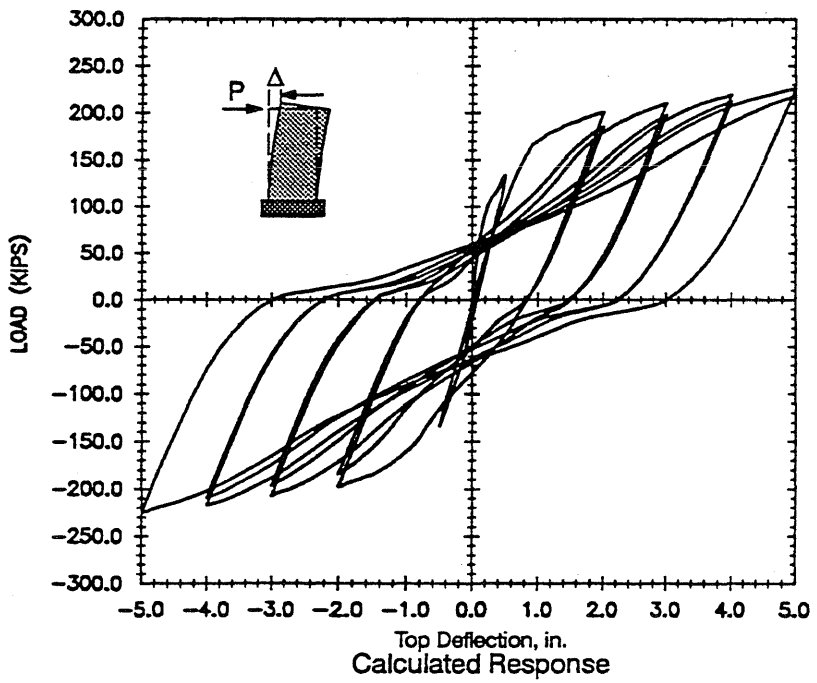
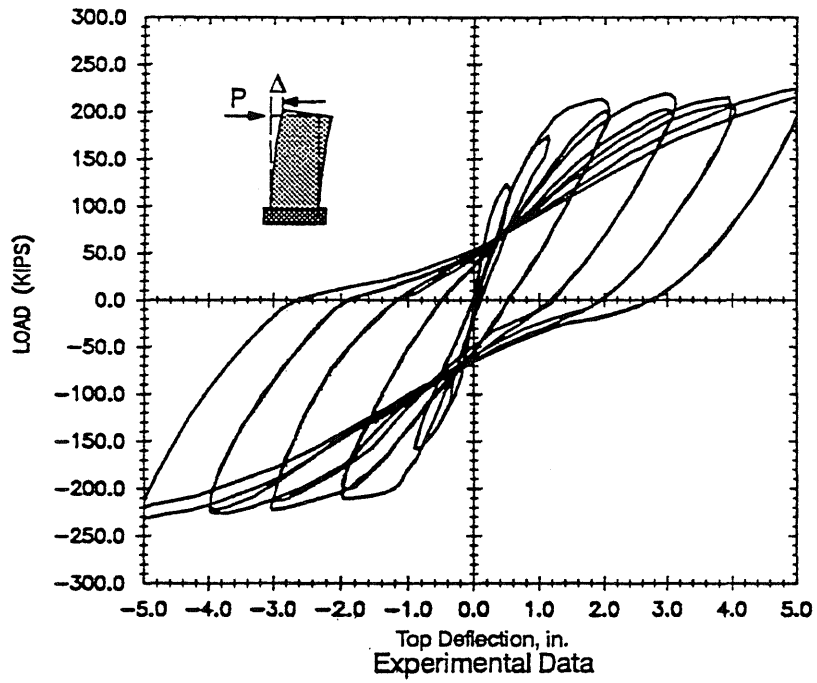


Fig. 6.31 Load vs. Deflection Curve for Wall B7

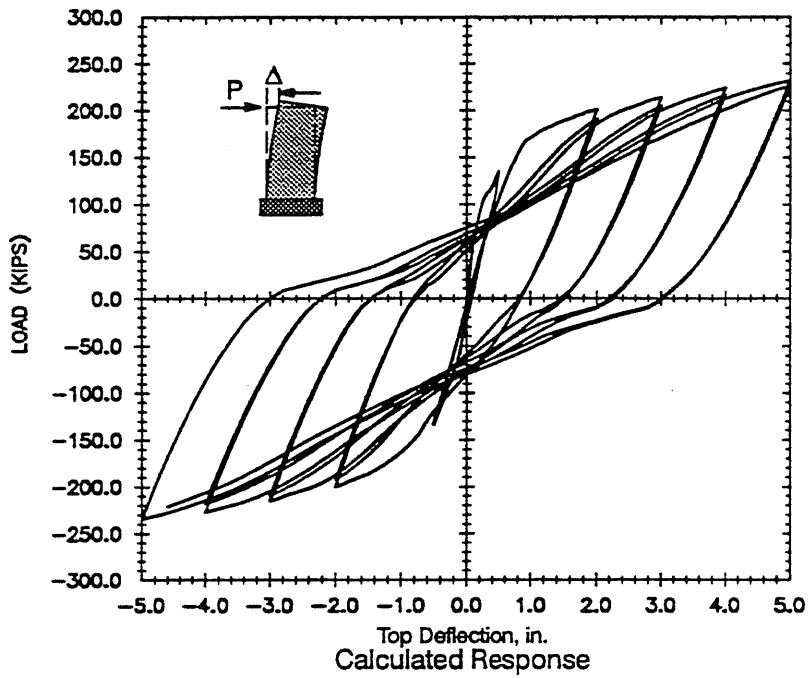
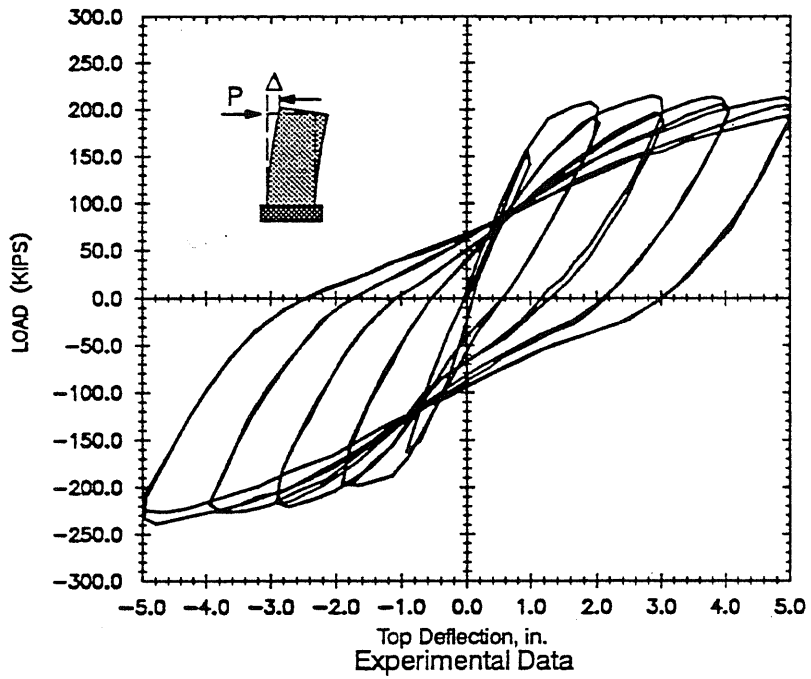


Fig. 6.32 Load vs. Deflection Curve for Wall B8

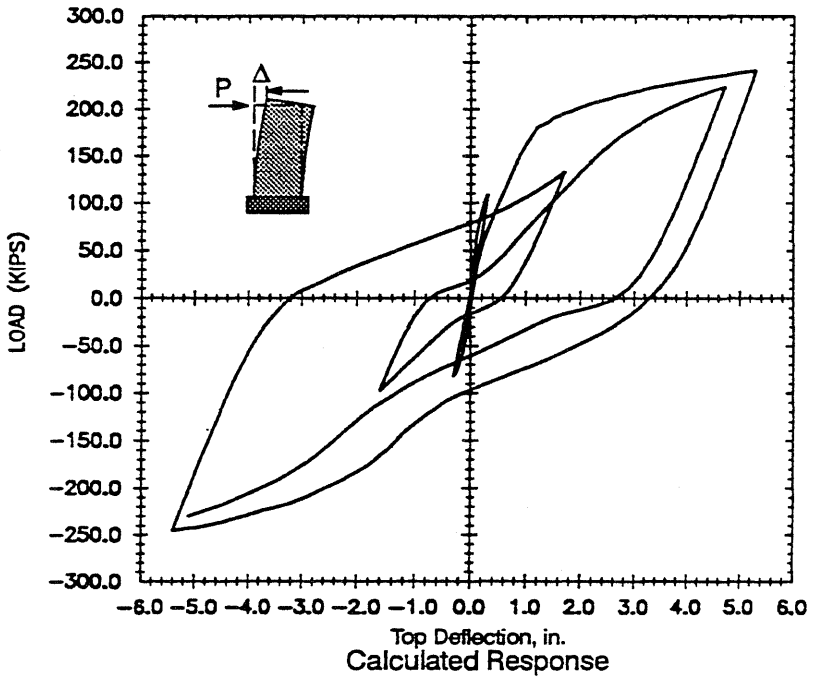
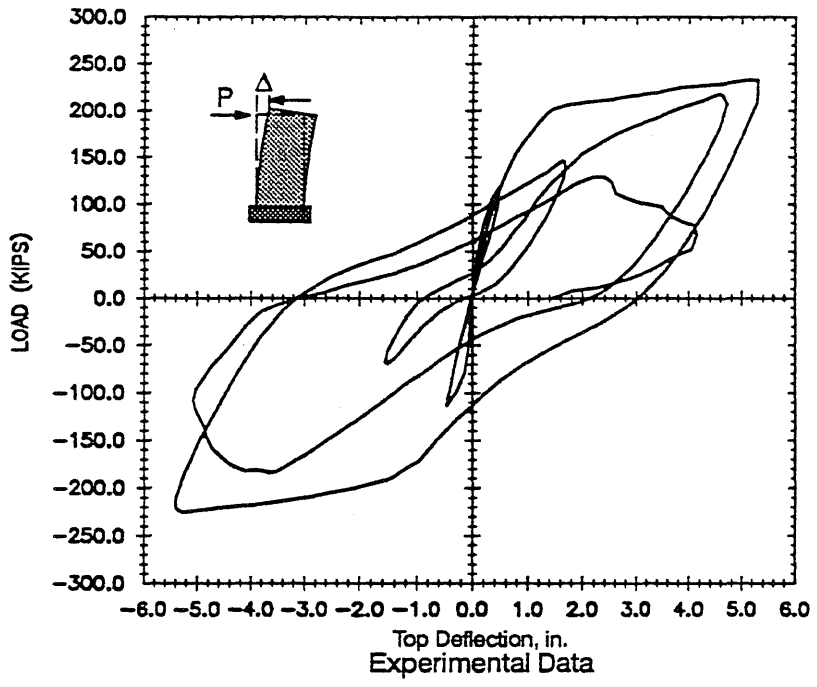
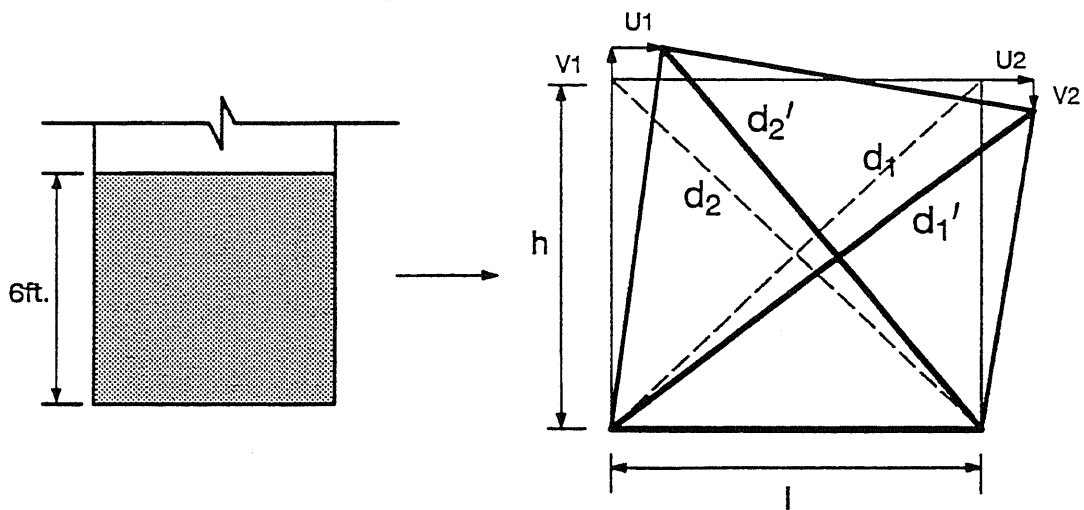


Fig. 6.33 Load vs. Deflection Curve for Wall B9





$$d_1' = \sqrt{(h + V_2)^2 + (l + U_2)^2}$$

$$d_2' = \sqrt{(h + V_1)^2 + (l - U_1)^2}$$

$$\gamma_{Avg} = \frac{(d_1' - d_1)d_1 - (d_2' - d_2)d_2}{2 h l}$$

Fig. 6.34 Estimation of Shear Distortion

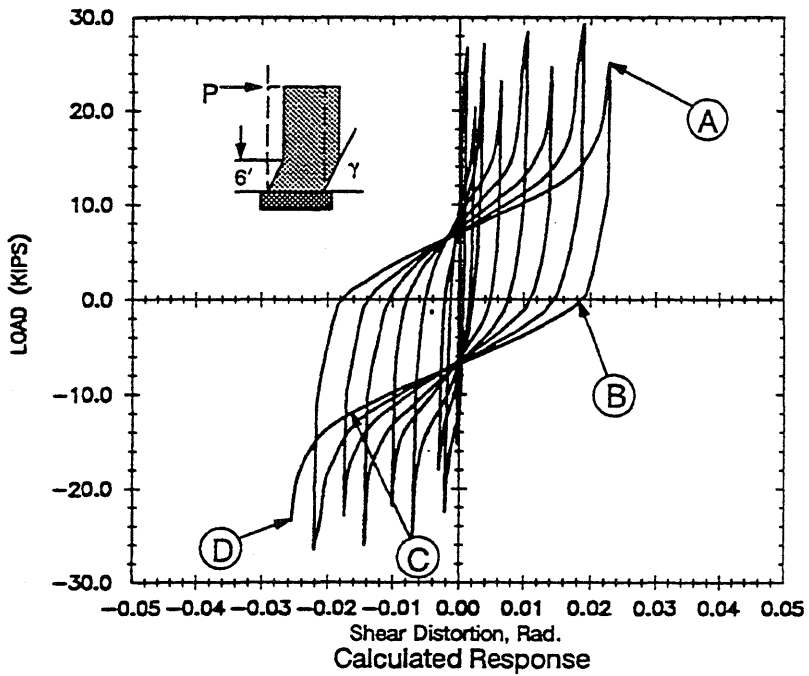
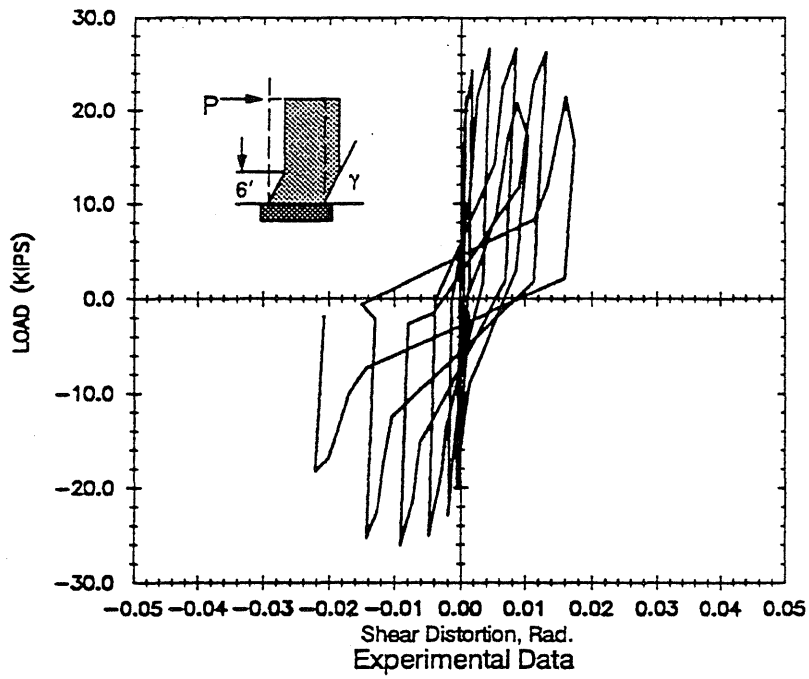


Fig. 6.35 Load vs. Shear Distortion at 6-ft Level: Wall R1

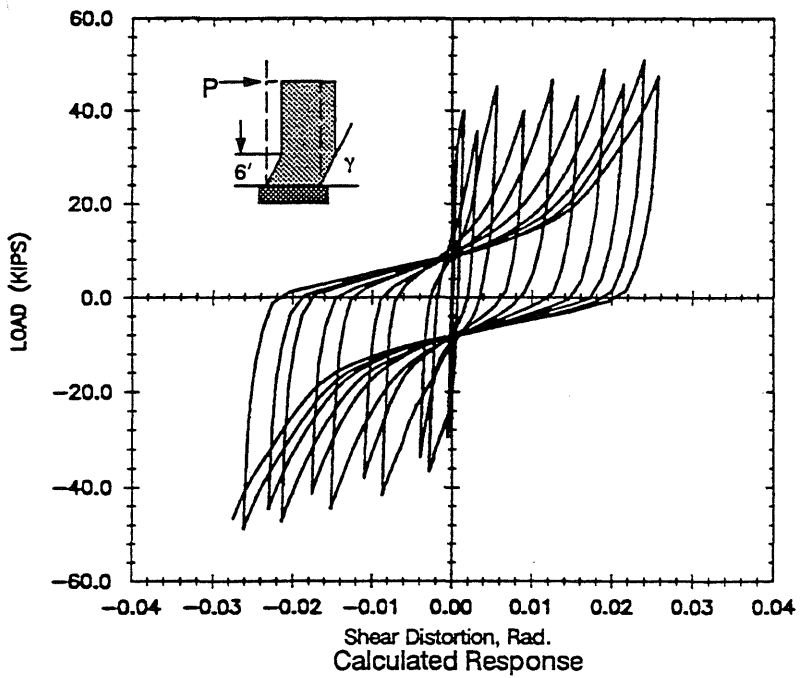
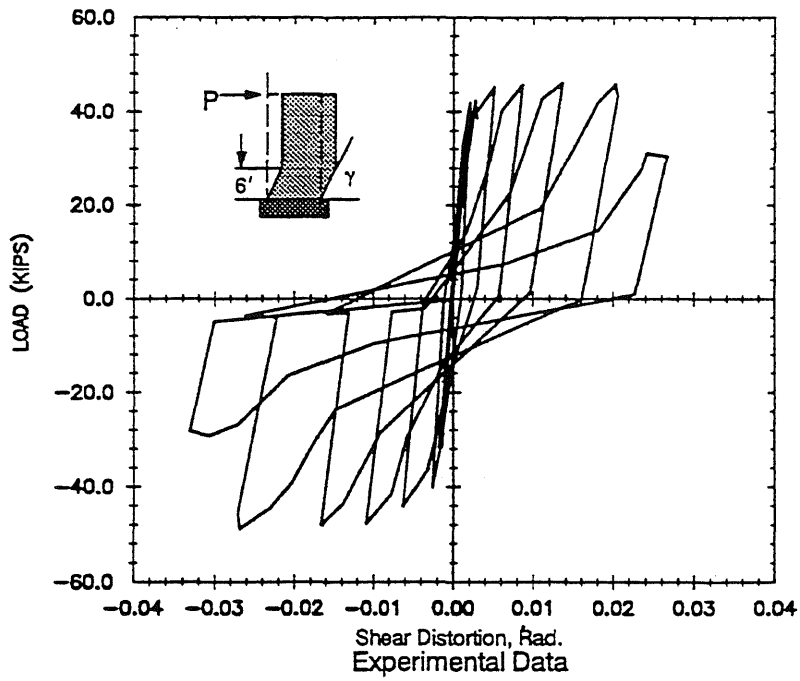


Fig. 6.36 Load vs. Shear Distortion at 6-ft Level: Wall R2

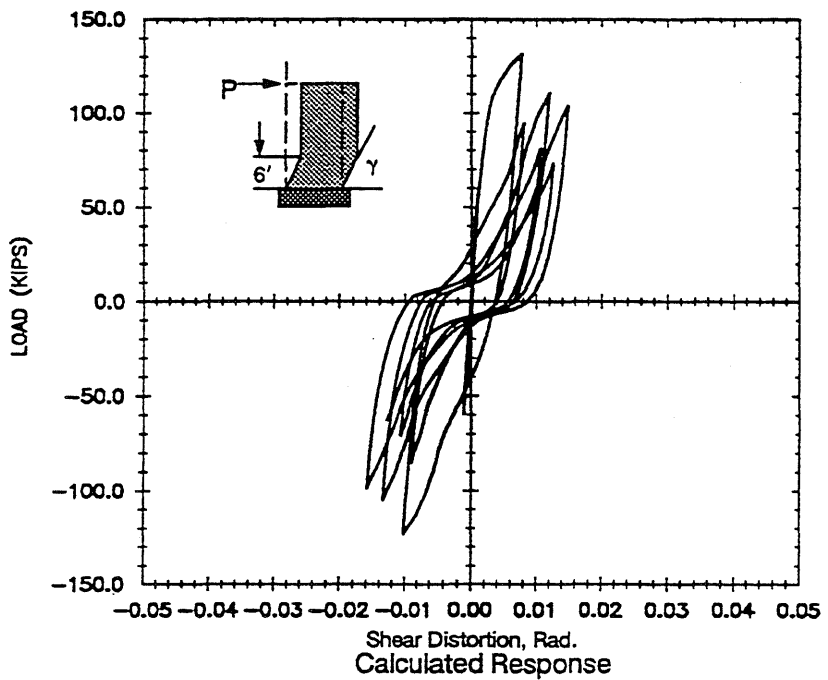
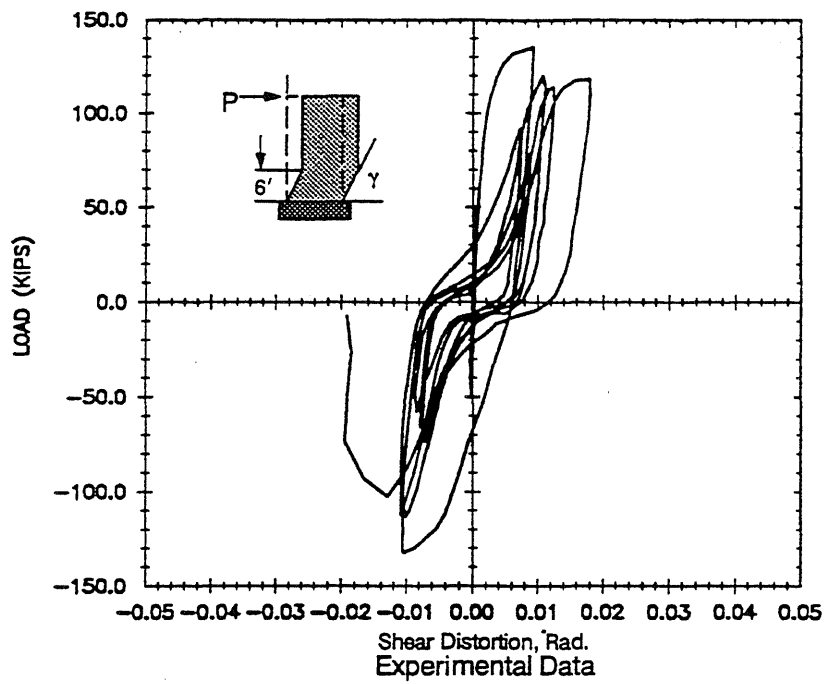


Fig. 6.37 Load vs. Shear Distortion at 6-ft Level: Wall R3

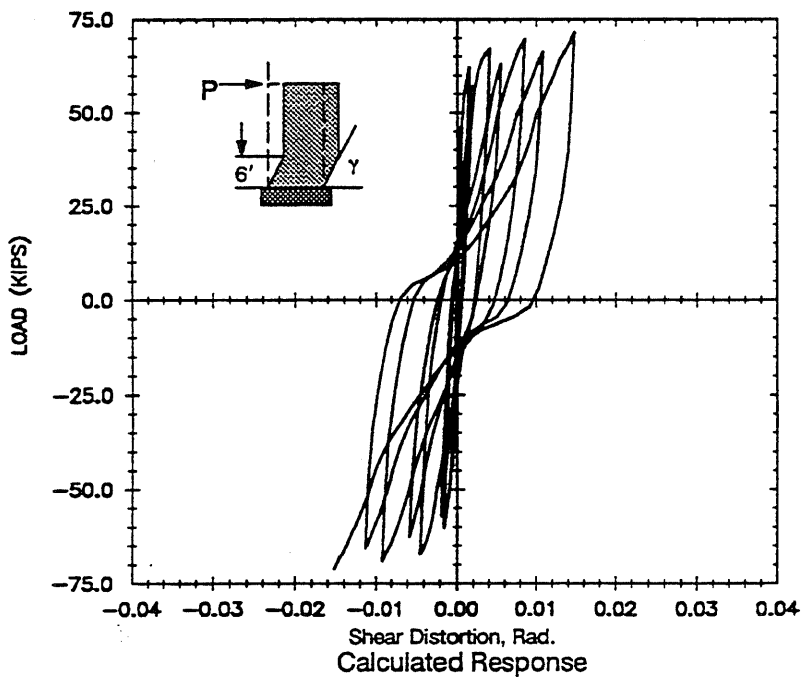
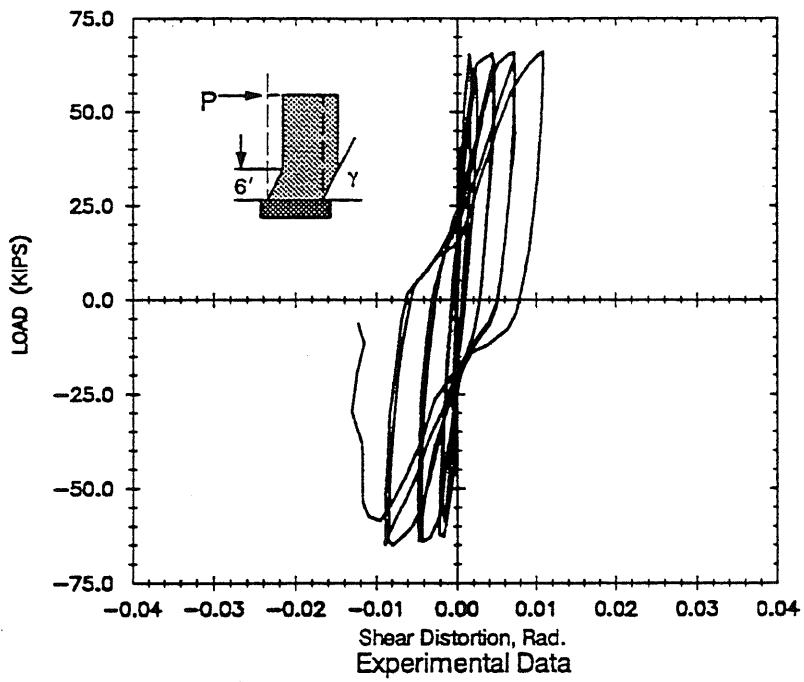


Fig. 6.38 Load vs. Shear Distortion at 6-ft Level: Wall R4

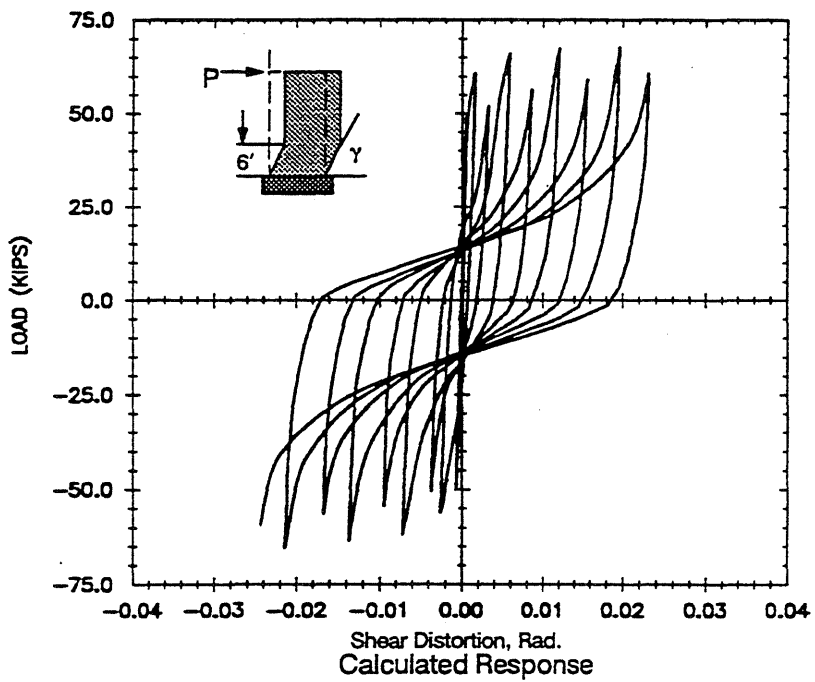
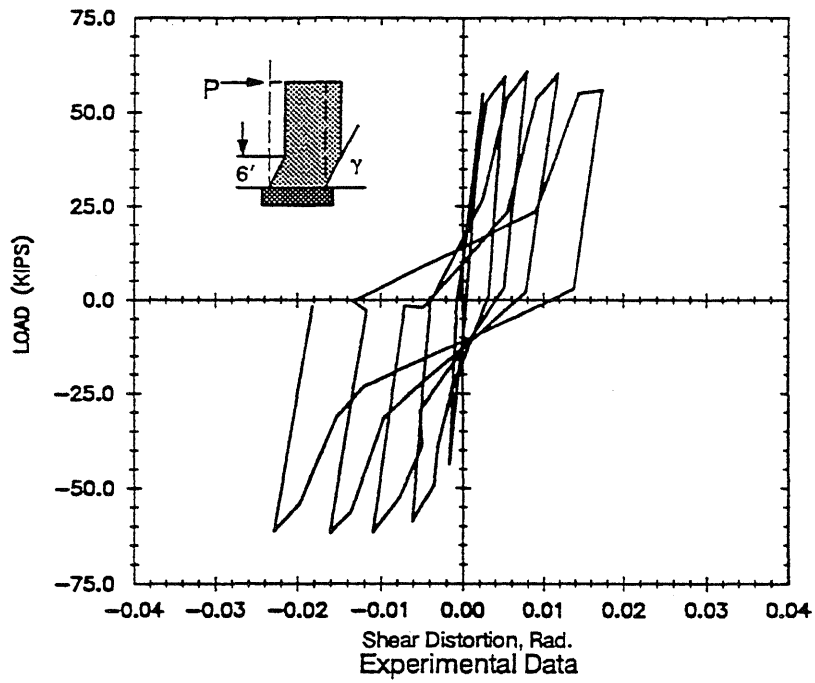


Fig. 6.39 Load vs. Shear Distortion at 6-ft Level: Wall B1

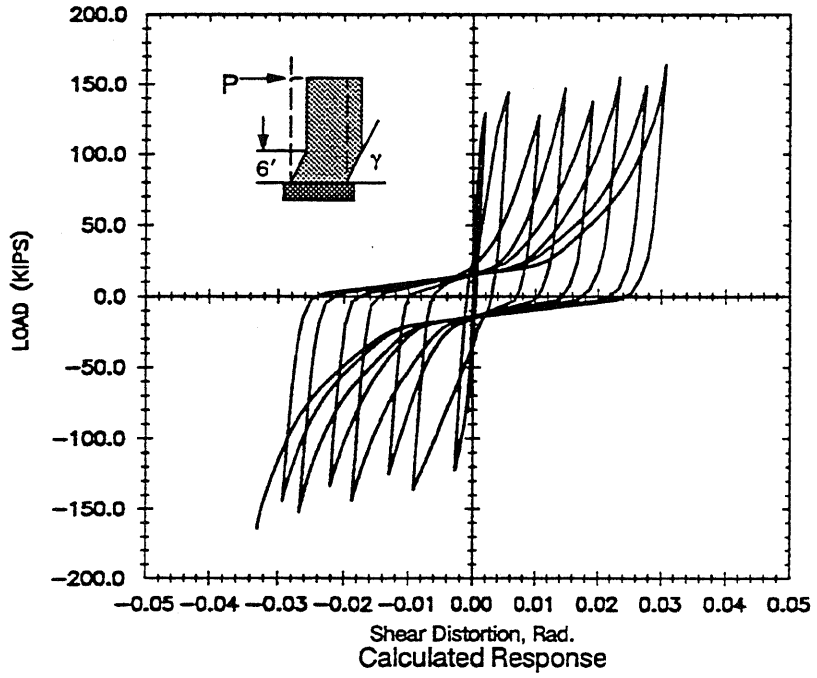
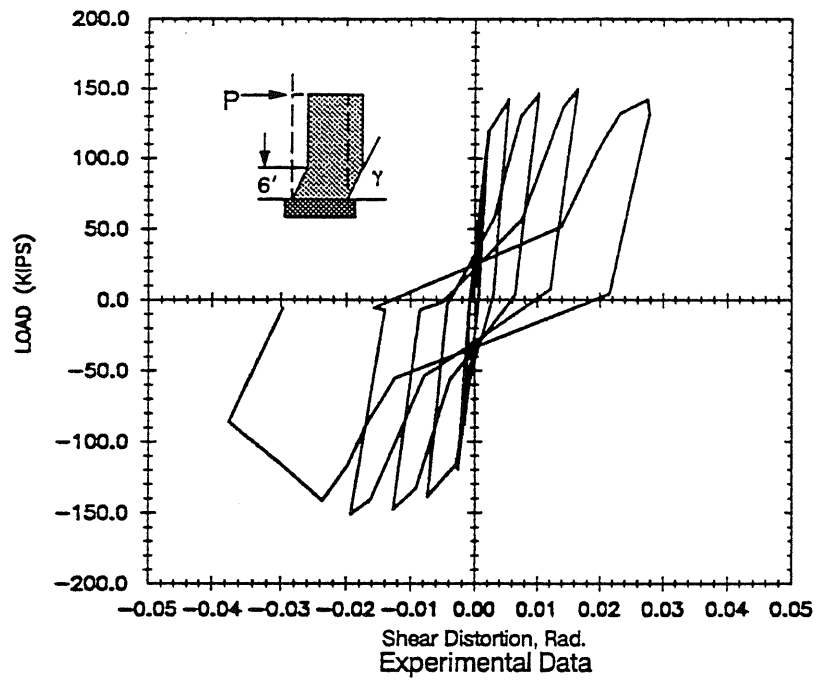


Fig. 6.40 Load vs. Shear Distortion at 6-ft Level: Wall B2

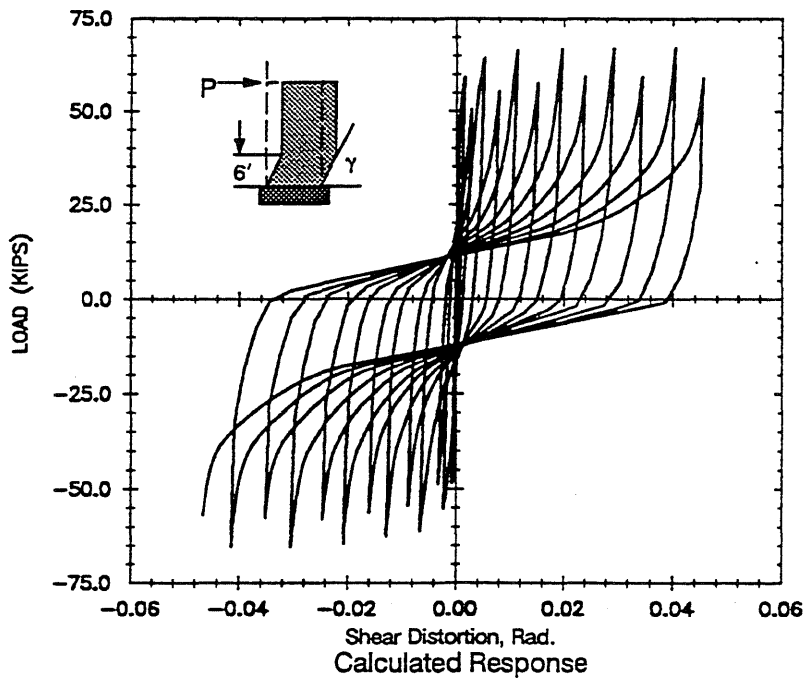
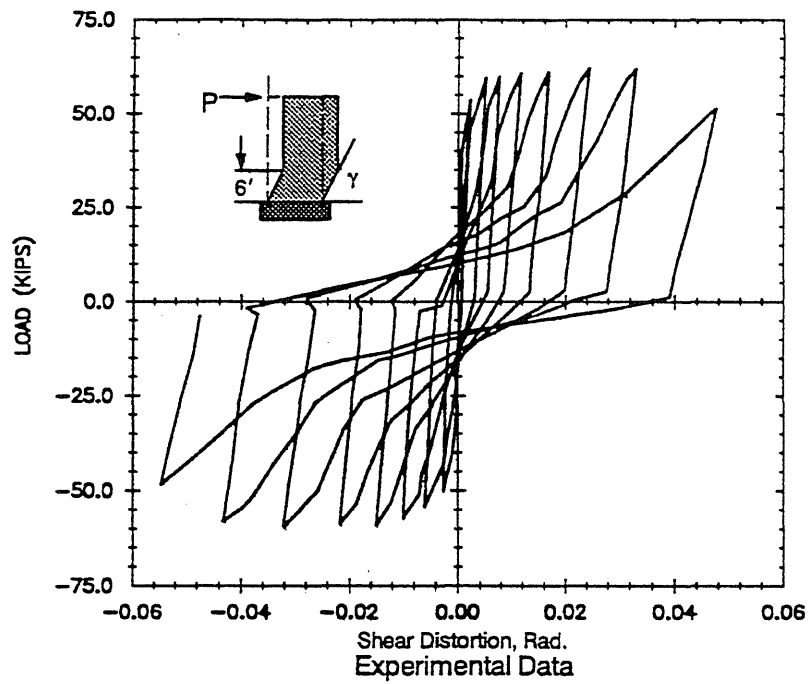


Fig. 6.41 Load vs. Shear Distortion at 6-ft Level: Wall B3



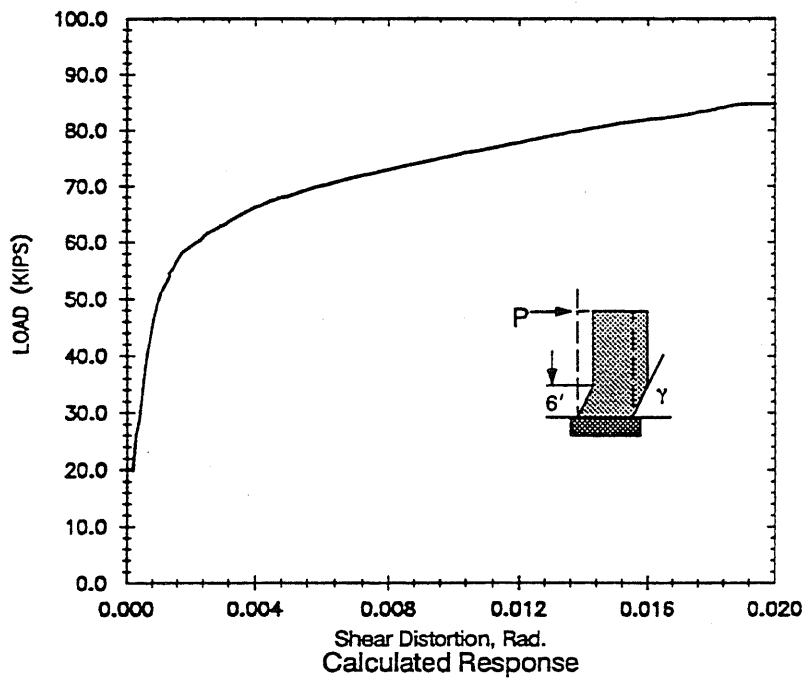
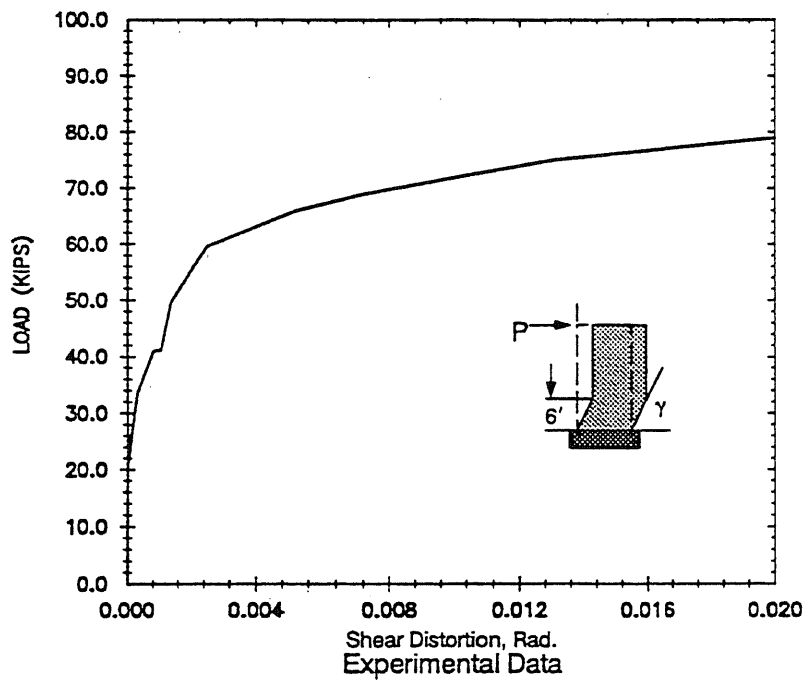


Fig. 6.42 Load vs. Shear Distortion at 6-ft Level: Wall B4

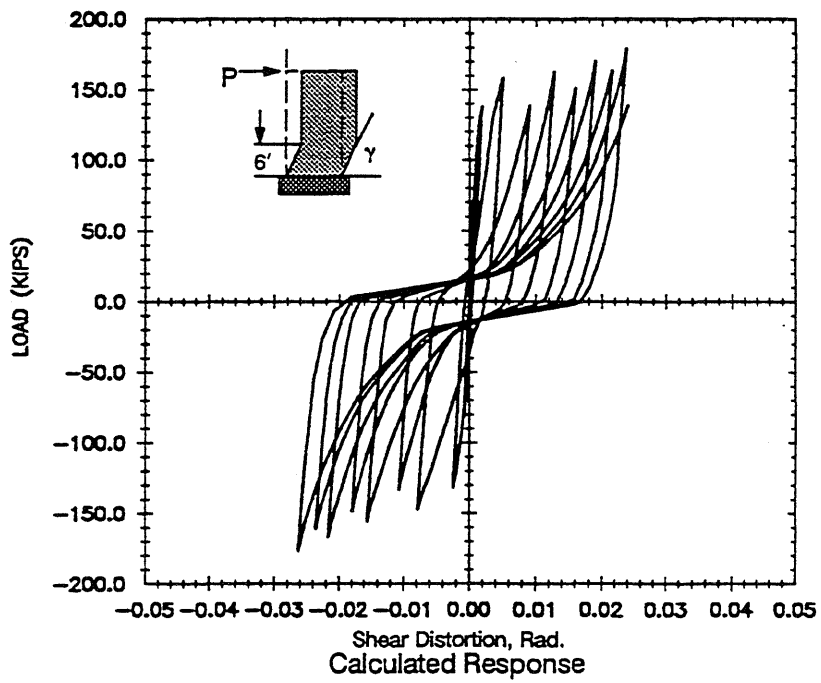
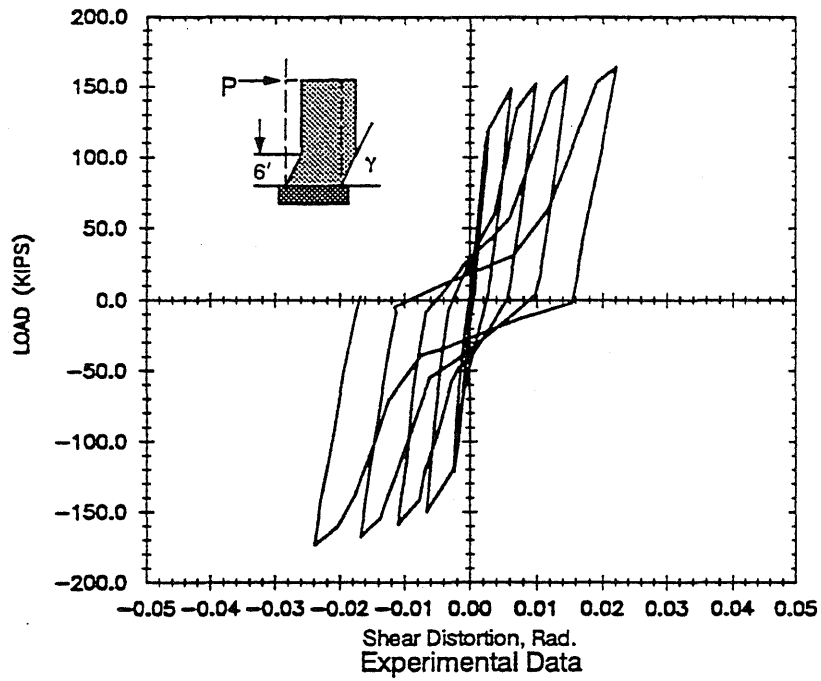


Fig. 6.43 Load vs. Shear Distortion at 6-ft Level: Wall B5

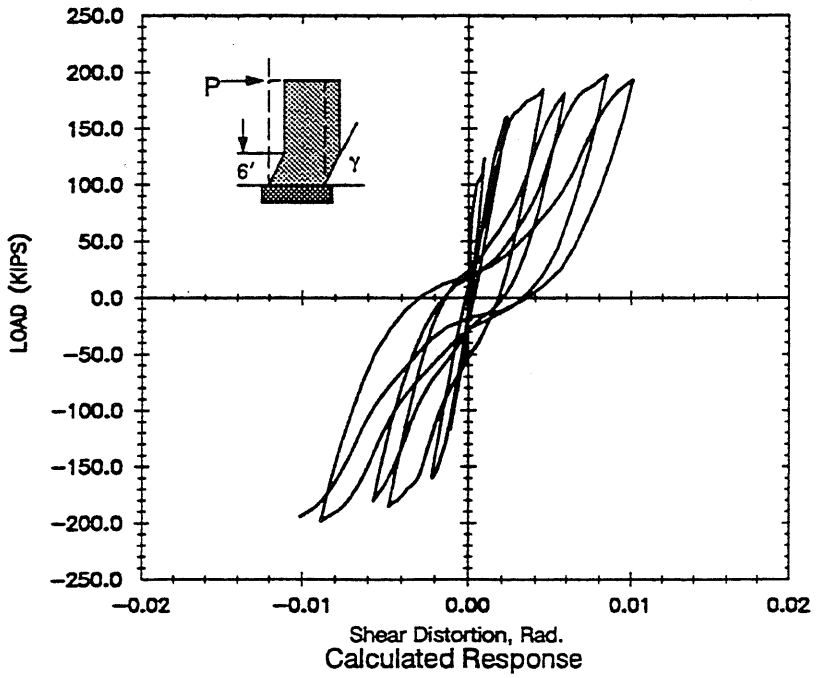
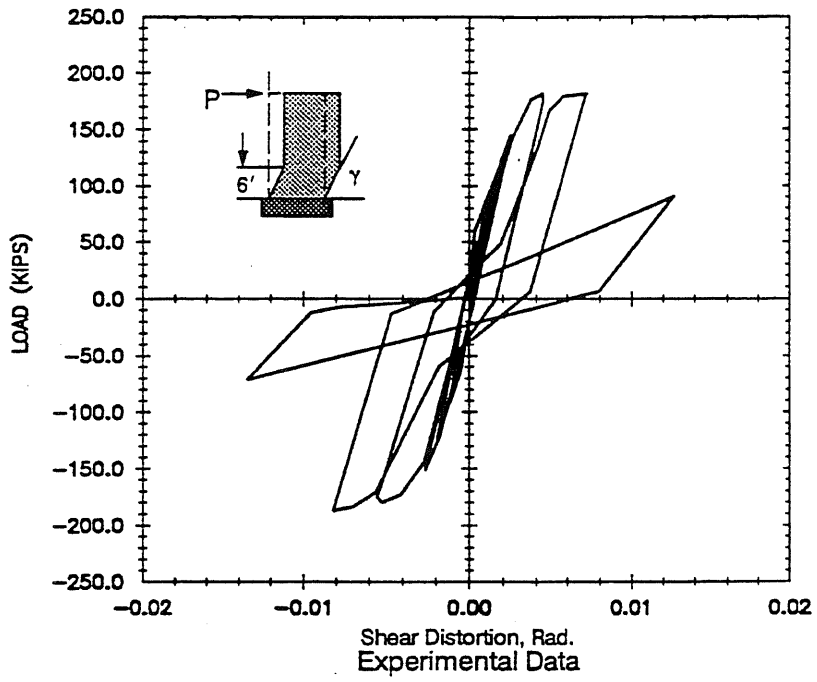


Fig. 6.44 Load vs. Shear Distortion at 6-ft Level: Wall B6

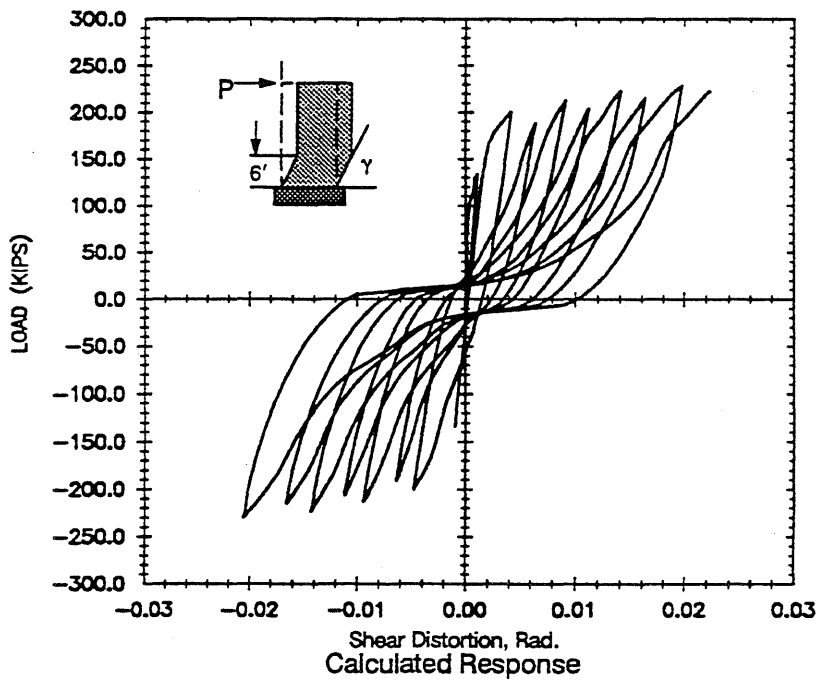
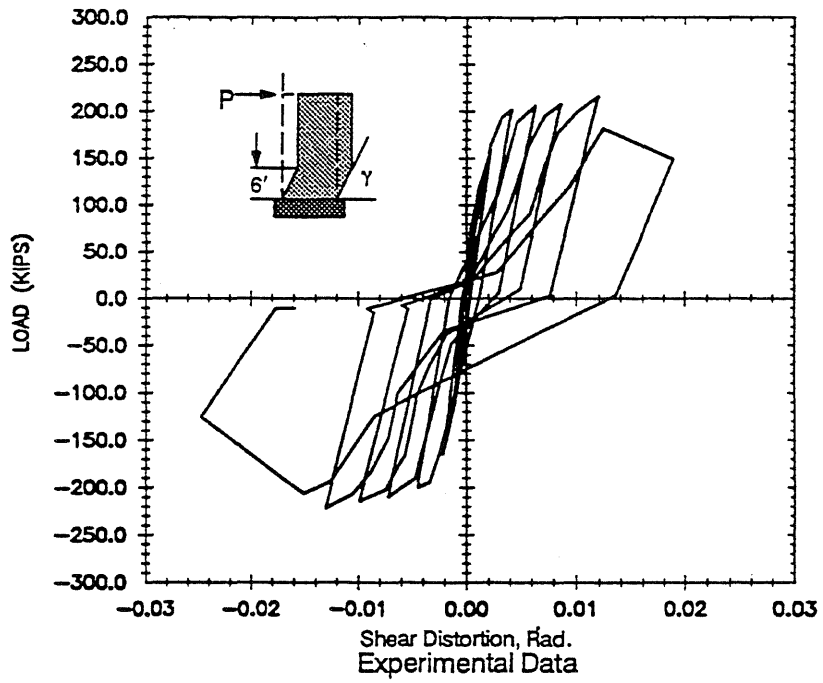


Fig. 6.45 Load vs. Shear Distortion at 6-ft Level: Wall B7

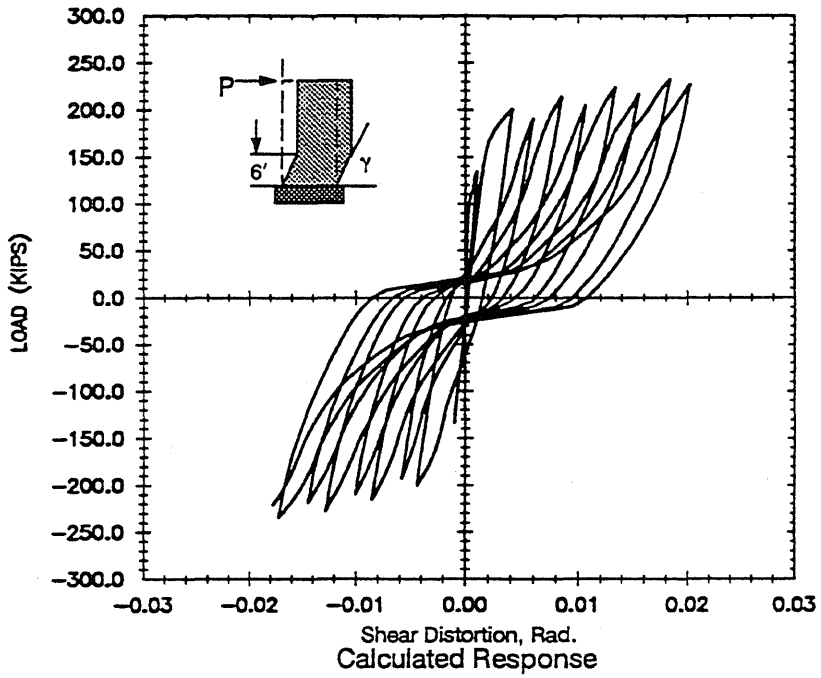
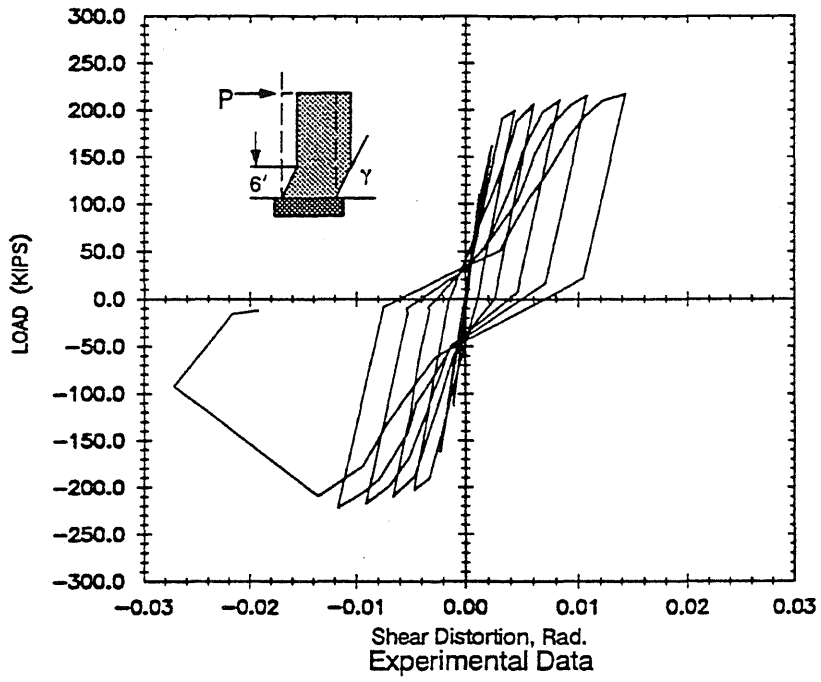


Fig. 6.46 Load vs. Shear Distortion at 6-ft Level: Wall B8

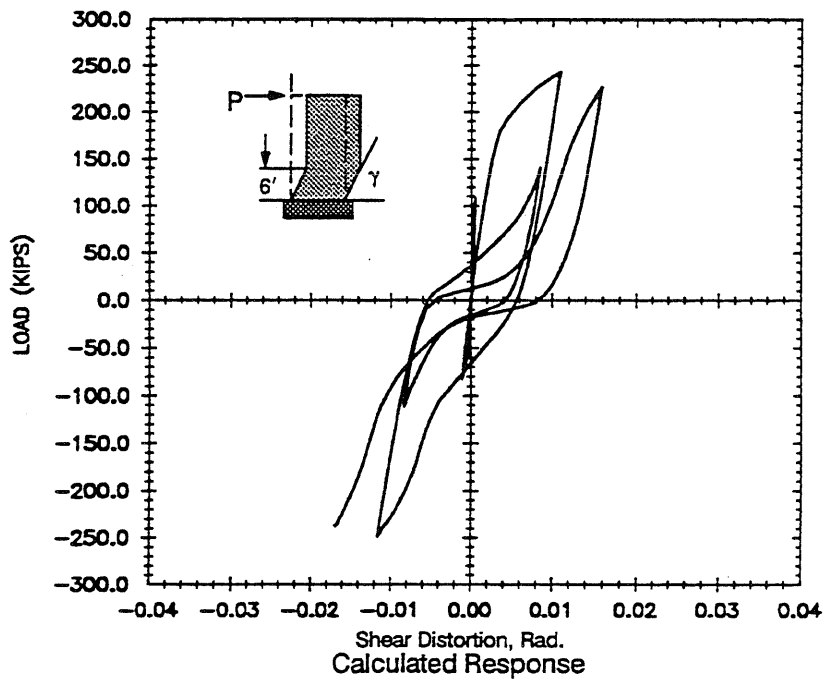
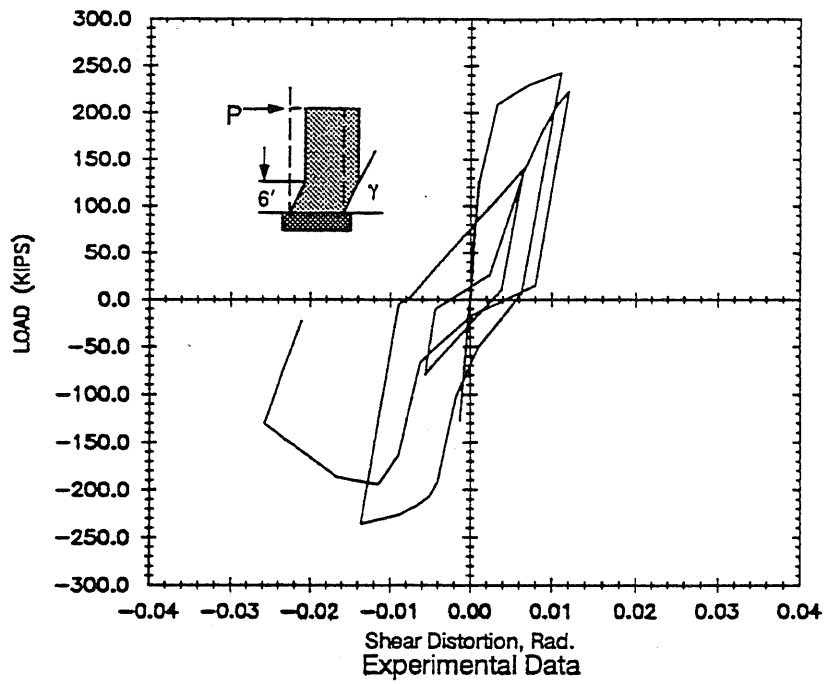


Fig. 6.47 Load vs. Shear Distortion at 6-ft Level: Wall B9

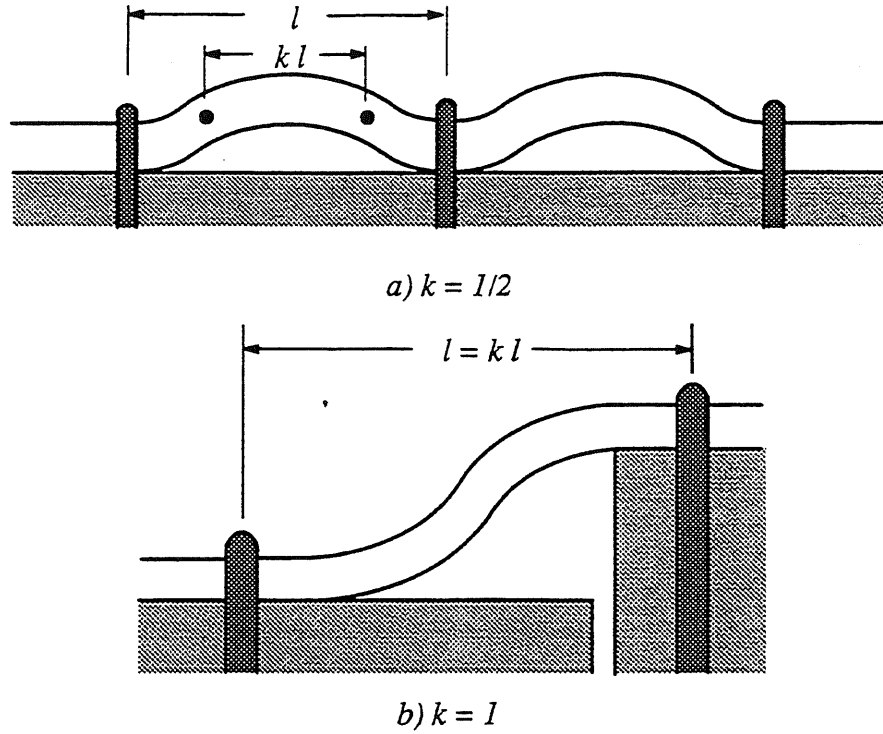
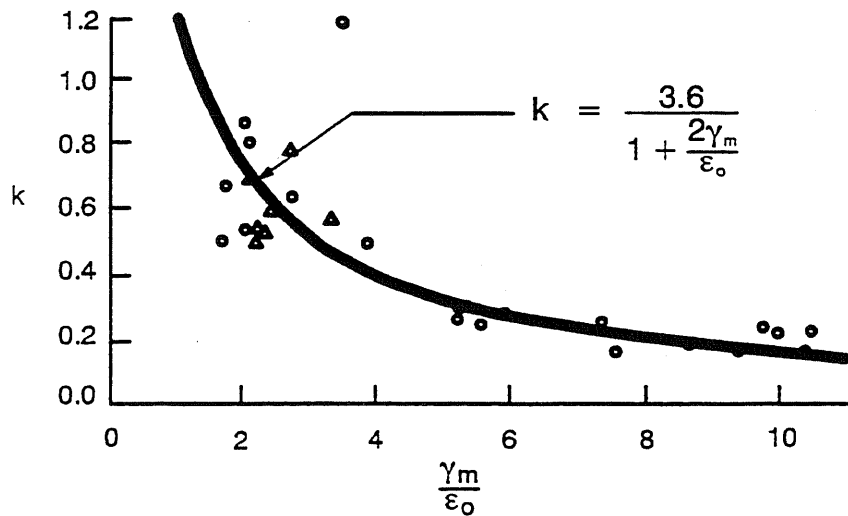
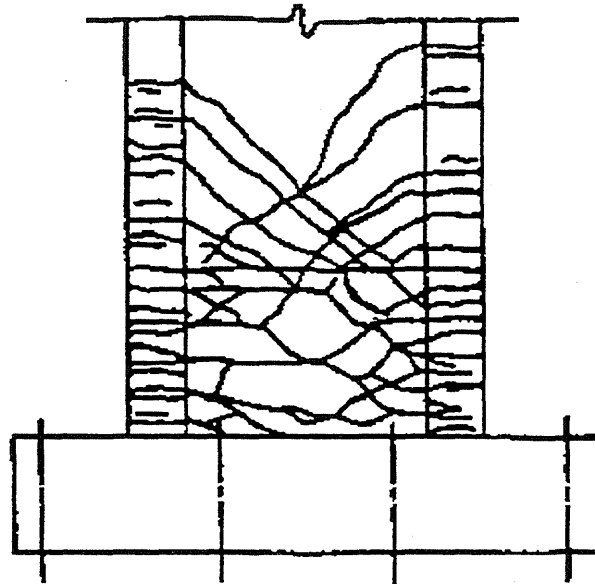


Fig. 6.48 Buckling Modes of Reinforcing Bars (from Gosain et al [62])

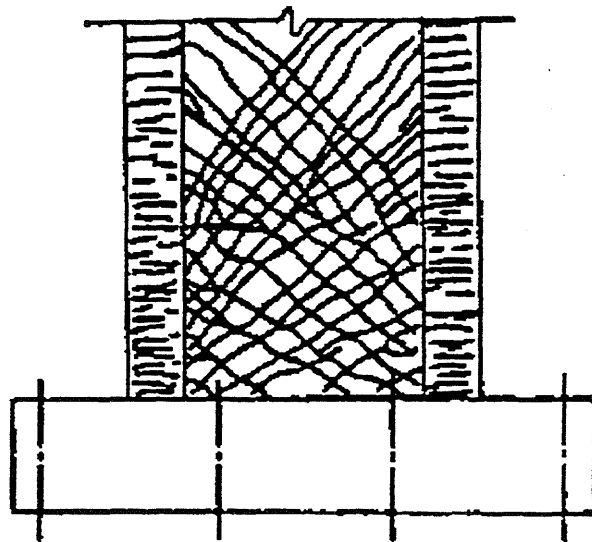


- $\gamma_m$  = maximum average shear distortions measured within the hinging region prior to web crushing
- $\epsilon_0$  = measured axial strain at maximum load from compressive tests of concrete cylinders

Fig. 6.49 Effective Strength Factors vs. Normalized Shear Distortion for Shear Walls (from [104])



a) Crack Pattern of a Wall Specimen Subjected to Low Nominal Shear Stress



b) Crack Pattern of a Wall Specimen Subjected to High Nominal Shear Stress

Fig. 6.50 Typical Crack Patterns in PCA Wall Specimens



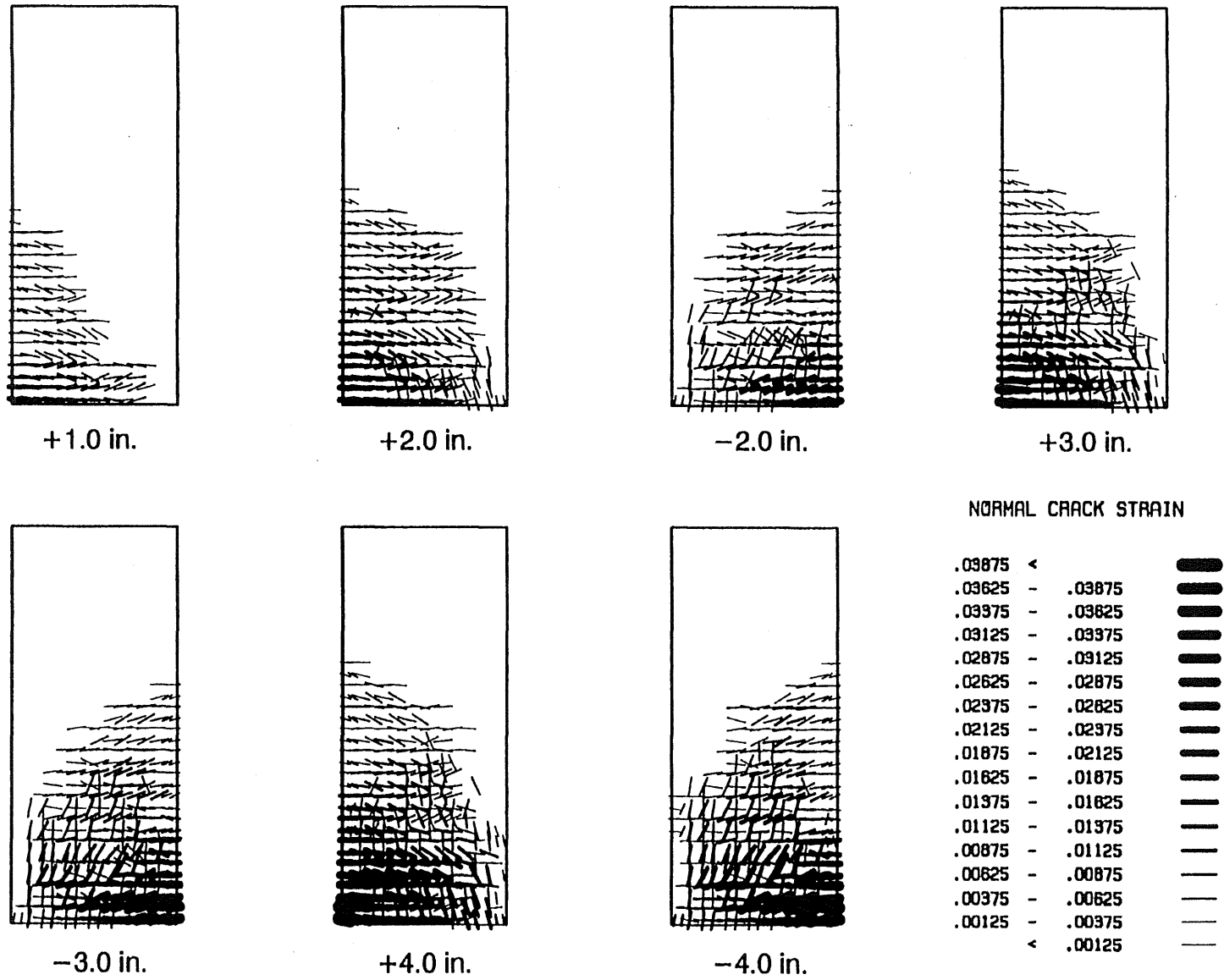


Fig. 6.51 Calculated Crack Patterns for Wall R1 at Different Top-Deflection Levels

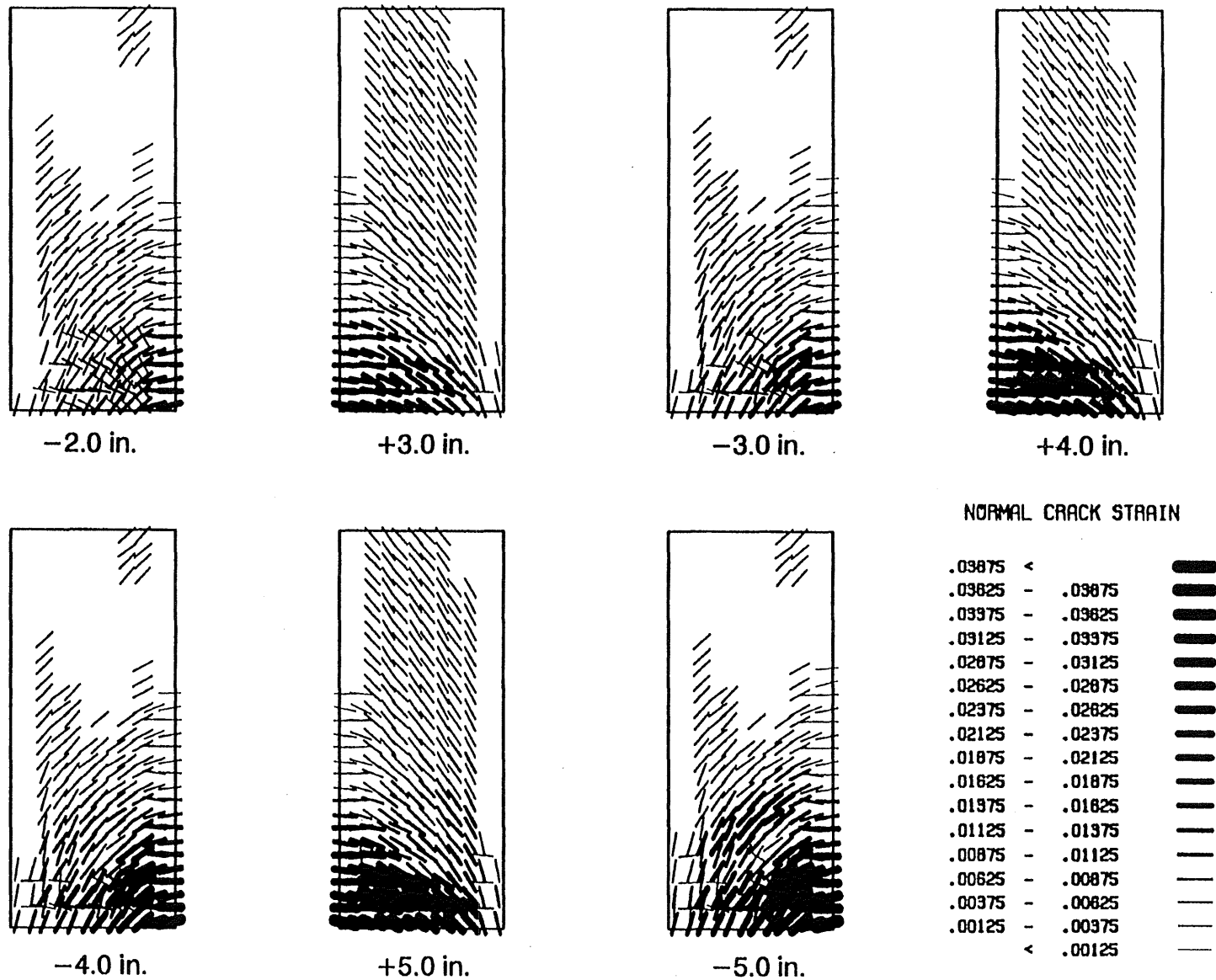


Fig. 6.52 Calculated Crack Patterns for Wall B7 at Different Top-Deflection Levels

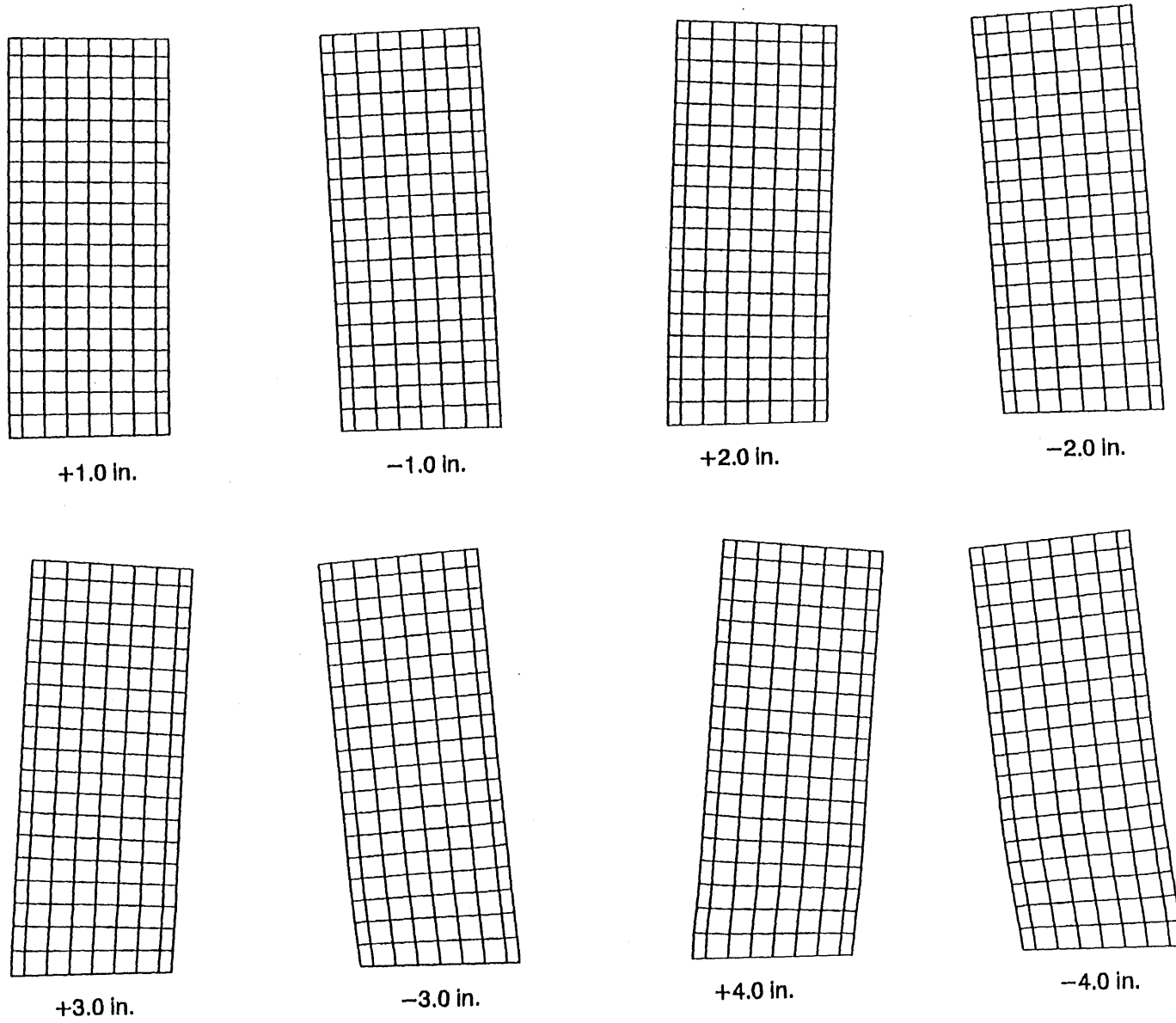


Fig. 6.53 Calculated Deformed Shape of Wall R1 at Different Top-Deflection Levels

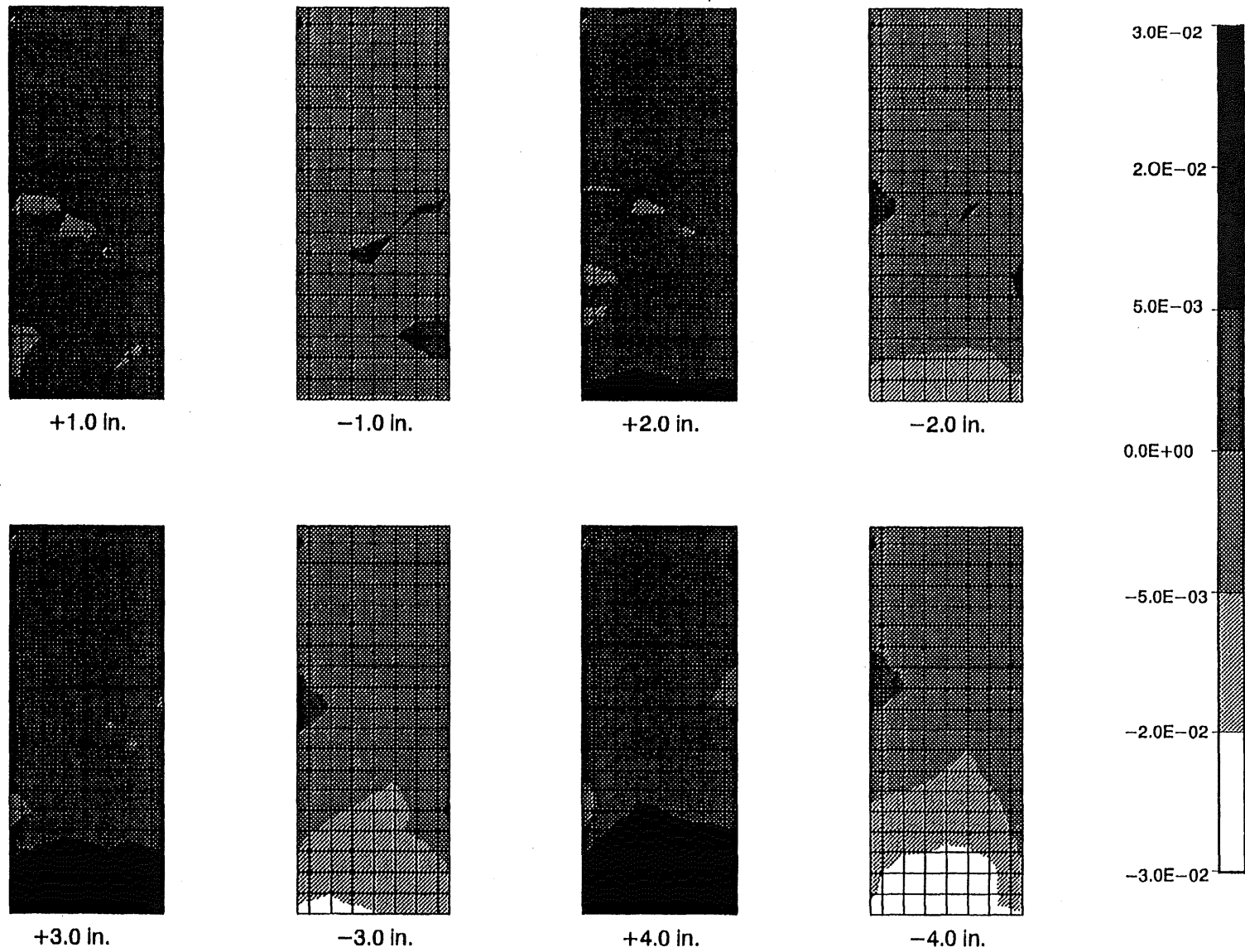


Fig. 6.54 Calculated Shear Strain Distribution in Wall R1 at Different Top-Deflection Levels

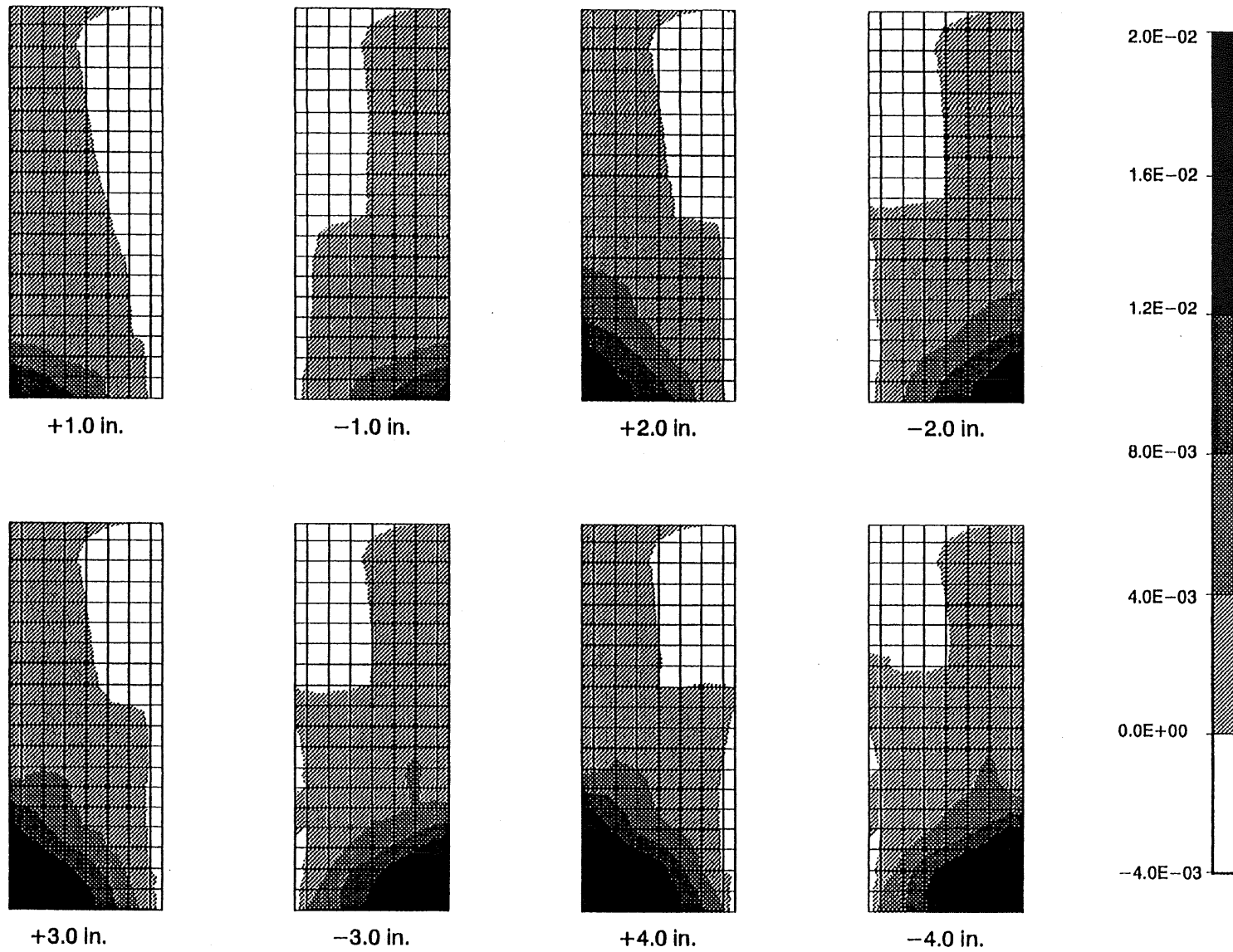


Fig. 6.55 Calculated  $\epsilon_{yy}$  Distribution in Wall R1 at Different Top-Deflection Levels

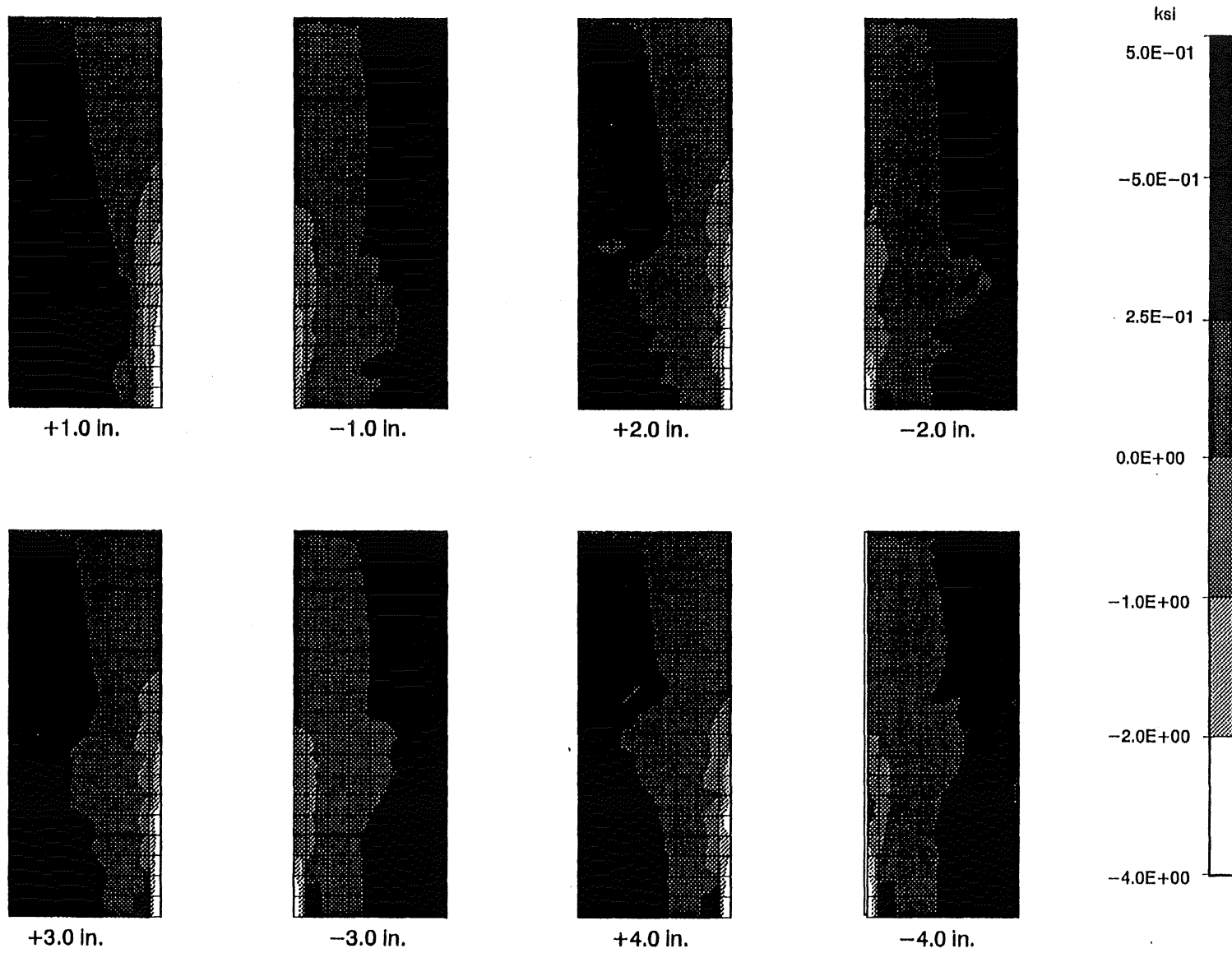


Fig. 6.56 Calculated  $\sigma_{yy}$  Distribution in Wall R1 at Different Top-Deflection Levels

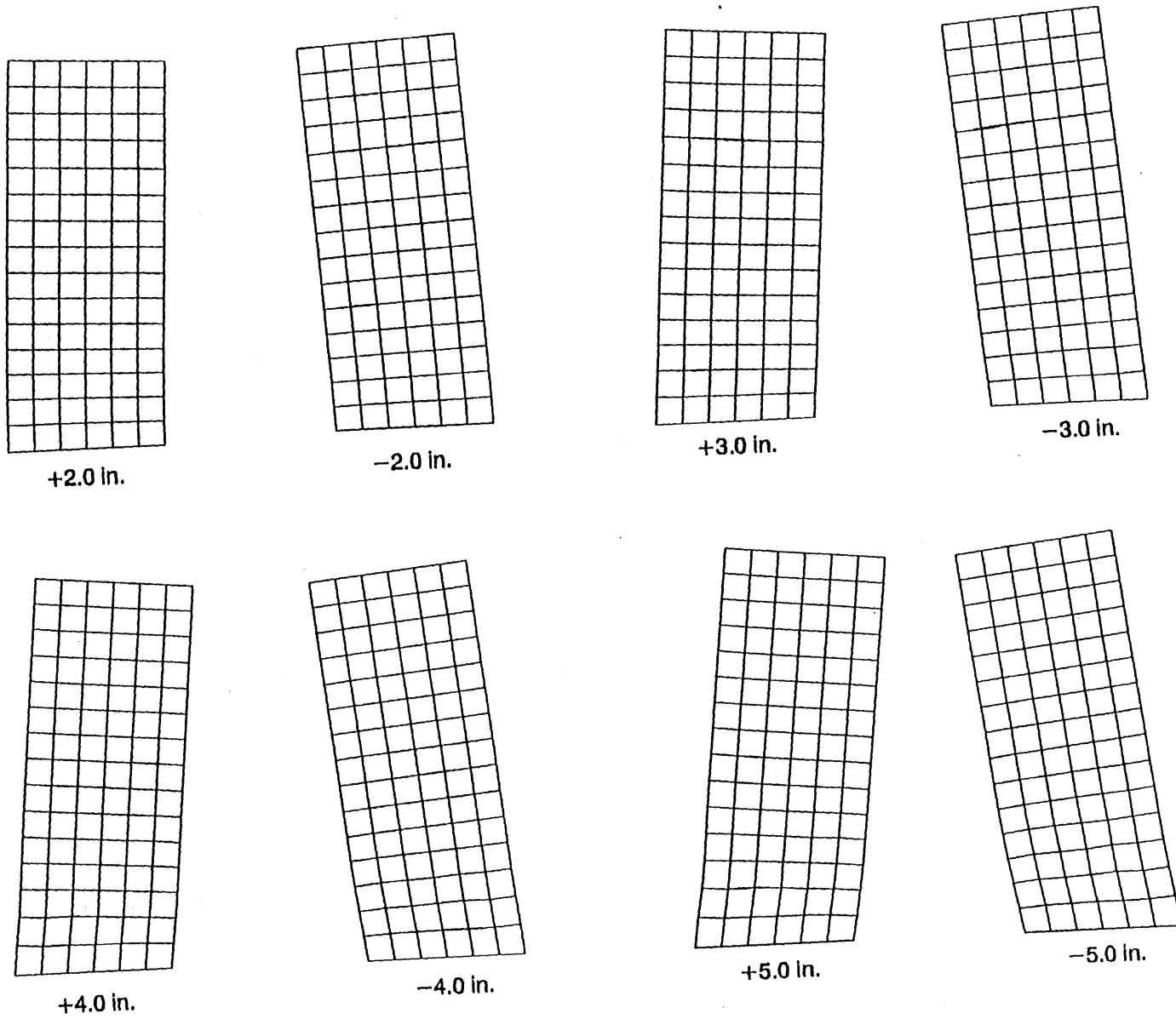


Fig. 6.57 Calculated Deformed Shape of Wall B7 at Different Top-Deflection Levels

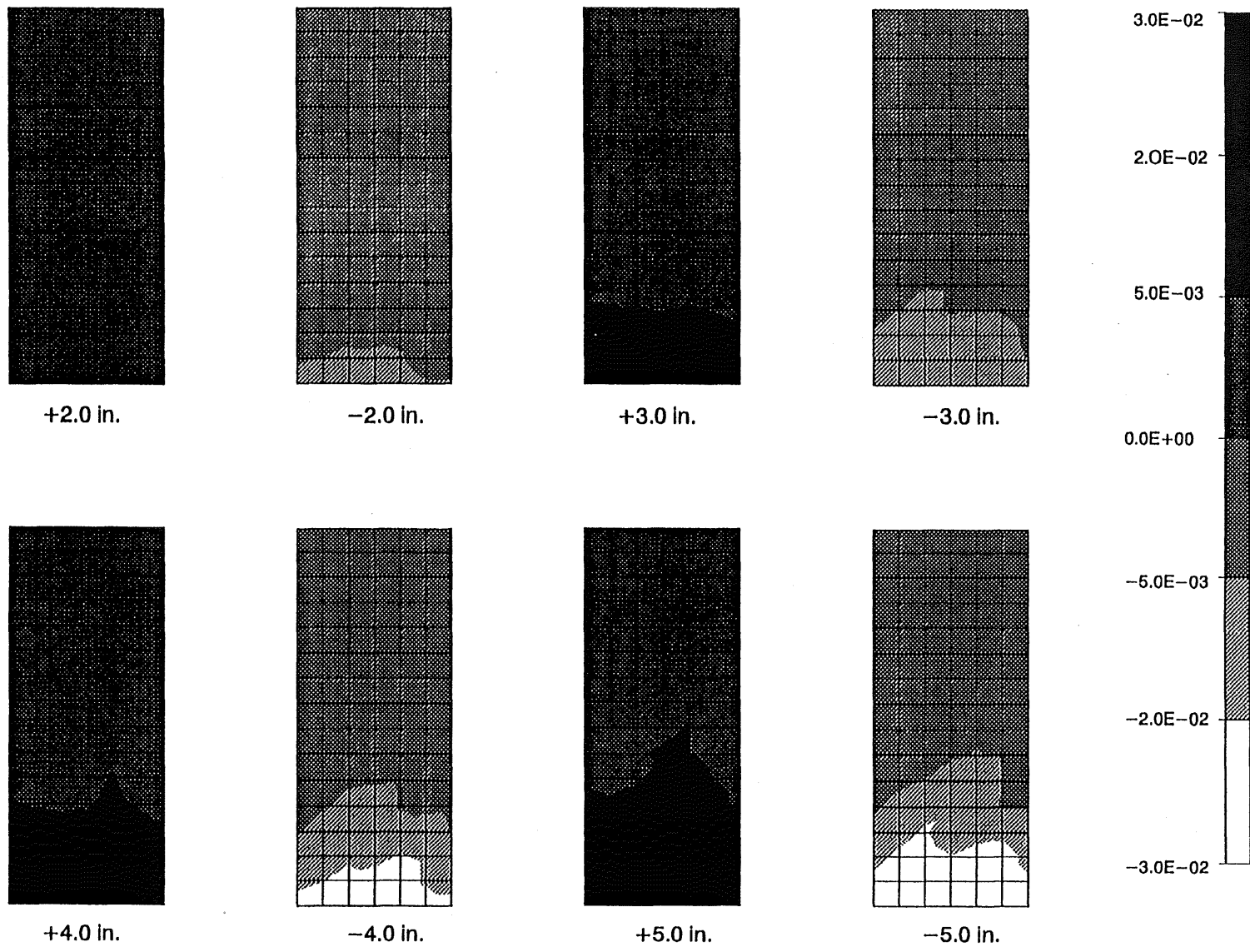


Fig. 6.58 Calculated Shear Strain Distribution in Wall B7 at Different Top-Deflection Levels



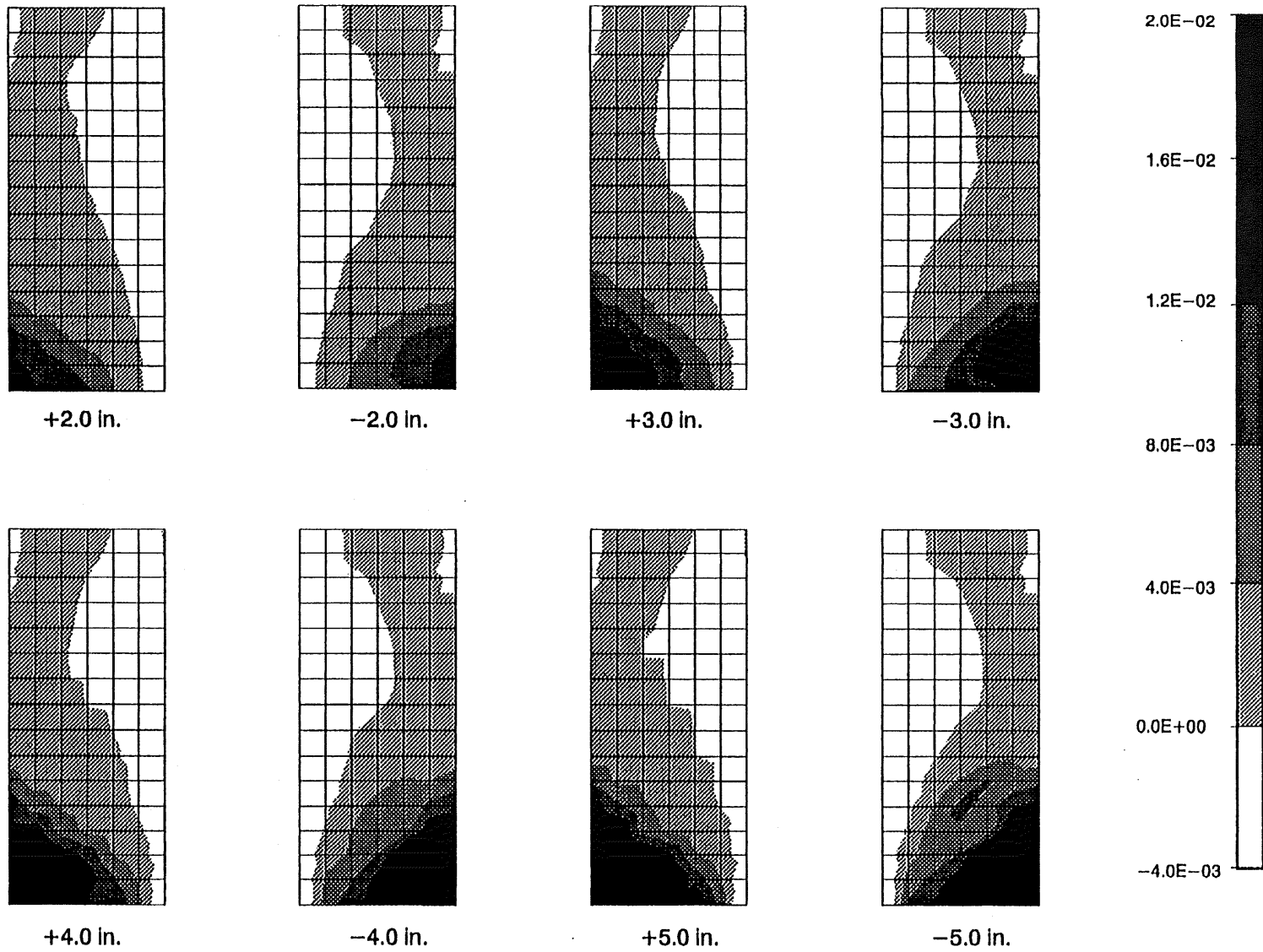


Fig. 6.59 Calculated  $\epsilon_{yy}$  Distribution in Wall B7 at Different Top-Deflection Levels

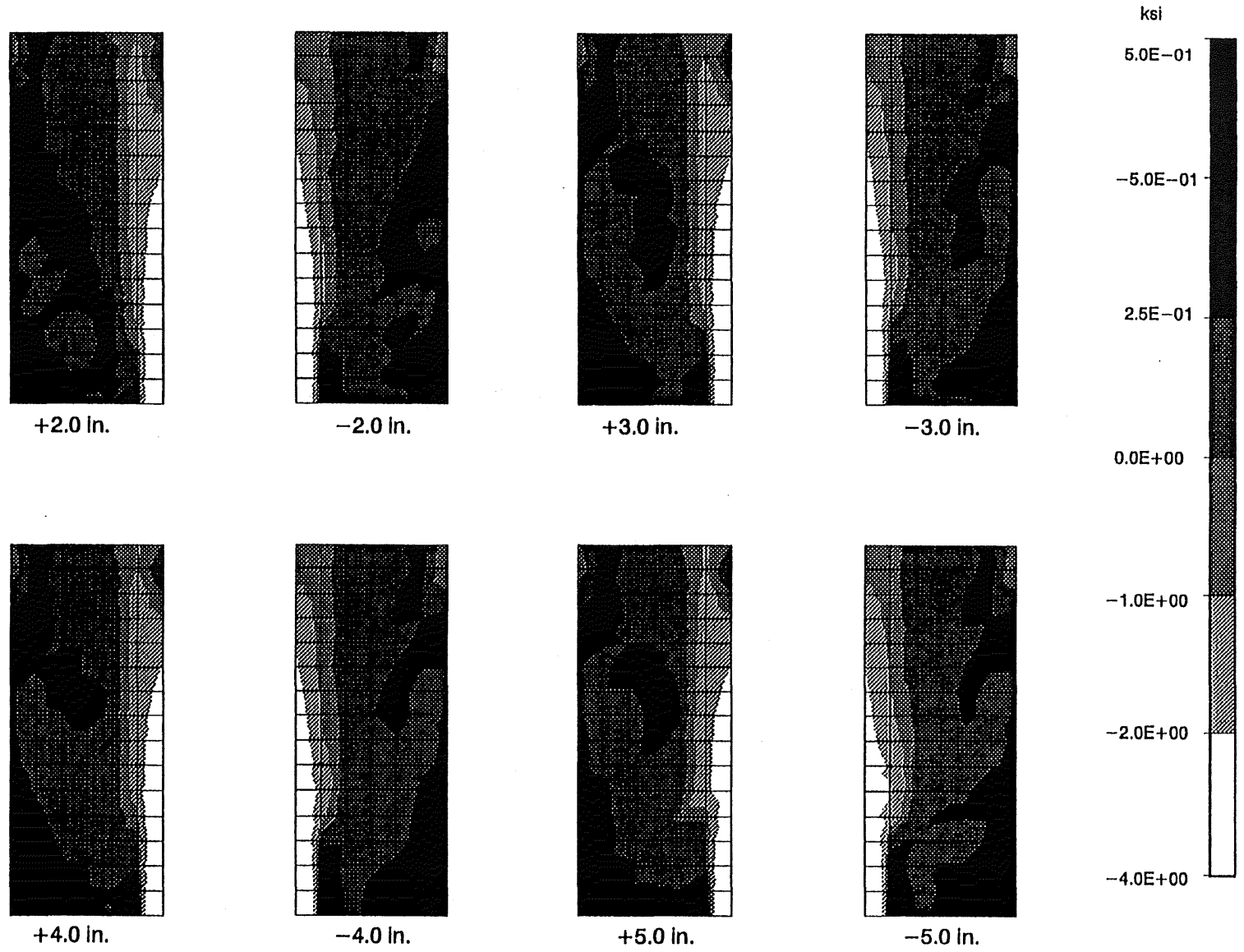


Fig. 6.60 Calculated  $\sigma_{yy}$  Distribution in Wall B7 at Different Top-Deflection Levels

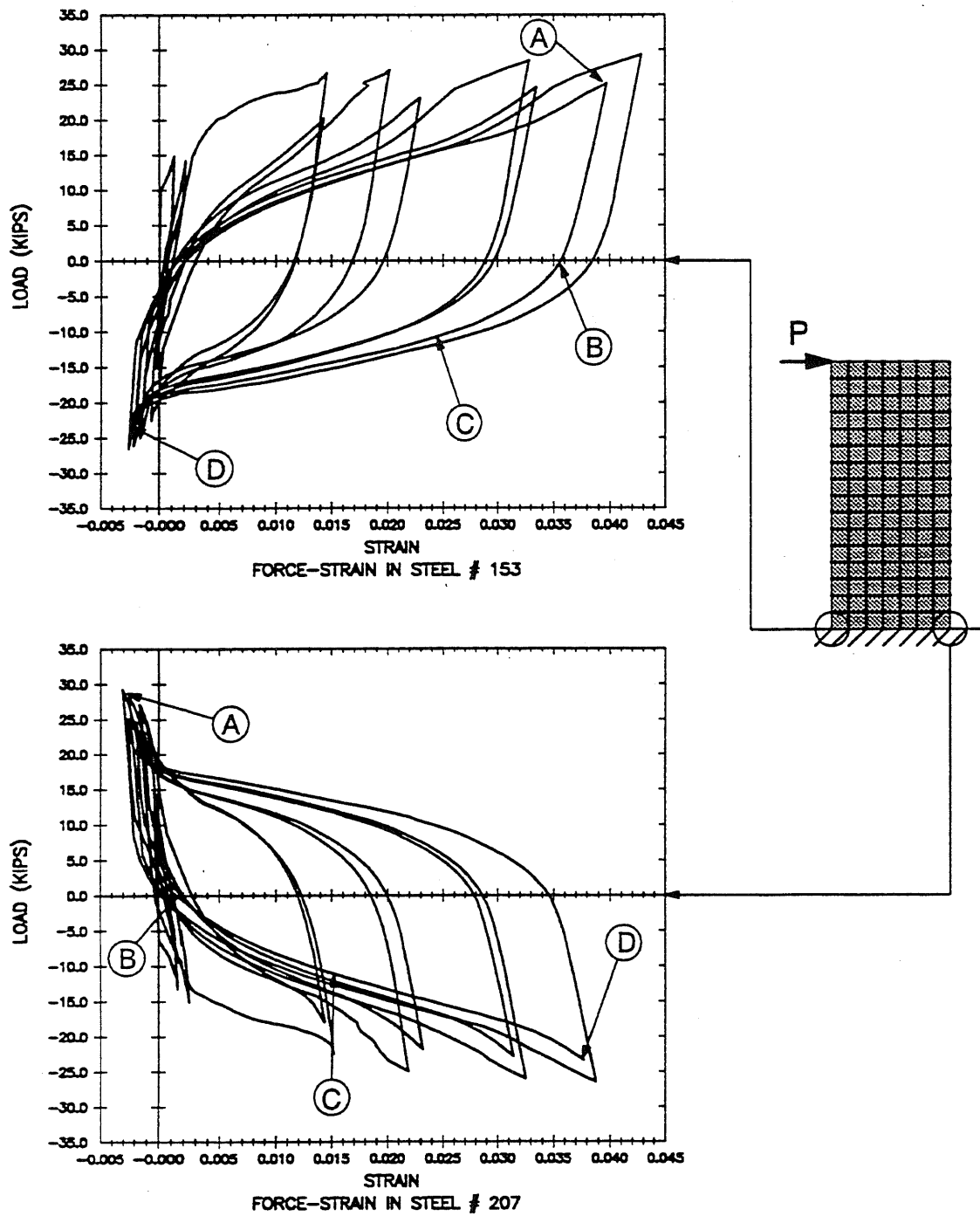


Fig. 6.61 Calculated Load vs. Strain in Flexural Reinforcement: Wall R1

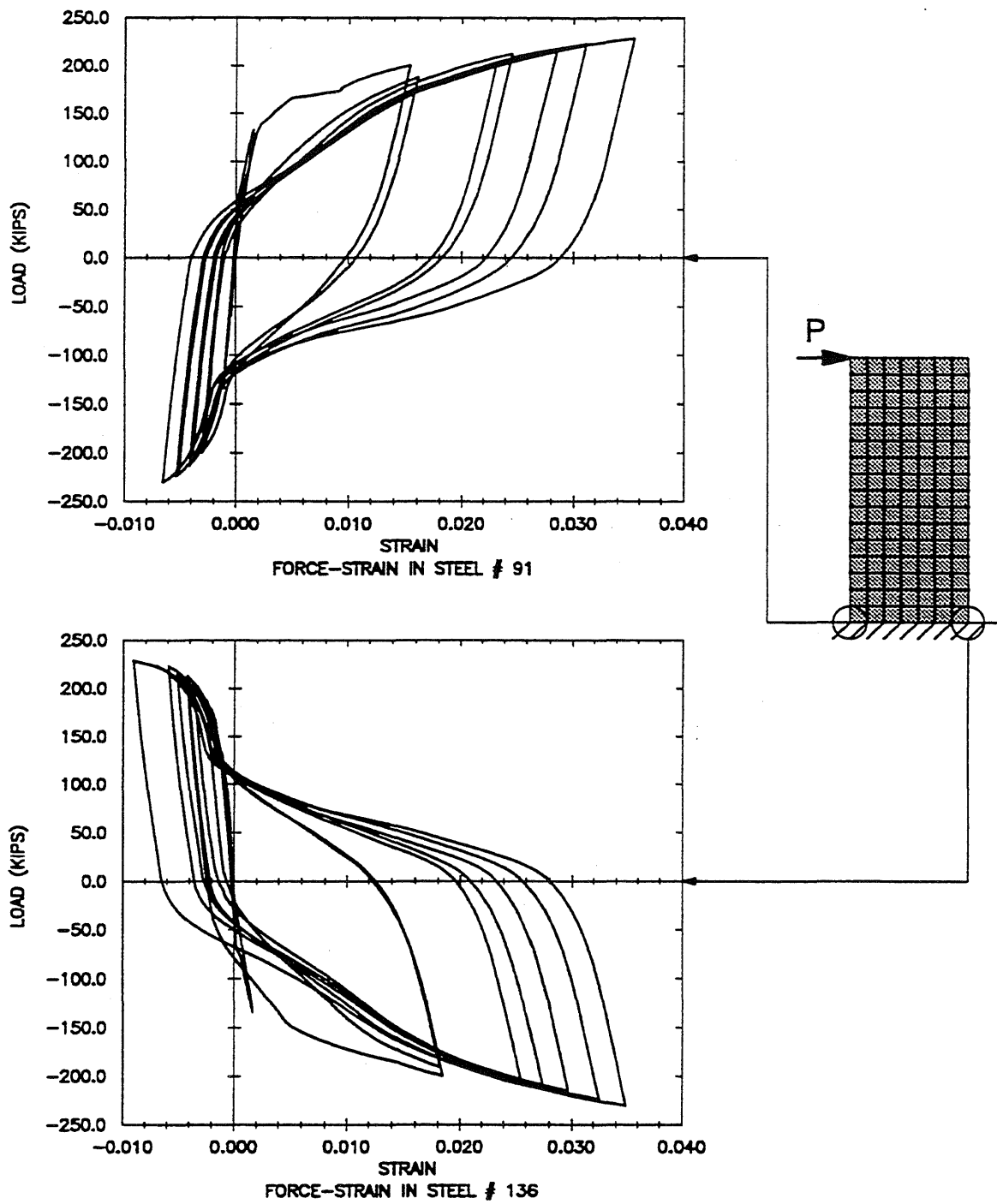


Fig. 6.62 Calculated Load vs. Strain in Flexural Reinforcement: Wall B7

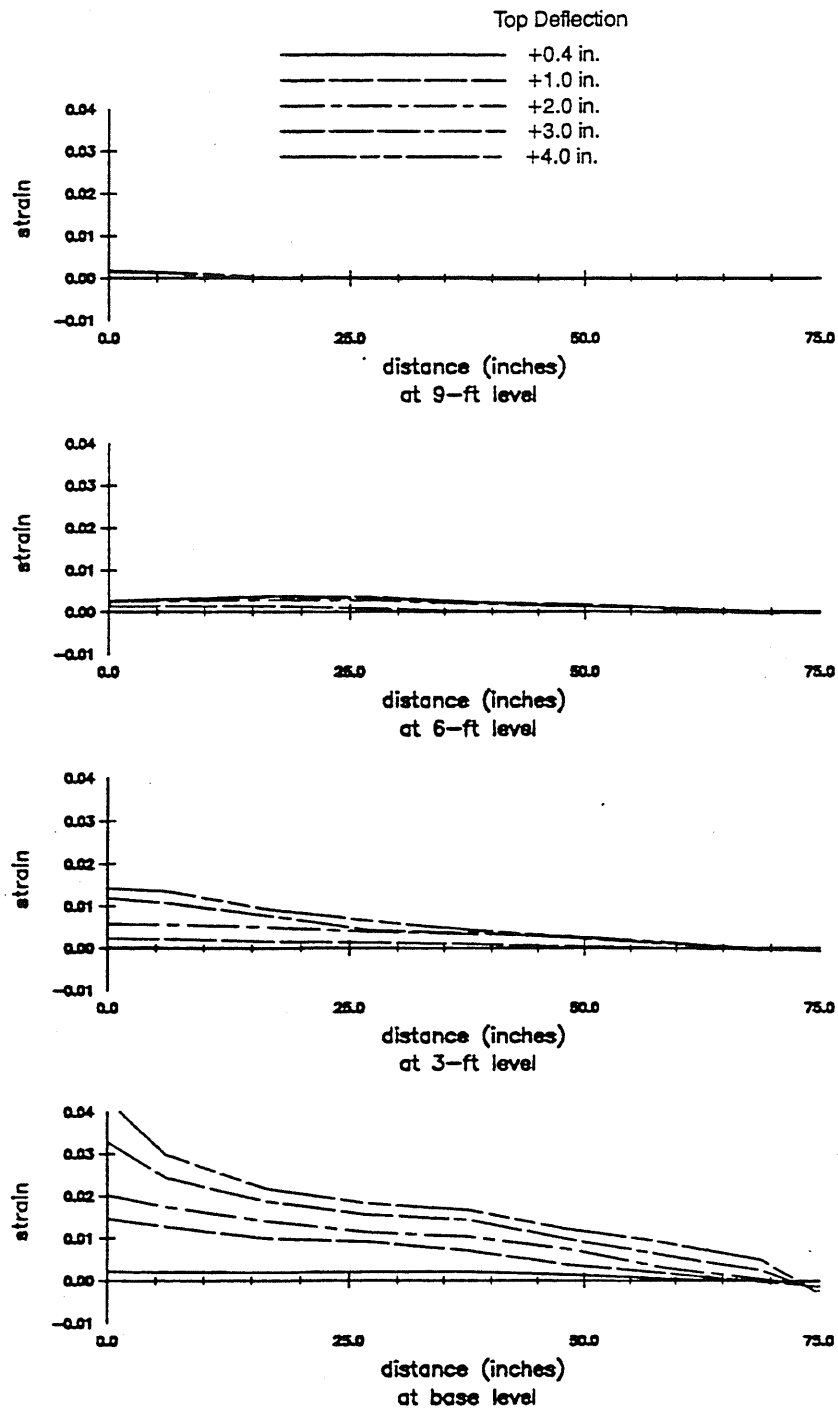


Fig. 6.63 Calculated Strain in Vertical Reinforcing Steel at Maximum Positive Loadings: Wall R1

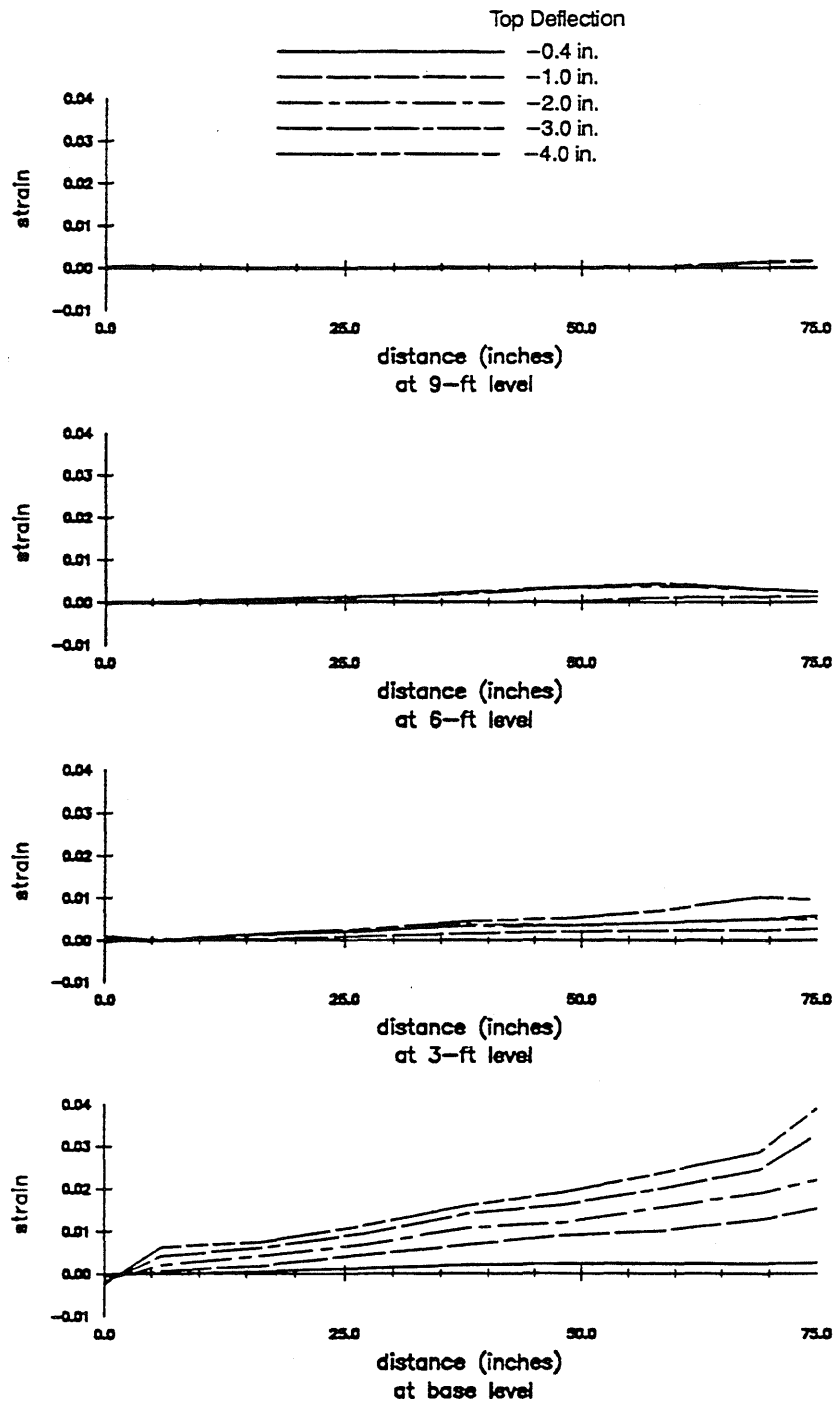


Fig. 6.64 Calculated Strain in Vertical Reinforcing Steel at Maximum Negative Loadings: Wall R1

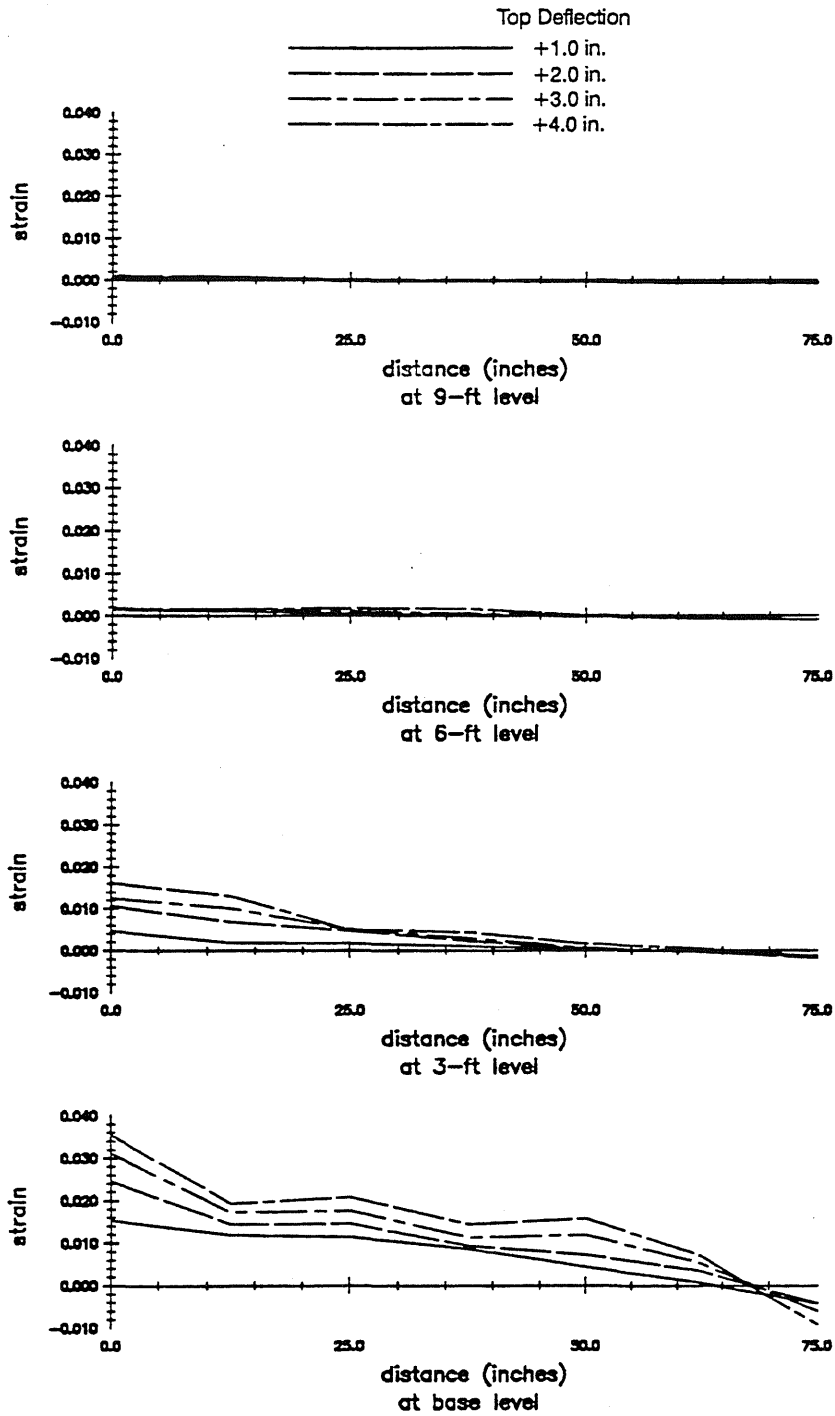


Fig. 6.65 Calculated Strain in Vertical Reinforcing Steel at Maximum Positive Loadings: Wall B7

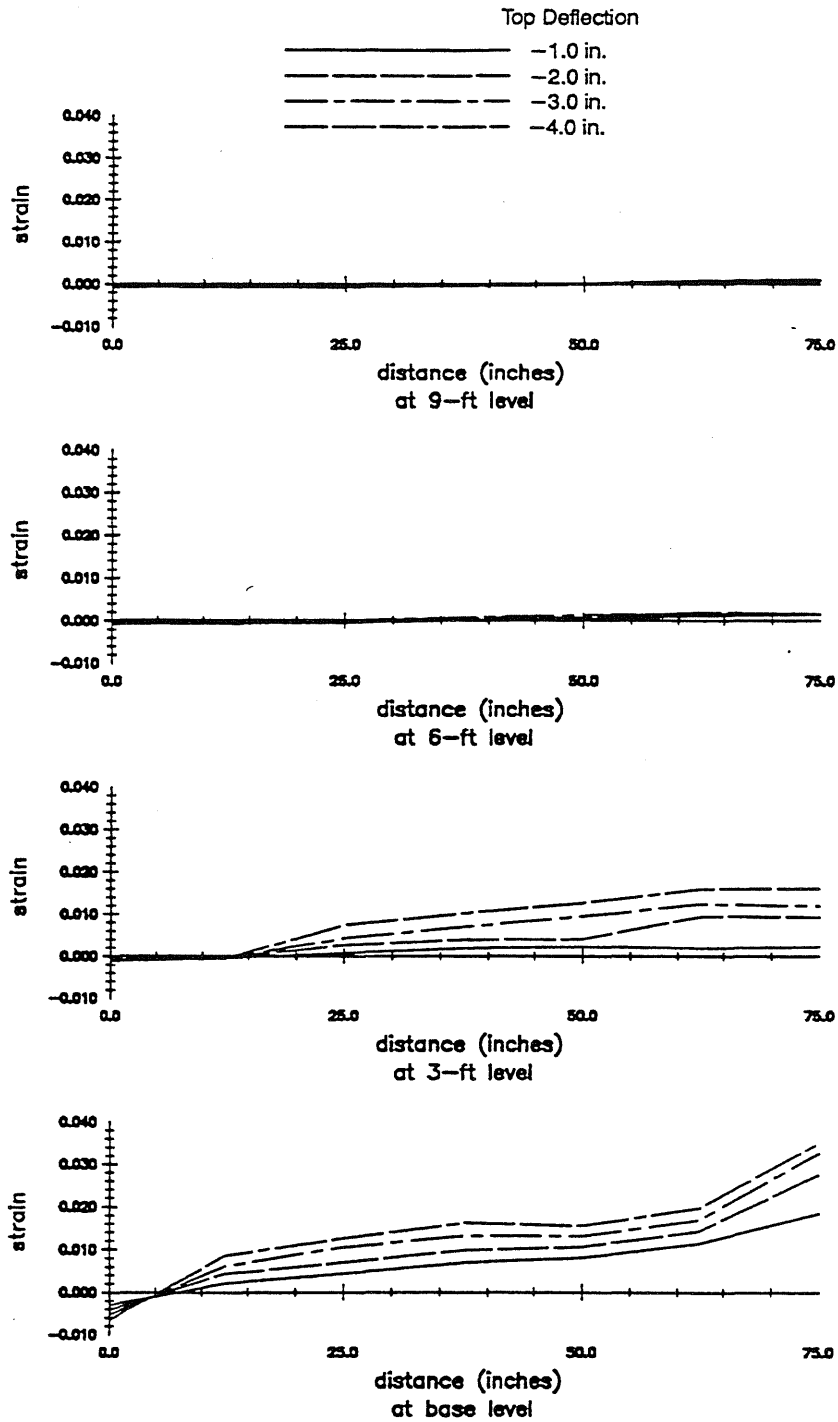


Fig. 6.66 Calculated Strain in Vertical Reinforcing Steel at Maximum Negative Loadings: Wall B7



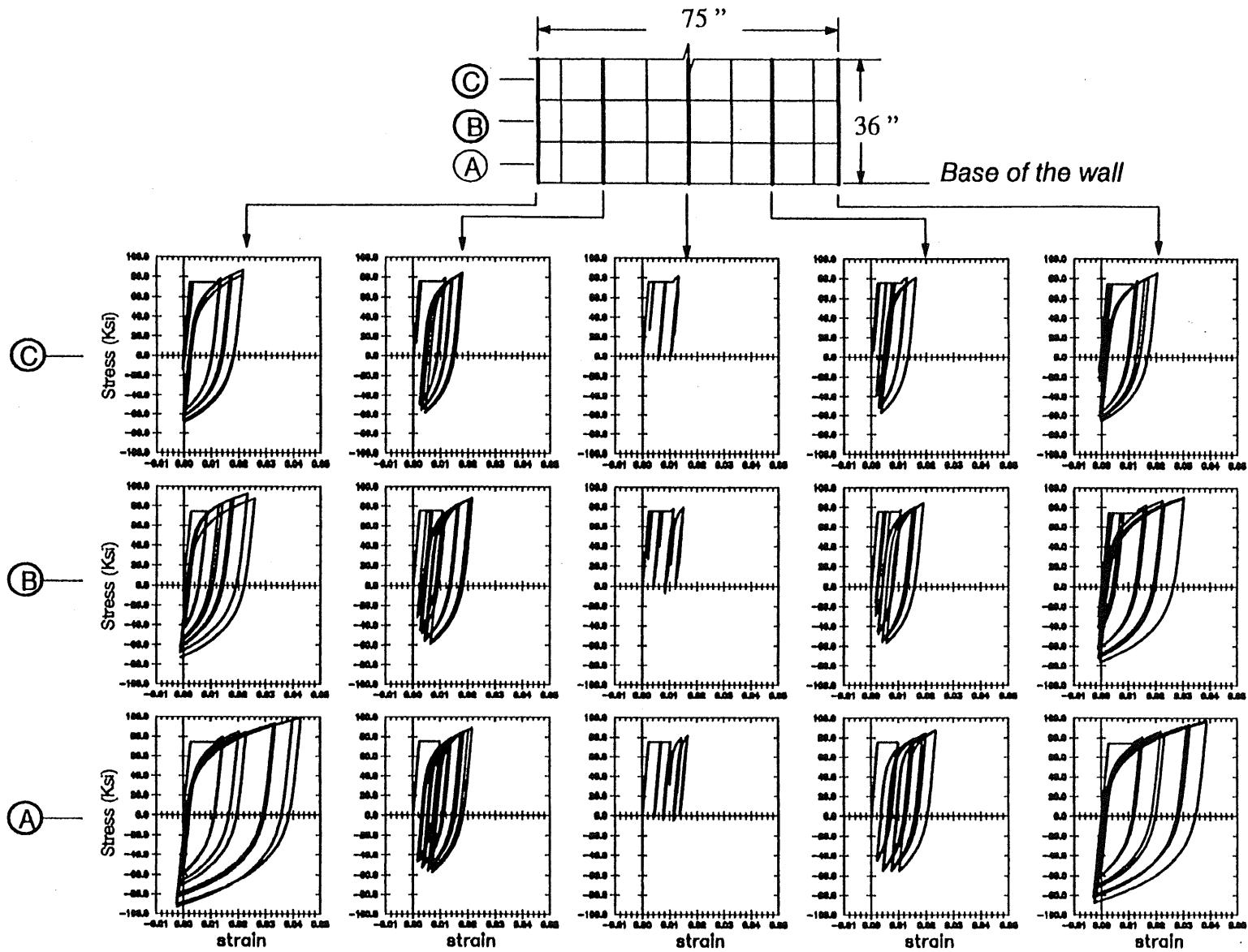


Fig. 6.67 Calculated Stress-Strain Relationship in Vertical Reinforcement for Wall R1

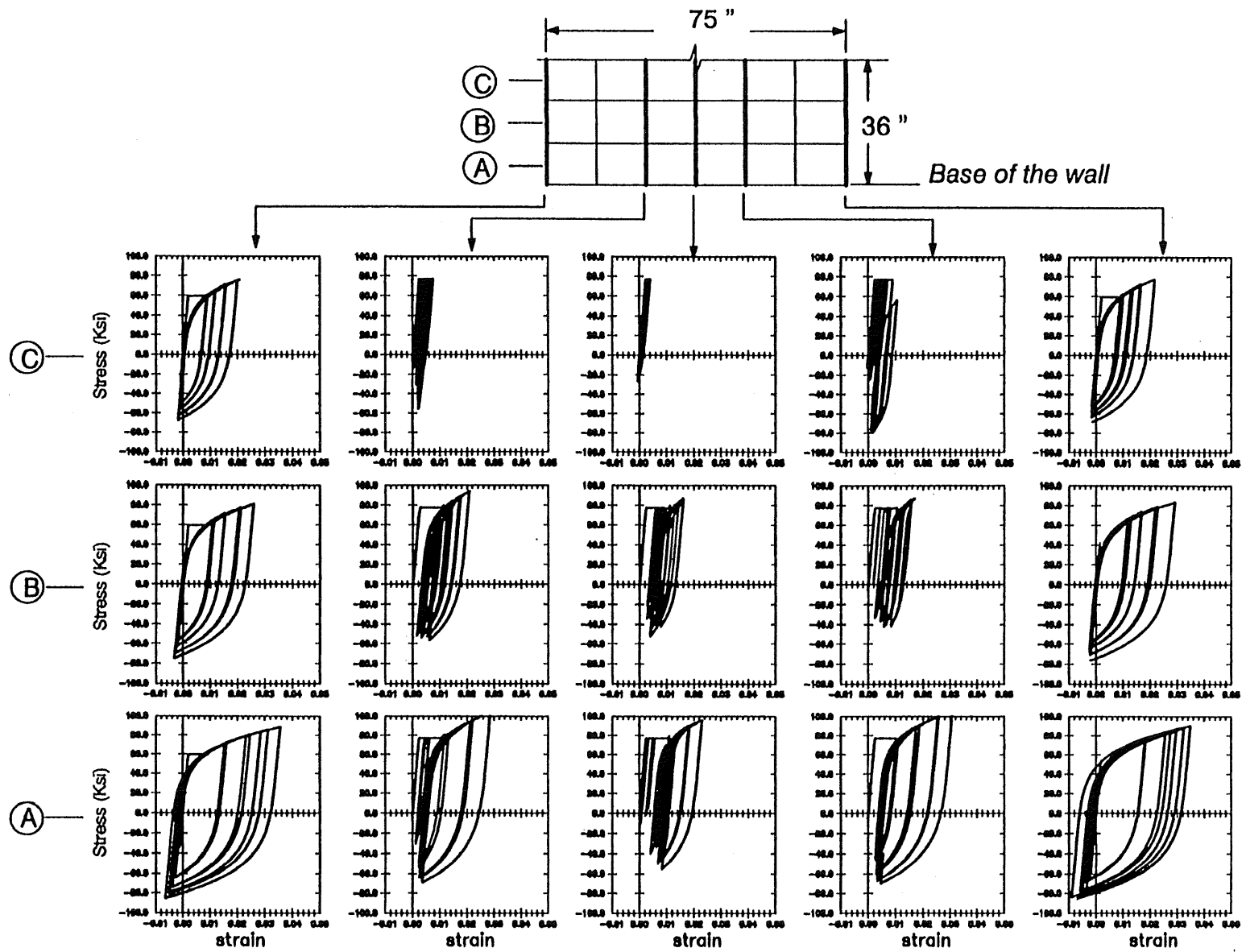
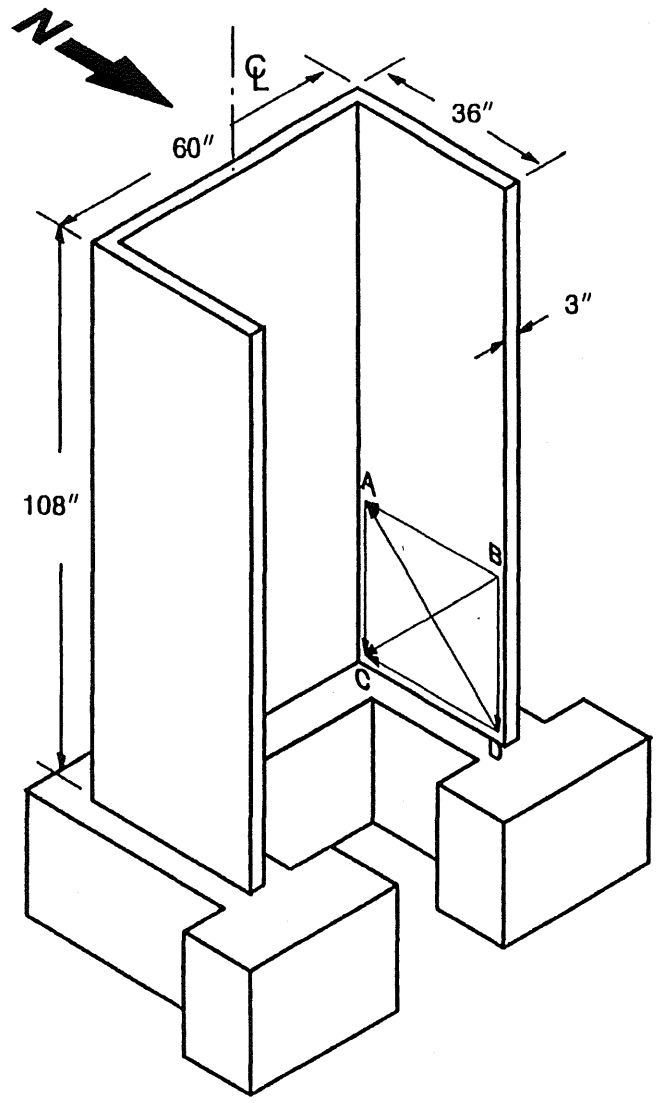
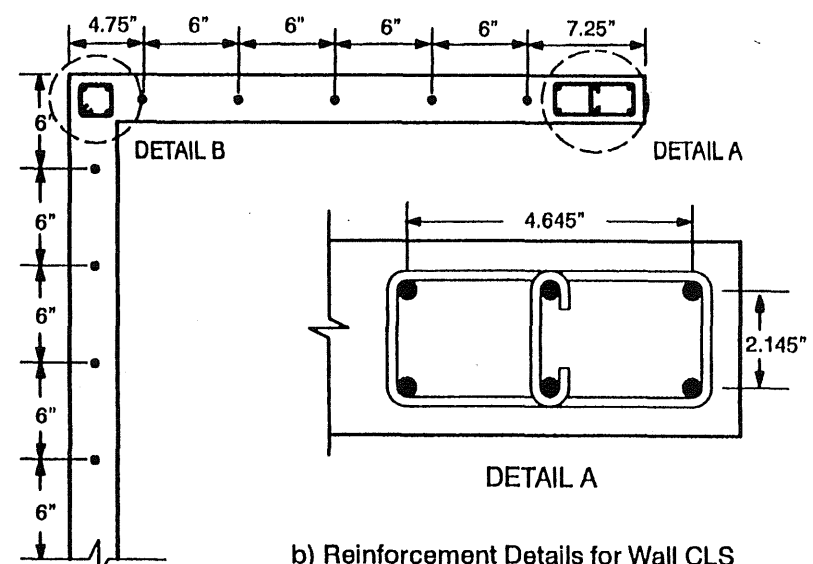


Fig. 6.68 Calculated Stress-Strain Relationship in Vertical Reinforcement for Wall B7

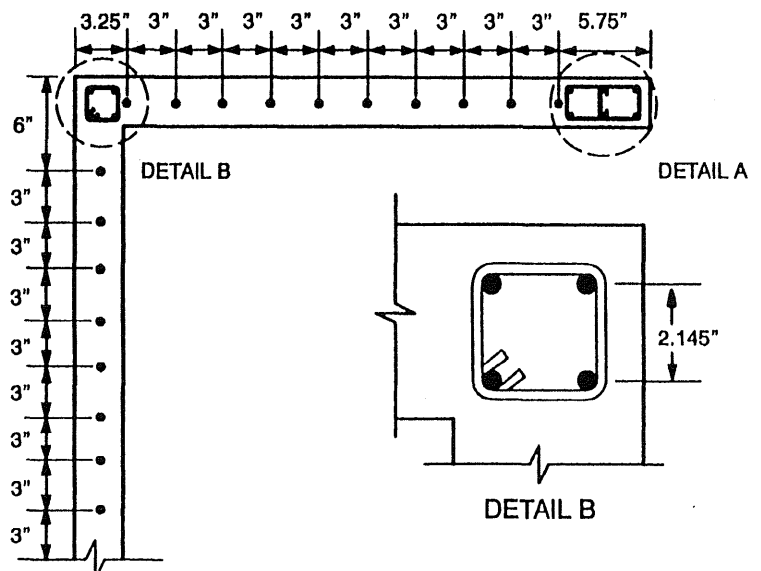


a) Overall Dimensions



b) Reinforcement Details for Wall CLS

Longitudinal Reinforcement: #3 Bars  
Web Reinforcement: #2 Bars  
Transverse Reinforcement: No. 10 Gage Wire



c) Reinforcement Details for Wall CMS

Fig. 7.1 Walls CLS and CMS

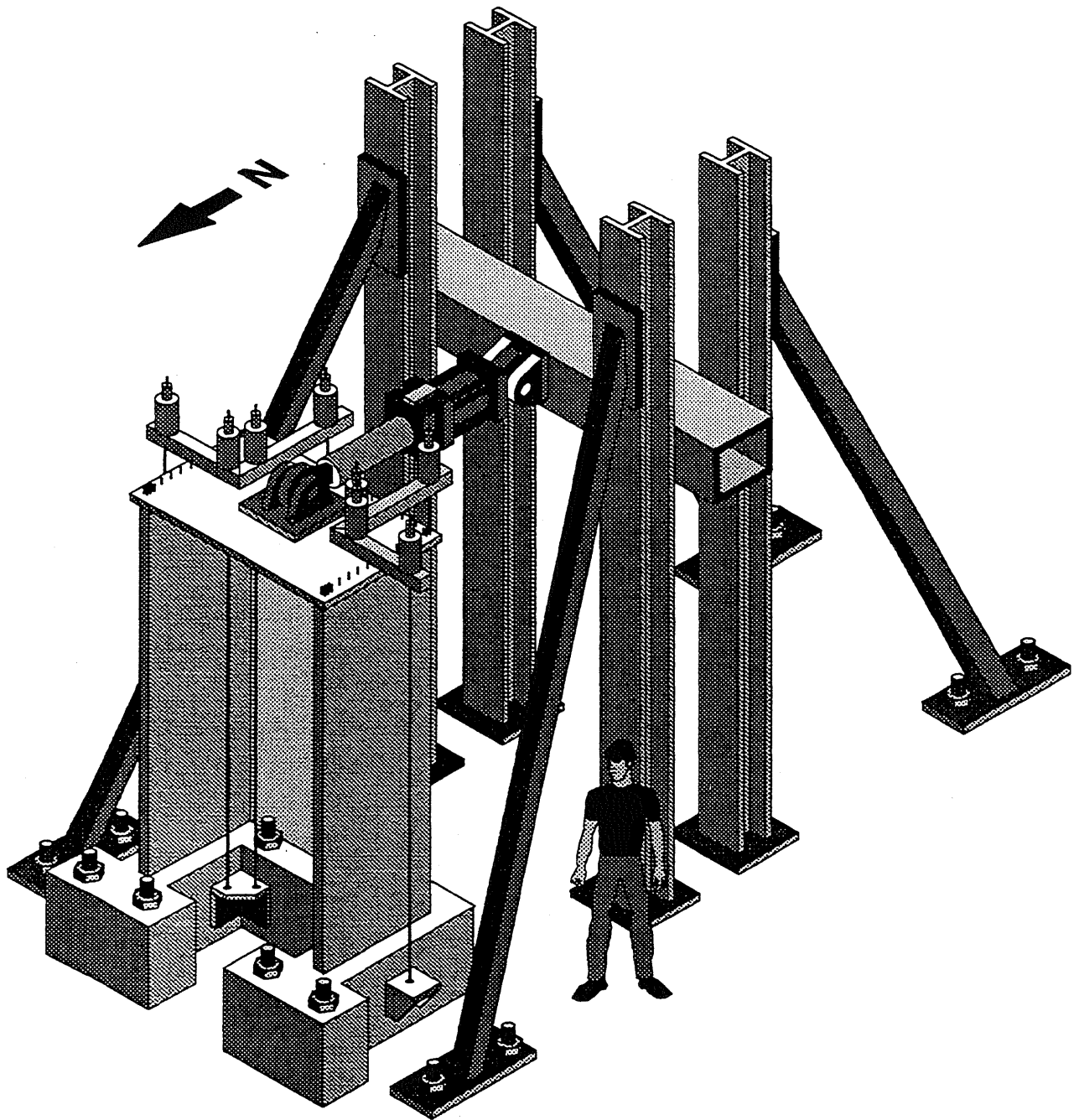
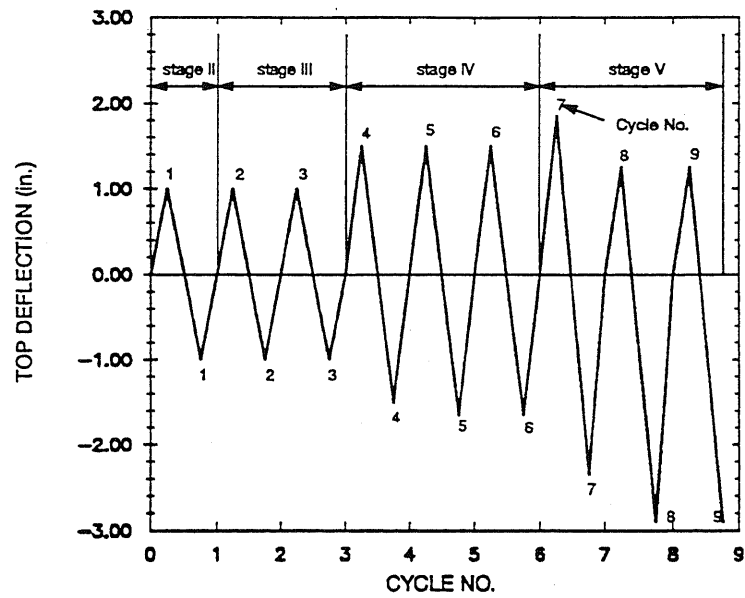
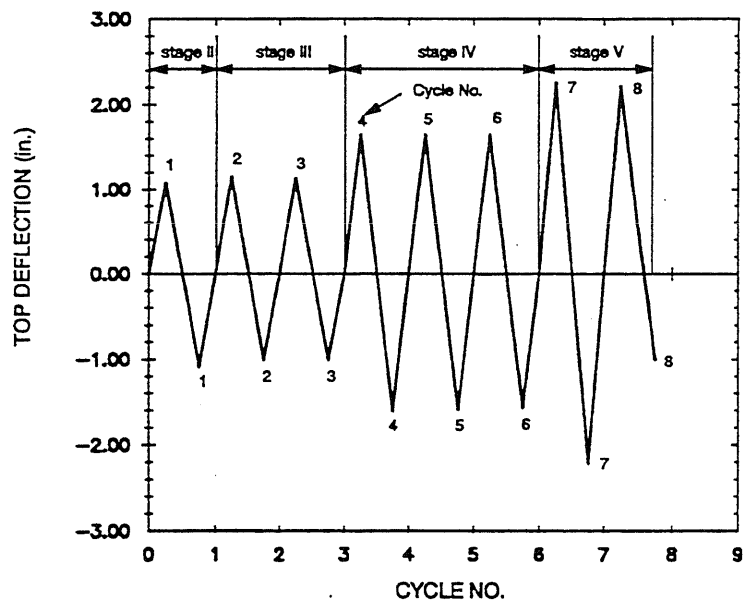


Fig. 7.2 Experimental Setup

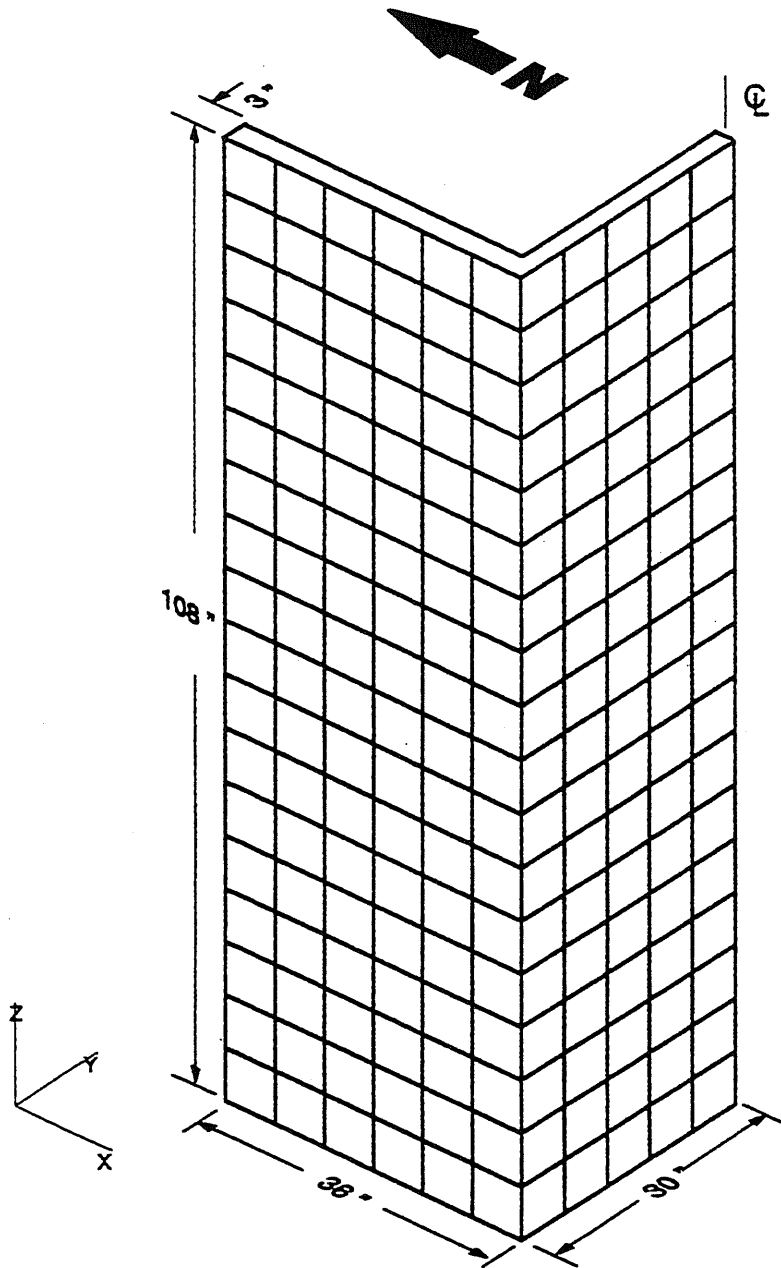


a) Loading History of Wall CLS



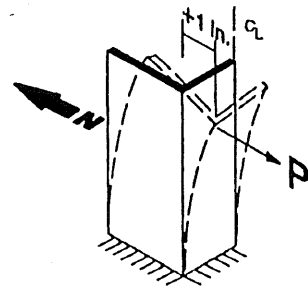
b) Loading History of Wall CMS

Fig. 7.3 Imposed Displacement Histories during Stages II through V for Walls CLS and CMS

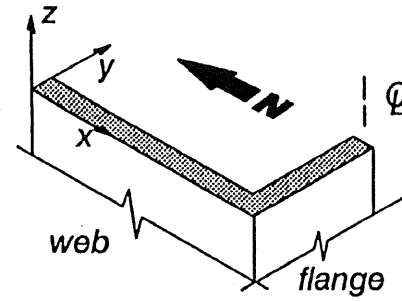


8-node plane stress elements (Q2DISOP) were used for two-dimensional analysis.  
8-node shell elements (QSHELL) were used for three-dimensional analysis.

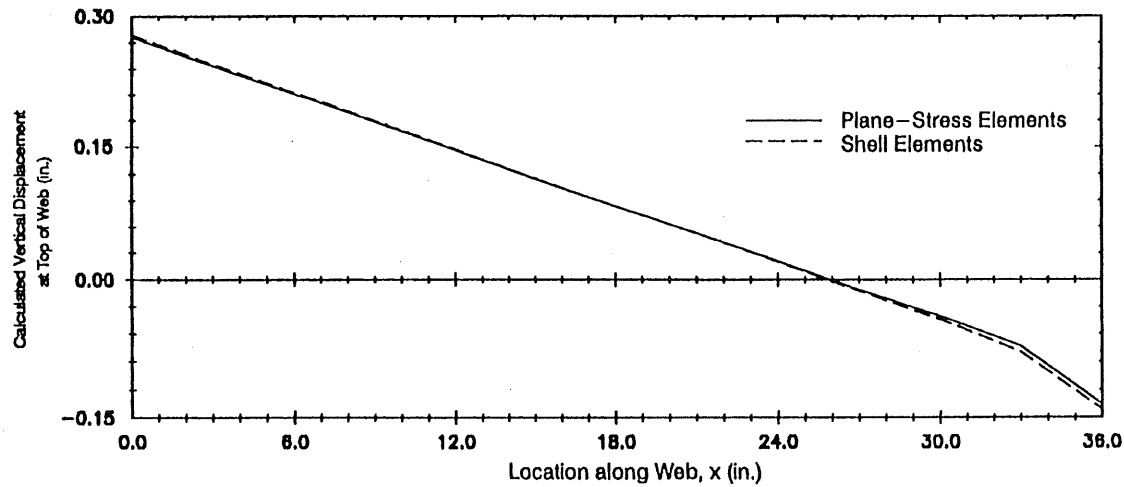
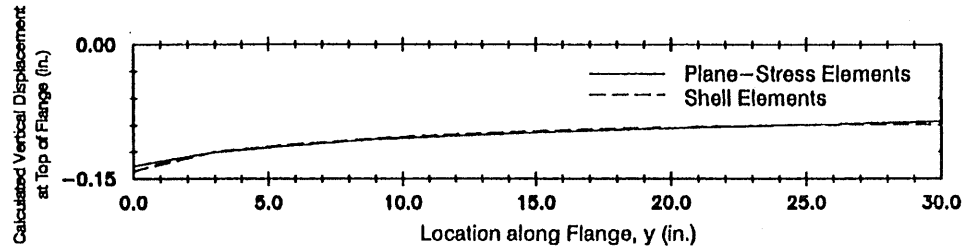
Fig. 7.4 Finite Element Model for Evaluating Differences between the Calculated Response using Plane Stress and Shell Elements



a) Imposed Loading in the Wall Model



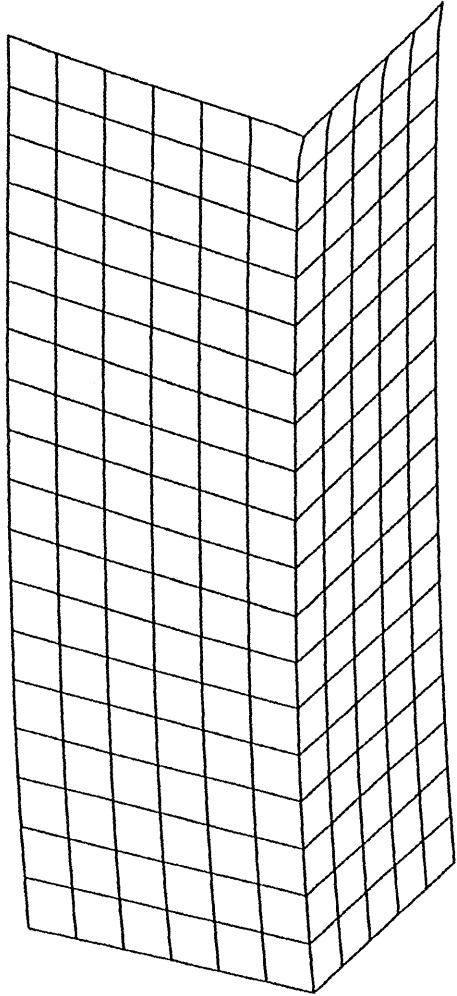
b) X-Y-Z Coordinate at the Top of the Wall



c) Calculated Vertical Displacement at the Top of the Flange and the Web

Fig. 7.5 Wall Model and the Calculated Vertical Displacements at the top of the Wall

Plane-Stress Elements



Shell Elements

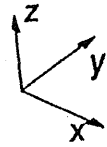
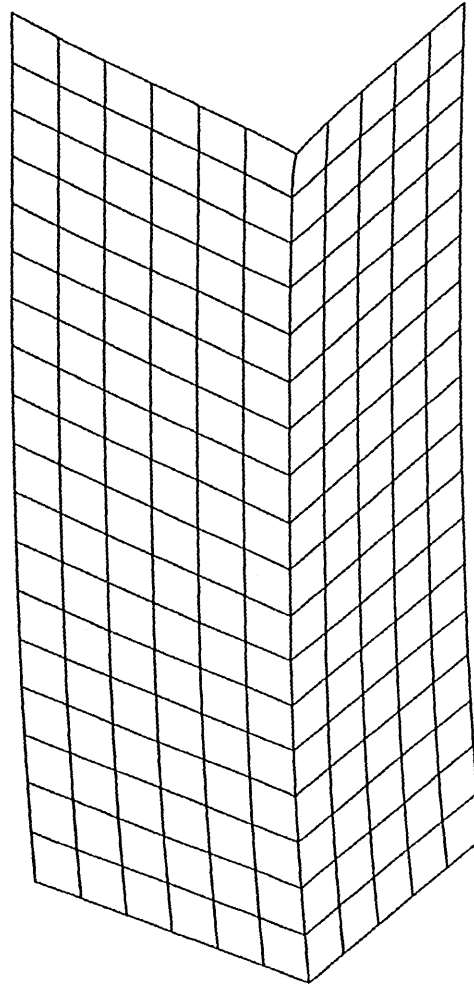


Fig. 7.6 Calculated Deformed Shapes of the C-Shaped Walls



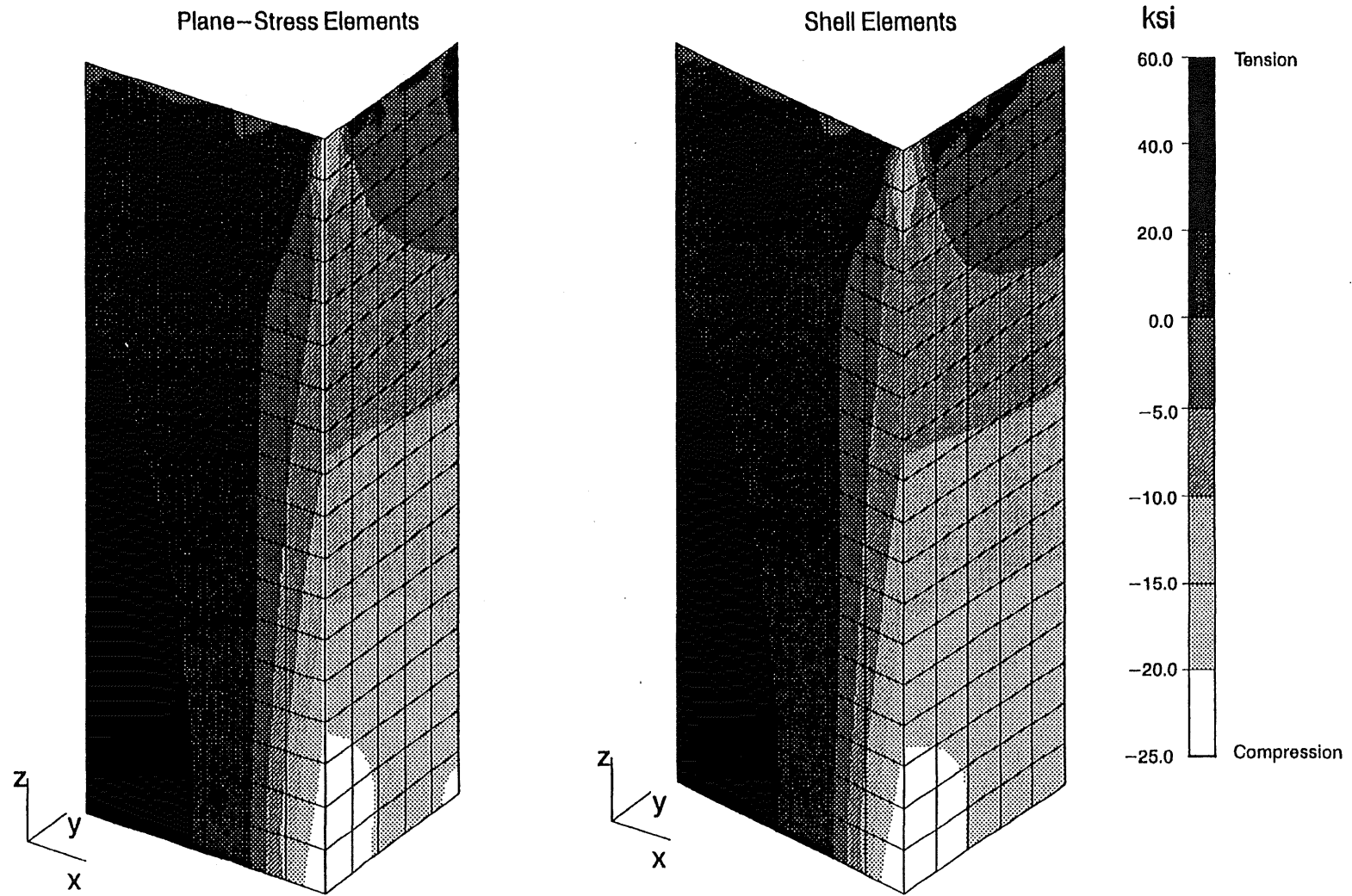


Fig. 7.7 Distribution of Calculated Axial Stress in the C-Shaped Wall Model

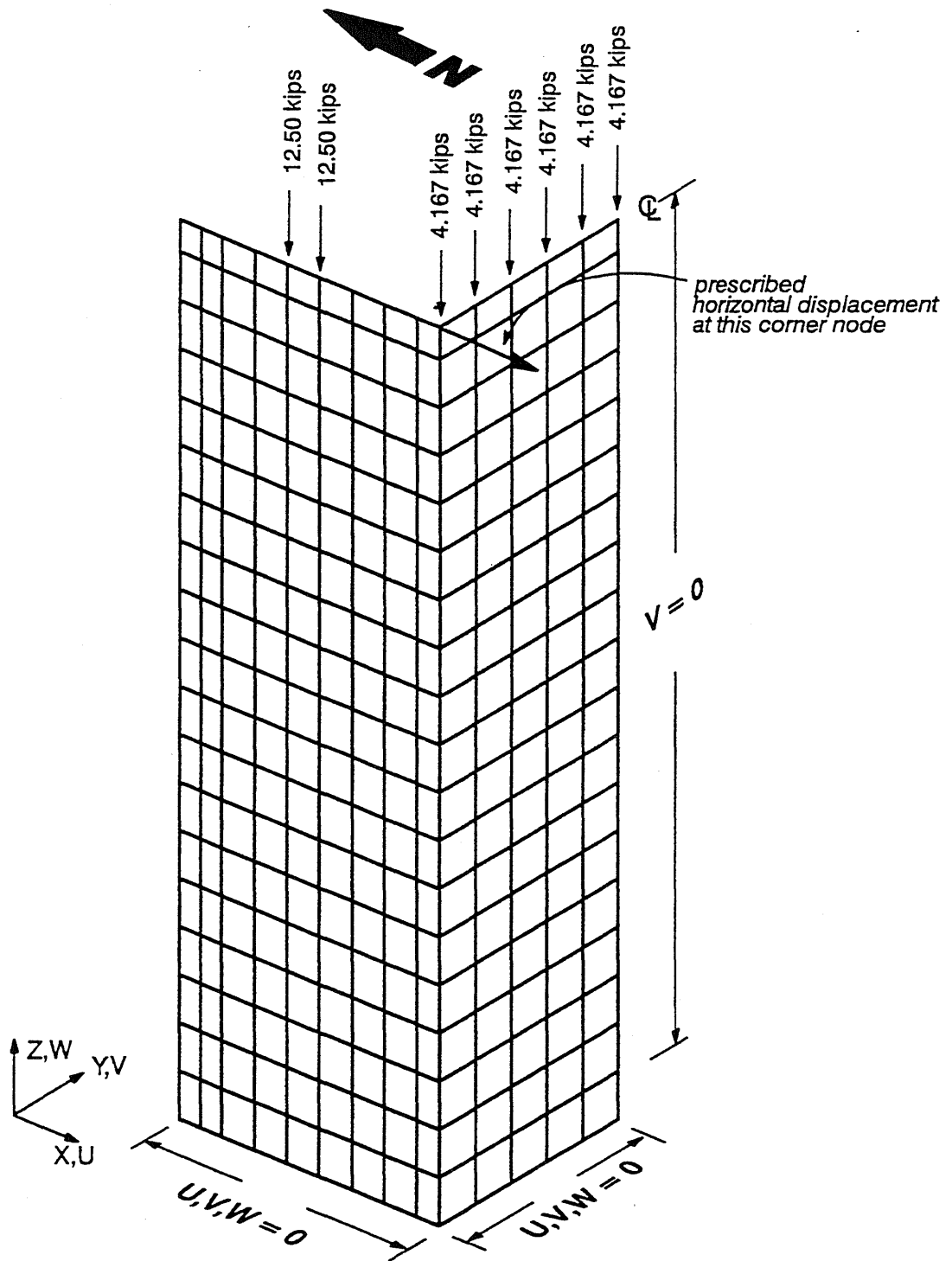
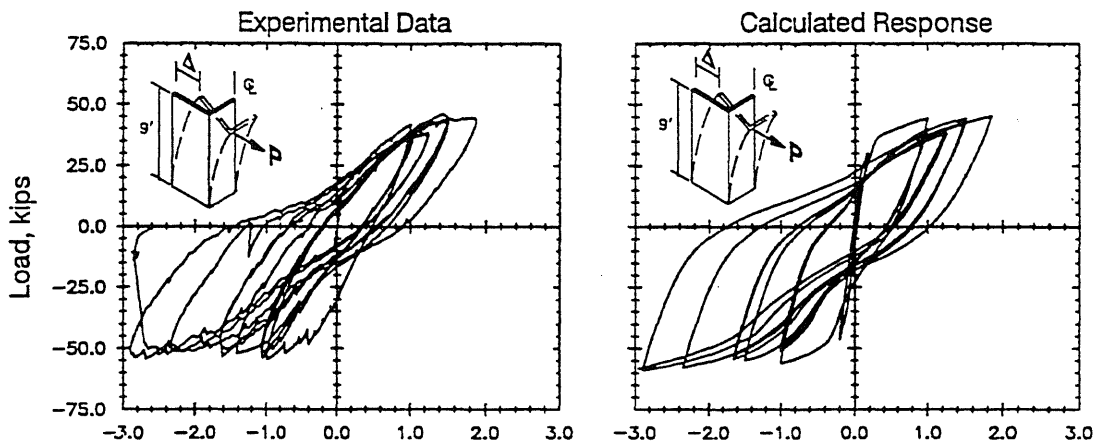
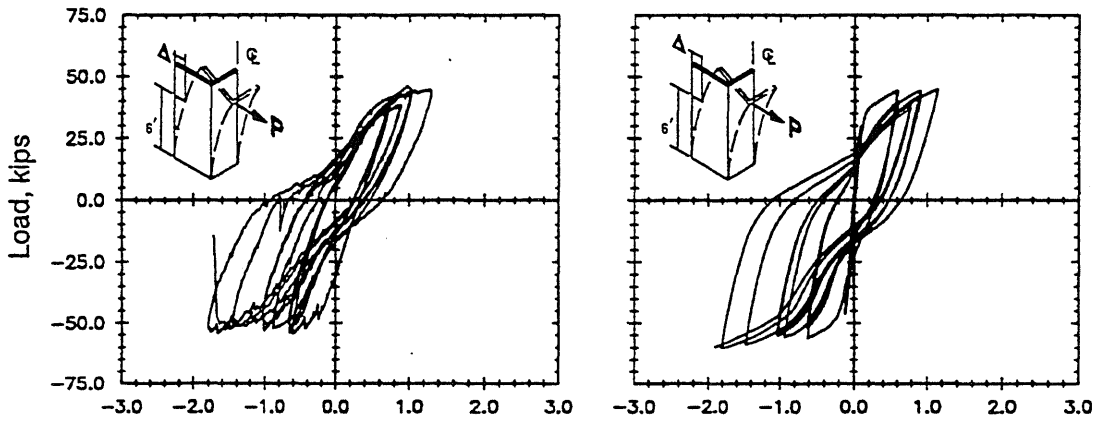


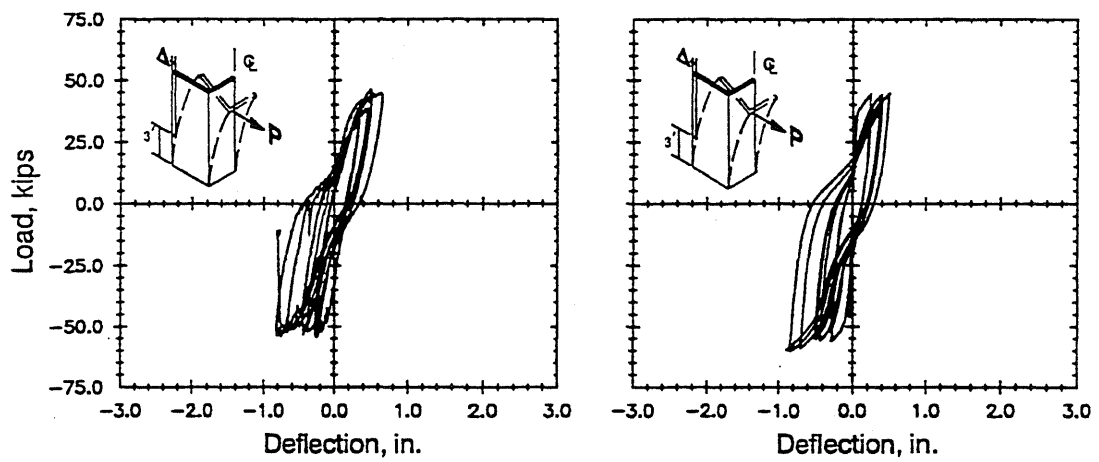
Fig. 7.8 Loading and Boundary Conditions for Finite Element Models of Walls CLS and CMS



a) 9-ft above the base



b) 6-ft above the base



c) 3-ft above the base

Fig. 7.9 Load vs. Deflection Curves at Different Levels for Wall CLS

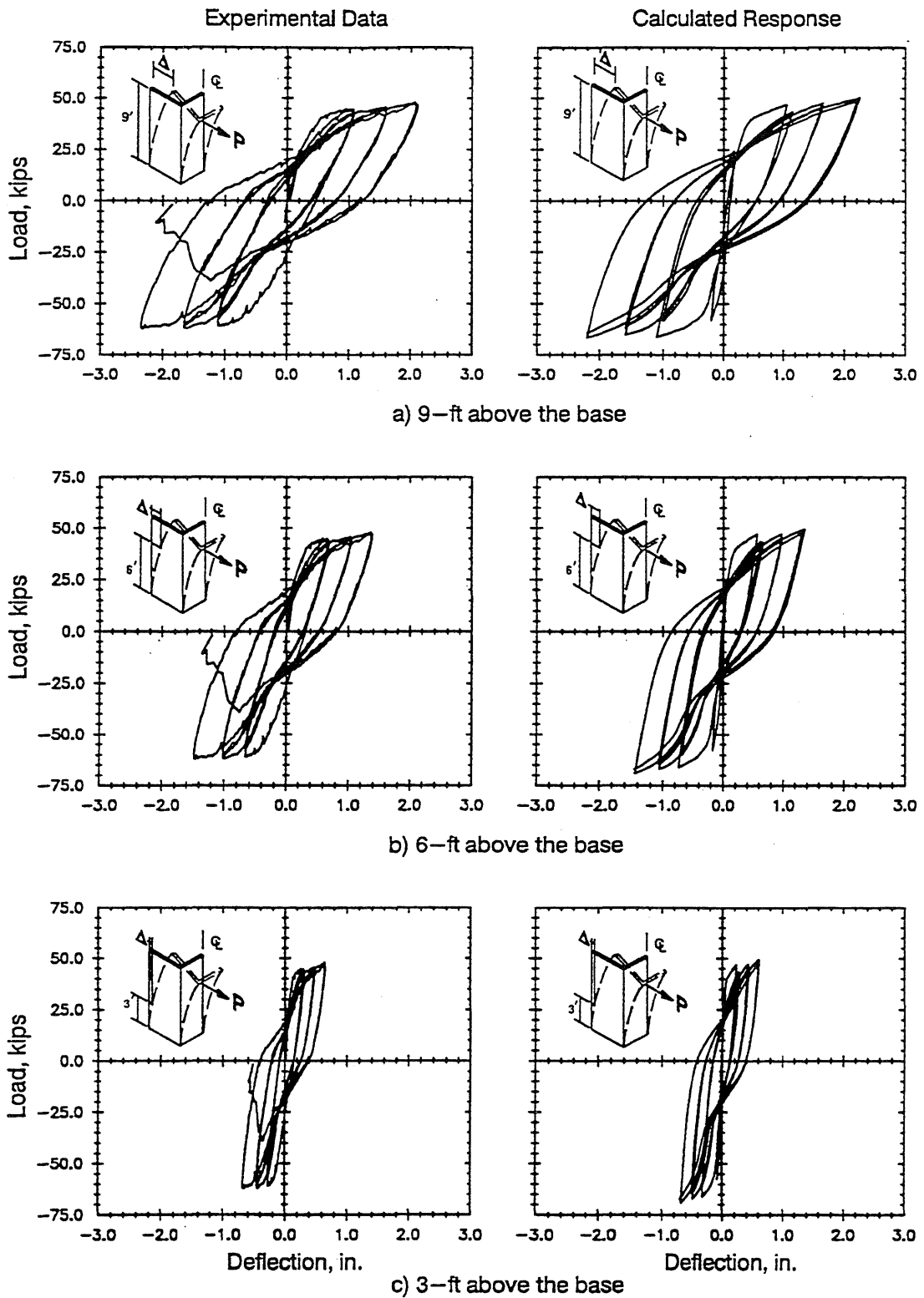


Fig. 7.10 Load vs. Deflection Curves at Different Levels for Wall CMS

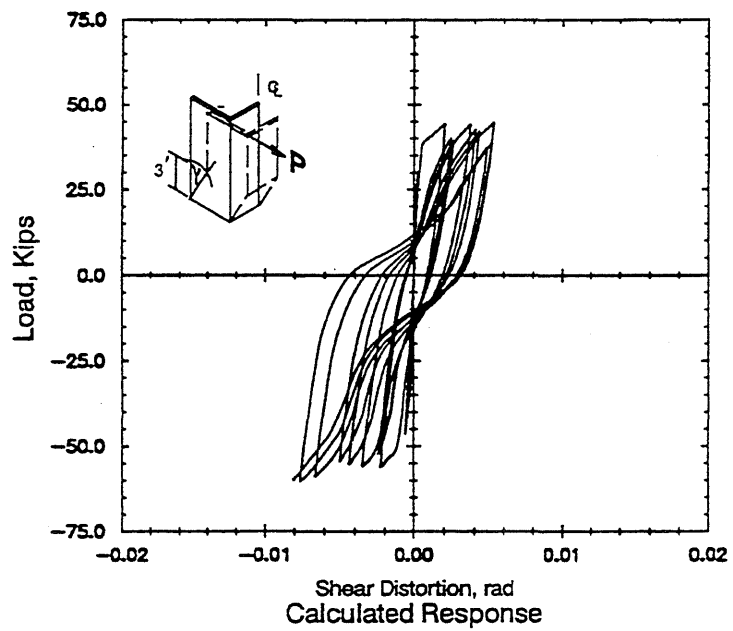
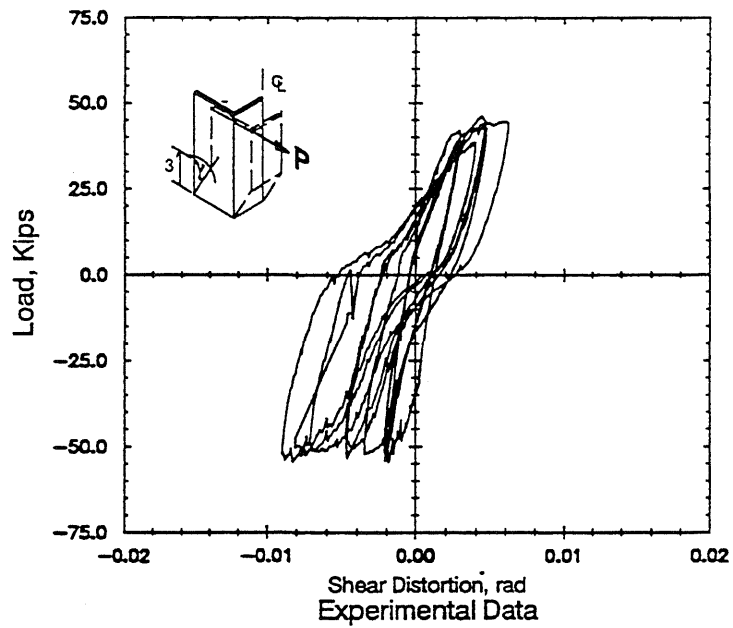


Fig. 7.11 Load vs. Shear Distortion at 3-ft Level: Wall CLS

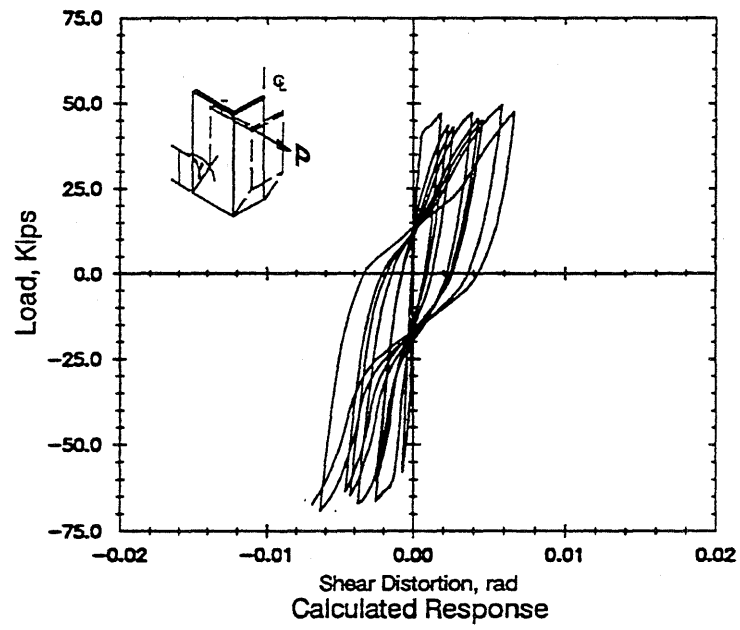
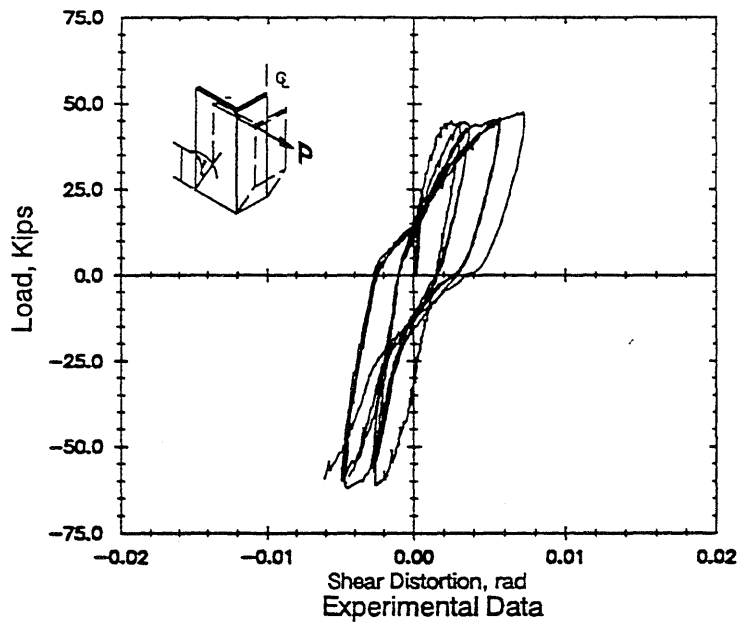


Fig. 7.12 Load vs. Shear Distortion at 3-ft Level: Wall CMS

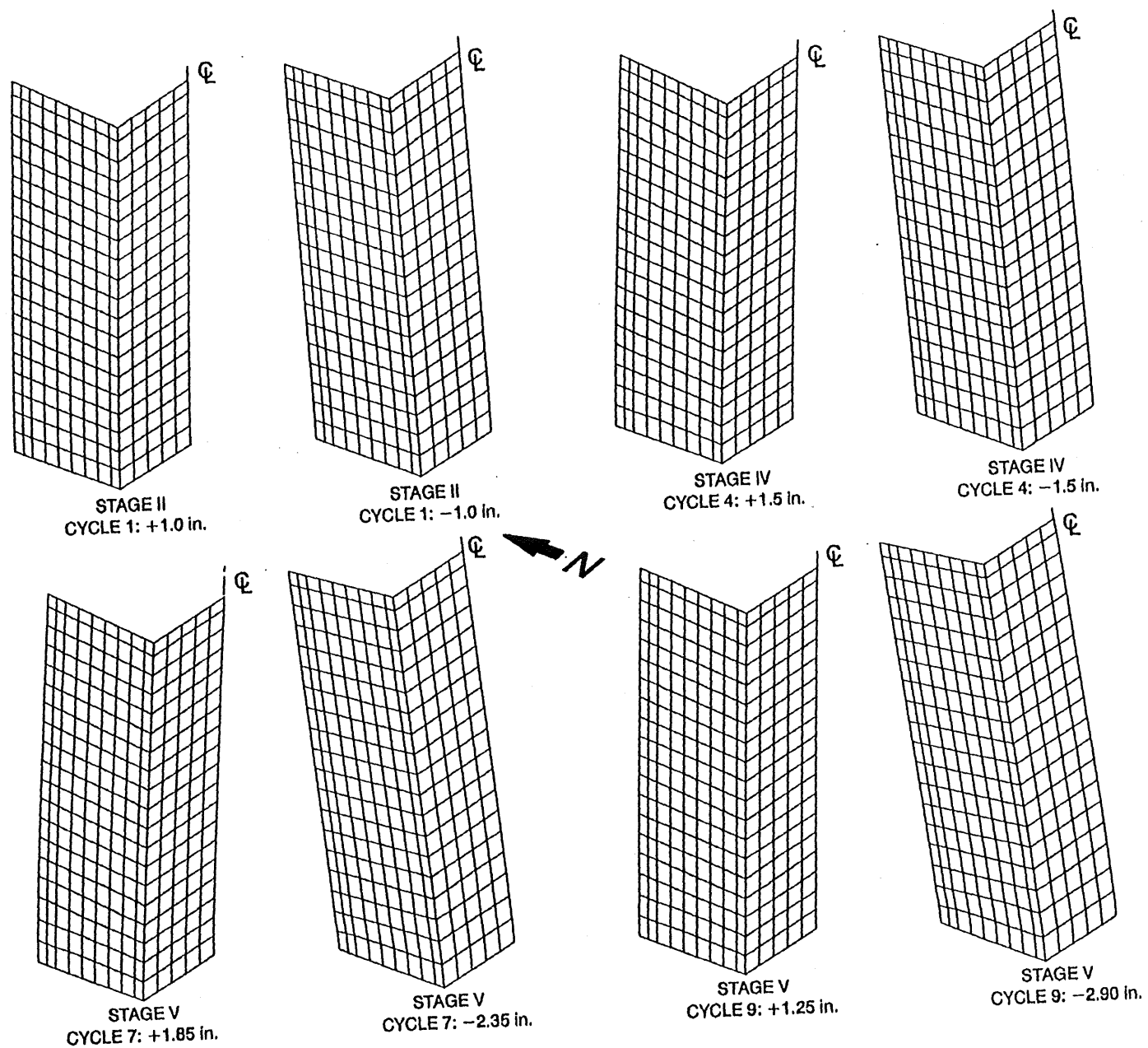


Fig. 7.13 Calculated Deformed Shape of Wall CLS

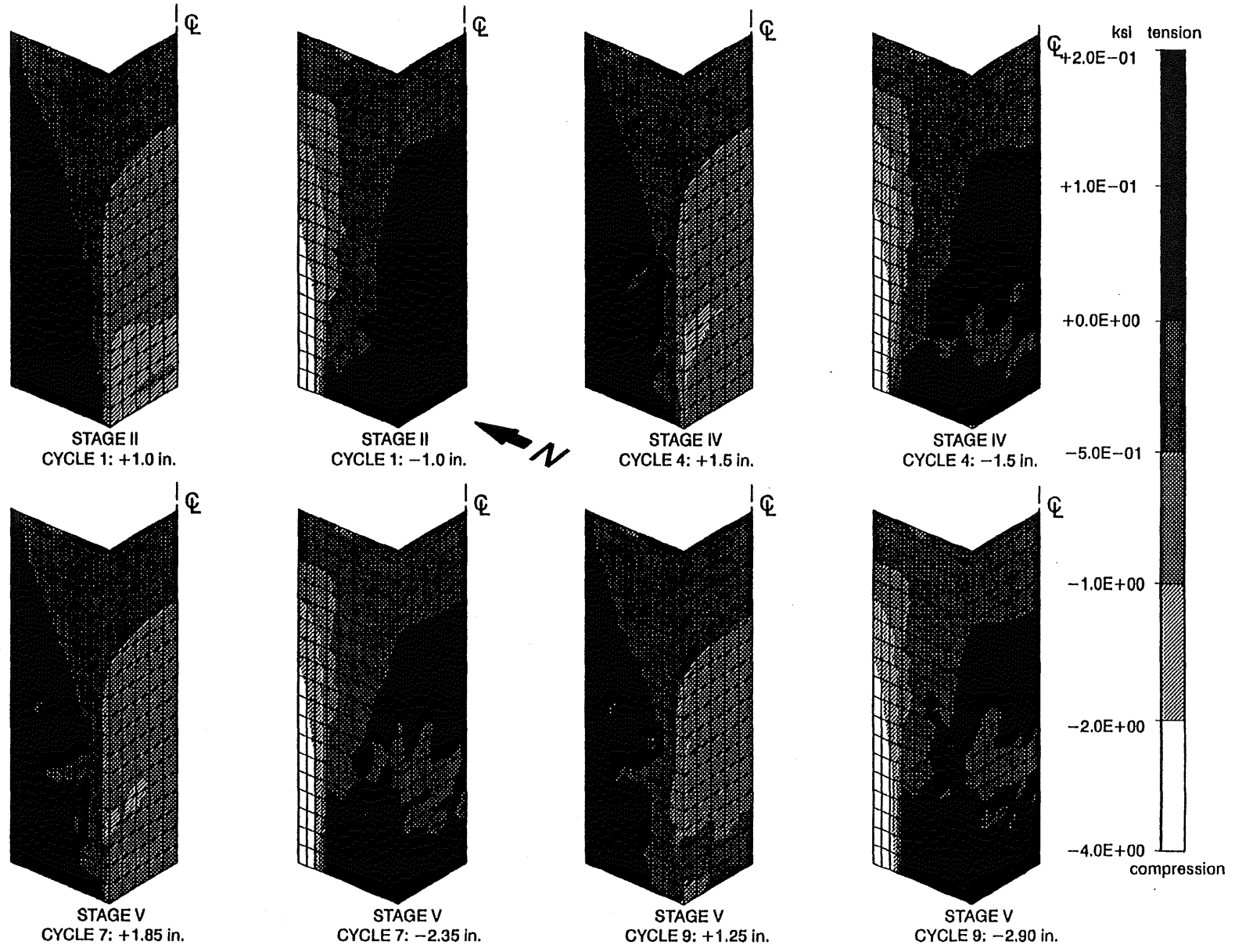


Fig. 7.14 Calculated Vertical Stress Distribution in Wall CLS



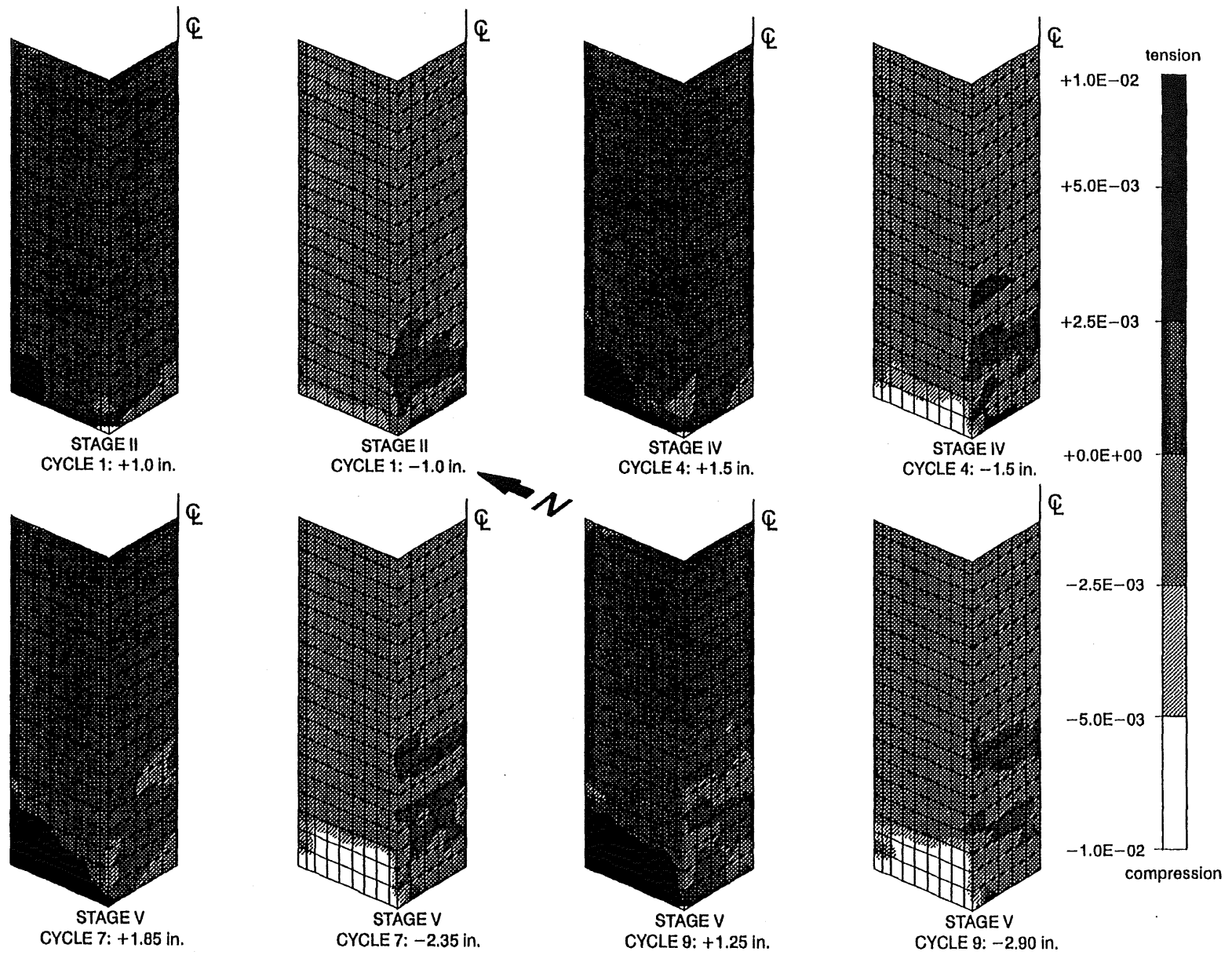


Fig. 7.15 Calculated In-plane Shear Strain Distribution in Wall CLS

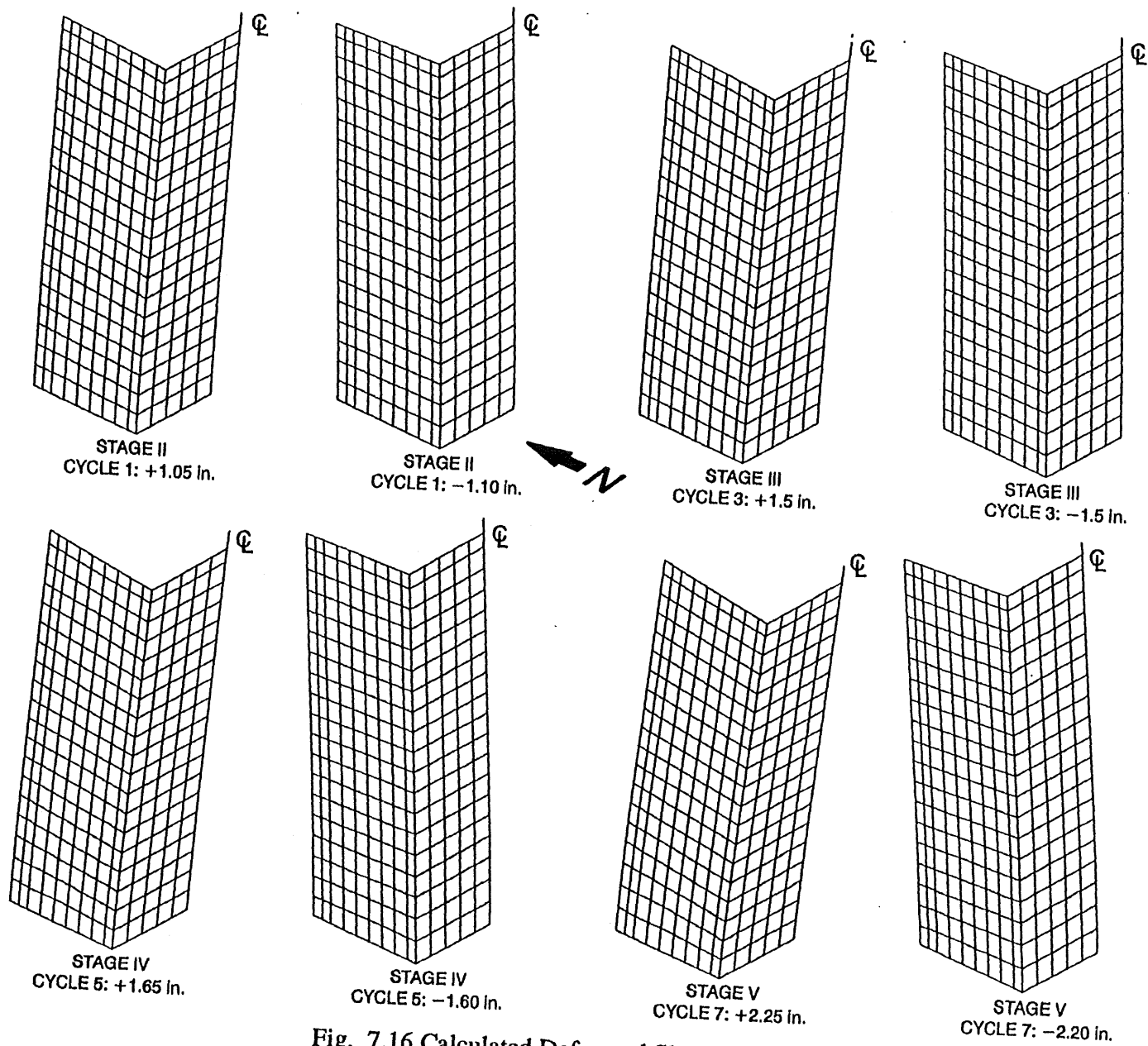


Fig. 7.16 Calculated Deformed Shape of Wall CMS

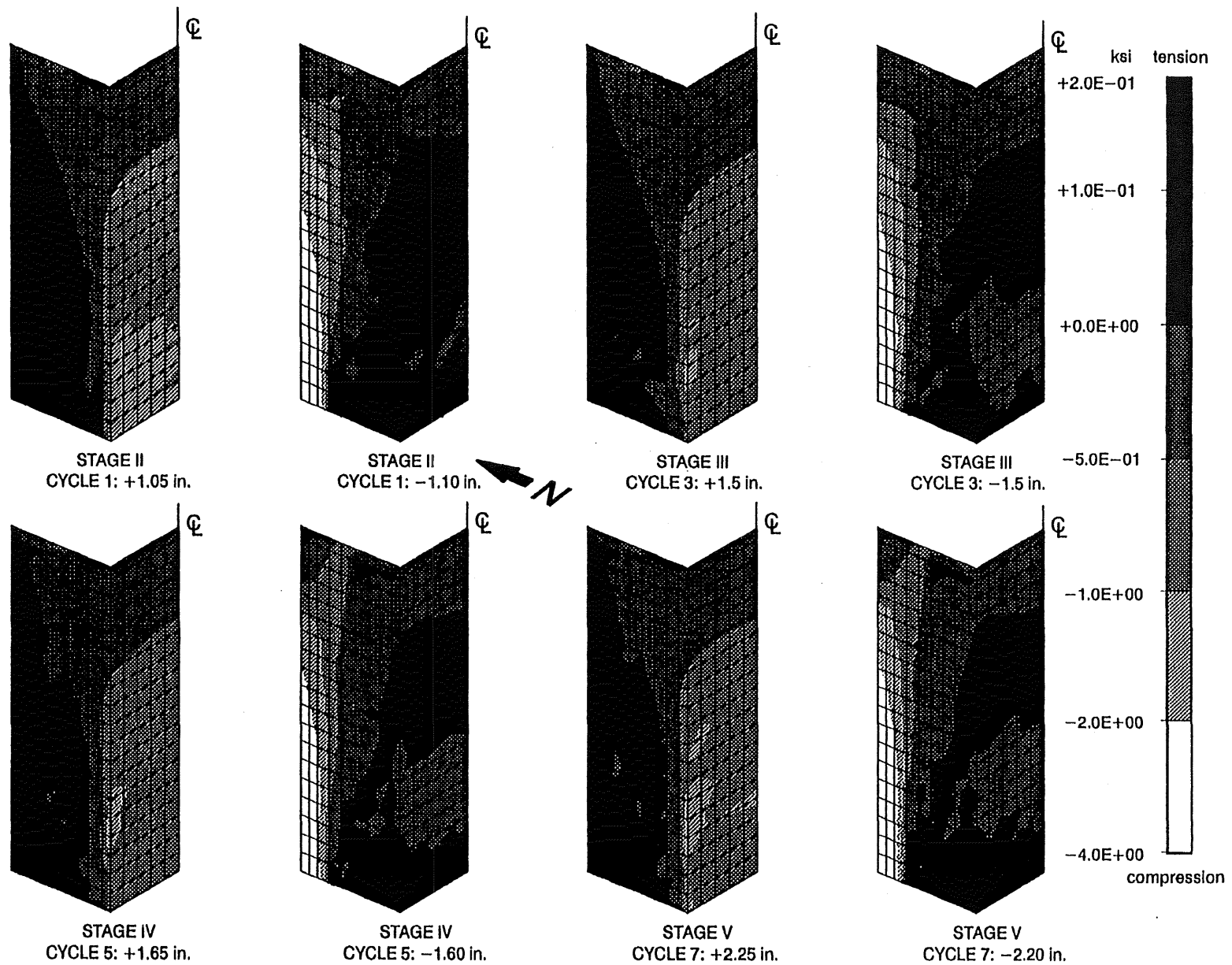


Fig. 7.17 Calculated Vertical Stress Distribution in Wall CMS

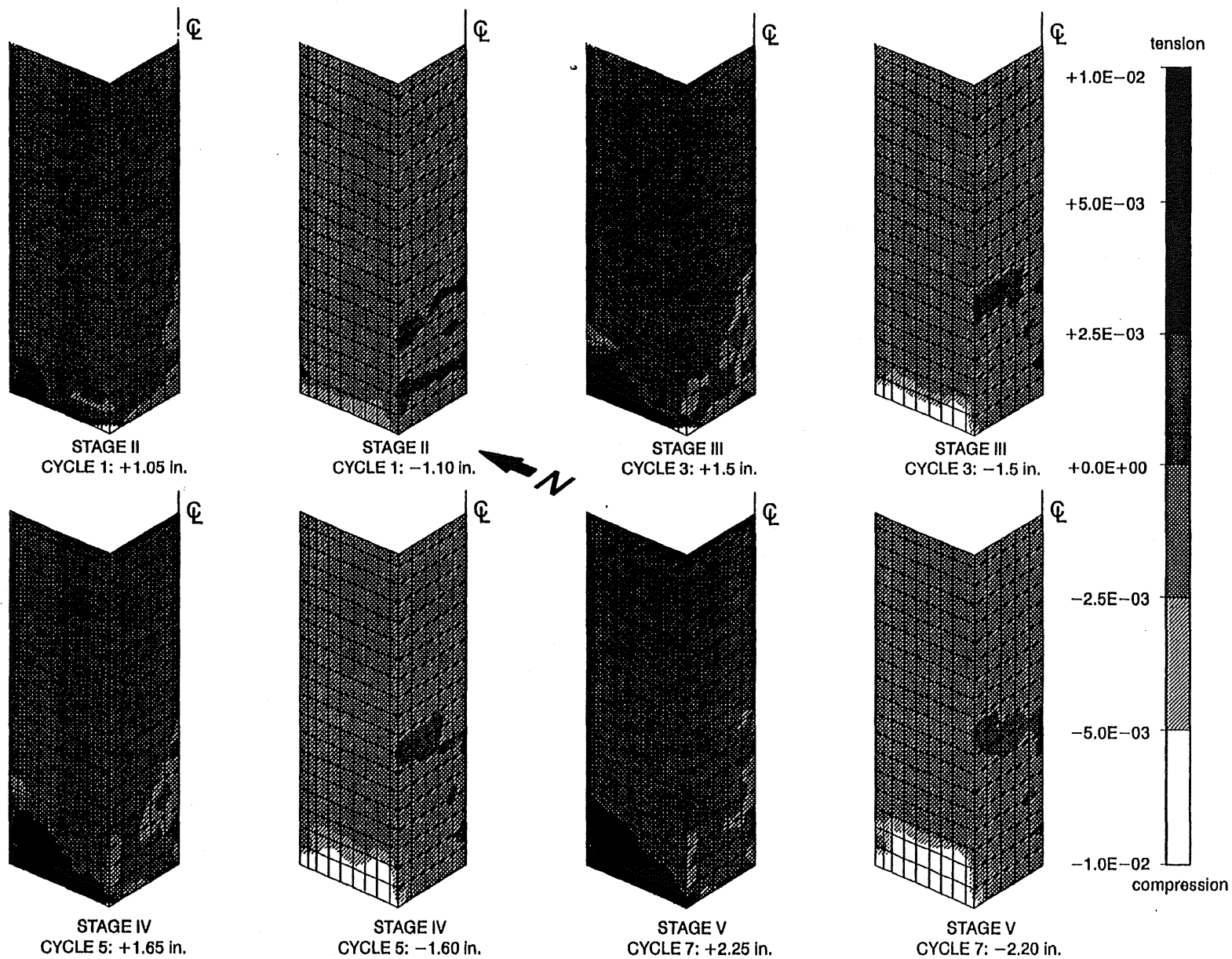


Fig. 7.18 Calculated In-plane Shear Strain Distribution in Wall CMS

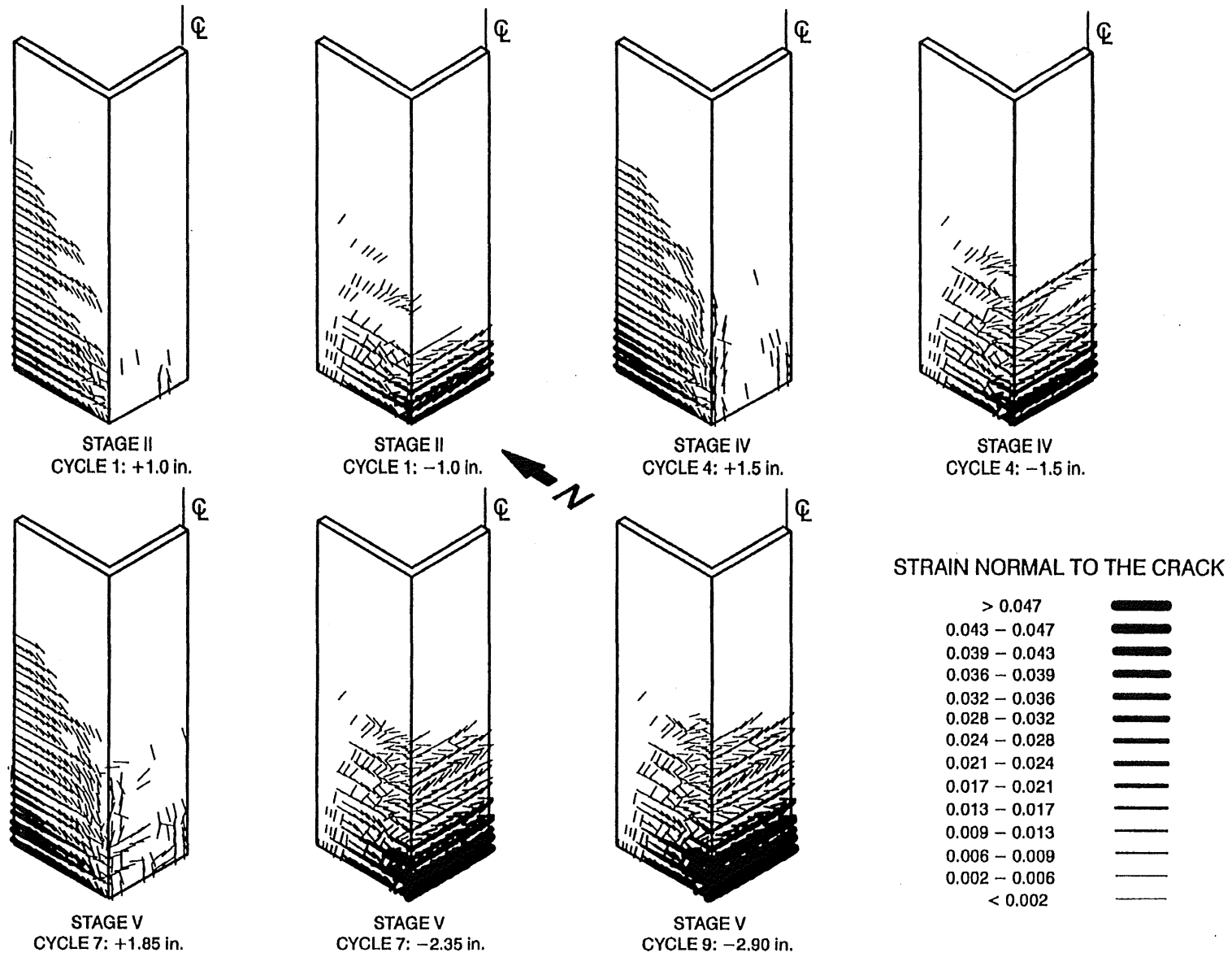


Fig. 7.19 Calculated Crack Patterns for Wall CLS at Different Top-Deflection Levels

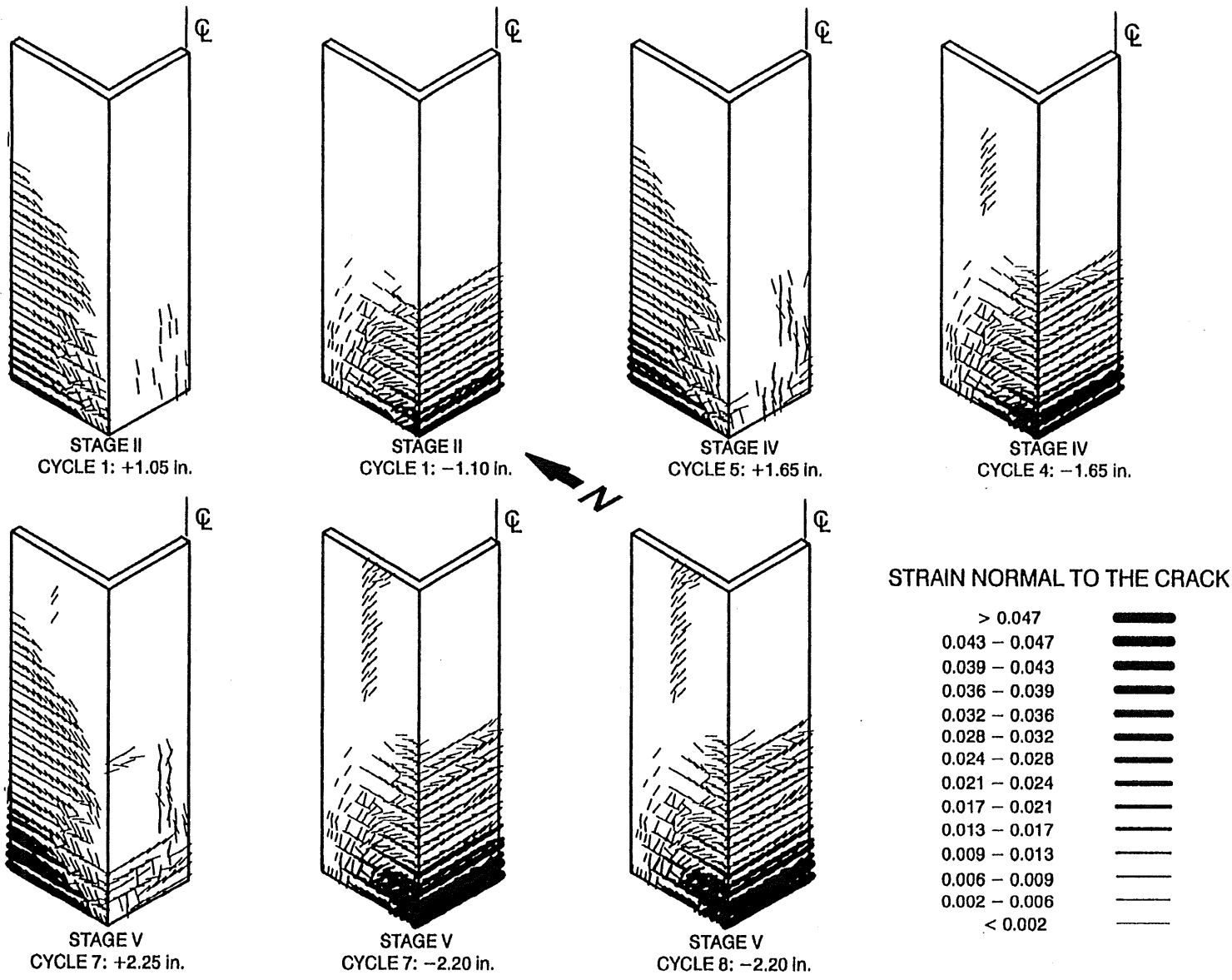


Fig. 7.20 Calculated Crack Patterns for Wall CMS at Different Top-Deflection Levels

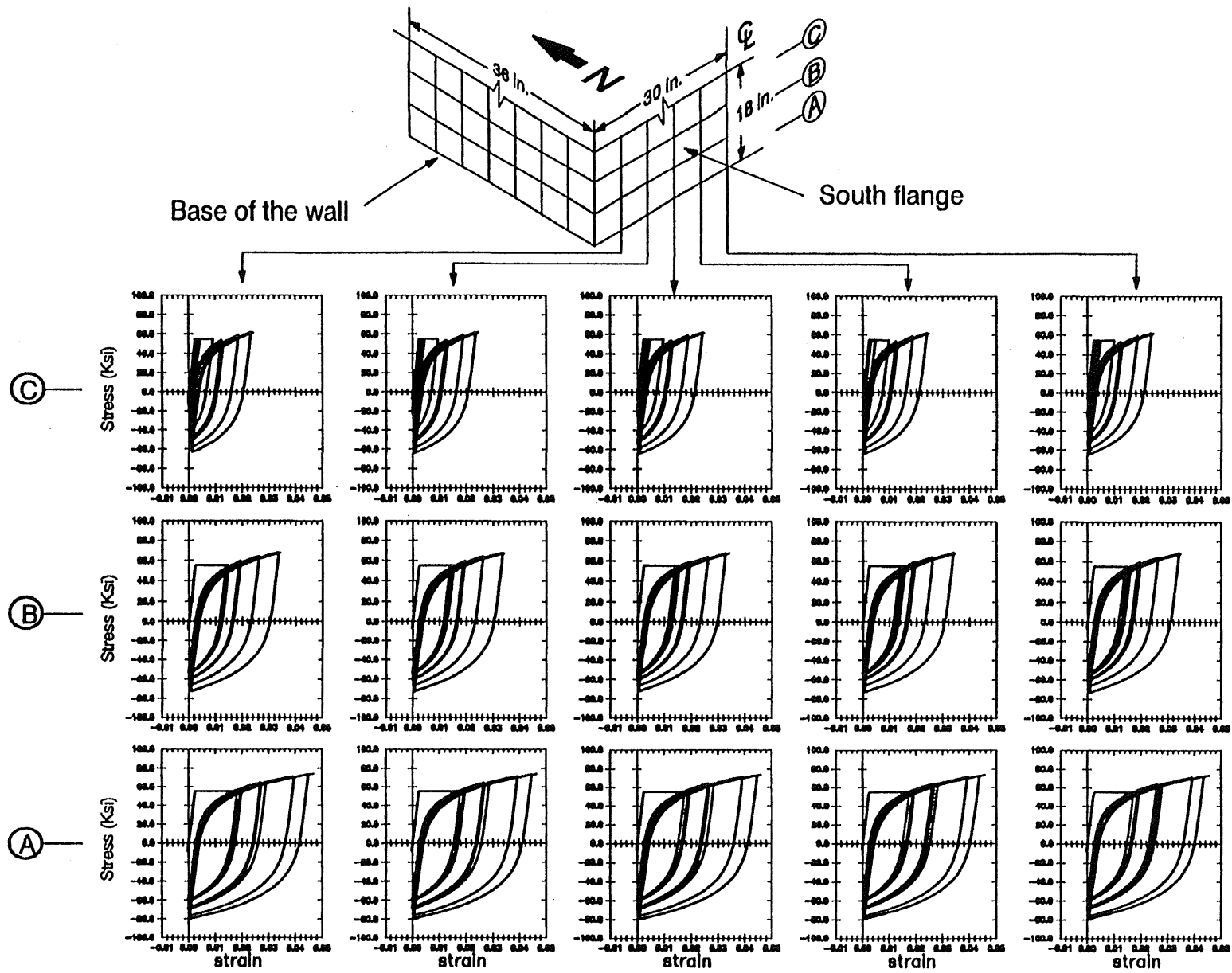


Fig. 7.21 Calculated Stress-Strain Relationship in Vertical Reinforcement in South Flange for Wall CLS

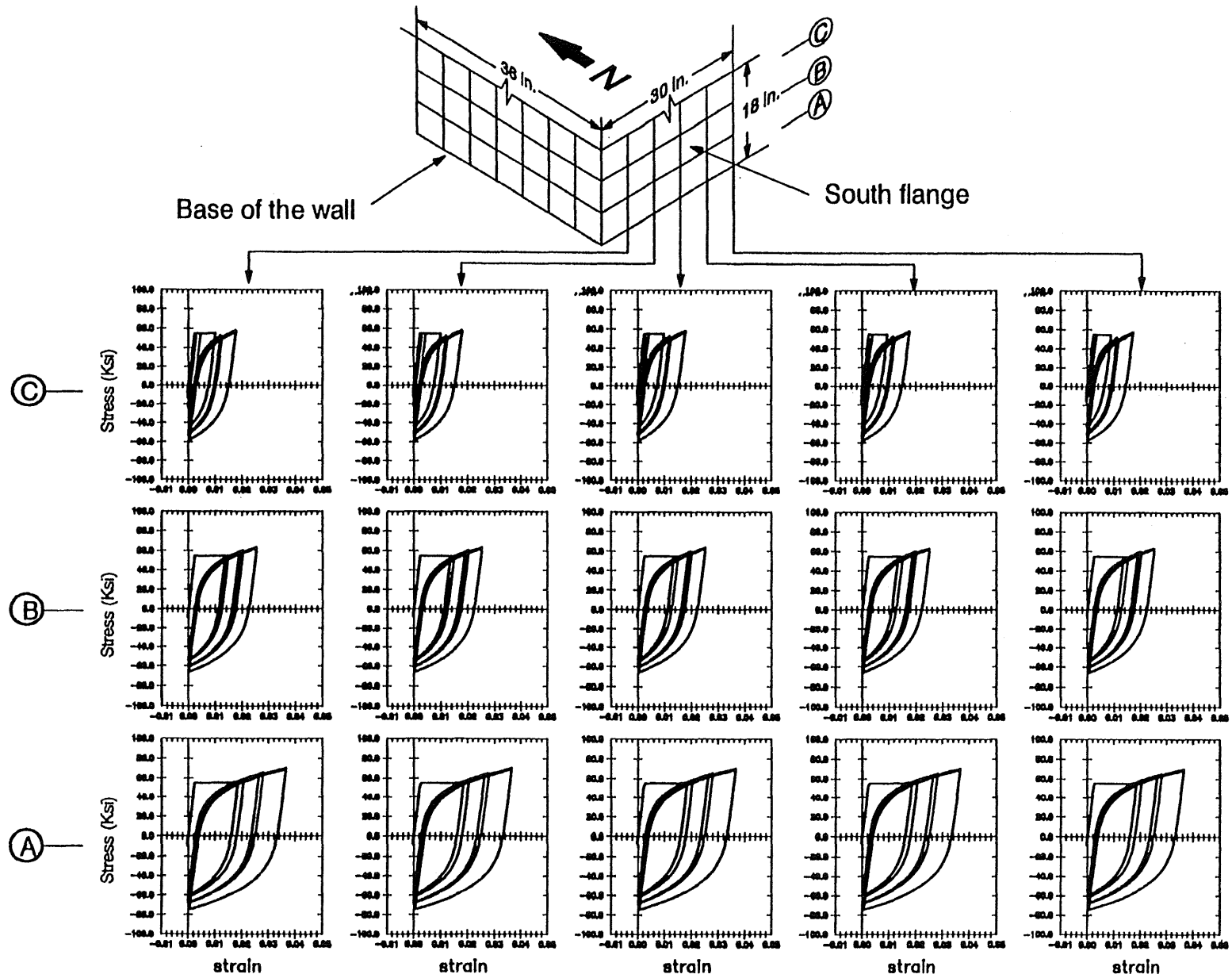
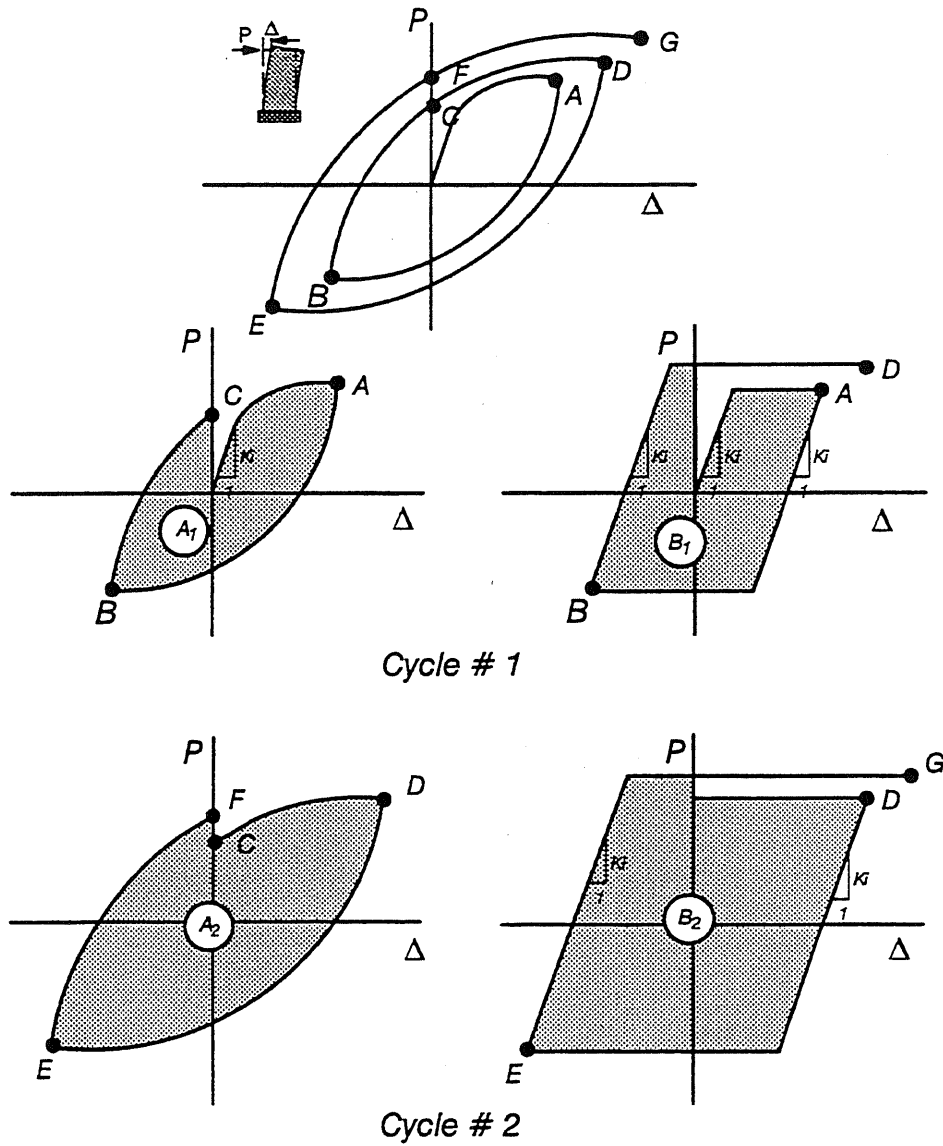


Fig. 7.22 Calculated Stress-Strain Relationship in Vertical Reinforcement in South Flange for Wall CMS





$A_i$  is the energy dissipation capacity of each cycle.  
 $B_i$  is the energy dissipation capacity of an elasto-plastic material with the same max. load and max. displacement of each cycle.  
 $K_i$  is the uncracked stiffness of the wall

The accumulated energy dissipation ratio of cycle  $i =$

$$\frac{\sum_i A_i}{\sum_i B_i}$$

Fig. 8.1 Calculation of the Accumulated Energy Dissipation Ratio

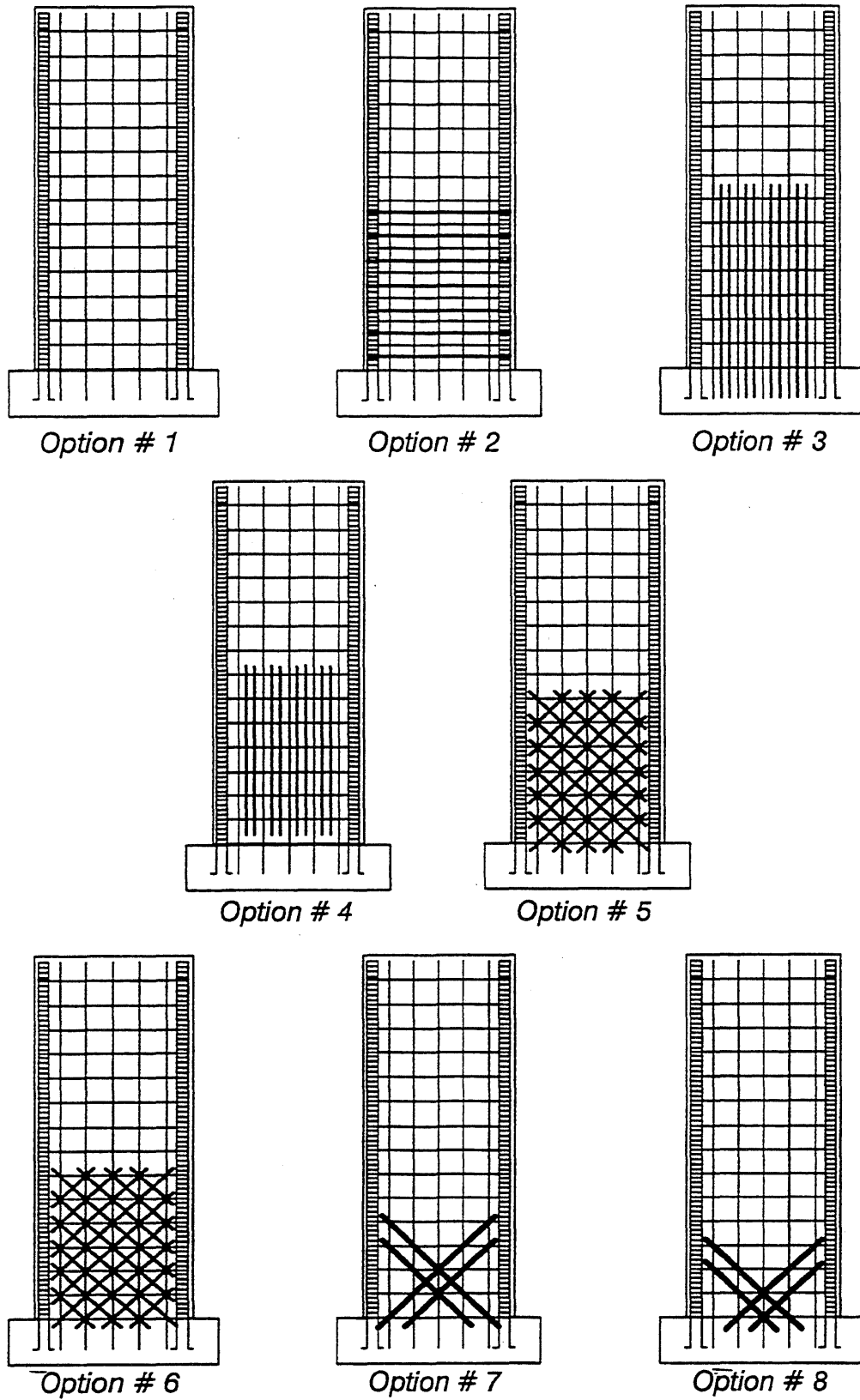


Fig. 8.2 Reinforcement Details Considered in the Finite Element Analyses

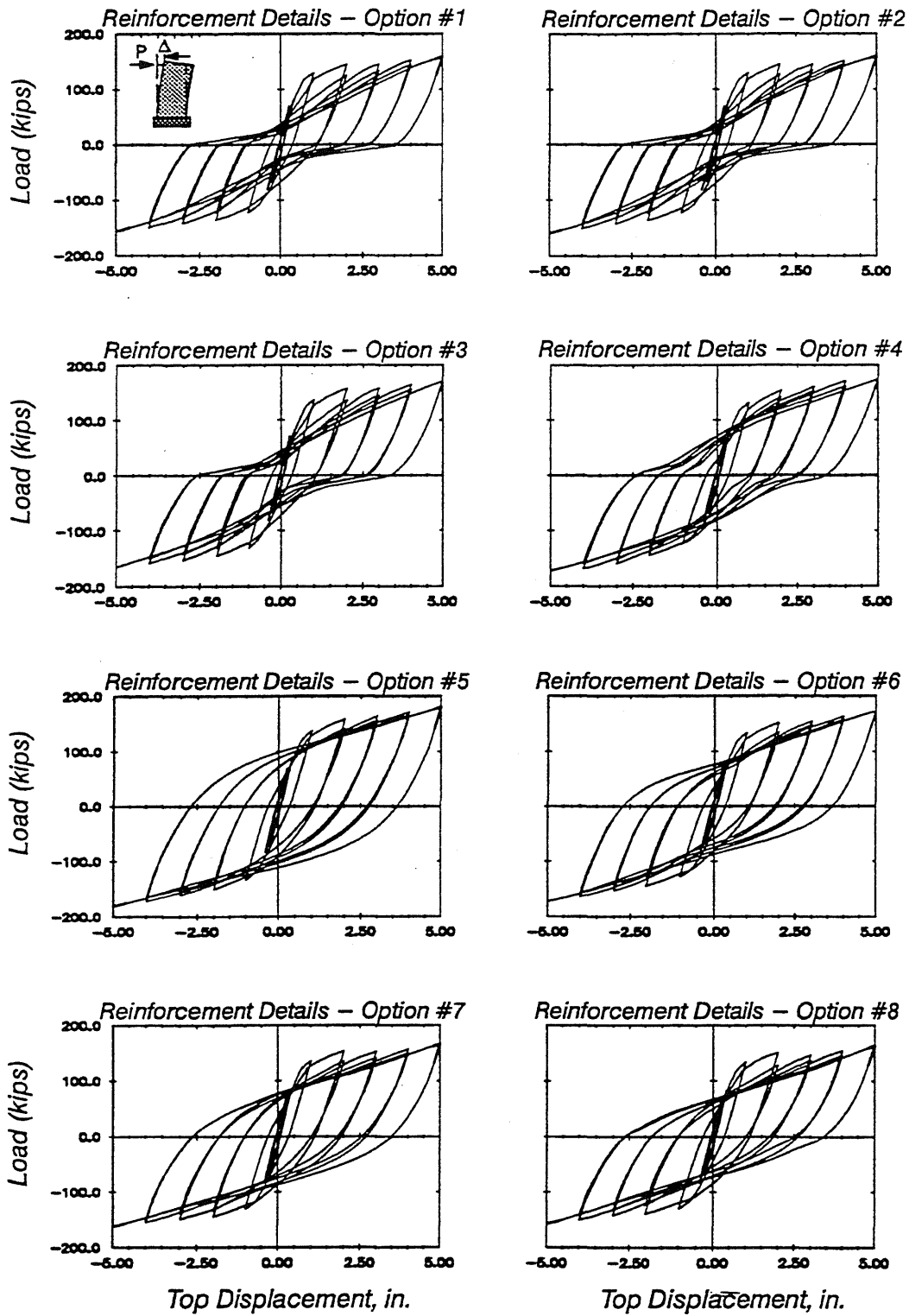


Fig. 8.3 Load vs. Top Deflection Curves for Wall B2 with Different Reinforcement Details

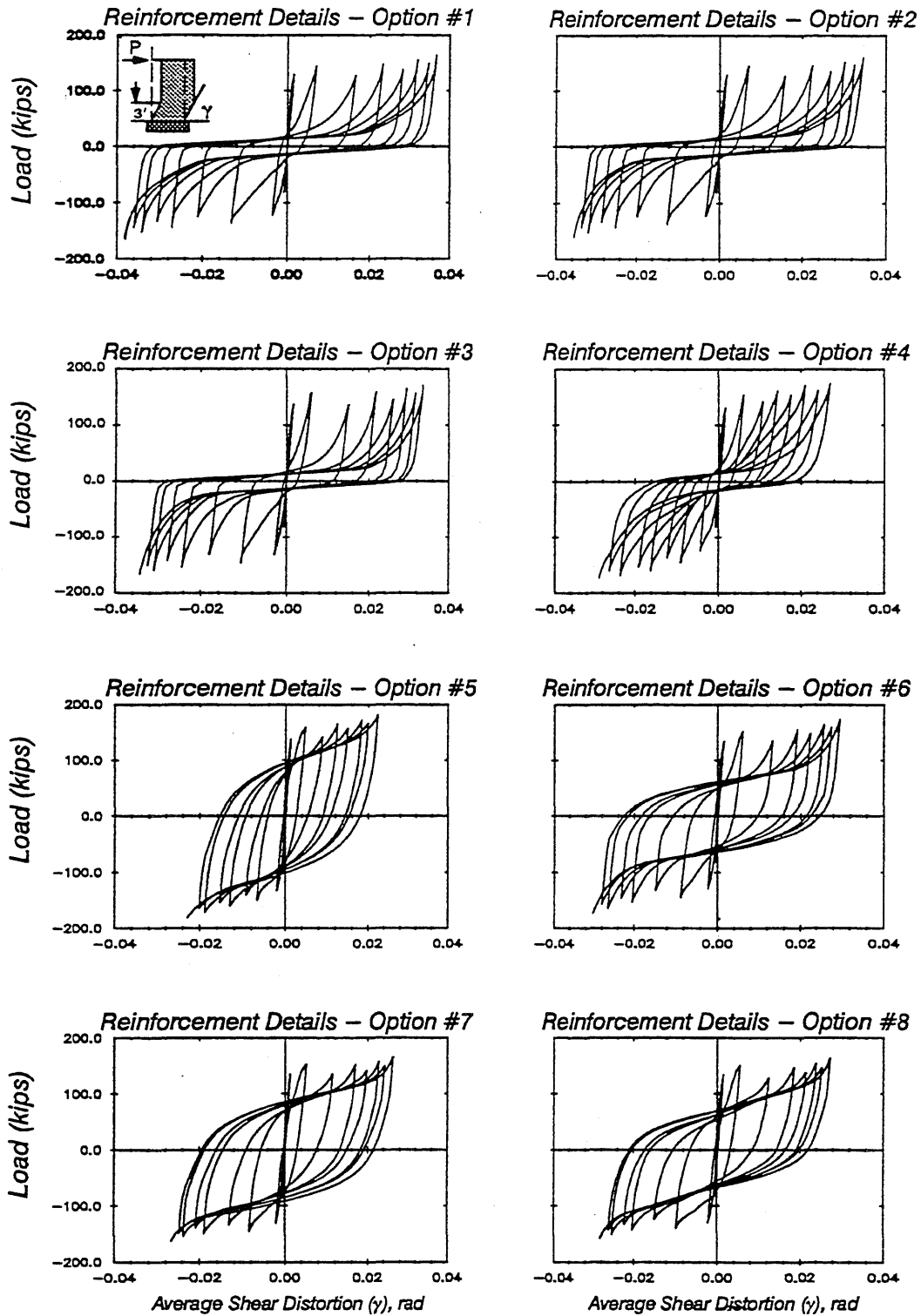


Fig. 8.4 Load vs. Shear Distortion Curves for Wall B2 with Different Reinforcement Details

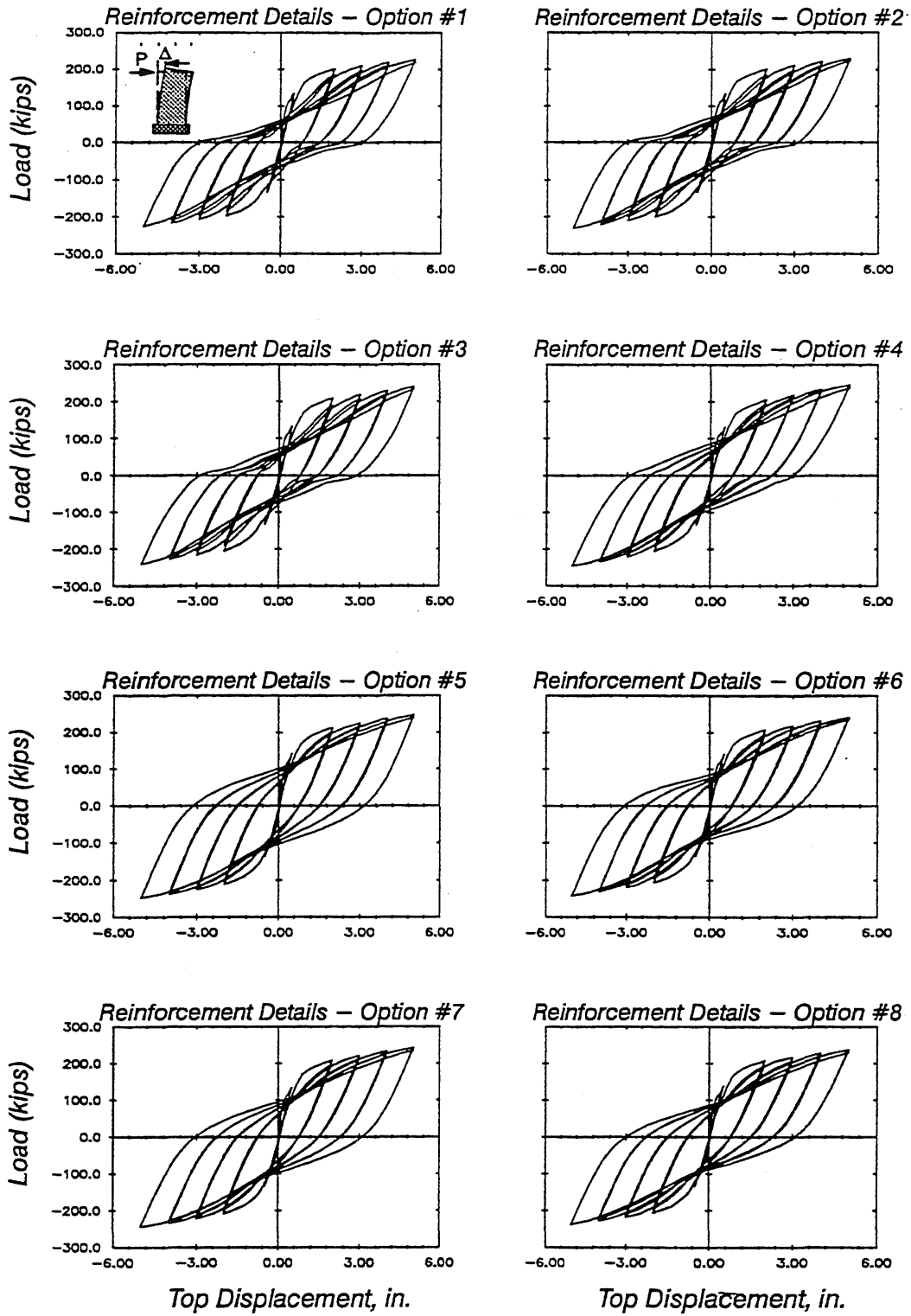


Fig. 8.5 Load vs. Top Deflection Curves for Wall B7 with Different Reinforcement Details

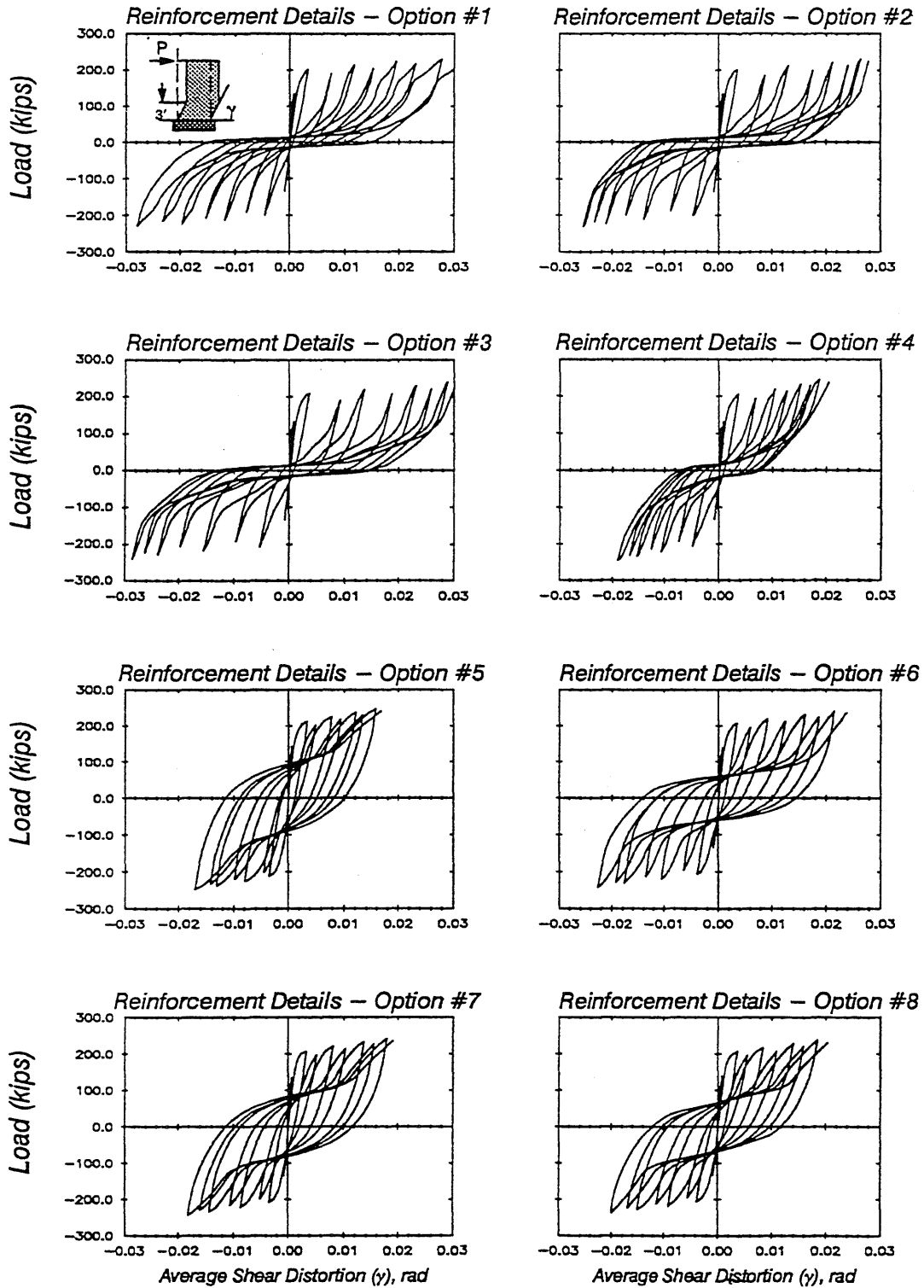


Fig. 8.6 Load vs. Shear Distortion Curves for Wall B7 with Different Reinforcement Details

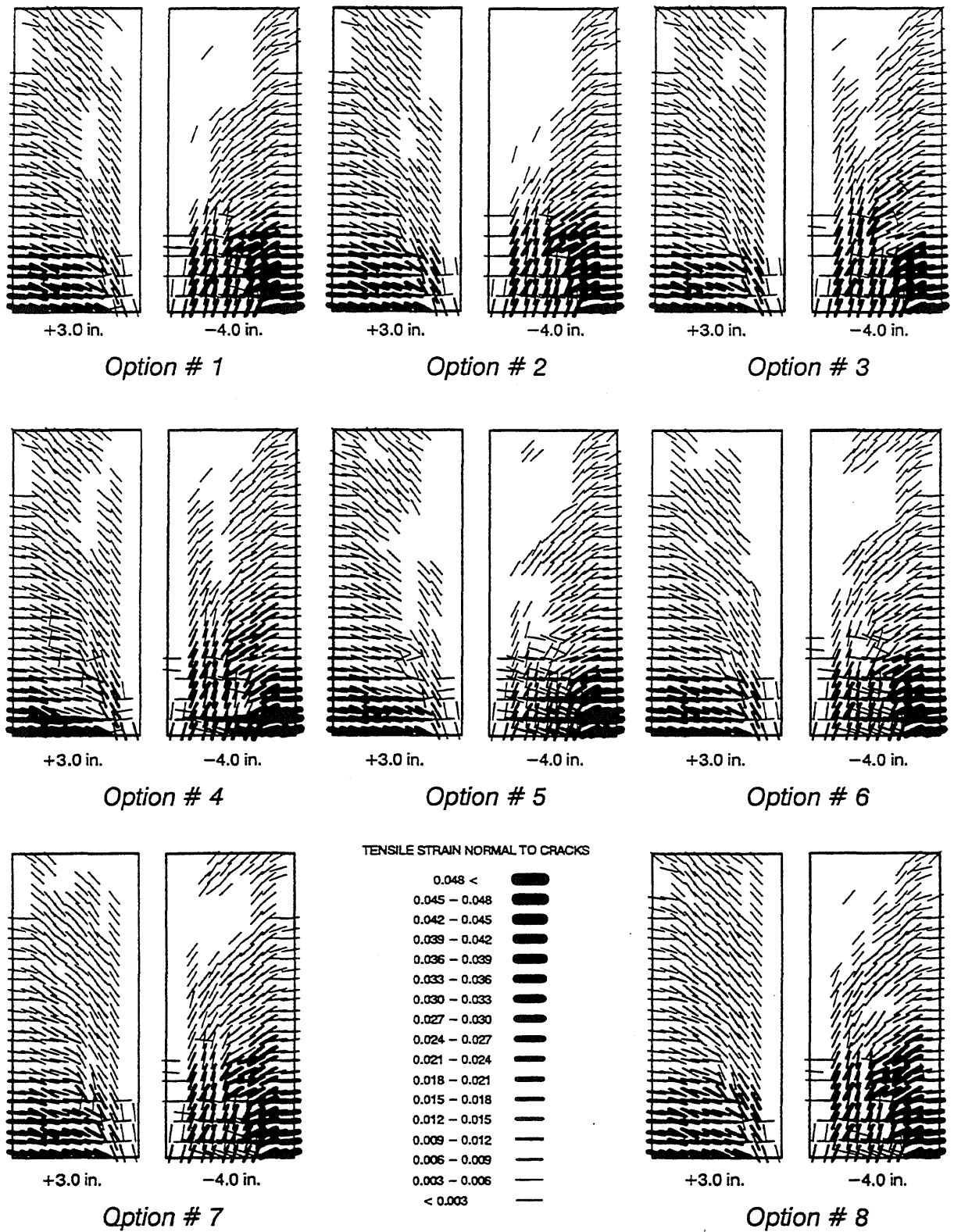


Fig. 8.7 Crack Patterns in Wall B2 with Different Reinforcement Details

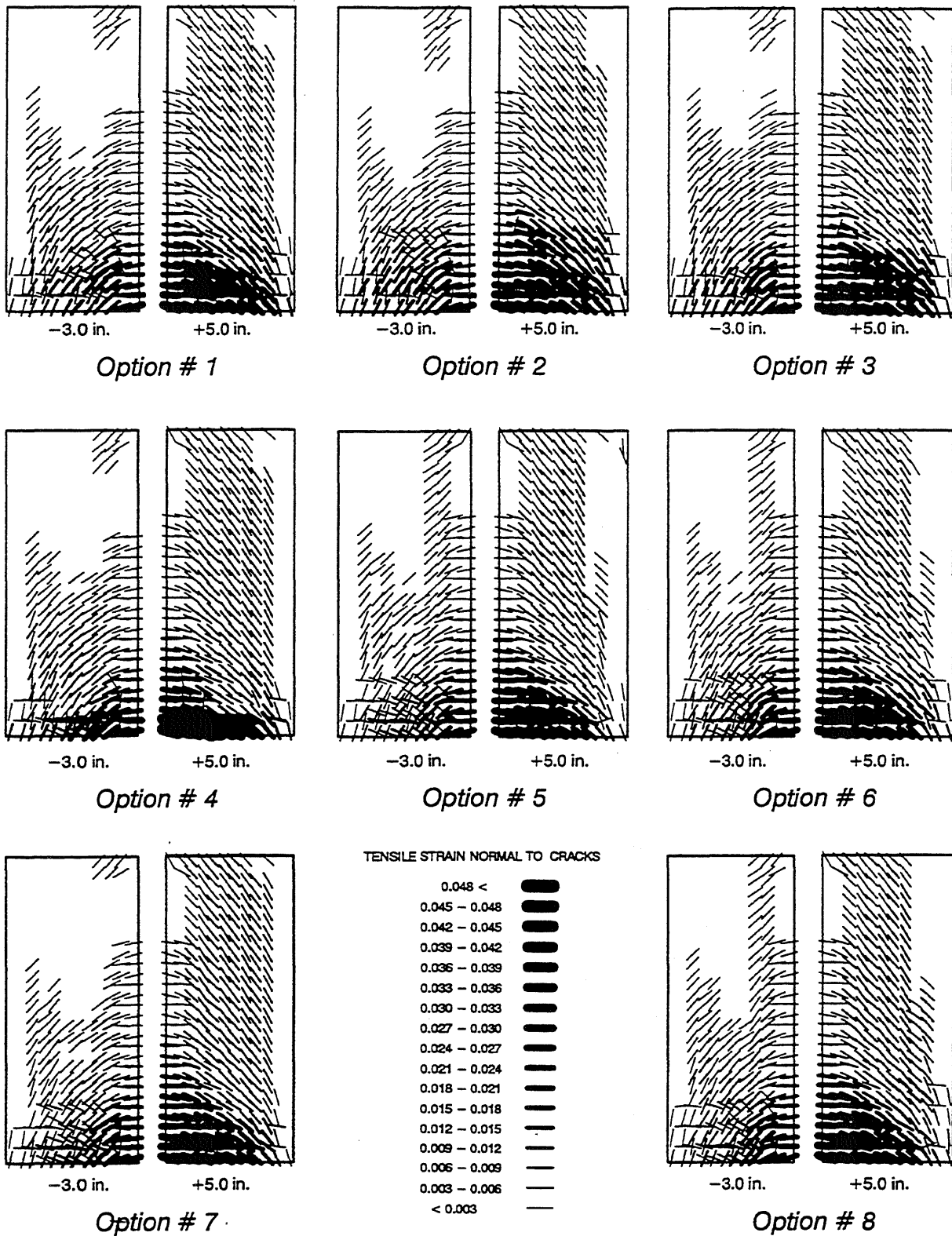
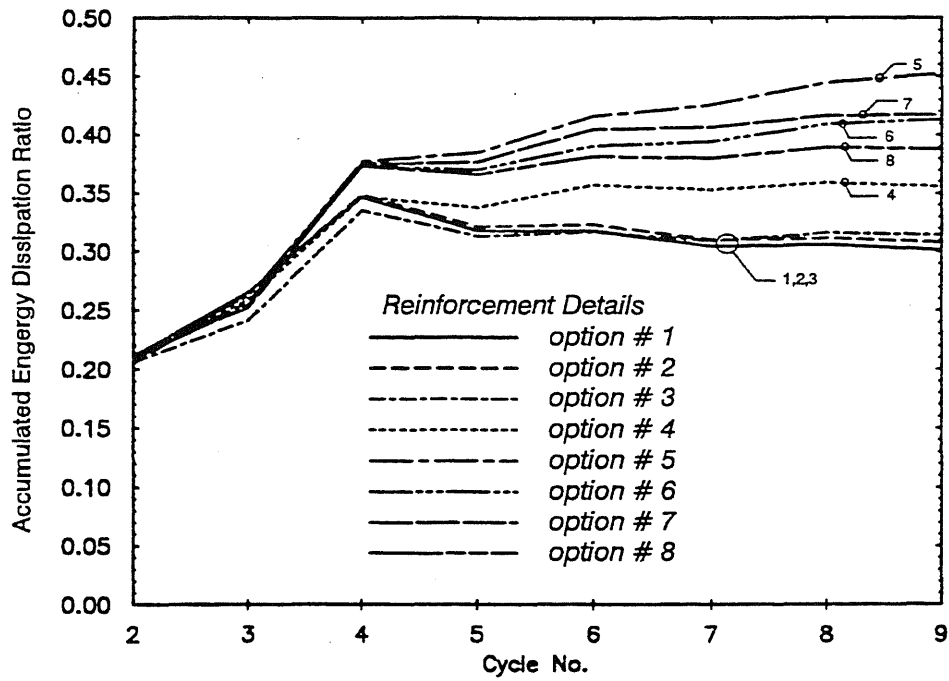
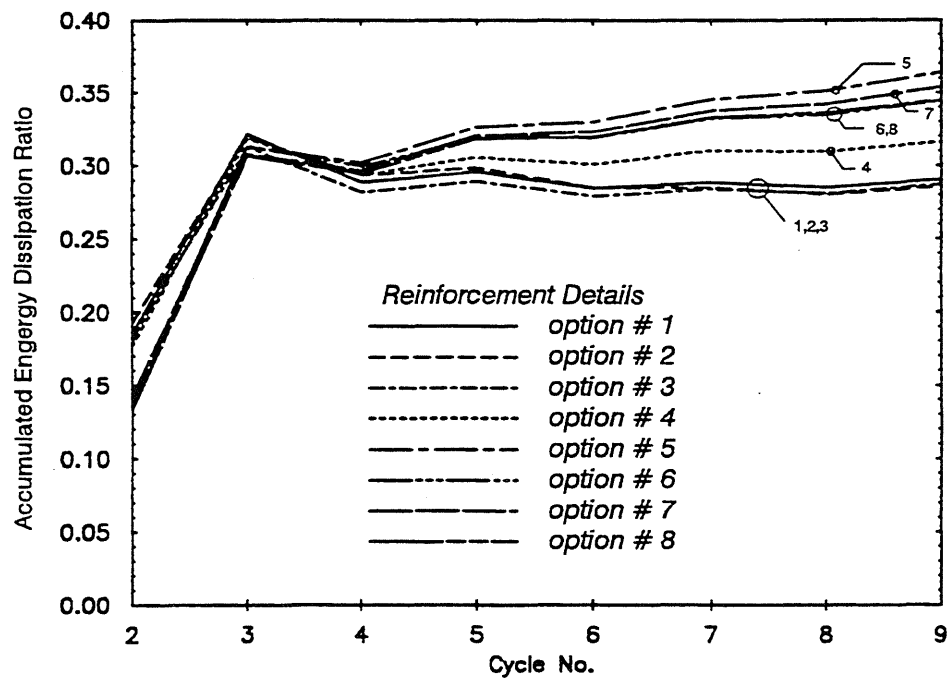


Fig. 8.8 Crack Patterns in Wall B7 with Different Reinforcement Details



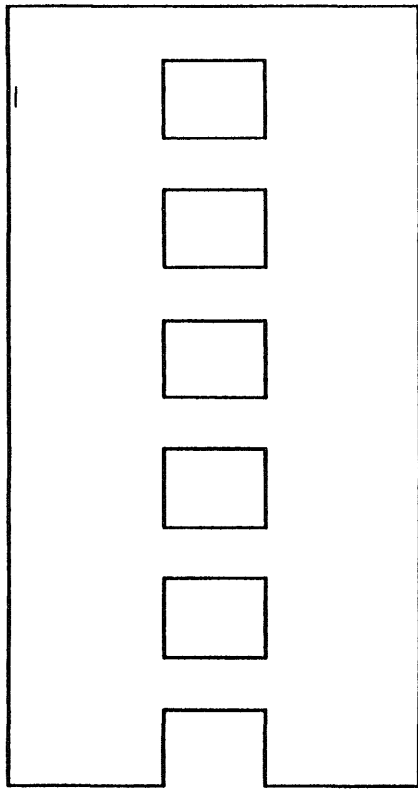


a) Wall B2

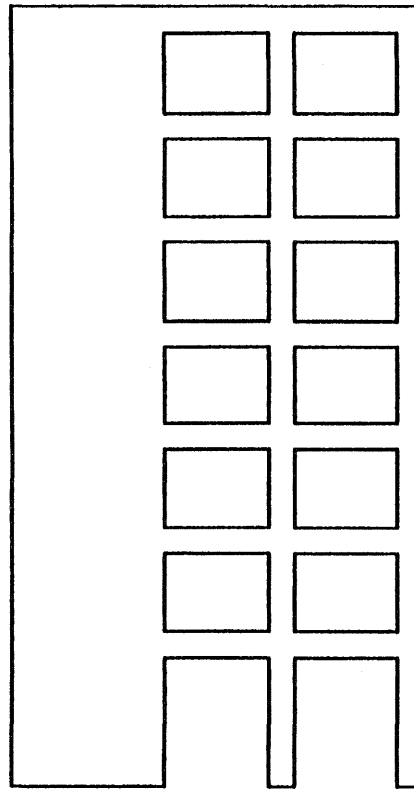


b) Wall B7

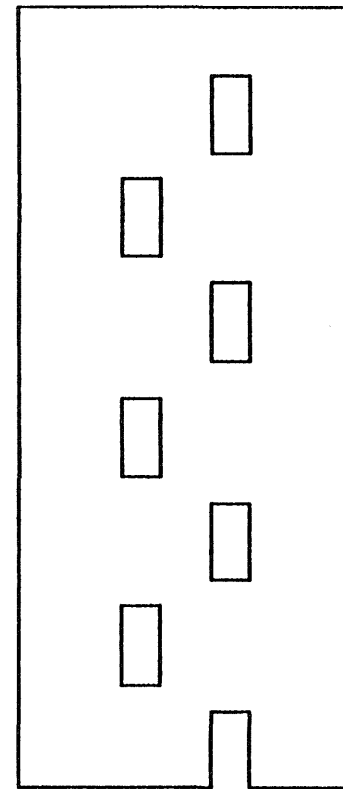
Fig. 8.9 Accumulated Energy Dissipation Ratio for Walls B2 and B7



a) Coupled Shear Walls



b) Wall-Frame Systems



c) Pierced Shear Walls

Fig. 8.10 Shear Wall Systems (from [126])

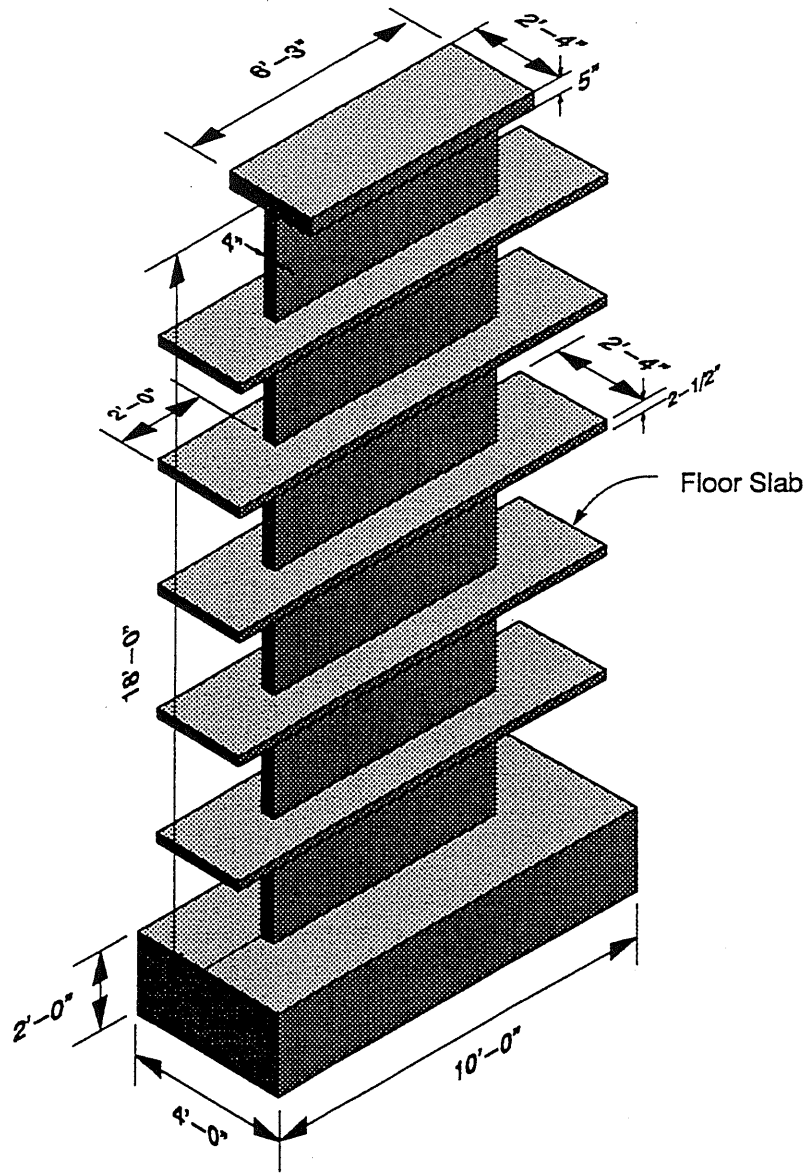


Fig. 8.11 Overall Dimensions of Walls CI1 and PW1

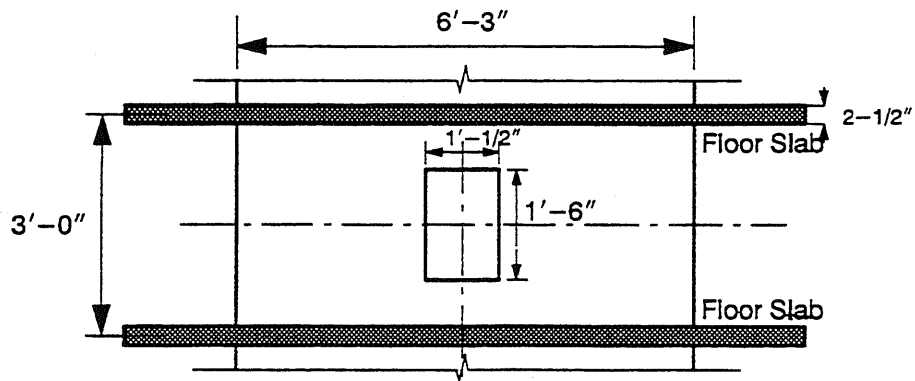


Fig. 8.12 Location and Dimensions of Openings in Wall PW1

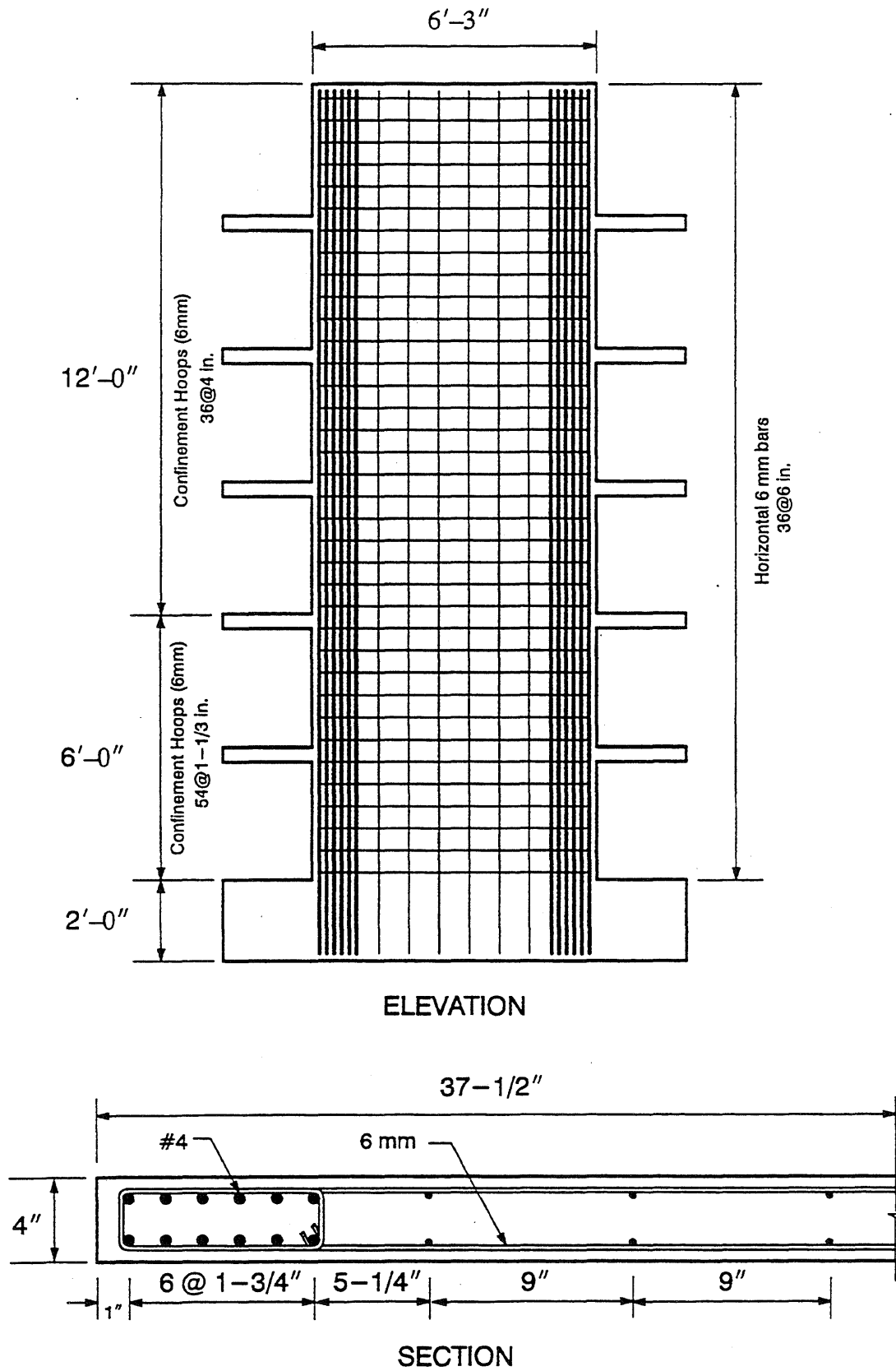
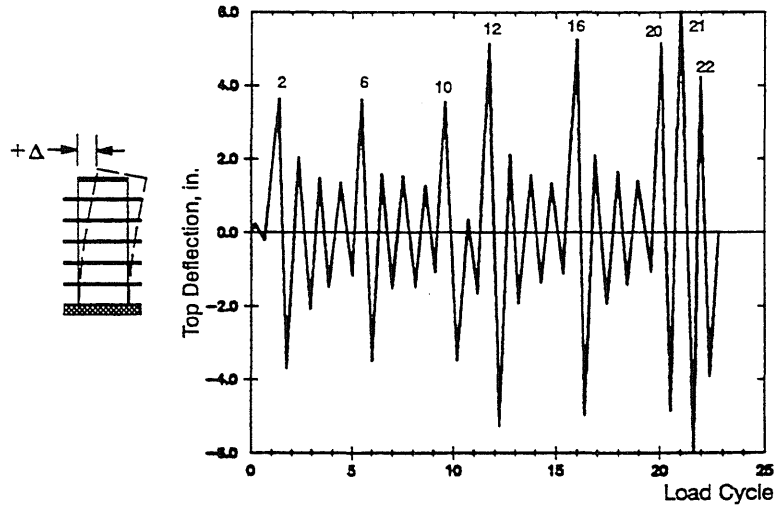
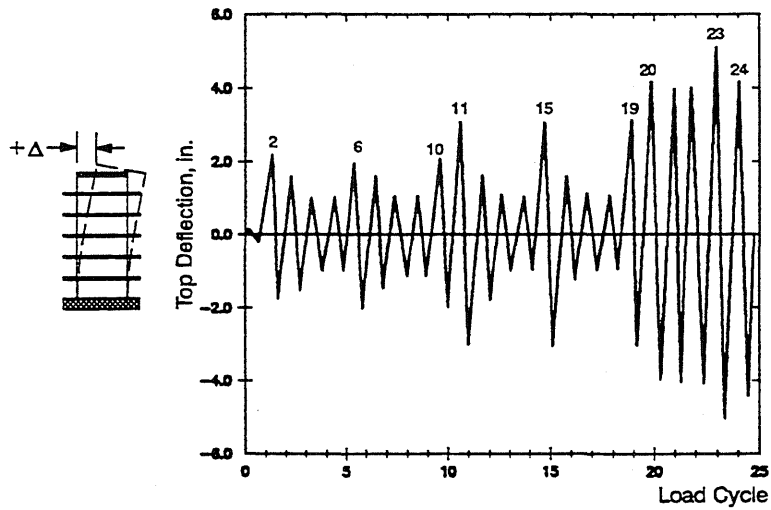


Fig. 8.13 Reinforcement Details in Wall CI1

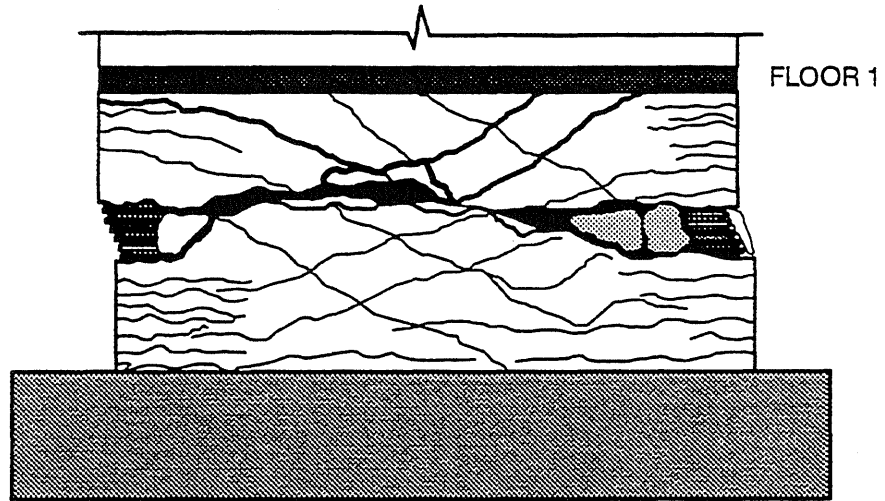


a) Wall CI1

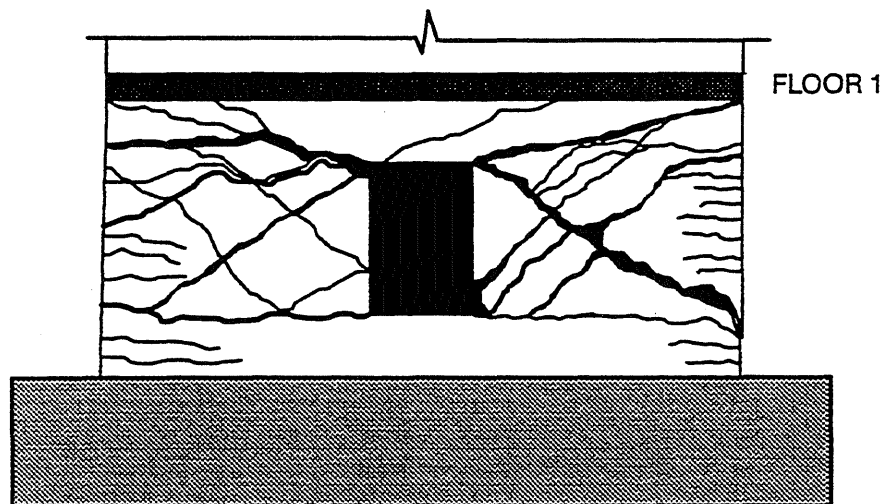


b) Wall PW1

Fig. 8.14 Top-Deflection History for Walls CI1 and PW1



Wall CI1 after failure



Wall PW1 after failure

Fig. 8.15 Specimens CI1 and PW1 after Failures

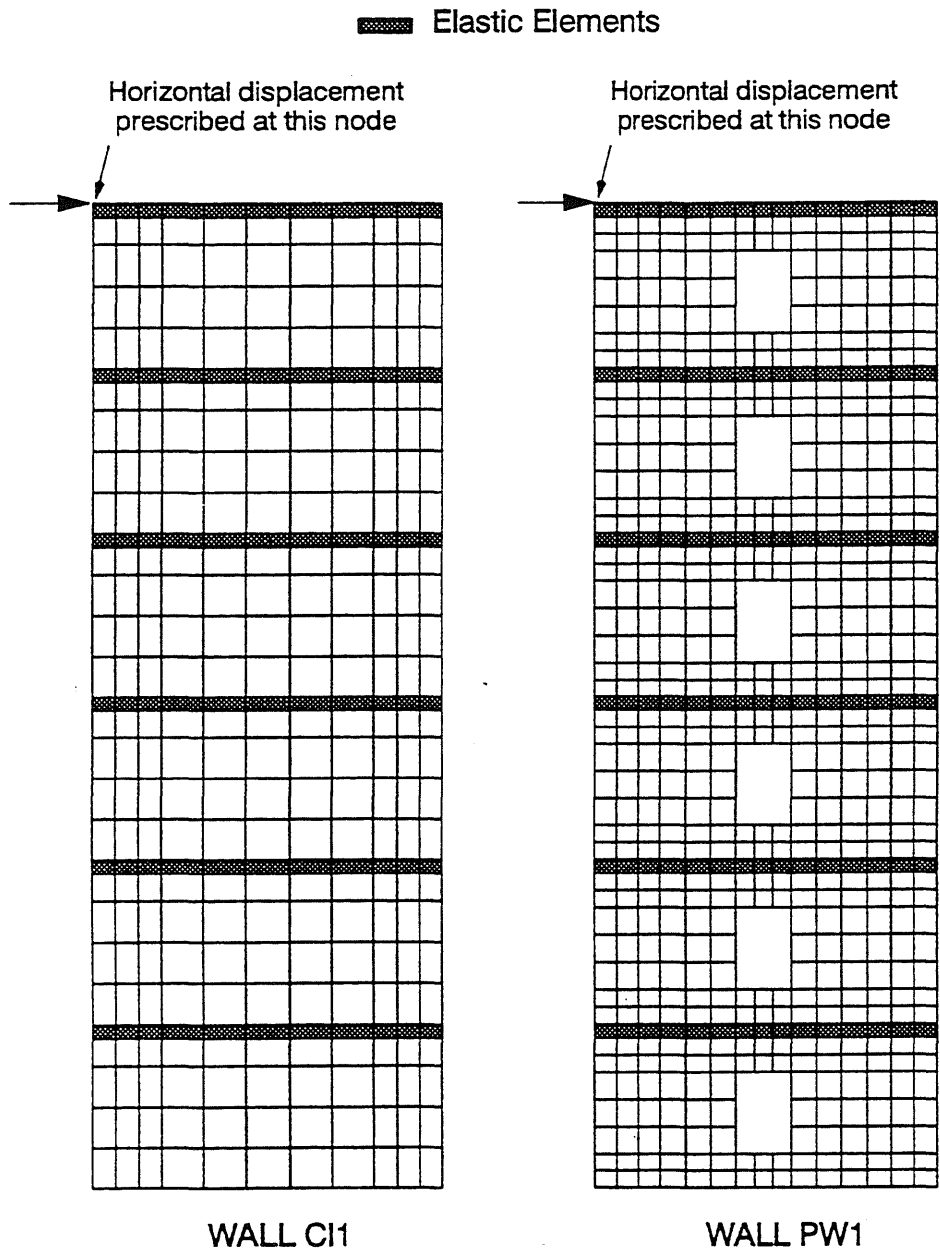
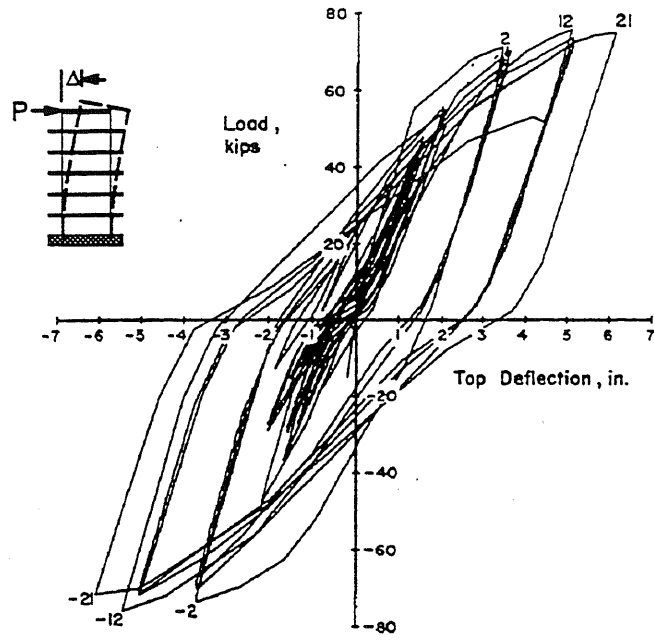
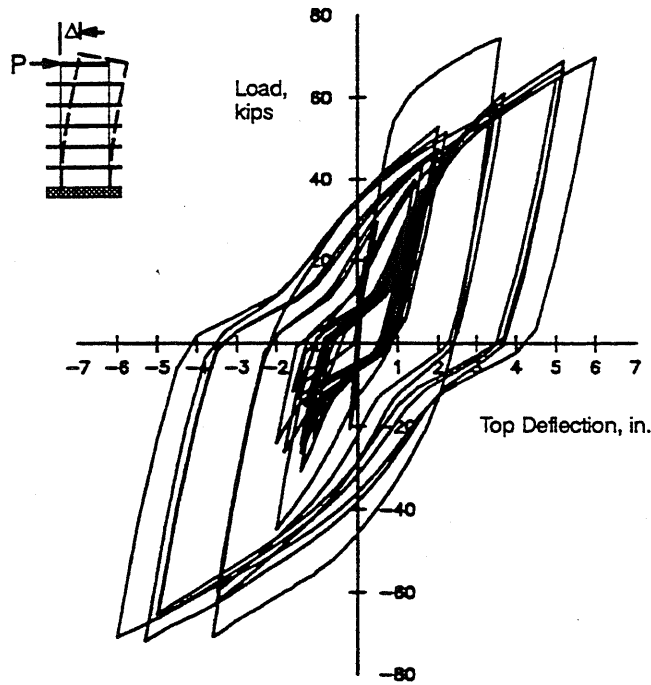


Fig. 8.16 Finite Element Meshes for Walls CI1 and PW1



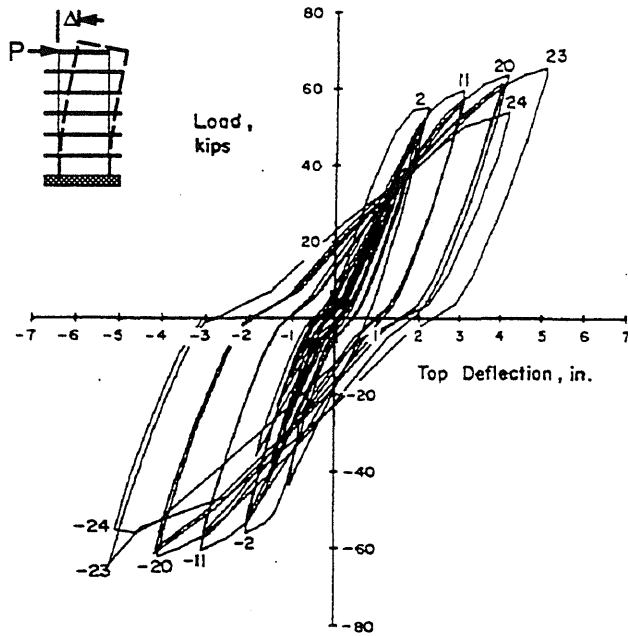
a) Experimental Results: Wall C11



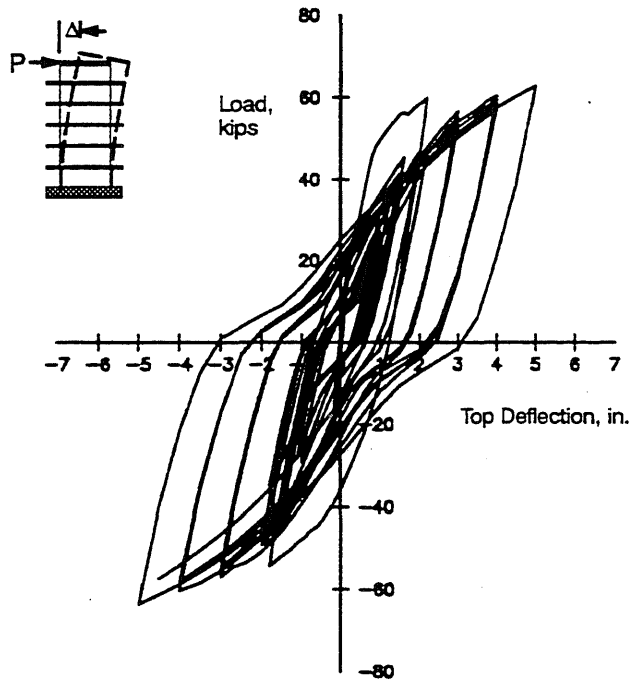
b) Calculated Results: Wall C11

Fig. 8.17 Load vs. Top Deflection Curves for Wall C11



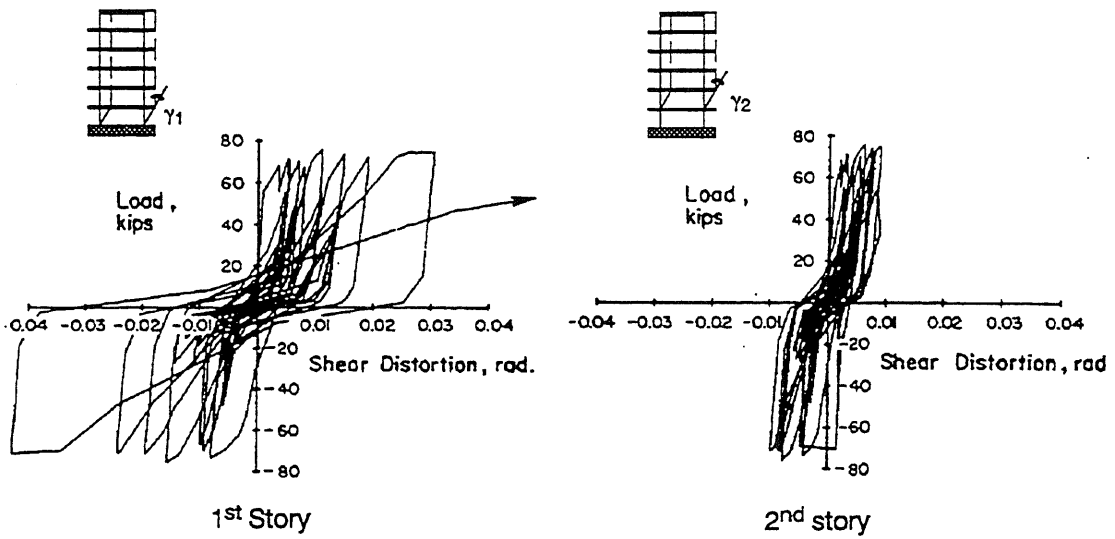


a) Experimental Results: Wall PW1

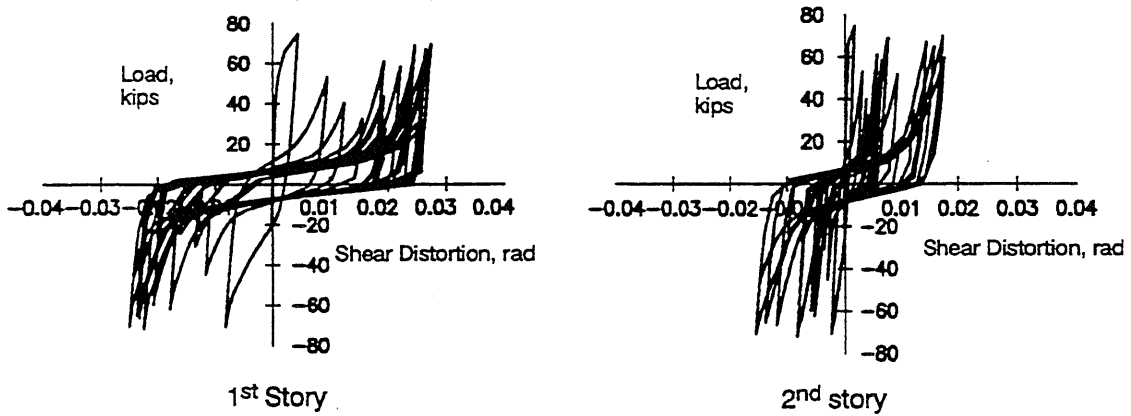


b) Calculated Results: Wall PW1

Fig. 8.18 Load vs. Top Deflection Curves for Wall PW1

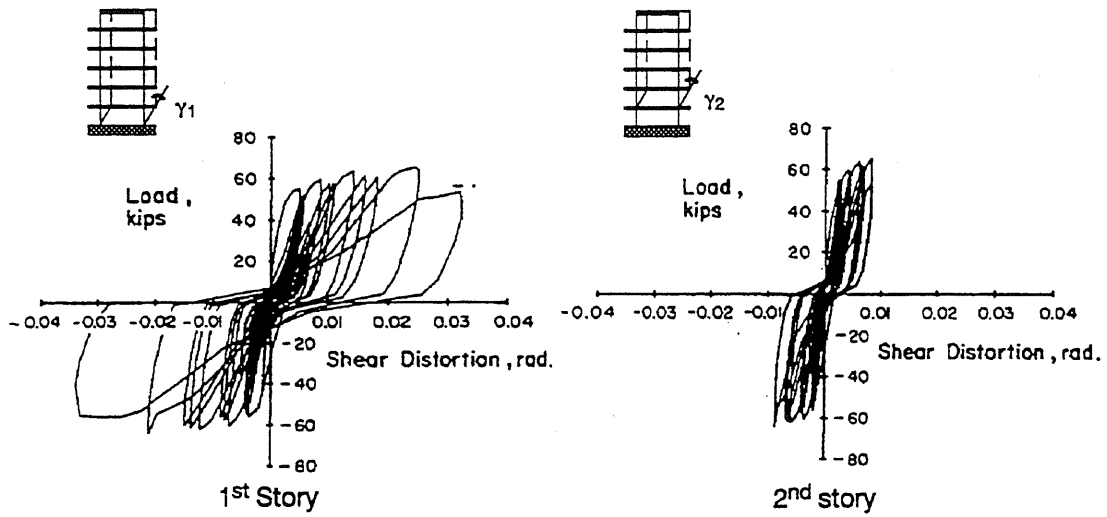


a) Experimental Results

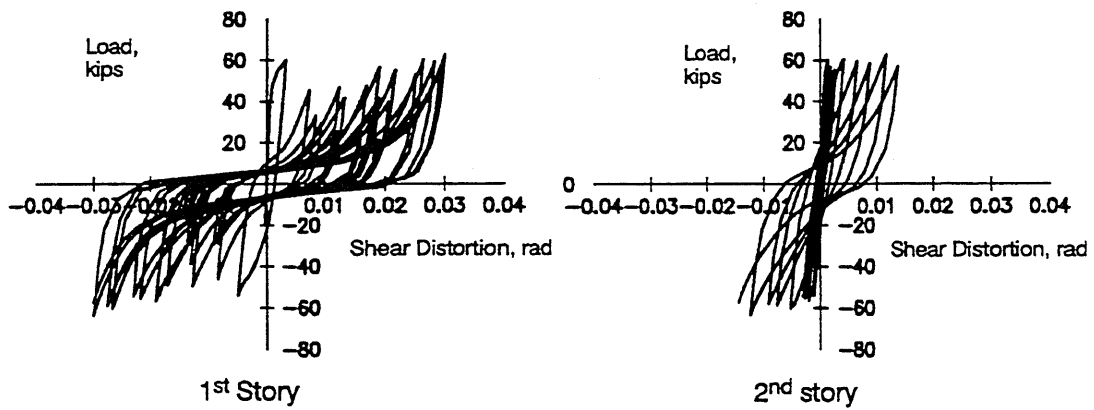


b) Calculated Results

Fig. 8.19 Load vs. Shear Distortion for Wall CI1

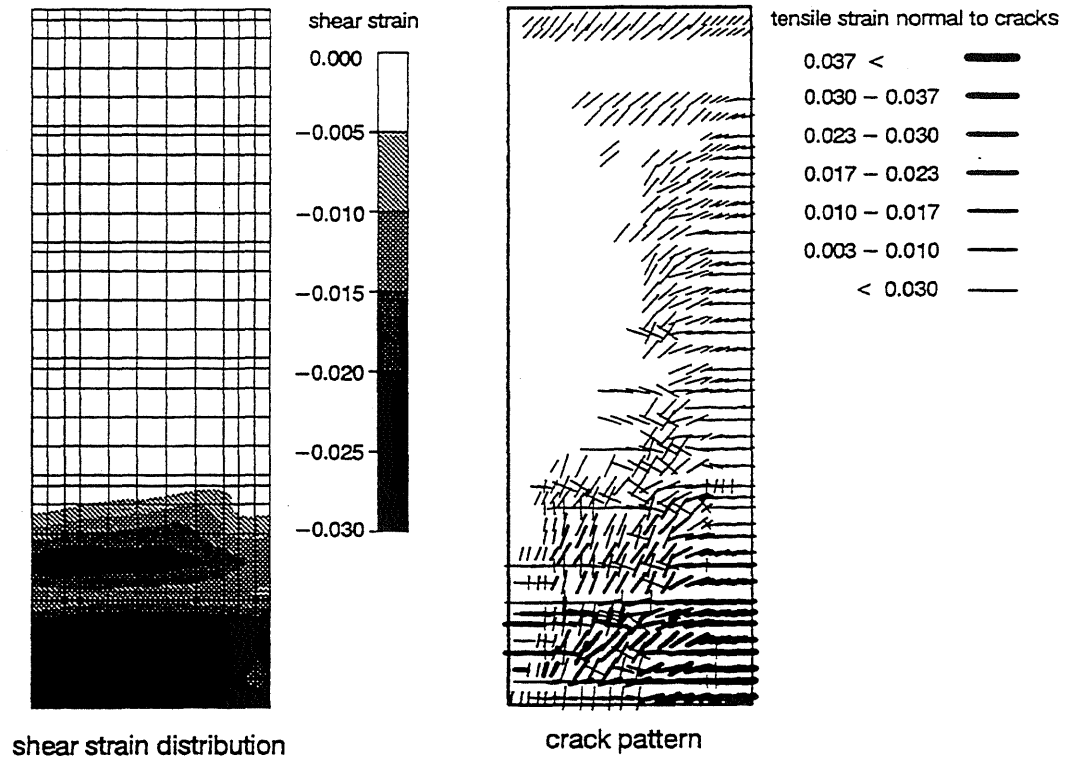


a) Experimental Results

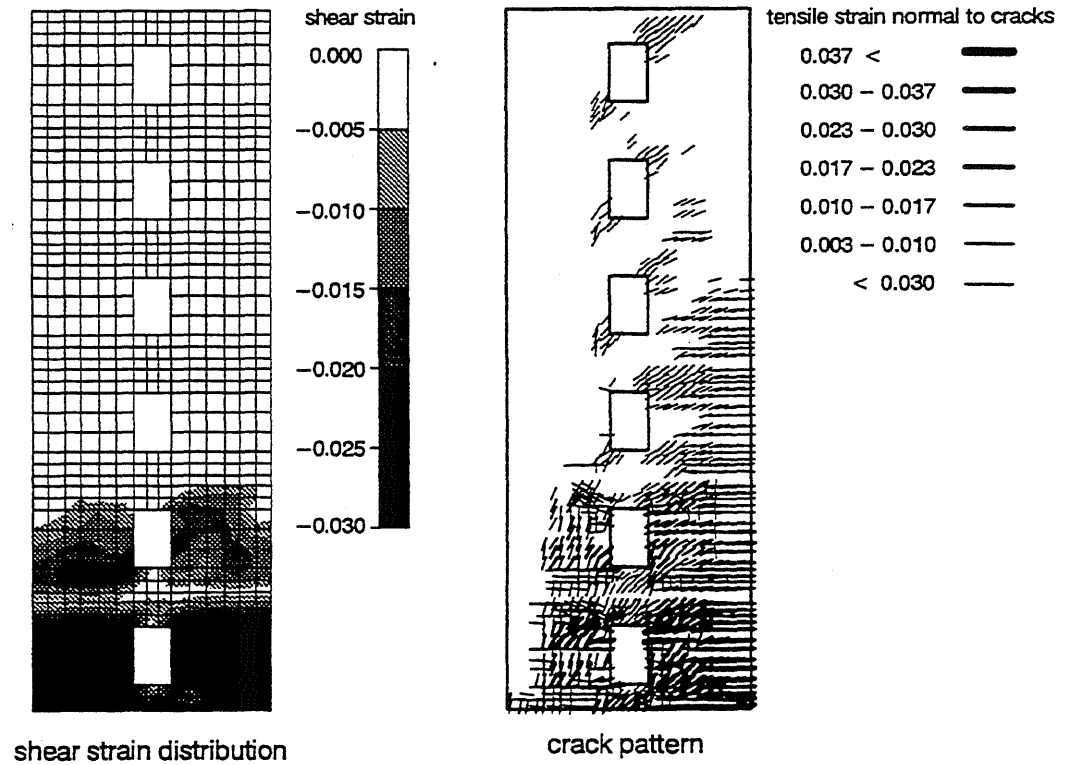


b) Calculated Results

Fig. 8.20 Load vs. Shear Distortion for Wall PW1

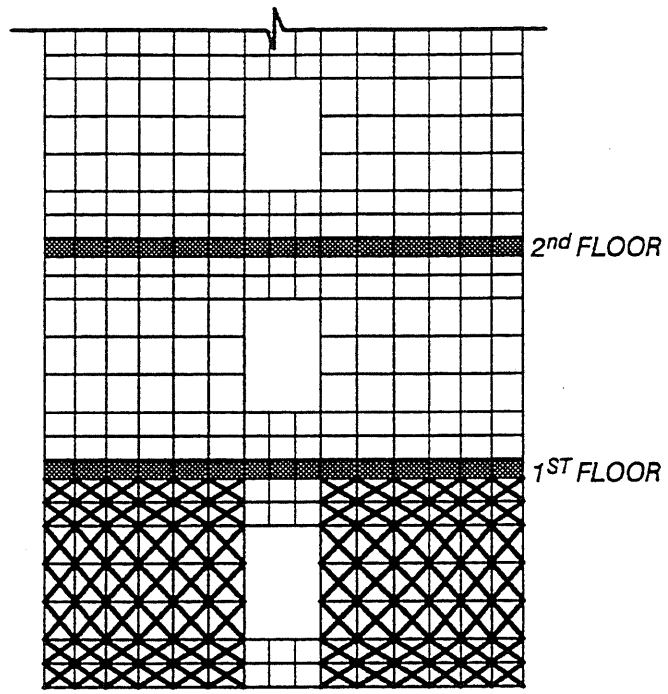


a) Calculated Response of Wall CI1 at Load Cycle #21 (-6.00 in.)

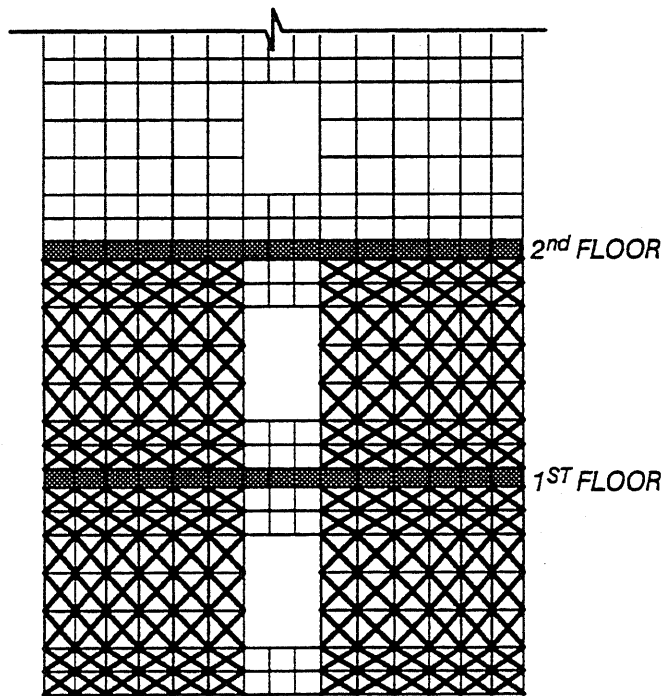


b) Calculated Response of Wall PW1 at Load Cycle #23 (-5.00 in.)

Fig. 8.21 Shear Strain Distribution and Crack Patterns for Walls CI1 and PW1

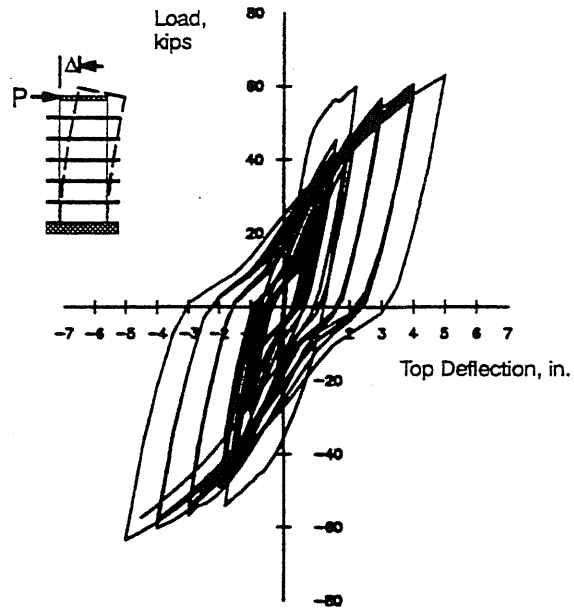


a) Wall PW1-A

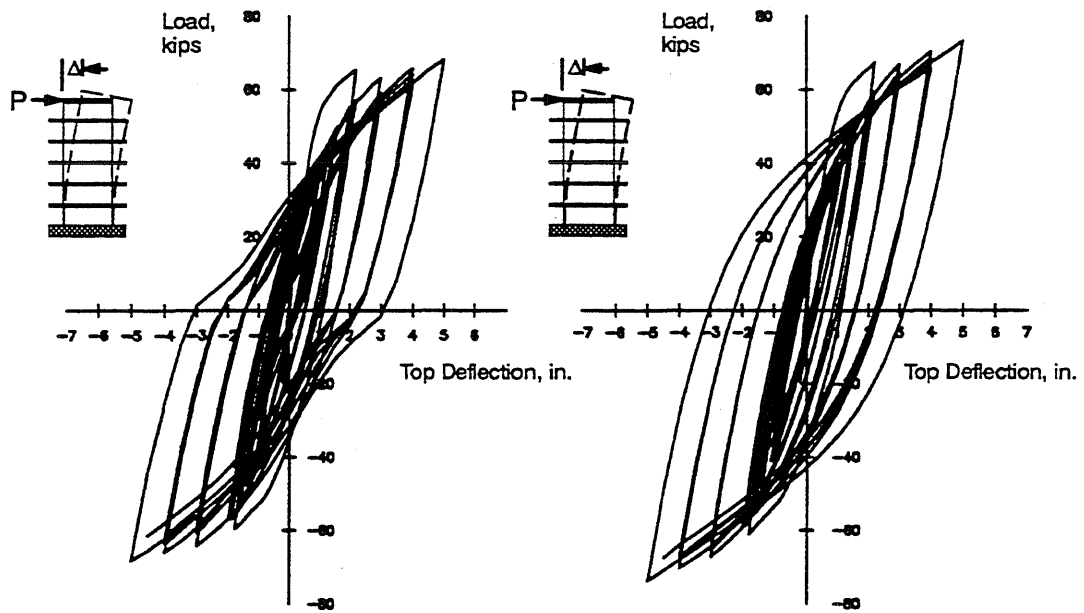


b) Wall PW1-B

Fig. 8.22 Diagonal Reinforcement in Wall PW1



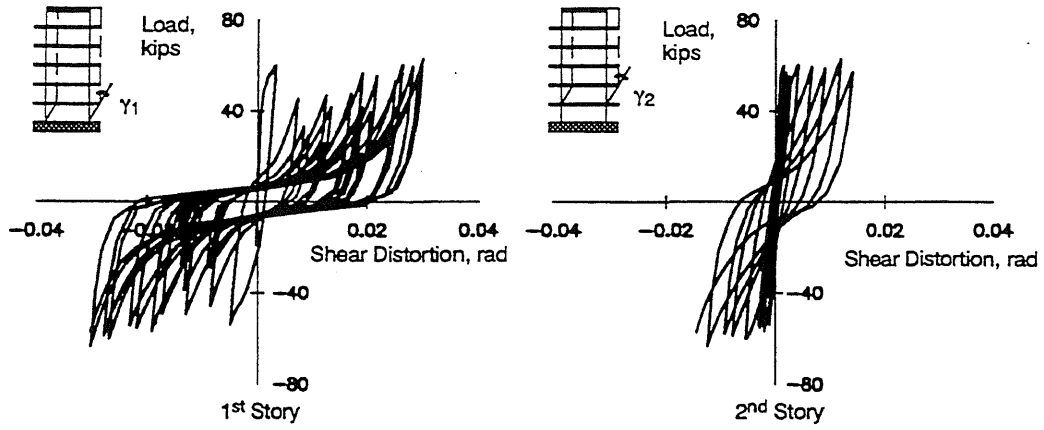
a) Wall PW1 with Original Reinforcement



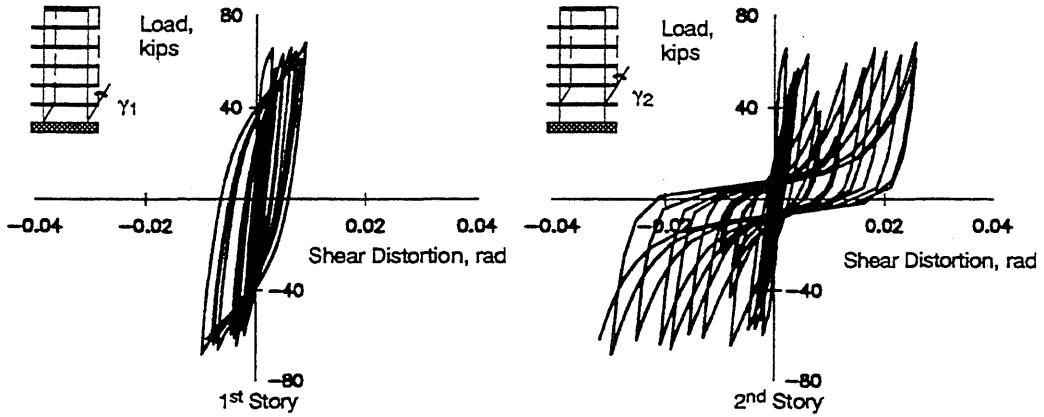
b) Wall PW1 with Diagonal Reinforcement Option A

c) Wall PW1 with Diagonal Reinforcement Option B

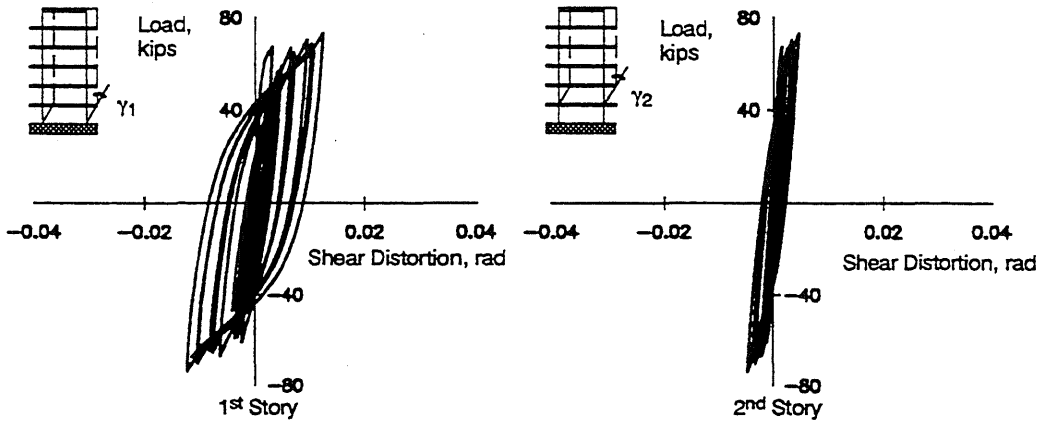
Fig. 8.23 Load vs. Top Deflection Curves for Wall PW1



a) Wall PW1 with Original Reinforcement



b) Wall PW1 with Diagonal Reinforcement Option A



c) Wall PW1 with Diagonal Reinforcement Option B

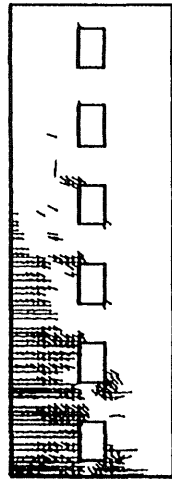
Fig. 8.24 Load vs. Shear Distortion Curves for Wall PW1



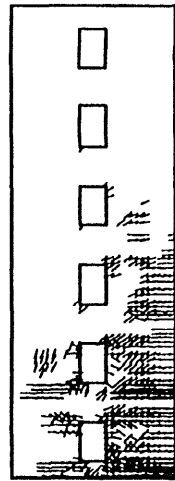
a) Original Reinforcement Details

Fig. 8.25 Crack Patterns in Wall PW1

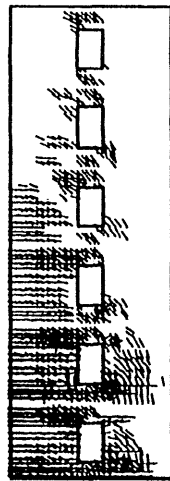




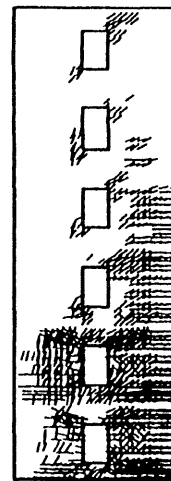
CYCLE#2 +2.20 in.



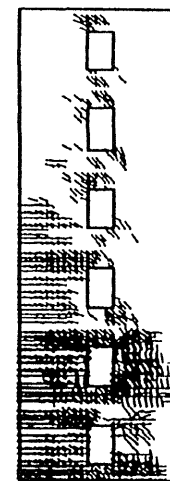
CYCLE#2 -1.80 in.



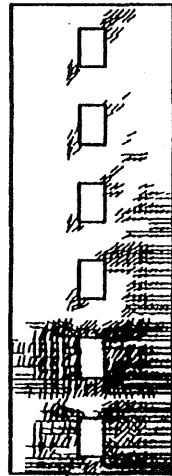
CYCLE#11 + 3.00 in.



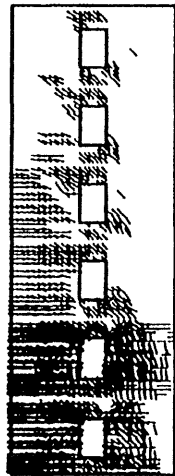
CYCLE#11 - 3.00 in.



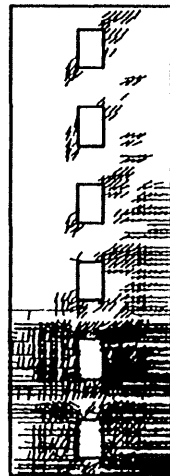
CYCLE#119 +3.00 in.



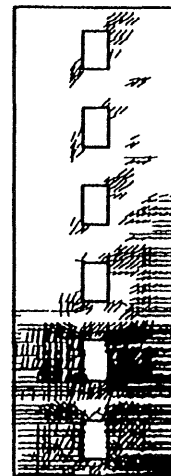
CYCLE#19 -3.00 in.



CYCLE#23 +5.00 in.

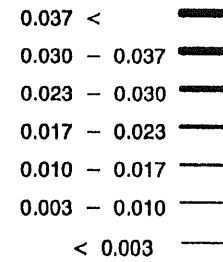


CYCLE#23 -5.00 in.



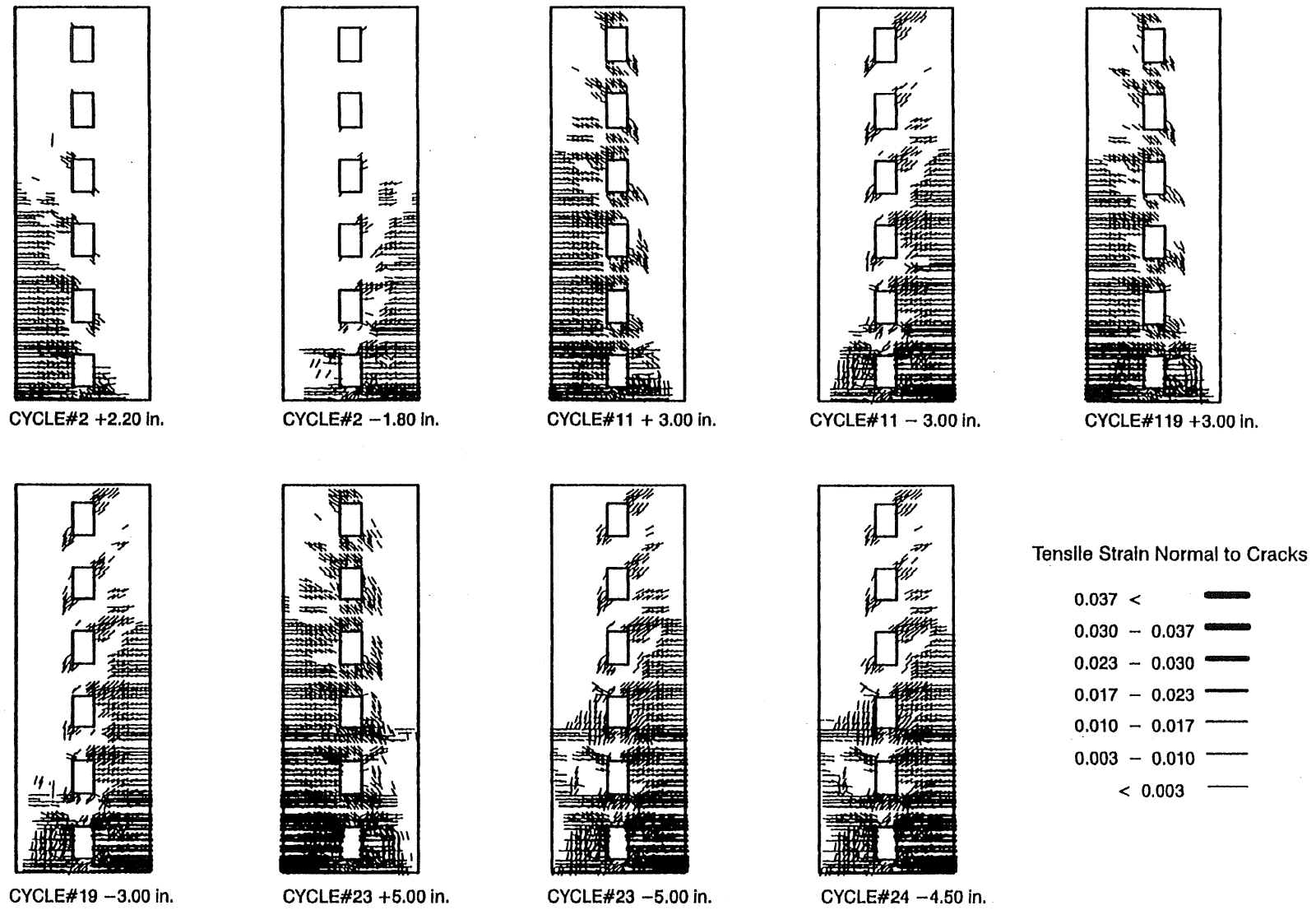
CYCLE#24 -4.50 in.

Tensile Strain Normal to Cracks



b) Reinforcement Option A: Diagonal Reinforcement in 1<sup>st</sup> Story

Fig. 8.25 Crack Patterns in Wall PW1 (Cont.)



c) Reinforcement Option B: Diagonal Reinforcement in 1<sup>st</sup> and 2<sup>nd</sup> Stories

Fig. 8.25 Crack Patterns in Wall PW1 (Cont.)

Load Cycle #23 (-5.0 in.)

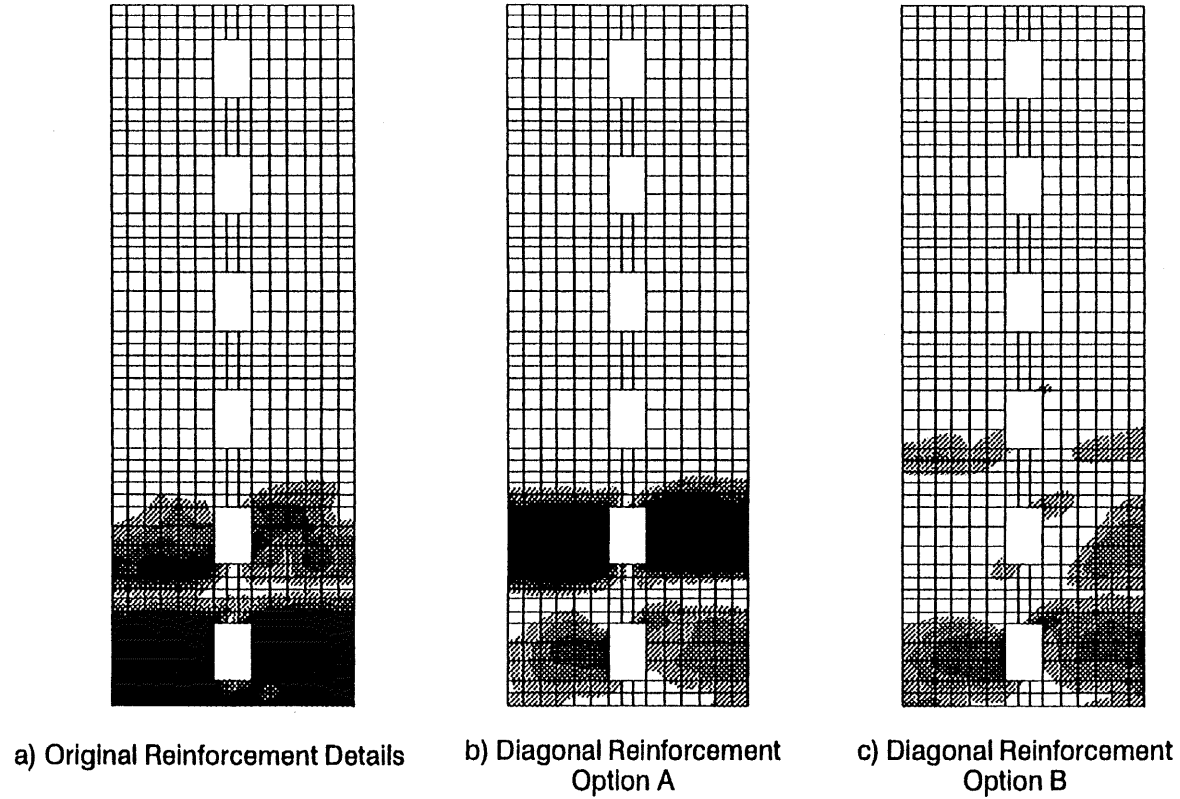


Fig. 8.26 Shear Strain Distribution in Wall PW1

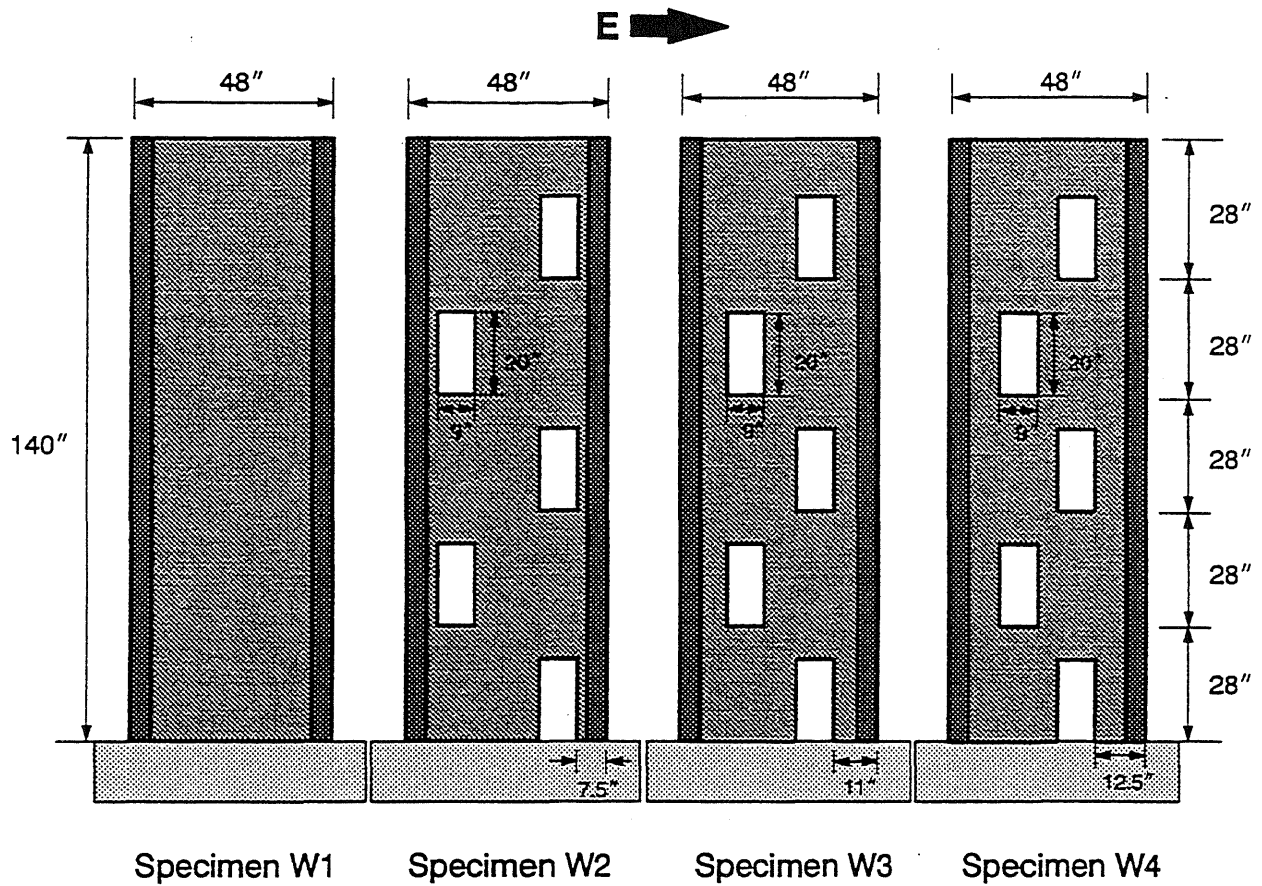


Fig. 8.27 Dimensions of Wall Specimens Tested at the University of Michigan

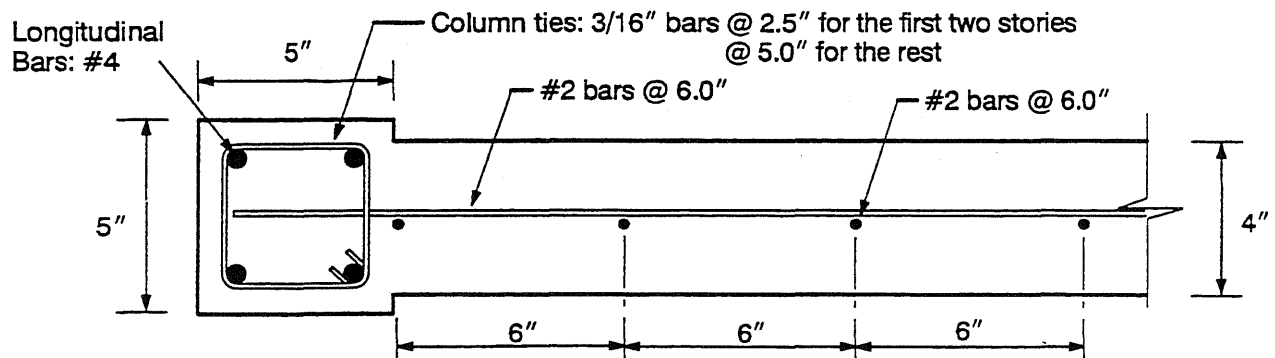
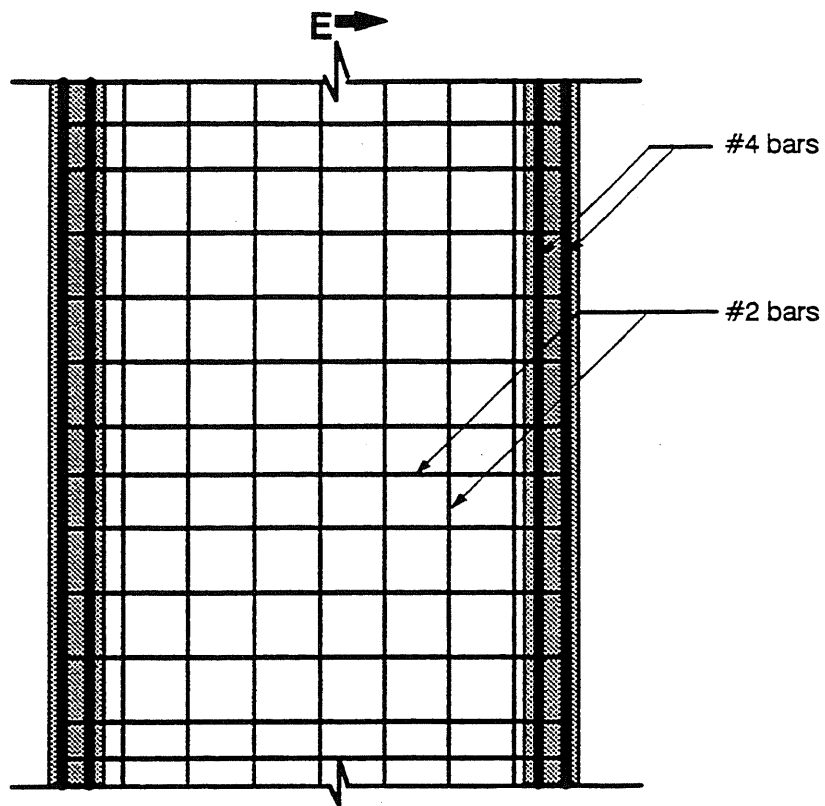
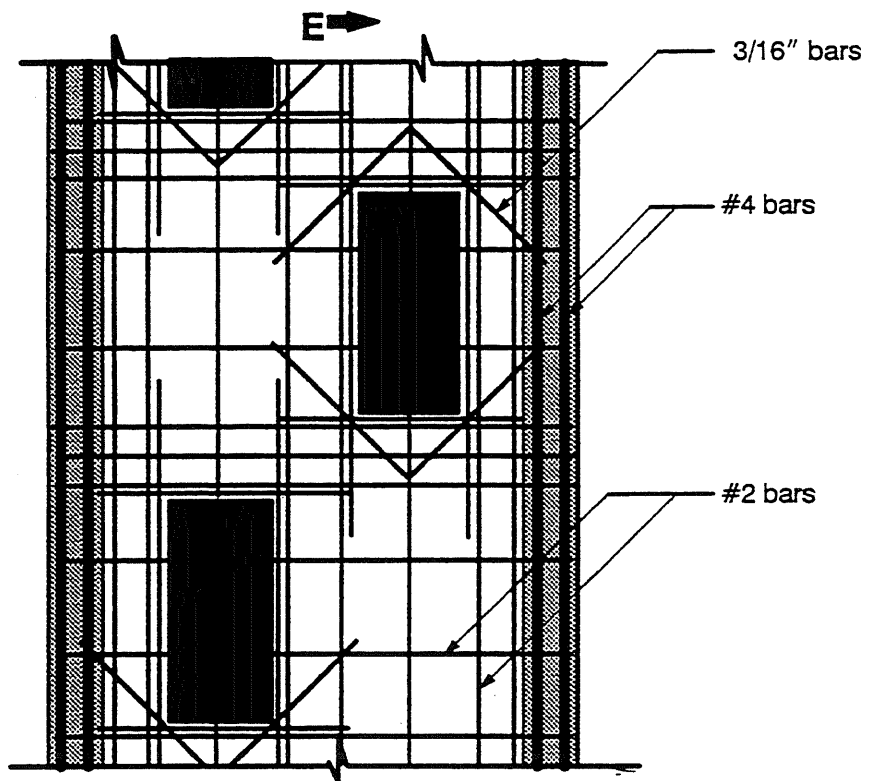


Fig. 8.28 Reinforcement Details for Wall W1: Cross Section



a) Wall W1



b) Wall W3

Fig. 8.29 Reinforcement Details for Wall Specimens: Elevation

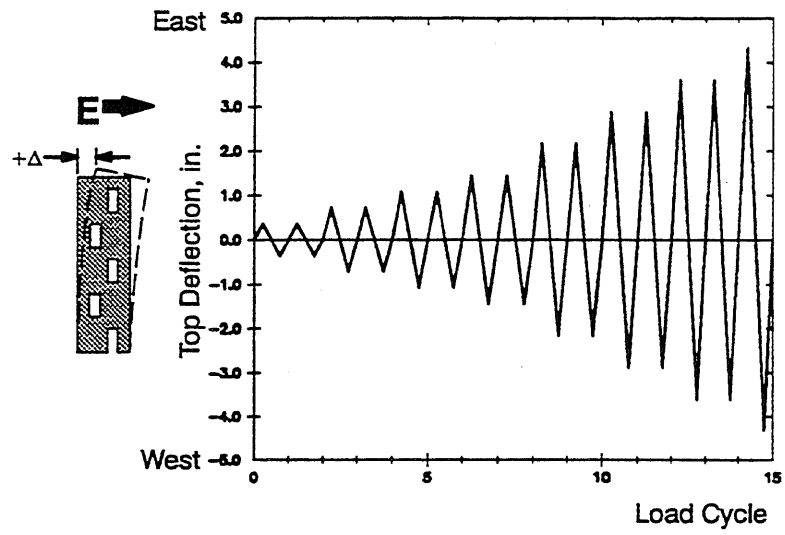


Fig. 8.30 Typical Top-Deflection History for Walls W1, W2, W3, and W4

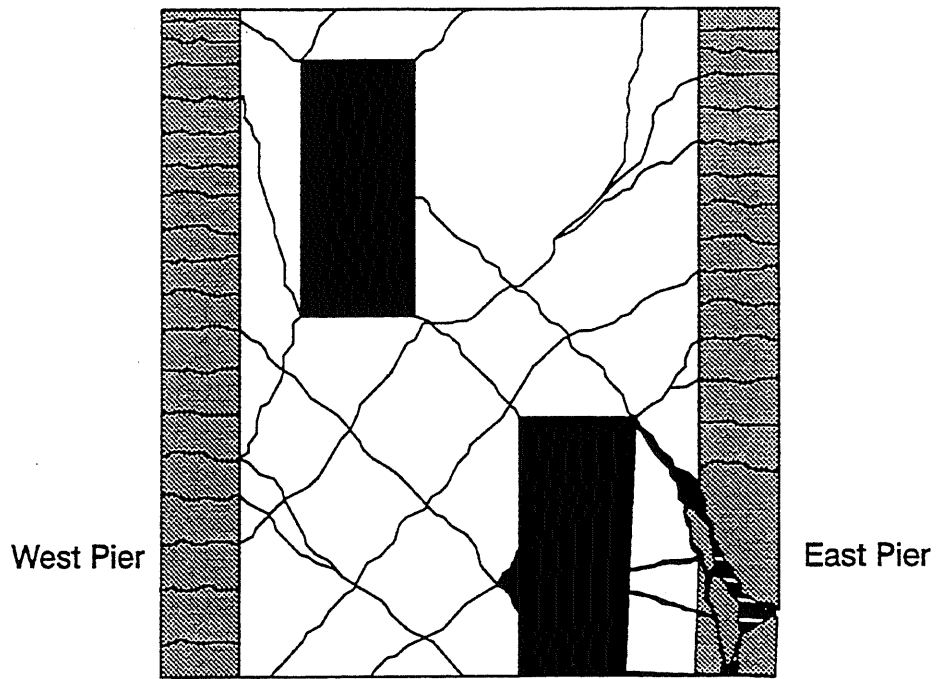


Fig. 8.31 Crack Patterns in Wall W2 after Failure



Fig. 8.32 Diagonal Tension Shear Failure in Reinforced Concrete Beam (from [56])

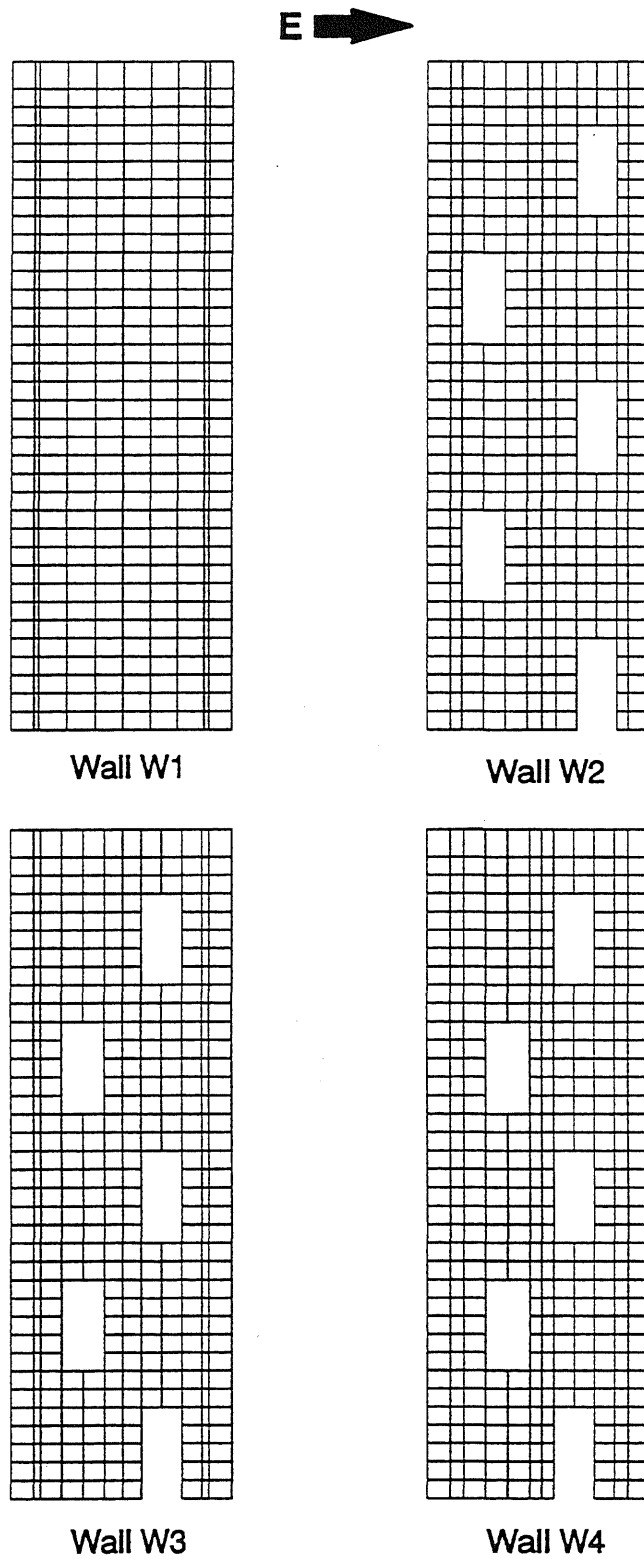
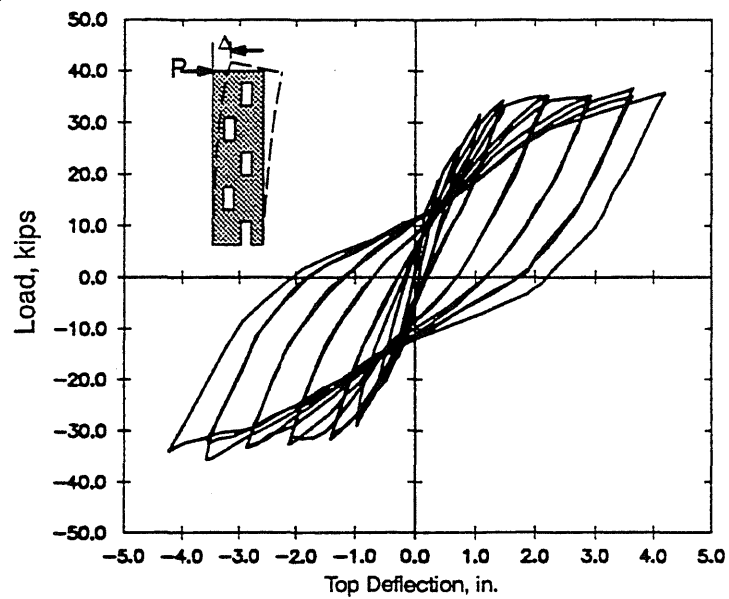
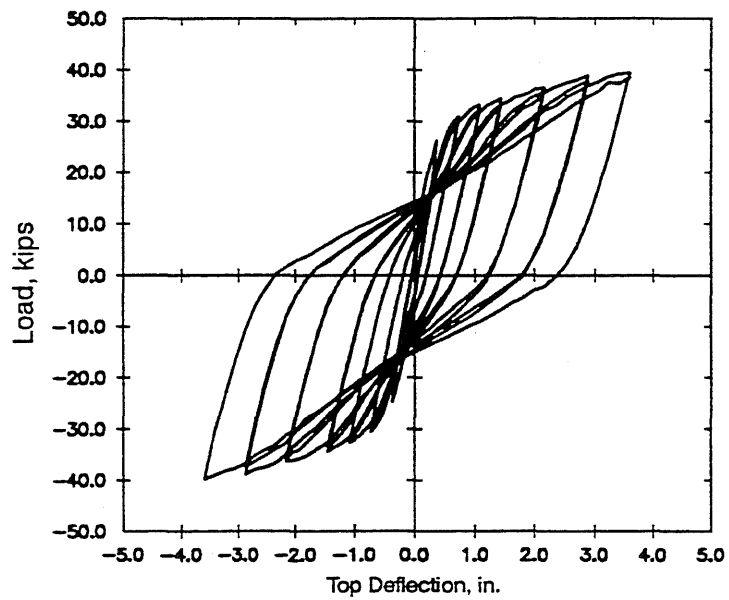


Fig. 8.33 Finite Element Meshes for Wall Specimens



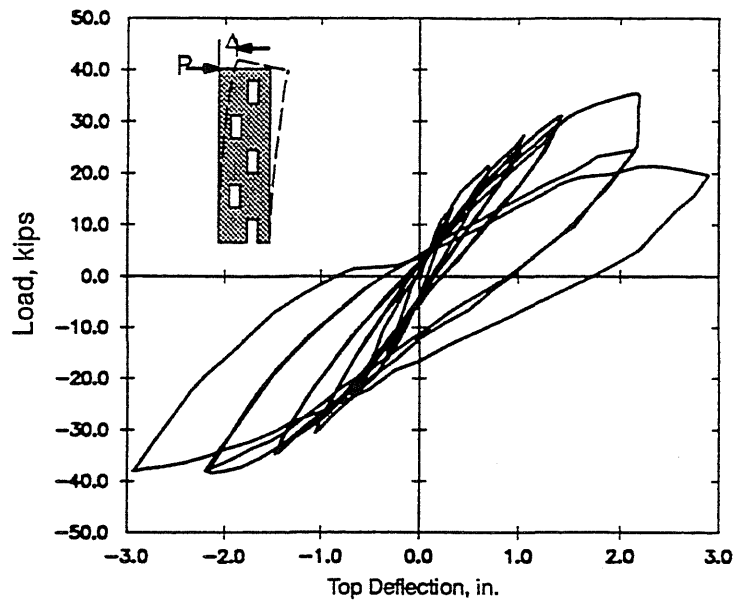


a) EXPERIMENTAL RESULT

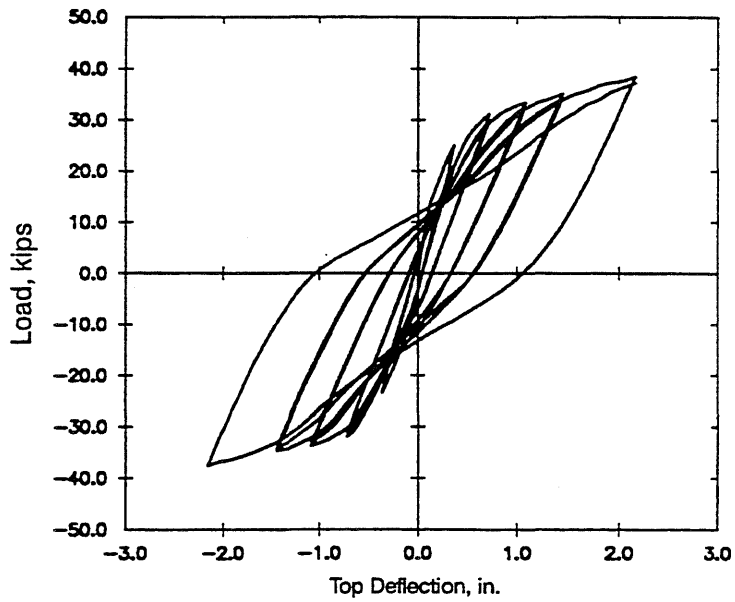


b) CALCULATED RESULT

Fig. 8.34 Load vs. Top Deflection Curve for Wall W1



a) EXPERIMENTAL RESULT



b) CALCULATED RESULT

Fig. 8.35 Load vs. Top Deflection Curve for Wall W2

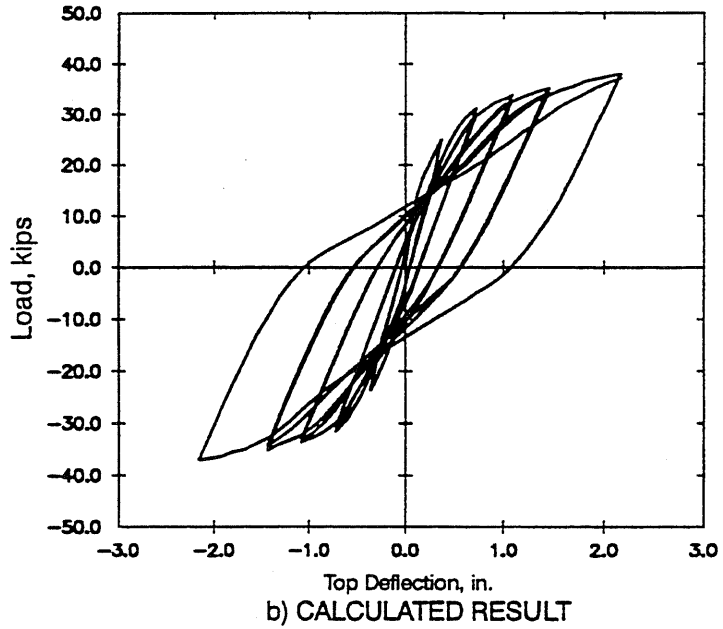
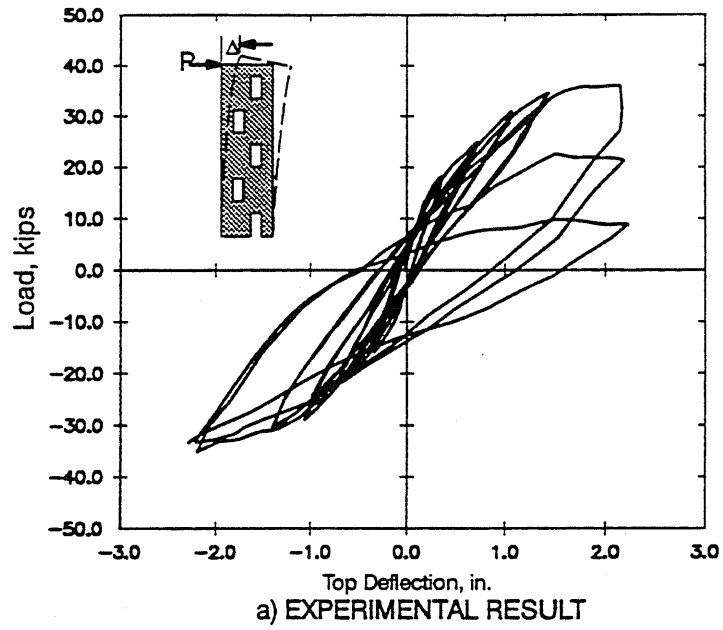
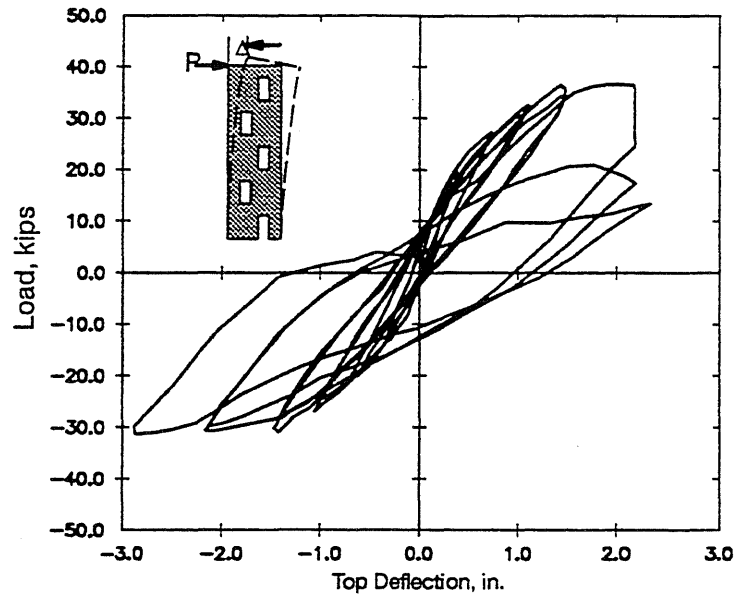
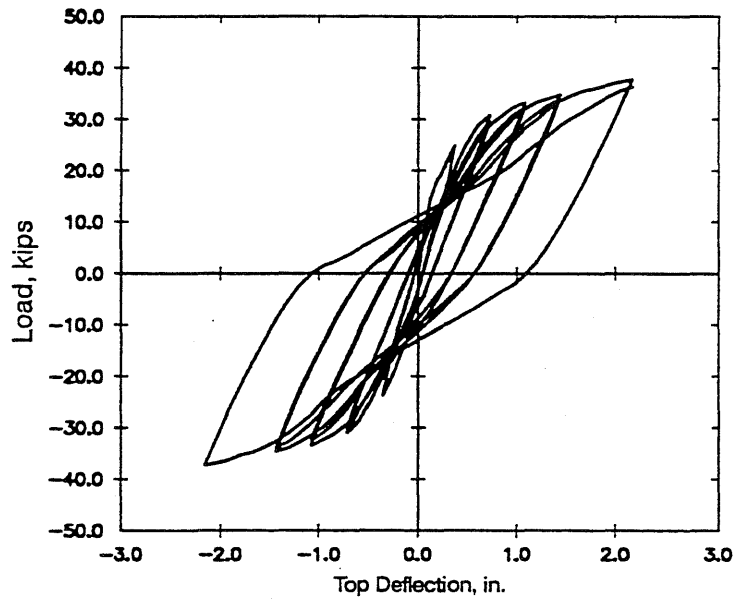


Fig. 8.36 Load vs. Top Deflection Curve for Wall W3



a) EXPERIMENTAL RESULT



b) CALCULATED RESULT

Fig. 8.37 Load vs. Top Deflection Curve for Wall W4

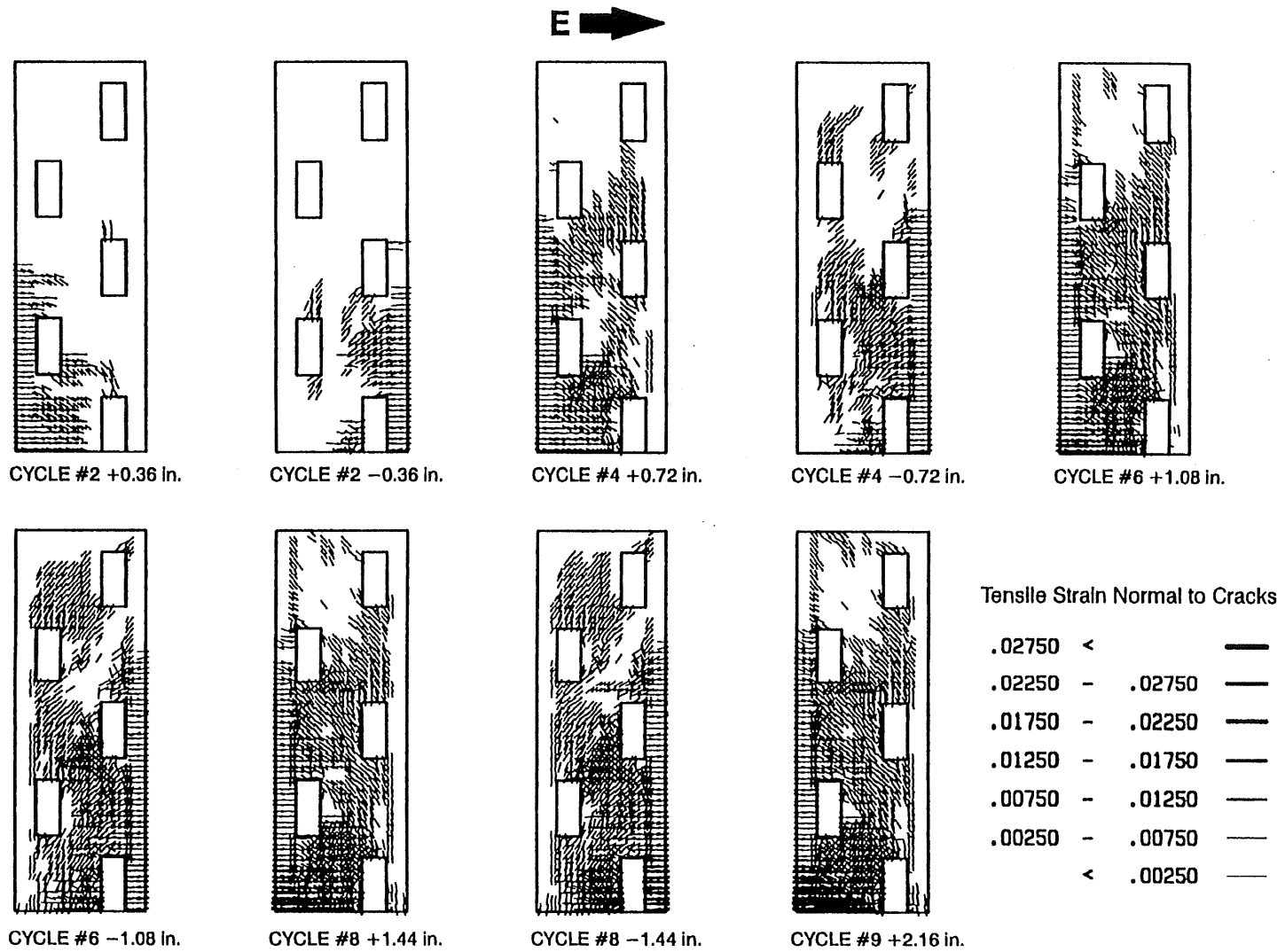


Fig. 8.38 Crack Patterns in Wall W2: Original Reinforcement Details

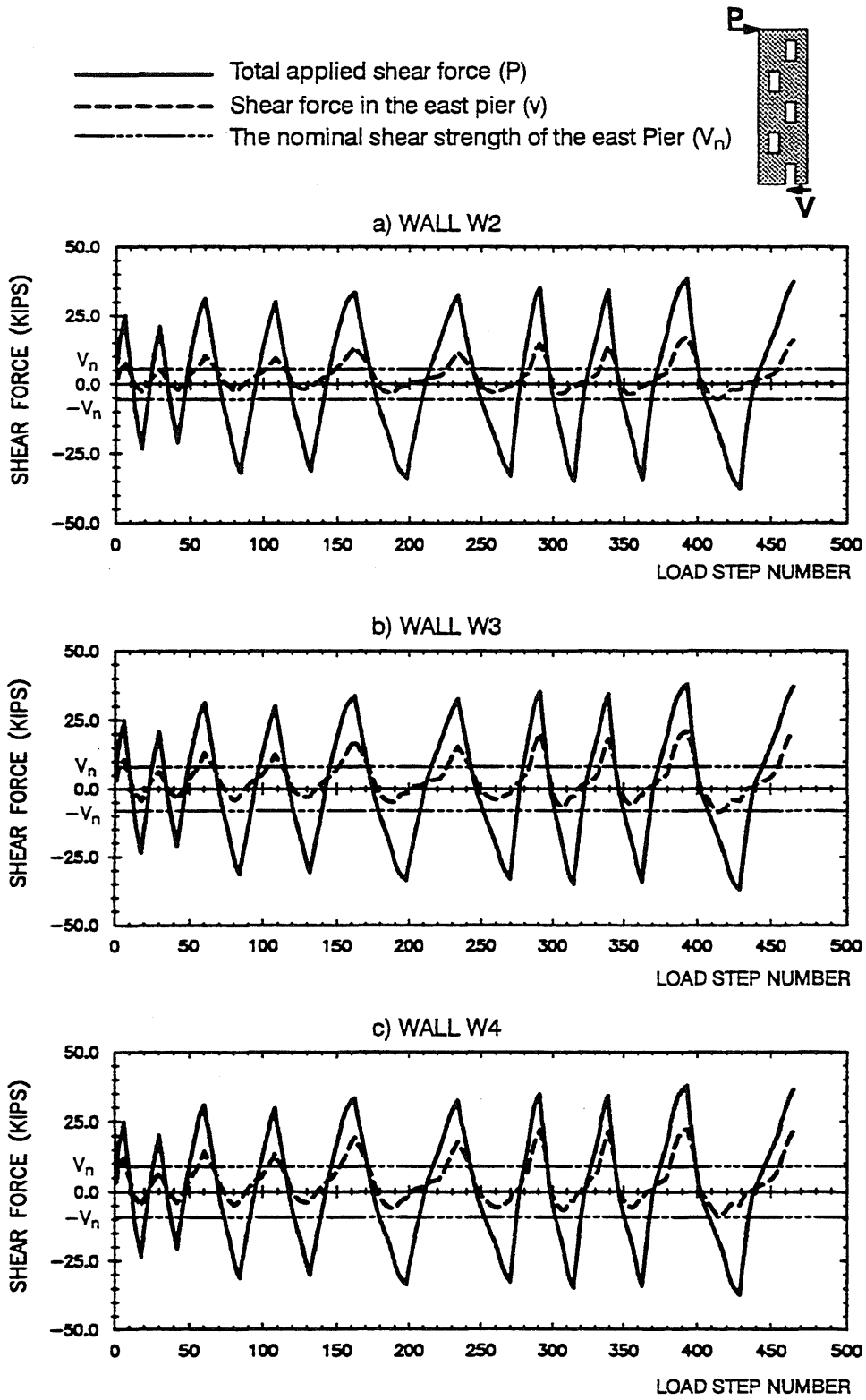


Fig. 8.39 Shear Forces Distribution in Walls W2, W3, and W4

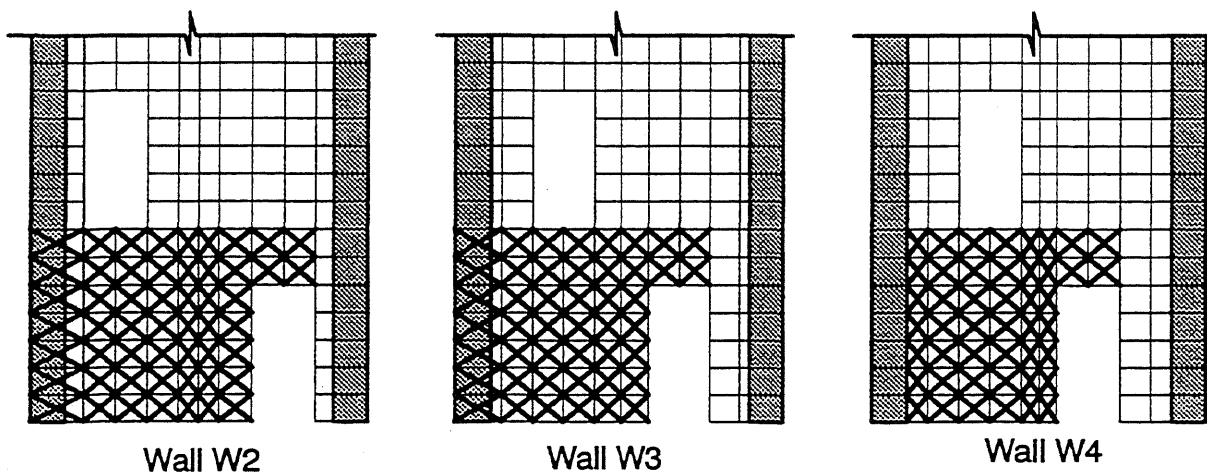


Fig. 8.40 Diagonal Reinforcement in Walls W2, W3, and W4

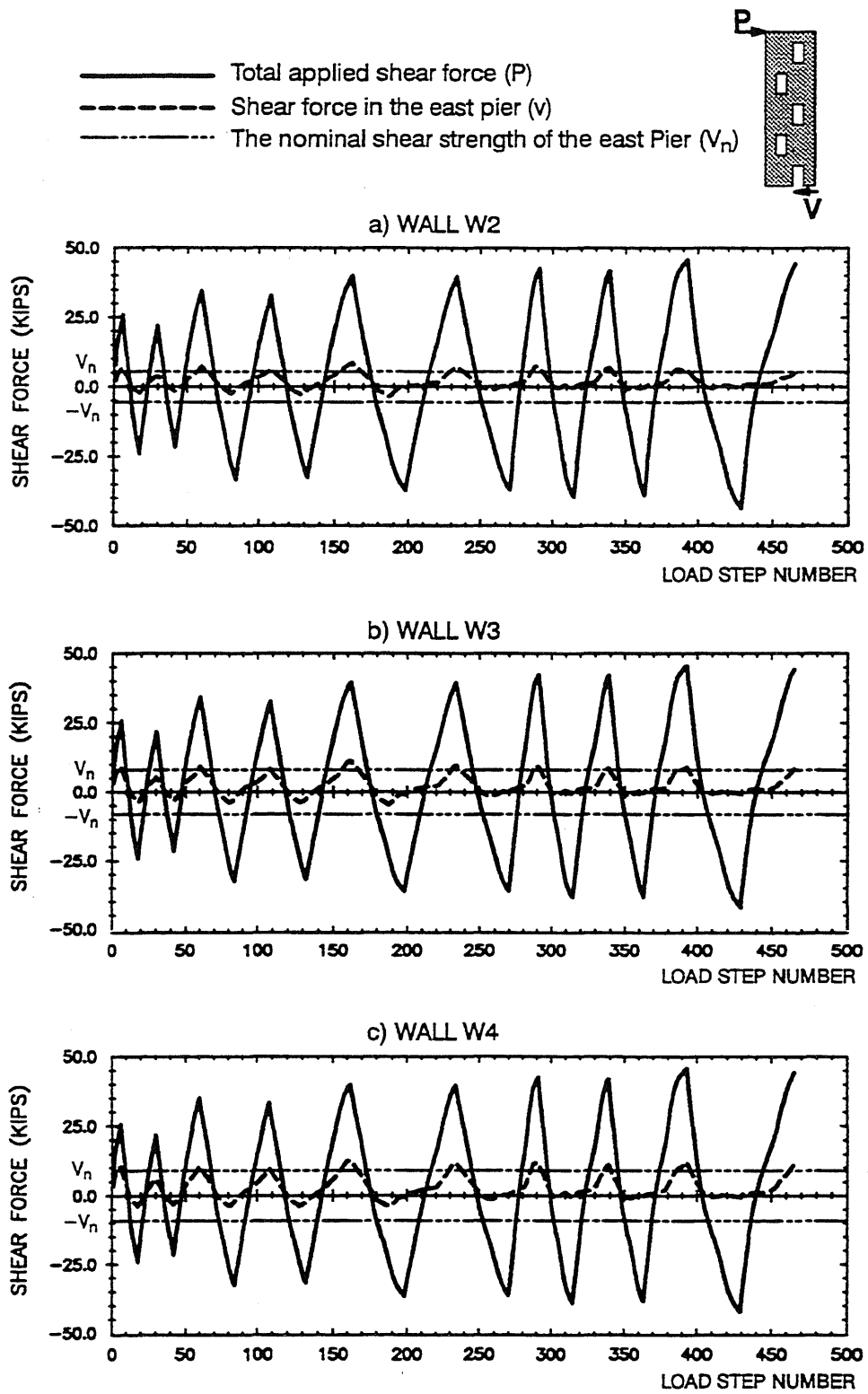


Fig. 8.41 Shear Forces in Walls W2, W3, and W4: with Diagonal Reinforcement



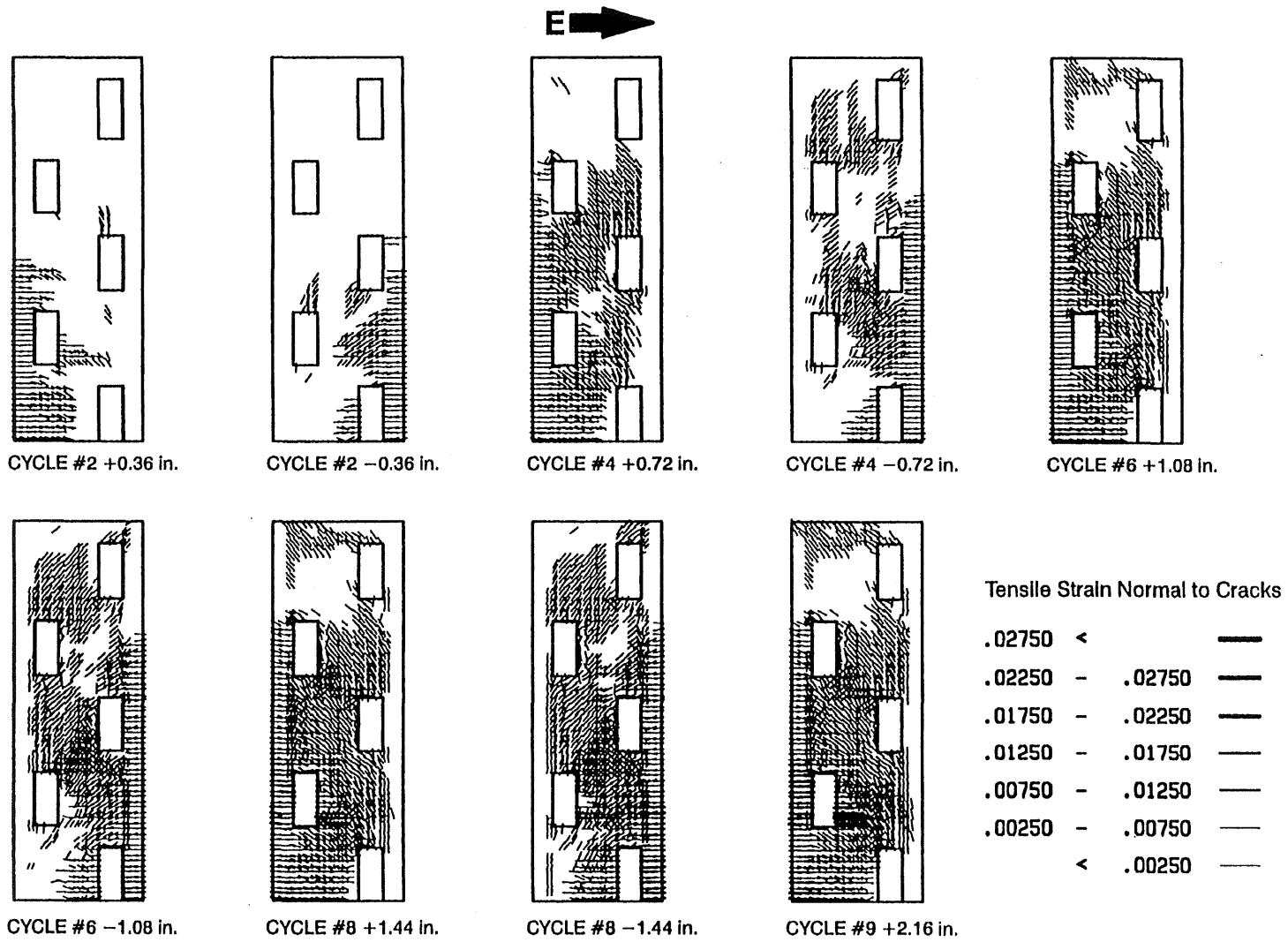


Fig. 8.42 Crack Patterns in Wall W2: with Diagonal Reinforcement

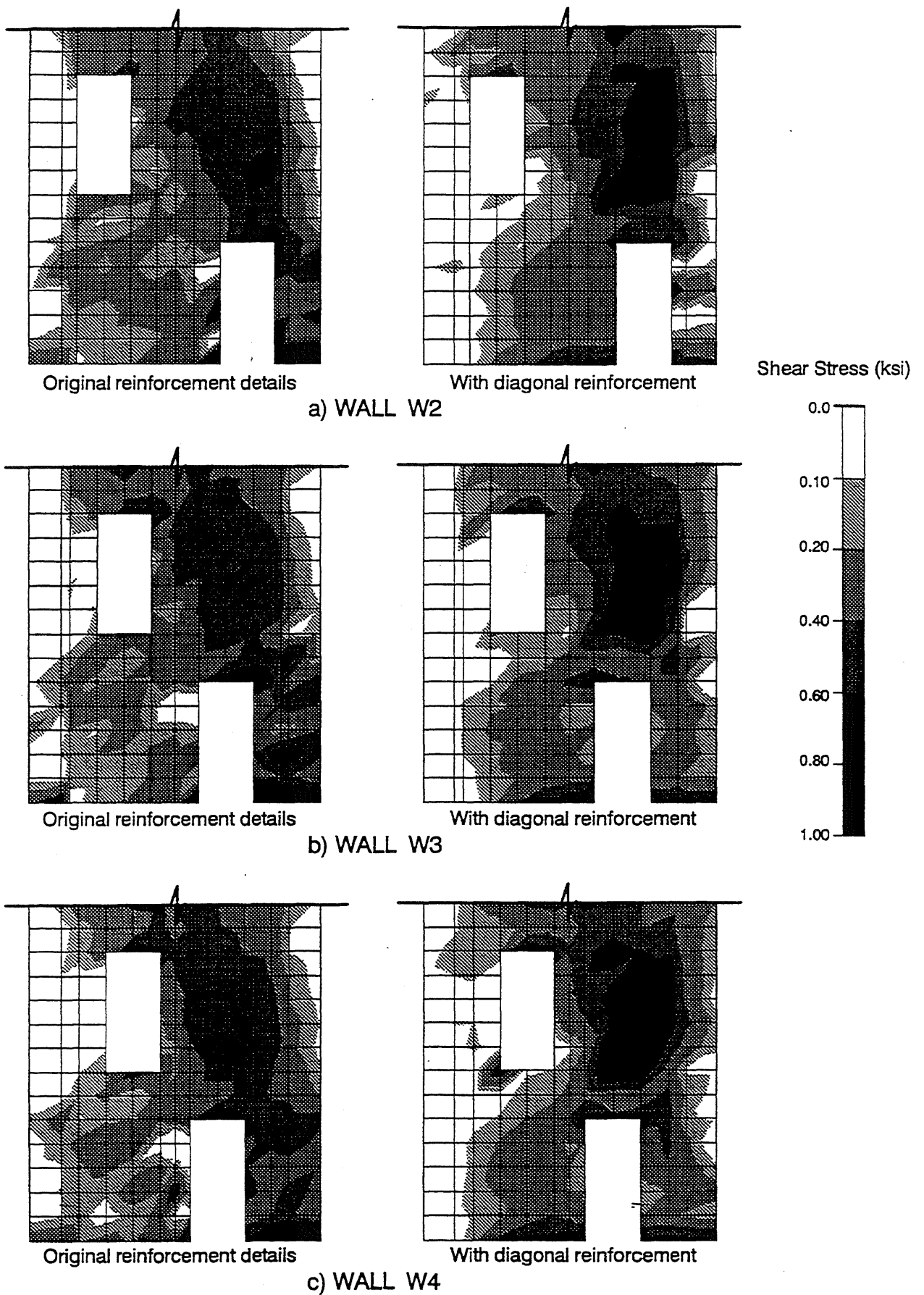


Fig. 8.43 Influence of Diagonal Reinforcement on the Shear Stress Distribution in Walls W2, W3, and W4

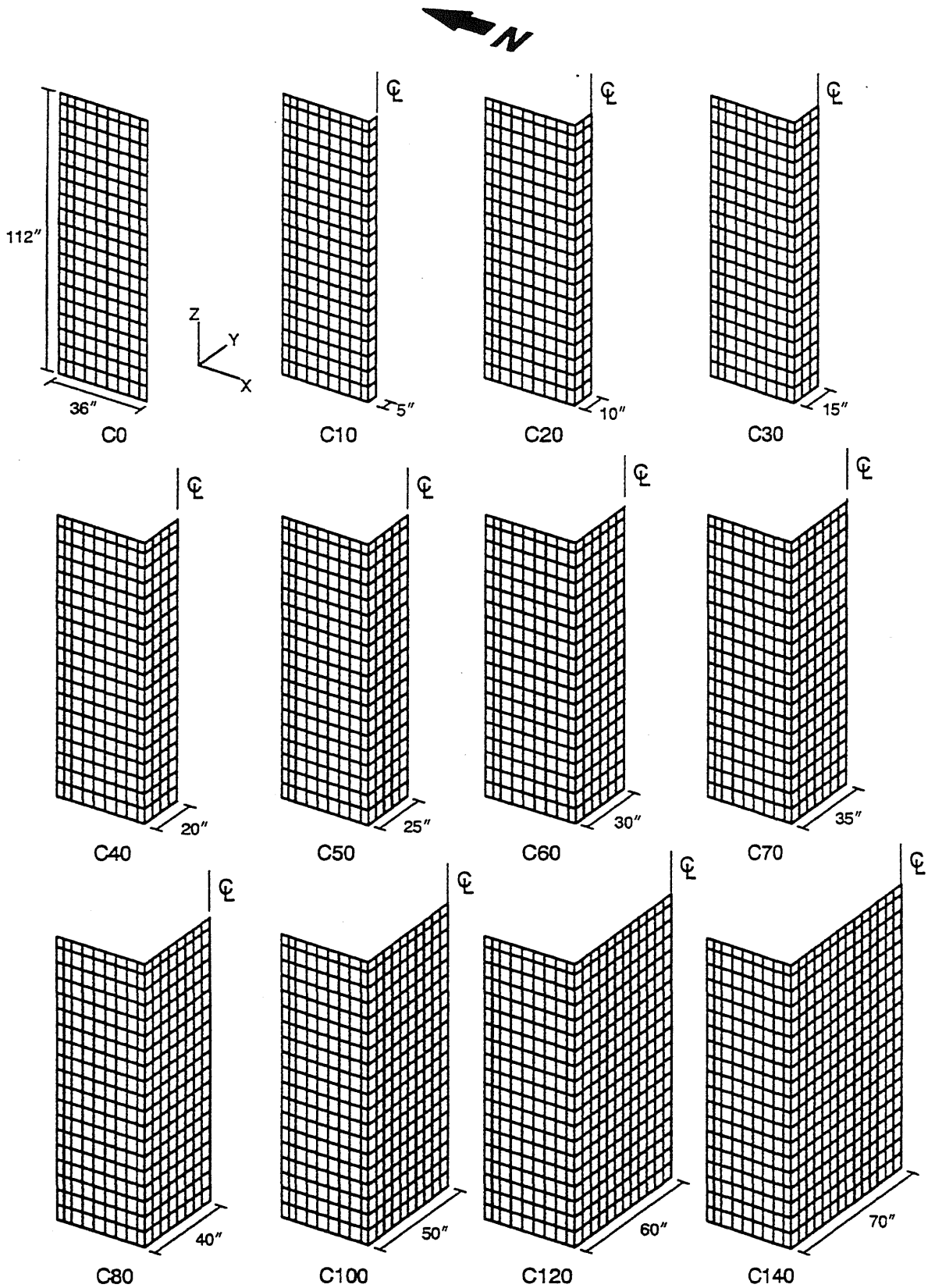


Fig. 8.44 Finite Element Meshes for C-Shaped Wall Models

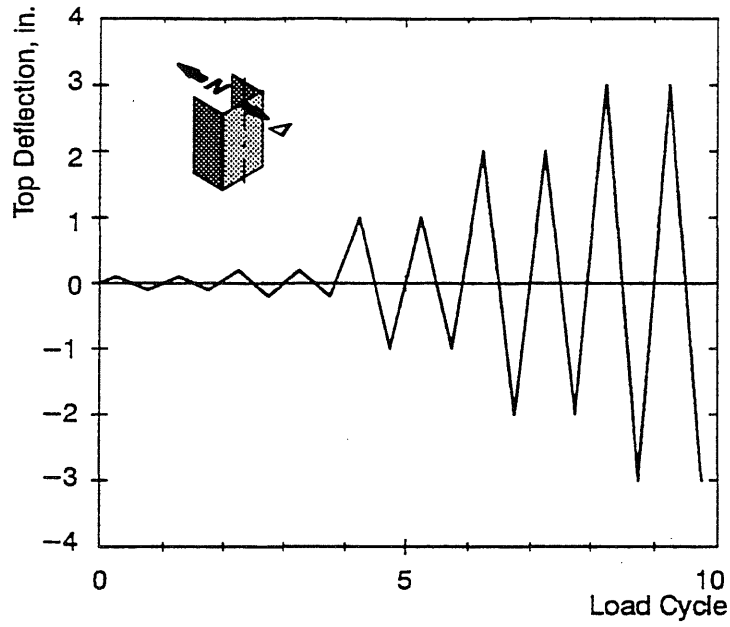


Fig. 8.45 Top-Deflection History for C-Shaped Walls: Case D

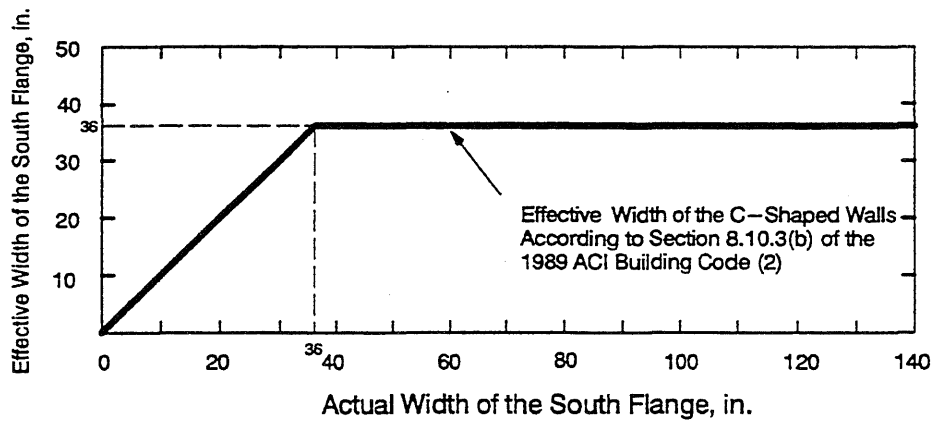
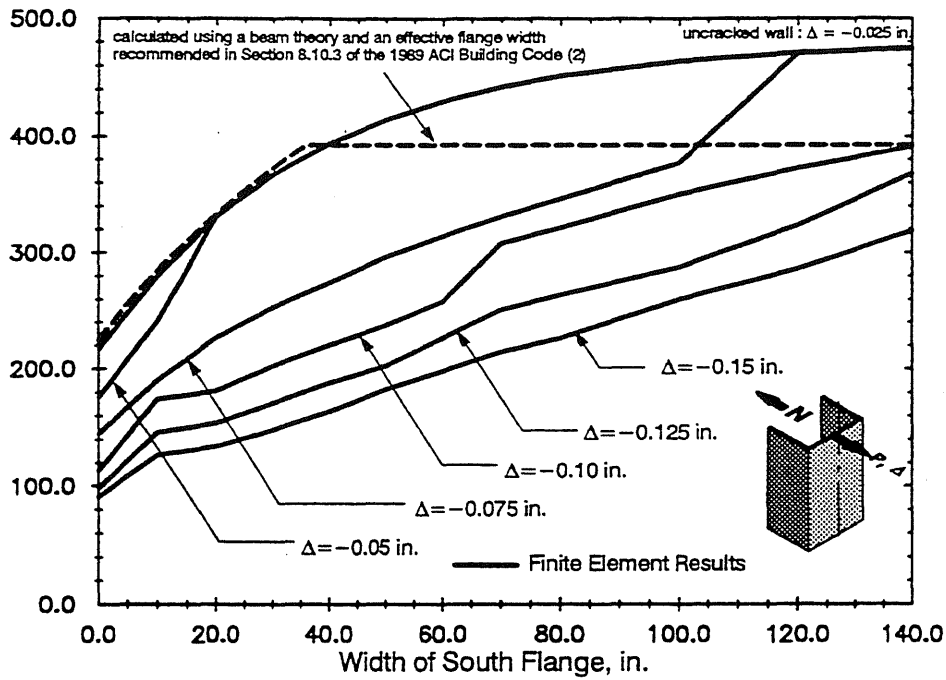
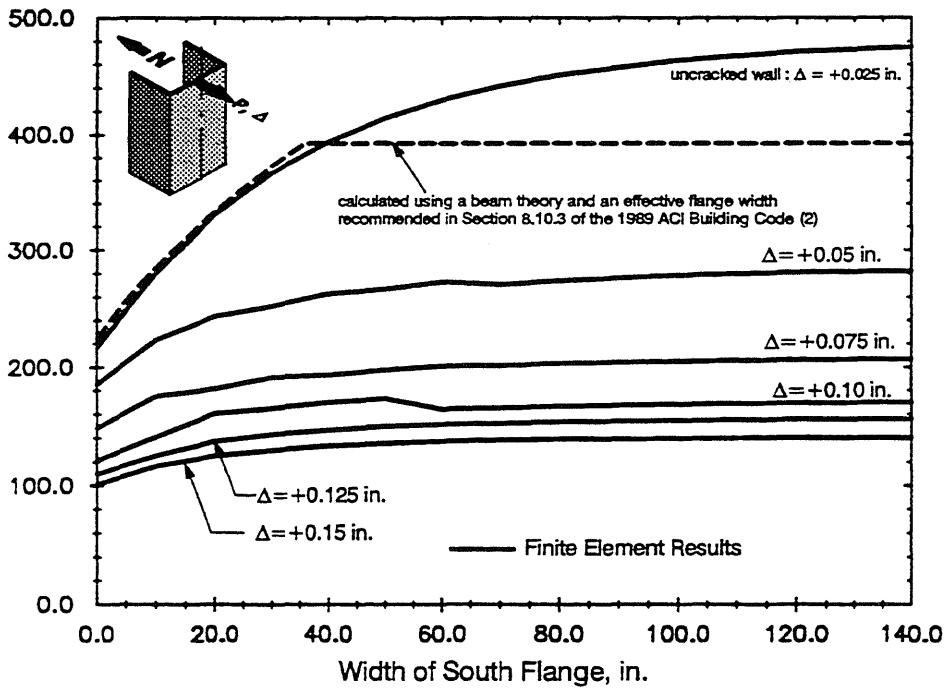


Fig. 8.46 Effective Width of the South Flange for C-Shaped Walls



a) Stiffness of C-Shaped Walls Loaded in the North Direction



b) Stiffness of C-Shaped Walls Loaded in the South Direction

Fig. 8.47 Secant Stiffnesses of C-Shaped Walls at Different Deformation Levels

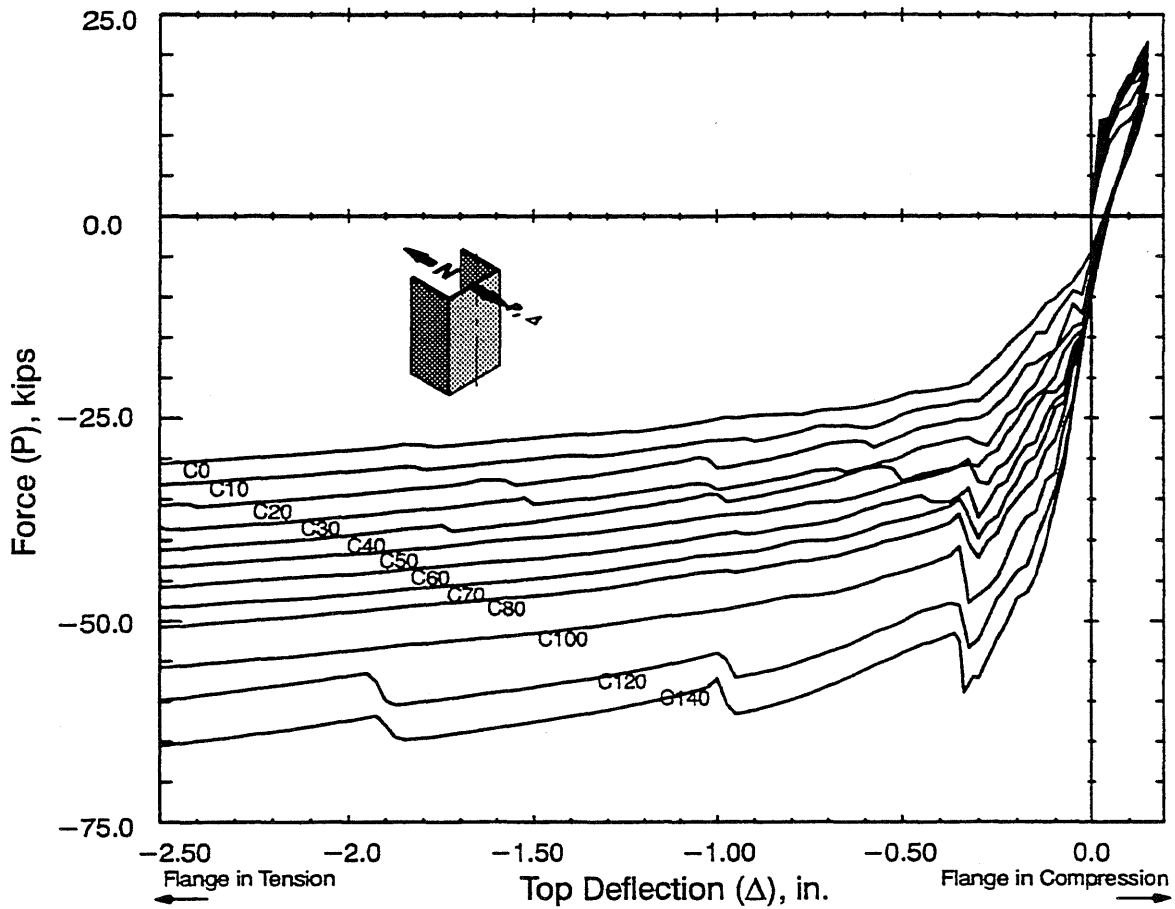


Fig. 8.48 Calculated Load vs. Top Deflection Curves for C-Shaped Walls: Case A

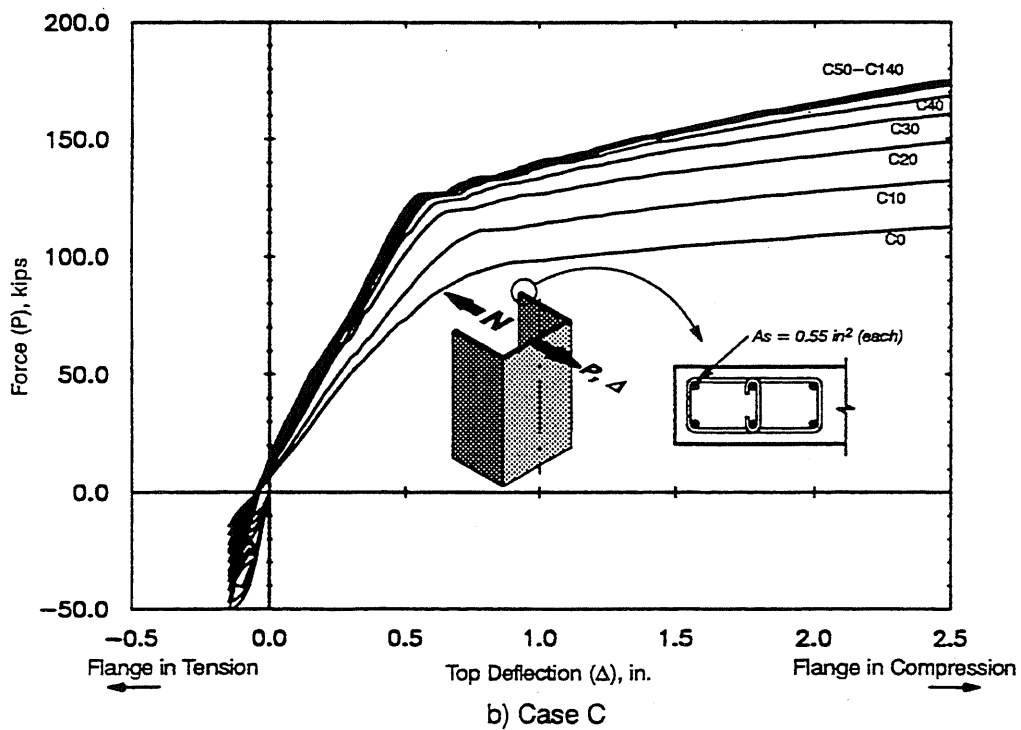
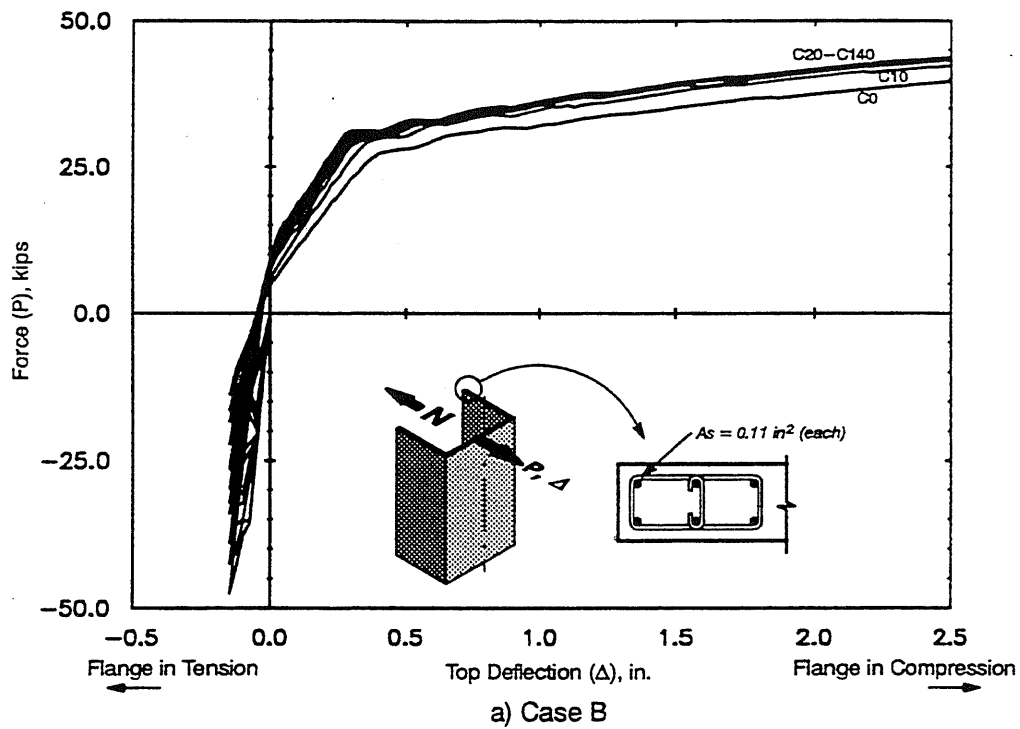


Fig. 8.49 Calculated Load vs. Top Deflection Curves for C-Shaped Walls: Cases B and C

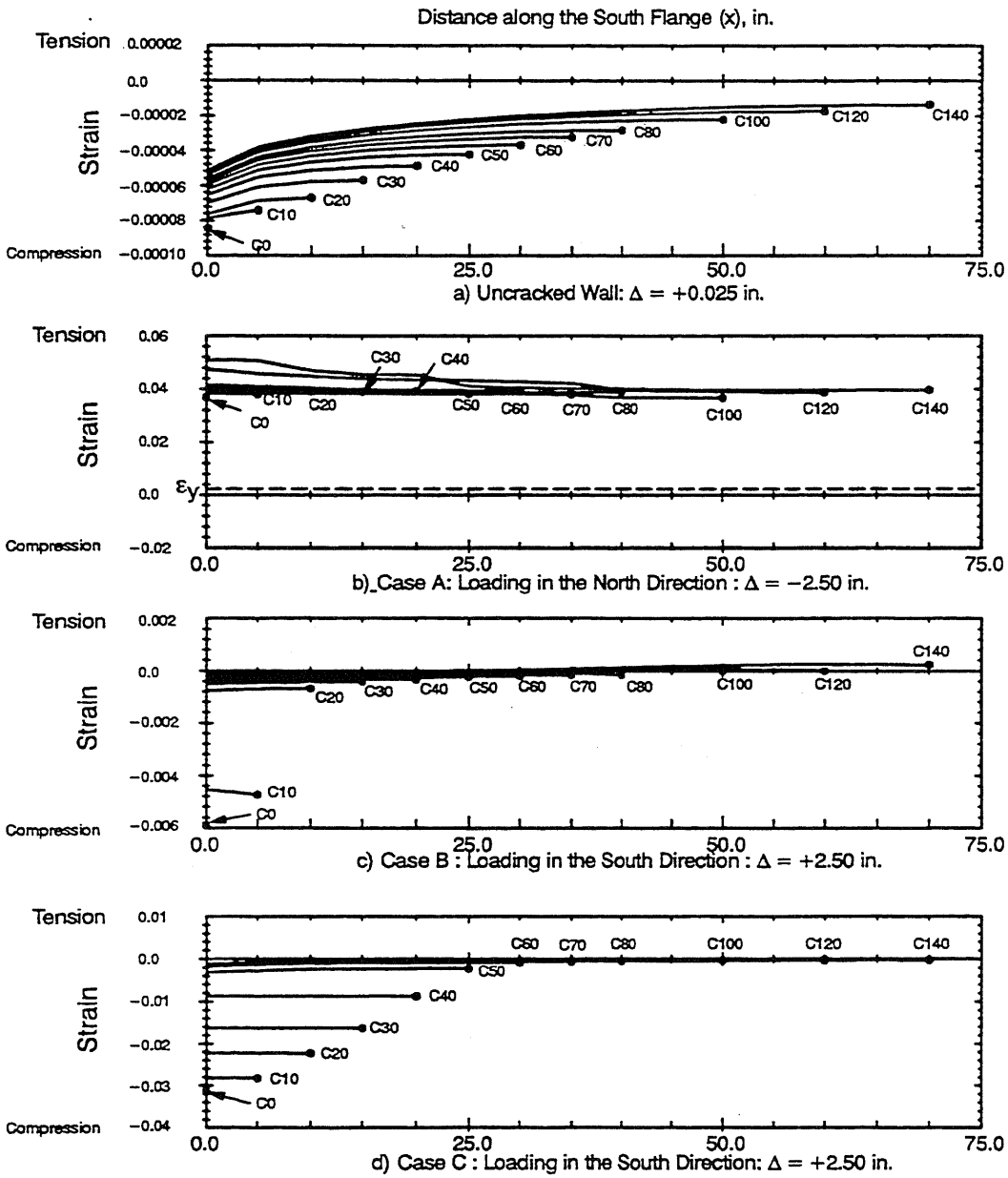
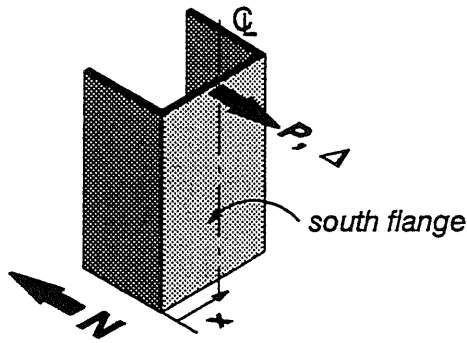


Fig. 8.50 Distribution of Strain in Vertical Reinforcing Bars along the Base of the South Flange



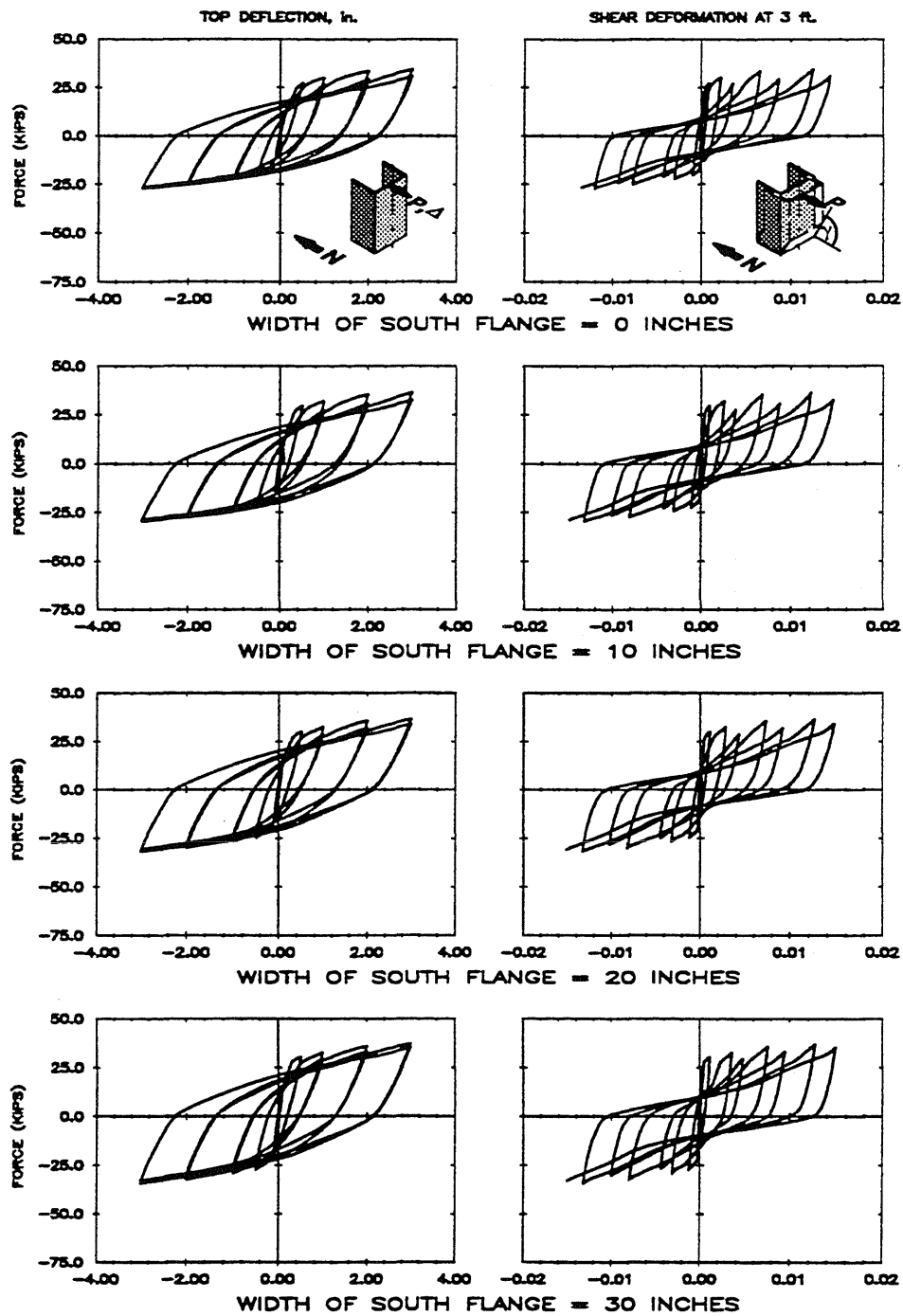


Fig. 8.51 Calculated Results of C-Shaped Walls subjected to Cyclic Loadings

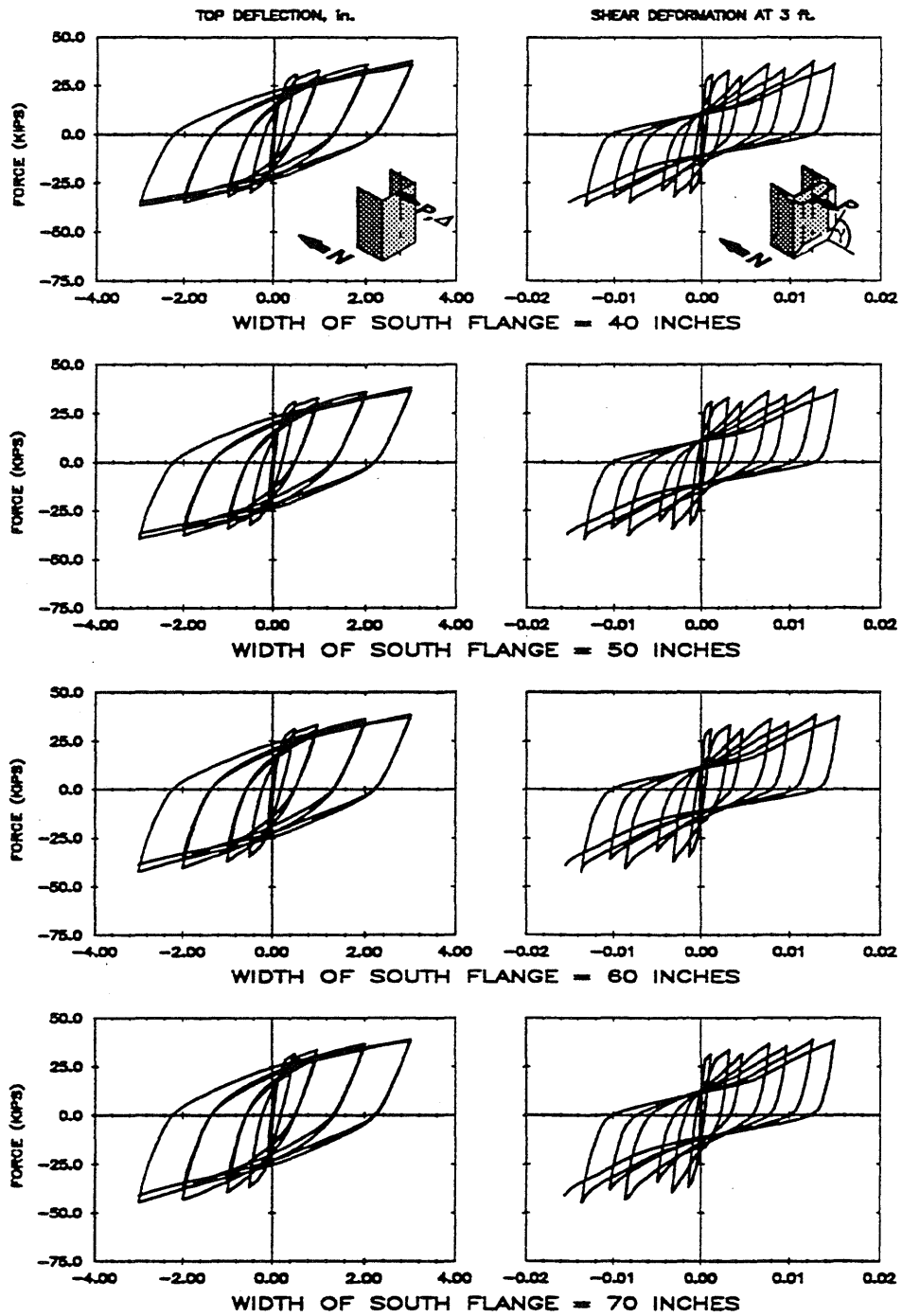


Fig. 8.51 Calculated Results of C-Shaped Walls subjected to Cyclic Loadings (Cont.)

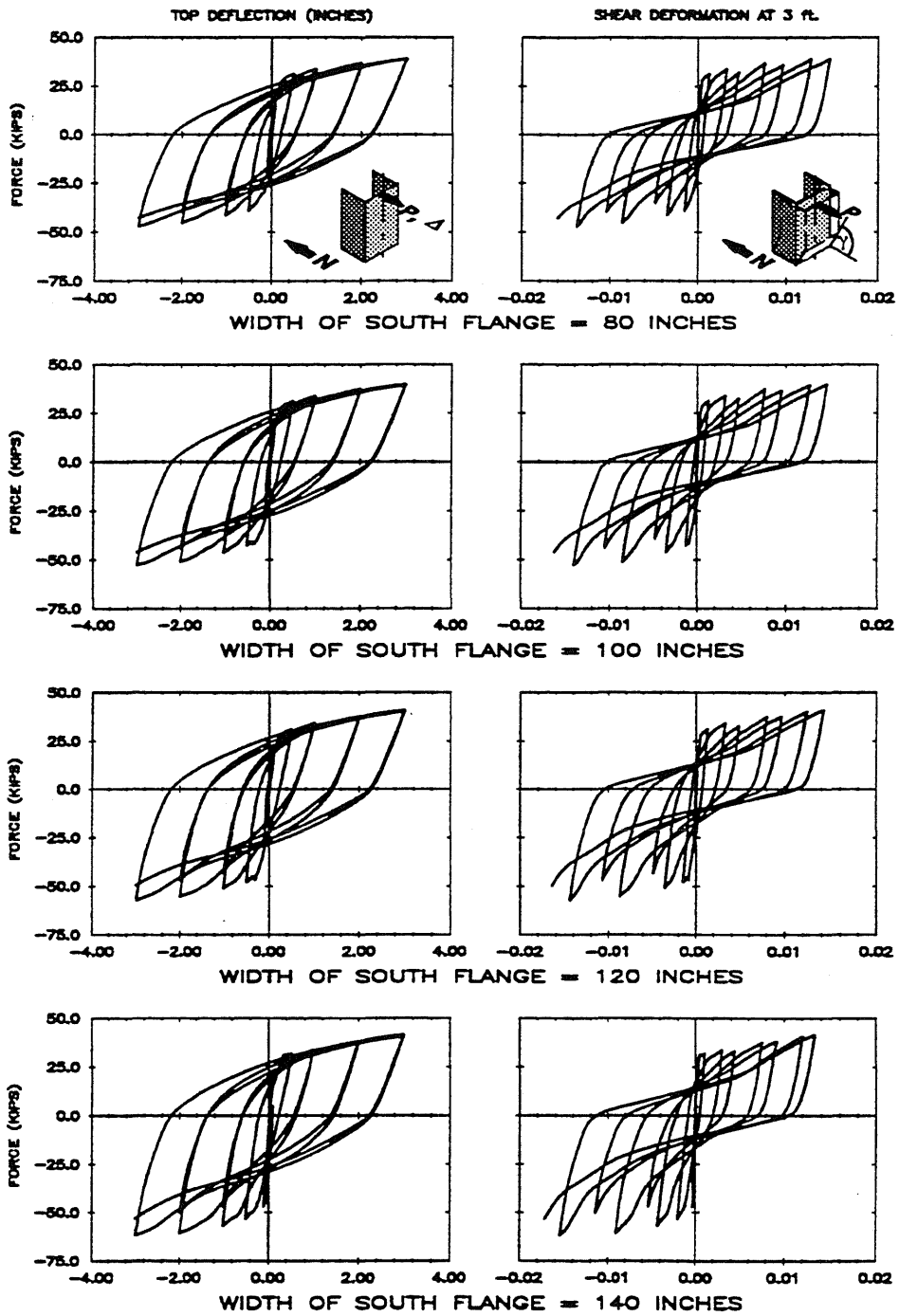


Fig. 8.51 Calculated Results of C-Shaped Walls subjected to Cyclic Loadings (Cont.)

## APPENDIX A

### COMPRESSION STIFFENING AND COMPRESSION SOFTENING CURVES FOR THE CONCRETE MODEL

#### A.1 COMPRESSION STIFFENING CURVE

A compression stiffening curve (curve A-B in Fig. A.1) is defined by the following equation:

$$\frac{\varepsilon_c - \varepsilon_n}{\varepsilon_{os}} = \frac{\sigma_c - \sigma_n}{\sigma_{os}} + \left( \frac{\sigma_c - \sigma_n}{\sigma_{os}} \right)^s \quad (\text{A.1})$$

where

$$s = \left( \frac{E_c}{E_t} - 1 \right) \left( \frac{k_2}{k_1 E_c - k_2} \right)$$

$$\sigma_{os} = \frac{|k_2|^{\frac{s}{s-1}}}{|k_1 E_c - k_2|^{\frac{1}{s-1}}}$$

$$\varepsilon_{os} = \frac{\sigma_{os}}{E_c}$$

$$k_1 = \varepsilon_c - \varepsilon_n$$

$$k_2 = \sigma_c - \sigma_n$$

$E_t$  = the tangent stiffness at the beginning of the unloading curve

$E_c$  = the initial modulus of elasticity for concrete

$(\varepsilon_c, \sigma_c)$  = the strain and stress at the current load step

$(\varepsilon_n, \sigma_n)$  = the strain and stress at the end of the compression stiffening curve

## A.2 COMPRESSION SOFTENING CURVE

A compression softening curve (curve B–C in Fig. A.2) is defined by the following equation:

$$\text{when } \varepsilon > \varepsilon_n \quad \sigma = E_c \varepsilon \quad (\text{A.2})$$

$$\text{when } \varepsilon < \varepsilon_n \quad \frac{\sigma - \sigma_n}{\sigma_{oc}} = \frac{\varepsilon - \varepsilon_n}{\varepsilon_{oc}} e^{\left(1 - \frac{\varepsilon - \varepsilon_n}{\varepsilon_{oc}}\right)} \quad (\text{A.3})$$

where

$$\sigma_{oc} = f_{cult} - \sigma_n$$

$$\varepsilon_{oc} = \frac{\sigma_{oc} e}{E_c}$$

$f_{cult}$  = the compressive strength of concrete

$E_c$  = the initial modulus of elasticity for concrete

$e$  = the base of the natural logarithms

$(\varepsilon_n, \sigma_n)$  = the strain and stress at the beginning of the compression softening curve

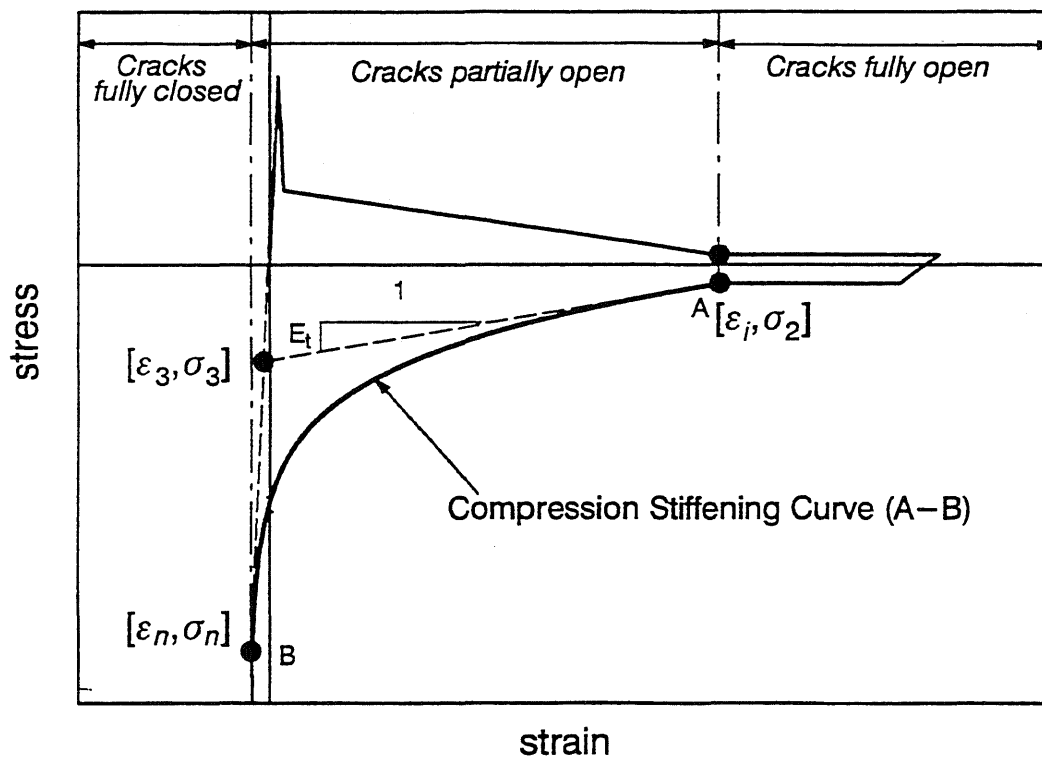


Fig. A.1 Compression Stiffening Curve

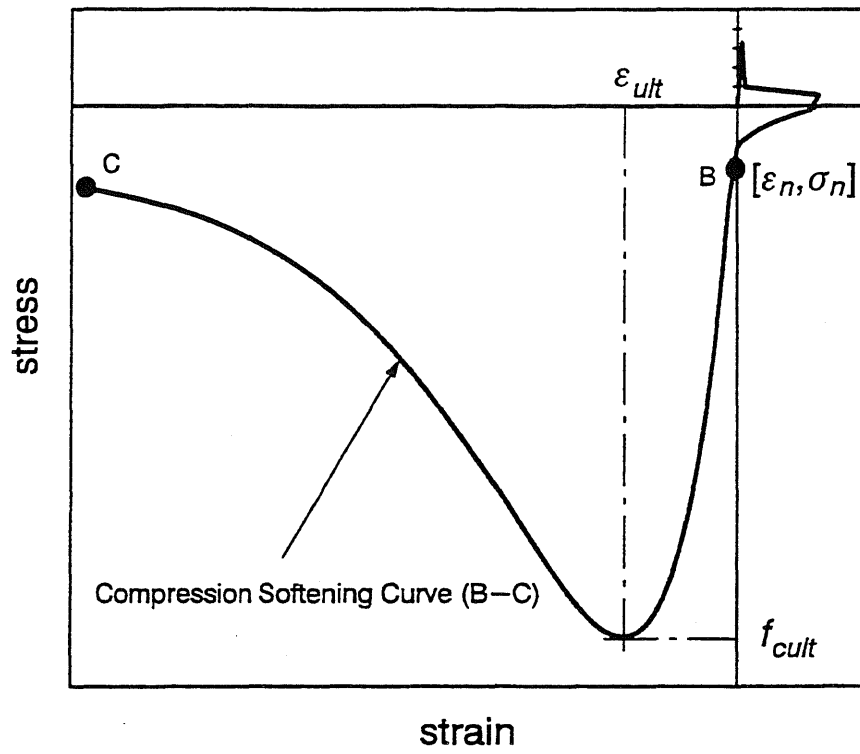


Fig. A.2 Compression Softening Curve

## APPENDIX B

### STRESS-STRAIN RELATIONSHIP FOR CONFINED CONCRETE

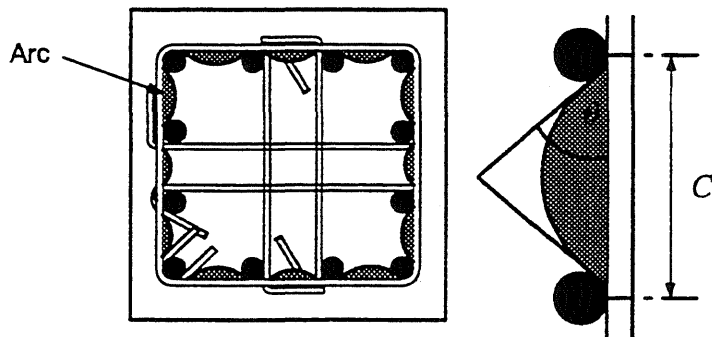
The stress-strain relationship for confined concrete proposed by Shiekh and Uzumeri (125) was adopted in the proposed concrete model. Parameters of the relationship, which include  $f_{cu}$ ,  $\epsilon_1$ ,  $\epsilon_2$ , and  $\epsilon_{85}$  (Fig. B.1), are calculated as follows:

step 1: Determine volumetric ratio of tie steel :

$$\rho_s = \frac{\text{volume of tie steel at a level}}{\text{volume of core (center to center of outer ties)}}$$

step 2: Determine  $\lambda$  :

$$\lambda = 1 - \frac{\sum_{i=1}^n C_i^2}{\alpha A_{co}}$$



$n$  = the number of arcs

$A_{co}$  = the area enclosed by the center line of outer tie

$C$  = the center-to-center distance between longitudinal bars

$\alpha = 5.5$

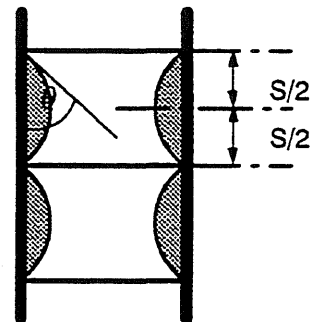
step 3: Determine  $\lambda^*$  :

$$\lambda^* = \lambda (B - 0.5 s \tan \theta) (H - 0.5 s \tan \theta)$$

$B$  and  $H$  = the center-to-center distance of perimeter tie of rectangular core.

$\theta$  = 45 degrees

$s$  = spacing between transverse reinforcement



step 4: Determine  $P_{occ}$  :

$$P_{occ} = 0.85 f'_c (A_{oc} - A_s)$$

step 5: Determine  $K_s$  and  $f_{cult}$  :

$$k_s = 2.73 \frac{\lambda^* B^2}{P_{occ}} \sqrt{\rho_s f'_s} \quad f_{cult} = k_s f'_c$$

step 6: Determine  $\varepsilon_1$  :

$$\varepsilon_1 = 0.55 k_s f'_c \times 10^{-6} \quad f'_c \text{ in psi}$$

step 7: Determine  $\varepsilon_2$  :

$$\frac{\varepsilon_2}{\varepsilon_{00}} = 1 + \frac{0.81}{C} \left( 1 + 5.0 \left( \frac{s}{B} \right)^2 \right) \frac{\rho_s f'_c}{\sqrt{f'_c}}$$

$\varepsilon_{00}$  = strain corresponding to the maximum stress in plain concrete

step 8: Determine  $\varepsilon_{85}$  :

$$\varepsilon_{85} = 0.225 \rho_s \sqrt{\frac{B}{s}} + \varepsilon_2$$

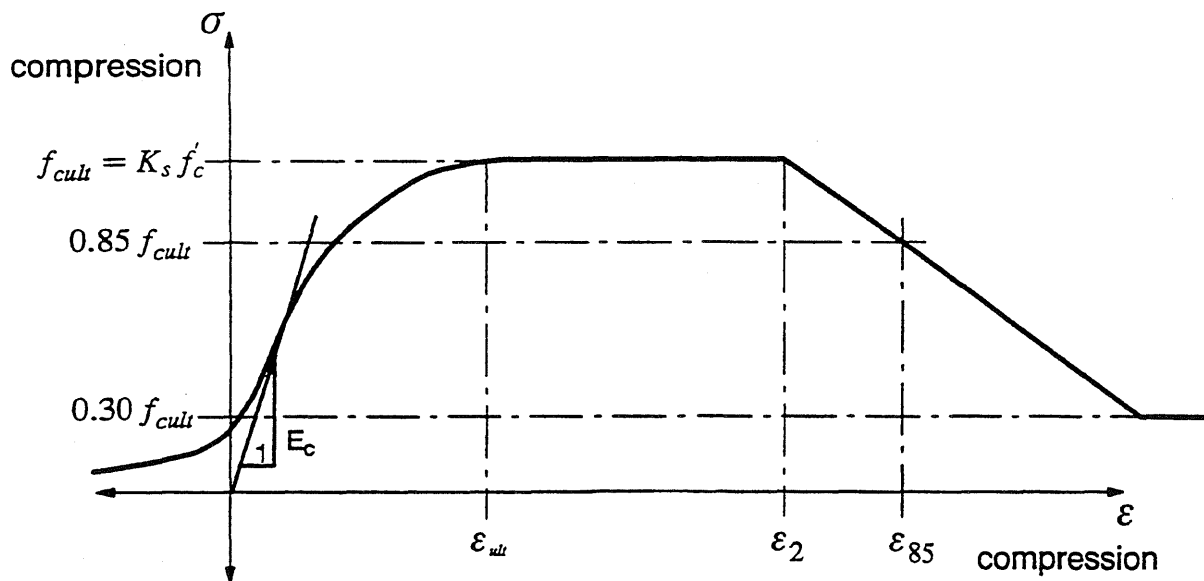


Fig. B.1 Stress-Strain Relationship for Confined Concrete



## APPENDIX C

### RULES FOR CYCLIC STRESS-STRAIN RELATIONSHIP OF CONCRETE

[  $\sigma, \varepsilon$  ] = stress and strain at the current load step

#### ENVELOPE CURVE:

$$\sigma_{env} = \sigma_{oc} * \left[ \frac{\varepsilon - \varepsilon_n}{\varepsilon_{oc}} \right] e^{1 - \frac{\varepsilon - \varepsilon_n}{\varepsilon_{oc}}} + \sigma_n \quad (C.1)$$

where

$$\sigma_{oc} = f_{cult} - \sigma_n$$

$$\varepsilon_{oc} = \frac{\sigma_{oc} e}{E_c}$$

( $\varepsilon_n, \sigma_n$ ) = the strain and stress at the beginning of the compression softening curve

#### COMMON POINTS:

$$\sigma_{cp} = \sigma_n + 0.85 * (\sigma_{env} - \sigma_n) \quad (C.2)$$

#### PERMANENT COMPRESSIVE STRAIN $\varepsilon_p$ :

$\varepsilon_p$  is the permanent compressive strain for the current cycle

$$\varepsilon_p = \frac{\varepsilon_{ult} [1.0 - 0.425e^{(1-s)}]}{1 - (s e^{(1-s)})} \quad (C.3)$$

$$\text{if } \varepsilon_p < 0.70 \cdot \varepsilon_{max}^c \quad \varepsilon_p = 0.70 \cdot \varepsilon_{max}^c$$

where

$$s = \frac{\varepsilon_{max}^c}{\varepsilon_{ult}}$$

$\varepsilon_{ult}$  = the compressive strain at the compressive strength of concrete,  $f_{cult}$

$\varepsilon_{max}^c$  = the previous maximum compressive strain

There are 5 values of tangent stiffness used in the relationship :

$$E1 = E_c = \text{the initial modulus of elasticity for concrete} \quad (C.4)$$

$$E2 = \frac{\sigma_{cp} - \sigma_{pr}}{\varepsilon_{\max}^c - \varepsilon_{pr}} \quad (C.5)$$

where  $\sigma_{pr}, \varepsilon_{pr} =$  stress-strain of the previous load step

$$E3 = 0.10 E_c \quad (C.6)$$

if ( $E3 < E2$ ) then  $E3 = E2$

$$E4 = \frac{0.30 f_{\text{cult}}}{\varepsilon_{0.3} - \varepsilon_p} \quad (C.7)$$

where  $\varepsilon_{0.3} =$  strain at stress =  $0.30 f_{\text{cult}}$  when unloading  
with tangent stiffness =  $E_{\text{conc}}$  from  $[\sigma_v, \varepsilon_{\max}^c]$

$$E5 = \frac{\sigma_c}{\varepsilon_{\max}^c} \quad (C.8)$$

Value of  $\varepsilon_n$  in each cycle is adjusted as follows :

$$\varepsilon_n = \frac{\sigma_n}{E5} \quad (C.9)$$

$[\sigma, \varepsilon]$	=	stress, strain at the current load step
$[\sigma_{pr}, \varepsilon_{pr}]$	=	stress, strain at the previous load step
$E_t$	=	tangent stiffness of the current load step
$\sigma_v$	=	stress on the envelope curve at strain = $\varepsilon_{\max}^c$
$E_v$	=	tangent stiffness of the envelope curve at strain = $\varepsilon_{\max}^c$

The rules for loading and unloading are described in Table C.1.

Table C.1 Loading and Unloading Rules for Unconfined Concrete

LOADING: $\epsilon < \epsilon_{pr}$	Description
<p>                     if <math>\epsilon_{max}^c &gt; \epsilon_{ult}</math> then _____  <math>E_t = E_1</math> _____                      else _____                      if <math>\epsilon &lt; \epsilon_{max}^c</math> then _____  <math>E_t = E_3</math> _____                      else _____  <math>E_t = E_2</math> _____                      endif _____                      endif _____  <math>\sigma = \sigma_{pr} + E_t(\epsilon - \epsilon_{pr})</math> _____                      if <math>\sigma &lt; \sigma_v</math> then _____  <math>\sigma = \sigma_v</math> _____  <math>E_t = E_v</math> _____                      endif _____                      B - C } _____                      H - I } _____                      A - B } _____                      G - H } _____                      C - D } _____                      I - J } _____                 </p>	<p>                     concrete has not been crushed yet                      use elastic <math>E_c</math>                      concrete has previously been crushed                      current strain less than previous max.strain                      use <math>E_3</math>                      current strain is greater than prev. max.strain                      use secant stiffness between <math>(\sigma_{pr}, \epsilon_{pr})</math> and <math>(\sigma_v, \epsilon_{max}^c)</math> <math>E_2</math>                      update stress at current step                      if the current stress is less that the stress on the envelop curve, stress-strain curve follows the envelope curve                 </p>
UNLOADING: $\epsilon > \epsilon_{pr}$	Description
<p> <math>E_t = E_1</math> _____  <math>\sigma = \sigma_{pr} + E_t(\epsilon - \epsilon_{pr})</math> _____                      if <math>\sigma &lt; 0.30 f_{cult}</math> then _____  <math>E_t = E_4</math> _____  <math>\sigma = \sigma_{pr} + E_t(\epsilon - \epsilon_{pr})</math> _____                      endif _____                      if <math>\sigma &lt; 0.0</math> then _____  <math>\sigma = 0.0</math> _____  <math>E_t = 0.0</math> _____                      endif _____                      D - E } _____                      E - F } _____                      F - G } _____                 </p>	<p>                     use elastic <math>E_c</math>                      update stress at current step                      if the current stress is greater that 0.30 <math>f_{cult}</math> use <math>E_4</math> instead.                      if the current stress is greater than 0.0, set stress and stiffness to be 0.0                 </p>

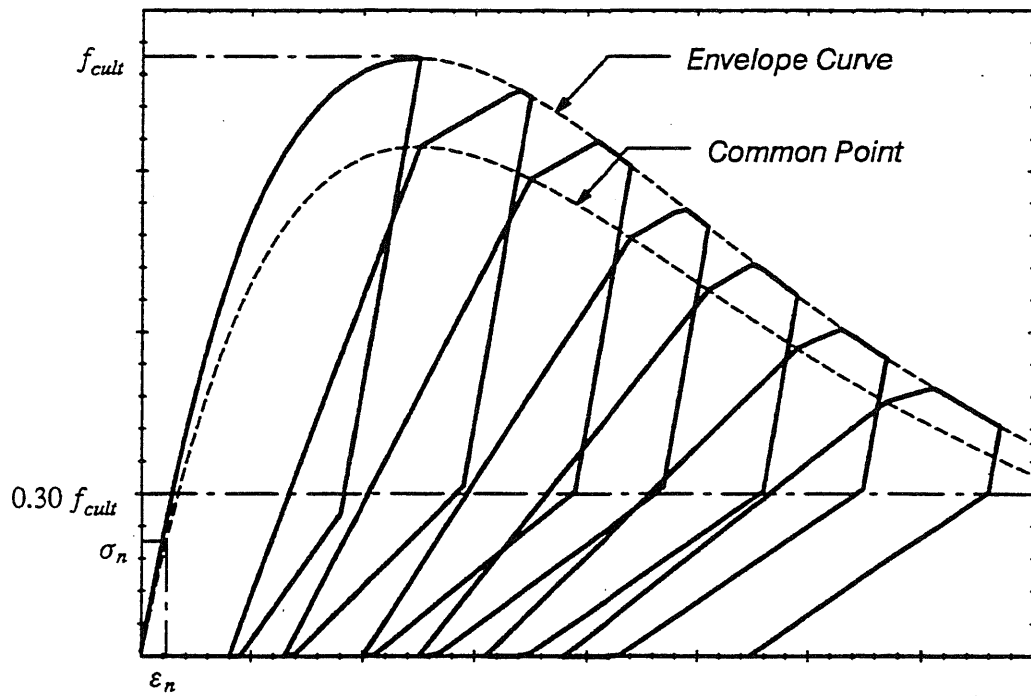


Fig. C.1 : Stress–strain of Unconfined Concrete subjected to Cyclic Compressive Loading

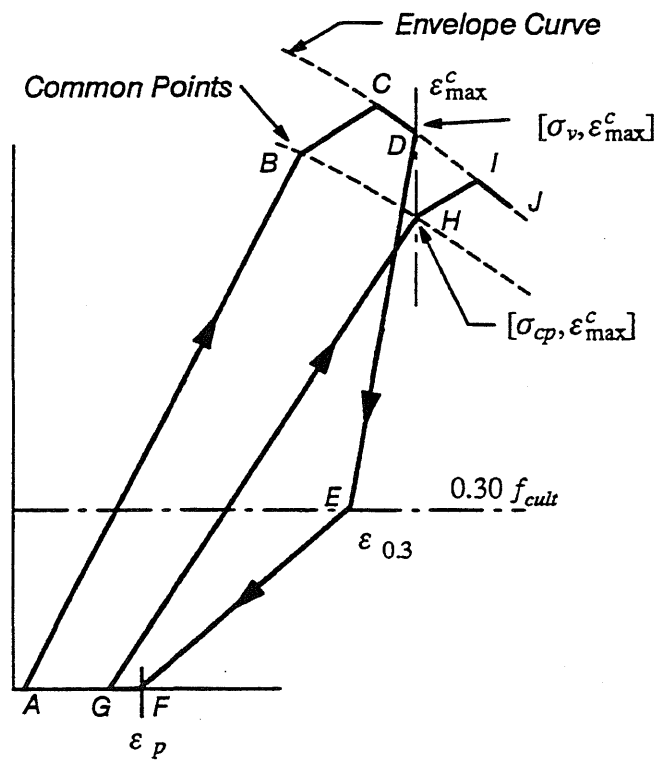


Fig. C.2 : Rules for Cyclic Compressive Loading

# APPENDIX D

## FINITE ELEMENT MESHES FOR WALLS

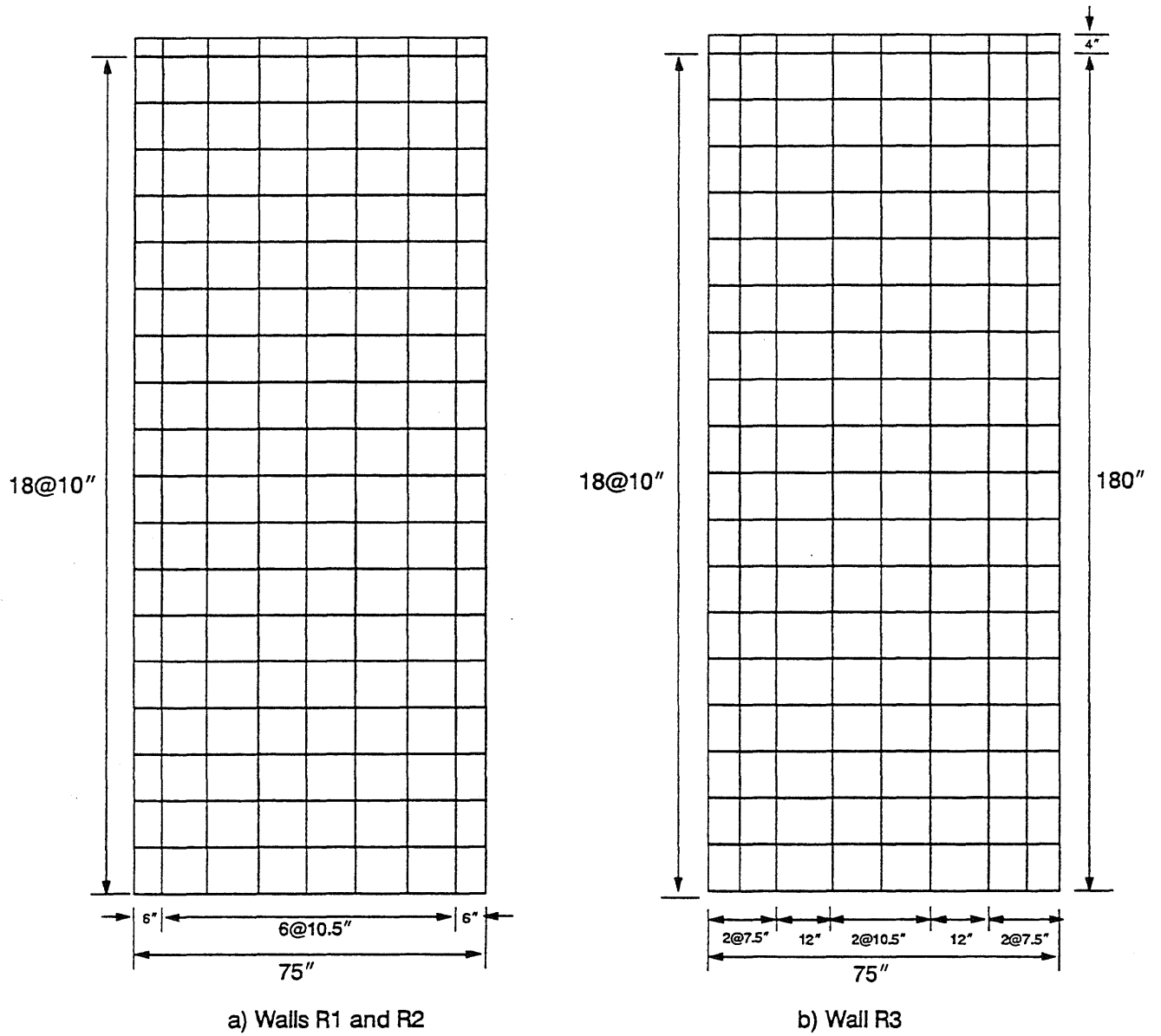
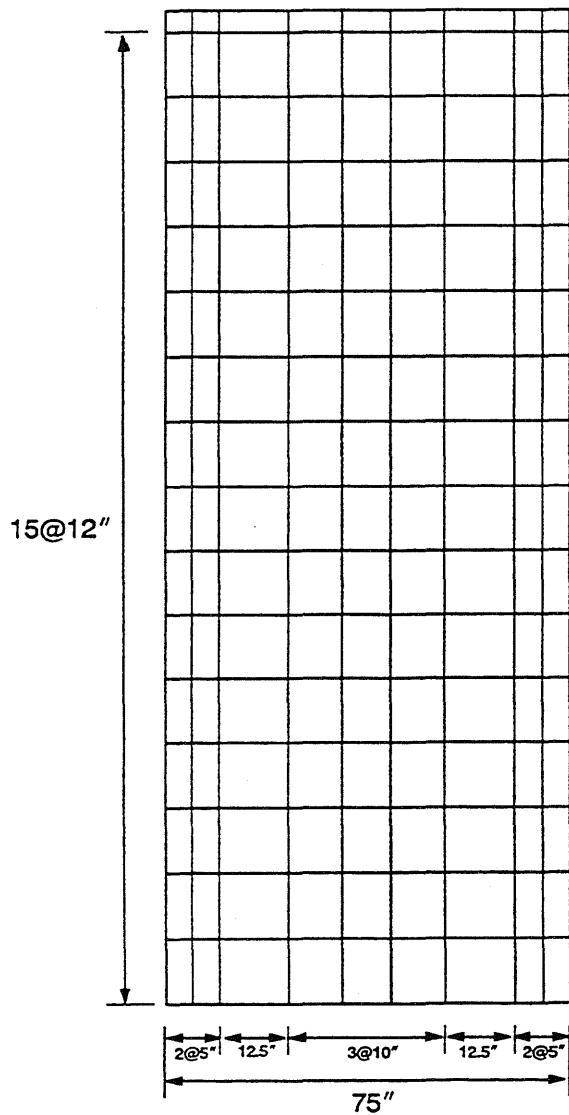
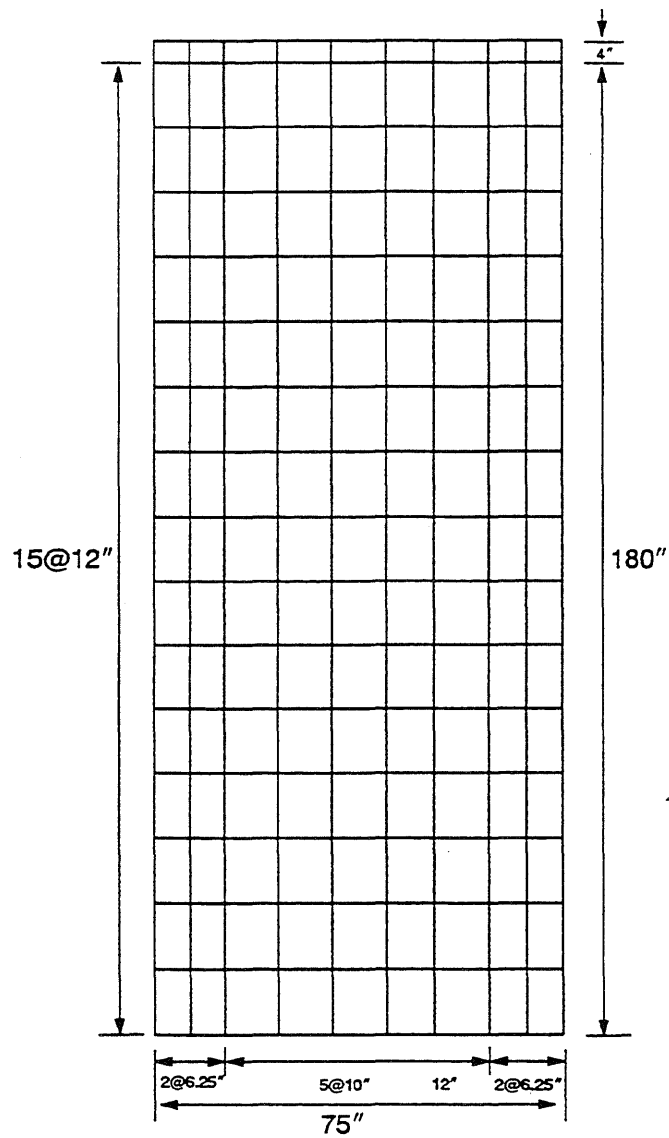


Fig. D.1 Finite Element Meshes for PCA Walls

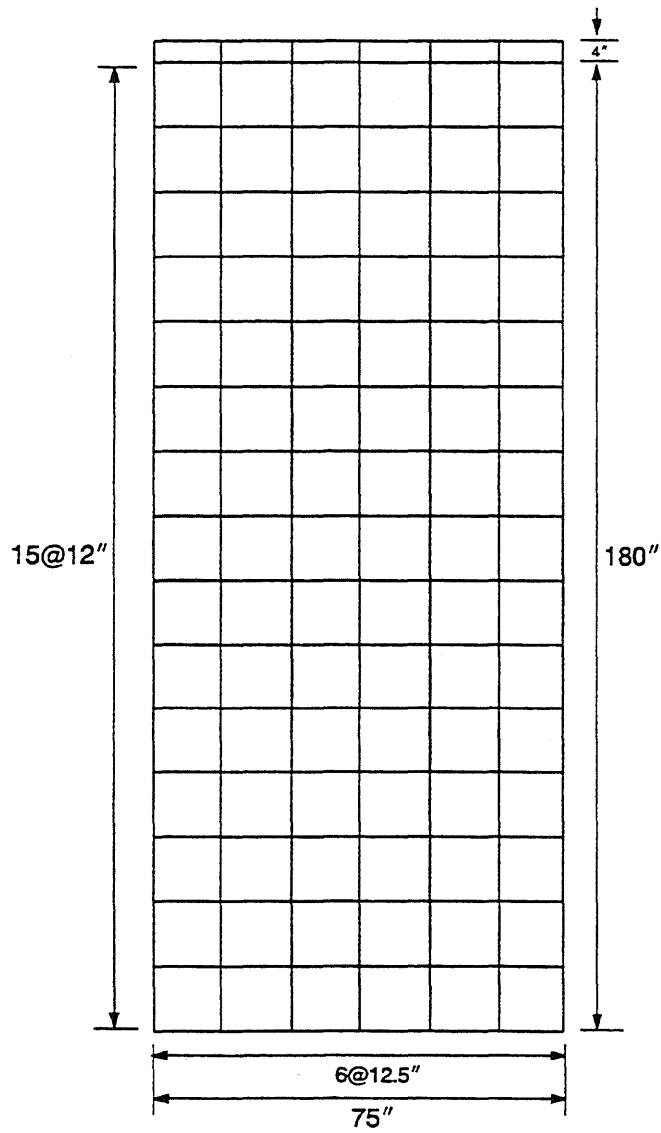


c) Wall R4



d) Walls B1, B3, B4, and B9

Fig. D.1 Finite Element Meshes for PCA Walls (cont.)



e) Walls B2, B5, B6, B7, and B8

Fig. D.1 Finite Element Meshes for PCA Walls (cont.)

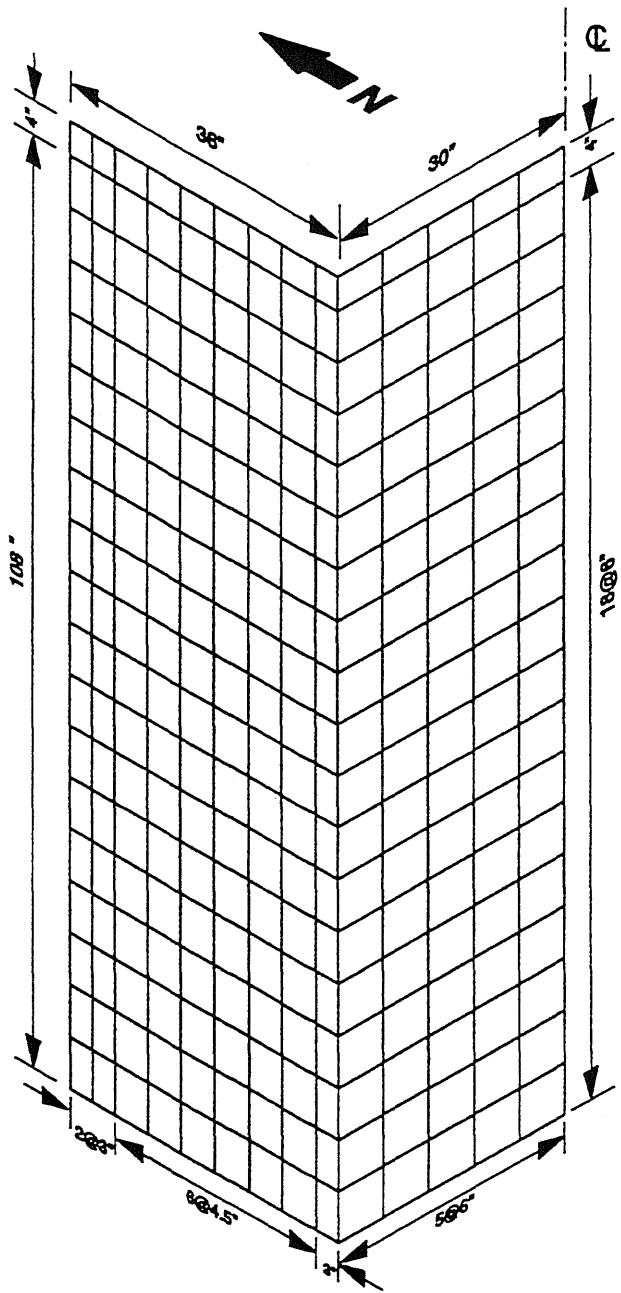
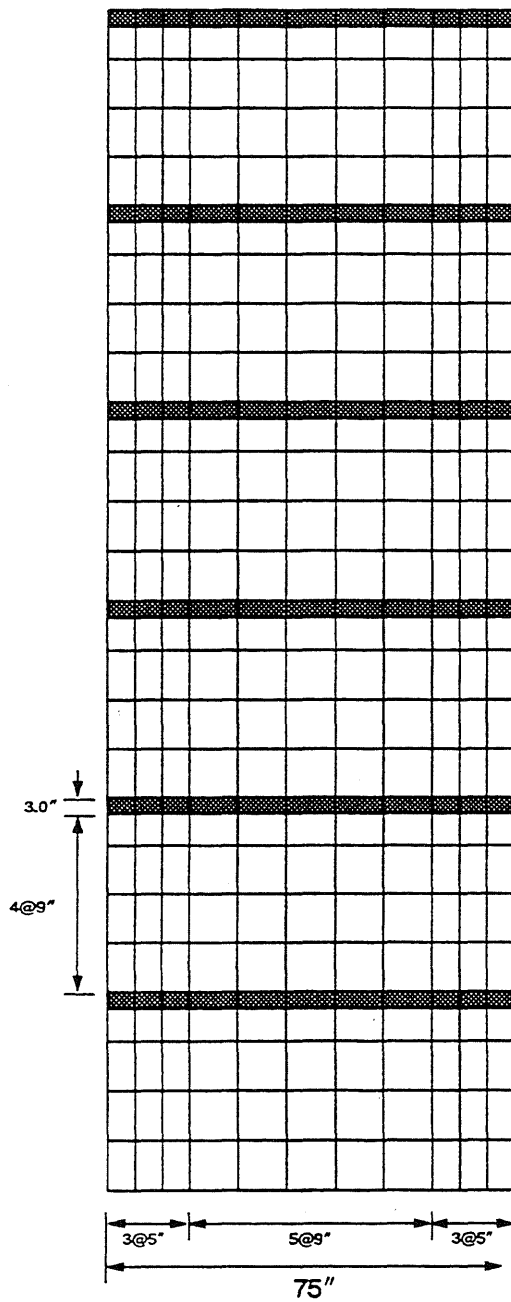
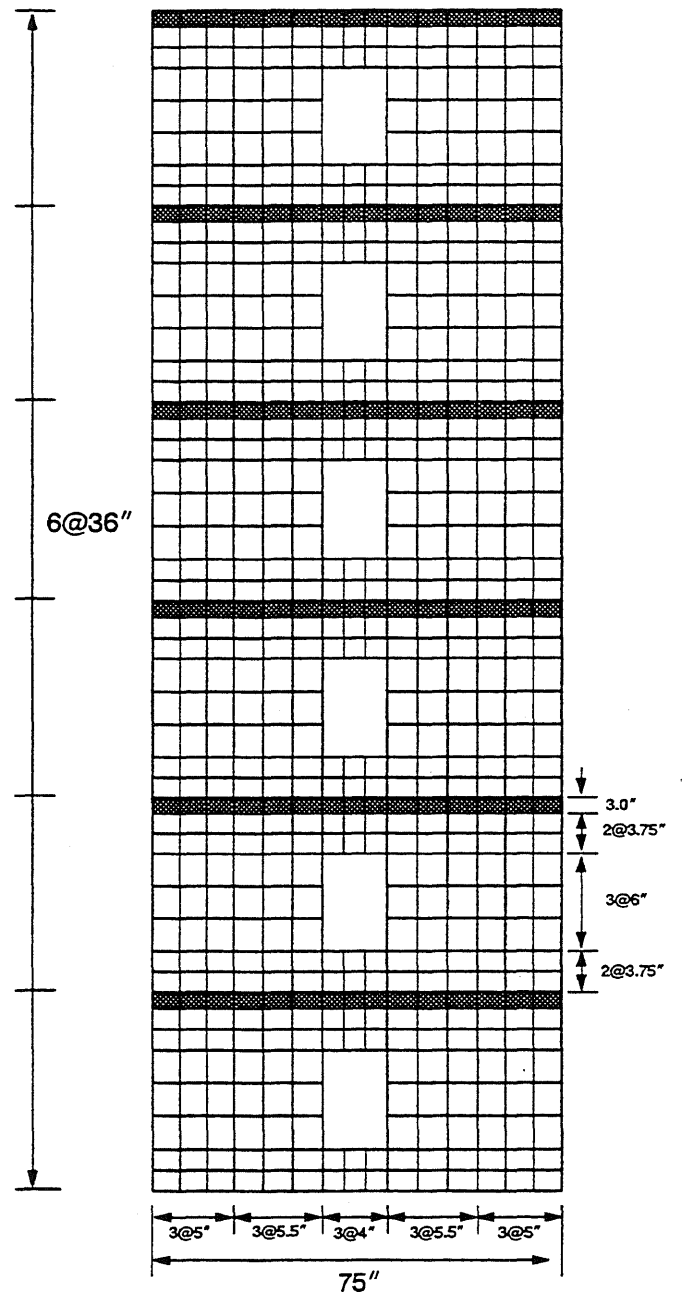


Fig. D.2 Finite Element Meshes for Walls CLS and CMS





a) Wall CI1



b) Wall PW1

Fig. D.3 Finite Element Meshes for Walls CI1 and PW1

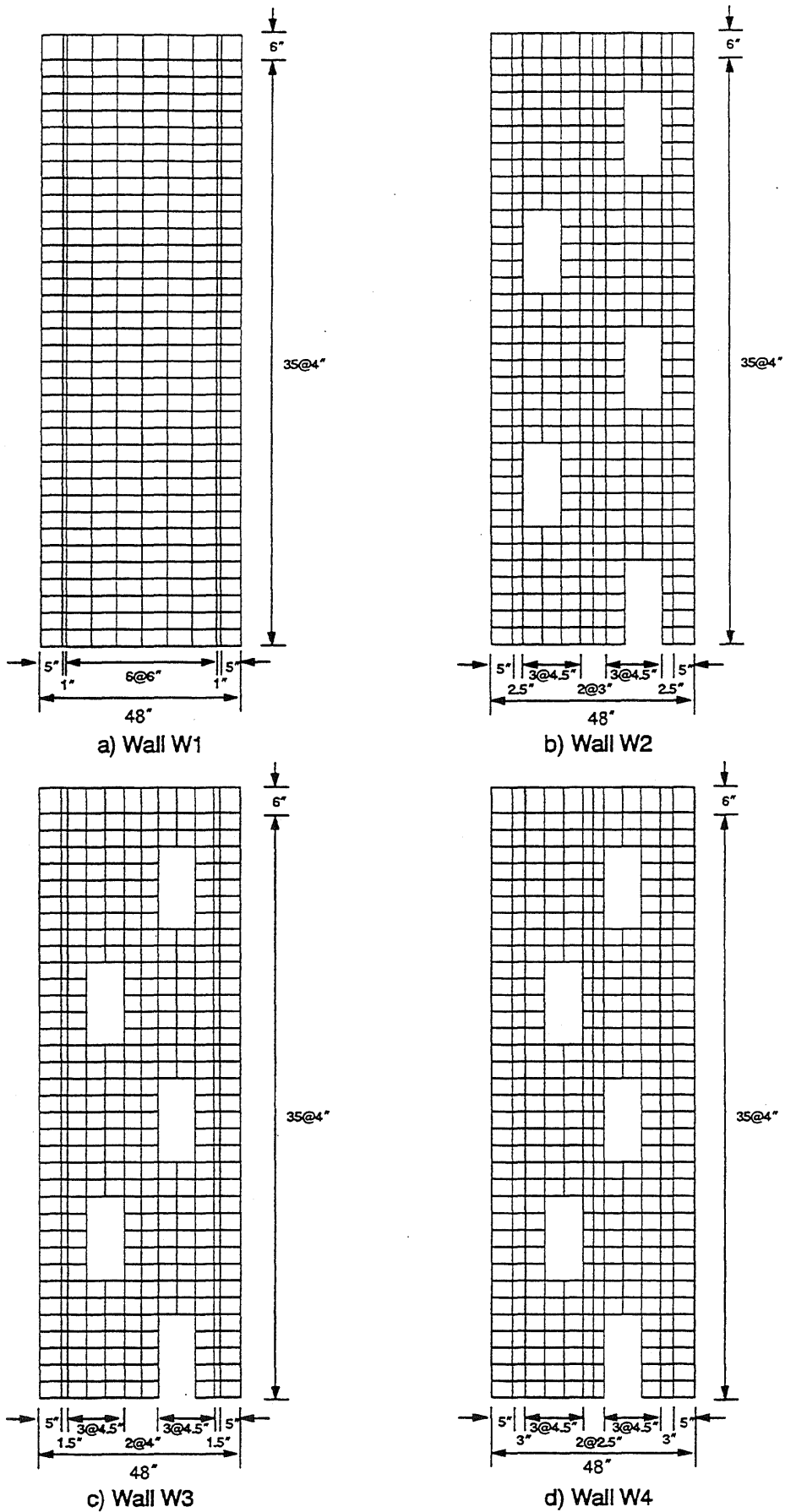


Fig. D.4 Finite Element Meshes for Walls W1, W2, W3, and W4

## APPENDIX E

### MATERIAL PROPERTIES FOR PCA WALL TESTS

Table E.1 Measured Concrete Properties (from (105, 106,103))

Specimen	$f_c'$ (psi)	$f_r$ (psi)	$E_c$ (ksi)
R1	6490	655	4030
R2	6735	650	3890
R3	3535	-	-
R4	3285	-	-
B1	7685	730	4080
B2	7775	710	4200
B3	6860	635	3960
B4	6530	680	4100
B5	6570	625	3970
B6	3164	657	3350
B7	7155	873	4310
B8	6085	614	3900
B9	6396	633	3940

$f_c'$  = average compressive strength of concrete  
 $f_r$  = average modulus of rupture of concrete  
 $E_c$  = average modulus of elasticity of concrete

Table E.2 Measured Reinforcing Steel Properties (from (105, 106, 103))

Size	Properties	Specimen												
		R1	R2	R3	R4	B1	B2	B3	B4	B5	B6	B7	B8	B9
D3	$f_y$ (ksi)	66.0	70.4	70.0	70.0	68.7	67.1	69.0	73.8	69.2	70.7	-	-	-
	$f_{su}$ (ksi)	72.0	76.2	-	-	75.1	74.4	76.8	78.8	75.4	74.0	-	-	-
	$E_s$ (ksi x $10^3$ )	30.6	28.3	-	-	33.0	33.8	32.5	28.4	31.2	30.0	-	-	-
6mm	$f_y$ (ksi)	75.7	77.6	75.0	75.0	75.5	77.2	69.4	73.2	72.8	74.2	71.0	65.8	66.9
	$f_{su}$ (ksi)	101.5	100.2	-	-	100.8	101.6	95.5	98.8	97.4	98.0	101.0	89.3	88.9
	$E_s$ (ksi x $10^3$ )	31.4	32.6	-	-	32.5	32.1	30.4	31.9	31.4	30.4	28.5	28.2	28.6
No. 3	$f_y$ (ksi)	74.2	-	-	-	-	-	-	-	-	-	-	-	-
	$f_{su}$ (ksi)	111.0	-	-	-	-	-	-	-	-	-	-	-	-
	$E_s$ (ksi x $10^3$ )	27.8	-	-	-	-	-	-	-	-	-	-	-	-
No. 4	$f_y$ (ksi)	-	65.3	78.3	71.2	65.2	-	63.5	65.3	-	-	-	-	-
	$f_{su}$ (ksi)	-	102.7	-	-	102.7	-	101.1	102.5	-	-	-	-	-
	$E_s$ (ksi x $10^3$ )	-	26.9	-	-	28.3	-	25.9	27.5	-	-	-	-	-
No. 6	$f_y$ (ksi)	-	-	-	-	-	59.5	-	-	64.4	63.9	66.4	64.9	62.3
	$f_{su}$ (ksi)	-	-	-	-	-	100.8	-	-	106.4	106.3	108.8	108.2	106.5
	$E_s$ (ksi x $10^3$ )	-	-	-	-	-	30.2	-	-	29.5	28.5	28.4	27.5	27.6

$f_y$  = yielding strength of reinforcing steel  
 $f_{su}$  = strength of reinforcing steel  
 $E_s$  = modulus of elasticity of reinforcing steel

## APPENDIX F

### MATERIAL PROPERTIES FOR C-SHAPED WALLS

Table F.1 Measured Concrete Properties

Specimen	f <sub>c</sub> ' (psi)	f <sub>t</sub> (psi)	f <sub>r</sub> (ksi)
CLS	4500	425	940
CMS	4050	420	1070

f<sub>c</sub>' = average compressive strength of concrete  
 f<sub>t</sub> = average splitting tensile strength of concrete  
 f<sub>r</sub> = average modulus of rupture of concrete

Table F.2 Measured Steel Properties

Reinforcing Steel	f <sub>y</sub> (ksi)	f <sub>su</sub> (ksi)	E <sub>s</sub> (ksi)
No. 2 Bar	55	71	27,750
No. 3 Bar	62	91	28,400
#10 Wire	85	112	24,300

f<sub>y</sub> = yielding strength of reinforcing steel  
 f<sub>su</sub> = strength of reinforcing steel  
 E<sub>s</sub> = modulus of elasticity of reinforcing steel

## APPENDIX G

### MATERIAL PROPERTIES FOR WALL CI1 AND PW1

Table G.1 Measured Concrete Properties (from (126))

Specimen	f <sub>c</sub> ' (psi)	f <sub>t</sub> (psi)	E <sub>c</sub> (ksi)
CI-1	3375	480	3385
PW-1	3030	430	2815

f<sub>c</sub>' = average compressive strength of concrete  
 f<sub>t</sub> = average splitting tensile strength of concrete  
 E<sub>c</sub> = average modulus of elasticity of concrete

Table G.2 Measured Steel Properties (from (126))

Specimen	Reinforcing Steel	f <sub>y</sub> (ksi)	f <sub>su</sub> (ksi)	E <sub>s</sub> (ksi)
CI-1	No. 4 Bar	69.1	110.5	26,100
	6 mm bar	68.6	94.3	29,500
	D-3 wire	70.8	81.9	27,700
PW-1	No. 4 Bar	60.4	110.0	24,000
	6 mm bar	67.0	90.5	35,000
	D-3 wire	78.0	87.7	28,500

f<sub>y</sub> = yielding strength of reinforcing steel  
 f<sub>su</sub> = strength of reinforcing steel  
 E<sub>s</sub> = modulus of elasticity of reinforcing steel

## APPENDIX H

### MATERIAL PROPERTIES OF WALLS W1, W2, W3, AND W4

Table H.1 Material Properties for Concrete (from (6))

Specimen	$f_c'$ (psi)		Split Cylinder Strength (psi)	Modulus of Rupture (psi)
	28 days	on test date		
W-1	4940	4960	416	847
W-2	4690	4830	425	816
W-3	4790	5160	394	814
W-4	4960	5260	409	852

Table H.2 Material Properties for Reinforcing Steel (from (6))

Reinforcing Steel	Yield Stress, $f_y$ ksi	Young's Modulus ksi	Yield Strain, $\epsilon_y$ in./in.
#4 Bar	78.4	29000	0.0027
#2 Bar	81.5	29000	0.0028
3/16 " Bar	90.0	29000	0.0031

## LIST OF REFERENCES

1. ACI Committee 318, "Building Code Requirements for Reinforced Concrete", ACI 318-77, American Concrete Institute, Detroit, 1977, 102 pp.
2. ACI Committee 318, "Building Code Requirements for Reinforced Concrete", ACI 318-89, American Concrete Institute, Detroit, 1989, 353 pp.
3. Agrawal, A.B., L.G. Jaeger, and A.A. Mufti, "Crack Propagation and Plasticity of Reinforced Concrete Shear-Wall under Monotonic and Cyclic Loading," Conference on Finite Element Methods in Engineering, Adelaide, Australia, December 1976.
4. Aktan, H.M. and R.D. Hanson, "Nonlinear Cyclic Analysis of Reinforced Concrete Plane Stress Members," Special Publication SP63-6, American Concrete Institute, 1980, pp. 135-152.
5. Aktan, A.E., B.I. Karlson, and M.A. Sozen, "Stress-Strain Relationships of Reinforcing Bars Subjected to Large Strain Reversals," Civil Engineering Studies, Structural Research Series No. 397, University of Illinois at Urbana-Champaign, Urbana, Illinois, June 1973.
6. Ali A. and J.K. Wight, "Reinforced Concrete Structural Walls with Staggered Opening Configurations under Reversed Cyclic Loading," Report No. UMCE90-05, Department of Civil and Environmental Engineering, The University of Michigan, Ann Arbor, Michigan, April 1990, pp. 241.
7. Al-Mahaidi, R.S.H., "Nonlinear Finite Element Analysis of Reinforced Concrete Deep Members," Ph.D. Thesis, Department of Structural Engineering, Cornell University, Ithaca, New York, May 1978.
8. Balakrishnan, S., A.E. Elwi, and D.W. Murray, "Effect of Modeling on NLFE Analysis of Concrete Structures," Journal of Structural Engineering, ASCE, Vol. 114, No.7, July 1988, pp. 1467-1487.



9. Balakrishnan, S. and D.W. Murray, "Concrete Constitutive Model for NLFE Analysis of Structures," Journal of Structural Engineering, ASCE, Vol. 114, No. 7, July 1988, pp. 1449–1466.
10. Balakrishnan, S. and D.W. Murray, "Prediction of R/C Panel and Deep Beam Behavior by NLFEA," Journal of Structural Engineering, ASCE, Vol. 114, No. 10, October 1988, pp. 2323–2342.
11. Barzegar, F., "Analysis of RC Membrane Elements with Anisotropic Reinforcement," Journal of Structural Engineering, ASCE, Vol. 115, No. 3, March 1989, pp. 647–665.
12. Bashur, F.K. and D. Darwin, "Nonlinear Model for Reinforced Concrete Slabs," Journal of the Structural Division, ASCE, Vol. 104, No. ST1, January 1978, pp. 157–158.
13. Bathe, K.J., Finite Element Procedures in Engineering Analysis, Prentice–Hall Inc., Englewood Cliffs, N.J. 1982.
14. Bathe, K.J. and A.P. Cimento, "Some Practical Procedures for the Solution of Nonlinear Finite Element Equations," Computer Methods in Applied Mechanics and Engineering, Vol. 22, 1980, pp. 59–85.
15. Bathe, K.J. and S. Ramaswamy, "On Three–Dimensional Nonlinear Analysis of Reinforced Concrete Structures," Nuclear Engineering and Design, Vol. 52, 1979, pp. 385–409.
16. Bazant, Z.P., "Comment of Orthogonal Models for Concrete and Geomaterials," Journal of the Engineering Mechanics, ASCE, Vol. 109, No. 3, June 1983, pp. 849–865.
17. Bazant, Z.P. and L. Cedolin, "Blunt Crack Band Propagation in Finite Element Analysis," Journal of the Engineering Mechanics Division, ASCE, Vol. 105, No. EM2, April 1979, pp. 397–315.
18. Bazant, Z.P. and L. Cedolin, "Fracture Mechanics of Reinforced Concrete," Journal of the Engineering Mechanics Division, ASCE, Vol. 106, No. EM6, December 1980, pp. 1287–1306.

19. Bazant, Z.P. and P. Gambarova, "Rough Cracks in Reinforced Concrete," Journal of the Structural Division, ASCE, Vol. 106, No. ST4, April 1980, pp. 819–842.
20. Bazant, Z.P. and S. Kim, "Plastic–Fracturing Theory of Concrete," Journal of the Engineering Mechanics Division, ASCE, Vol. 105, No. EM3, June 1979, pp. 407–478.
21. Bazant, Z.P. and C. Sheih, "Hysteretic Fracturing Endochronic Theory for Concrete," Journal of the Engineering Mechanics Division, ASCE, Vol. 106, No. EM5, October 1980, pp. 929–950.
22. Belarbi, A. and T.T.C. Hsu, "Constitutive Laws of Reinforced Concrete in Biaxial Tension–Compression," Research Report No. UHCEE 91–2, Department of Civil Engineering, University of Houston, Houston, Texas, July 1991, 155 pp.
23. Bergan, N.B. and I. Holand, "Nonlinear Finite Element Analysis of Concrete Structures," Computer Methods in Applied Mechanics and Engineering, Vol. 17, NO. 18, 1979, pp. 443–467.
24. Bertero, V.V. and R.G. Collins, "Investigation of the Failures of the Olive View Stairtowers during the San Fernando Earthquake and their Implications on Seismic Design," Report No. EERC 73–36, Earthquake Engineering Research Center, University of California, Berkeley, August 1970.
25. Bolander, J.E. and J.K. Wight, "Towards Realistic FE Models for Reinforced Concrete Shear Wall Dominant Buildings subjected to Lateral Loadings," Report No. UMCE89–2, Department of Civil Engineering, The University of Michigan, Ann Arbor, Michigan, January 1989, pp. 192.
26. Bolander, J.E. and J.K. Wight, "Finite Element Modeling of Shear–Wall–Dominant Buildings," Journal of Structural Engineering, ASCE, Vol. 117, No. 6, June 1991, pp. 1719–1739.
27. Buyukozturk, O., "Nonlinear Analysis of Reinforced Concrete Structures," Computers & Structures, Vol. 7, 1977, pp. 149–156.

28. Buyukozturk, O. , J.J. Connor, and P. Leombruni, "Research on Modeling Shear Transfer in Reinforced Concrete Nuclear Structures," Nuclear Engineering and Design, Vol. 59, 1980, pp. 67–83.
29. Cardenas, A.E. and D.D. Magura, "Strength of High–Rise Shear Walls – Rectangular Cross Section," Special Publication SP36–7, American Concrete Institute.
30. Cedolin, L. and Z.P. Bazant, "Effect of Finite Element Choice in Blunt Crack Band Analysis," Computer Methods in Applied Mechanics and Engineering, Vol. 24, 1980, pp. 305–316.
31. Cedolin, L. and A.H. Nilson, "A Convergence Study of Iterative Methods Applied to Finite Element Analysis of Reinforced Concrete," International Journal for Numerical Methods in Engineering, Vol. 12, 1978, pp. 437–451.
32. Cedolin, L. and S.D. Poli, "Finite Element Studies of Shear–Critical R/C Beams," Journal of the Engineering Mechanics Division, ASCE, Vol. 103, No. EM3, June 1977, pp. 395–410.
33. Cervenka, V., "Inelastic Finite Element Analysis of Reinforced Concrete Panels under In–Plane Loads," Ph.D. Thesis, Department of Civil Engineering, University of Colorado, Boulder, Colorado, 1970.
34. Cervenka, V., "Inelastic Finite Element Analysis of Reinforced Concrete Panels under In–plane Loads," Ph.D. Dissertation, Department of Civil Engineering, The University of Colorado, Boulder, Colorado, 1980, pp. 239.
35. Cervenka, V., "Constitutive Model for Cracked Reinforced Concrete," Journal of the American Concrete Institute, Vol. 82, No. 6, November–December 1985, pp. 877–882.
36. Cervenka, V. and K.H. Gerstle, "Inelastic Analysis of Reinforced Concrete Panels: Theory" Publication of International Association for Bridge and Structural Engineering, Vol. 31–II, 1971, pp. 31–45.

37. Cervenka, V. and K.H. Gerstle, "Inelastic Analysis of Reinforced Concrete Panels: Experimental Verification and Application," Publication of International Association for Bridge and Structural Engineering, Vol. 32-II, 1971, pp. 25-39.
38. Chang, T.Y., H. Taniguchi, and W.F. Chen, "Nonlinear Finite Element Analysis of Reinforced Concrete Panels," Journal of Structural Engineering, ASCE, Vol. 113, No. 1, January 1987, pp. 122-140.
39. Chen, W.F., Plasticity in Reinforced Concrete, McGraw-Hill Co., New York, 1981.
40. Collins, M.P., "Towards a Rational Theory for Reinforced Concrete Members in Shear," Journal of the Structural Division, Vol. 104, No. ST4, April 1978, pp. 649-660.
41. Colville, J. and J. Abbasi, "Plane Stress Reinforced Concrete Finite Elements," Journal of the Structural Division, ASCE, Vol. 100, No. ST5, May 1974, pp. 1067-1083.
42. Crisfield, M.A. and J. Wills, "Analysis of R/C Panels Using Different Concrete Models," Journal of Engineering Mechanics, ASCE, Vol. 115, No. 3, March 1989, pp. 578-597.
43. Darwin, D., "Concrete Crack Propagation," Finite Element of Reinforced Concrete Structures, ASCE, May 1985, pp. 184-203.
44. Darwin, D. and D.A.W. Pecknold, "Inelastic Model for Cyclic Biaxial Loading of Reinforced Concrete," Civil Engineering Studies, Structural Research Series No. 409, University of Illinois at Urbana-Champaign, Urbana, Illinois, 1974.
45. Darwin, D. and D.A.W. Pecknold, "Analysis of RC shear panels under Cyclic Loading," Journal of the Structural Division, ASCE, Vol. 107, No. ST2, February 1976, pp. 355-369.
46. De Borst, R., "Smearred Cracking, Plasticity, Creep, and Thermal Loading - A Unnified Approach," Computer Methods in Applied Mechanics and Engineering, Vol. 62, 1987, pp. 89-110.
47. De Borst, R. and P. Nauta, "Non-Orthogonal Cracks in a Smearred Finite Element Method," Engineering Computations, Vol. 2, March 1985, pp. 35-46.

48. Derecho, A.T., S.K. Ghosh, M. Iqbal, and M. Fintel, "Strength, Stiffness, and Ductility Required in Reinforced Concrete Structural Walls for Earthquake Resistance," ACI Journal, Vol. 76, August 1979, pp. 875–895.
49. Dodds, R.H., "Numerical and Software Requirements for General Nonlinear Finite Element Analysis," Ph.D. Dissertation, Department of Civil Engineering, University of Illinois at Urbana–Champaign, Urbana, Illinois, 1978.
50. Dodds, R.H., D. Darwin, J.L. Smith, and L.D. Leibengood, "Grid Size Effects with Smeared Cracking in Finite Element Analysis of Reinforced Concrete," Structural Engineering and Engineering Materials Report No. 6, The University of Kansas Center for Research Inc., August 1982.
51. Dodds, R.H., M. Keppel, P. Vargas, R. Schmidt, and S. Schiff, "Release Notes for POLO-FINITE: Version 8.0", University of Illinois, Urbana, Illinois, July 1990.
52. Dulacska, H., "Dowel Action of Reinforcement Crossing Cracks in Concrete," Journal of the American Concrete Institute, Vol. 69, December 1972, pp. 754–757.
53. Elliot, A.F., "An Experimental Investigation of Shear Transfer across Crack in Reinforced Concrete," M.S. Thesis, Department of Structural Engineering, Cornell University, Ithaca, New York, June 1974.
54. El-Mezaini, N. and E. Citipitioglu "Finite Element Analysis of Prestressed and Reinforced Concrete Structures," Journal of Structural Engineering, ASCE, Vol. 117, No. 10, October 1991, pp. 2851–2864.
55. Fardis, M.N. and O. Buyukozturk, "Shear Stiffness of Concrete by Finite Elements," Journal of the Structural Division, ASCE, Vol. 106, No. ST6, June 1980, pp. 1311–1327.
56. Ferguson, P.M., J.E. Breen, and J.O. Jirsa, "Reinforced Concrete Fundamentals," John Wiley & Sons Inc., Fifth Edition, 1988, 746 pp.

57. Fintel, M., "Ductile Shear Walls in Earthquake Resistant Multistory Buildings," Journal of the American Concrete Institute, Vol. 71, No. 6, June 1974, pp. 296–365.
58. Floegl, H, and H.A. Mang, "Tension Stiffening Concept Based on Bond Slip," Journal of the Structural Division, ASCE, Vol. 108, No. ST12, December 1982, pp. 2681–2701.
59. Gajer, G. and P.F. Dux, "Crack Band Based Model for FEM Analysis of Concrete Structures," Journal of Structural Engineering, ASCE, Vol. 116, No. 6, June 1990, pp. 1696–1714.
60. Gilbert, R.I. and R.F. Warner, "Tension Stiffening in Reinforced Concrete Slabs," Journal of the Structural Division, ASCE, Vol. 104, No. ST12, December 1978, pp. 1885–1900.
61. Gopalaratnam, V.S. and S.P. Shah, "Post-Cracking Characteristics of Concrete in Uniaxial Tension," Engineering Mechanics, pp. 1393–1398.
62. Gosain, N.K., R.H. Brown, and J.O. Jirsa, "Shear Requirements for Load Reversals on RC Members," Journal of the Structural Division, ASCE, Vol. 103, No. ST7, July 1977, pp. 1461–1476.
63. Gupta, A.K. and H. Akbar, "Cracking in Reinforced Concrete Analysis," Reinforced Concrete Shell Research Report, Civil Engineering Department, North Carolina State University, Raleigh, North Carolina, January 1983.
64. Gupta, A.K. and S.R. Maestrini, "Unified Approach to Modeling Post-Cracking Membrane Behavior of Reinforced Concrete," Journal of Structural Engineering, ASCE, Vol. 115, No. 4, April 1989, pp. 977–993.
65. Hand, F.R., D.A. Pecknold, and W.C. Schnobrich, "Nonlinear Layered Analysis of RC Plates and Shells," Journal of the Structural Division, ASCE, Vol. 99, No. ST7, July 1973, pp. 1491–1505.
66. Hegemier, G.A., H. Murakami, and L.J. Hageman, "On Tension Stiffening in Reinforced Concrete," Mechanics of Material 4, 1985, pp. 161–179.

67. Hillerborg, A., M. Modeer, and P-E. Peterson, "Analysis of Crack Formation and Crack Growth in Concrete by Means of Fracture Mechanics and Finite Elements," Cement and Concrete Research, Vol. 6, 1976, pp. 773-782.
68. Hofbeck, J.A., I.O. Ibrahim, and H. Mattock, "Shear Transfer in Reinforced Concrete," Journal of the American Concrete Institute, Vol. 66, No. 3, February 1969, pp. 119-128.
69. Hognestad, E., N.W. Hanson, and D. McHenry, "Concrete Stress Distribution in Ultimate Strength Design," Journal of the American Concrete Institute, Vol. 27, No. 4, December 1955, pp. 455-479.
70. Houde, J. and M.S. Mirza, "A Finite Element Analysis of Shear Strength of Reinforced Concrete Beams," Shear in Reinforced Concrete, Special Publication SP42-5, American Concrete Institute, 1974, pp. 103-128.
71. Hu, H. and W.C. Schnobrich, "Nonlinear Analysis of Plane Stress State Reinforced Concrete under Short Term Monotonic Loading," Civil Engineering Studies, Structural Research Series No. 539, University of Illinois at Urbana-Champaign, Urbana, Illinois, 1988.
72. Hu, H. and W.C. Schnobrich, "Nonlinear Analysis of Cracked Reinforced Concrete," ACI Structural Journal, Vol. 87, No. 2, March-April 1990, pp. 199-207.
73. Inoue, N., N. Koshika, and N. Suzuki, "Analysis of Shear Wall Based on Collins Panel Test," Finite Element of Reinforced Concrete Structures, ASCE, May 1985, pp. 288-299.
74. International Conference of Building Officials, "Uniform Building Code," 1988 Edition, Whittier, California, 1988.
75. Izumo, J., H. Shin, K. Maekawa, and J. Okamura, "Analytical Model for RC panels under Cyclic Load," Structural Design, Analysis, and Testing, Proceedings of the sessions related to design, analysis and testing at Structures Congress' 89, ASCE, May 1989, pp. 39-48.

76. Jimenez-Perez, R., P. Gergely, and R.N. White, "Shear Transfer across Cracks in Reinforced Concrete," Report No. 78-4, Department of Structural Engineering, Cornell University, August 1978.
77. Jimenez, R., P. Perdikaris, P. Gergely, and R. White, "Interface Shear Transfer and Dowel Action in Cracked Reinforced Concrete Subject to Cyclic Shear," Proceedings of the Specialty Conference of Structural Analysis, ASCE, August 1976, pp. 457-475.
78. Jofriet, J.C. and G.M. McNeice, "Finite Element Analysis of Reinforced Concrete Slab," Journal of the Structural Division, ASCE, Vol. 97, No. ST3, March 1971, pp. 785-806.
79. Karsan, I.D. and J.O. Jirsa, "Behavior of Concrete Under Compressive Loading," Journal of the Structural Division, ASCE, Vol. 95, No. ST12, December 1969, pp. 2543-2563.
80. Kent, D.C and R. Park, "Cyclic Load Behavior of Reinforcing Steel," Strain, Vol. 9, No. 3, July 1973, pp. 98-103.
81. Kupfer, H.B. and H.K. Hilsdorf, "Behavior of Concrete under Biaxial Stresses," Journal of the American Concrete Institute, Vol. 66, No. 8, August 1969, pp. 656-666.
82. Laible, J.P., R.N. White, and P. Gergely, "Experimental Investigation of Seismic Shear Transfer Across Cracks in Concrete Nuclear Containment Vessels," Reinforced Concrete Structures in Seismic Zone, Special Publication SP53-9, American Concrete Institute, 1977, pp. 203-226.
83. Leibengood, L.C., D. Darwin, and R.H. Dodds, "Finite Element Analysis of Concrete Fracture Specimens," Structural Engineering and Engineering Materials, The University of Kansas, Lawrence, Kansas, May, 1984.
84. Lin, C.S. and A.C. Scordelis, "Nonlinear Analysis of RC shells of General Forms," Journal of the Structural Division, ASCE, Vol. 101, No. ST3, March 1975, pp. 523-538.



85. Link, R.A., A.E. Elwi, and A. Scanlon, "Biaxial Tension Stiffening due to Generally Oriented Reinforcing Layers," Journal of Engineering Mechanics, ASCE, Vol. 115, No. 8, August 1989, pp. 1647–1662.
86. Liu, T.C.Y., A.H. Nilson, and F.O. Slate, "Biaxial Stress–Strain Relations for Concrete," Journal of the Structural Division, ASCE, Vol. 98, No. ST5, May 1972, pp. 1025–1034.
87. Liu, T.C.Y., A.H. Nilson, and F.O. Slate, "Stress–Strain Response and Fracture of Concrete in Uniaxial and Biaxial Compression," Journal of the American Concrete Institute, Vol. 69, No. 5, May 1972, pp. 291–295.
88. Lopez, L.A., R.H. Dodds, D.R. Rehak, and R.J. Schmidt, "POLO–FINITE: A Structural Mechanics System for Linear and Nonlinear, Static and Dynamic Analysis," University of Illinois, Urbana–Champaign, IL.
89. Ma, S.–Y., V.V. Betero, and E.G. Popov, "Experimental and Analytical Studies on the Hysteretic Behavior of Reinforced Concrete Rectangular and T–Beams," Report No. EERC 76–2, Earthquake Engineering Research Center, University of California, Berkeley, May 1976.
90. Massicotte, B. and J.G. MacGregor, "Tension–Stiffening Model of Planar Reinforced Concrete Members," Journal of Structural Engineering, Vol. 116, No. 11, November 1990, pp. 3039–3058.
91. Massicotte, B., J.G. MacGregor, and A.E. Elwi, "Behavior of Concrete Panels Subjected to Axial and Lateral Loads," Journal of Structural Engineering, ASCE, Vol. 116, No. 9, September 1990, pp. 2324–2343.
92. Matsuzaki, Y., H. Fukuyama, T. Iizuka, and J. Noguchi, "Behavior of Crack under Reversed Cyclic Loading," Finite Element of Reinforced Concrete Structures, ASCE, May 1985, pp. 11–30.
93. Mattock, A.H., "Shear Transfer in Concrete Having Reinforcement at an Angle to the Shear Plane," Shear in Reinforced Concrete, Special Publication SP42–2, American Concrete Institute, 1974, pp. 17–41.

94. Mattock, A.H., "Cyclic Shear Transfer and Type of Interface," Journal of the Structural Division, ASCE, Vol. 107, No. ST10, October 1981, pp. 1945–1964.
95. Meyer, C. and K.J. Bathe, "Nonlinear Analysis of R/C Structures in Practice," Journal of the Structural Division, ASCE, Vol. 108, No. ST7, July 1982, pp. 1605–1622.
96. Mikame, A., H. Yoshikawa, I. Shiraishi, Y. Kamiyama, S. Iizuka, K. Sato, K. Kawasaki, and H. Noguchi, "Parametric Analyses of RC Shear Walls by FEM," Structural Design, Analysis, and Testing, Proceedings of the sessions related to design, analysis and testing at Structures Congress' 89, ASCE, May 1989, pp. 301–310.
97. Milford, R.V., "Nonlinear Behavior of Reinforced Concrete Cooling Tower," Ph.D. Disstertation, Department of Civil Engineering, University of Illinois at Urbana–Champaign, Urbana, Illinois, 1984.
98. Nam, C. and C.G. Salmon, "Finite Element Analysis of Concrete Beams," Journal of the Structural Division, ASCE, Vol. 100, No. ST12, December 1974, pp. 2419–2432.
99. Ngo, D. and A.C.Scordelis, "Finite Element Analysis of Reinforced Concrete Beams," Journal of the American Concrete Institute, Vol. 65, No. 9, September 1968, pp. 152–163.
100. Nilson, A.H., "Nonlinear Analysis of Reinforced Concrete by the Finite Element Method," Journal of the American Concrete Institute, Vol. 65, No. 9, September 1968, pp. 757–766.
101. Nilson, A.H., "Internal Measurement of Bond Slip," ACI Journal, Vol. 69, No. 7, July 1972, pp. 439–441.
102. Noguchi, H., "Analytical Models for Cyclic Loading of RC Members," Finite Element of Reinforced Concrete Structures, ASCE, May 1985, pp. 486–506.
103. Oesterle, R.G., "Inelastic Analysis of In–Plane Strength of Reinforced Concrete Shear Walls," Ph.D. Dissertation, Department of Civil Engineering, Northwestern University, Evanston, Illinois, June 1986.

104. Oesterle, R.G., J.D. Aristizabal-Ochoa, K.N. Shiu, and W.G. Corley, "Web Crushing of Reinforced Concrete Structural Walls," Journal of the American Concrete Institute, Vol. 81, No. 3, May-June 1984, pp. 231-241.
105. Oesterle, R.G., A.E. Fiorato, L.S. Johal, J.E. Carpenter, H.G. Russel, and W.G. Corley, "Earthquake Resistant Structural Walls - Tests of Isolated Walls," Report to National Science Foundation, Concrete Technology Laboratories, Portland Cement Association, Skokie, Illinois, October 1975.
106. Oesterle, R.G., A.E. Fiorato, L.S. Johal, J.E. Carpenter, H.G. Russel, and W.G. Corley, "Earthquake Resistant Structural Walls - Tests of Isolated Walls - Phase II," PCA Construction Technology Laboratory / National Science Foundation, Washington D.C., 1978.
107. Okamura, H., H. Shin, and K. Maekawa, "Development of Analytical Model for Reinforced Concrete," Structural Design, Analysis, and Testing, Proceedings of the sessions related to design, analysis and testing at Structures Congress' 89, ASCE, May 1989, pp. 49-58.
108. Ozcebe, G. and M. Saatcioglu, "Hysteretic Shear Model for Reinforced Concrete Members," Journal of Structural Engineering, Vol. 115, No. 1, January 1989, pp. 132-148.
109. Park, R., "Constitutive Relations of Steel : Effects on Hysteretic Behavior of Structural Concrete Members and on Strength Considerations in Seismic Design," Proceedings, Workshop on Earthquake-Resistant Reinforced Concrete Building Construction (ERCBC), University of California at Berkeley, Berkeley, California, July 1977, pp. 683-695.
110. Park, R., D.C. Kent, and A.S. Richard, "Reinforced Concrete Members with Cyclic Loading," Journal of the Structural Division, ASCE, Vol. 98, No. ST7, July 1972, pp. 1341-1360.
111. Park, R. and T. Paulay, "Reinforced Concrete Structures," John Wiley & Sons Inc., 1975, 769 pp.
112. Paulay, T., "Ductility of Reinforced Concrete Shearwalls for Seismic Areas," Reinforced Concrete Structures in Seismic Zone, Special Publication SP53-7, American Concrete Institute, 1977, pp. 127-147.

113. Paulay, T., "Earthquake-Resisting Shearwalls - New Zealand Design Trends," ACI Journal, Vol. 77, May-June 1980, pp. 144-152.
114. Paulay, T. and P.J. Loeber, "Shear Transfer by Aggregate Interlock," Shear in Reinforced Concrete, Special Publication SP42-1, American Concrete Institute, 1974, pp. 1-15.
115. Paulay, T., R. Park, and M.H. Phillips, "Horizontal Construction Joints in Cast-In-Place Reinforced Concrete," Shear in Reinforced Concrete, Special Publication SP42-27, American Concrete Institute, 1974, pp. 599-616.
116. Perdikaris, P.C. and H. Miller, "Tension Stiffening in Reinforced Concrete under Repeated Uniaxial Tension," Engineering Mechanics, pp. 1412-1415.
117. Placas, A. and P.E. Regan, "Shear Failures of Reinforced Concrete Beams," Journal of the American Concrete Institute, Vol. 68, October 1971, pp. 763-773.
118. Popov, E.G., "Mechanical Characteristics and Bond of Reinforcing Steel under Seismic Conditions," Proceedings, Workshop on Earthquake-Resistant Reinforced Concrete Building Construction (ERCBC), University of California at Berkeley, Berkeley, California, July 1977, pp. 658-682.
119. Popovics, S., "A State-of-the-Art Report : A Review of Stress-Strain Relationships for Concrete," Journal of the American Concrete Institute, Vol. 67, March 1970, pp. 243-248.
120. Rashid, Y.R., "Analytical of Prestressed Concrete Vessels," Nuclear Engineering and Design, Vol. 7, No. 4, April 1968, pp. 334-344.
121. Scanlon, A. and D.W. Murray, "Time-Dependent Reinforced Concrete Slab Deflections," Journal of the Structural Division, ASCE, Vol. 100, No. ST4, September 1974, pp. 1911-1924.
122. Schnobrich, W.C., "The Role of Finite Element Analysis of Reinforced Concrete Structures," Finite Element of Reinforced Concrete Structures, ASCE, May 1985, pp. 1-24.

123. SEAOC, "Recommended Lateral Force Requirements and Commentary," Seismology Committee, Structural Engineers' Association of California, San Francisco, 1973, 146 pp.
124. Seckin, M. "Hysteretic Behavior of Cast-in-Place Exterior Beam-Column Sub-Assemblies," Ph.D. Thesis, University of Toronto, 1981, 266 pp.
125. Shiekh, S.A. and S.M. Uzumeri, "Analytical Model for Concrete Confinement in Tied Columns," Journal of the Structural Division, ASCE, Vol. 108, No. ST12, December 1982, pp. 2703-2722.
126. Shiu, K.N., J.I. Daniel, J.D. Aristizabal-Ochoa, A.E. Fiorato, and W.G. Corley, "Earthquake Resistant Structural Walls - Tests of Walls with and without Openings," Report to National Science Foundation, Concrete Technology Laboratories, Portland Cement Association, Skokie, Illinois, July 1981.
127. Singh, A., K.H. Gerstle, and L.G. Tulin, "The Behavior of Reinforcing Steel Under Reversal Loading," Journal ASTM, Materials Research and Standards, Vol. 5, No. 1, January 1965, pp. 12-17.
128. Sinha, B.P., K.H. Gerslte, and L.G. Tulin, "Stress-Strain Relations for Concrete Under Cyclic Loadings," Journal of the American Concrete Institute, Vol. 61, No. 2, February 1964, pp. 195-211.
129. Smith, G.M. and L.E. Young, "Ultimate Flexural Analysis Based on Stress-Strain Curves of Cylinders,"
130. Somayaji, S., "Composite Response, Bond Stress-Slip Relationships and Cracking in Ferrocement and Reinforced Concrete," Ph.D. Thesis, University of Illinois at Chicago Circle, Chicago, Illinois, 1979.
131. Sotomura, K. adn Y. Murazumi, "Nonlinear Analysis of Shear Walls with Numerous Small Openings," Finite Element of Reinforced Concrete Structures, ASCE, May 1985, pp. 300-307.

132. Spooner, D.C. and J.W. Dougill, "A Quantitative Assessment of Damage Sustained in Concrete During Compressive Loadings," Magazine of Concrete Research, Vol. 27, No. 92, September 1975, pp. 155-160.
133. Stanton, J. "The Dowel Action of Reinforcement and the Nonlinear Dynamic Analysis of Concrete Nuclear Containment Vessels," M.S. Thesis, Cornell University, August 1976.
134. Stevens, N.J., S.M. Uzumeri, and M.P. Collins, "Analytical Modelling of Reinforced concrete Subjected to Monotonic and Reversed Loadings," Publication No. 87-1, Department of Civil Engineering, University of Toronto, Toronto, Canada, January 1987.
135. Suidan, M. and W.C. Schnobrich, "Finite Element Analysis of Reinforced Concrete," Journal of the Structural Division, ASCE, Vol.99, No. ST10, October 1973, pp. 2109-2122.
136. Task Committee on Finite Element Analysis of Reinforced Concrete Structures, State-of-the-Art Report on Finite Element Analysis of Reinforced Concrete, American Society of Civil Engineers, New York, N.Y., 1982, 545 pp.
137. Tassios, T.P. and E.N. Vintzeleou, "Concrete-to-Concrete Friction," Journal of Structural Engineering, ASCE, Vol. 113, No. 4, April 1987, pp. 832-849.
138. Taylor, H.P., "The Fundamental of Reinforced Concrete Beams in Bending and Shear," Shear in Reinforced Concrete, Vol. 1, Special Publication SP-42, American Concrete Institute, Detroit, Michigan, 1974.
139. Ueda, M. and T. Kawai, "Discrete Limit Analysis of R/C Shear Walls," Finite Element of Reinforced Concrete Structures, ASCE, May 1985, pp. 277-287.
140. Vallenias, J.M., B. Vitelmov, and E.P. Popov, "Hysteresis Behavior of Reinforced Concrete Structural Walls," Report No. UCB/EERC-79/20, Earthquake Engineering Research Center, University of California, Berkeley, California, August 1979.
141. Valliappan, S. and T.F. Doolan, "Nonlinear Stress Analysis of Reinforced Concrete," Journal of the Structural Division, ASCE, Vol. 90, No. ST4, April 1972, pp. 885-898.

142. Vecchio, F.J., "Nonlinear Finite Element Analysis of Reinforced Concrete Membranes," ACI Structural Journal, Vol. 86, No. 1, January–February 1989, pp. 26–35.
143. Vecchio, F.J. and M.P. Collins, "The Response of Reinforced Concrete to In-plane Shear and Normal Stresses," Publication No. 82–03, Department of Civil Engineering, University of Toronto, March 1982.
144. Vecchio, F.J. and M.P. Collins, "The Modified Compression Field Theory for Reinforced Concrete Elements Subjected to Shear," Journal of the American Concrete Institute, Vol. 83, March–April 1986, pp. 219–231.
145. Vintzeleou, E.N. and T.P. Tassios, "Behavior of Dowels under Cyclic Deformations," ACI Structural Journal, Vol. 84, July–February 1987, pp. 18–30.
146. White, R.N. and M.J. Holley, "Experimental Studies of Membrane Shear Transfer," Journal of the Structural Division, ASCE, Vol. 98, No. ST8, August 1972, pp. 1835–1852.
147. William, K.J., B. Hurlbut, and S. Sture, "Experimental and Constitutive Aspects of Concrete Failure," Finite Element of Reinforced Concrete Structures, ASCE, May 1985, pp. 226–254.
148. Wood, S.L., "Experimental Investigation of the Strength, Stiffness, and Deformation Capacity of Slender Reinforced Concrete Walls," A Proposal to the National Science Foundation, 1989.
149. Wood, S.L., "Observed Behavior of Slender Reinforced Concrete Walls Subjected to Cyclic Loadings," Earthquake-Resistant Concrete Structures – Inelastic Response and Design, SP-127, American Concrete Institute, Detroit, 1991.
150. Wood, S.L., J.K. Wight, and J.P. Moehle, "The 1985 Chile Earthquake: Observations on Earthquake-Resistant Construction in Vina Del Mar," Civil Engineering Studies, Structural Research Series No. 532, University of Illinois at Urbana–Champaign, Urbana, Illinois, February 1987.

151. Xu, C., "Analytical Model for Reinforced Concrete under Cyclic Loading," Ph.D. Dissertation, Department of Civil Engineering, University of Illinois at Urbana-Champaign, Urbana, Illinois, 1991.
152. Yamaguchi, E. and W.F. Chen, "Cracking Model for Finite Element Analysis of Concrete Materials," Journal of Engineering Mechanics, ASCE, Vol. 116, No. 6, June 1990, pp. 1242-1260.
153. Yamaguchi, H. and S. Nomura, "Analysis of RC Walls by Plastic-Fracturing Theory," Structural Design, Analysis, and Testing, Proceedings of the sessions related to design, analysis and testing at Structures Congress' 89, ASCE, May 1989, pp. 204-213.
154. Yankelevsky, D.Z. and H.W. Reinhardt, "Response of Plain Concrete to Cyclic Tension," ACI Materials Journal, Vol. 84-M37, September-October 1987, pp. 365-373.
155. Yankelevsky, O.Z. and H.W. Reinhardt, "Uniaxial Behavior of Concrete in Cyclic Tension," Journal of Structural Engineering, ASCE, Vol. 115, No. 1, January 1989, pp. 166-182.
156. Yankelevsky, D.Z. and H.W. Reinhardt, "Model for Cyclic Compressive Behavior of Concrete," Journal of Structural Engineering, ASCE, Vol. 113, No. 2, February 1987, pp. 228-240.
157. Yuzugullu, D., "Finite Element Approach for the Prediction of Inelastic Behavior of Shear Wall-Frame System," Ph.D. Dissertation, Department of Civil Engineering, University of Illinois at Urbana-Champaign, Urbana, Illinois, 1972.
158. Zhen-hai, G. and Z. Xiu-qin, "Investigation of Complete Stress-Deformation Curves for Concrete in Tension," ACI Materials Journal, Vol. 84-M29, July-August 1987, pp. 278-285.